

Ordnung und Unordnung am Beispiel Lichtmanagement in Solarzellen

HABILITATIONSSCHRIFT

zur Erlangung des akademischen Grades

Dr. rer. nat. habil.

vorgelegt der

Naturwissenschaftlichen Fakultät II
Chemie, Physik und Mathematik
der Martin-Luther-Universität Halle-Wittenberg

von

Herrn Dr. rer. nat. Alexander Nicolas Sprafke
geb. am 18.10.1979 in Oberhausen

Gutachter

1. Prof. Dr. Ralf B. Wehrspohn (Martin-Luther-Universität Halle-Wittenberg)
2. Prof. Dr. Kurt Busch (Humboldt-Universität zu Berlin)
3. Prof. Dr. Thomas Pertsch (Friedrich-Schiller-Universität Jena)

Halle (Saale), verteidigt am 19. Juni 2023, Probevorlesung gehalten am 25. Juli 2023

Unordnung ist das halbe Leben.

Inhaltsverzeichnis

Verzeichnis wissenschaftlicher Publikationen	iii
1 Einleitung	1
2 Lichtmanagement mit Unordnung: Schwarzes Silizium	5
2.1 Einführung.....	5
2.2 Antireflexion.....	6
2.3 Lichtwegverlängerung und Lichteinfang (<i>Light trapping</i>).....	8
2.4 Oberflächenrekombination und -passivierung.....	9
2.5 Reaktives Ionenätzen bei nicht-kryogenen Temperaturen.....	11
2.6 MACE für Nanostrukturierung und gleichzeitige Aufreinigung.....	14
2.7 Vergleich unterschiedlicher Herstellungstechnologien.....	16
3 Lichtmanagement mit Ordnung: Gitter und photonische Kristalle	19
3.1 Einführung.....	19
3.2 Großflächige Rückseitengitter für ultradünne c-Si Solarzellen.....	21
3.3 Rückseitengitter für CIGSe-Dünnschicht-Solarzellen.....	23
3.4 Effiziente Phasengitter für Lichtmanagement im Solarmodul.....	25
3.5 Sprühbeschichtung für die Herstellung 3D Photonischer Kristalle.....	27
4 Lichtmanagement mit geordneter Unordnung: Hyperuniformität	31
4.1 Einführung.....	31
4.2 Unordnung in dichtgepackten Kugelmonolagen.....	33
4.3 Hyperuniforme Unordnung.....	36
4.4 Skalierbare Fabrikation nahezu-hyperuniformer ungeordneter Substrate....	39
4.5 Maßgeschneiderte Lichtstreuung durch hyperuniforme Unordnung.....	43
4.6 Hyperuniforme Unordnung für Antireflexion in Heterojunction-Solarzellen..	48
5 Fazit und Ausblick	51
6 Literaturverzeichnis	55
7 Ausgewählte Publikationen	65
Danksagung	178
Lebenslauf	179
Eidesstattliche Erklärung	180

Verzeichnis wissenschaftlicher Publikationen

Im Rahmen dieser Habilitation wurden folgende Publikationen in ausgewiesenen Fachzeitschriften veröffentlicht (*peer-reviewed*). Eine Auswahl ist in Kapitel 7 ab Seite 65 zu finden, in der folgenden Aufzählung mit (*) und unter Angabe der Seitenzahl gekennzeichnet.

P. M. Piechulla, R. B. Wehrspohn, A. Sprafke. Towards hyperuniform disorder via self-assembly of bidisperse colloidal patterns at an electrode (2022, eingereicht bei *Adv. Mater. Interfaces*).

P. M. Piechulla, Y. J. Donie, R. B. Wehrspohn, U. Lemmer, G. Gomard, A. Sprafke. Correlated disorder substrate-integrated nanodisk scatterers for light extraction in OLEDs (2022, eingereicht bei *Adv. Opt. Mater.*).

- [1] (* **S. 156**) P. M. Piechulla, B. Fuhrmann, E. Slivina, C. Rockstuhl, R. B. Wehrspohn, A. Sprafke. Tailored Light Scattering through Hyperuniform Disorder in Self-Organized Arrays of High-Index Nanodisks, *Adv. Opt. Mater.* **9**, 2100186 (2021) (inkl. Cover der Ausgabe).
- [2] (* **S. 168**) P. M. Piechulla, E. Slivina, D. Baetzner, I. Fernandez-Corbaton, P. Dhawan, R. B. Wehrspohn, A. Sprafke, C. Rockstuhl. Antireflective Huygens' Metasurface with Correlated Disorder Made from High-Index Disks Implemented into Silicon Heterojunction Solar Cells, *ACS Photonics* **8**, 3476–3485 (2021).
- [3] P. Dhawan, M. Gaudig, A. Sprafke, R. B. Wehrspohn, C. Rockstuhl. Light-trapping structures for planar solar cells inspired by transformation optics, *Opt. Express* **29**, 19903-19919 (2021).
- [4] J. Sievers, M. Below, C. Reinhardt, F. Heyroth, S. Schlenker, G. Schmidt, A. Sprafke, and J. Schilling. Periodic metal resonator chains for Surface Enhanced Raman Scattering (SERS), *J. Appl. Phys.* **130**, 223104 (2021).
- [5] (* **S. 105**) T. Schneider, J. Tröndle, B. Fuhrmann, F. Syrowatka, A. Sprafke, R. Scheer. Ultrathin CIGSe Solar Cells with Integrated Structured Back Reflector, *Solar RRL* **4**, 2000295 (2020).
- [6] (* **S. 97**) Y.-C. Chang, M. E. Pollard, David N. R. Payne, A. Sprafke, S. Pillai, D. M. Bagnall. Large-Area Nanosphere Gratings for Light Trapping and Reduced Surface Losses in Thin Solar Cells, *IEEE J. Photovoltaics* **9**, 1012 (2019).
- [7] S. Nanz, A. Abass, P. M. Piechulla, A. Sprafke, R. B. Wehrspohn, C. Rockstuhl. Light-Trapping Front Textures for Solar Cells from Tailored Mixtures of Nanospheres, *Phys. Status Solidi A* **215**, 1800699 (2018).

Verzeichnis wissenschaftlicher Publikationen

- [8] (* **S. 146**) P. M. Piechulla, L. Mühlenbein, R. B. Wehrspohn, S. Nanz, A. Abass, C. Rockstuhl, A. Sprafke. Fabrication of nearly-hyperuniform substrates by tailored disorder for photonic applications, *Adv. Opt. Mater.* **6**, 1701272 (2018) (gewählt zum *Best of Adv. Opt. Mat. 2018*).
- [9] (* **S. 133**) S. Nanz, A. Abass, P. M. Piechulla, A. Sprafke, R. B. Wehrspohn, C. Rockstuhl. Strategy for tailoring the Size Distribution of Nanospheres to Optimize Rough Backreflectors of Solar Cells, *Opt. Express* **26**, A111-A123 (2018).
- [10] K. Ilse, T. Schneider, J. Ziegler, A. Sprafke, R. B. Wehrspohn. Integrated low-temperature process for the fabrication of amorphous Si nanoparticles embedded in Al₂O₃ for non-volatile memory application, *Phys. Status Solidi A* **213**, 2446-2451 (2016) (inkl. Rückseitencover der Ausgabe).
- [11] N. Sardana, V. Talalaev, F. Heyroth, G. Schmidt, C. Bohley, A. Sprafke, J. Schilling. Localized surface plasmon resonance in the IR regime, *Opt. Express* **24**, 254-261 (2016).
- [12] X. Li, J.-H. Lee, A. Sprafke, Ralf B. Wehrspohn. Black Metallurgical Silicon for Solar Energy Conversion, *Semicond. Sci. Technol.* **31**, 014009 (2016) (Übersichtsartikel).
- [13] (* **S. 112**) M. Muchow, T. Büchner, A. Sprafke, Gerhard Seifert. Femtosecond laser-written high-efficiency blazed phase gratings in the volume of soda lime glass for light management in solar modules, *Opt. Express* **23**, 33540-33549 (2015).
- [14] M. F. Schuhmann, S. Wiesendanger, J. C. Goldschmidt, B. Bläsi, K. Bittkau, U. W. Paetzold, A. Sprafke, R. B. Wehrspohn, C. Rockstuhl, M. Wegener. Cloaked contact grids on solar cells by coordinate transformations: designs and prototypes, *Optica* **2**, 850-853 (2015).
- [15] (* **S. 66**) M. Gaudig, J. Hirsch, T. Schneider, A. Sprafke, J. Ziegler, N. Bernhard, R. B. Wehrspohn. Properties of black silicon obtained at room-temperature by different plasma modes, *J. Vac. Sci. Technol. A* **33**, 05E132 (2015).
- [16] J. Ziegler, M. Mews, K. Kaufmann, T. Schneider, A. Sprafke, L. Korte, R. B. Wehrspohn. Plasma-enhanced atomic-layer-deposited MoO_x emitters for silicon heterojunction solar cells, *Appl. Phys. A* **120**, 811-816 (2015).
- [17] (* **S. 79**) M. Otto, M. Algasinger, H. Branz, B. Gesemann, T. Gimpel, K. Füchsel, T. Käsebier, S. Kontermann, X. Li, V. Naumann, J. Oh, A. Sprafke, J. Ziegler, M. Zilk, R. B. Wehrspohn. Black Silicon Photovoltaics *Adv. Opt. Mater.* **3**, 147-164 (2015).
- [18] X. Li, C. Yan, J. Wang, A. Graff, S. L. Schweizer, A. Sprafke, O. G. Schmidt, R. B. Wehrspohn. Stable Silicon Anodes for Lithium-Ion Batteries Using Mesoporous Metallurgical Silicon, *Adv. Energy Mater.* **5**, 1401556 (2015).

- [19] X. Li, Y. Xiao, K. Zhou, J. Wang, S. L. Schweizer, A. Sprafke, J.-H. Lee, R. B. Wehrspohn. Photoelectrochemical hydrogen evolution of tapered silicon nanowires, *Phys. Chem. Chem. Phys.* **17**, 800-804 (2015).
- [20] (* S. 74) X. Li, Y. Xiao, K. Zhou, C. Yan, K. Zhou, P.-T. Miclea, S. Meyer, S. L. Schweizer, A. Sprafke, J.-H. Lee, R. B. Wehrspohn. Self-purification model for metal-assisted chemical etching of metallurgical silicon, *Electrochim. Acta* **138**, 476-480 (2014).
- [21] J. Ziegler, J. Haschke, T. Käsebier, L. Korte, A. Sprafke, R. B. Wehrspohn. Influence of black silicon surfaces on the performance of back-contacted back silicon heterojunction solar cells, *Opt. Express* **22**, A1469-A1476 (2014).
- [22] J. Ziegler, A. Sprafke, M. Otto, R. B. Wehrspohn. Activation of Al₂O₃ passivation layers on silicon by microwave annealing, *Appl. Phys. A* **113**, 285-290 (2013).
- [23] (* S. 122) A. Sprafke, D. Schneevoigt, S. Seidel, S. L. Schweizer, R. B. Wehrspohn. Automated spray coating process for the fabrication of large-area artificial opals on textured substrates, *Opt. Express* **21**, A528-A538 (2013).
- [24] X. Li, Y. Xiao, C. Yan, J. Song, V. Talaev, S. L. Schweizer, K. Piekielska, A. Sprafke, J.-H. Lee, R. B. Wehrspohn. Fast electroless fabrication of uniform mesoporous silicon layers, *Electrochim. Acta* **94**, 57-61 (2013).
- [25] X. Li, Y. Xiao, C. Yan, K. Zhou, S. L. Schweizer, A. Sprafke, J.-H. Lee, R. B. Wehrspohn. Influence of the Mobility of Pt Nanoparticles on the Anisotropic Etching Properties of Silicon, *ECS Solid State Lett.* **2**, 22-24 (2013).
- [26] M. Otto, M. Kroll, T. Käsebier, J. Ziegler, A. Sprafke, R. B. Wehrspohn. Passivation of Optically Black Silicon by Atomic Layer Deposited Al₂O₃, *Energy Procedia* **38**, 862-865 (2013).
- [27] A. Sprafke, R. B. Wehrspohn. Light Trapping Concepts for Photon Management in Solar Cells, *Green*, **2**, 177-187 (2012) (Übersichtsartikel).

Buchkapitel (begutachtet)

- [28] A. Sprafke, J. Schilling. *Buch*: Dielectric Metamaterials: Fundamentals, Designs and Applications, *Kapitel*: Non-resonant dielectric metamaterials, Herausgeber: Woodhead Publishing, Editoren: I. Brener, J. Valentine, I. Staude, C. Holloway, S. Liu, ISBN: 978-008102403-4 (2020).
- [29] A. Sprafke, R. B. Wehrspohn. *Buch*: Photon Management in Solar Cells, *Kapitel*: Current Concepts for Optical Path Enhancement in Solar Cells, Herausgeber: Wiley, Editoren: R. B. Wehrspohn, U. Rau, A. Gombert, ISBN: 978-3527411757 (2015).

1 Einleitung

Die Energiekonversion in Solarzellen beginnt mit der Absorption solarer Photonen in einem Halbleiter, dem Absorber. Die primäre Aufgabenstellung des Lichtmanagements in Solarzellen ergibt sich damit aus der trivialen Einsicht, für einen hohen Wirkungsgrad eine möglichst hohe Absorption zu erreichen. Dies bedeutet zum einen, dem Absorber durch Entspiegelung alle eintreffenden Photonen zur Verfügung zu stellen, zum anderen, dass möglichst viele Photonen absorbiert werden. Mögliche Lösungsansätze hierfür möchte ich in dieser Habilitationsschrift darlegen.

Die weit überwiegende Mehrheit der produzierten Solarzellen basiert auf kristallinem Silizium (c-Si) [30]. Silizium steht als zweithäufigstes Element der Erdkruste quasi grenzenlos zur Verfügung und es verfügt auch über eine Bandlücke, die nach dem Limit des detaillierten Gleichgewichts eine günstige Größe für die solare Energiekonversion aufweist [31,32]. Einer der wichtigsten Gründe, der das Erreichen dieses Limits verhindert: Es werden nicht alle auftreffenden Photonen absorbiert. Der hohe Brechungsindex bewirkt eine Reflexion, die sich auch schon augenscheinlich am metallischen Glanz polierter Siliziumoberflächen ablesen lässt. Als indirekter Halbleiter kommen schlechte Absorptionseigenschaften hinzu. Z.B. für eine Lichtwellenlängen von $\lambda = 780 \text{ nm}$ übertrifft die Absorptionslänge von Silizium $10 \mu\text{m}$ und steigt für größere Wellenlängen schnell an (Abb. 1.1a). Nimmt man eine Solarzelle mit perfekter Entspiegelung (Antireflexion) an, die nicht absorbiertes Licht nach dem ersten Durchgang auf der Rückseite wieder entlässt, liesse sich maximal die in Abb. 1.1b aufgetragene elektrische Stromdichte extrahieren. Auf Anheb ist aus dieser Abbildung die Notwendigkeit von lichtwegverlängernden Maßnahmen in kristallinen Silizium-Solarzellen abzulesen. Diese Ausführungen lassen sich auch auf andere Halbleitermaterialien für die Photovoltaik übertragen. Zwar sind diese in der Regel direkte Halbleiter mit entsprechend kürzeren Absorptionslängen, sie werden für sog. Dünnschicht-Solarzellen allerdings in so geringen Schichtdicken verwendet, dass auch für diese das Sonnenlicht nach dem ersten Durchgang nicht vollständig absorbiert wurde, während das Problem des Reflexionsverlustes genauso wie für Silizium besteht.

Martin Green (UNSW, Australien) stellte 1991 ein äußerst erfolgreiches Solarzellendesign vor (Abb. 1.1c), das mehr als 20 Jahre den höchsten Wirkungsgrad für c-Si-Solarzellen vor-

1 Einleitung

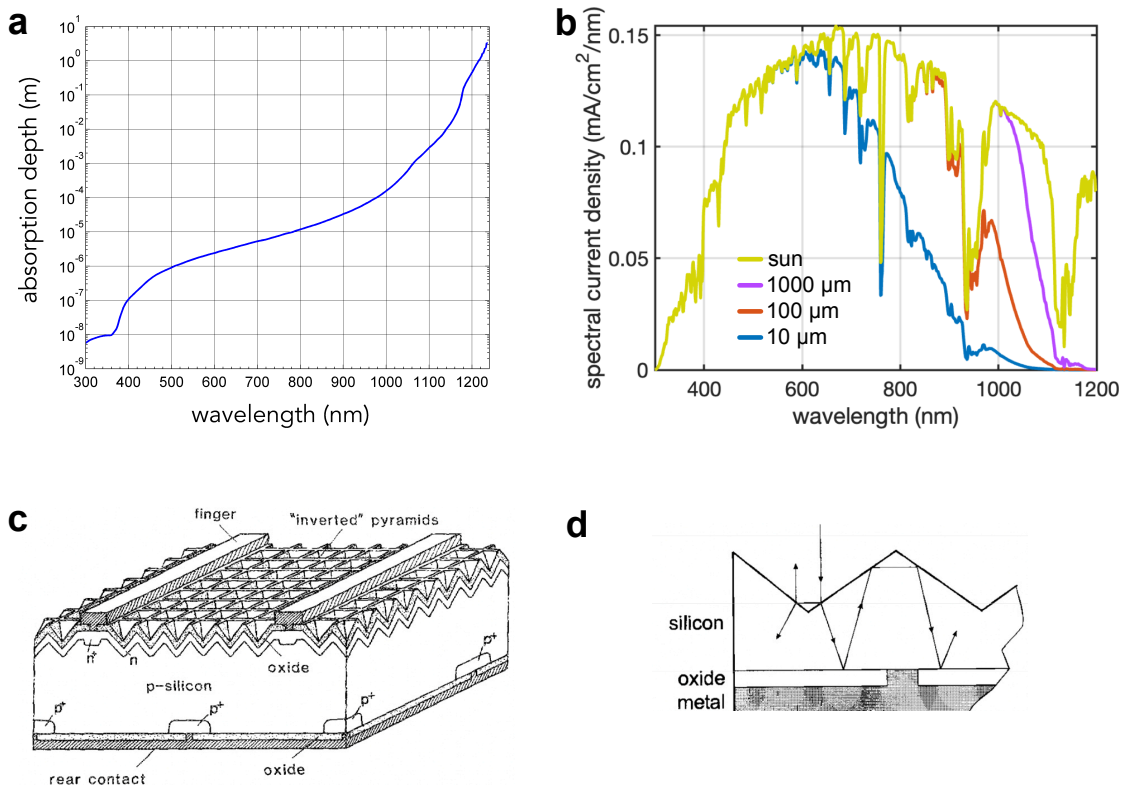


Abb. 1.1: (a) Wellenlängenabhängige Absorptionslänge von kristallinem Silizium. (b) Berechnete photogenerierte Stromdichte pro Wellenlängenintervall unter der Annahme perfekter Entspiegelung aber nur maximal einem Durchgang durch einen Si-Absorber unterschiedlicher Dicke. Die gelbe Kurve stellt die maximal erreichbare Stromdichte dar. (c) Aufbau der von Martin Green 1991 vorgestellten c-Si-Solarzelle mit invertierten Pyramiden als Frontseitentextur. Solarzellen mit diesem Design hielten über viele Jahre den Weltrekord mit einem Wirkungsgrad von 24%. (d) Die Pyramid-Textur bewirkt Antireflexion und Lichtwegverlängerung Abb. aus [29,33,34].

weisen konnte [33,35,36]. Dies lag nicht zuletzt an der verwendeten Frontseiten-Textur aus nasschemisch geätzten, invertierten Pyramiden. Ausgestattet mit einer transparenten Dünnschicht zur Reflexionsminderung der Grenzfläche auf ca. $R_0 \approx 10\%$ bewirken die gekippten Flächen, dass an den Oberflächenstrukturen reflektiertes Licht eine zweite Chance bekommt, in den Absorber einzudringen (Abb. 1.1d). Damit wird der resultierende Reflexionsgrad $R_{\text{res}} = R_0^2$ auf nur noch ca. 1% herabgesetzt. In Kombination mit einem metallischen Rückseitenspiegel ermöglichen die Pyramiden zusätzlich Totalreflexion an der Vorderseite. Schwach absorbiertes Licht kann auf diese Weise mehrere Durchgänge durch den Absorber vollziehen, bevor es schlussendlich entweder absorbiert wird oder doch die Solarzelle verlässt.

Auf dem Weg zu höheren Wirkungsgraden, höherer Material- und Kosteneffizienz werden jedoch neue Ansätze notwendig. c-Si-Solarzellen werden beispielsweise immer dünner und

das Lichtmanagement der Pyramid-Textur reicht nicht nur nicht mehr aus, sondern ihre Fabrikation ist unterhalb einer gewissen Dicke auch nicht mehr durchführbar. Dies gilt ebenso für neue Solarzellen-Konzepte, die heute noch Gegenstand der Forschung sind, beispielsweise Dünnschicht-Solarzellen. Ein Solarzellen-Konzept, das aufgrund hoher Wirkungsgrade derzeit große Aufmerksamkeit erfährt, sind Perowskit-Silizium-Tandemsolarzellen [36–38]. In diesen Solarzellen ist eine Perowskit-Dünnschicht auf einem c-Si-Absorber aufgebracht und neue Lichtmanagement-Ansätze sind gefragt, die kompatibel sind.

Vielversprechende Ansätze bietet die Nanophotonik. Da ihre Strukturen charakteristische Größen im Bereich der Lichtwellenlänge aufweisen, basieren diese nicht mehr auf geometrischer Optik, sondern auf Wellenoptik. Dielektrische Nanopartikel mit hohem Brechungsindex beispielsweise besitzen Streuquerschnitte, die ein Vielfaches ihres geometrischen Querschnitts betragen können [39,40]. Darauf basierend sind zwischenzeitlich eine Fülle nanophotonischer Ansätze sowohl für Antireflexion wie auch für Lichtwegverlängerung in Solarzellen vorgeschlagen worden [41–43].

Unabhängig von den vorgestellten nanophotonischen Texturen spielt die strukturelle Anordnung der jeweiligen Streuelemente eine entscheidende Rolle. Wir bewegen uns im Wellenbild, weshalb räumliche Korrelationen die Interferenz gestreuter Wellen und damit das Streuverhalten der ganzen Textur bestimmen [44]. Räumliche Korrelationen von Lichtmanagement-Strukturen bilden einen Schwerpunkt meiner Arbeit. Anordnungen können keine bzw. sehr geringe Korrelationen aufweisen und dementsprechend zufällig sein. Interferenz ist dann wellenlängenunabhängig inkohärent und im idealisierten Fall diffus-isotrop. Überraschenderweise stellt dieser Fall ein schwer zu schlagendes Limit bzgl. Lichtwegverlängerung bereit, das sog. $4n^2$ -Limit. Neben den hier behandelten Texturen aus schwarzem Silizium reicht interessanterweise auch die Pyramiden-Textur an dieses Limit heran [17,45–47]. Unkorreliert-ungeordneten Anordnungen stehen geordnet-periodischen gegenüber, die eine sehr hohe Korrelation aufweisen, beispielsweise Gitter und photonische Kristalle. Interferenz ist dann kohärent und Streuung findet nur in wenige diskrete Beugungsrichtungen statt. Sie bieten potentiell sehr hohe Lichtwegverlängerungen an, die allerdings spektral eng begrenzt sind. Dies erfordert hohe Anforderungen an das konkrete Design, das an das jeweilige Absorbiermaterial und die Ausführung der nanophotonischen Struktur angepasst werden muss.

Neben diesen eher als konventionell anzusehenden Strukturtypen (zufällig-ungeordnet und periodisch-geordnet) stelle ich einen weiteren Typus vor, die korrelierte Unordnung. Eine besondere Klasse innerhalb der korrelierten Unordnung stellt die sog. hyperuniforme Unordnung dar. Obwohl ungeordnet, teilen hyperuniform-ungeordnete Strukturen Eigenschaften mit periodischen Strukturen, die andere ungeordnete Strukturen nicht aufweisen. Dazu gehören insbesondere unterdrückte Dichtefluktuationen auf großen Längenskalen [48]. Die-

1 Einleitung

se recht abstrakt anmutende Feststellung hat konkrete Auswirkungen auf die Lichtstreuung hyperuniform-ungeordneter Texturen. Wie für eine Gitterstruktur lässt sich einerseits Lichtstreuung für bestimmte (Raum-)Winkelbereiche effizient unterdrücken. Wie für eine zufällige Struktur kann andererseits für andere Winkelbereiche diffuse Lichtstreuung stattfinden. Hyperuniform ungeordnete Strukturen bergen demnach das Potential, eine zuvor nicht beobachtete Kombination aus den bevorzugten Eigenschaften von zufällig-ungeordneten und periodisch-geordneten Texturen bereitzustellen. Mit meinem Team konnte ich auf diesem Gebiet einige der ersten experimentellen Arbeiten zu diesem Thema beitragen.

Jeder in Frage kommende Ansatz für die Absorptionserhöhung in Solarzellen muss Nebenbedingungen erfüllen. Die Energie absorbierter Photonen wird in chemische Energie in Form von Elektron-Loch-Paaren umgewandelt. Diese gilt es effizient zu extrahieren, der Vorgang kann jedoch durch zu große Rekombination von Elektron-Loch-Paaren behindert werden und der Gewinn der erreichten Absorptionserhöhung wird zunichte gemacht [34]. Potentielle Ansätze müssen deshalb immer sicherstellen, dass Absorptions- und Extraktionsbemühungen sich nicht gegenseitig im Weg stehen. Eine weitere offensichtliche, aber nicht trivial zu erfüllende, Anforderung ist die skalierbare Fabrikation von nanophotonischen Strukturen auf großen Flächen. Selbst in einem Forschungskontext, in dem grundlegende Abhängigkeiten untersucht werden und Kostenüberlegungen in den Hintergrund rücken, sollte dies Berücksichtigung finden. Nicht nur ist die Möglichkeit einer (im Labormaßstab) großflächigen Fabrikationsmethode für das Experiment sehr hilfreich, solche Methoden lassen sich bei entsprechendem Potential natürlich auch eher in solche weiterentwickeln, die den Anforderungen der Industrie genügen.

Aufbau der Arbeit

Die vorliegende Arbeit ist eine kumulative Habilitationsschrift und stellt eine Übersicht über meine bisherigen wissenschaftlichen Arbeiten zum Lichtmanagement in Solarzellen dar. Die folgenden Kapitel behandeln Untersuchungen zu ungeordneten photonischen Strukturen am Modellsystem schwarzes Silizium in Kapitel 2, geordneten Strukturen in Kapitel 3 und schließlich ungeordneten aber stark korrelierten bzw. hyperuniformen Strukturen in Kapitel 4. Nach einer kurzen Zusammenfassung und einem Ausblick auf mögliche Fortsetzungsarbeiten in Kapitel 5 ist in Kapitel 7 eine Auswahl meiner Publikationen zu finden.

2 Lichtmanagement mit Unordnung: Schwarzes Silizium

2.1 Einführung

Als schwarzes Silizium werden Oberflächen von kristallinem Silizium mit ausgeprägter Mikro- bzw. Nanostrukturierung bezeichnet [17]. Ein Beispiel ist in Abb. 2.1 gezeigt. Die nadelförmige Struktur führt zu einer starken Verminderung von Lichtreflexion im sichtbaren Spektralbereich, sodass eine entsprechend behandelte Siliziumscheibe schwarz erscheint [49]. Die Nadelstrukturen weisen häufig eine konische Verbreiterung auf, womit geometrische Dimensionen sowohl im Bereich weniger Nanometer (sub-Wellenlängenbereich für sichtbares Licht) an der Spitze als auch einiger hundert Nanometer (Größenordnung der Wellenlänge) im unteren Teil auftreten. Damit treten neben Antireflexion auch Lichtfallen-Eigenschaften aufgrund von Lichtstreuung auf [50], wodurch die Lichtabsorption derart texturierter Si-Scheiben in einem hohen Maß verstärkt ist, siehe auch Abb. 2.1c. Diese besonderen optischen Eigenschaften machen schwarzes Silizium äußerst attraktiv für optoelektronische Anwendung wie Solarzellen [51–54], aber u. a. auch photoelektrochemische Wasserspaltung [19,55], Photodioden [56], Terahertzemitter [56] oder hochsensitive optisch-chemische Sensoren [57].

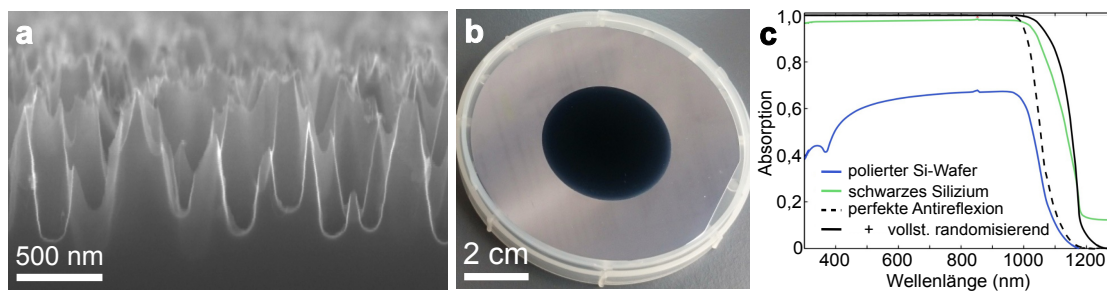


Abb. 2.1: (a) Mikrostruktur (Rasterelektronenaufnahme) und (b) makroskopisches Erscheinungsbild sowie (c) Absorptionsspektrum (grüne Kurve) einer typischen schwarzes-Silizium-Textur hergestellt mittels reaktivem Ionenätzen. Außerdem ist die Absorption für eine glatt polierte Scheibe gezeigt sowie die hypothetischen Fälle perfekter Antireflexion sowie perfekter Antireflexion in Kombination mit vollständig randomisierender Textur (siehe Legende). Die Dicke aller Si-Scheiben beträgt $W = 250 \mu\text{m}$.

2.2 Antireflexion

Die Lichtreflexion einer glatt polierten Siliziumoberfläche lässt sich nach Fresnel berechnen (hier: senkrechter Lichteinfall) [58]:

$$R = \left| \frac{n_{\text{Si}} - n_{\text{Vac}}}{n_{\text{Si}} + n_{\text{Vac}}} \right|^2. \quad (2.1)$$

Im Spektralbereich des VIS und NIR ergibt sich aufgrund des verhältnismäßig hohen Brechungsindexkontrasts zwischen Silizium mit $n_{\text{Si}} \approx 3,5$ (wellenlängenabhängig) und Luft bzw. Vakuum mit $n_{\text{Vac}} = 1$ ein Wert zwischen 30-40% (vgl. Abb. 2.2a und b, gestrichelte Kurven). Für oben genannte Anwendungen, insbesondere für die Photovoltaik, stellt dies einen Reflexionsverlust dar, da hierdurch die Effizienz der angestrebten Energiekonversion von vornherein signifikant reduziert wird. Ein konventioneller Ansatz, diesen Reflexionsverlust zu verringern, besteht im Aufbringen eines dünnen transparenten Films (*antireflection coating ARC*) auf die Grenzschicht zwischen Silizium und Luft (bzw. Einkapselungsmaterial) [27,29]. Die Beschichtung sollte eine Dicke von $\lambda_{\text{des}}/4$ aufweisen, so dass Licht, das von der oberen Grenzfläche des Films zurück reflektiert wird und jenes, das von der unteren Grenzfläche reflektiert wird, destruktiv interferiert, idealerweise zu $R = 0$ (wenn $n_{\text{ARC}} = \sqrt{n_{\text{Vac}} n_{\text{Si}}}$) für die Designwellenlänge λ_{des} (vgl. Abb. 2.2a und b, violette Kurven). Die durchschnittliche Reflexion kann so auf rund $R_{\text{avg}} = 11\%$ für den Wellenlängen-Bereich 350-1100 nm gesenkt werden.

Eine entscheidende Schwäche solcher ARC-Schichten ist ihre Wellenlängen-Selektivität sowie ihre starke Abhängigkeit vom Einfallswinkel. Insbesondere für Solarzellen sind die Auswirkungen nachteilig, da sowohl das Sonnenspektrum spektral sehr breitbandig ist sowie sich der Einfallswinkel der Sonne über den Tagesverlauf stark ändert. Eine verbesserte Antireflexion würde eine Grenzschicht bieten mit einem Brechungsindex, der sich graduell von jenem des oberen Halbraums (z.B. Luft, Einkapselungsmaterial) zu dem des unteren Halbraums (Si) verändert. Die Vermeidung von abrupten bzw. größeren Sprüngen des Brechungsindex' führt zu einer starken Verringerung der Fresnel-Reflexion: Ein graduell variierender Brechungsindex lässt sich gedanklich in viele dünne, übereinander gestapelte parallele Schichten mit geringem Brechungsindexkontrast unterteilen. Da R nach Gl. 2.1 vom Brechungsindexkontrast der angrenzenden Materialien abhängt, lässt sich auf diese Weise ein Schichtstapel mit insgesamt sehr kleiner Reflexion R erreichen. Schon eine Gradientenschicht mit der Dicke in der Größenordnung der Lichtwellenlänge ist einer konventionellen ARC-Beschichtung bzgl. durchschnittlicher Reflexion, spektraler Bandbreite und Einfallswinkel-Abhängigkeit weit überlegen [17,59]. Die Reflexion einer Gradientenschicht mit linearem Brechungsindexprofil ist in Abb. 2.2a und b (orange Kurve) gezeigt. Die durchschnittlicher Reflexion beträgt $R_{\text{avg}} = 1,0\%$, ist also sehr viel geringer im Vergleich zur konventionellen ARC-Beschichtung. Weiter re-

2.2 Antireflexion

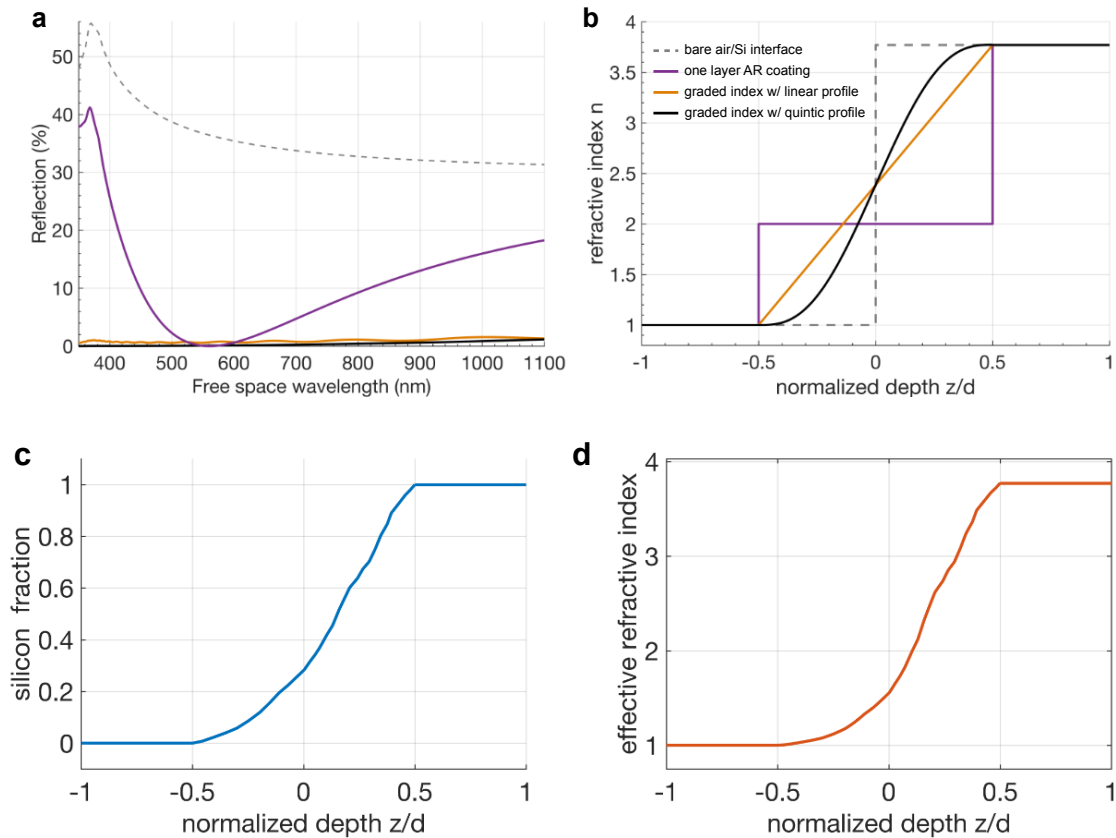


Abb. 2.2: (a) Berechnete Reflexionsspektren und (b) zugehörige Brechungsindexprofile für unterschiedliche Si-Grenzflächen. (c) Experimentell bestimmter Si-Füllfaktor einer typischen schwarzes-Silizium-Textur hergestellt mittels reaktivem Trockenätzen und (d) daraus bestimmter effektiver Brechungsindex ($\lambda = 700 \text{ nm}$) nach dem Bruggeman-Modell aufgetragen gegen die normalisierte Tiefe z/d . Abbildungen aus [28]

duzieren lässt sich die Reflexion durch andere Brechungsindexprofile, wie bspw. ein quintisches Profil, welches mit $R_{\text{avg}} = 0,4\%$ eine noch bessere Performance bzgl. Antireflexion aufweist [59], wobei der Unterschied zum linearen Profil relativ gesehen groß, absolut gesehen jedoch nur noch klein ist.

Realistisch lassen sich derartige Brechungsindexprofile mit homogenen Materialien bzw. Materialkompositen nicht realisieren, da eine entsprechende Vielfalt an benötigten Brechungsindices nicht existiert. Poröse Materialien wie schwarzes Silizium hingegen stellen sehr wohl solche Brechungsindexprofile bereit. Unterteilt man seine Textur gedanklich in viele dünne Schichten, kann für jede dieser Schichten ein optisch effektives Medium angenommen werden, dessen effektiver Brechungsindex in vertikaler Richtung aufgrund der konischen Nadelform variiert [28]. Von den Spitzen bis zum Erreichen des Volumenmaterials nimmt der Füllfaktor von Silizium zu, siehe Abb. 2.2c. Der effektive Brechungsindex $n_{\text{eff}} = \sqrt{\epsilon_{\text{eff}}}$ (dielek-

2 Lichtmanagement mit Unordnung: Schwarzes Silizium

trische Funktion ϵ) lässt sich nach dem Bruggemann-Modell durch Nullstellen-Bestimmung von

$$f \frac{\epsilon_1 - \epsilon_{\text{eff}}}{\epsilon_1 + 2\epsilon_{\text{eff}}} + (1 - f) \frac{\epsilon_2 - \epsilon_{\text{eff}}}{\epsilon_2 + 2\epsilon_{\text{eff}}} = 0, \quad (2.2)$$

mit dem Füllgrad f des höherbrechenden Mediums ($n_{\text{Si}} = \sqrt{\epsilon_1}$) im niedrigbrechenden Medium ($n_{\text{Vac}} = \sqrt{\epsilon_2}$) errechnen [28]. Das (effektive) Brechungsindexprofil einer fabrizierten schwarzes-Silizium-Textur ist in in Abb. 2.2d gezeigt. Der Vergleich mit Abb. 2.2b zeigt, dass diese Probe ein graduelles Brechungsindexprofil aufweist, dessen Verlauf zwischen dem des linearen und des quintischen Profils liegt. Somit lassen sich die überragenden Antireflexionseigenschaften von schwarzem Silizium auf den graduell ansteigenden Brechungsindex eines effektiven Mediums zurückführen.

2.3 Lichtwegverlängerung und Lichteinfang (*Light trapping*)

Die Antireflexionseigenschaften von schwarzem Silizium führen zu einer fast idealen Einkoppelung von Licht in das Siliziumvolumen, d.h. die auftreffende Lichtenergie steht fast vollständig für die Energiekonversion zur Verfügung. In Abb. 2.1c erkennt man dies an der sehr viel größeren Absorption im Vergleich zu einer glatt-polierten Si-Scheibe. Vergleicht man die Absorption mit dem hypothetischen Fall einer perfekten Antireflexion, ist zu erkennen, dass die schwarzes-Silizium-Textur sogar signifikant erhöhte Absorption im Bereich $\lambda_0 = 1000 - 1200$ nm in der Umgebung der Si-Bandkante aufweist.

Die effektives-Medium-Theorie erklärt zwar die Antireflexionseigenschaften, sie lässt sich dennoch nur eingeschränkt auf die Textur anwenden, da die wichtige Bedingung, dass alle beteiligten Strukturgrößen sehr viel kleiner als die Lichtwellenlänge sind, nicht durchweg eingehalten werden kann. Sie gilt noch für den Bereich der Spitzen, jedoch nicht mehr für den Bereich weiter unten. Dort sind die Nadeln stark verbreitert (einige 100 nm) und es tritt ausgeprägte Lichtstreuung auf, die der Annahme eines homogenen effektiven Mediums widerspricht. Dies wird zusätzlich verstärkt durch den verhältnismäßig hohen Brechungsindex von Silizium. Da die Wellenlänge λ in Materie gegenüber der Vakuumwellenlänge λ_0 um den Brechungsindex n_{Si} verkürzt ist, $\lambda = \lambda_0 / n_{\text{Si}}$, mag die Mikrostruktur von der Luftseite aus alle subwellenlängen-groß erscheinen, von der Silizium-Seite aus gesehen sicherlich nicht.

Die Streuung an diesen Strukturen führt zu einer Lichtwegverlängerung innerhalb des Siliziums [17,60]. Dies spielt für die Absorption von Wellenlängen, für welche die Absorptionslänge von Silizium größer als die Dicke der Solarzelle bzw. Si-Scheibe ist, eine wichtige Rolle, da hierdurch ihre Absorptionswahrscheinlichkeit erhöht wird. Für eine Siliziumscheibe mit einer Dicke von 250 μm gilt dies beispielsweise für $\lambda_0 > 1000$ nm. Totalreflexion an der Grenz-

2.4 Oberflächenrekombination und -passivierung

fläche, z.B. nach Reflexion von der Rückseite, verlängert den Lichtwegverlängerung und damit die Absorption weiter. Die Absorptionsverstärkung α_{abs} für den Fall einer vollständig randomisierenden Textur wurde von Yablonovitch hergeleitet und beträgt [61,62],

$$\alpha_{\text{abs}} = 4n^2, \quad (2.3)$$

auch ergodisches oder Yablonovitch-Limit genannt, und gilt als eine wichtige Referenzgröße bzgl. Absorption in Solarzellen. Hierbei wird die quadratische Abhängigkeit der photonischen Zustandsdichte im Material vom Brechungsindex n berücksichtigt, wobei die randomisierende Textur die Besetzung aller Zustände im photonischen Phasenraum bewirkt; ein Faktor 2 rührt her von der Annahme einer perfekt weiß reflektierenden zweiten Grenzfläche der Scheibe, während die Mittelung über den Raumwinkel einen weiteren Faktor 2 ergibt.

In Abb. 2.1c ist die Absorption nach Yablonovitch ebenfalls eingezeichnet¹, und wir erkennen, dass die Kurve für schwarzes Silizium diesem Limit nahe kommt. Abweichungen lassen sich darauf zurückführen, dass schwarzes Silizium das einfallende Licht nicht vollständig randomisiert streut, wie beispielsweise der idealisierte Lambertscher Streuer, welcher Licht isotrop abstrahlt. Ursachen hierfür sind in Nadel-eigenen Resonanzen zu suchen. Mit charakteristischen Durchmessern im Bereich der Wellenlänge und aufgrund des hohen Brechungsindex' fällt schwarzes Silizium in den Bereich der Mie-Streuung und eine Vielzahl von Resonanzen können auftreten [41,63]. Die Untersuchung dieser Resonanzen liegt nicht im Rahmen dieser Arbeit, jedoch kann davon ausgegangen werden, dass die Abstrahlung der Textur, gemittelt über alle Resonanzen, nicht der isotropen Abstrahlcharakteristik des Lambertschen Streuers entspricht.

2.4 Oberflächenrekombination und -passivierung

In einer auf schwarzem Silizium basierenden Solarzelle bedeutet die Absorptionserhöhung eine verstärkte Elektron-Loch-Paar-Generation und damit einen Zuwachs an photogenerierter Stromdichte j_{ph} . Der Wirkungsgrad einer Solarzelle ist im Weiteren jedoch limitiert durch die detaillierte Bilanz von Generation von Elektron-Loch-Paaren und Rekombination dieser bevor sie an den elektrischen Kontakten abgeführt werden können. Nur für ausreichend unterdrückte Rekombination wird durch erhöhten j_{ph} auch die Kurzschlussstromdichte j_{sc} sowie, auf einer logarithmischen Skala, die offene Klemmspannung U_{OC} vergrößert, was dann zu einem höheren Wirkungsgrad η der Solarzelle führen kann [34].

Es treten strahlende sowie nicht-strahlende Rekombinationsprozesse wie Auger-, Shockley-

¹Da hier kein weißer Rückreflektor vorliegt, sondern eine beidseitig texturierte Probe, gilt hier nun $\alpha_{\text{abs}} = 2n^2$.

2 Lichtmanagement mit Unordnung: Schwarzes Silizium

Read-Hall- und Oberflächendefektrekombination auf [31,64,65]. Da Rekombination im Volumen mit der Waferdicke W skaliert [31,64], lässt sie sich durch die Verwendung dünner Si-Scheiben minimieren, was auch im Sinne der Material- und Kosteneffizienz ist. Mit steigendem Oberflächen-zu-Volumen-Verhältnis dominiert die Rekombination an der Oberfläche [66]. Eine Solarzelle kann somit nur effizient sein, wenn neben den optischen Eigenschaften auch angemessene elektronische Eigenschaften vorliegen, die Oberflächenrekombination also durch eine sog. Oberflächenpassivierung, welche die Defekte neutralisiert, möglichst klein gehalten wird [67].

Die Flächendichte rekombinationsaktiver Defekte $D_{S,\text{ref}}$ einer planaren Referenz-Siliziumoberfläche ist im Vergleich zu jener von schwarzem Silizium, $D_{S,\text{nano}}$, stark erhöht, was den Gewinn an Absorptions zunichte machen kann. Eine wichtige Ursache für die erhöhte Defektdichte ist der Fabrikationsprozess, der Oberflächendefekte und Verunreinigungen einbringt. Selbst nach Passivierung (s.u.) kann beispielsweise für einen nass-chemischen Herstellungsprozess die Defektdichte um das 100-fache erhöht sein ($\delta = D_{S,\text{nano}}/D_{S,\text{ref}} \approx 100$), für einen Femtosekundenlaserprozess um das 1500-fache ($\delta \approx 1500$) [17]. Dies hat direkte Auswirkungen auf die effektive Lebensdauer τ_{eff} der Minoritätsladungsträger bzw. die effektive Oberflächenrekombinationsgeschwindigkeit $S_{\text{eff}} = W/2\tau_{\text{eff}}$ [68], da $S_{\text{eff}} = \nu_{\text{th}}\sigma D_S$ ist, mit der thermischen Geschwindigkeit ν_{th} und dem Einfangquerschnitt σ [67]. τ_{eff} ist eine experimentell bestimmbare Größe, beispielsweise mittels quasistatischer Photoleitfähigkeitsmessung (*quasi-steady state photoconductance method* QSSPC) messbar [69].

Auch eine reine Siliziumoberfläche hält aufgrund des Kristallsymmetriebruchs Grenzflächenzustände als Rekombinationszentren bereit. Damit führt die mit der (gewünschten) Strukturierung einhergehende Oberflächenvergrößerung $\gamma = A_{\text{nano}}/A_{\text{ref}}$, mit der wahren Fläche A_{nano} und der projizierten Grundfläche A_{ref} , zu einer weiteren Erhöhung von S_{eff} . γ kann je nach Herstellungstechnologie Werte von $\gamma = 2$ bis zu $\gamma = 45$ erreichen [17]. Für das Verhältnis von S_{eff} bzw. τ_{eff} von texturierter und glatter Grenzfläche finden wir nun

$$\frac{S_{\text{nano}}}{S_{\text{ref}}} = \frac{\tau_{\text{ref}}}{\tau_{\text{nano}}} = \frac{A_{\text{nano}}}{A_{\text{ref}}} \cdot \frac{S_{D,\text{nano}}}{D_{S,\text{ref}}} = \gamma\delta. \quad (2.4)$$

An Gl. 2.4 lässt sich u.a. ablesen, dass eine texturierte Grenzfläche immer eine erhöhte Oberflächenrekombination aufweisen wird, da selbst für ein vollständiges Ausheilen von fabrikationsinduzierten Schäden ($\delta = 1$) immer noch $S_{\text{nano}}/S_{\text{ref}} = \gamma > 1$ ist, was eine effektive Passivierung umso wichtiger macht. Hierfür haben sich dünne (10 – 50 nm) Al_2O_3 -Schichten hervorgetan [70,71], die speziell auch für schwarze-Silizium-Texturen in unserer Gruppe untersucht wurden [17,26,72,73]. Al_2O_3 bietet zum einen die Kombination zweier komplementärer Effekte für die Passivation: Eine hohe Dichte an fixen (hier: negativen) Ladungen lässt

2.5 Reaktives Ionenätzen bei nicht-kryogenen Temperaturen

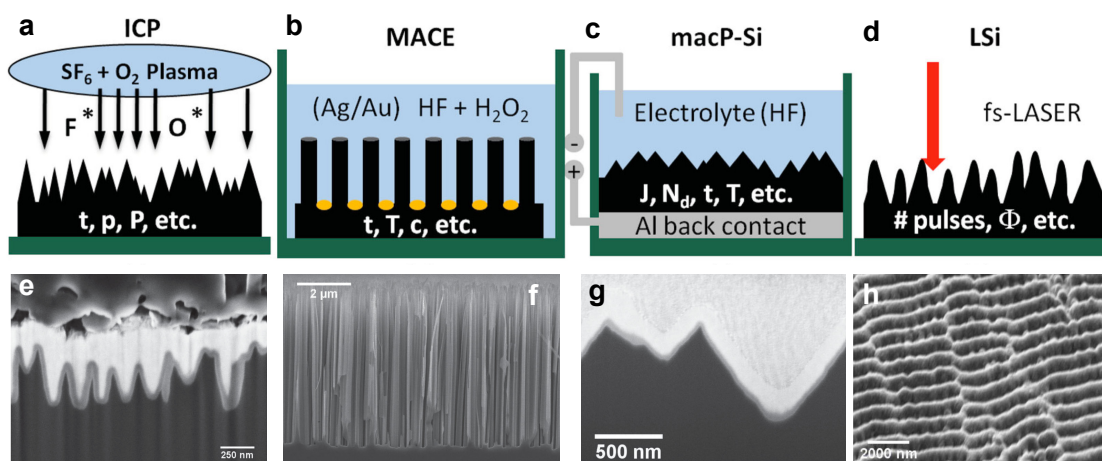


Abb. 2.3: Schematische Darstellung verschiedener Herstellungsmethoden von schwarzem Silizium und REM-Aufnahmen typischer resultierender Oberflächentexturen. (a), (e) Reaktives Ionenätzen, (b), (f) MACE, (c), (g) elektrochemisches Ätzen, (d), (h) Laserstrukturierung. In (e) lässt sich im mittigen Bereich als graue Schicht der konformal aufgetragene Al_2O_3 -Passivierfilm erkennen. Abb. [17] entnommen.

die *Feldefekt-Passivierung* in Erscheinung treten. Aufgrund der Coulomb-Abstoßung wird eine Ladungsträgersorte (hier: Elektronen) von der Grenzfläche ferngehalten und auf diese Weise dort Rekombination unterdrückt. Durch die sog. *chemischen Passivierung* werden Defektzustände an der Grenzfläche abgesättigt und D_S reduziert. Zum anderen lässt sich Al_2O_3 mittels Atomlagenabscheidung (*atomic layer deposition* ALD) konformal aufbringen, was für schwarzes Silizium mit mitunter hohen Aspektverhältnissen in der Mikrostruktur einen unschätzbaren Vorteil darstellt (siehe auch Abb. 2.3e).

2.5 Reaktives Ionenätzen bei nicht-kryogenen Temperaturen

Es existieren verschiedene Methoden, schwarzes Silizium herzustellen. Die gängigsten sind reaktives Ionenätzen (*reactive ion etching* RIE, auch Plasma- oder Trockenätzen) [50,72,74], stromloses metall-unterstütztes chemisches Ätzen (*metall-assisted chemical etching* MACE) [51,53,75], photoelektrochemisches Ätzen [57] und Laserpulsstrukturierung [76] (siehe Übersicht in Abb. 2.3). Diese Methoden führen bei korrekter Wahl der Herstellungsparameter zu makroskopisch schwarzen Siliziumscheiben [17]. Mikrostrukturell allerdings resultieren sie in deutlich unterscheidbaren Strukturen, was sich sowohl in den optischen Eigenschaften dieser Oberflächentexturierungen als auch in den elektronischen Eigenschaften niederschlägt. Reaktives Ionenätzen und MACE sind die in unserer Gruppe präferierten Methoden für die Herstellung von schwarzem Silizium.

2 Lichtmanagement mit Unordnung: Schwarzes Silizium

Reaktive Ionenätzen ist ein etabliertes Verfahren zur Mikrobearbeitung von Silizium [77,78]. Schwarzes Silizium war über eine lange Zeit als unerwünschtes Nebenprodukt bekannt, bevor es für optoelektronische Anwendungen entdeckt wurde [79]. Im Labormaßstab wurden bereits auch schon Solarzellen aus RIE-geätztem schwarzen Silizium hergestellt [21,54,80].

In unserer Arbeitsgruppe wird RIE maskenklos mit einer Mischung aus SF_6 und O_2 und einem induktiv (*inductive coupled plasma* ICP) oder kapazitiv (*capacitive coupled plasma* CCP) gekoppeltem Plasma, oder einer Kombination aus beidem (ICP-CCP), verwendet. Die im Plasma gebildeten F^* -Radikale reagieren mit der Siliziumoberfläche zu flüchtigem SiF_4 . In einem konkurrierendem Prozess formen sich Siliziumoxyfluoride, $\text{SiF}_4 + \text{O}^* \rightarrow \text{SiO}_x\text{F}_y$, welche als Ätzstop für F^* wirken [81]. Auf horizontalen Flächen wird diese Selbstmaskierung durch das Ionenbombardement physikalisch durchbrochen, das durch eine Gleichspannung zwischen Plasma und Probe in der Größenordnung 10-100 V erzeugt wird. Aufgrund der Direktionalität der auftreffenden Plasma-Ionen ist dieser Effekt jedoch auf vertikalen Flächen schwächer, so dass Seitenwände größtenteils geschützt sind vor dem chemischen Ätzen durch F^* -Radikale. Im Ergebnis ist der RIE-Prozess stark anisotrop und führt bei entsprechender Parameterwahl zu zufällig verteilten nadelartigen Strukturen [82]. Bestimmte Morphologien, wie das Aspektverhältnis der Nadeln, lassen sich durch die Prozessparameter variieren.

Der Vorteil bei der Herstellung von schwarzem Silizium mittels RIE ist die Vermeidung toxischer Chemikalien und eine Texturierung unabhängig von Kristallorientierung und Dotierung. Nachteilig ist, dass die Si-Scheiben für reproduzierbare Ergebnisse bisher auf kryogene Temperaturen (zwischen -110°C und -70°C) heruntergekühlt werden mussten, was der Volatilität der Siliziumoxyfluoride zugeschrieben wird [83]. Der Selbstmaskierungseffekt wird aufgrund der Desorption bei höheren Temperaturen vermindert und die Texturbildung instabil. Ein Prozess bei höheren Temperaturen, z.B. Raumtemperatur, ist für eine kosteneffiziente industrielle Produktion jedoch erstrebenswert. Es würde nicht nur die aufwendige Kühlung wegfallen, der Prozess würde auch technologisch vereinfacht und beschleunigt, beispielsweise aufgrund geringerer zu kontrollierenden Temperaturdifferenzen und Ausbleiben von Kondenswasserbildung beim Be- und Entladen der (zu evakuierenden) Ätzkammer.

Schwarzes Silizium bei $T > 0^\circ\text{C}$ ist nicht grundsätzlich unmöglich wie vereinzelte Arbeiten in der Literatur zeigen konnten [84,85], jedoch wird das Prozessfenster mit steigender Temperatur immer kleiner. In unserer Gruppe haben wir deshalb untersucht, unter welchen Bedingungen schwarzes Silizium reproduzierbar präpariert werden kann und inwiefern dieses hinsichtlich seiner optoelektronischen Performance abschneidet [15].

Mit der Zielgröße möglichst hoher gemittelter² Absorption A_{avg} konnten wir für den Plasma-Modus CCP und ICP-CCP schwarzes Silizium bei $T = 5^\circ\text{C}$ herstellen. Die Mikrostruktur,

²Mittelung über den Spektralbereich $\lambda_0 = 300 - 1150 \text{ nm}$

2.5 Reaktives Ionenätzen bei nicht-kryogenen Temperaturen

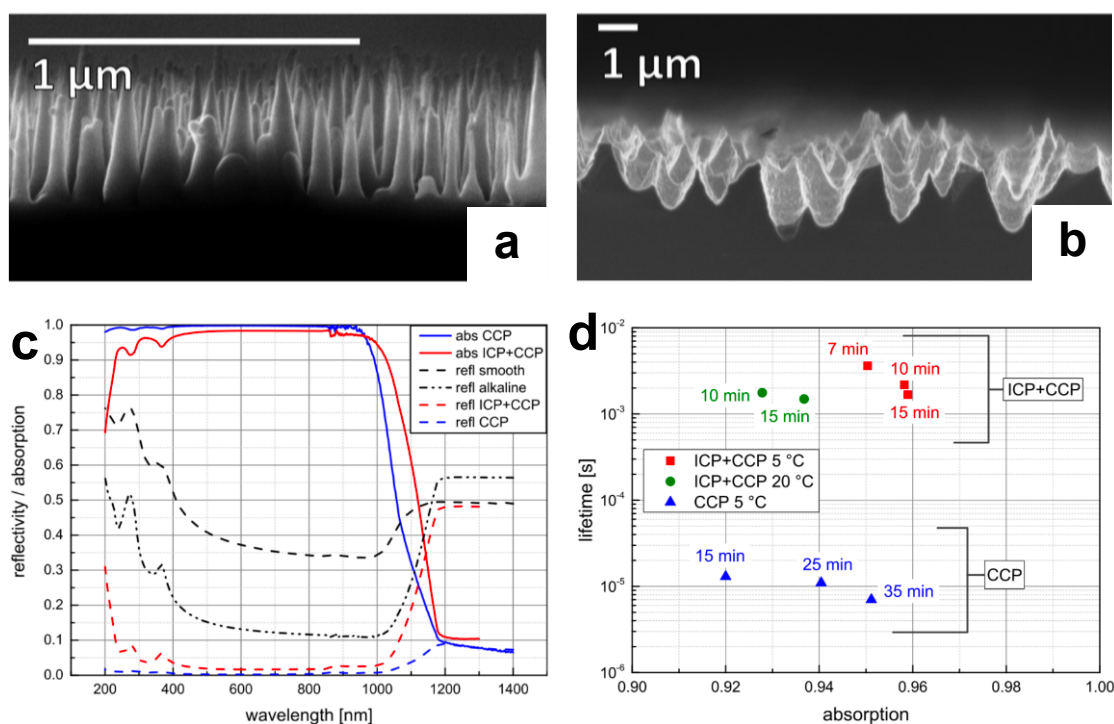


Abb. 2.4: Mikrostruktur von schwarzem Silizium präpariert unter Verwendung eines (a) kapazitiven (CCP) und (b) induktiv-kapazitivem (ICP-CCP) Plasmaprozess. (c) Absorptions- (durchgezogene Kurven) und Reflexionsspektren (unterbrochene Kurven) sowie (d) Lebensdauer der Minoritätsladungsträger aufgetragen gegen die gemittelte ($\lambda_0 = 300 - 1150 \text{ nm}$) Absorption A_{avg} der hergestellten Texturen nach Al_2O_3 -Passivierung. Die Zeitangaben stellen die Ätzdauern dar. Abb. aus [15]

siehe Abb. 2.4a und b, ist für die beiden Fälle unterschiedlich. Während der CCP-Prozess Nadeln mit hohen Aspektverhältnissen hervorbringt (man beachte die unterschiedlichen Maßstäbe), sind die ICP-CCP-Strukturen krater-ähnlich. Die Höhe der Nadeln aus dem CCP-Prozess beträgt ca. 500 nm und der durchschnittliche laterale Abstand beträgt ca. 100 nm; die Kratertiefe und -abstände aus dem ICP-CCP-Prozess sind im Bereich von 1 μm . Die Unterschiede in der Mikrostruktur ziehen Unterschiede in den optischen Eigenschaften nach sich, siehe Abb. 2.4c. Die eng stehenden, dünnen Nadeln der CCP-Struktur erfüllen eher die Näherung des effektiven Mediums, s.o., und bewirken eine bessere Antireflexion und damit Absorption von $A \approx 99\%$ für $\lambda_0 \lesssim 950 \text{ nm}$. Für $\lambda_0 \gtrsim 950 \text{ nm}$ allerdings ist die Absorption der ICP-CCP-Struktur höher. Aufgrund der charakteristischen Größe im Bereich der Wellenlänge streut sie das Licht besser, was zu einer erhöhten Lichtwegverlängerung führt. Die ICP-CCP-Struktur kann so seine etwas schlechtere Antireflexion mehr als kompensieren, so dass seine gemittelte Absorption A_{avg} größer ist als für die CCP-Struktur.

Deutliche Unterschiede sind für die Minoritätslebensdauern τ_{eff} der Al_2O_3 -passivierten

Proben zu beobachten. In Abb. 2.4d sind sie zusammen mit der gemittelten Absorption aufgetragen. Für Anwendungen in der Photovoltaik werden Lebensdauern von mindestens $\tau_{\text{eff}} > 100 \mu\text{s}$ benötigt, was wir nur für die ICP-CCP-Strukturen ($1 < \tau_{\text{eff}} < 3,6 \text{ ms}$) erreichen konnten. Die Ursache für die starke Degradation der CCP-Strukturen ($\tau_{\text{eff}} < 10 \mu\text{s}$) ist in der offensichtlichen stärkeren Oberflächenvergrößerung γ zu suchen, vermutlich aber noch vielmehr in der relativ hohen Vorspannung (*DC bias*, hier 100 V), ohne die wir bei dieser Temperatur keine Textur erhalten. Die Vorspannung beschleunigt Plasma-Ionen auf die Si-Oberfläche und bewirkt tiefe Defekte, die selbst die Al_2O_3 -Passivierung nicht mehr ausheilt [86,87] und demnach zu einem hohen δ führt. Wie man an der Abhängigkeit von τ_{eff} von der Ätzdauer erkennt, trifft dies auch für die ICP-CCP-Strukturen zu, jedoch in viel geringerem Maße.

Den ICP-CCP-Prozess konnten wir unter weiterer Prozessparameteranpassung bis zu einer Temperatur von $T = 20^\circ\text{C}$ treiben. Die optischen Eigenschaften von so hergestelltem schwarzem Silizium sind zwar etwas schlechter als für $T = 5^\circ\text{C}$, die elektronischen Eigenschaften können jedoch ihr hohes Niveau halten, siehe Abb. 2.4d (grüne Datenpunkte). Der ICP-CCP-Prozess stellt demnach einen potentiellen Kandidaten für die kosteneffektive Herstellung von schwarzem Silizium in der Photovoltaikindustrie dar.

2.6 MACE für Nanostrukturierung und gleichzeitige Aufreinigung

Das stromlose metall-unterstützte nasschemische Ätzen wird in wässrigen Lösungen aus Flußsäure (HF) und Wasserstoffperoxid (H_2O_2) durchgeführt [75,88]. Auf die Siliziumoberfläche aufgebrachte Edelmetallnanopartikel, z.B. Silber- oder Goldnanopartikel, agieren als Katalysatoren, um Silizium zügig und ohne das Anlegen einer elektrischen Spannung zu ätzen. Der Ätzmechanismus beruht auf der Reduktion von H_2O_2 auf der Metalloberfläche, d.h. das Metall gibt Elektronen ab. Die dem Metall fehlenden Elektronen werden aus dem Valenzband des Siliziums durch Elektronentransfer über die Metall/Si-Grenzfläche ausgeglichen. Die resultierenden Löcher diffundieren an die Si/Elektrolyt-Grenzfläche nahe des Metallpartikels, was einer lokalen divalenten oder tetravalenten Oxidation des Siliciums entspricht. HF ätzt daraufhin das (teiloxydierte) Silizium unter Bildung eines $[\text{SiF}_6]^{2-}$ -Komplexes. Dieses selektive Ätzen geschieht in unmittelbarer Umgebung und hauptsächlich unterhalb des Metallnanopartikels, sodass das Metallpartikel in das Silizium einsinkt und einen vertikalen Kanal bildet.

Der Ätzprozess ist ausgeprochen anisotrop, MACE-prozessiertes schwarzes Silizium zeichnet sich beispielsweise durch Nadelstrukturen mit praktisch vertikalen Seitenwänden aus, die konische Verbreiterung wie sie z.B. bei RIE-prozessiertem schwarzem Silizium auftritt, ist minimal (vgl. Abb. 2.3f). Der MACE-Prozess ist streng genommen ein elektrochemischer

2.6 MACE für Nanostrukturierung und gleichzeitige Aufreinigung

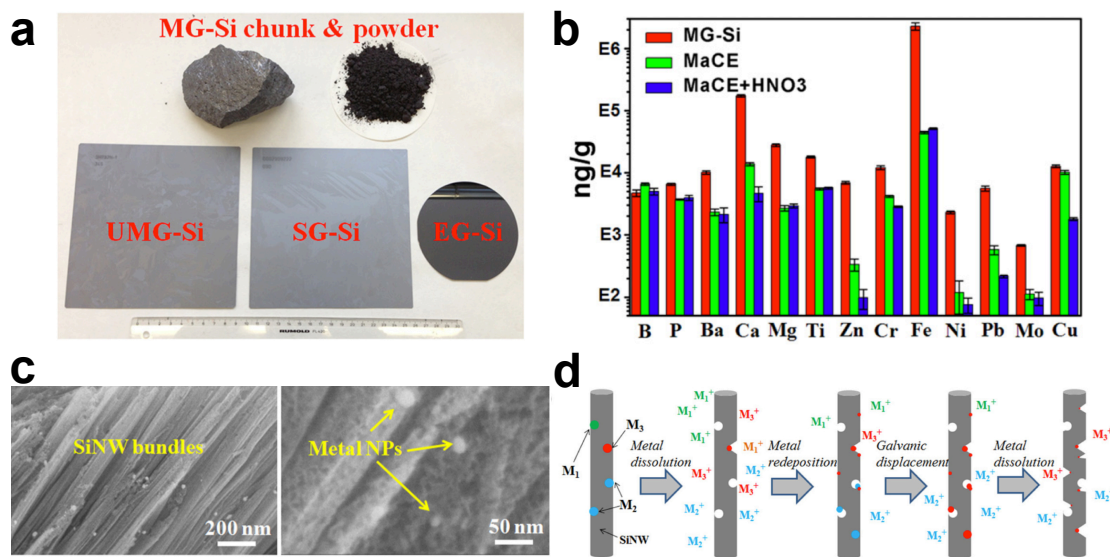


Abb. 2.5: (a) Silizium unterschiedlicher Reinheitsgrade. (b) Verunreinigungslevel (ICP-MS) aufgeschlüsselt nach Elementen für unbehandeltes MG-Si (rote Balken), nach MACE-Ätzung (grüne Balken) und nach MACE- und anschließender HNO₃-Ätzung. (c) REM-Aufnahmen der Nanostruktur nach MACE-Ätzung. (d) Skizze zum Mechanismus der MACE-Aufreinigung. Abb. aus [12,20,92]

Prozess, da zwischen dem Metall als (lokale) Kathode und Silizium als Anode ein Strom fließt, es muss allerdings keine äußere Spannungsquelle angeschlossen werden. Der Metallkatalysator kann auf der zu ätzenden Siliziumoberfläche zufällig angeordnet werden (was hier der Fall ist) oder für deterministische Siliziumstrukturen als gezielt präparierte Maskenstruktur aufgebracht sein. MACE ist verhältnismäßig einfach und kosteneffektiv zu implementieren und kann sowohl auf p- als auch auf n-Typ Silizium angewendet werden, weshalb er schnell an Popularität gewann und vielfältig Anwendung findet [75]. So sind nicht nur im Labormaßstab Solarzellen aus schwarzem Silizium mittels MACE hergestellt worden [53,89], sondern auch erste Ansätze zur Marktkommerzialisierung erfolgt [90,91].

In unserer Gruppe wurde erstmals beobachtet, dass sich sog. metallurgisches Silizium (MG-Si) durch MACE aufreinigen lässt [20,92]. MG-Si (Reinheit > 99 %) ist eine Vorstufe des industriell genutzten *solar grade* (SC-Si, Reinheit > 99,9999%) bzw. *electronic grade* (EG-Si, Reinheit > 99,999999%) Siliziums, wobei die Aufreinigung im kosten- und energieintensiven Siemens-Prozess bei einer Temperatur von $T = 1100^{\circ}\text{C}$ geschieht. Setzt man MG-Si-Pulver dem Ag-MACE-Prozess und einer nachfolgenden Behandlung mit Salpetersäure HNO₃ aus, findet eine Aufreinigung von 99,74 % auf 99,9884 % statt, für *upgraded metallurgical silicon* (UMG-Si) von 99,999772 % auf 99,999899 % und damit fast auf das Niveau von SC-Si. Abb. 2.5b zeigt mittels Massenspektrometrie mit induktiv gekoppeltem Plasma (*inductively coupled plasma mass spectrometry* ICP-MS) gemessene Verunreinigungslevel aufgeschlüsselt nach Elementen

2 Lichtmanagement mit Unordnung: Schwarzes Silizium

ten und Prozessschritten. Aufgrund der potentiellen Reduktion des ökologischen Fussabdrucks und von Kosten aufgrund geringeren Energieeinsatz handelt es sich um einen bemerkenswerten Ansatz, insbesondere da hier die Aufreinigung mit der Nanostrukturierung zu schwarzem Silizium einhergeht.

Der Mechanismus der MACE-Aufreinigung ist komplex und beinhaltet mehrere Faktoren [20]. Verunreinigungen treten aufgrund ihrer meist geringen Löslichkeit in Si mikroskopisch nicht homogen auf. Während des Erstarrens scheiden sie sich gehäuft an Korngrenzen ab [93,94]. Da Korngrenzen morphologische Defekte in der Kristallstruktur darstellen, findet die Nukleation der Metallnanopartikel-Katalysatoren (hier Ag) bevorzugt an diesen statt. Es wird also verstärkt an Korngrenzen entlang geätzt und damit neben Si auch Verunreinigungen gelöst.

Im Weiteren zeigt die Mikrostrukturanalyse, dass die entstandenen Nadelstrukturen in MG-Si im Gegensatz zu MACE an SC- bzw. EG-Si porös sind und (vor der abschliessenden HNO_3 -Behandlung) ihre Seitenwände mit Metallnanopartikeln, vornehmlich Ag, bedeckt sind, vgl. Abb. 2.5c. Neben den ausgelösten metallischen Verunreinigungen wird auch immer etwas Ag der initialen Nanopartikel während des MACE-Prozesses gelöst [95]. Diese scheiden sich an einer Si-Seitenwand ab, verstärkt an Korngrenzen, wo dann ein weiterer MACE-Prozess stattfindet. So findet nach dem ersten Ätzen entlang der Korngrenzen mit entsprechend erhöhter Verunreinigung eine weitere Iteration des gleichen MACE-Prozesses statt, nun aber an Stellen, die erst durch den vorherigen zugänglich geworden sind. Dieses Modell wird u.a. gestützt durch die Beobachtung, dass die Konzentrationen der Dotierelemente Bor und Phosphor mutmaßlich aufgrund ihrer hohen Kompatibilität in das Si-Kristallgitter kaum eine Veränderung erfahren.

Wir können die gelösten Elemente in drei Kategorien einteilen, solche mit großem negativen Redox-Potential, M_1 (Ba, Ca, Mg, Ti, Zn, Cr, Fe), mit moderatem negativen Redox-Potential, M_2 (Ni, Pb, Mo) und kleinem positiven Redox-Potential, M_3 (Cu, Ag). M_1 -Metalle sind als Ionen (Fe, Cr, Fe) oder Präzipitate (MgF_2 , Ca_2 , Ba_2) zu stabil, um nach dem Herauslösen eine weitere Rolle bei der Aufreinigung zu spielen. M_2 -Metalle renukleieren auf der Si-Oberfläche und können einen weiteren MACE-Prozess induzieren, sind allerdings zu instabil, um tief zu ätzen und werden schnell wieder gelöst. M_3 -Metalle hingegen haben nicht nur eine katalytische Wirkung, sondern lösen sich zudem nur langsam und renukleieren schnell für weitere Ätzprozesse.

2.7 Vergleich unterschiedlicher Herstellungstechnologien

Die starke Performance-Abhängigkeit von den Herstellungsparametern bei RIE-prozessiertem schwarzem Silizium (Abschnitt 2.5), insbesondere der Lebensdauern der Minoritäts-

2.7 Vergleich unterschiedlicher Herstellungstechnologien

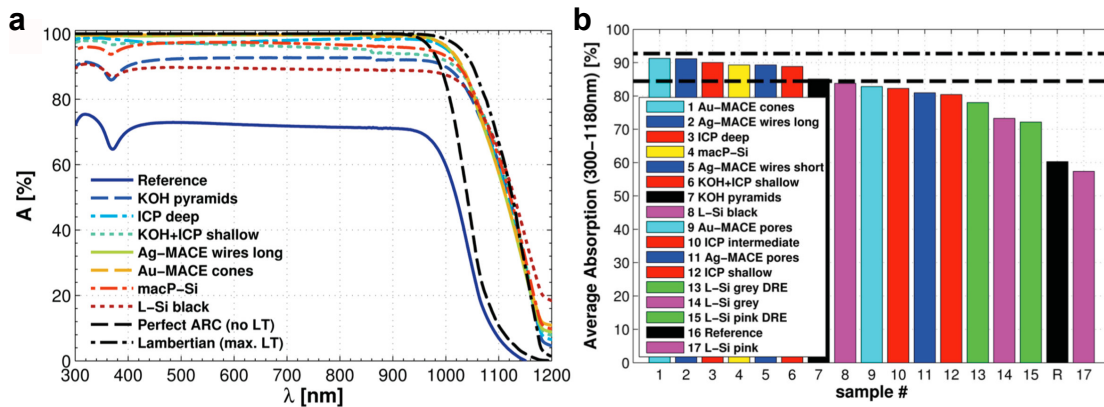


Abb. 2.6: (a) Absorptionsspektren $A(\lambda)$ und (b) gemittelte Absorption A_{avg} verschiedener schwarzer Silizium-Texturen. Mit *ICP* bezeichnete Proben sind mittels reaktivem Ionenätzen hergestellt, *macP-Si* mittels elektrochemischem Ätzen, *L-Si* mittels Laserpulsstrukturierung. Als Vergleichskurven bzw. -werte dienen eine untexturierte glatte Probe (*Reference*), eine KOH-Pyramid-Textur (*KOH pyramids*), perfekte Antireflexion (*Perfect ARC (no LT)*) und das Limit nach Yablonoivitch (*Lambertian (max. LT)*). Abbildungen aus [17] entnommen.

ladungsträger, lässt die Frage nach einem Vergleich unterschiedlicher Herstellungstechnologien aufkommen. Um diese Frage zu beantworten, haben wir uns in einer Kooperation mit weiteren Gruppen zusammen getan, die sich mit der Herstellung von schwarzem Silizium für photovoltaische Anwendungen befassen [17]. Jede dieser Gruppen hat sich auf eine jeweils andere Herstellungstechnologie spezialisiert: ICP-RIE (Friedrich-Schiller-Universität Jena und Fraunhofer IAP), MACE mit Ag- (Ag-MACE, Martin-Luther-Universität Halle-Wittenberg) und Au-Katalyst (Au-MACE, National Renewable Energy Laboratory NREL, USA), photoelektrochemisches Ätzen (*mac-P*, Martin-Luther-Universität Halle-Wittenberg) und Femtosekunden-Laserpuls-Prozessierung (*L-Si*, Fraunhofer HHI).

Typische Mikrostrukturen der unterschiedlichen Methoden sind in Abb. 2.3 beispielhaft gezeigt. Um Vergleichbarkeit zu gewährleisten, wurde allen Gruppen gleichartiges Basismaterial³ übergeben, das nach Texturierung an uns zurück gesendet wurde. Daraufhin haben wir die Proben per ALD mit 35 nm Al_2O_3 passiviert und die optische und optoelektronische Charakterisierung durchgeführt, d.h. Absorption $A(\lambda)$ und Minoritätsträger-Lebensdauer τ_{eff} gemessen. Als experimentelle Referenzen dienten eine untexturierte Probe und eine KOH-Textur (invertierte Pyramiden) welche auch Jahrzehnte nach ihrer Einführung als Industriestandard gilt [45,46].

$A(\lambda)$ von Proben mit der höchsten gemittelten⁴ Absorption A_{avg} ist in Abb. 2.6a gezeigt, A_{avg} aller Proben in Abb. 2.6b. Bis auf einen Ausreißer (Probe #17) weisen alle Proben deutlich erhöhte A_{avg} gegenüber der flachen Referenz auf, was in erster Linie auf die unterdrückte

³glatt polierte Si-Scheiben aus einer Charge, p-Typ, Dotierung $(1,00 \pm 0,25) \Omega \text{ cm}$, 250 μm Dicke, 6" Durchmesser

⁴Mittelung über den Spektralbereich $\lambda_0 = 300 - 1180 \text{ nm}$

2 Lichtmanagement mit Unordnung: Schwarzes Silizium

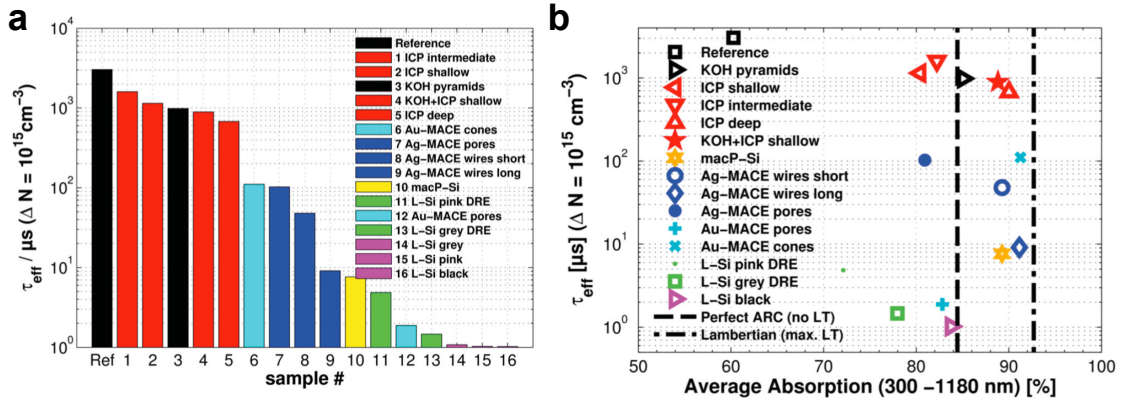


Abb. 2.7: (a) Lebensdauern τ_{eff} der unterschiedlichen schwarzes-Silizium-Texturen. (b) τ_{eff} aufgetragen gegen die gemittelte Absorption $A(\lambda)$. Abb. aus [17]

Reflexion zurück zu führen ist. Hierbei tun sich insbesondere die MACE-prozessierten Proben hervor mit $A(300 \text{ nm} < \lambda_0 < 950 \text{ nm}) > 99\%$. Nur sechs der 16 Proben absorbieren im Mittel mehr als die KOH-Textur. Diese zeichnen sich, wie auch die KOH-Textur selbst, durch ausgeprägtes *light trapping* für $\lambda_0 > 1000 \text{ nm}$ aus. Keine der Laser-prozessierten Proben konnte die KOH-Textur übertreffen.

In Abb. 2.7a sind die effektiven Lebensdauern τ_{eff} aufgetragen. Wie erwartet besitzt die untexturierte Referenzprobe mit $\tau_{\text{eff}} = 3,6 \mu\text{s}$ die höchste Lebensdauer. Alle ICP-RIE-Proben ($0,68 \text{ ms} < \tau_{\text{eff}} < 1,6 \text{ ms}$) sowie die KOH-Textur ($\tau_{\text{eff}} = 0,98 \text{ ms}$) zeigen ebenfalls sehr hohe Werte an. MACE-Texturen haben noch annehmbare $\tau_{\text{eff}} > 100 \mu\text{s}$, wenn die Strukturen keine allzu hohen Aspektverhältnisse aufweisen und beispielsweise kraterförmig sind, während für alle anderen Proben $\tau_{\text{eff}} < 10 \mu\text{s}$ ist. Auffällig sind die sehr geringen Lebensdauern der Laser-texturierten Proben.

Abb. 2.7b fasst die Ergebnisse zusammen und zeigt τ_{eff} aufgetragen gegen A_{avg} . Hier zeigt sich die Überlegenheit Al_2O_3 -passivierter ICP-RIE-Texturen in der Kombination aus langen Lebensdauern, fast auf dem Niveau der unprozessierten Probe, gepaart mit einer Absorption, die höher sein kann als jene der KOH-Textur. Das gute Abschneiden der ICP-RIE-Texturen macht diese Herstellungstechnologie insbesondere interessant für den Fall zukünftiger dünner, auch ultradünner ($5 - 50 \mu\text{m}$) c-Si-Solarzellen, wenn die KOH-Texturierung nicht mehr anwendbar ist. Ähnliches gilt für den MACE-Prozess. Mit hoher Absorption und noch annehmbaren Lebensdauern ist dieser Prozess ebenfalls ein potentieller Kandidat für ultradünne Solarzellen. Die Laser-Prozessierung, zumindest in der hier verwendeten Form, scheint aufgrund ihres nur mäßigen Abschneidens bzgl. A_{avg} und vor allem sehr kleinen τ_{eff} weniger geeignet für die Texturierung für photovoltaische Anwendung.

3 Lichtmanagement mit Ordnung: Gitter und photonische Kristalle

3.1 Einführung

Geht man von einer plan-parallelen Absorberschicht als vereinfachtes Modell für eine Solarzelle aus, ist die größte Lichtwegverlängerung offensichtlich dann erreicht, wenn das Licht im Absorber parallel zu den Grenzflächen propagiert. Für senkrechten Lichteinfall bedeutet dies eine Propagationsrichtungsänderung von 90° . Solch große Änderungen lassen sich durch diffraktive Strukturen wie Gitter erreichen, also Strukturen, die eine hohe Ordnung aufweisen. Ein möglicher Lichtpfad sieht folgendermaßen aus (siehe auch Abb. 3.1): Sonnenlicht tritt in den Absorber ein, durchquert diesen und trifft auf ein rückseitig angebrachtes Gitter. Hier wird es zurück reflektiert, aber es findet Beugung in einen Winkel statt, der vom Lot aus gesehen größer ist als der Einfallswinkel, so dass ein längerer Weg bis zur Vorderseite zurückgelegt wird. Dort trifft das Licht unter einem Winkel größer als der Winkel der Totalreflexion θ_{tot} auf, wird also unter demselben Winkel wieder zum Rückseitengitter reflektiert. Dort angekommen kann das Licht unter gleichem Winkel reflektiert werden und wieder Totalreflexion erfahren oder, da Reziprozität der Lichtwege gilt, auch in den Winkel der ersten Durchquerung gebeugt und an der Vorderseite entweder zurück reflektiert oder transmittiert werden und die Solarzelle wieder verlassen.

Gitter scheinen offensichtlich für die Absorptionserhöhung durch Lichtwegverlängerung geeignet. Um die Antireflexion von der Lichtwegverlängerung zu entkoppeln, werden sie meist

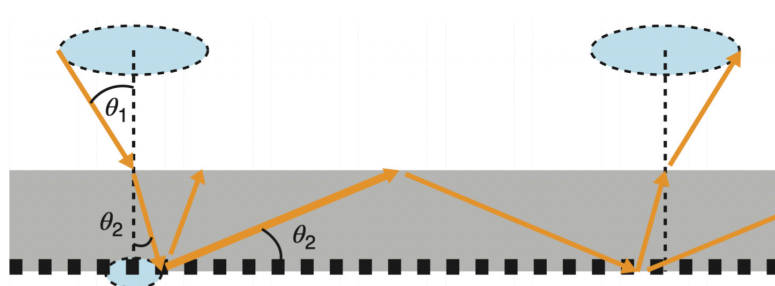


Abb. 3.1: Möglicher Lichtpfad für eine Solarzelle mit Rückseitengitter. Abb. aus [29]

3 Lichtmanagement mit Ordnung: Gitter und photonische Kristalle

auf der Rückseite des Absorbers implementiert und müssen spektral angepasst werden auf Wellenlängen, die während des ersten Durchgang nicht absorbiert wurden [5,6,96–104]. In kristallinen Silizium-Solarzellen trifft dies auf den Spektralbereich nahe der Bandkante von Silizium bei $\lambda_0 = 1150$ nm zu. Je dünner der Absorber ist, desto größer wird der Bereich, was insbesondere für ultradünne c-Si-Solarzellen mit Dicken < 50 μm und den wesentlich dünneren Dünnschicht-Solarzellen, z.B. CIGSe-Solarzellen, zutrifft.

Eine korrekte Bestimmung der potentiellen optischen Wegverlängerung α_{opt} berücksichtigt die Divergenz Θ des Sonnenlichts durch Erhaltung der Étendue [100,105,106]. Peters *et al.* haben für diesen Fall

$$\alpha_{\text{opt}} = \frac{2n\Theta}{1 - \cos\Theta} \quad (3.1)$$

hergeleitet und für Sonnenlicht nach dem Durchgang durch die Erdatmosphäre mit $\Theta_c \approx 0,44$ mrad ergibt sich für einen Siliziumabsorber $\alpha_{\text{opt}} \approx 318$ [106]. Dies zeigt das hohe Potential diffraktiver Strukturen auf. Jedoch muss berücksichtigt werden, dass dieser Wert nur für eine Wellenlänge λ Gültigkeit besitzt. Die oben angesprochene spektrale Breite und die Tageszeitabhängigkeit des Lichteinfalls limitieren das auf den ersten Blick hohe Potential von diffraktiven Strukturen, da Beugung am Gitter (Gitterkonstante a) stark Wellenlängen- und Einfallswinkel-abhängig ist. Dies wird durch die Gittergleichung beschrieben,

$$a(\sin\theta_{\text{in}} - \sin\theta_m) = m\lambda \quad (3.2)$$

(Einfallswinkel bzw. Ausfallswinkel θ_{in} und θ_m , Beugungsordnung m , Wellenlänge im Material λ), welche einen Spezialfall der Bragg- bzw. im reziproken Raum der Laue-Bedingung

$$\mathbf{k}_{\text{in}} - \mathbf{k}_m = m\mathbf{G} \quad (3.3)$$

(einfallender bzw. gebeugter Wellenvektor \mathbf{k}_{in} und \mathbf{k}_m , reziproker Gittervektor \mathbf{G}) darstellt [44].

Für aktuelle c-Si-Solarzellen mit typischen Absorberdicken von $W \approx 200$ μm konnte noch kein auf Gitterbeugung basierendes Konzept überzeugen im Vergleich zu Konzepten, die auf diffuse Streuung (schwarzes Silizium) oder geometrische Optik (Pyramiden) basieren und sich dem Yablonovitch-Limit annähern. Beugungsbasierte Konzepte koppeln das einfallende Lichts mit Moden der Absorberschicht. Die geringstmögliche Dicke der Schicht ist damit durch das Monomodens-Regime bestimmt. Von theoretischer Seite scheint das $4n^2$ -Limit in diesem Regime zu schlagen zu sein [107], ein experimenteller Nachweis steht noch aus. Ein Ansatz für noch geringere Schichtdicken stellt die Entkopplung von Absorber- und lichtführender Schicht dar.

3.2 Großflächige Rückseitengitter für ultradünne c-Si Solarzellen

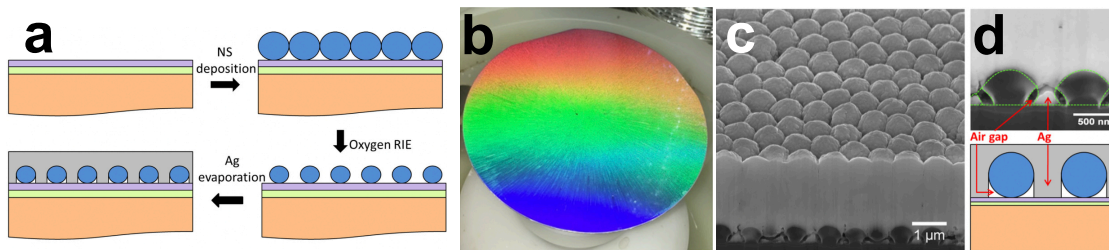


Abb. 3.2: Prozesskette für die Herstellung des Rückseitengitters. (b) Photo einer 4"-Si-Scheibe nach Auskristallisation der Nanokugeln zu einem hexagonalen Gitter. (c) REM-Querschnittsaufnahme der finalen Struktur. (d) REM-Nahansicht und Skizze. Abb. aus [6]

3.2 Großflächige Rückseitengitter für ultradünne c-Si Solarzellen

Jeder in Frage kommende nanophotonische Ansatz für das Lichtmanagement in Solarzellen muss unbedingt den Einfluss auf die elektronische Oberflächenrekombination berücksichtigen. Der Absorber bzw. die Absorberoberfläche sollte im besten Fall gar nicht modifiziert werden, weder strukturell (Defekte) noch geometrisch (Oberflächenvergrößerung), vgl. z.B. Abschnitt 2.4. Um diesem Umstand Rechnung zu tragen, wurde in einer Arbeit zusammen mit der UNSW (Sydney, Australien) ein Gitter als externe Struktur auf eine glatte, zuvor passivierte, ultradünne (30 µm Dicke) c-Si-Scheibe aufgebracht [6]. Es fand also keine Oberflächenvergrößerung an der c-Si-Oberfläche statt. Für die Gitterherstellung wurde Nanokugel-Lithographie (*nanosphere lithography* NSL) gewählt [108–110]. NSL ist eine kosteneffektive und verhältnismäßig simple Methode für die großflächige Fabrikation von geordneten Nanopartikel-Feldern und damit interessant für die Integration in Solarzellen [6,103,104].

Abb. 3.2a zeigt schematisch die Prozessschritte für die Gitterherstellung. Eine monodisperse Lösung mit Polystyrol-Kugeln wird auf eine (mittels $\text{Al}_2\text{O}_3/\text{Si}_3\text{O}_4$ -Schichtstapel passivierte) ultradünne, glatte Si-Scheibe aufgeschleudert. Beim Trocknen ordnen sich die Kugeln hexagonal an mit einer Gitterkonstante a , die durch den Kugeldurchmesser D bestimmt ist. Mit einer nachfolgenden Sauerstoffplasma-Behandlung lässt sich D nachträglich verkleinern. Im letzten Schritt wurde ein 2,5 µm dicker Silberfilm aufgebracht. Dieser erhöht die Reflexion des Gitters und dient in einer Solarzelle auch als elektrischer Rückkontakt.

Für die Parameter a und D wurden im Vorfeld numerische Berechnung durchgeführt. Eine 30 µm dicke Si-Scheibe vollständig in rigorose numerischen Rechnungen einzubeziehen ist rechen- und zeitaufwendig, weswegen hier rigorose und geometrische Ansätze kombiniert wurden. Die optische Antwort des Rückseitengitters wurde mittels der FEM-Methode (Softwarepaket *JCMsuite* [111]) berechnet. Hierbei reicht es, eine Einheitszelle des Gitters mit periodischen Randbedingungen zu berücksichtigen, die nur wenige 100 nm ins Si hineinreicht.

3 Lichtmanagement mit Ordnung: Gitter und photonische Kristalle

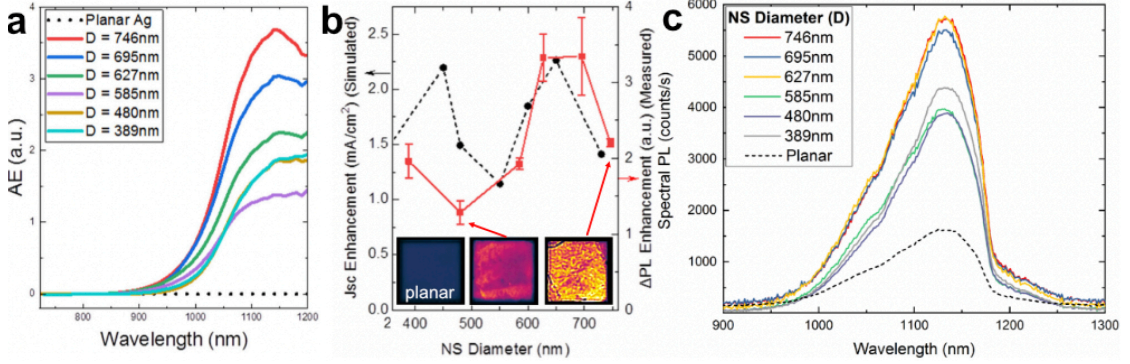


Abb. 3.3: (a) Experimentell gemessene Absorptionsverstärkung AE, (b) berechnete Kurzschlussstromerhöhung Δj_{ph} und gemessene flächengemittelte (1 cm^2) Photolumineszenz-Erhöhung ΔP_L und (c) gemessene spektral aufgelöste Photolumineszenz von ultradünnen Si-Pseudozellen mit Rückseitengitter für verschiedene Kugeldurchmesser D bei konstanter Gitterkonstante $a = 747 \text{ nm}$. Der größtmögliche Kugeldurchmesser ist durch die Gitterkonstante begrenzt. Abb. aus [6]

Die unstrukturierte Vorderseite lässt sich allein mit Fresnel-Gleichungen berechnen. Vorder- und Rückseite sowie die Si-Scheibe dazwischen können dann mit dem Softwarepaket OP-TOS effizient *inkohärent* gekoppelt werden, um die Absorption $A(\lambda)$ des Systems zu bestimmen [112]. Mit $A(\lambda)$ lässt sich dann die photogenerierte Stromdichte

$$j_{ph} = e \int \frac{\lambda}{hc} A(\lambda) I_{AM1.5}(\lambda) d\lambda \quad (3.4)$$

bestimmen, mit der Elementarladung e , Plancksches Wirkungsquantum h und dem solaren Bestrahlungsspektrum $I_{AM1.5}$. Unter der idealisierten Annahme, dass Rekombination vollständig unterdrückt ist, d.h. $\text{IQE}(\lambda) = A(\lambda)$ (interne Quanteneffizienz IQE), entspricht die maximal erreichbare Kurzschlussstromdichte der Photostromdichte, $j_{sc} = j_{ph}$.

Abb. 3.3a zeigt die experimentell gemessene Absorptionsverstärkung

$$\text{AE}(\lambda) = \frac{A(\lambda) - A_{\text{ref}}(\lambda)}{A_{\text{ref}}(\lambda)} \quad (3.5)$$

(Absorption $A_{\text{ref}}(\lambda)$ der Referenzprobe ohne Rückseitengitter) der Pseudozellen (Solarzellen ohne elektrische Kontakte) für $a = 746 \text{ nm}$. Deutlich ist der Effekt des Rückseitengitters als erhöhte Absorption mit bis zu $\text{AE}_{\text{max}} = 3,7$ für $\lambda > 900 \text{ nm}$ zu erkennen. Die Kugelgröße beeinflusst die Beugungseffizienzen und damit die Absorption. Allerdings kann ein Teil der gemessenen Absorption parasitär sein, also statt im Silizium z.B. im Silber stattfinden. Insbesondere auf strukturierten Metalloberflächen lassen sich resonant Oberflächenplasmon-Polaritonen (*surface plasmon polaritons* SPPs) mit hoher parasitärer Absorption anregen [113–116].

Um parasitäre von nützlicher Absorption zu trennen, wurden Photolumineszenz-Messungen

3.3 Rückseitengitter für CIGSe-Dünnschicht-Solarzellen

(PL) durchgeführt. Bei erhöhter Absorption werden Elektron-Loch-Paare vermehrt strahlend rekombinieren, also zu einem erhöhten PL-Signal beitragen, allerdings nur, wenn andere Rekombinationsmechanismen wie z.B. Oberflächendefekt-Rekombination nicht dominieren. Wird das emittierte Licht selektiv auf die Emission von Silizium gefiltert, lassen sich so Aussagen zu Absorptionserhöhung sowie Rekombination treffen [117,118].

Abb. 3.3b zeigt die Erhöhung des PL-Signals ΔPL zusammen mit der berechneten Erhöhung des Photostroms Δj_{ph} . Eine Übereinstimmung der Trends ist zu erkennen. Spektral aufgelöste PL-Messungen $PL(\lambda)$ sind in Abb. 3.3c dargestellt. Die Emission hat ihr Maximum bei $\lambda = 1130$ nm, was typisch für Si ist und zeigt, dass die Ursache von ΔPL in der Absorptionserhöhung in Si zu suchen ist. Aus dem PL-Signal lässt sich AE unabhängig bestimmen. Mit

$$PL(\lambda) = BB(\lambda) \cdot A(\lambda) \cdot e^{\frac{V}{kT}} \quad (3.6)$$

(Schwarzkörperemission $BB(\lambda)$, Quasi-Fermi-Niveau-Abstand V) [119], ist $AE(\lambda) = \Delta PL / PL_{\text{planar}}$. Die so bestimmte Absorptionsverstärkung ist in guter Übereinstimmung mit den in Abb. 3.3a gezeigten, ebenfalls mit Werten bis zu $AE_{\text{max}} = 3,7$. Die lässt den Schluss zu, dass die Prozessschritte für die Fabrikation des Rückseitengitters keinen bis wenig schädigenden Einfluss auf die Si-Grenzfläche hat. NSL-basierte Rückseitengitter besitzen demnach durchaus das Potential, Anwendung für die Wirkungsgraderhöhung von ultradünnen c-Si-Solarzellen zu finden.

3.3 Rückseitengitter für CIGSe-Dünnschicht-Solarzellen

Auch in Dünnschicht-Solarzellen sind Lichtmanagement-Konzepte nötig. Zwar sind die verwendeten Materialien wie z.B. amorphes Silizium oder Kupfer-Indium-Gallium-Diselenid (CIGSe) direkte Halbleiter mit entsprechend kürzeren Absorptionslängen, jedoch sind ihre Filmdicken meist derart dünn, 100 nm bis wenige μm , dass auch in diesen das Sonnenlicht nicht beim ersten Durchgang vollständig absorbiert wird. Die Ausgangsmaterialien können verhältnismäßig teuer sein, z.B. Indium in CIGSe-Solarzellen, so dass die Verwendung noch dünnerer Absorberschichten zu einer deutlichen Kosteneinsparung führt, wenn die Materialeffizienz entsprechend gesteigert werden kann.

In einer Zusammenarbeit mit der Photovoltaik-Gruppe an der MLU haben wir eine neue nanophotonische Rückseitenstruktur in eine CIGSe-Solarzelle integriert [5]. Das Ziel dieser Arbeit war, die Dicke des Absorbers auf weniger als ein Viertel zu reduzieren, von 2,6 μm auf 600 nm, den Wirkungsgrad jedoch auf gleichbleibendem Niveau zu halten. Hierfür wurden zwei Lichtmanagement-Ansätze kombiniert. Statt eines Molybden-Rückkontakts und-reflektors wurde ein Al/Indium-Zinnoxid (ITO)-Schichtsystem verwendet. Mo ist zwar kompatibel mit CIGSe und deswegen als Rückkontakt etabliert, jedoch ist seine Reflektivität ge-

3 Lichtmanagement mit Ordnung: Gitter und photonische Kristalle

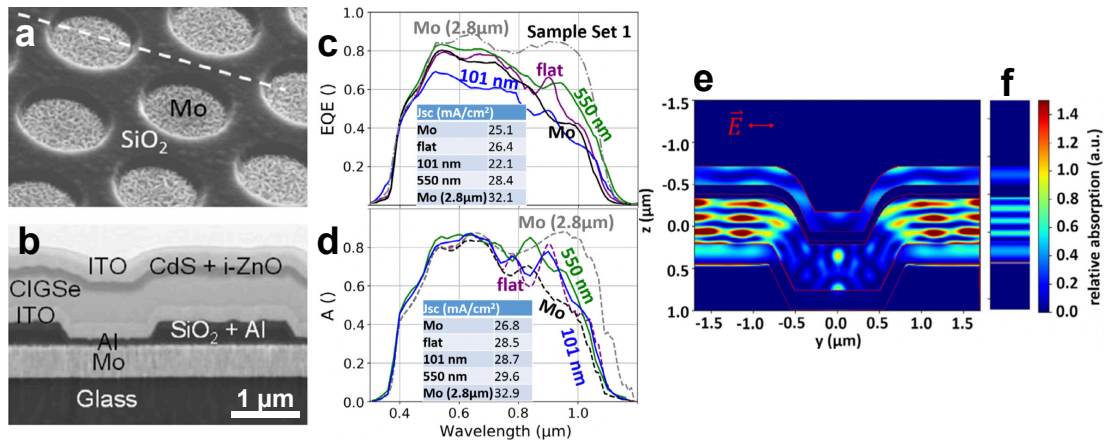


Abb. 3.4: (a) REM-Aufnahme eines strukturierten Substrats (197 nm Strukturhöhe, $a = 2 \mu\text{m}$) vor Aufbringen der restlichen Schichten. (b) Querschnitt einer fertigen CIGSe-Dünnschicht-Zelle. (c) Gemessene EQE und (b) berechnete Absorption von fabrizierten CIGSe-Solarzellen mit 600 nm dicker Absorberschicht und flachem Mo-Rückkontakt, flachem Al/ITO-Rückkontakt, strukturiertem Al/ITO-Rückkontakt mit 101 nm bzw. 550 nm Strukturhöhe und flachem Mo-Rückkontakt und 2,8 μm Absorberschichtdicke. (e) Berechnete lokale Absorption einer strukturierten Zelle (Querschnitt durch eine Einheitszelle) und einer (f) flachen Zelle. Abb. aus [5]

ring und die Rekombination an der Mo/CIGSe-Grenzfläche hoch [120–122]. Al als Rückkontakt verspricht mit besseren Reflexions- und Absorptionseigenschaften eine erhöhte Photostromgeneration, allerdings muss eine leitfähige ITO-Schicht als Diffusionsbarriere dienen, da es ansonsten zu unerwünschten chemischen Reaktionen mit der CIGSe-Schicht kommen kann. Im Weiteren wurde der Rückkontakt periodisch strukturiert, um durch Gitterbeugung Lichtwegverlängerung und damit höhere Absorption zu bewirken.

Anders als bei c-Si-Solarzellen wird der Absorber hier jedoch in der Regel auf ein Substrat aufgebracht, auf das vorher der Rückkontakt appliziert wurde. Damit ist ein Vorgehen wie im Beispiel des vorherigen Abschnitts, d.h. eine nachträgliche Integration des Gitters mit einer flachen Absorberschicht, nicht möglich. Stattdessen muss das Substrat bzw. der Rückkontakt vorstrukturiert und dann die Absorberschicht darauf deponiert werden. In dieser Arbeit erfolgte die Strukturierung mittels Laserinterferenz-Lithographie auf einem photoempfindlichen Lack und nachfolgendem Lift-off einer SiO_2 -Schicht. Abb. 3.4a zeigt beispielhaft ein derart strukturiertes Substrat, Abb. 3.4b zeigt den Querschnitt einer fertigen Zelle.

Die experimentell bestimmte externe Quanteneffizienz (EQE) verschiedener fabrizierter Zellen mit einer CIGSe-Absorberschichtdicke von 600 nm ist in Abb. 3.4c gezeigt. Der Wechsel von Mo zu Al/ITO führt zu einer breitbandig erhöhten EQE für $\lambda > 600 \text{ nm}$, wie der Vergleich der beiden flachen Zellen mit verschiedenen Rückreflektoren zeigt (vgl. schwarze und violette Kurven). Der Photostrom j_{sc} wird um 5% gesteigert. Mit Strukturierung (550 nm Struktur-

3.4 Effiziente Phasengitter für Lichtmanagement im Solarmodul

höhe, grüne Kurve) erfährt j_{sc} eine weitere Erhöhung um rund 8% (13% im Vergleich zum Mo-Rückkontakt). Damit konnte hier durch ein nanophotonisches Lichtmanagement-Konzept in Kombination mit angepasstem Rückseitenmaterial ein j_{sc} erreicht werden, der noch 88% einer CIGSe-Solarzellen mit 2,8 μm Absorberschichtdicke entspricht (graue Kurve).

In Abb. 3.4e und f ist die mittels *Finite Difference Time Domain*-Methode (FDTD) berechnete lokale Absorption,

$$A(\mathbf{r}) = \text{Im}(\mathbf{E}^*(\mathbf{r})\mathbf{D}(\mathbf{r})), \quad (3.7)$$

mit und ohne Strukturierung gezeigt. Im Vergleich zum flachen Fall sind für den strukturierten Fall deutlich lokale Absorptionserhöhungen zu erkennen. Diese sind auf die Anregung von Wellenleitermoden in dem Schichtstapel der Solarzelle zu erklären [123,124], welche erst durch die Einführung der periodischen Struktur möglich werden. Im flachen Fall können keine Wellenleitermoden angeregt werden.

In Abb. 3.4d sind berechnete Absorptionskurven dargestellt. Diese sind im Wesentlichen im Einklang mit dem Experiment, weisen allerdings meist höhere Werte auf, so ergibt beispielsweise die Strukturierung inklusive Al/ITO-Rückkontakt noch 90% des j_{sc} der Zelle mit 2,8 μm dicker CIGSe-Schicht. Die Abweichungen zwischen Simulation und Experiment stammen vermutlich aus zusätzlicher parasitärer Absorption im Al/ITO-Schichtstapel sowie nicht berücksichtigter Rekombination in diesem. Für ein optimiertes Wirken des strukturierten Rückkontakts ist eine materialeitige Anpassung des Schichtstapels sowie der geometrischen Gitterparameter notwendig.

3.4 Effiziente Phasengitter für Lichtmanagement im Solarmodul

Nicht nur auf der Ebene der Solarzelle können Lichtmanagement-Konzepte Anwendung finden, sondern auch auf der Ebene des Solarmoduls [125,126]. Hierbei soll Sonnenlicht, das auf optisch nicht-aktive Flächen trifft, z.B. die Frontkontakte der Solarzellen oder die Fläche zwischen den Solarzellen, auf die absorbierenden Flächen abgelenkt werden, siehe Abb. 3.5a. Diese Fläche kann z.B. bei gängigen c-Si-Solarmodulen, je nach Aufbau des Moduls, einen Anteil von 5 – 10% der Gesamtfläche einnehmen.

In einer Zusammenarbeit mit der Hochschule Anhalt und dem Fraunhofer CSP haben wir in das Modulglas eingeschriebene Phasengitter für das Lichtmanagement im Solarmodul untersucht [13,127]. Phasengitter weisen wie alle periodischen Strukturen Gitterbeugung auf, sie zeichnen sich allerdings dadurch aus, dass der Ursprung der interferierenden Lichtwellen nicht auf Streuung einer jeden Einheitszelle beruht, sondern auf Laufzeitunterschiede beim

3 Lichtmanagement mit Ordnung: Gitter und photonische Kristalle

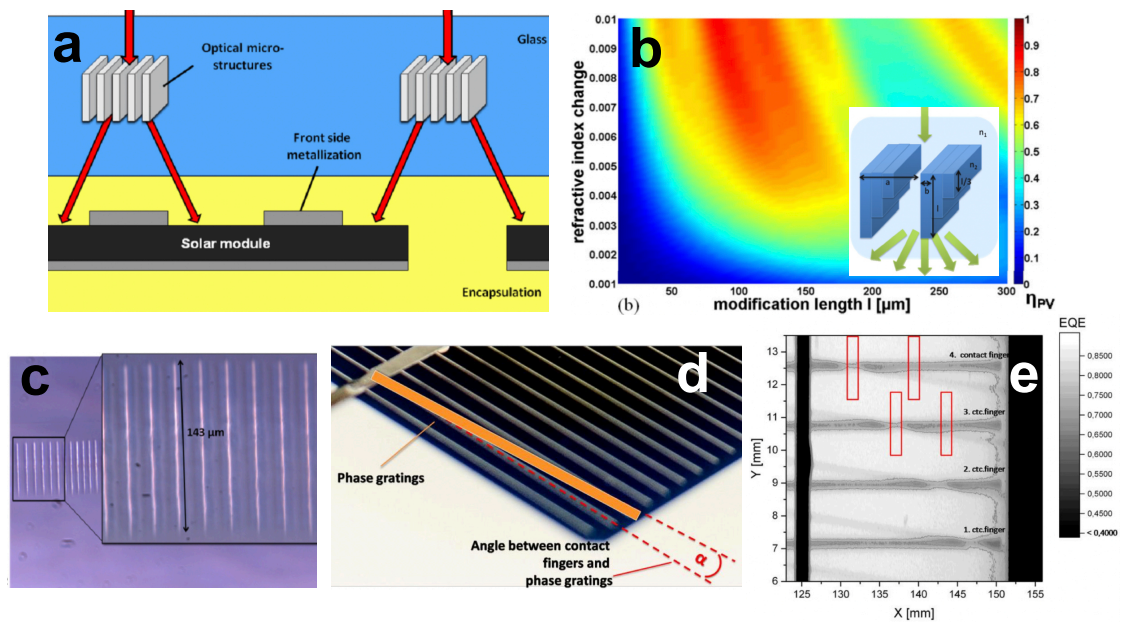


Abb. 3.5: (a) Funktionsweise von Phasengittern für das Lichtmanagement im Solarmodul. (b) Berechnete gemittelte Beugungseffizienz η_{PV} in Abhängigkeit von Tiefe und Brechungsindexkontrast lasereingeschriebener Phasengitter. Die Einheitszelle ist asymmetrisch aufgebaut (siehe Inset). (c) Phasenkontrast-Mikroskopie eines laserbehandelten Glasses (Querschnitt). (d) Schema zur Ausrichtung der Phasengitter bzgl. der Solarzelle. (e) Ortsaufgelöste EQE-Messungen eines Minimoduls mit eingeschriebenen Phasengittern ($\lambda = 405 \text{ nm}$). Abb. aus [13,127].

Durchlauf durch diese. Die Laufzeitunterschiede entstehen in der Regel durch eingebrachte geringe Brechungsindexunterschiede. Phasengitter operieren in Transmission, da ihre Reflexion aufgrund des geringen Indexkontrastes sehr klein ist. Damit eignen sie sich gut für die Integration in das Solarmodulglas oder das Solarzellen-Einkapselungsmaterial.

In dieser Arbeit wurden diffraktive Strukturen mittels fokussierten Femtosekunden-Laserpulsen in Modulglas eingebracht. Die hohe Energiedichte im Fokus generiert ein Elektronenplasma, welches permanente strukturelle Veränderungen nach sich zieht [128,129]. Größere SiO_2 -Verbände innerhalb des Glasses brechen auf, wodurch sich unter Bildung kleinerer Strukturen lokal Dichte und Brechungsindex erhöhen.

Das Phasenkontrast-Bild in Abb. 3.5c zeigt die strukturellen Veränderungen durch Laserpuls-Beschuss als längliche Kanäle mit Längen im Bereich von $130 - 150 \mu\text{m}$ und Durchmessern von $2 - 3 \mu\text{m}$. Sie befinden sich ca. $650 \mu\text{m}$ tief unter der Glasoberfläche. Durch Vergleich mit numerischen Rechnungen mittels *rigorous coupled-wave analysis* (RCWA) finden wir für unsere Strukturen $\Delta n \approx 0,6\%$. Durch gezieltes Setzen dieser Kanäle können cm^2 große Flächen mit Phasengittern in Glas eingeschrieben werden; auch kann die Einheitszelle zur Erhöhung der Beugungseffizienz ähnlich einem *blazed grating* asymmetrisch aufgebaut werden.

3.5 Sprühbeschichtung für die Herstellung 3D Photonischer Kristalle

Mit dem Ziel, dass die über den relevanten Spektralbereich¹ gemittelte akkumulierte Beugungseffizienz

$$\eta_{PV} = \frac{\int \eta_D(\lambda) d\lambda}{\int d\lambda}, \quad (3.8)$$

mit $\eta_D = \sum_m \eta_m$ ($m \neq 0$, Beugungseffizienz η_m), unter Berücksichtigung der technologischen Möglichkeiten, möglichst groß sein soll, konnten wir Parameter für ein Phasengitter ausmachen, das experimentell gemessene $\eta_{PV} = 77\%$ aufweist, d.h. 77% des einfallenden Lichts wird zur Seite abgelenkt. Dieses Phasengitter wurde in Solarmodulglas eingeschrieben und in ein Mini-Solarmodul integriert. Da eine entsprechende Vorrichtung fehlte, mit der das Phasengitter genau oberhalb der Kontaktfinger der Solarzelle ausgerichtet werden kann, wurde es mit einem Winkel von $\alpha = 5^\circ$ zu den Kontaktfingern hergestellt, um einen Überlapp zu garantieren, siehe Abb. 3.5d. Das Solarmodul wurde mit orts aufgelöster EQE vermessen, d.h. die Modulfläche wird mit einem Laserstrahl (Durchmesser ca. $150 \mu\text{m}$, λ einstellbar) abgerastert und der Kurzschlussstrom gemessen, siehe Abb. 3.5e. An den Positionen, an denen das Phasengitter über den Kontaktfingern steht (z.B. die beiden linken rot umrandeten Flächen), ist eine erhöhte EQE zu finden, was auf das seitliche Ablenken von Licht auf die aktive Fläche der Solarzelle zurückgeführt werden kann. Die weitere Auswertung der Messungen führt zu dem Ergebnis, dass für den Fall einer vollständigen und ausgerichteten Abdeckung aller Kontaktfinger eine relative Wirkungsgraderhöhung des Moduls von 1% zu erwarten ist.

3.5 Sprühbeschichtung für die Herstellung 3D Photonischer Kristalle

Dreidimensionale photonische Kristalle (*3D photonic crystals* 3DPC) [130,131], z.B. künstliche Opale, stellen eine weitere vielversprechende Materialklasse für das Lichtmanagement in Solarzellen dar. Zusätzlich zur Beugung von Gittern, die als 2D photonische Kristalle angesehen werden können, besitzen 3DPC komplexe Bandstrukturen im Volumen mit richtungsabhängigen Reflexions- und Transmissionseigenschaften, die für neuartige winkel- und frequenzselektive Filter oder Rückseitenstrukturen verwendet werden können [132–134].

Hervorgetan haben sich (invertierte) Opal-Strukturen aus sphärischen Kolloiden, da sie kosteneffektiv fabriziert werden können [135,136]. Allerdings ist ihre Herstellung sehr zeintensiv. Bei der sog. Tauchbeschichtung (*Dip coating*) wird ein Substrat in eine Kolloidlösung getaucht und langsam herausgezogen [137]. An dem Meniskus, der sich auf dem Substrat an der Lösung/Luft-Grenzfläche ausbildet, setzen sich die Kolloide, getrieben durch Kapillarkraft und Oberflächenspannung, selbstorganisiert auf dem Substrat ab und bilden

¹ $\lambda = 300 - 1100 \text{ nm}$

3 Lichtmanagement mit Ordnung: Gitter und photonische Kristalle

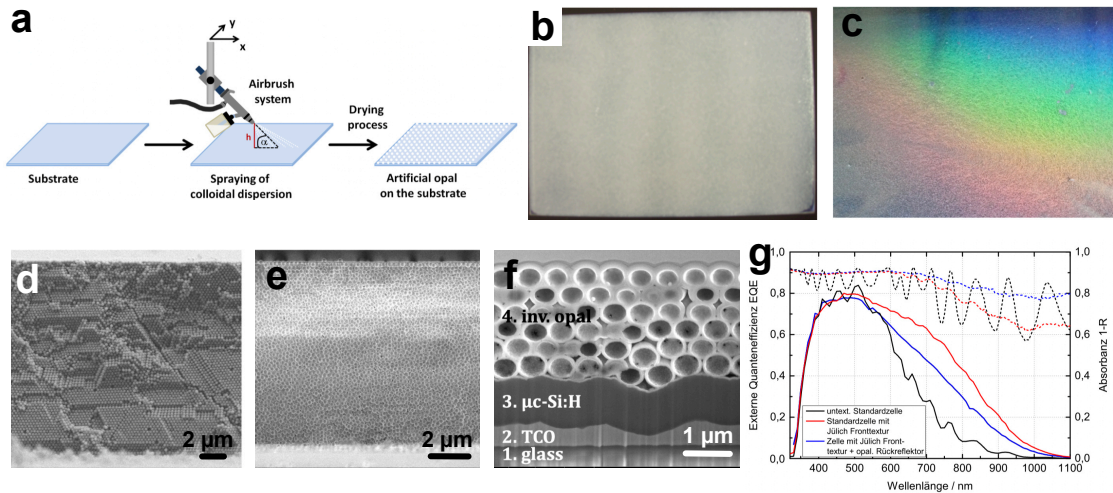


Abb. 3.6: (a) Schema zur automatisierten Sprühbeschichtung. (b) Photographie eines 10 cm × 15 cm Glassubstrats kurz nach Sprühbeschichtung und (c) nach Trocknung der Schicht (70 min). Die resultierenden kolloidalen Filme können je nach Herstellungsparameter (d) periodisch oder (e) amorph sein. Die Schichtdicke lässt sich ebenfalls einstellen, z.B. (f) nur wenige Lagen dick. Auch Deposition auf texturierten Substraten ist möglich, hier als Rückseitenstruktur für $\mu\text{c-Si}$ -Dünnschichtsolarzellen. (g) EQE (volle Kurven) und Absorption (gestrichelte Kurven) von $\mu\text{c-Si}$ -Dünnschichtsolarzellen: Untexturiert (schwarz), texturiert (rot), texturiert + 3DPC-Rückseitenkontakt (blau). Abb. aus [23,138,139].

dabei eine 3D periodische Struktur, den Opal. Aufgrund der geringen Ziehgeschwindigkeit ($\approx 1 - 10 \mu\text{m}/\text{min}$) werden beispielsweise mehrere Tage benötigt, um Flächen von der Größe eines handelsüblichen Mikroskopie-Objektträgers zu beschichten.

Wir haben ein Verfahren entwickelt, mit dem großflächig Opalstrukturen in deutlich kürzerer Zeit fabrizieren werden können [23]. Es basiert auf einer automatisierten Sprühbeschichtung des Substrats mit der Kolloidlösung in einer kontrollierten Umgebung. Während des Trocknungsvorgangs kristallisiert innerhalb ca. 1h ein großflächiger Opal aus, vgl. Abb. 3.6b-c. Der mikroskopische Mechanismus entspricht dabei dem der Tauchbeschichtung, allerdings besteht der Meniskus an allen Rändern des Substrats und überstreicht während der Trocknungszeit die gesamte Substratfläche aufgrund der flächigen Evaporation des Lösungsmittels. Durch Variation der Bestandteile der versprühten Lösung lässt sich die Dicke des resultierenden Opals einstellen, auch ist die Beschichtung texturierter Substrate möglich, vgl. Abb. 3.6d-f.

In einer Zusammenarbeit mit dem Forschungszentrum Jülich (FZ Jülich) haben wir Sprühbeschichtung verwendet, um invertierte Opale als Rückseitenstrukturen in Dünnschicht-Solarzellen aus mikrokristallinem Silizium ($\mu\text{c-Si}$) zu integrieren [138,139]. Hierbei wurde ein invertierter Opal auf der Rückseite mit einem nassgeätzten Substrat auf der Vorderseite kombiniert. Ziel war, das ungeordneten Substrat mit seinen streuenden sowie antireflektiven Ei-

3.5 Sprühbeschichtung für die Herstellung 3D Photonischer Kristalle

genschaften zu erhalten, während der 3D photonische Kristall Lichtwegverlängerung durch Beugung bei gleichzeitiger Reflexion aufgrund seiner photonischen Bandlücke bereitstellt. Da die Absorberschicht mit 1 μm Dicke sehr dünn ist, bleibt die Textur durch die Schicht hindurch erhalten (siehe Abb. 3.6f). Eine einfache Gitterstruktur lässt sich auf diese Struktur nicht anwenden, da die Rauigkeit die benötigten räumlichen Korrelationen des Gitters zerstört. Opale aus unserer Sprühbeschichtung jedoch gleichen die Rauigkeit innerhalb 2-3 Kugellagen aus und bilden dann eine periodische Kristallstruktur aus. Absorptionsmessungen (Abb. 3.6g), gestrichelte Kurven) zeigen, dass die Absorption im Vergleich zu einer glatten und auch einer texturierten Solarzelle, die als Stand der Technik gilt, erhöht ist, d.h. das Lichtmanagement wurde durch unsere Rückseitenstruktur verbessert. Eine erhöhte EQE (durchgezogene Linien) und damit auch Wirkungsgrad konnte jedoch nicht gezeigt werden. Da der invertierte Opal auch die Funktion als elektrischer Rückkontakt inne hat, bestand dieser aus ALD-deponiertem leitfähigen Al:ZnO, wurde im Rahmen der Arbeit jedoch nicht dahingehend optimiert und konnte damit nicht mit dem technologisch hoch-optimierten $\mu\text{-Si/Al:ZnO/Ag}$ -Rückkontakt des FZ Jülich konkurrieren.

4 Lichtmanagement mit geordneter Unordnung: Hyperuniformität

4.1 Einführung

Kapitel 2 hat sich mit schwarzem Silizium beschäftigt, dessen nadelförmige Mikrostruktur zufällig angeordnet ist und deshalb in einem hohen Maß diffuse Lichtstreuung aufweist. Kapitel 3 behandelt periodische Strukturen, an welchen Lichtstreuung in wenige, präzise festgelegte Richtungen erfolgt, den Beugungsordnungen. Die Streuung zufälliger Strukturen ist spektral breitbandig, während periodische Strukturen sehr schmalbandig operieren. Damit sind die Möglichkeiten, Lichtstreuung nach Bedarf zu steuern, stark eingeschränkt.

Wie eine solche Streuung beispielsweise an einer Rückseitenstruktur für die Lichtwegverlängerung in Solarzellen aussehen könnte, ist in Abb. 4.1 skizziert. Hierfür ist es instruktiv, in den reziproken Raum zu wechseln und die Wellenvektoren \mathbf{k} des gestreuten Lichts zu veranschaulichen [9,140,141]. Abb. 4.1b zeigt $k_{||}$, d.h. den Anteil des gestreuten Wellenvektors parallel zur Absorberschicht. Lichtstreuung in den Bereich A ($0 \leq k_{||} < k_{\text{tot}}$) fällt unter einem Winkel kleiner als der Winkel der Totalreflexion θ_{tot} (sog. Emissionskegel) auf die Vordersei-

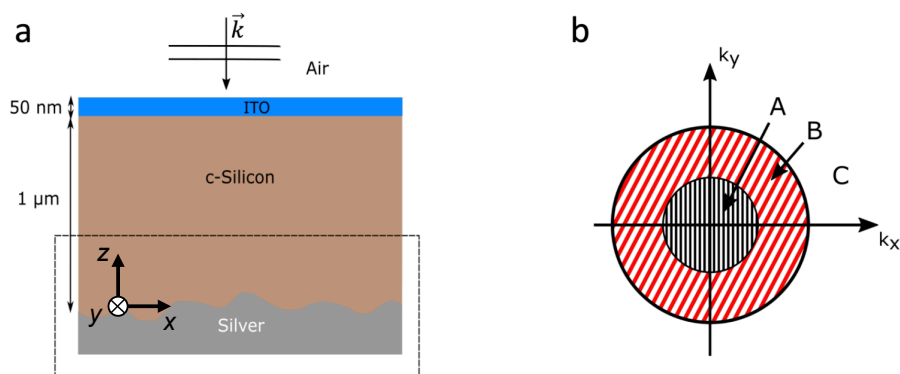


Abb. 4.1: (a) Allgemeine Rückseitenstruktur für die Lichtwegverlängerung in einer Solarzelle. (b) Laterale Komponente (parallel zur Grenzfläche) des gestreuten Wellenvektors $\mathbf{k}_{||} = (k_x, k_y)$. Streuung in den Emissionskegel A kann die Solarzelle wieder verlassen, im Bereich B findet Totalreflexion statt und in Bereich C wird \mathbf{k} evaneszent. Abbildungen aus [9].

4 Lichtmanagement mit geordneter Unordnung: Hyperuniformität

te ein, kann dort also wieder die Solarzelle verlassen. Streuung in Winkeln größer als θ_{tot} sind durch den Bereich B ($k_{\text{tot}} \leq k_{\parallel} \leq k_{\text{in}}$ mit $k_{\text{in}} = n \frac{\omega}{c_0}$) gekennzeichnet. Dieses Licht wird nicht nur aufgrund Totalreflexion an der Vorderseite vollständig zurück reflektiert, sondern erfährt auch eine größere Lichtwegverlängerung. In Bereich C ($k_{\parallel} > k_{\text{in}}$) können Lichtmoden angeregt werden, die evaneszent an die Rückseite gebunden sind und sollten gemieden werden. Für metallisch Strukturen beispielsweise können hierdurch Oberflächenplasmon-Polaritonen (SPPs) angeregt werden, die signifikante parasitäre Absorption aufweisen können [141–144]. Das Ziel ist demnach, ausschließliche oder zumindest verstärkte Streuung im Bereich B zu erreichen.

Lichtstreuung lässt sich als Impulsübertrag eines Objekts wie z.B. einer Textur auf das einfallende Licht auffassen [44]. Wie das Licht seinen Wellenvektor \mathbf{k} ändert hängt dabei von den Raumfrequenzen \mathbf{q} ab, welche die Textur bereitstellt, $\mathbf{k}_{\parallel} = \mathbf{k}_{\text{in},\parallel} + \mathbf{q}$. Ein erster Ansatz, Streuung in Bereich B zu erreichen, ist demnach eine Struktur, die ebenfalls B abdeckt. In einer Darstellung wie Abb. 4.1b deckt eine zufällige Textur alle Bereiche homogen ab. Im Gegensatz dazu nehmen die Beugungsordnungen einer periodischen Textur nur einen verschwindend kleinen Teil ein¹, der durchaus ganz in B liegen kann, allerdings mit starker Wellenlängen-Abhängigkeit. Zwischen diesen beiden zueinander diametral stehenden Strukturtypen, *völlige Unordnung* (zufällig) und *strenge Ordnung* (periodisch), liegt der weite und noch wenig erforschte Bereich der *korrelierten Unordnung* vor, welcher in dem vorliegenden Kapitel behandelt wird. Strukturen korrelierter Unordnung erfahren ein stark zunehmendes Interesse, da ihnen das Potential zugeschrieben wird, eine neuartige Materialklasse zu bilden [1,48,145–150].

Bisherige ungeordnete Materialien sind in der Regel nur wenig korreliert bzw. die jeweilige Herstellungstechnologie kann gewisse Korrelationen einbringen. Nasschemische geätzte Substrate wie die sog. Asahi-U- oder die Jülich-Textur weisen für Dünnschicht-Solarzellen gute Streueigenschaften auf [151]. Ein Nachteil bisheriger Verfahren ist jedoch, dass Variation der Unordnung nur in sehr beschränktem Maße möglich ist, weshalb korrelierte Unordnung bisher nur unzureichend untersucht wurde und vieles dafür spricht, dass das Potential streuender Oberflächen noch nicht ausgeschöpft ist.

Wird Korrelation gezielt verwendet, eröffnen sich neue Wege, das Fourier-Spektrum einer Struktur (ihr Erscheinen im reziproken Raum) zu manipulieren und damit dem Ziel, Lichtstreuung maßzuschneidern, entscheidend näher zu kommen. So liessen sich beispielsweise die Vorteile periodischer Strukturen wie intensitätsstarke (aber schmalbandige) Beugung mit den Vorteilen ungeordneter Strukturen wie spektrale breitbandige (aber intensitätsschwache) Streuung und Robustheit in der Fabrikation, zusammen bringen. Derartige Eigenschaft-

¹Für ein unendlich ausgedehntes perfektes Gitter sind die Beugungsordnungen Dirac-Spitzen im k -Raum

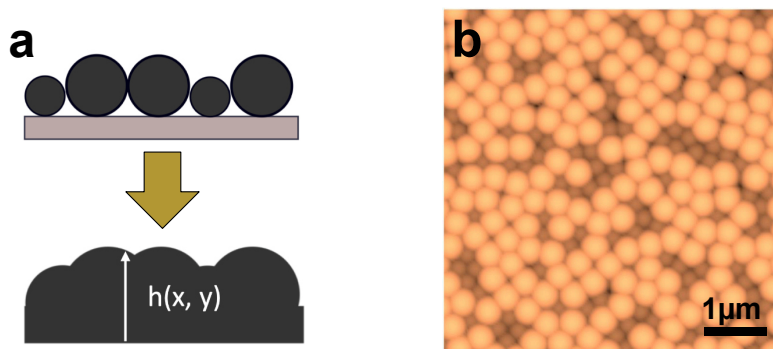


Abb. 4.2: (a) Eine Kugelmonolage dient als Templat für eine Oberfläche, deren Höhenprofil durch die Größenverteilung der Kugeln bestimmt ist. (b) Computer-generierte dichte Kugelmonolage aus 60 % mit $r_1 = 170 \text{ nm}$ und 40 % mit $r = 120 \text{ nm}$, bedeckt mit einer isotrop gewachsenen 100 nm dicken Ag-Schicht. Abb. aus [9].

en sind insbesondere für Anwendungen mit spektral breitbandiger Funktion wie Solarzellen oder (O)LED-Lichterzeugung interessant [2,7,9,141,152–156].

Eine Korrelation besteht beispielsweise, wenn die genaue räumliche Verteilung von (streuenden) Elementen zwar zufällig ist, die Wahrscheinlichkeit für einen bestimmten mittleren Abstand der Elemente zueinander aber erhöht ist. Von diesem Ansatz ausgehend hat sich in den letzten Jahre auf dem Gebiet der korrelierten Unordnung insbesondere das von Salvatore Torquato eingeführte Konzept der *Hyperuniformität* hervorgetan [48,146,157], welches ich ab Abschnitt 4.3 bespreche. Hyperuniform-ungeordnete Strukturen stellen eine exotische Teilmenge von Strukturen mit korrelierter Unordnung dar. Unser Team konnte wichtige experimentelle Arbeiten auf diesem Gebiet beitragen, z.B. haben wir ein skalierbares und kosteneffektives Verfahren für die Herstellung fast-hyperuniformer Nanopartikelfelder entwickelt [8]. Weiter konnten wir Mechanismen aufzeigen, wie mittels hyperuniformer Unordnung maßgeschneiderte Streuung ermöglicht wird [1].

4.2 Unordnung in dichtgepackten Kugelmonolagen

Ausgehend von oben eingeführtem Ansatz für maßgeschneiderte Lichtstreuung haben wir in einer Zusammenarbeit mit dem Karlsruher Institut für Technologie KIT die Auswirkung von Unordnung in einer Rückseitenstruktur numerisch untersucht (vgl. Skizze Abb. 4.1a) [9]. Hierzu wählten wir einen Ansatz, der prinzipiell auch experimentell eine systematische Variation der Textur erlaubt. So wird die Textur durch eine dicht gepackte Kugelmonolage definiert. Der Algorithmus zur Erstellung der Monolage beruht auf einer zufälligen Platzierung der Kugeln auf der Substratoberfläche und anschließendem Zusammenschieben der Kugeln. Durch Materialdeposition auf die Monolage wird die streuende Oberfläche generiert, siehe

4 Lichtmanagement mit geordneter Unordnung: Hyperuniformität

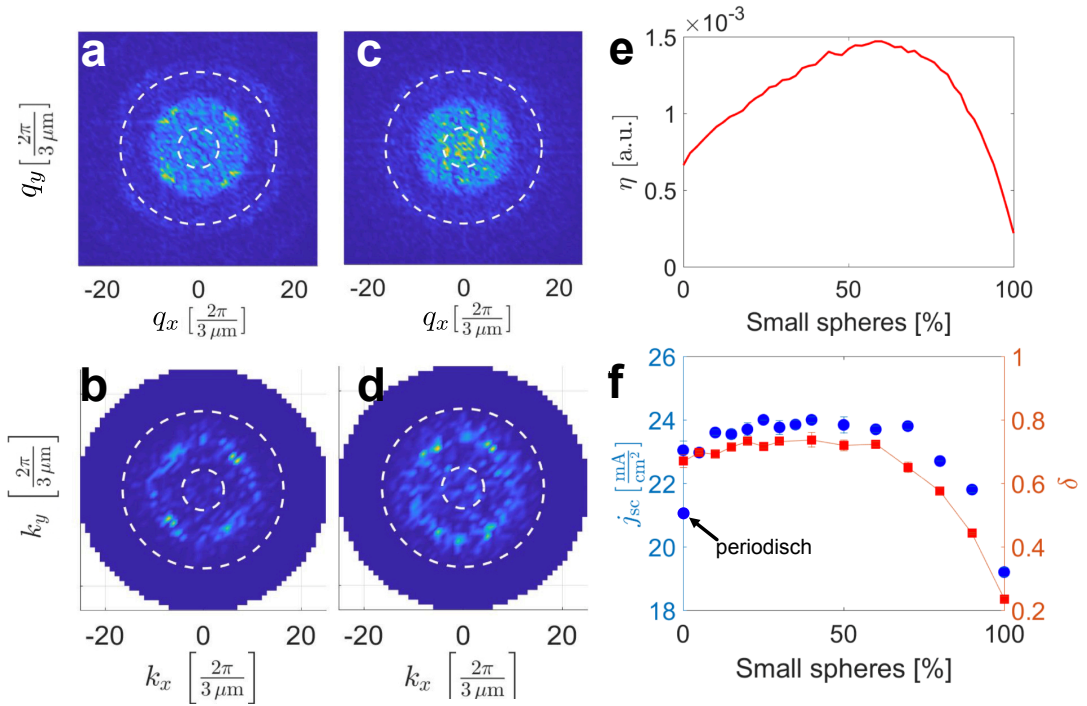


Abb. 4.3: PSD einer Textur basierend auf einer bidispersen Monolage mit einem Anteil von großen ($r = 170$ nm) und kleinen ($r = 120$ nm) Kugeln von (a) 90%/10% und (b) 60%/40%. (b),(d) zugehörige Streuverteilung. Die weißen Kreise markieren die Grenzen der Bereiche A, B und C ($\lambda_0 = 700$ nm). (e) Anteil der PSD, (f) Streuung (rote Datenpunkte) in Region B und j_{sc} (blaue Datenpunkte) in Abhängigkeit vom Anteil der kleineren Kugelgröße. Abb. aus [9].

Abb. 4.2. Bei der Verwendung einer einzigen Kugelgröße wird die resultierende Anordnung der Kugeln im wesentlichen periodisch sein, durch den Algorithmus wird keine perfekte Periodizität erzwungen, so dass kleine Abweichungen auch für diesen Fall auftreten. Mit der Zugabe einer weiteren Kugelgröße jedoch nimmt die Unordnung immer weiter zu.

Die Charakterisierung der resultierenden Topographie erfolgt mittels (diskreter) Fouriertransformation des Höhenprofils $h(\mathbf{r})$, der spektralen Leistungsdichte (*Power spectral density* PSD)

$$\text{PSD}(\mathbf{q}) = \frac{1}{L^2} \left| \sum_i h(r_i) e^{-i\mathbf{q}r_i} \Delta L^2 \right|^2, \quad (4.1)$$

mit der Seitenlänge L des betrachteten Ausschnitts und der lateralen Auflösung ΔL des Profils. In Abb. 4.3a und c ist die PSD beispielhaft gezeigt für die Fälle, dass neben der Kugelgröße $r = 170$ nm ein Anteil von 10% bzw. % 40% von Kugeln mit $r = 120$ nm vorliegt. Für den kleineren Anteil sind noch einzelne verstärkte Raumfrequenz-Bereiche zu erkennen, die auf eine noch teilweise bestehende Periodizität deuten, also aus verbreiterten Beugungsordnungen

4.2 Unordnung in dichtgepackten Kugelmonolagen

resultieren [158]. Insgesamt ist das Fourier-Spektrum jedoch im Vergleich zu einer perfekten Periodizität schon stark verbreitert. Für den Fall mit höherem Anteil sind die sichtbaren Maxima verschwunden und weicht einer homogenen Verteilung der PSD. Für eine bessere Vergleichbarkeit unterschiedlicher Muster zeigt Abb. 4.3e die Summe der PSD-Anteile in Zielbereich B

$$\eta = \sum_j \text{PSD}(\mathbf{q}_j), \quad (4.2)$$

mit $k_{\text{tot}} < q_j < n \frac{\omega}{c_0}$, in Abhängigkeit vom Anteil kleiner Kugeln. Hierbei wurde über viele Konfigurationen gemittelt, um eine statistisch signifikante Aussage zu erhalten und wir erkennen, dass η am größten wird für einen Anteil kleiner Kugeln von 60%.

Um den Zusammenhang zwischen PSD-Verteilung einer Textur mit seiner Streuung zu untersuchen, wurden rigorose Berechnung mittels FEM (Softwarepaket *JCMSuite* [111]) durchgeführt. Die Geometrie der Rechnungen ist in Abb. 4.1a skizziert: Die mit Silber bedeckte Kugelmonolage bildet die Rückseitenstruktur für einen ultradünnen Si-Absorber mit 1 μm Dicke. Für eine Wellenlänge $\lambda_0 = 700 \text{ nm}$ ist die Verteilung des Streulichts im reziproken Raum in Abb. 4.3b und d gezeigt. Eine verstärkte Streuung in den ringförmigen Bereich B ist für beide Fälle zu erkennen. Die Textur mit höherem Anteil kleiner Kugeln füllt diesen Bereich besser aus, allerdings auch den zentralen Bereich A und ein Zusammenhang zwischen PSD und Streuung ist schwer auszumachen. In Teilbild f (rote Datenpunkte) ist δ dargestellt, welches sich analog zu η aus dem in B hinein gestreuten Anteil berechnet. Ein zu η ähnlicher, aber schwächer ausgeprägter Verlauf lässt sich für δ ablesen mit einem (flachen) Maximum für einen Anteil kleiner Kugeln von 40%.

Für eine Solarzelle muss Lichtwegverlängerung nicht nur für eine einzelne Wellenlänge, sondern für einen ganzen Wellenlängenbereich in B bestehen. Um dies zu evaluieren, betrachten wir statt einer Mittelung von δ über diesen Bereich den photogenerierten Strom j_{sc} nach Gl. 3.4. Dieser ist geeigneter, da auf diese Weise die resultierende Absorptionserhöhung durch die Textur und nicht nur die initiale Streuung an dieser berücksichtigt wird. Es gehen auch weitere Größen wie die (Total-)Reflexion an der Vorderseite und die Gewichtung des einfallenden Sonnenspektrums ein. j_{sc} ist in Abb. 4.3f (blaue Datenpunkte) aufgetragen. Für einen flachen, untexturierten Ag-Rückseitenspiegel finden wir $j_{\text{sc}} = 15,3 \frac{\text{mA}}{\text{cm}^2}$ und schon für eine Textur auf Basis einer periodischen Anordnung der großen Kugeln finden wir $j_{\text{sc}} = 21,1 \frac{\text{mA}}{\text{cm}^2}$. Bleiben wir bei einer Kugelsorte, erlauben aber Unordnung, wird $j_{\text{sc}} = 23,0 \frac{\text{mA}}{\text{cm}^2}$ erreicht. Erhöhen wir die Unordnung durch Zugabe kleiner Kugeln, lässt sich dieser Wert für einen Anteil kleiner Kugeln von 40% weiter auf $j_{\text{sc}} = 24,1 \frac{\text{mA}}{\text{cm}^2}$ steigern, was einer Erhöhung um 58% bzw. 13,7% im Vergleich zum flachen bzw. periodischen Fall entspricht.

Diese Arbeit zeigt, dass Unordnung durch gezielte Manipulation der Raumfrequenzen ein

hohes Potential für eine maßgeschneiderte Lichtstreuung verspricht. Unser Vorgehen, Unordnung und Raumfrequenzen einzubringen war hier nichtsdestotrotz eher phänomenologischer Natur. Eine neue Materialklasse, die kontrollierte Unordnung von vornherein mitbringt, beschreibe ich im folgenden Abschnitt.

4.3 Hyperuniforme Unordnung

Eine intuitive und verbreitete Weise, flächige Strukturen bzw. Texturen zu charakterisieren, ist die Darstellung ihrer Raumfrequenzen im reziproken Raum durch Fourier-Transformation ihrer Ortsdarstellung. Wenn die Struktur aus einer Anordnung von identischen Elementen bzw. Streuern besteht, genügt es auch, das Punktmuster ihrer Positionen im Ortsraum zu transformieren. Die Fourier-Transformierte eines Punktmusters ist der Strukturfaktor

$$S(\mathbf{q}) = \frac{1}{N} \left| \sum_{j=1}^N e^{i\mathbf{q}\mathbf{r}_j} \right|^2 \quad (4.3)$$

mit der Anzahl N von Punkten an den Positionen \mathbf{r}_j [159]. Anhand des Strukturfaktors lassen sich unterschiedliche Typen von Ordnung bzw. Unordnung feststellen. Eine mögliche Kategorisierung ist in Abb. 4.4 dargestellt. Der Strukturfaktor eines periodischen Musters von Streuelementen, z.B. eines Gitters, weist aufgrund der hohen Korrelation scharfe Maxima auf, die sich vollständig durch reziproke Gittervektoren konstruieren lassen. Im Gegensatz dazu steht ein vollständig zufälliges Muster mit einer Poisson-Verteilung der Streuelemente. Benachbarte Elemente können einen beliebigen Abstand zueinander aufweisen und Agglomeration und Überlappung sind auch möglich. Ein solches Muster weist keinerlei Korrelationen auf, so dass der Strukturfaktor konstant ist bzw. einem Rauschen um $S = 1$ entspricht. Beispiele für solche Streuensembles sind beispielsweise Staub- oder Wasserteilchen (Nebel) in Luft.

Zwischen diesen beiden extremen Fällen existiert ein Regime, in dem die Elemente weder streng periodisch aber auch nicht völlig zufällig angeordnet sind, sondern trotz Unordnung korreliert sind. Korrelierte Unordnung liegt beispielsweise in der Anordnung von Atomen in amorpher Materie vor, in welchem die Länge der chemischen Bindung die Distanz der Atome zu ihren nächsten Nachbarn festlegt, die Winkel zwischen den Bindungen aber variieren können. Eine exotische Untergruppe von Punktmustern mit korrelierter Unordnung bilden solche mit *hyperuniformer Unordnung* [48,146]. Strukturen, deren Elemente ungeordnet aber hyperuniform sind, weisen eine auf den ersten Blick nicht sichtbare, versteckte Ordnung auf: Langreichweitige Dichte-Fluktuationen sind unterdrückt. Für den hier betrachteten 2D Fall bedeutet dies, dass für ein sphärischen Fensters mit wachsendem Radius R die Varianz der

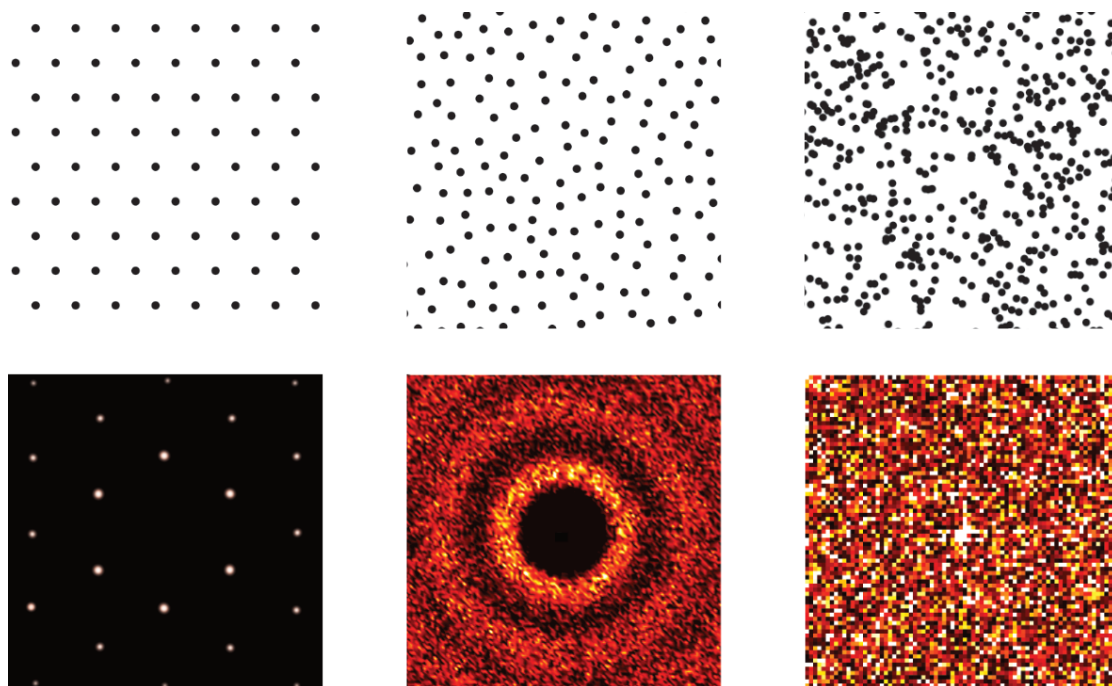


Abb. 4.4: Klassen unterschiedlicher Ordnung: Die obere Reihe zeigt 2D Punktmuster im Realraum, die z.B. die Positionen streuender Elemente darstellen können, während die untere Reihe den zugehörigen Strukturfaktor zeigt. Ein periodisches Punktmuster (linke Spalte) weist im Spektrum des Strukturfaktors scharfe Maxima auf, welche beispielsweise den Beugungsreflexen eines Gitters entspricht. Für ein zufälliges Muster (rechte Spalte), zeigt der Strukturfaktor keinerlei Besonderheiten auf und entspricht einem Rauschen. Strukturen mit korrelierter Unordnung (mittlere Spalte) ähneln amorphen Strukturen, in denen die Elemente zwar zufällig angeordnet sind, die nächste-Nachbar-Abstände trotzdem nur wenig streuen. Im hier gezeigten Fall besteht eine starke Korrelation, die in einem Strukturfaktor resultiert, der am Ursprung und in einem Bereich um diesen verschwindet. Eine solche Struktur ist ungeordnet *stealthy* hyperuniform. Abb. aus [28].

eingeschlossenen Anzahl von Punkten, $\sigma_N^2(R) \equiv \langle N^2(R) \rangle - \langle N(R) \rangle^2$, schwächer als R^2 ansteigt. Eine äquivalente Formulierung dazu ist ein verschwindender Strukturfaktor im Ursprung des reziproken Raums:

$$\lim_{q \rightarrow 0} S(\mathbf{q}) = 0 \quad (4.4)$$

Ein Beispiel für eine ungeordnete hyperuniforme (*hyperuniform disordered* HuD) Anordnung ist in der mittleren Spalte von Abb. 4.4 gezeigt. Der Strukturfaktor dieser Anordnung weicht deutlich von der zufälligen Anordnung ab und wie gefordert ist $S(q \rightarrow 0) = 0$. Darüber hinaus verschwindet S für einen ganzen Bereich um den Ursprung herum, $q < q_s$; eine solche Anordnung wird *stealthy* hyperuniform genannt. Diese Anforderung wird auch für alle periodische und auch quasi-periodische Muster erfüllt (siehe z.B. das periodische Muster in der linken Spalte), womit überraschend eine übergeordnete Klassifizierung gefunden wurde, unter die sowohl (quasi-)periodische als auch HuD-Muster fallen.

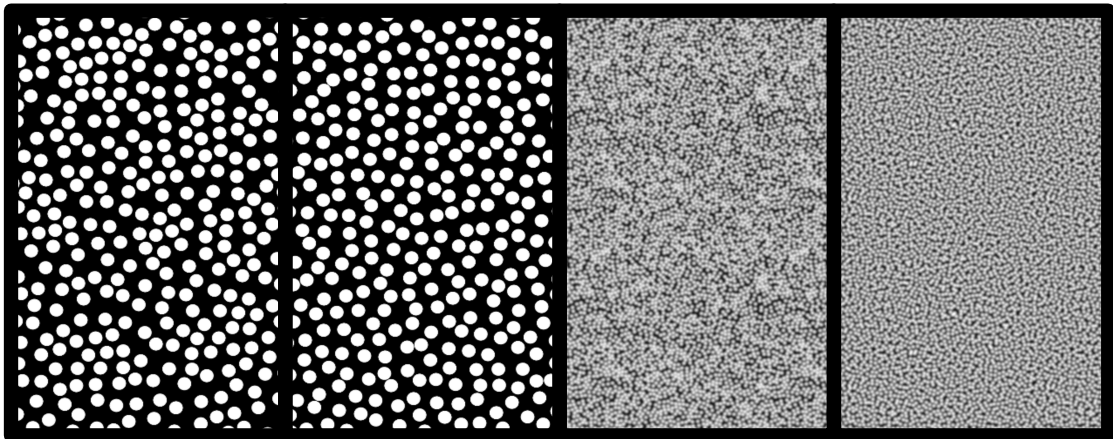


Abb. 4.5: Vergleich eines nicht-HuD-Musters (1. & 3.v.l.) mit einem HuD-Muster in Nahansicht und Übersicht.

Hyperuniformität ist meist nur schwer augenscheinlich zu bestimmen. Abb. 4.5 stellt zwei Punktmuster gegenüber, von denen eins HuD ist, das andere nicht. In der Nahansicht sind die Unterschiede kaum auszumachen. Erst wenn wir herauszoomen und uns ein großes Feld der Verteilung ansehen, wird die Definition nach Gl. 4.3 fassbar, denn mit einem Mal werden die Dichtefluktuationen des nicht-HuD-Musters sichtbar, während das HuD-Muster immer homogener erscheint, insbesondere wenn man sich die Abbildung aus einigen Metern Entfernung anschaut. Dass HuD nicht nur eine theoretische Kuriosität darstellt, zeigen inzwischen gefundene Nachweise in der Natur [160–163]. So wurde beispielsweise gezeigt, dass die Anordnung von Photorezeptoren auf der Retina von Haushühnern *multi*-hyperuniform ist, d.h. jede Rezeptorensorte stellt für sich ein hyperuniformes Muster dar, worauf vermutlich das außerordentliche Sehvermögen von Haushühnern zurückzuführen ist [160].

In der Optik und Photonik versprechen HuD-Materialien u.a. Eigenschaften, die bisher nur periodischen Strukturen zugeschrieben wurden. Ein Beispiel ist die Existenz einer strukturell bedingten photonischen Bandlücke in ungeordneten aber hyperuniformen Medien, die auch schon experimentell nachgewiesen wurden [164–169]. Im Gegensatz zu den photonischen Bandlücken in (periodischen) photonischen Kristallen weist diese in ungeordneten hyperuniformen Strukturen allerdings keine Richtungsabhängigkeit auf, was beispielsweise beliebig geformte Wellenleiter ermöglichen könnte. Im Rahmen von streuenden Texturen für das Lichtmanagement in Solarzellen fällt die große Ähnlichkeit des Strukturfaktors eines HuD-Musters mit dem gewünschten Streuprofil auf, das in Abb. 4.1b gezeigt ist. Für das Lichtmanagement in Solarzellen sind HuD-Texturen deshalb von hohem Interesse.

4.4 Skalierbare Fabrikation nahezu-hyperuniformer ungeordneter Substrate

Die großflächige und skalierbare Herstellung von maßgeschneiderten ungeordneten Oberflächen ist eine zentrale Herausforderung in der Optik-Industrie, insbesondere im Sektor Photovoltaik, aber z.B. auch für die (O)LED-Produktion. In diesen Anwendungen ist spektrale Breitbandigkeit gekoppelt mit effizientem Lichteinfang in (bzw. Lichtextraktion) aus dünnen Schichten im Mikro- oder Nanometerbereich ein wesentlicher Faktor für die Materialeffizienz. Die vorherigen Abschnitte zeigen, dass dies Eigenschaften sind, für die Unordnung ein noch ungenutztes Potential birgt, wenn sie denn kontrolliert eingebracht wird. Es existieren natürlich deterministische Ansätze für die Herstellung maßgeschneiderter ungeordneter Oberflächen, wie z.B. Elektronenstrahl-Lithographie. Diese sind äußerst flexibel, jedoch auch langsam und teuer und daher nicht für den großflächigen (industriellen) Einsatz geeignet. Mit konventionellen skalierbaren Technologien, z.B. Nasschemisches Ätzen oder Plasmatexturierung (vgl. Kapitel 2), lassen sich ungeordnete Grenzflächen herstellen, jedoch bieten sie nur eine begrenzte Kontrolle über die resultierenden Unordnung.

Als skalierbare und kosteneffektive *Bottom up*-Methode ist selbstorganisierte Nanokugeldeposition vielversprechend, jedoch wurde diese bisher fast ausschließlich für die Herstellung periodischer Strukturen wie Gitter oder photonische Kristalle angewandt (vgl. Kapitel 3) [23,108–110,135,136]. Wenige Arbeiten existieren, in denen gezielt ungeordnete Kugelmonolagen hergestellt wurden und auch in diesen konnte die Unordnung nicht eingestellt werden [170]. Im Rahmen der hier vorgestellten Arbeit habe ich mit meinem Team ein Verfahren entwickelt, das diese Lücke schließt [8,171].

Depositionsprozess

Unser Prozess (siehe Abb. 4.6) macht sich zunutze, dass kommerziell erhältliche Nanokugel-Dispersionen (hier PMMA-Kolloide) zur Stabilisierung (negative) Oberflächenladungen aufweisen. Ein zuvor Al_2O_3 -funktionalisiertes Substrat wird in die Dispersion getaucht. Die dünne (10-20 nm) Al_2O_3 -Schicht weist positive Oberflächenladungen auf, so dass die Kugeln nach Diffusion zur Substratoberfläche dort immobilisieren. Aufgrund ihrer Oberflächenladung bestimmen schon immobilisierte Kugeln auch die Positionen weiterer Kugeln, da sie sowohl Ladungen der Substratoberfläche abschirmen als auch mit anderen Kugeln wechselwirken. Hierdurch wird zum einen sichergestellt, dass sich immer nur eine Kugelmonolage bildet, zum anderen sind die Partikelpositionen nicht rein zufällig, d.h. sie korrelieren. Die Deposition funktioniert aufgrund dieses selbstorganisierten und selbstlimitierenden Mechanismus äußerst homogen. Das Substrat ist bis zu den Rändern gleichmäßig mit einer unge-

4 Lichtmanagement mit geordneter Unordnung: Hyperuniformität

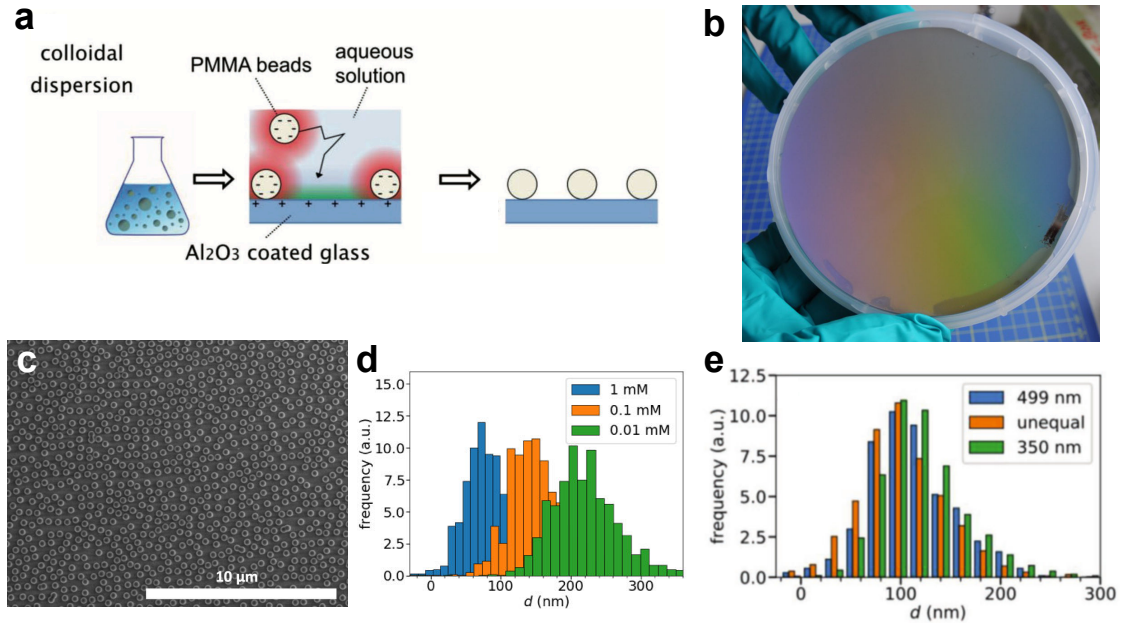


Abb. 4.6: Herstellung von ungeordneten Kugelmonolagen. (a) Skizze zum Depositionsprozess. (b) 4-Zoll-Si-Scheibe nach Deposition. (c) REM-Aufnahme (Aufsicht) einer typischen Kugelmonolage. (d) Histogramm nächster-Nachbar-Abstände d für drei unterschiedliche Ionenstärken μ . (e) Histogramm von d bei der gleichzeitigen Deposition von zwei unterschiedlichen Kugelgrößen. Abbildungen teilweise entnommen aus [8].

ordneten Kugelmonolage bedeckt, siehe Abb. 4.6b und c. Darüberhinaus ist der Prozess nicht nur flexibel bzgl. der Substratgröße, sondern auch bzgl. des Substratmaterials, solange eine Al_2O_3 -Funktionalisierung vorliegt. Eine Al_2O_3 -Abscheidung mittels ALD erlaubt auch eine gleichmäßige Funktionalisierung von texturierten Substraten, so dass eine ungeordnete Kugelmonolage auch auf solchen möglich ist.

Das Potential $W_{\text{DLVO}}(d)$ zwischen Substrat und Kugeln bzw. zwischen zwei Kugeln in Abstand d lässt sich durch die Derjaguin-Landau-Verwey-Overbeek-Theorie (DLVO) beschreiben [172]:

$$W_{\text{DLVO}}(d) = W_{\text{el}}(d) + W_{\text{vdW}}(d) \quad (4.5)$$

mit $W_{\text{el}}(d) \propto e^{-\kappa d}$, $W_{\text{vdW}}(d) \propto \frac{1}{d}$,

Substrat-Kugel- bzw. Kugel-Kugel-Abstand d (Oberflächenabstand) und Debye-Länge (Abschirmlänge) $1/\kappa$. Die elektrostatische Wechselwirkung W_{el} der Kugeln untereinander ist abstoßend, mit der anziehenden van-der-Waals-Wechselwirkung W_{vdW} kann sich im resultierenden Potential allerdings ein schwaches Minimum bei d_0 mit einer Potentialtiefe in der Größenordnung von $W_{\text{DLVO}}(d_0) \approx 1 k_{\text{B}} T$ ausbilden. Für d_0 ist die Wahrscheinlichkeit einer

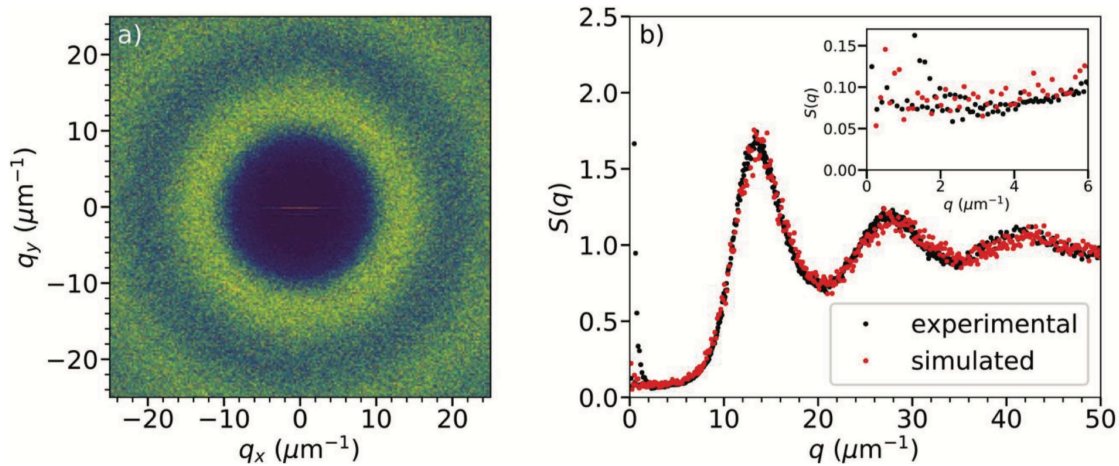


Abb. 4.7: (a) Strukturfaktor $S(\mathbf{q})$ einer typischen Probe extrahiert aus einer REM-Aufnahme (Kugeldurchmesser 350 nm). (b) Über den Betrag von $|\mathbf{q}| = q$ gemittelter experimenteller (schwarz) bzw. simulierter (rot) Strukturfaktor $S(q)$. Abb. aus [8].

Kugelplatzierung demnach vergrößert. Die Lage von d_0 ist abhängig von κ , welches sich wiederum über die experimentell einfach zugängliche Ionenstärke μ (Ionenkonzentration) der wässrigen Umgebung einstellen lässt, so dass $d_0 = d_0(\mu)$. Das Histogramm Abb. 4.6d über die Häufigkeit gefundener Kugelabstände zeigt, wie sich der wahrscheinlichste Abstand d_0 mit der Ionenstärke μ verschiebt. Wir konnten mittlere Abstände (Mittelpunkt-zu-Mittelpunkt) in einem weiten Bereich von etwa 160 nm bis 1400 nm realisieren. Im Weiteren stellt sich der Oberfläche-zu-Oberfläche-Abstand als praktisch unabhängig vom verwendeten Kugeldurchmesser heraus. So lassen sich mit dieser Methode sogar verschiedene Kugelgrößen in der verwendeten Lösung mischen und mit demselben mittleren Abstand in einem Schritt deponieren, siehe Abb. 4.6e.² Dies stellt einen zusätzlichen Freiheitsgrad in der Herstellung maßgeschneiderter ungeordneter Substrate dar. Wir sind damit nicht nur in der Lage, Unordnung in lateraler Richtung zu kontrollieren, sondern über die Kugelgrößen-Verteilung auch in vertikaler Richtung Einfluss zu nehmen.

Struktureigenschaften

Anhand von REM-Aufnahmen lassen sich computer-gestützt die Positionen der deponierten Nanokugeln entnehmen und der Strukturfaktor $S(\mathbf{q})$ nach Gl. 4.3 berechnen, welcher in Abb. 4.7a gezeigt ist. $S(\mathbf{q})$ ist rotationsinvariant, was auf ein isotropes Muster schließen lässt und uns erlaubt, über den Betrag von $|\mathbf{q}| = q$ zu mitteln, siehe Abb. 4.7b. Die Merkmale von $S(q)$ lassen auf eine stark korrelierte Konfiguration schließen. Die Maxima bei $q = 13,5 \mu\text{m}^{-1}$,

²In der Praxis müssen die Kugelgrößen in der gleichen Größenordnung vorliegen.

4 Lichtmanagement mit geordneter Unordnung: Hyperuniformität

$28\mu\text{m}^{-1}$ und $42\mu\text{m}^{-1}$ sind Ausdruck von einem gehäuften Vorkommen eines bestimmten Punktabstandes, dem mittleren Partikelabstand d_0 . Nahe $q = 0$ wird $S(q)$ klein, d. h. langreichweitige Dichte-Fluktuationen sind unterdrückt. Damit deutet $S(q)$ unserer Strukturen auf ein hyperuniformes Muster hin, da $S(q)$ für einen Bereich um den Ursprung $q \leq 10\mu\text{m}^{-1}$ klein wird, sogar auf eine stealthy hyperuniforme Struktur.

Im Experiment hergestellte Muster werden nie ganz dem theoretischen Ideal $S(q \rightarrow 0) = 0$ genügen können. Für eine Einordnung bezüglich Hyperuniformität wurde in der Literatur vorgeschlagen, die Hyperuniformitätsmetrik H ,

$$H \equiv \frac{S(q \rightarrow 0)}{S_{\max}(q)}, \quad (4.6)$$

hinzuzuziehen und ein Muster für H in der Größenordnung $\approx 10^{-4}$ tatsächlich bzw. effektiv hyperuniform [48,173,174] und für $\approx 10^{-2}$ nahezu hyperuniform [164,175,176] zu bezeichnen. Für unsere Strukturen erreichen wir $H \approx 3 \cdot 10^{-2}$, wir können sie demzufolge als nahezu hyperuniform bezeichnen. Da bisher nur wenige experimentelle Arbeiten zu dieser Thematik existieren, ist bzgl. der Bewertung fabrizierter Strukturen jedoch noch kein allgemeiner Konsens gefunden.

Im Weiteren haben wir ein *random-sequential adsorption* (RSA)-Modell formuliert und den Gegebenheiten unseres Depositionsprozesses angepasst. Das Modell basiert auf dem Ansatz, Partikel sequentiell und zufällig auf einer Oberfläche aufzusetzen. Die Wahrscheinlichkeit, dass ein Partikel die jeweilige Position auch einnimmt, wird durch vorgefundene Potentiallandschaft bestimmt, hängt also von den Positionen schon vorliegender Partikel ab. Das Modell ist semi-phänomenologisch, d. h. die Wahrscheinlichkeiten leiten sich von den physikalischen Abhängigkeiten (Gl. 4.5) ab, wobei die eingesetzten Konstanten aus einigen wenigen Experimenten zur Kalibration extrahiert wurden. Vergleichen wir die Strukturfaktoren aus dem Simulationsmodell mit dem Experiment, finden wir eine sehr gute Übereinstimmung, siehe Abb. 4.7b. Auch wenn unterschiedliche Kugeldurchmesser verwendet werden, stimmt unser Modell mit den experimentellen Daten überein. Damit werden Vorhersagen von experimentell realisierbaren Partikelmustern ermöglicht, ohne diese tatsächlich herzustellen (in möglicherweise langen Versuchsreihen), was in Vorbereitung für Experimente von hohem Nutzen ist.

4.5 Maßgeschneiderte Lichtstreuung durch hyperuniforme Unordnung

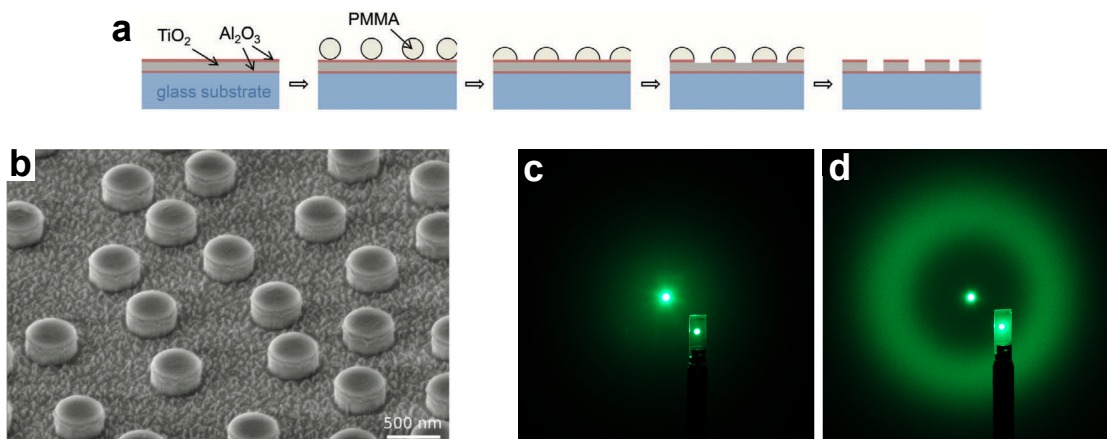


Abb. 4.8: (a) Skizze zur Prozessierung der nahezu-HuD-Kugelmonolagen zu TiO_2 -Nanoscheibchen-Arrays. Auf dem $\text{Al}_2\text{O}_3/\text{TiO}_2/\text{Al}_2\text{O}_3$ -Schichtstapel wird unsere Kugeldeposition ausgeführt. Nach einem Tempersschritt für eine flächigere Bedeckung folgt ein Al_2O_3 -selektiver Trockenätzschritt (BCl_3/Ar -Atmosphäre), danach ein TiO_2 -selektiver Trockenätzschritt ($\text{CF}_4/\text{O}_2/\text{Ar}$ -Atmosphäre), so dass schlussendlich TiO_2 -Nanoscheibchen entstehen. (b) REM-Aufnahme der Nanoscheibchen mit Höhe 231 nm und Durchmesser ($455,0 \pm 5,4$) nm. Vorwärtsstreuung ($\lambda = 532$ nm, unpolarisiert) identischer Nanoscheibchen auf Glas in einer (c) unkorrelierten und einer (b) nahezu-HuD-Anordnung auf einen Schirm. Im Vordergrund ist jeweils die Probe zu erkennen. Abb. aus [1,171].

4.5 Maßgeschneiderte Lichtstreuung durch hyperuniforme Unordnung

Auf Basis unserer nahezu-HuD-Substrate untersuchten wir die Lichtstreuung von Feldern (Arrays) identischer Nanopartikel, die eine HuD-Anordnung aufweisen [1]. Mit dem Ziel, neue Möglichkeiten für maßgeschneiderte Lichtstreuung aufzutun, stand dabei insbesondere die Wechselwirkung von HuD mit den Streueigenschaften des individuellen Nanopartikels im Mittelpunkt. Da die PMMA-Kugeln selbst mit ihrem verhältnismäßig geringen Brechungsindex ($n=1,5$) keine starken Streuer sind, haben wir den Prozess weiterentwickelt, um Arrays aus hochbrechenden Nanoscheiben aus TiO_2 ($n = 2,4$) zu erhalten. Die Kugelmonolage dient dabei als Templat, so dass die nahezu-HuD-Anordnung erhalten bleibt. Die Präparation erfolgt auf einer TiO_2 -Schicht (Dicke 231 nm), die zwischen zwei dünnen Al_2O_3 -Schichten (Dicke 10-20 nm) vorliegt, siehe Abb. 4.8a für eine Skizze zum Prozess. Die oberste Al_2O_3 -Schichten dient einerseits der Kugeldeposition (siehe vorherigen Abschnitt), zusammen mit der unteren Schicht aber auch als Hartmaske bzw. Ätzstop für zwei nachfolgende Trockenätz-Prozesse, mit denen das Kugeltemplat in die TiO_2 -Schicht übertragen wird und wir auf diese Weise großflächige Arrays hochbrechender TiO_2 -Nanoscheibchen erhalten, siehe Abb. 4.8b.

Nanopartikel aus hochbrechenden Dielektrika haben sich in den letzten Jahren aufgrund ihrer besonderen Streueigenschaften im Rahmen optischer Metamaterialien hervorgerufen und

4 Lichtmanagement mit geordneter Unordnung: Hyperuniformität

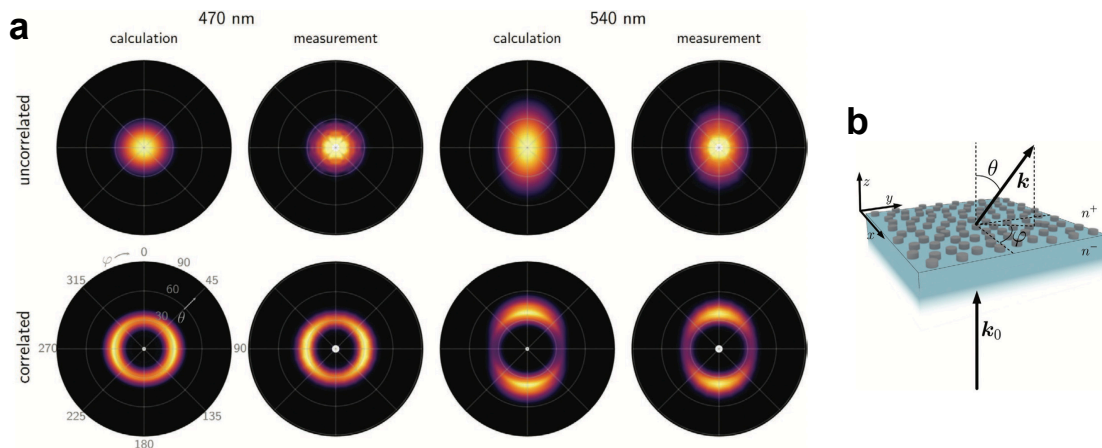


Abb. 4.9: (a) Experimentell gemessene und berechnete Vorwärtsstreuung $ARS(\theta, \phi)$ für den unkorrelierten und nahezu-HuD-Fall für zwei verschiedene Wellenlängen (\hat{x} -polarisiert). (b) Skizze zur verwendeten Notation und Koordinatensystem. k_0 bzw. k sind einfallender und gestreuer Wellenvektor. Abb. aus [1].

eignen sich mit hohen Streuquerschnitten auch für unsere Untersuchung [39–41,177,178]. Sie ermöglichen beispielsweise neben der Anregung elektrischer Resonanzen auch die Anregung magnetischer Resonanzen bei optischen Frequenzen sowie neuartige Wege der Nah- und Fernfeldmanipulation. Hierbei haben sich insbesondere Nanoscheibchen durchgesetzt, da sie über die Geometrie eine gute Kontrolle über ihr Streuspektrum erlauben.

In Abb. 4.8c und d sind Photographien der Vorwärtsstreuung zweier Proben auf einen Schirm gezeigt. In beiden Fällen streuen TiO_2 -Nanoscheibchen mit identischer Geometrie, in c befinden sie sich jedoch in einer unkorrelierten, d.h. zufälligen, Anordnung und in d in einer hochkorrelierten nahezu-HuD-Anordnung auf dem Substrat. Während die Streuung der unkorrelierten Ensembles dem des Einzelpartikels entspricht und sich dementsprechend vornehmlich in kleine Streuwinkel konzentriert, wird sie durch die HuD-Anordnung offensichtlich stark modifiziert. Die Streuung weist ein Maximum in Ringform auf, während sie für den Bereich innerhalb des Rings unterdrückt ist. Die Ursache hierfür ist in der hohen Korrelation des HuD-Musters zu finden. Die Korrelation führt zu Streurichtungen, in welche die Summe aller gestreuten Wellen konstruktiv oder destruktiv interferieren. Dies ist ganz ähnlich zur Gitterbeugung in periodische Strukturen, allerdings mit zwei wichtigen Unterschieden: Zum einen ist die Beugung nicht diskreten Richtungen zugeordnet, sondern ist aufgrund der lateralen Isotropie des Nanoscheibchenmusters kontinuierlich erlaubt, so dass sich ein Ring ausbildet. Zum anderen existiert statt eines diskreten nächster-Nachbar-Abstandes eine kontinuierliche Verteilung dieser, was zu einer Verbreiterung des Beugungsmaximums sowohl im Winkel (in radialer Richtung des Rings) als auch spektral entspricht.

Winkelaufgelöste Streuantwort

Im Fernfeld lässt sich das gestreute Feld des Einzelpartikel $E_s(\mathbf{r})$ schreiben als [44,179]

$$E_s(\mathbf{r}) = E_0 \frac{e^{i\mathbf{k}\cdot\mathbf{r}}}{r} \mathbf{f}_0. \quad (4.7)$$

mit dem Formfaktor \mathbf{f}_0 , der die normalisierte Streufeldamplitude für gegebene Polarisati-on, Wellenlänge und Einfalls- sowie Streuwinkel darstellt. \mathbf{f}_0 lässt sich hier mittels rigorosen Methoden wie FEM bestimmen, im Falle sphärischer Kugeln im homogenen Medium auch analytisch mittels Mie-Theorie [180]. In Anlehnung an die Born-Näherung interferieren für ein Ensemble identischer Partikel alle am Einzelpartikel gestreuten Felder und die experi-mentell messbare winkelabhängige Streuintensität (*angular resolved scattering* ARS) kann als Modulation der Einzelpartikel-Streuintensität $|\mathbf{f}_0|^2$ mit dem Strukturfaktor S des Ensembles formuliert werden [1,44]

$$ARS = \frac{P_{\text{sca}}}{\int_{\Omega} |\mathbf{f}_0|^2 S d\Omega} \cdot |\mathbf{f}_0(\mathbf{k})|^2 S(k_{\parallel}) \quad (4.8)$$

Der erste Term dient der Normierung mit der Integration über den Raumwinkel und der Be-rücksichtigung von transmittiertem bzw. reflektiertem Spekularanteil $P_{\text{sca}} = 1 - T - R$, d.h. es ist $ARS \propto f_0^2 S$.

In Abb. 4.9 ist die Winkelabhängigkeit der ARS in Vorwärtsrichtung nach Gl. 4.8 zusam-men mit der experimentell vermessenen ARS für den unkorrelierten und den nahezu HuD-Fall für zwei unterschiedliche Wellenlängen aufgetragen. Wir finden eine gute Übereinstim-mung, insbesondere die Ringstruktur mit unterdrückter Streuung im Ringinnern lässt sich reproduzieren. Ferner lässt sich eine Anisotropie in der Streuung erkennen. Da der Struktur-faktor S rotationssymmetrisch ist, muss die Ursache hierfür im Formfaktor \mathbf{f}_0 der einzelnen Nanoscheibchen liegen. In der Tat können wir durch weitere numerische Untersuchungen im Rahmen einer Multipolentwicklung der Nahfelder das Auftreten unterschiedlicher Reso-nanztypen für die Anisotropie verantwortlich machen [181,182]. Für $\lambda = 470$ nm dominieren elektrische Dipol-, Quadrupol- und Oktupolmoden, während für $\lambda = 540$ nm ihre magne-tischen Gegenstücke dominieren. Elektrische und magnetische Moden weisen zueinander senkrechte Abstrahlprofile auf, die sich hier bemerkbar machen. Die Anisotropie ist auch im unkorrelierten Fall erkennbar, allerdings ist der Kontrast, d.h. das Verhältnis der Streuinten-sitäten entlang der x - und y -Achse, kleiner ($= 2,2$) als im nahezu-HuD-Fall ($= 5,2$).

Spektrale Abhängigkeit der Streuantwort

Abb. 4.10 zeigt wieder die ARS der unkorrelierten und nahezu-HuD-Probe, nun jedoch in-klusive ihrer spektralen Abhängigkeit und über den Azimuthwinkel φ gemittelt. Für die un-

4 Lichtmanagement mit geordneter Unordnung: Hyperuniformität

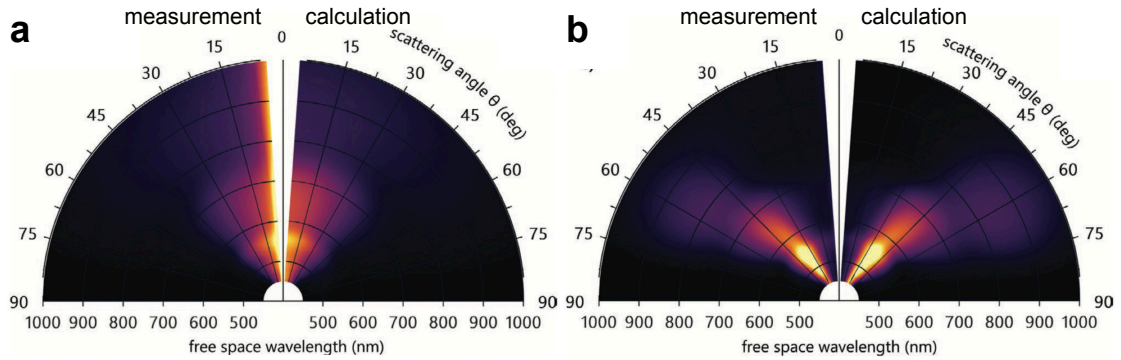


Abb. 4.10: Experimentell gemessene und berechnete Vorwärtsstreuung $ARS(\theta, \lambda)$ für den (a) unkorrelierten und (b) nahezu-HuD-Fall in Abhängigkeit von Streuwinkel und Wellenlänge. Abb. aus [1].

korrelierte Probe erkennt man ein Streumaximum um $\lambda = 560$ nm, was auf die dort besonders starke Anregung von magnetischen Multipolen zurückzuführen ist, und dass sich die Streuung innerhalb $\theta < 30^\circ$ konzentriert. Im Gegensatz dazu ist Streuung in kleine Winkel für die HuD-Probe über den gesamten Spektralbereich unterdrückt. Vielmehr konzentriert sie sich für $\lambda = 450 - 750$ nm in einem Winkelbereich $30^\circ < \theta < 50^\circ$ und wechselt dann für $\lambda = 800 - 1000$ nm in den Bereich $50^\circ < \theta < 70^\circ$.³

Dieses Verhalten überrascht. Da die besonderen Streueigenschaften einer HuD-Anordnung wie bei einer periodischen Struktur auf Interferenz beruht, wird hier eine viel stärkere Wellenlängen-Abhängigkeit des Streuwinkels erwartet. In Abb. 4.11a ist S aufgetragen, allerdings wurde die Abhängigkeit von der Raumfrequenz q zu einer von λ und Streuwinkel θ konvertiert gemäß $\theta = \arcsin \frac{\lambda q}{2\pi}$ (für senkrechten Lichteinfall). Die schwarze Kurve kennzeichnet den Verlauf des Maximum S_{\max} . Die Kurve entspräche gleichzeitig der Abhängigkeit einer Beugungsordnung eines periodischen Gitters mit einer Gitterkonstante a , die gleich dem mittleren Abstand r_0 (hier 828 nm) der HuD-Struktur ist. Für ein Gitter sind erlaubte Richtungen stark eingeschränkt, da nur genau die Beugungsordnungen sind erlaubt (Gl. 3.2). Im Gegensatz dazu ermöglicht HuD aufgrund des kontinuierlichen Verlaufs von S sehr viel mehr Möglichkeiten. Nur für kleine Winkel θ ist Streuung aufgrund des gegen null strebenden Strukturfaktors S unterdrückt.

Nichtsdestotrotz erklärt der Verlauf von S noch nicht die beobachtete ARS , wir müssen noch das Streuverhalten des Einzelpartikels f_0 hinzuziehen. In Abb. 4.11b ist f_0^2 aufgetragen. Für eine bessere Visualisierung sind die Daten auf den Maximalwert für jede Wellenlänge normiert. Während Vorwärtsstreuung für das Einzelpartikel dominiert, kann man auch ablesen, dass für $\lambda = 800 - 1000$ nm ein größerer Winkelbereich abgedeckt wird, als für $\lambda = 450 -$

³Die angegebenen Bereiche entsprechen den in Abb. 4.8d und Abb. 4.9 beobachteten Ringen. Diese liegen in der Ebene senkrecht zur Zeichenebene von Abb. 4.10b.

4.5 Maßgeschneiderte Lichtstreuung durch hyperuniforme Unordnung

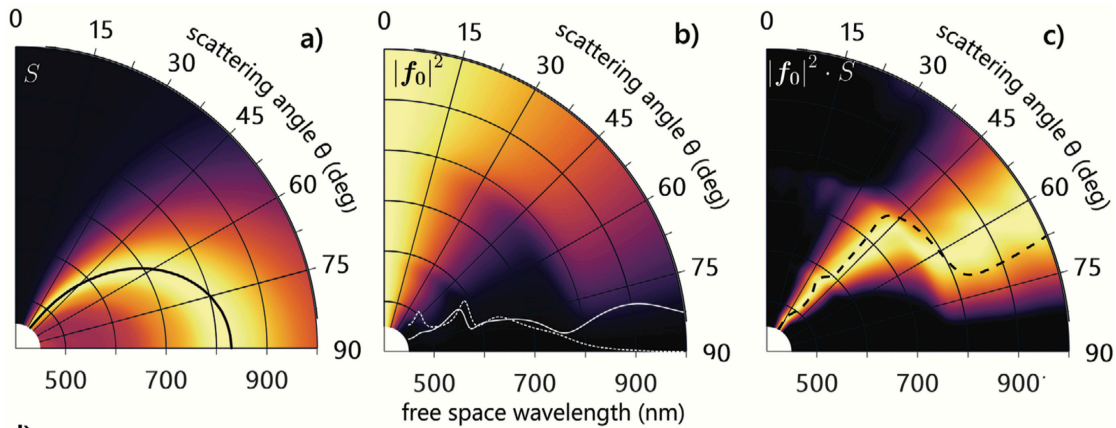


Abb. 4.11: (a) Strukturfaktor $S(\theta, \lambda)$ der in Abb. 4.9 und Abb. 4.10 vermessenen nahezu-HuD-Probe extrahiert aus REM-Aufnahmen. (b) Formfaktor bzw. Streuintensität $|f_0|^2$ des einzelnen Nanoscheibchens, normiert auf den Maximalwert für die jeweilige Wellenlänge. Die überlagerte durchgezogene weiße Kurve deutet die Beiträge zur Streuung von elektrischem und magnetischem Dipol an, die gestrichelte Linie Beiträge von Multipolen höherer Ordnung. (c) ARS der nahezu-HuD-Probe, normiert auf den Maximalwert für die jeweilige Wellenlänge. Die gestrichelte Linie stellt eine Konturlinie der Daten in (b) dar, $|f_0|^2 = 0,35$. Abb. aus [1].

750 nm. Multipolentwicklung ergibt, dass im langwelligen Bereich ausschließlich elektrische und magnetische Dipolstrahlung auftritt, während für den kurzwelligen Bereich elektrische und magnetische Dipol-, Quadrupol- sowie Oktupolstrahlung signifikante Beiträge leisten (siehe auch weiße Kurven). Interferenz insbesondere mit höheren Multipol-Ordnungen führt wie auch hier zu Streuverteilungen, die auf engere Winkelbereiche beschränkt sind und somit das Verhalten begründet.

Um nun die experimentell vermessene ARS (Abb. 4.10b, linke Seite) zu erklären, ist in Abb. 4.11c das Produkt $f_0^2 \cdot S$ dargestellt. Es handelt sich dabei um dieselben Daten wie in Abb. 4.10b, rechte Seite, allerdings ebenfalls normiert auf den Maximalwert für jede Wellenlänge, um die dominante Streurichtung zu visualisieren. Zusätzlich ist eine Konturlinie eingezeichnet, die dem Wert von f_0^2 am Streumaximum der Probe folgt ($\lambda = 560$ nm, $\theta = 35^\circ$, siehe Abb. 4.10b, linke Seite).

In dieser Darstellung wird offensichtlich, dass Lichtstreuung in einer HuD-Struktur nicht allein von S abhängt. Die Konturlinie, die sich auf f_0^2 des Einzelpartikels bezieht, folgt eindeutig dem Verlauf maximaler Streuung des HuD-Ensembles (hell-gelbe Bereiche), d.h. die Winkelabhängigkeit des einzelnen Streuelements ist der Winkelabhängigkeit des Ensembles ausgeprägt. Dies steht in starkem Kontrast zur Beugung in periodischen Strukturen. In diesen ist der Einfluss des Formfaktors f_0 beschränkt auf die Intensitätsverteilung zwischen den Beugungsordnungen und besitzt keinerlei Einfluss auf die Winkelabhängigkeit. In zufälligen Strukturen wiederum bestimmt f_0 allein die Winkelabhängigkeit, da für diese $S = 1$ ist, so

4 Lichtmanagement mit geordneter Unordnung: Hyperuniformität

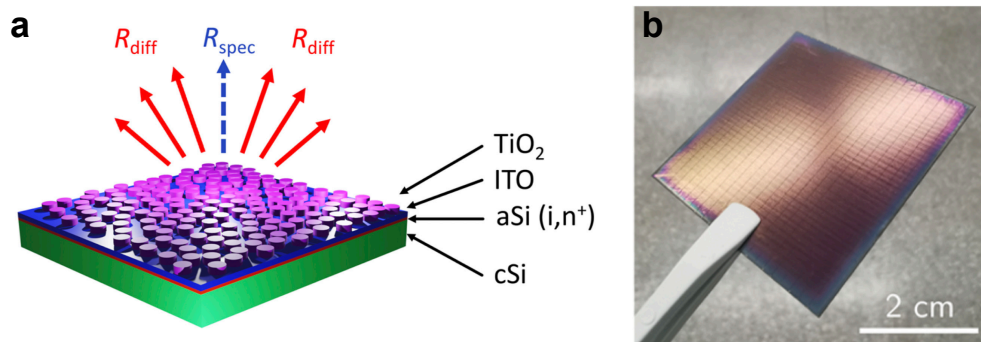


Abb. 4.12: (a) Schichtstruktur der Vorderseite. Basis ist eine HJT-Solarzelle mit Rückseitenemitter. Auf der Vorderseite wird der c-Si-Absorber durch eine dünne Schicht aus amorphem Si passiviert, während eine ITO-Schicht als ARC und elektrischer Kontakt fungiert. Auf die Solarzelle wurde unser in 4.5 beschriebene Fabrikationsprozess angewandt. (b) Foto der fertigen Solarzelle. Abb. aus [2].

dass HuD-Strukturen auch zu diesen im Kontrast stehen. In HuD-Strukturen dominiert weder S noch f_0 ; stattdessen wird eine wechselseitige Abhängigkeit ermöglicht.

Korrelationen allein reichen für diese Eigenschaft nicht aus. So gut wie alle in der Nanophotonik verwendeten Nanopartikel weisen Vorwärtsstreuung in kleine Winkel θ auf. Solange S für $q \rightarrow 0$ nicht gegen null tendiert, wird die Ensemblestreuung immer ein Maximum bei kleinen θ aufweisen, da das Produkt $S f_0^2$ dort groß sein wird. Um Streuung in kleine Winkel zu unterdrücken, muss S im entsprechenden q -Bereich so klein wie möglich sein und ansonsten groß, welches genau der Definition hyperuniformer Unordnung entspricht. Diese Eigenschaft stellt einen neuartigen Ansatz dar, Lichtstreuung nach Bedarf maßzuschneidern und ebnet den Weg zu einer neuen Klasse optischer Metamaterialien.

4.6 Hyperuniforme Unordnung für Antireflexion in Heterojunction-Solarzellen

Mit der richtigen Geometrie lassen sich in dielektrischen Nanoscheibchen elektrische und magnetische Dipolresonanz gleichzeitig für eine Wellenlänge anregen [183,184]. Ist die Resonanz von gleicher Amplitude, ist für dieses sog. duale System Rückstreuung vollständig unterdrückt und ein Array solcher Streuer wird auch Huygenssche Metaoberfläche (*metasurface*) genannt, da es an die nur vorwärts abstrahlenden Emitter aus Huygens Elementarwellen-Theorie erinnert [177,185,186]. In einer erweiterten Betrachtung basiert dieser Effekts auf der Erhaltung der Helizität des einfallenden Lichts, wozu neben der Dualität auch eine Rotations-symmetrie $2\pi/l$, mit $l \geq 3$, bestehen muss [187–189]. Darunter fallen auch HuD-Muster, da sie statistisch isotrop sind ($l \rightarrow \infty$).

4.6 Hyperuniforme Unordnung für Antireflexion in Heterojunction-Solarzellen

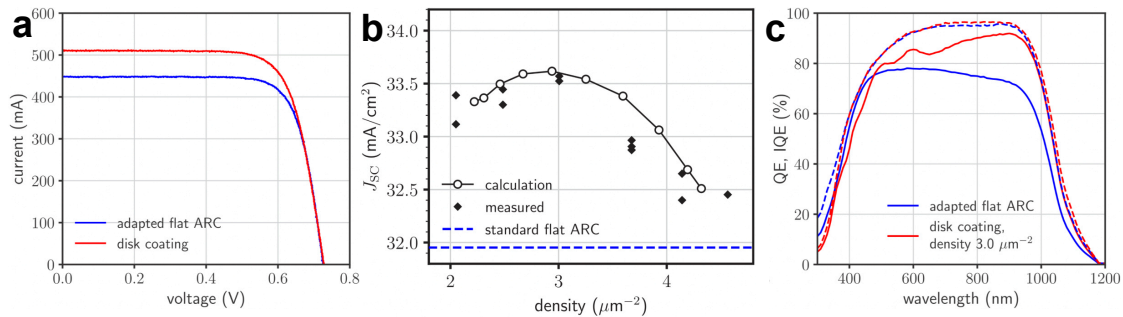


Abb. 4.13: (a) IV-Kennlinie einer Solarzelle vor (adapted flat ARC) und nach (disk coating) Aufbringen der Nanoscheibchen-Vorderseitenstruktur. (b) Experimentell gemessene und berechnete Kurzschlussstromdichte. Die blau gestrichelte Linie stellt den Wert für den flach-optimierten Fall dar. (c) Externe (durchgezogene Kurven) und interne (gestrichelte Kurven) Quanteneffizienzen der in (a) gezeigten Solarzellen. Abb. aus [2].

Derartige Systeme stellen einen völlig neuartigen Ansatz für Antireflexion in Solarzellen dar [190–192]. In Zusammenarbeit mit dem Karlsruher Institut für Technologie KIT sowie dem Solarzellen- und -modul-Hersteller Meyer Burger AG haben wir ungeordnete hochbrechende Nanoscheibchen mit unserem oben beschriebenen Prozess auf industrielle Silizium-Heterojunction-Solarzellen als Vorderseiten-Struktur aufgebracht [2], siehe Abb. 4.12. Im Gegensatz zu ähnlichen Arbeiten aus der Literatur handelt es sich hierbei um die erste Anwendung einer derartigen photonischen Struktur auf großflächigen Solarzellen, was u.a. die Skalierbarkeit unseres Prozesses in einem industriellen Kontext unterstreicht.

Nahezu-HuD-Arrays aus TiO_2 -Nanoscheibchen (Durchmesser 370 nm, Höhe 122 nm) wurden auf untexturierten Solarzellen von Meyer Burger auf Basis ihrer Heterojunction-Technologie (HJT) mit flacher Antireflexionsschicht aus Indiumzinnoxid (ITO, Dicke 50 nm) aufgebracht. Der Vorher-Nachher-Vergleich der Strom-Spannungs-Kennlinien (IV) in Abb. 4.13a zeigt keine Einbußen in der Kurzschluss-Spannung ($V_{OC, \text{flach}} = 726 \text{ mV}$, $V_{OC, \text{disk}} = 728 \text{ mV}$), was die Kompatibilität unseres Prozesses unter potentiellen Bedingung in der Solarzellenproduktion aufzeigt. Die Funktion der Struktur, spektral breite Absorptionserhöhung, macht sich hingegen im Kurzschlussstrom bemerkbar, welcher von $I_{SC, \text{flach}} = 448 \text{ mA}$ auf $I_{SC, \text{disk}} = 511 \text{ mA}$ steigt, was einer Erhöhung um 14% entspricht. Die resultierende relative Wirkungsgradsteigerung beträgt 10,4% (von $\eta_{\text{flach}} = 16,5\%$ auf $\eta_{\text{disk}} = 18,2\%$). Wird eine untexturierten Solarzelle von Meyer Burger mit optimierter Antireflexionsschicht (ITO-Schichtdicke 80 nm) als Referenz verwendet, so messen wir auch dann einen um 5% gesteigerten Kurzschlussstrom.

In Abb. 4.13b ist die gemessene und vorhergesagt Kurzschlussstromdichte j_{sc} für unterschiedliche Nanoscheibchen-Bedeckungsgrade aufgetragen. Die Vorhersage beruht auf unserem Ansatzes für die Berechnung der optischen Antwort von HuD-Texturen (Gl. 4.8). Den darin einflussenden Strukturfaktor S haben wir hierfür nicht experimentell bestimmt, son-

4 Lichtmanagement mit geordneter Unordnung: Hyperuniformität

dem unserem adaptierten RSA-Modell für die Kugeldeposition entnommen. Wir erkennen auch hier wieder eine gute Übereinstimmung zwischen unserem Modell und dem Experiment und ferner, dass die Nanoscheiben für den gesamten betrachteten Bereich zu höheren j_{scs} führen als die flach-optimierte Referenzstruktur. Die signifikante Steigerung ist auf die erhöhte Lichtabsorption durch die Nanoscheibchen-Textur zurückzuführen. Die EQE in Abb. 4.13 (durchgezogene Kurven) ist aufgrund der besseren Antireflexion bis auf $\lambda < 500$ nm über den gesamten Wellenlängenbereich erhöht. Absorptionserhöhung für $\lambda > 1000$ nm aufgrund Lichtwegverlängerung durch Vorwärtsstreuung in große Winkel ist anzunehmen, wurde in dieser Arbeit aber nicht näher untersucht. Eine weitere Analyse zeigt, dass diffus zurückgestreutes Licht noch nicht vollständig unterdrückt werden konnte. Eine diesbezügliche Verbesserung mit stärkerer Absorptionserhöhung ist für HuD-Anordnungen mit verringerter Hyperuniformitätsmetrik H (Gl. 4.6) zu erwarten, z.B. durch Optimierung bzw. Adaption des Depositionsprozesses der ungeordneten Templat-Kugelmonolage.

5 Fazit und Ausblick

In dieser Arbeit wurden optische Ansätze für die Erhöhung des Wirkungsgrads photovoltaischer Anwendungen wie Solarzellen untersucht. Aus Sicht des Lichtmanagements entspricht eine Wirkungsgraderhöhung einer verstärkten Absorption im Basismaterial. Die von mir behandelten Ansätze basieren auf einer Absorptionserhöhung durch verbesserte Antireflexion und Lichtwegverlängerung. Erstere soll sicherstellen, dass der Solarzelle die größtmögliche Lichtenergie für die Energiekonversion zu Verfügung steht. Das Ziel letzterer ist, auch Photonen mit geringer Absorptionswahrscheinlichkeit nutzbar zu machen.

Die untersuchten Ansätze müssen wichtige Anforderungen berücksichtigen, die über rein optische Überlegungen hinausgehen. Die wichtigste Bedingung auf physikalischer Ebene ist, dass neben der erhöhten Generation von Elektron-Loch-Paaren durch einfallende Photonen auch die Nutzung dieser gewährleistet ist (Abschnitt 2.4). Schlüsselfaktor hierfür stellt eine ausreichend unterdrückte Oberflächenrekombination dar. In einigen wenigen Fällen wie bei ICP-RIE-generiertem schwarzen Silizium kann dies durch fortgeschrittene Passivierschichten sichergestellt werden (Abschnitt 2.7). Der geeignetste Weg ist jedoch, die empfindlichen Absorbergrenzflächen planar zu belassen und nicht zu texturieren. Eine gut passivierte, planare Grenzfläche wird immer eine niedrigere Oberflächenrekombination aufweisen, als eine entsprechende nicht-planare Grenzfläche.

Eine weitere Rahmenbedingung ist die technische Umsetzbarkeit des Ansatzes für die potentielle Anwendung in einer realen Solarzelle. Solarzellen sind in ihrer Art großflächige Elemente, weshalb die jeweilige Herstellungsmethode zumindest prinzipiell auf diese Flächen hochskalierbar sein muss. Die Solarzellen-Produktion ist außerdem äußerst kostensensitiv, so dass selbst für vielversprechende Ansätze nur solche in Frage kommen, die nur geringe zusätzliche Kosten verursachen. Diesbezüglich sind insbesondere der MACE-Prozess (Abschnitt 2.6), die von uns entwickelte Fabrikation 3D photonischer Kristalle mittels Sprühbeschichtung (Abschnitt 3.5) sowie die Nanokugeldeposition für nahezu-HuD-Substrate (Abschnitt 4.4) zu nennen.

Mittelpunkt der vorliegenden Arbeit ist die Auswirkung der strukturellen Anordnung der lichtstreuenden Elemente auf die erreichbare Absorptionserhöhung. Die nadelförmigen Streuelemente der schwarzen Siliziumtexturen aus Kapitel 2 sind im wesentlichen zufällig ange-

5 Fazit und Ausblick

ordnet. Die Kombination aus charakteristischen Größen im Bereich weniger Nanometer an den Spitzen und Größen im Bereich der Lichtwellenlänge am unteren Ende führt zu exzellenten optischen Eigenschaften. Antireflexion ist für schwarzes Silizium annähernd ideal und die Lichtwegverlängerung nähert sich dem $4n^2$ -Limit. Im Gegenzug vermindern sich allerdings die elektronischen Eigenschaften des Materials aufgrund des schwerwiegenden strukturellen Eingriffs in die Grenzfläche. Die beobachtete Degradation ist stark von der eingesetzten Herstellungsmethode abhängig, einzig für ICP-RIE- und in Ansätzen auch für MACE-Texturierung kann die Lebensdauer der Minoritätsladungsträger durch optimierte Passivierschichten zumindest in die Größenordnung einer untexturierten Si-Oberfläche zurückgeholt werden.

In Kapitel 3 sind die Streuelemente streng periodisch angeordnet und anstatt diffuser Streuung besteht das Lichtmanagement in diesen Strukturen in einem Umlenken des einfallenden Lichts, hervorgerufen durch Gitterbeugung. Periodische Strukturen sind aufgrund ihrer starken Wellenlängen- und Winkelabhängigkeit schwierig mit der benötigten spektralen Breitbandigkeit zu vereinbaren bzw. zu optimieren. Sie bieten allerdings potentiell sehr hohe Lichtwegverlängerungen, weswegen sie immer noch Gegenstand aktueller Forschung sind. So können Gitter beispielsweise für sehr geringe Absorberdicken wie ultradünne c-Si-Solarzellen (Abschnitt 3.2) und den noch dünneren Dünnschicht-Solarzellen (Abschnitt 3.3) Licht effektiv in Richtungen außerhalb des Emissionskegels beugen und durch Totalreflexion an der vorderen Grenzfläche in schichteigene Wellenleitermoden koppeln.

Aufbauend auf den Erkenntnissen der vorherigen Kapitel wird in Kapitel 4 korrelierte Unordnung und insbesondere hyperuniforme Unordnung als neuartiger Lichtmanagement-Ansatz eingeführt. Die gezielte Anpassung der Raumfrequenzen einer Textur an die Anforderungen der gestreuten Wellenvektoren wird erst durch ein vertieftes Verständnis über korrelierte Unordnung ermöglicht. Das Konzept der Hyperuniformität mit seiner systematischen Kategorisierung von Struktur im reziproken Raum bietet hierfür einen in diesem Rahmen bisher kaum verfolgten Zugang. Mit meinem Team konnte ich eine der ersten Arbeiten zur experimentellen Realisation von nahezu-HuD-Strukturen beitragen (Abschnitt 4.4), die nicht nur skalierbar sind, sondern sich auch in einem industriellen Kontext auf Solarzellen nach aktuellem Stand der Technik beweisen konnten (Abschnitt 4.6). Weiter konnten wir aufzeigen, wie HuD neuartige Möglichkeiten für die maßgeschneiderte Lichtstreuung ermöglicht. Anders als in konventionellen Strukturen, in denen die Streuwinkelverteilung entweder allein durch den einzelne Streuer und seinen Formfaktor f_0 (zufällige Strukturen) bestimmt ist oder nur durch ihre Anordnung untereinander mit dem Strukturfaktor S (periodische Strukturen), erlaubt HuD ein präzises Wechselspiel zwischen beiden.

Der nächste wichtige Meilenstein im Zuge der vorgestellten Arbeiten ist eine HuD-Rück-

seitenstruktur für die Lichtwegverlängerung in Solarzellen. Aus meiner Sicht ist eine solche Struktur besonders vielversprechend, da schon ihr zugehöriger Strukturfaktor S allein die gewünschte Streulicht-Winkelabhängigkeit (Abb. 4.1b) aufweisen kann. Mit dem richtigen Formfaktor f_0 , beispielsweise hochbrechenden Nanoscheibchen mit hohen Streuquerschnitten, kann die Streuung voraussichtlich nicht nur effizient, sondern auch von ausreichender spektraler Breite sein.

Die Forschung zu HuD steht noch am Anfang. Nachdem das Thema für viele Jahre nur von theoretischer Seite bearbeitet wurde, kommen langsam mehr und mehr experimentelle Arbeiten wie auch die unseren hinzu und das Interesse steigt nicht nur im Bereich Optik und Photonik. Diese spannende Entwicklung liegt nicht zuletzt an der grundsätzlichen Bedeutung von *Struktur* in praktisch allen Bereichen der Physik. Einerseits lassen sich die beobachteten Phänomene aus der Wechselwirkung von Licht mit HuD-Strukturen natürlich auch auf andere Wellentypen übertragen, z.B. Phononen [193], andererseits werden HuD-Strukturen auch neuartige Transport- und mechanische Eigenschaften zugesprochen [157,194–198]. Eine wichtige experimentelle Herausforderung ist dann die gezielte Herstellung von und Kontrolle über HuD auf den jeweiligen Größenskalen, insbesondere bei dem Übergang von den in dieser Arbeit behandelten 2D- zu 3D-Strukturen.

6 Literaturverzeichnis

1. Piechulla, P. M. *et al.* Tailored Light Scattering through Hyperuniform Disorder in Self-Organized Arrays of High-Index Nanodisks. *Adv. Opt. Mater.* **9**, 2100186 (2021).
2. Piechulla, P. M. *et al.* Antireflective Huygens' Metasurface with Correlated Disorder Made from High-Index Disks Implemented into Silicon Heterojunction Solar Cells. *ACS Photonics* **8**, 3476–3485 (2021).
3. Dhawan, P. *et al.* Light-Trapping Structures for Planar Solar Cells Inspired by Transformation Optics. *Opt. Express* **29**, 19903–19919 (2021).
4. Sievers, J. *et al.* Periodic Metal Resonator Chains for Surface Enhanced Raman Scattering (SERS). *J. Appl. Phys.* **130**, 223104 (2021).
5. Schneider, T. *et al.* Ultrathin CIGSe Solar Cells with Integrated Structured Back Reflector. *Solar RRL* **4**, 2000295 (2020).
6. Chang, Y.-C. *et al.* Large-Area Nanosphere Gratings for Light Trapping and Reduced Surface Losses in Thin Solar Cells. *IEEE J. Photovoltaics* **9**, 1012–1019 (2019).
7. Nanz, S. *et al.* Light-Trapping Front Textures for Solar Cells from Tailored Mixtures of Nanospheres: A Numerical Study. *Phys. Status Solidi A* **215**, 1800699 (2018).
8. Piechulla, P. M. *et al.* Fabrication of Nearly-Hyperuniform Substrates by Tailored Disorder for Photonic Applications. *Adv. Opt. Mater.* **6**, 1701272 (2018).
9. Nanz, S. *et al.* Strategy for Tailoring the Size Distribution of Nanospheres to Optimize Rough Backreflectors of Solar Cells. *Opt. Express* **26**, A111–A123 (2018).
10. Ilse, K., Schneider, T., Ziegler, J., Sprafke, A. & Wehrspohn, R. B. Integrated Low-Temperature Process for the Fabrication of Amorphous Si Nanoparticles Embedded in Al₂O₃ for Non-Volatile Memory Application. *Physica Status Solidi A* **213**, 2446–2451 (2016).
11. Sardana, N. *et al.* Localized Surface Plasmon Resonance in the IR Regime. *Opt. Express* **24**, 254–261 (2016).
12. Li, X., Lee, J.-H., Sprafke, A. N. & Wehrspohn, R. B. Black Metallurgical Silicon for Solar Energy Conversion. *Semicond. Sci. Technol.* **31**, 014009 (2016).
13. Muchow, M., Büchner, T., Sprafke, A. & Seifert, G. Femtosecond Laser-Written High-Efficiency Blazed Phase Gratings in the Volume of Soda Lime Glass for Light Management in Solar Modules. *Opt. Express* **23**, 33540–33549 (2015).
14. Schumann, M. F. *et al.* Cloaked Contact Grids on Solar Cells by Coordinate Transformations: Designs and Prototypes. *Optica* **2**, 850–853 (2015).
15. Gaudig, M. *et al.* Properties of Black Silicon Obtained at Room-Temperature by Different Plasma Modes. *J. Vac. Sci. Technol. A* **33**, 05E132 (2015).
16. Ziegler, J. *et al.* Plasma-Enhanced Atomic-Layer-Deposited MoO_x Emitters for Silicon Heterojunction Solar Cells. *Appl. Phys. A* **120**, 811–816 (2015).

6 Literaturverzeichnis

17. Otto, M. *et al.* Black Silicon Photovoltaics. *Adv. Opt. Mater.* **3**, 147–164 (2015).
18. Li, X. *et al.* Stable Silicon Anodes for Lithium-Ion Batteries Using Mesoporous Metallurgical Silicon. *Adv. Energy Mater.* **5**, 1401556 (2015).
19. Li, X. *et al.* Photoelectrochemical Hydrogen Evolution of Tapered Silicon Nanowires. *Phys. Chem. Chem. Phys.* **17**, 800–804 (2015).
20. Li, X. *et al.* Self-Purification Model for Metal-Assisted Chemical Etching of Metallurgical Silicon. *Electrochim. Acta* **138**, 476–480 (2014).
21. Ziegler, J. *et al.* Influence of Black Silicon Surfaces on the Performance of Back-Contacted Back Silicon Heterojunction Solar Cells. *Opt. Express* **22**, A1469–A1476 (2014).
22. Ziegler, J., Otto, M., Sprafke, A. N. & Wehrspohn, R. B. Activation of Al₂O₃ Passivation Layers on Silicon by Microwave Annealing. *Appl. Phys. A* **113**, 285–290 (2013).
23. Sprafke, A. N., Schneevoigt, D., Seidel, S., Schweizer, S. L. & Wehrspohn, R. B. Automated Spray Coating Process for the Fabrication of Large-Area Artificial Opals on Textured Substrates. *Opt. Express* **21**, A528–A538 (2013).
24. Li, X. *et al.* Fast Electroless Fabrication of Uniform Mesoporous Silicon Layers. *Electrochim. Acta* **94**, 57–61 (2013).
25. Li, X. *et al.* Influence of the Mobility of Pt Nanoparticles on the Anisotropic Etching Properties of Silicon. *ECS Solid State Lett.* **2**, P22 (2013).
26. Otto, M. *et al.* Passivation of Optically Black Silicon by Atomic Layer Deposited Al₂O₃. *Energy Procedia. Proceedings of the 3rd International Conference on Crystalline Silicon Photovoltaics (SiliconPV 2013)* **38**, 862–865 (2013).
27. Sprafke, A. N. & Wehrspohn, R. B. Light Trapping Concepts for Photon Management in Solar Cells. *Green* **2**, 177–187 (2012).
28. Sprafke, A. & Schilling, J. in *Dielectric Metamaterials* (Hrsg. Brener, I., Liu, S., Staude, I., Valentine, J. & Holloway, C.) 249–288 (Woodhead Publishing, 2020).
29. Sprafke, A. N. & Wehrspohn, R. B. in *Photon Management in Solar Cells* (Hrsg. Wehrspohn, R. B., Rau, U. & Gombert, A.) 1–20 (Wiley-VCH Verlag GmbH & Co. KGaA, Weinheim, Germany, 2015).
30. VDMA. *International Technology Roadmap for Photovoltaic (ITRPV)* Techn. Ber. (2022).
31. Shockley, W. & Queisser, H. J. Detailed Balance Limit of Efficiency of *P-n* Junction Solar Cells. *J. Appl. Phys.* **32**, 510–519 (1961).
32. Ehrler, B., Hutter, E. M. & Berry, J. J. The Complicated Morality of Named Inventions. *ACS Energy Lett.* **6**, 565–567 (2021).
33. Green, M. A. *Recent Advances in Silicon Solar Cell Performance in Tenth EC Photovolt. Sol. Energy Conf.* (Hrsg. Luque, A., Sala, G., Palz, W., Santos, G. & Helm, P.) (Springer Netherlands, Dordrecht, 1991), 250–253.
34. Würfel, P. & Würfel, U. *Physics of Solar Cells: From Basic Principles to Advanced Concepts* 3rd edition (Wiley-VCH Verlag GmbH & Co. KGaA, Weinheim, 2016).
35. Wang, A., Zhao, J. & Green, M. A. 24% Efficient Silicon Solar Cells. *Appl. Phys. Lett.* **57**, 602–604 (1990).
36. *Best Research-Cell Efficiency Chart* <https://www.nrel.gov/pv/cell-efficiency.html>.
37. Al-Ashouri, A. *et al.* Monolithic Perovskite/Silicon Tandem Solar Cell with >29% Efficiency by Enhanced Hole Extraction. *Science* **370**, 1300–1309 (2020).
38. Fu, F. *et al.* Monolithic Perovskite-Silicon Tandem Solar Cells: From the Lab to Fab? *Adv. Mater.* **34**, 2106540 (2022).

39. Kuznetsov, A. I., Miroshnichenko, A. E., Brongersma, M. L., Kivshar, Y. S. & Luk'yanchuk, B. Optically Resonant Dielectric Nanostructures. *Science* **354**, aag2472 (2016).
40. Kruk, S. & Kivshar, Y. Functional Meta-Optics and Nanophotonics Governed by Mie Resonances. *ACS Photonics* **4**, 2638–2649 (2017).
41. Brongersma, M. L., Cui, Y. & Fan, S. Light Management for Photovoltaics Using High-Index Nanostructures. *Nat. Mater.* **13**, 451–460 (2014).
42. Polman, A., Knight, M., Garnett, E. C., Ehrler, B. & Sinke, W. C. Photovoltaic Materials: Present Efficiencies and Future Challenges. *Science* **352**, aad4424 (2016).
43. Garnett, E. C., Ehrler, B., Polman, A. & Alarcon-Llado, E. Photonics for Photovoltaics: Advances and Opportunities. *ACS Photonics* **8**, 61–70 (2021).
44. Born, M. & Wolf, E. *Principles of Optics: Electromagnetic Theory of Propagation, Interference and Diffraction of Light* 7th expanded ed (Cambridge University Press, Cambridge ; New York, 1999).
45. Campbell, P. & Green, M. A. Light Trapping Properties of Pyramidally Textured Surfaces. *J. Appl. Phys.* **62**, 243–249 (1987).
46. Campbell, P. Enhancement of Light Absorption from Randomizing and Geometric Textures. *J. Opt. Soc. Am. B* **10**, 2410 (1993).
47. Ingenito, A., Isabella, O. & Zeman, M. Experimental Demonstration of 4n² Classical Absorption Limit in Nanotextured Ultrathin Solar Cells with Dielectric Omnidirectional Back Reflector. *ACS Photonics* **1**, 270–278 (2014).
48. Torquato, S. Hyperuniform States of Matter. *Phys. Reports* **745**, 1–95 (2018).
49. Huang, Y.-F. *et al.* Improved Broadband and Quasi-Omnidirectional Anti-Reflection Properties with Biomimetic Silicon Nanostructures. *Nat. Nanotechnol.* **2**, 770–774 (2007).
50. Kroll, M. *et al.* *Black Silicon for Solar Cell Applications* in *SPIE Photonics Europe* (Hrsg. Wehrspohn, R. & Gombert, A.) (Brussels, Belgium, 2012), 843817.
51. Koynov, S., Brandt, M. S. & Stutzmann, M. Black Nonreflecting Silicon Surfaces for Solar Cells. *Appl. Phys. Lett.* **88**, 203107 (2006).
52. Halbwx, M. *et al.* Micro and Nano-Structuration of Silicon by Femtosecond Laser: Application to Silicon Photovoltaic Cells Fabrication. *Thin Solid Films* **516**, 6791–6795 (2008).
53. Oh, J., Yuan, H.-C. & Branz, H. M. An 18.2%-Efficient Black-Silicon Solar Cell Achieved through Control of Carrier Recombination in Nanostructures. *Nat. Nanotechnol.* **7**, 743–748 (2012).
54. Savin, H. *et al.* Black Silicon Solar Cells with Interdigitated Back-Contacts Achieve 22.1% Efficiency. *Nat. Nanotechnol.* **10**, 624–628 (2015).
55. Oh, I., Kye, J. & Hwang, S. Enhanced Photoelectrochemical Hydrogen Production from Silicon Nanowire Array Photocathode. *Nano Lett.* **12**, 298–302 (2012).
56. Steglich, M., Zilk, M., Schrempel, F., Tünnermann, A. & Kley, E.-B. Improvement of Ge-on-Si Photodiodes by Black Silicon Light Trapping. *Appl. Phys. Lett.* **102**, 111110 (2013).
57. Gesemann, B., Wehrspohn, R., Hackner, A. & Müller, G. Large-Scale Fabrication of Ordered Silicon Nanotip Arrays Used for Gas Ionization in Ion Mobility Spectrometers. *IEEE Trans. Nanotechnology* **10**, 50–52 (2011).
58. Jackson, J. D. *Classical Electrodynamics* 3rd ed (Wiley, New York, 1999).
59. Southwell, W. H. Gradient-Index Antireflection Coatings. *Opt. Lett.* **8**, 584–586 (1983).
60. Kroll, M. *et al.* *Optical Modeling of Needle like Silicon Surfaces Produced by an ICP-RIE Process* in *Photonics Sol. Energy Syst. III* **7725** (SPIE, 2010), 36–45.

6 Literaturverzeichnis

61. Yablonovitch, E. & Cody, G. Intensity Enhancement in Textured Optical Sheets for Solar Cells. *IEEE Trans. Electron Devices* **29**, 300–305 (1982).
62. Yablonovitch, E. Statistical Ray Optics. *J. Opt. Soc. Am.* **72**, 899–907 (1982).
63. Wang, Z. Y. *et al.* Broadband Optical Absorption by Tunable Mie Resonances in Silicon Nanocone Arrays. *Sci. Rep.* **5**, 7810 (2015).
64. Tiedje, T., Yablonovitch, E., Cody, G. & Brooks, B. Limiting Efficiency of Silicon Solar Cells. *IEEE Trans. Electron Devices* **31**, 711–716 (1984).
65. Green, M. Limits on the Open-Circuit Voltage and Efficiency of Silicon Solar Cells Imposed by Intrinsic Auger Processes. *IEEE Trans. Electron Devices* **31**, 671–678 (1984).
66. Green, M. A. Limiting Efficiency of Bulk and Thin-Film Silicon Solar Cells in the Presence of Surface Recombination. *Prog. Photovolt: Res. Appl.* **7**, 327–330 (1999).
67. Yablonovitch, E., Allara, D. L., Chang, C. C., Gmitter, T. & Bright, T. B. Unusually Low Surface-Recombination Velocity on Silicon and Germanium Surfaces. *Phys. Rev. Lett.* **57**, 249–252 (1986).
68. Sproul, A. B. Dimensionless Solution of the Equation Describing the Effect of Surface Recombination on Carrier Decay in Semiconductors. *J. Appl. Phys.* **76**, 2851–2854 (1994).
69. Sinton, R. A. & Cuevas, A. Contactless Determination of Current–Voltage Characteristics and Minority-carrier Lifetimes in Semiconductors from Quasi-steady-state Photoconductance Data. *Appl. Phys. Lett.* **69**, 2510–2512 (1996).
70. Agostinelli, G. *et al.* Very Low Surface Recombination Velocities on P-Type Silicon Wafers Passivated with a Dielectric with Fixed Negative Charge. *Solar Energy Materials and Solar Cells* **90**, 3438–3443 (2006).
71. Hoex, B., Heil, S. B. S., Langereis, E., van de Sanden, M. C. M. & Kessels, W. M. M. Ultra-low Surface Recombination of C-Si Substrates Passivated by Plasma-Assisted Atomic Layer Deposited Al₂O₃. *Appl. Phys. Lett.* **89**, 042112 (2006).
72. Otto, M. *et al.* Extremely Low Surface Recombination Velocities in Black Silicon Passivated by Atomic Layer Deposition. *Appl. Phys. Lett.* **100**, 191603 (2012).
73. Otto, M. *Effective passivation of black silicon surfaces by conformal thermal ALD deposited Al₂O₃ layers* Diss. (Martin Luther University Halle-Wittenberg, 2015).
74. Füchsel, K. *et al.* *Black Silicon Photovoltaics in Photonics Sol. Energy Syst. IV* **8438** (SPIE, 2012), 98–105.
75. Huang, Z., Geyer, N., Werner, P., de Boor, J. & Gösele, U. Metal-Assisted Chemical Etching of Silicon: A Review. *Adv. Mater.* **23**, 285–308 (2011).
76. Gimpel, T., Höger, I., Falk, F., Schade, W. & Kontermann, S. Electron Backscatter Diffraction on Femtosecond Laser Sulfur Hyperdoped Silicon. *Appl. Phys. Lett.* **101**, 111911 (2012).
77. Schwartz, G. C. & Schaible, P. M. Reactive Ion Etching of Silicon. *Journal of Vacuum Science and Technology* **16**, 410–413 (1979).
78. Perry, A. J. & Boswell, R. W. Fast Anisotropic Etching of Silicon in an Inductively Coupled Plasma Reactor. *Appl. Phys. Lett.* **55**, 148–150 (1989).
79. Gittleman, J. I., Sichel, E. K., Lehmann, H. W. & Widmer, R. Textured Silicon: A Selective Absorber for Solar Thermal Conversion. *Appl. Phys. Lett.* **35**, 742–744 (1979).
80. Repo, P. *et al.* N-Type Black Silicon Solar Cells. *Energy Procedia* **38**, 866–871 (2013).
81. Mellhaoui, X. *et al.* SiO_xF_y Passivation Layer in Silicon Cryoetching. *J. Appl. Phys.* **98**, 104901 (2005).

82. Gaudig, M., Maiberg, M., Plapp, M. & Wehrspohn, R. B. Model for Black Silicon Formation Just from Surface Temperature Non-Uniformities. *J. Appl. Phys.* **124**, 233302 (2018).
83. Schnell, M., Ludemann, R. & Schaefer, S. *Plasma Surface Texturization for Multicrystalline Silicon Solar Cells* in *28th IEEE Photovolt. Spec. Conf.* (IEEE, Anchorage, AK, USA, 2000), 367–370.
84. Yoo, J., Yu, G. & Yi, J. Large-Area Multicrystalline Silicon Solar Cell Fabrication Using Reactive Ion Etching (RIE). *Sol. Energy Mater. Sol. Cells* **95**, 2–6 (2011).
85. Allen, T., Bullock, J., Cuevas, A., Baker-Finch, S. & Karouta, F. *Reactive Ion Etched Black Silicon Texturing: A Comparative Study* in *IEEE 40th Photovolt. Spec. Conf. PVSC* (IEEE, Denver, CO, USA, 2014), 0562–0566.
86. Macdonald, D. *et al.* Texturing Industrial Multicrystalline Silicon Solar Cells. *Solar Energy* **76**, 277–283 (2004).
87. Deenapanray, P. N. K., Hörteis, M., Macdonald, D. & Weber, K. J. Minority Carrier Lifetime Properties of Reactive Ion Etched P-Type Float Zone Si. *Electrochem. Solid-State Lett.* **8**, G78 (2005).
88. Archer, R. Stain Films on Silicon. *J. Phys. Chem. Solids* **14**, 104–110 (1960).
89. Ye, X. *et al.* 18.45%-Efficient Multi-Crystalline Silicon Solar Cells with Novel Nanoscale Pseudo-Pyramid Texture. *Adv. Funct. Mater.* **24**, 6708–6716 (2014).
90. Hutchins, Mark. *Black Is the New Black* <https://www.pv-magazine.com/magazine-archive/black-is-the-new-black/>. 2017.
91. Beetz, B. *Suntech's Black Silicon Solar Cells Enter Mass Production* <https://www.pv-magazine.com/2018/01/04/suntechs-black-silicon-solar-cells-enter-mass-production/>. 2018.
92. Li, X. *et al.* Upgraded Silicon Nanowires by Metal-Assisted Etching of Metallurgical Silicon: A New Route to Nanostructured Solar-Grade Silicon. *Adv. Mater.* **25**, 3187–3191 (2013).
93. McHugo, S. A., Thompson, A. C., Périchaud, I. & Martinuzzi, S. Direct Correlation of Transition Metal Impurities and Minority Carrier Recombination in Multicrystalline Silicon. *Appl. Phys. Lett.* **72**, 3482–3484 (1998).
94. Ma, X., Zhang, J., Wang, T. & Li, T. Hydrometallurgical Purification of Metallurgical Grade Silicon. *Rare Metals* **28**, 221–225 (2009).
95. Zhong, X., Qu, Y., Lin, Y.-C., Liao, L. & Duan, X. Unveiling the Formation Pathway of Single Crystalline Porous Silicon Nanowires. *ACS Appl. Mater. Interfaces* **3**, 261–270 (2011).
96. Heine, C. & Morf, R. H. Submicrometer Gratings for Solar Energy Applications. *Appl. Opt.* **34**, 2476 (1995).
97. Zeng, L. *et al.* Efficiency Enhancement in Si Solar Cells by Textured Photonic Crystal Back Reflector. *Appl. Phys. Lett.* **89**, 111111 (2006).
98. Bermel, P., Luo, C., Zeng, L., Kimerling, L. C. & Joannopoulos, J. D. Improving Thin-Film Crystalline Silicon Solar Cell Efficiencies with Photonic Crystals. *Opt. Express* **15**, 16986 (2007).
99. Dewan, R. & Knipp, D. Light Trapping in Thin-Film Silicon Solar Cells with Integrated Diffraction Grating. *J. Appl. Phys.* **106**, 074901 (2009).
100. Peters, M., Rüdiger, M., Hauser, H., Hermle, M. & Bläsi, B. Diffractive Gratings for Crystalline Silicon Solar Cells—Optimum Parameters and Loss Mechanisms: Diffractive Gratings for Crystalline Silicon Solar Cells. *Prog. Photovolt: Res. Appl.* **20**, 862–873 (2012).
101. Mellor, A. *et al.* Nanoimprinted Diffraction Gratings for Crystalline Silicon Solar Cells: Implementation, Characterization and Simulation. *Opt. Express* **21**, A295 (2013).

6 Literaturverzeichnis

102. Rothemund, R. *et al.* Light Trapping in Pyramidally Textured Crystalline Silicon Solar Cells Using Back-Side Diffractive Gratings: Diffractive Gratings for Pyramidally Textured Silicon Solar Cells. *Prog. Photovolt: Res. Appl.* **21**, 747–753 (2013).
103. Eisenlohr, J. *et al.* Hexagonal Sphere Gratings for Enhanced Light Trapping in Crystalline Silicon Solar Cells. *Opt. Express* **22**, A111 (2014).
104. Eisenlohr, J. *et al.* Rear Side Sphere Gratings for Improved Light Trapping in Crystalline Silicon Single Junction and Silicon-Based Tandem Solar Cells. *Sol. Energy Mater. Sol. Cells* **142**, 60–65 (2015).
105. Peters, M. *et al.* in *Photon Management in Solar Cells* (Hrsg. Wehrspohn, R. B., Rau, U. & Gombert, A.) 49–90 (Wiley-VCH Verlag GmbH & Co. KGaA, Weinheim, Germany, 2015).
106. *Physics of Nanostructured Solar Cells* (Hrsg. Badescu, V. & Paulescu, M.) (Nova Science Publishers, New York, 2010).
107. Yu, Z., Raman, A. & Fan, S. Fundamental Limit of Nanophotonic Light Trapping in Solar Cells. *PNAS* **107**, 17491–17496 (2010).
108. Hulsteen, J. C. & Van Duyne, R. P. Nanosphere Lithography: A Materials General Fabrication Process for Periodic Particle Array Surfaces. *J. Vac. Sci. Technol. A* **13**, 1553–1558 (1995).
109. Jensen, T. R., Malinsky, M. D., Haynes, C. L. & Van Duyne, R. P. Nanosphere Lithography: Tunable Localized Surface Plasmon Resonance Spectra of Silver Nanoparticles. *J. Phys. Chem. B* **104**, 10549–10556 (2000).
110. Haynes, C. L. & Van Duyne, R. P. Nanosphere Lithography: A Versatile Nanofabrication Tool for Studies of Size-Dependent Nanoparticle Optics. *J. Phys. Chem. B* **105**, 5599–5611 (2001).
111. *JCMwave - Complete Finite Element Technology for Optical Simulations* <https://jcmwave.com/>.
112. Tucher, N. *et al.* 3D Optical Simulation Formalism OPTOS for Textured Silicon Solar Cells. *Opt. Express* **23**, A1720 (2015).
113. Raether, H. *Surface Plasmons on Smooth and Rough Surfaces and on Gratings* (Springer Berlin Heidelberg, Berlin, Heidelberg, 1988).
114. Maier, S. A. *Plasmonics: Fundamentals and Applications* (Springer US, New York, NY, 2007).
115. Pillai, S. & Green, M. Plasmonics for Photovoltaic Applications. *Sol. Energy Mater. Sol. Cells* **94**, 1481–1486 (2010).
116. Green, M. A. & Pillai, S. Harnessing Plasmonics for Solar Cells. *Nat. Photonics* **6**, 130–132 (2012).
117. Barugkin, C., Wan, Y., Macdonald, D. & Catchpole, K. R. Evaluating Plasmonic Light Trapping With Photoluminescence. *IEEE J. Photovoltaics* **3**, 1292–1297 (2013).
118. Barugkin, C. *et al.* Light Trapping Efficiency Comparison of Si Solar Cell Textures Using Spectral Photoluminescence. *Opt. Express* **23**, A391 (2015).
119. Delamarre, A., Lombez, L. & Guillemoles, J. F. *Characterization of Solar Cells Using Electroluminescence and Photoluminescence Hyperspectral Images in SPIE OPTO* (Hrsg. Freundlich, A. & Guillemoles, J.-F. E.) (San Francisco, California, USA, 2012), 825614.
120. Jarzembowski, E. *et al.* The Influence of Sodium on the Molybdenum/Cu(In,Ga)Se₂ Interface Recombination Velocity, Determined by Time Resolved Photoluminescence. *Appl. Phys. Lett.* **107**, 051601 (2015).
121. Vermang, B. *et al.* Highly Reflective Rear Surface Passivation Design for Ultra-Thin Cu(In,Ga)Se₂ Solar Cells. *Thin Solid Films* **582**, 300–303 (2015).
122. Jarzembowski, E., Fuhrmann, B., Leipner, H., Fränzel, W. & Scheer, R. Ultrathin Cu(In,Ga)Se₂ Solar Cells with Point-like Back Contact in

- Experiment and Simulation. *Thin Solid Films* **633**, 61–65 (2017).
123. Ferry, V. E., Polman, A. & Atwater, H. A. Modeling Light Trapping in Nanostructured Solar Cells. *ACS Nano* **5**, 10055–10064 (2011).
 124. Paetzold, U. W., Lehnen, S., Bittkau, K., Rau, U. & Carius, R. Nanoscale Observation of Waveguide Modes Enhancing the Efficiency of Solar Cells. *Nano Lett.* **14**, 6599–6605 (2014).
 125. Yamada, T., Nakamura, H., Sugiura, T., Sakuta, K. & Kurokawa, K. Reflection Loss Analysis by Optical Modeling of PV Module. *Sol. Energy Mater. Sol. Cells* **67**, 405–413 (2001).
 126. Schneider, J. *et al.* Combined Effect of Light Harvesting Strings, Anti-Reflective Coating, Thin Glass, and High Ultraviolet Transmission Encapsulant to Reduce Optical Losses in Solar Modules: Optical Loss Reduction by Combining Innovative Solar Module Technologies. *Prog. Photovolt: Res. Appl.* **22**, 830–837 (2014).
 127. Muchow, M., Sprafke, A., Turek, M., Eiternick, S. & Seifert, G. *Increasing the Efficiency of Solar Modules by Femtosecond Laser Written Blazed Phase Gratings in the Volume of Soda Lime Glass in Light Energy Environ.* (OSA, Leipzig, 2016), PW5A.3.
 128. Chan, J., Huser, T., Risbud, S. & Krol, D. Modification of the Fused Silica Glass Network Associated with Waveguide Fabrication Using Femtosecond Laser Pulses. *Appl. Phys. A* **76**, 367–372 (2003).
 129. Voigtländer, C., Richter, D., Thomas, J., Tünnermann, A. & Nolte, S. Inscription of High Contrast Volume Bragg Gratings in Fused Silica with Femtosecond Laser Pulses. *Appl. Phys. A* **102**, 35–38 (2011).
 130. Yablonovitch, E. Inhibited Spontaneous Emission in Solid-State Physics and Electronics. *Phys. Rev. Lett.* **58**, 2059–2062 (1987).
 131. John, S. Strong Localization of Photons in Certain Disordered Dielectric Superlattices. *Phys. Rev. Lett.* **58**, 2486–2489 (1987).
 132. Ulbrich, C. *et al.* Directional Selectivity and Ultra-Light-Trapping in Solar Cells: Directional Selectivity and Ultra-Light-Trapping in Solar Cells. *phys. stat. sol. (a)* **205**, 2831–2843 (2008).
 133. Üpping, J. *et al.* Three-Dimensional Photonic Crystal Intermediate Reflectors for Enhanced Light-Trapping in Tandem Solar Cells. *Adv. Mater.* **23**, 3896–3900 (2011).
 134. Peters, M., Christoph Goldschmidt, J. & Bläsi, B. Efficiency Limit and Example of a Photonic Solar Cell. *J. Appl. Phys.* **110**, 043104 (2011).
 135. Ozin, G. A. & Yang, S. M. The Race for the Photonic Chip: Colloidal Crystal Assembly in Silicon Wafers. *Adv. Funct. Mater.* **11**, 95–104 (2001).
 136. Von Freymann, G., Kitaev, V., Lotsch, B. V. & Ozin, G. A. Bottom-up Assembly of Photonic Crystals. *Chem. Soc. Rev.* **42**, 2528–2554 (2013).
 137. Zhou, Z. & Zhao, X. S. Opal and Inverse Opal Fabricated with a Flow-Controlled Vertical Deposition Method. *Langmuir* **21**, 4717–4723 (2005).
 138. Sprafke, A. *et al.* *Opaline Backside Structures for Photon Management in Solar Cells in Light Energy Environ. 2015* (OSA, Suzhou, 2015), PTu2B.4.
 139. Schneevoigt, D. *3D-photonische Kristalle für optimiertes Photonmanagement in Silizium-Dünnschichtsolarzellen* Diss. (Martin Luther University Halle-Wittenberg, 2020).
 140. Martins, E. R., Li, J., Liu, Y., Zhou, J. & Krauss, T. F. Engineering Gratings for Light Trapping in Photovoltaics: The Supercell Concept. *Phys. Rev. B* **86**, 041404 (2012).
 141. van Lare, M.-C. & Polman, A. Optimized Scattering Power Spectral Density of Photovol-

6 Literaturverzeichnis

- taic Light-Trapping Patterns. *ACS Photonics* **2**, 822–831 (2015).
142. Paetzold, U. W., Moulin, E., Pieters, B. E., Carrius, R. & Rau, U. Design of Nanostructured Plasmonic Back Contacts for Thin-Film Silicon Solar Cells. *Opt. Express* **19**, A1219–A1230 (2011).
143. Van Lare, M., Lenzmann, F. & Polman, A. Dielectric Back Scattering Patterns for Light Trapping in Thin-Film Si Solar Cells. *Opt. Express* **21**, 20738–20746 (2013).
144. Disney, C. E. R., Pillai, S. & Green, M. A. The Impact of Parasitic Loss on Solar Cells with Plasmonic Nano-Textured Rear Reflectors. *Sci. Rep.* **7**, 12826 (2017).
145. Wiersma, D. S. Disordered Photonics. *Nat. Photonics* **7**, 188–196 (2013).
146. Torquato, S. Hyperuniformity and Its Generalizations. *Phys. Rev. E* **94**, 022122 (2016).
147. Wiersma, D. S., Bartolini, P., Lagendijk, A. & Righini, R. Localization of Light in a Disordered Medium. *Nature* **390**, 671–673 (1997).
148. Vynck, K., Burrelli, M., Riboli, F. & Wiersma, D. S. Photon Management in Two-Dimensional Disordered Media. *Nat. Mater.* **11**, 1017–1022 (2012).
149. Sheinfux, H. H. *et al.* Observation of Anderson Localization in Disordered Nanophotonic Structures. *Science* **356**, 953–956 (2017).
150. Yu, S., Piao, X. & Park, N. Disordered Potential Landscapes for Anomalous Delocalization and Superdiffusion of Light. *ACS Photonics* **5**, 1499–1505 (2018).
151. Rockstuhl, C. *et al.* Comparison and Optimization of Randomly Textured Surfaces in Thin-Film Solar Cells. *Opt. Express* **18**, A335–A342 (2010).
152. Wiesendanger, S., Zilk, M., Pertsch, T., Lederer, F. & Rockstuhl, C. A Path to Implement Optimized Randomly Textured Surfaces for Solar Cells. *Appl. Phys. Lett.* **103**, 131115 (2013).
153. Wiesendanger, S., Zilk, M., Pertsch, T., Rockstuhl, C. & Lederer, F. Combining Randomly Textured Surfaces and Photonic Crystals for the Photon Management in Thin Film Microcrystalline Silicon Solar Cells. *Opt. Express* **21**, A450 (2013).
154. Bittkau, K., Hoffmann, A., Paetzold, U. & Carrius, R. Broadening of Light Coupling to Waveguide Modes in Solar Cells by Disordered Grating Textures. *Applied Sciences* **7**, 725 (2017).
155. Donie, Y. J. *et al.* Light Trapping in Thin Film Silicon Solar Cells *via* Phase Separated Disordered Nanopillars. *Nanoscale* **10**, 6651–6659 (2018).
156. Paetzold, U. W. *et al.* Disorder Improves Nanophotonic Light Trapping in Thin-Film Solar Cells. *Appl. Phys. Lett.* **104**, 131102 (2014).
157. Zhang, G., Stillinger, F. H. & Torquato, S. Transport, Geometrical, and Topological Properties of Stealthy Disordered Hyperuniform Two-Phase Systems. *J. Chem. Phys.* **145**, 244109 (2016).
158. Oskooi, A. *et al.* Partially Disordered Photonic-Crystal Thin Films for Enhanced and Robust Photovoltaics. *Appl. Phys. Lett.* **100**, 181110 (2012).
159. Allen, S. M. & Thomas, E. L. *The Structure of Materials* (J. Wiley, New York, 1999).
160. Jiao, Y. *et al.* Avian Photoreceptor Patterns Represent a Disordered Hyperuniform Solution to a Multiscale Packing Problem. *Phys. Rev. E* **89**, 022721 (2014).
161. Mayer, A., Balasubramanian, V., Mora, T. & Walczak, A. M. How a Well-Adapted Immune System Is Organized. *PNAS* **112**, 5950–5955 (2015).
162. Getzin, S. *et al.* Discovery of Fairy Circles in Australia Supports Self-Organization Theory. *PNAS* **113**, 3551–3556 (2016).
163. Xie, R. *et al.* Hyperuniformity in Amorphous Silicon Based on the Measurement of the

- Infinite-Wavelength Limit of the Structure Factor. *PNAS* **110**, 13250–13254 (2013).
164. Florescu, M., Torquato, S. & Steinhardt, P. J. Designer Disordered Materials with Large, Complete Photonic Band Gaps. *PNAS* **106**, 20658–20663 (2009).
 165. Man, W. *et al.* Isotropic Band Gaps and Free-form Waveguides Observed in Hyperuniform Disordered Photonic Solids. *PNAS* **110**, 15886–15891 (2013).
 166. Man, W. *et al.* Photonic Band Gap in Isotropic Hyperuniform Disordered Solids with Low Dielectric Contrast. *Opt. Express* **21**, 19972–19981 (2013).
 167. Sellers, S. R., Man, W., Sahba, S. & Florescu, M. Local Self-Uniformity in Photonic Networks. *Nat. Commun.* **8**, 14439 (2017).
 168. Muller, N., Haberko, J., Marichy, C. & Schefold, F. Silicon Hyperuniform Disordered Photonic Materials with a Pronounced Gap in the Shortwave Infrared. *Adv. Opt. Mater.* **2**, 115–119 (2014).
 169. Muller, N., Haberko, J., Marichy, C. & Schefold, F. Photonic Hyperuniform Networks Obtained by Silicon Double Inversion of Polymer Templates. *Optica* **4**, 361–366 (2017).
 170. Trompoukis, C. *et al.* Disordered Nanostructures by Hole-Mask Colloidal Lithography for Advanced Light Trapping in Silicon Solar Cells. *Opt. Express* **24**, A191–A201 (2016).
 171. Piechulla, P. M., Wehrspohn, R. B. & Sprafke, A. N. Toward Hyperuniform Disorder via Self-Assembly of Bidisperse Colloidal Patterns at an Electrode. *Adv. Mater. Interfaces* **10**, 2201395 (2022).
 172. Israelachvili, J. N. *Intermolecular and Surface Forces* 3rd ed (Academic Press, Burlington, MA, 2011).
 173. Atkinson, S., Zhang, G., Hopkins, A. B. & Torquato, S. Critical Slowing down and Hyperuniformity on Approach to Jamming. *Phys. Rev. E* **94**, 012902 (2016).
 174. Kim, J. & Torquato, S. Effect of Imperfections on the Hyperuniformity of Many-Body Systems. *Phys. Rev. B* **97**, 054105 (2018).
 175. Torquato, S., Uche, O. U. & Stillinger, F. H. Random Sequential Addition of Hard Spheres in High Euclidean Dimensions. *Phys. Rev. E* **74**, 061308 (2006).
 176. Hejna, M., Steinhardt, P. J. & Torquato, S. Nearly Hyperuniform Network Models of Amorphous Silicon. *Phys. Rev. B* **87**, 245204 (2013).
 177. Decker, M. *et al.* High-Efficiency Dielectric Huygens' Surfaces. *Adv. Opt. Mater.* **3**, 813–820 (2015).
 178. Koshelev, K. *et al.* Subwavelength Dielectric Resonators for Nonlinear Nanophotonics. *Science* **367**, 288–292 (2020).
 179. Keller, J. B. *Stochastic Equations and Wave Propagation in Random Media in Proc Symp. Appl Math Vol XVI* (Amer. Math. Soc., Providence, R.I., 1964), 145–170.
 180. Mie, G. Beiträge Zur Optik Trüber Medien, Speziell Kolloidaler Metallösungen. *Ann. Phys.* **330**, 377–445 (1908).
 181. Grahm, P., Shevchenko, A & Kaivola, M. Electromagnetic Multipole Theory for Optical Nanomaterials. *New J. Phys.* **14**, 093033 (2012).
 182. Santiago, X. G. *et al.* Decomposition of Scattered Electromagnetic Fields into Vector Spherical Wave Functions on Surfaces with General Shapes. *Phys. Rev. B* **99**, 045406 (2019).
 183. Van de Groep, J. & Polman, A. Designing Dielectric Resonators on Substrates: Combining Magnetic and Electric Resonances. *Opt. Express* **21**, 26285–26302 (2013).
 184. Staude, I. *et al.* Tailoring Directional Scattering through Magnetic and Electric Resonances in Subwavelength Silicon Nanodisks. *ACS Nano* **7**, 7824–7832 (2013).
 185. Huygens, C. *Traité de La Lumière : Où Sont Expliquées Les Causes de Ce Qui Lui Arrive Dans*

6 Literaturverzeichnis

- La Reflexion, & Dans La Refraction et Particulièrement Dans l'étrange Réfraction Du Cristal d'Islande* (Chez Pierre vander Aa, marchand libraire, A Leide, 1690).
186. Love, Augustus E. H. I. The Integration of the Equations of Propagation of Electric Waves. *Phil. Trans. R. Soc. Lond. A* **197**, 1–45 (1901).
187. Fernandez-Corbaton, I. Forward and Backward Helicity Scattering Coefficients for Systems with Discrete Rotational Symmetry. *Opt. Express* **21**, 29885–29893 (2013).
188. Fernandez-Corbaton, I. *et al.* Electromagnetic Duality Symmetry and Helicity Conservation for the Macroscopic Maxwell's Equations. *Phys. Rev. Lett.* **111**, 060401 (2013).
189. Slivina, E. *et al.* Insights into Backscattering Suppression in Solar Cells from the Helicity-Preservation Point of View. *Phys. Rev. Applied* **12**, 054003 (2019).
190. Spinelli, P., Verschuuren, M. A. & Polman, A. Broadband Omnidirectional Antireflection Coating Based on Subwavelength Surface Mie Resonators. *Nat. Commun.* **3**, 692 (2012).
191. Stevens, L. *et al.* Broadband Antireflection Mie Scatterers Revisited: A Solar Cell and Module Analysis. *Opt. Express* **27**, A524–A535 (2019).
192. Visser, D., Chen, D. Y., Désières, Y., Ravishankar, A. P. & Anand, S. Embossed Mie Resonator Arrays Composed of Compacted TiO₂ Nanoparticles for Broadband Anti-Reflection in Solar Cells. *Sci. Rep.* **10**, 12527 (2020).
193. Gkantzounis, G., Amoah, T. & Florescu, M. Hyperuniform Disordered Phononic Structures. *Phys. Rev. B* **95**, 094120 (2017).
194. Xu, Y., Chen, S., Chen, P.-E., Xu, W. & Jiao, Y. Microstructure and Mechanical Properties of Hyperuniform Heterogeneous Materials. *Phys. Rev. E* **96**, 043301 (2017).
195. Chen, D. & Torquato, S. Designing Disordered Hyperuniform Two-Phase Materials with Novel Physical Properties. *Acta Materialia* **142**, 152–161 (2018).
196. Kim, J. & Torquato, S. Multifunctional Composites for Elastic and Electromagnetic Wave Propagation. *PNAS* **117**, 8764–8774 (2020).
197. Kim, J. & Torquato, S. Effective Elastic Wave Characteristics of Composite Media. *New J. Phys.* **22**, 123050 (2020).
198. Chen, D. *et al.* Nearly Hyperuniform, Non-hyperuniform, and Antihyperuniform Density Fluctuations in Two-Dimensional Transition Metal Dichalcogenides with Defects. *Phys. Rev. B* **103**, 224102 (2021).

7 Ausgewählte Publikationen

- ab Seite 66 M. Gaudig, J. Hirsch, T. Schneider, A. Sprafke, J. Ziegler, N. Bernhard, R. B. Wehrspohn. Properties of black silicon obtained at room-temperature by different plasma modes, *J. Vac. Sci. Technol. A* **33**, 05E132 (2015).
- ab Seite 74 X. Li, Y. Xiao, K. Zhou, C. Yan, K. Zhou, P.-T. Miclea, S. Meyer, S. L. Schweizer, A. Sprafke, J.-H. Lee, R. B. Wehrspohn. Self-purification model for metal-assisted chemical etching of metallurgical silicon, *Electrochim. Acta* **138**, 476-480 (2014).
- ab Seite 79 M. Otto, M. Algasinger, H. Branz, B. Gesemann, T. Gimpel, K. Fücksel, T. Käsebier, S. Kontermann, X. Li, V. Naumann, J. Oh, A. Sprafke, J. Ziegler, M. Zilk, R. B. Wehrspohn. Black Silicon Photovoltaics *Adv. Opt. Mater.* **3**, 147-164 (2015).
- ab Seite 97 Y.-C. Chang, M. E. Pollard, David N. R. Payne, A. Sprafke, S. Pillai, D. M. Bagnall. Large-Area Nanosphere Gratings for Light Trapping and Reduced Surface Losses in Thin Solar Cells, *IEEE J. Photovoltaics* **9**, 1012 (2019).
- ab Seite 105 T. Schneider, J. Tröndle, B. Fuhrmann, F. Syrowatka, A. Sprafke, R. Scheer. Ultrathin CIGSe Solar Cells with Integrated Structured Back Reflector, *Solar RRL* **4**, 2000295 (2020).
- ab Seite 112 M. Muchow, T. Büchner, A. Sprafke, Gerhard Seifert. Femtosecond laser-written high-efficiency blazed phase gratings in the volume of soda lime glass for light management in solar modules, *Opt. Express* **23**, 33540-33549 (2015).
- ab Seite 122 A. Sprafke, D. Schneevoigt, S. Seidel, S. L. Schweizer, R. B. Wehrspohn. Automated spray coating process for the fabrication of large-area artificial opals on textured substrates, *Opt. Express* **21**, A528-A538 (2013).
- ab Seite 133 S. Nanz, A. Abass, P. M. Piechulla, A. Sprafke, R. B. Wehrspohn, C. Rockstuhl. Strategy for tailoring the Size Distribution of Nanospheres to Optimize Rough Backreflectors of Solar Cells, *Opt. Express* **26**, A111-A123 (2018).
- ab Seite 146 P. M. Piechulla, L. Mühlenbein, R. B. Wehrspohn, S. Nanz, A. Abass, C. Rockstuhl, A. Sprafke. Fabrication of nearly-hyperuniform substrates by tailored disorder for photonic applications, *Adv. Opt. Mater.* **6**, 1701272 (2018)
- ab Seite 156 P. M. Piechulla, B. Fuhrmann, E. Slivina, C. Rockstuhl, R. B. Wehrspohn, A. Sprafke. Tailored Light Scattering through Hyperuniform Disorder in Self-Organized Arrays of High-Index Nanodisks, *Adv. Opt. Mater.* **9**, 2100186 (2021).
- ab Seite 168 P. M. Piechulla, E. Slivina, D. Baetzner, I. Fernandez-Corbaton, P. Dhawan, R. B. Wehrspohn, A. Sprafke, C. Rockstuhl. Antireflective Huygens' Metasurface with Correlated Disorder Made from High-Index Disks Implemented into Silicon Heterojunction Solar Cells, *ACS Photonics* **8**, 3476-3485 (2021).

Properties of black silicon obtained at room-temperature by different plasma modes

Maria Gaudig^{a)}

Photovoltaics Group, Anhalt University of Applied Sciences, Bernburger Str. 55, 06366 Köthen, Germany and Group μ MD, Institute of Physics, Martin Luther University Halle-Wittenberg, Heinrich-Damerow-Str. 4, 06120 Halle (Saale), Germany

Jens Hirsch

Photovoltaics Group, Anhalt University of Applied Sciences, Bernburger Str. 55, 06366 Köthen, Germany

Thomas Schneider, Alexander N. Sprafke, and Johannes Ziegler

Group μ MD, Institute of Physics, Martin Luther University Halle-Wittenberg, Heinrich-Damerow-Str. 4, 06120 Halle (Saale), Germany

Norbert Bernhard

Photovoltaics Group, Anhalt University of Applied Sciences, Bernburger Str. 55, 06366 Köthen, Germany

Ralf B. Wehrspohn

Group μ MD, Institute of Physics, Martin Luther University Halle-Wittenberg, Heinrich-Damerow-Str. 4, 06120 Halle (Saale), Germany and Fraunhofer Institute for Mechanics of Materials IWM, Walter-Hülse-Str. 1, 06120 Halle (Saale), Germany

(Received 2 June 2015; accepted 14 August 2015; published 4 September 2015)

Black silicon plasma technology begins to be integrated into the process flow of silicon solar cells. However, most of the current technology is used at cryogenic or very low substrate temperatures. Here, the authors investigate the temperature-dependent properties of black silicon prepared by two different plasma etching techniques for black silicon, a pure capacitively coupled process (CCP), and an inductively and capacitively coupled process (ICP + CCP). It turns out that the ICP + CCP process at room-temperature yields black silicon samples with 93% absorption and minority carrier lifetime above 1 ms. The authors show that these optoelectronic properties are comparable to samples obtained at low temperatures. © 2015 American Vacuum Society.

[<http://dx.doi.org/10.1116/1.4929540>]

I. INTRODUCTION

A promising alternative to wet-chemical etching for the fabrication of black silicon (b-Si) for silicon solar cells is the maskless plasma texturing in an SF₆/O₂ atmosphere.^{1,2} The key benefits of b-Si prepared by plasma etching are their excellent optical properties, such as a strongly antireflective surface. Thus, no additional deposition of an antireflection layer is needed for optimal light incoupling into the substrate. Further advantages of the dry plasma texturing method are (1) less silicon waste, (2) no usage of toxic chemicals, (3) the easy adjustment of the prepared structures in size and shape by varying the plasma parameters, and (4) the possibility to texture silicon independent of its crystal orientation or prior surface treatment. Plasma texturing allows the etching of mono- and multicrystalline wafers for solar cells with the same process, which is an advantage over wet-chemical etch processes. However, the strong increase of the surface area and the surface degradation by ion bombardment during plasma etching result in a strongly enhanced surface recombination. Thus, a sufficient surface passivation to reduce this recombination is needed for photovoltaic (PV) applications of b-Si.

The b-Si formation in an SF₆/O₂ atmosphere^{3,4} can be summarized as follows: The fluorine radicals from the plasma react isotropically with silicon to volatile SiF₄. For anisotropic

etching, it is assumed that an accidental local masking layer (SiF_xO_y) is built on the silicon surface causing an initial roughening of the silicon surface due to the competition between deposition of SiF_xO_y and Si etching.^{5,6} This layer also acts as side wall passivation of the formed silicon structures during the further etching. Furthermore, a physical etching due to ion bombardment on the sample can as well influence the texturing. This last mechanism is called reactive ion etching (RIE) and enables the creation of high aspect textures.

However, up to now b-Si for PV applications is commonly prepared by a cryogenic plasma process, i.e., etching at temperatures well below 0 °C.^{4,7–11} In this work, we focus on high temperature etch processes with an SF₆/O₂ plasma and optimize them with the concrete application for solar cells, in contrast to other reported b-Si processes prepared by plasma etching at temperatures above 0 °C.^{12–15} Regarding cryogenic b-Si processes, a possible explanation of why low temperatures are preferred for b-Si formation by plasma etching is given in Schnell *et al.*⁷ It is supposed that the self-masking film is volatile and desorbs at higher wafer temperatures. Thus, less sufficient masking can be achieved for b-Si texturing and the b-Si formation is rather unstable. For this reason, the experimental efforts seem to be less extensive for cryogenic etch temperatures than for room-temperature to attain a stable b-Si etch regime.

However, there would be a great advantage of a high temperature plasma process at room temperature: The possibility

^{a)}Electronic mail: m.gaudig@emw.hs-anhalt.de

of a noncryogenic process would reduce costs as well as time for sufficient chamber and wafer cooling. Furthermore, the temperature control of the whole wafer surface is difficult in vacuum under plasma exposure because the sample is heated during plasma treatment. Control is easier to accomplish at higher temperatures, i.e., for smaller temperature differences. At last, when an cooled chamber is opened, water vapor condensates on the chamber surfaces, which in turn considerably decelerates the following evacuation of the chamber. This effect would not occur with a room temperature process.

In fact, investigations on such plasma processes at $T > 0^\circ\text{C}$ are subject of current research.^{16–18} Yoo *et al.*¹⁶ prepared textured surfaces on multicrystalline silicon wafers with a water cooled electrode ($\leq 20^\circ\text{C}$) and could achieve a higher solar cell efficiency than with planar wafers. Ziegler *et al.*¹⁷ showed first results of silicon solar cells with a textured front side prepared by plasma etching at 20°C . Moreover, promising b-Si wafers with low reflection and high lifetimes are produced by a plasma process at 15°C by Allen *et al.*¹⁸ These works already prove that it is possible to produce b-Si by plasma etching at $T > 0^\circ\text{C}$.

Following these studies, investigations on plasma processes at etch temperatures above 0°C to texture monocrystalline silicon are presented in this work. We show that it is possible to fabricate b-Si with optoelectrical properties as good as those prepared by cryogenic processes as reported in literature. Specifically, we optimized plasma processes at two different temperatures: 5°C and 20°C . Besides, the influence of the plasma ignition is investigated. For this purpose, two b-Si processes are presented with different plasma generation: For one process, the plasma is solely ignited capacitively. In the other process, a capacitive and at the same time inductive plasma generation is used. These processes are referred to as capacitively coupled power (CCP) and inductively and capacitively coupled (ICP + CCP) process in the following, respectively. The etched surfaces are analyzed concerning their microstructure, optical and electrical characteristics and discussed with regard to PV applications. To estimate and compare the electrical performance of the b-Si wafers, the effective minority charge carrier lifetime is measured. For this purpose, the samples are passivated by an optimized atomic layer deposition (ALD) process for the deposition of a thin (30 nm) Al_2O_3 layer on the silicon surface.⁹ This oxide layer is known to be an excellent chemical and electrical passivator for silicon surfaces^{19,20} and also provides good results for highly textured b-Si samples.⁹

In this work, the investigations are limited to the optoelectrical characterization of the b-Si samples. In this regards, the suitability of the prepared b-Si for the use as solar cells is evaluated; mechanical or thermal stability investigations were not applied.

II. EXPERIMENT

To create the textured silicon surfaces, an etch chamber of Oxford Instruments (Plasmalab System 100 ICP 65) is used. The wafer is mechanically clamped onto the lower

electrode, which can be cooled or heated to control the wafer temperature. For an improved thermal contact between the sample and the electrode, gaseous helium is supplied to the backside of the sample. The chamber includes a CCP generator as well as an ICP generator working at 13.56 MHz with a maximum in-coupling power of 300 and 600 W, respectively. By applying the radio frequency, a potential is built between plasma and the lower electrode, introducing an acceleration of positive ions on the sample surface. This DC bias is an important parameter influencing the RIE texturing. A high DC bias is also responsible for a decreased effective lifetime of the sample due to stronger surface degradation.^{21,22} The advantage of the inductively coupled plasma generation over the CCP generation is the decoupling of the ion density and ion energy in the plasma. Through this independence, the plasma density can be increased for quick etching without enhancing the ion bombardment on the sample.

Monocrystalline, polished float-zone silicon wafers with a thickness of $250\ \mu\text{m}$ are used (p-doped, $2.0\ \Omega\ \text{cm}$, $\langle 100 \rangle$).

For the experimental procedure, the black silicon method of Jansen *et al.*³ was used to find the b-Si regime. We first started to etch at 5°C to optimize the etch parameters of the CCP and ICP + CCP process aiming at low reflectivity. Both optimizations have been performed independently of each other. These etch parameters are only discussed here and are listed in Table I (first and second column). Homogeneously etched wafers with high antireflective front sides could be achieved. However, the electrical characterization of these samples revealed that samples etched by the ICP + CCP process are much more qualified for PV applications. So, we further focused on the ICP + CCP process and optimized one process at 20°C etch temperature. An etch process at 20°C with the CCP generator is not introduced in this work. Different etch temperatures also require different values for the other etch parameters, such as the $\text{O}_2:\text{SF}_6$ ratio or the capacitive power to achieve a b-Si texture. Thus, etching parameters needed to be optimized for each investigated temperature regarding the optical properties (Table I, third column).

The spectrally resolved reflectivity R and transmission T was measured with an integrating sphere to also consider diffuse reflection and transmission. The absorption A is calculated by $A = 1 - R - T$. For microscopic analysis, scanning electron microscopy (SEM) has been employed.

For measuring the effective minority carrier lifetime, the wafers were etched bifacially. After the etch process, the wafers are treated with an RCA cleaning. For this purpose, they are first dipped for 10 min into a 80°C $\text{H}_2\text{O}:\text{NH}_4\text{OH}:\text{H}_2\text{O}_2$ solution with 5:1:1 ratio, followed by a one minute HF dip at room temperature and dip into 5:1:1 solution of $\text{H}_2\text{O}:\text{HCl}:\text{H}_2\text{O}_2$ at 80°C for 10 min. Subsequently, Al_2O_3 is deposited on the cleaned surface by thermal ALD as a passivation layer using trimethylaluminum and water as precursors at 180°C . Ellipsometry measurements on smooth reference wafers show that the Al_2O_3 layer has a thickness of $32\ \text{nm} \pm 1\ \text{nm}$ for all samples. To activate the passivation, the samples were annealed at 385°C for 30 min. The effective

TABLE I. Etch parameters and the maximum measured DC bias voltage of the observed experiments.

Etch parameters	CCP (5 °C)	ICP + CCP (5 °C)	ICP + CCP (20 °C)
SF ₆ flow (sccm)	40	50	47
O ₂ flow (sccm)	55	42	44
Pressure (μbar)	50	45	45
Capacitively coupled power (W)	110	27	20
Inductively coupled power (W)	0	600	600
Max. DC bias (V)	98	53	34

minority carrier lifetimes τ_{eff} are measured using the quasi steady-state photoconductivity (QSSPC) method.²³

III. RESULTS AND DISCUSSION

In Table I, the etch parameters of the performed processes including the measured DC bias are shown. To observe the temporal trend, the etch time was varied. For the ICP + CCP process, dark samples (by visual appearance) are obtained already after 7 min of etching; whereas the process with just capacitively ignited plasma has lasted more than 15 min to create comparably dark surfaces. The ratio of the gas flows SF₆:O₂ is about 1:1 for the three processes which seem to be the optimal balance between side wall passivation and etching for b-Si formation. With 600 W, a high coil power was applied for the ICP + CCP process to allow high plasma density as possible. The capacitively coupled power for the process at 20 °C is smaller than for the process at 5 °C and, thus, the DC bias is decreased. Furthermore, the DC bias of ICP + CCP processes is smaller than half the value of the CCP process. So, RIE texturing should rather influence the CCP process.

Before looking into the introduced processes in detail, we want to discuss the influence of the sample temperature on the b-Si formation. As a general observation, it was not possible to use the same plasma parameters of a successful b-Si process for a process at another wafer temperature to fabricate b-Si, which made the experimental approach time-consuming. Considering, for example, the ICP + CCP processes in Table I, when the plasma parameters of the b-Si process at 5 °C are kept constant but the temperature is increased to 20 °C, the silicon wafer will be etched smoothly; no b-Si is formed because the balance between etching and passivation by the SiF_xO_y layer for the creation of textured silicon is displaced.²⁴ Thus, the plasma parameters have to be adjusted for higher sample temperatures to produce b-Si. Fortunately, mostly small parameter changes are sufficient to find the b-Si parameter regime, as one can see in Table I for the ICP + CCP process at 20 °C.

We furthermore investigated optically the b-Si formation at temperatures above 20 °C up to 40 °C and came to the conclusion that the plasma parameters have to be adjusted at increased sample temperatures as follows: (1) lowering the capacitively coupled power and (2) increase the O₂:SF₆ flow ratio. These adjustments are in general observed for ICP + CCP processes and also appear for the ICP + CCP

processes etched at 5 and 20 °C (see Table I). Furthermore, we observed that the b-Si process is rather unstable with higher etch temperatures: Small changes of the plasma condition result in modified etch results. Following assumptions are made to explain these observations:^{5,25,26} The plasma particles reacting with the silicon can desorb faster from a warmer surface. Thus, the SiF_xO_y layer, which is important for the initial masking and sidewall passivation of the created structures, desorbs partially at higher wafer temperatures. Following this, more O₂ particles are needed to perpetuate this passivation layer, which explains the higher O₂:SF₆ flow rate needed for higher etch temperatures; second, a smaller ion bombardment should be enough to attack and remove this layer protecting the silicon on the bottom of the textures, which explains the reduced capacitive power (lower DC bias) for higher etch temperatures. How far other mechanisms at higher wafer temperatures (e.g., increased particle diffusion or reaction rate on the silicon surface) influence the etch process is still not understood.

For the CCP process, the wafer temperature does not influence the etch result to the extend as observed in the case of the ICP + CCP process, probably due to the higher physical etch component (DC bias). This process seems to be less limited to surface diffusion or desorption of the etching or passivating particles.

A. Microstructure

For the CCP process, needles or cones are created during the etching, as shown in Fig. 1.

The needle height is about 500 nm and independent of the etching time; whereas the average distance of the structures is increased from about 100 to 170 nm, resulting in an aspect ratio of 5:1 to 3:1, after 15 and 45 min, respectively. These high aspect ratios can be traced back to the high DC bias at 98 V during etching, increasing the physical etching component perpendicularly to the surface.

In Fig. 2, SEM micrographs of samples etched for different times (etch temperature: 5 °C) using the ICP + CCP process are shown. Etching a silicon wafer with this process results in a microstructure consisting of parabolic shaped pits on the surface. Only small differences can be observed with longer etching time, which are in contrast to the resulting texture of the CCP process. The structure height is about 2.5–2.9 μm. The average distance of the structures is about 1 μm, one order of magnitude larger than that of the CCP process. The aspect ratio in these structures is about 2:1. During these plasma conditions, the physical etching by ions should play a less important role due to the small DC bias (<53 V), which explains why needlelike structures are not formed in comparison with the CCP process. The root of the arising parabolic pits during the ICP + CCP processes can be related to the high plasma density with inductive plasma incoupling (power: 600 W) causing reaction limited processes on the surface. However, the detailed formation mechanism remains unclear.

For the textures etched at 20 °C (not shown), the structure height (1.7 μm) is smaller, and the average distance of the structures is increased to values of about 1.7 μm, but no

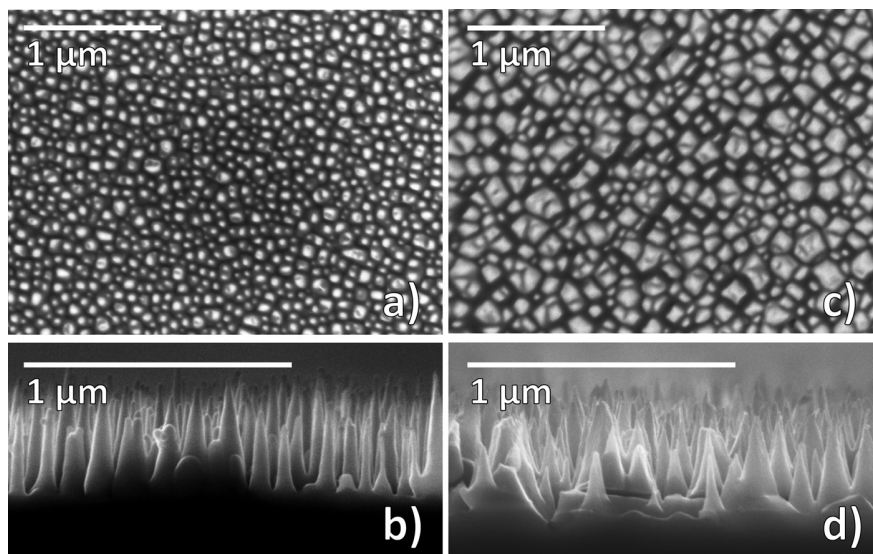


FIG. 1. SEM pictures from top [(a) and (c)] and side [(b) and (d)] view of two plasma etched samples at 5 °C (CCP process). The etching time is [(a) and (b)] 15 min and [(c) and (d)] 45 min, respectively.

further significant differences are observed. Thus, it is possible to create similar microstructures at different etch temperatures, also above 0 °C, by adapting the plasma parameters. Steglich *et al.*⁶ also observed b-Si etched at different temperatures. Their samples were etched with an ICP-RIE process at different temperatures (−38 and 20 °C) but with identical plasma parameters. The obtained microstructures look very similar, but at 20 °C, the average distance of the structures is slightly higher and the sidewalls are more porous, which can both be explained by the desorption of the sidewall passivation layer. A further comment in that work was that for accommodation of this effect the etch parameters should be adjusted, e.g., by increasing the O₂:SF₆ ratio. These explanations are consistent with our findings describing the influence

of the sample temperature on the parameters for b-Si formation (see above).

In conclusion, different shapes and dimensions of the surface textures are created with the two etch processes, which are correlated toward the different conditions during the plasma treatments: With the pure capacitive CCP process, a high DC bias about 100 V is generated, enhancing the ion acceleration on the surface for increased RIE texturing. This configuration creates high, needlelike structures. In contrast, for the ICP + CCP process, the DC bias is rather low (<53 V). The physical etching by ions is decreased. The parabolic form of the structures in the micrometer range is rather related to the high plasma density during the inductive plasma generation.

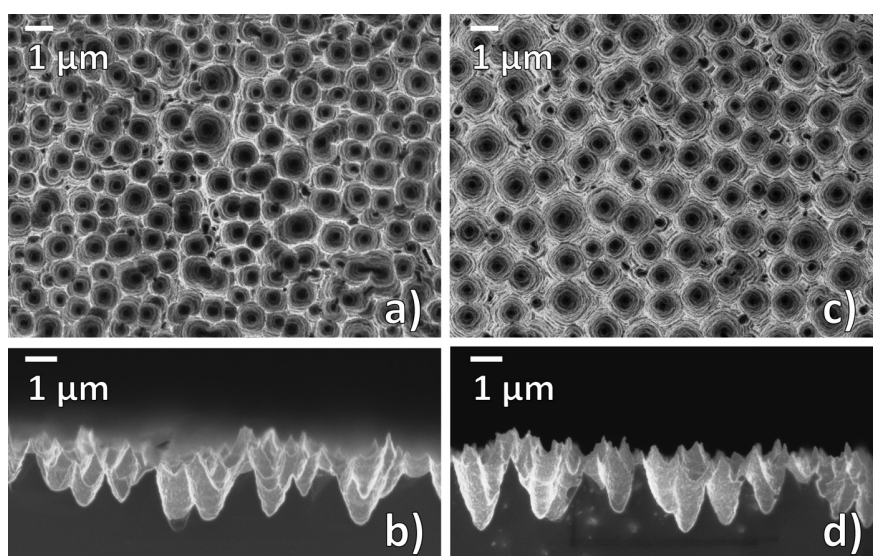


FIG. 2. SEM pictures from top [(a) and (c)] and side [(b) and (d)] view of two plasma etched samples at 5 °C (ICP + CCP process). The etching time is [(a) and (b)] 7 min and [(c) and (d)] 15 min, respectively.

B. Optics

In Fig. 3, reflectivity (dashed lines) and absorption spectra (solid lines) of CCP (dark) and ICP + CCP (bright) samples after passivation are shown. The reflectivity spectra of a smooth wafer (black dashed line) and an alkaline etched wafer (black dashed-dotted line) serve as a reference. For the sake of clarity, the best sample per etch process is presented in the graphs: CCP process etched for 35 min at 5 °C and ICP + CCP process etched for 15 min at 5 °C.

For both the CCP and the ICP + CCP process, a strong antireflection occurs. For the CCP process, the reflectivity is below 1% in the wavelength range from 300 to 950 nm. Whereas the sample etched with the ICP + CCP process never reaches values below 1%, but between 1% and 6% in the same wavelength range. With the alkaline etched surface, such high antireflection cannot be achieved. This observation demonstrates the optical advantage of the dry plasma process against the wet chemical etching for texturing silicon for PV applications. The absorption of the CCP process after passivation is higher than 99% from 300 to 950 nm due to the low reflectivity. In this wavelength range, the absorption of the ICP + CCP process is lower. However, this loss in absorption is regained in the infrared range from 1000 to 1200 nm, where the absorption of the ICP + CCP process clearly exceeds the absorption of the CCP process.

In Fig. 4, we zoom into the absorption spectra of Fig. 3; the spectra before Al_2O_3 deposition (dotted lines) are additionally included. The absorption is slightly increased after deposition of the thin Al_2O_3 layer due to lower reflection losses. We could observe this behavior for all passivated samples and explain it as a result of the smaller refractive indices contrast of Al_2O_3 and air (1.7:1.0) compared to that of silicon and air (3.5:1.0), leading to smaller Fresnel reflection at this interface.

The reason for different optical behavior of CCP and ICP + CCP samples can be explained by their different

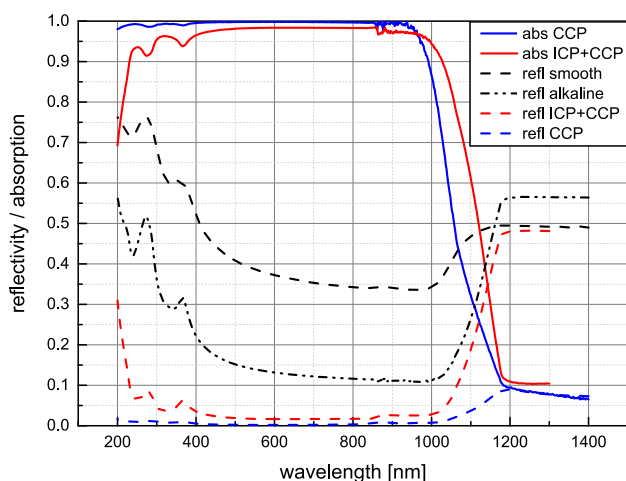


FIG. 3. (Color online) Absorption (solid lines) and reflectivity (dashed lines) spectra of a wafer etched with the ICP + CCP process (bright lines; 15 min etched, 5 °C) and with the CCP process (dark lines; 35 min etched, 5 °C) after passivation. As reference, the reflectivity spectra of a polished wafer (black dashed line) and an alkaline etched wafer with random pyramids (black dashed-dotted line).

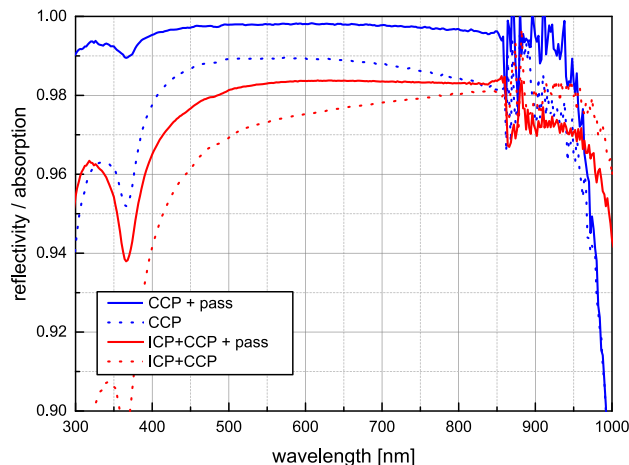


FIG. 4. (Color online) Zoom of Fig. 3: absorption spectra of the textured samples after passivation (solid lines) and before passivation (dotted lines) etched with the same process: bright lines—ICP + CCP (5 °C, 15 min) and dark lines—CCP (5 °C, 35 min).

textures. Regarding this issue, Steglich *et al.*⁶ and Otto *et al.*²⁷ investigated the optical properties of b-Si samples. In both the works, a connection between large correlation length (corresponding to the average distance of structures) and enhanced light trapping efficiency is observed. Through light trapping, in particular, the absorption of the photons near the band edge of silicon can be improved. Thus, the high absorption in the long wavelength range of the ICP + CCP samples is caused by their large lateral structure distance of about 1 μm . In contrast, etching with the CCP process generates smaller structures in lateral (<200 nm) and vertical (about 500 nm) dimension, resulting in a decreased light trapping. However, this structure is responsible for highly antireflective surfaces in the wavelength range from 300 to 950 nm. Here, the lateral texture resolution is too small for describing of the light propagation through the material with geometrical optics. A better picture to characterize the light propagation in this structure is illustrated with the help of the effective medium theory. In this picture, the structured surface can be assumed as a layer with smoothly changing refraction index.²⁸ In these kinds of layers, back reflection is strongly suppressed.^{6,27}

To conclude, the high aspect ratios and small dimensions of the textures etched by the CCP process result in a higher antireflective front side than for the ICP + CCP textures. Whereby the improved light trapping efficiency of the ICP + CCP process enhances the absorption from 1000 to 1200 nm.

C. Effective lifetime

The effective minority carrier lifetime is a figure of merit to estimate surface recombination and surface damage. In Fig. 5, the lifetime is plotted against the minority carrier density of samples etched for different durations with the CCP (triangle) or ICP + CCP (squares) process at 5 °C. For comparison, a QSSPC measurement of a smooth reference

(crosses) is included, which experienced the same passivation process as the textured samples did.

For the CCP process, the lifetimes are much lower than for the reference. The values are reduced to the range of 10 μ s, which is two orders of magnitude less compared to the smooth reference. As a reason for this degradation, the highly increased effective area can be suspected. However, the main effect is rather caused by the high ion impact due to the high DC bias (about 100 V, see Table I). The accelerated ions hit the surface and thereby generate defects, resulting in an increased surface recombination. These defects seem to grow deep within the bulk, too, since it is not possible to compensate them, even with a passivating Al₂O₃ layer. This surface degradation of silicon with high plasma power or high DC bias is already well-known.^{21,22} In this work, further experiments have been carried out with the aim to decrease the DC bias to improve the electrical properties of the CCP process. Unfortunately, it was not possible to noticeably improve the effective lifetime. Besides, the reflection increased by changing the plasma parameters.

In case of the ICP + CCP process, high lifetimes above 1 ms up to 3.6 ms are achievable, which are in the range of the effective lifetime of the smooth reference (4.9 ms). The surface damage of silicon seems to be smaller or can be passivated more effectively for the ICP + CCP process with inductive plasma ignition and reduced capacitive plasma power (27 W) in contrast to the purely capacitive CCP process at 110 W. As can be seen from Table I, the DC bias of the ICP + CCP process (53 V) is smaller than for the CCP process (100 V) decreasing the ion acceleration for the ICP + CCP process. Through the reduced ion bombardment, a smaller defect density should arise during etching, which can be passivated more effectively by Al₂O₃. Thus, the surface recombination is reduced, leading to an increased effective lifetime in the range of the smooth reference after passivation. However, also for the ICP + CCP process, surface damages arise during plasma etching, which is indicated by the reduced lifetime with higher etch times. Furthermore,

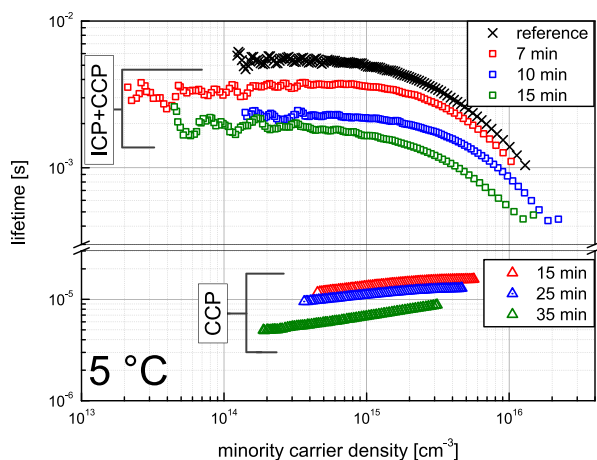


FIG. 5. (Color online) Effective lifetimes plotted against the minority carrier density for a polished reference wafer (dark crosses), ICP + CCP process at 5 °C (squares), and CCP process at 5 °C (triangle) for different etch times.

the effective surface area of the ICP + CCP process is smaller than of the CCP process, which as well improves the electrical performance.

For completeness, the lifetimes for the ICP + CCP process at 20 °C etch temperature are shown in Fig. 6. A slight decrease of the effective lifetime occurs in contrast to the samples etched at 5 °C, although the DC bias is further reduced from 53 to 34 V.

Regarding PV applications, the CCP process is not qualified for solar cell fabrication through electrical surface degradation. For the ICP + CCP process at 5 and 20 °C, high lifetimes are achievable in the range of the untextured reference, which qualifies this plasma process for PV application.

D. Discussion

To compare the electrical and optical properties of the textured and passivated samples, the lifetimes (at the minority carrier density of 10¹⁵ cm⁻³) are plotted against the absorption for all processes and etching times in Fig. 7: the ICP + CCP processes at 5 °C (red squares), at 20 °C (green circles) and the CCP processes at 5 °C (blue triangles). For the absorption, the spectra are weighted on the AM1.5 g spectrum from 300 nm to 1150 nm.

As a general observation for both etch modes, the absorption increases with increasing etch time, but at the same time the lifetimes is reduced. Therefore, depending on the application, the optical properties of b-Si should be evaluated against the electrical performance by varying the etch time. For b-Si solar cells, the etch time should be chosen for an optimal external quantum efficiency which is influenced by absorption gains and recombination losses. The decrease of the lifetimes with etch time for every plasma process shows furthermore that the silicon surface is damaged by the plasma treatment leading to an enhanced recombination: The longer the sample is exposed to the plasma, the higher the induced damage is created of the surface, independent of the plasma process.

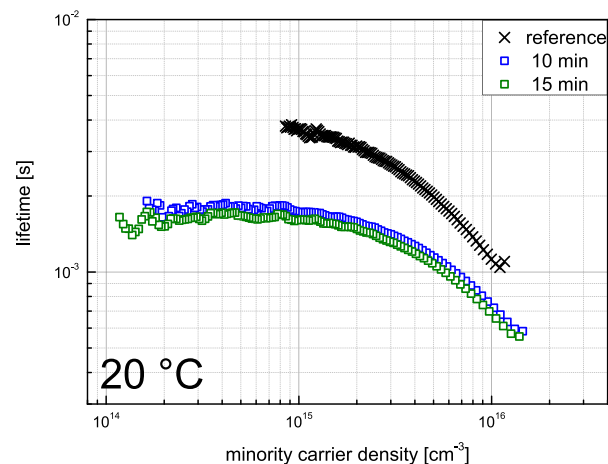


FIG. 6. (Color online) Effective lifetimes plotted against the minority carrier density for a polished reference wafer (dark crosses) and the ICP + CCP process at 20 °C (squares) after 10 and 15 min etching.

Furthermore, very high absorption values can be achieved by texturing with CCP and ICP + CCP plasma generation up to 95.9% for the ICP + CCP process at 5 °C after 15 min etching. So, highly antireflective surfaces with enhanced absorption can be provided by both plasma processes with different textures. Nevertheless, the etch time of the CCP process is longer than that of the ICP + CCP process to reach these high absorption values, which is a further benefit of the ICP + CCP process.

Whereas regarding the electrical performance of the samples, the ICP + CCP process clearly achieves better effective lifetimes above 1 ms in contrast to the CCP process. As already mentioned in Sec. III C, the effective lifetimes are mainly influenced by the surface damage created during plasma treatment. It can therefore be concluded that the silicon surface is much less attacked by the plasma during the ICP + CCP process contrary to the CCP process. This statement is confirmed by the measured DC bias for both processes (see Table I): During the CCP process, a high DC bias of about 100 V is created, which leads to an acceleration of the ions in the plasma on the silicon surface. The energy of the ions appears to be sufficient to generate defects on the surface, which grow deep within the bulk. Therefore, these defects cannot be passivated, even with the excellent Al₂O₃ passivation layer. The result is an increased surface recombination and, thus, a smaller lifetime, comparing to an untreated wafer. In contrast to this capacitive process, the ICP + CCP process provides just a small DC bias of <53 V. The ion energy is decreased and, using the same argumentation as above, this leads to a clearly higher lifetime, in contrary to the CCP process. For PV applications, the decreased lifetimes of the samples etched with the CCP process is too low to use these wafers in solar cell production. In contrast, the good optoelectronic properties of the ICP + CCP process provide potential for use in b-Si solar cell production.

Finally, the ICP + CCP process at 5 °C performs slightly better optically than the ICP + CCP process at 20 °C because

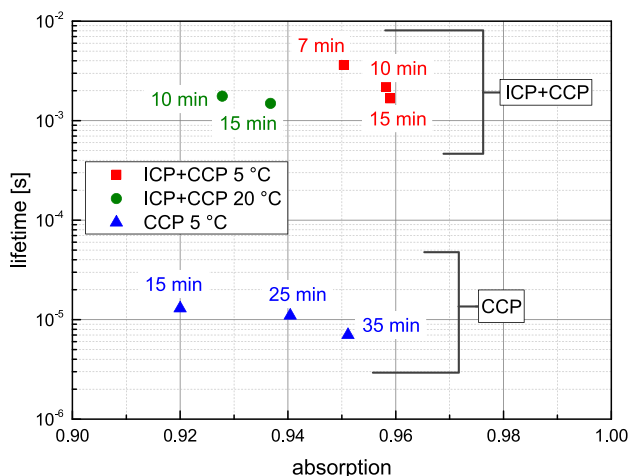


Fig. 7. (Color online) Effective lifetime at the minority carrier density of 10^{15} cm^{-3} plotted against the weighted absorption (300–1150 nm). The assigned times in minutes indicate the etch duration.

of the smaller average distance of the structures at 5 °C. Electronically, the 5 °C process also performs slightly better than the 20 °C process. However, similar good results confirm that it is possible to fabricate b-Si by plasma etching at room temperatures, which are qualified for PV applications.

As a final conclusion, we could demonstrate that it is possible to fabricate plasma textured b-Si at etch temperatures above 0 °C, up to at least 20 °C. Thus, the experimental advantages of a b-Si process at room temperature can be exploited for faster and easier etching in contrast to a cryogenic process. Furthermore, the optical properties of the etched samples with absorption values above 95% are in a comparable regime as b-Si prepared by cryogenic processes.

The investigation of the discussed etch processes, CCP and ICP + CCP, reveal great differences concerning the created textures, which can be explained by their respective different plasma etch conditions. However, regarding PV applications, the ICP + CCP process is much better suited due to clearly better optoelectrical performances.

IV. SUMMARY

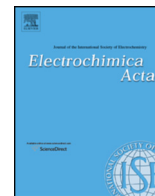
In this work, different plasma etching techniques for black silicon are compared with the focus on etch temperatures above 0 °C. The maskless etch process was realized in a plasma chamber with capacitive and inductive plasma ignition in a SF₆/O₂ atmosphere. Two different etch modes are evaluated: the CCP process at 5 °C with capacitively coupled power generation and second the ICP + CCP process at 5 °C and 20 °C with inductively and capacitively coupled plasma ignition. The wafers are characterized concerning their microstructure, optics, and minority carrier lifetime. For both etch modes, a longer etch time leads to an increased absorption but also to a reduction of the effective lifetime. The absorption in both cases could be increased to values about 95% from 300 to 1150 nm. The ICP + CCP process achieves better lifetimes of $\tau > 1 \text{ ms}$ as compared to the CCP process. Moreover, the optical and electrical characteristics of the ICP + CCP process at 20 °C are only slightly worse than those samples processed at 5 °C. We believe that b-Si obtained via a combined ICP + CCP process at 20 °C is a potential cost-effective candidate for use in silicon photovoltaics.

ACKNOWLEDGMENTS

This work was carried out within the joint research graduate school “StrukturSolar” of Anhalt University of Applied Sciences and Martin Luther University Halle-Wittenberg, which is funded by the German Ministry of Education and Research under identification code 03SF0417A.

- ¹J. Oh, H.-Ch. Yuan, and H. M. Branz, *Nat. Nanotechnol.* **7**, 743 (2012).
- ²A. Ingenito, O. Isabella, and M. Zeman, “Nano-cones on micro-pyramids: Modulated surface textures for maximal spectral response and high-efficiency solar cells,” *Prog. Photovoltaics: Res. Appl.* (in press).
- ³H. Jansen, M. de Boer, R. Legtenberg, and M. Elwenspoek, *J. Micromech. Microeng.* **5**, 115 (1995).
- ⁴M. Keller, S. Janz, S. Reber, and S. Lindekugel, *25th EU PVSEC* (2010), p. 2299.

- ⁵R. Dussart, T. Tillocher, P. Lefauchaux, and M. Boufnichel, *J. Phys. D: Appl. Phys.* **47**, 123001 (2014).
- ⁶M. Steglich, Th. Käsebier, Th. Pertsch, E.-B. Kley, M. Zilk, and A. Tünnermann, *J. Appl. Phys.* **116**, 173503 (2014).
- ⁷M. Schnell, R. Lüdemann, and S. Schaefer, *28th IEEE Photovoltaic Specialists Conference*, Anchorage, Alaska (2000), p. 367.
- ⁸S. H. Zaidi, D. S. Ruby, and J. M. Gee, *IEEE Trans. Electron Devices* **48**, 1200 (2001).
- ⁹M. Otto, M. Kroll, Th. Käsebier, R. Salzer, A. Tünnermann, and R. B. Wehrspohn, *Appl. Phys. Lett.* **100**, 191603 (2012).
- ¹⁰P. Repo, J. Benick, V. Vähänissi, J. Schön, G. von Gastrow, B. Steinhauser, M. C. Schubert, M. Hermle, and H. Savin, *Energy Procedia* **38**, 866 (2013).
- ¹¹G. von Gastrow, R. Alcubilla, P. Ortega, M. Yli-Koski, S. Conesa-Boj, A. F. i Morral, and H. Savin, *Sol. Energy Mater. Sol. Cells* **142**, 29 (2015).
- ¹²M. Stubenrauch, M. Fischer, C. Kremin, S. Stobenau, A. Albrecht, and O. Nagel, *J. Micromech. Microeng.* **16**, S82 (2006).
- ¹³C. Yang, S.-H. Ryu, Y.-A. Lim, and W. J. Yoo, *Nano* **03**, 169 (2008).
- ¹⁴S. Leopold, C. Kremin, A. Ulbrich, S. Krishchok, and M. Hoffmann, *J. Vac. Sci. Technol., B* **29**, 011002 (2011).
- ¹⁵J. Pezoldt, T. Kups, M. Stubenrauch, and M. Fischer, *Phys. Status Solidi C* **8**, 1021 (2011).
- ¹⁶J. Yoo, G. Yu, and J. Yi, *Sol. Energy Mater. Sol. Cells* **95**, 2 (2011).
- ¹⁷J. Ziegler, J. Haschke, Th. Käsebier, L. Korte, A. N. Sprafke, and R. B. Wehrspohn, *Opt. Express* **22**, A1469 (2014).
- ¹⁸T. Allen, J. Bullock, A. Cuevas, S. Baker-Finch, and F. Karouta, *40th IEEE Photovoltaic Specialists Conference* (2014), p. 0562.
- ¹⁹B. Hoex, J. J. H. Gielis, M. C. M. van de Sanden, and W. M. M. Kessels, *J. Appl. Phys.* **104**, 113703 (2008).
- ²⁰V. Naumann, M. Otto, C. Hagendorf, and R. B. Wehrspohn, *J. Vac. Sci. Technol., A* **30**, 04D106 (2012).
- ²¹D. H. Macdonald, A. Cuevas, M. J. Kerr, C. Samundsett, D. Ruby, and S. Winderbaum, *Sol. Energy* **76**, 277 (2004).
- ²²P. N. K. Deenapanray, M. Hörteis, D. Macdonald, and K. J. Weber, *Electrochem. Solid-State* **8**, G78 (2005).
- ²³R. A. Sinton and A. Cuevas, *Appl. Phys. Lett.* **69**, 2510 (1996).
- ²⁴T. Tillocher, R. Dussart, X. Mellhaoui, P. Lefauchaux, N. Mekkakia Maaza, P. Ranson, M. Boufnichel, and L. J. Overzet, *J. Vac. Sci. Technol., A* **24**, 1073 (2006).
- ²⁵H. Jansen, H. Gardeniers, M. de Boer, M. Elwenspoek, and J. Fluitman, *J. Micromech. Microeng.* **6**, 14 (1996).
- ²⁶R. Dussart, X. Mellhaoui, T. Tillocher, P. Lefauchaux, M. Volatier, C. Socquet-Clerc, P. Brault, and P. Ranson, *J. Phys. D: Appl. Phys.* **38**, 3395 (2005).
- ²⁷M. Otto *et al.*, *Adv. Opt. Mater.* **3**, 147 (2015).
- ²⁸R. B. Stephens and G. D. Cody, *Thin Solid Films* **45**, 19 (1977).



Self-purification model for metal-assisted chemical etching of metallurgical silicon



Xiaopeng Li^{a,b,1}, Yanjun Xiao^c, Chenglin Yan^d, Keya Zhou^c, Paul-Tiberiu Miclea^{b,e}, Sylke Meyer^e, Stefan L. Schweizer^b, Alexander Sprafke^b, Jung-Ho Lee^{c,*}, Ralf B. Wehrspohn^{b,f,*}

^a Max-Planck Institute of Microstructure Physics, Weinberg 2, Halle D-06120, Germany

^b Institute of Physics, Martin-Luther-Universität Halle-Wittenberg, Halle D-06120, Germany

^c Department of Chemical Engineering, Hanyang University, Ansan, Kyonggi 426-791, Korea

^d School of Energy, Soochow University, Suzhou, Jiangsu, 215006, PR China

^e Fraunhofer Center for Silicon Photovoltaics CSP, Halle D-06120, Germany

^f Fraunhofer Institute for Mechanics of Materials IWM, Halle D-06120, Germany

ARTICLE INFO

Article history:

Received 11 March 2014

Received in revised form 5 May 2014

Accepted 6 May 2014

Available online 30 June 2014

Keywords:

Metal assisted chemical etching
metallurgical silicon
purification effect
transitional metal impurity
etching model

ABSTRACT

Metal-assisted chemical etching (MaCE) of metallurgical-grade silicon (MG-Si) has improved the purity of MG-Si (~99%) to close to solar-grade (~99.9999%) by removing metal impurities during the successful preparation of porous silicon nanowires (SiNWs). A new etching principle is proposed to explain the different levels of chemical reduction between various metal impurities with pore formation during etching. This model provides chemical insights into the relationship between dissolved metal ions and pores evolved during the formation of SiNWs.

© 2014 Elsevier Ltd. All rights reserved.

1. Introduction

Semiconductor nanowires (NWs) with a diameter range ≤ 200 nm have been under intensive study in the past decades [1,2]. Substantial efforts have been devoted to investigating their distinct physical [3,4] and chemical [5] properties derived from the confined size and/or geometry. Some novel properties make semiconductor nanowires attractive for a broad spectrum of applications in solar cells [6], photodetectors [7], and sensors [8]. Recently, new methods for enhancing the optical/electrical/chemical activities of NWs have focused on integrating nanoscale morphological features, e.g. surface roughness [9], particle decoration [10], and pores [11]. Generating pores inside NWs, for instance, greatly improves the stability/capacity of lithium ion batteries because porous NWs can accommodate a

large amount of the mechanical strain developed during repeated charge/discharge cycles while providing a large surface area for full lithiation [11]. The presence of pores also suppresses phonon propagation, further reducing thermal conductivity of NWs, which is beneficial for thermoelectric applications [12].

To date, metal-assisted chemical etching (MaCE) has mostly received attention for its simplicity, room-temperature processing, and industry-friendly benefits [13–15]; moreover, porous SiNWs have only been obtained from ultrapure, electronic-grade Si (EG-Si, purity >99.999999%) [16,17]. We have reported that the MaCE of metallurgical Si (MG-Si, purity ~99%, ~US\$ 2/kg) produced porous SiNWs which were improved to near solar-grade (SG-Si, purity ~99.9999%) by removing impurities inside MG-Si [18]. This is normally not possible by traditional acid leaching methods [19]. Understanding the specified etching mechanism is therefore crucial for the possibility to rationally design/control porosity in the formation of MG-SiNWs and replace the costly ‘Siemens’ process [20] for purifying MG-Si. Here, we propose a new chemical etching model to explain different reduction levels among various kinds of metal impurities and their impacts on the formation of SiNWs after dissolving into the etchant.

* Corresponding authors.

E-mail addresses: jungho@hanyang.ac.kr (J.-H. Lee), Ralf.Wehrspohn@iwmh.fraunhofer.de (R.B. Wehrspohn).

¹ ISE member.

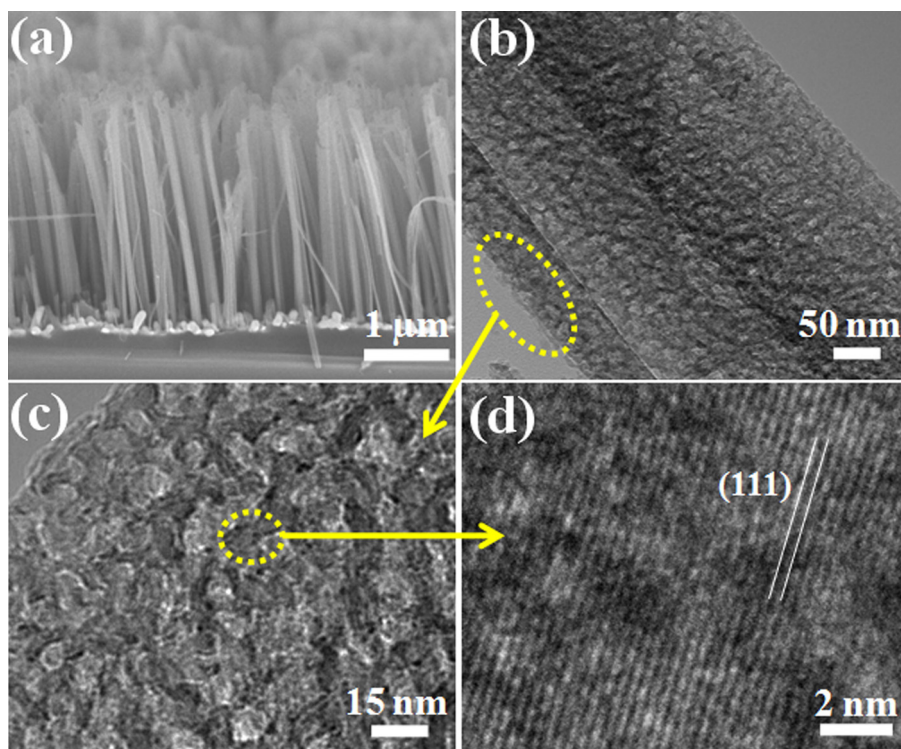


Fig. 1. (a) SEM image showing MG-SiNWs fabricated by MaCE, (b) TEM image of MG-SiNWs (MaCE followed by HNO₃ treatment). (c, d) are the magnified views.

2. Results and discussion

The fabrication process of MG-SiNWs has followed a two-step MaCE method suggested by Peng *et al.* [14] MG-Si pieces were first loaded with dense Ag nanoparticles (AgNPs) by galvanic displacement; then, they were etched in an HF and H₂O₂ solution to allow AgNPs to drill nanopores deep into MG-Si. SiNWs were spontaneously formed due to the contiguous Ag film. Meanwhile, metal impurities, such as silicides [21], were dissolved upon exposure to the acidic etchant solution. Fig. 1(a) shows a scanning electron microscopy (SEM) image of MG-SiNWs. The etching speed (0.1 μm/min) for the formation of MG-SiNWs is much slower than that for EG-SiNWs [0.36 μm/min, see Supporting Information (SI) Fig. S1]. Fig. 1(b,c) show transmission electron microscopy (TEM) images of MG-SiNWs after removing Ag catalysts by a HNO₃ cleaning step. The MG-SiNWs reveal a uniform distribution of pores in sizes of 8–15 nm. Fig. 1(d) confirms the presence of crystalline phase between pores.

Inductively coupled plasma optical emission spectroscopy (ICP-OES) was adopted to quantify the impurity levels inside MG-Si before and after etching. Three different treatments of MG-Si powders, i.e., MaCE, MaCE+HNO₃, and HF+H₂O₂/HNO₃ without Ag (acid wash), are compared in Fig. 2(a); the exact values of impurity concentration in non-treated and treated MG-Si powders are shown in SI, Table S1. Simple acid washing (not MaCE) removed 60–95% of the original impurities for all kinds of metals such that the MG-Si purity was improved from 99.74 to 99.975% (see SI Table S1). For MaCE treatment, AgNPs penetrated into MG-Si particles with depths of 1–2.5 μm (see SI Fig. S2). Fig. 3(d) lists the reduction ratios of metal impurities between MaCE and MaCE+HNO₃ samples compared to the acid-washed samples. Most metals (from Ba to Ni) normally revealed a higher removal ratio than the acid-washed sample because large surface areas were exposed to the etchant, owing to the nanowire morphologies formed by MaCE. However, Ca is an exception because it reacts with HF to form CaF₂ precipitates, which were then trapped or absorbed into the porous

MG-Si. In contrast, MaCE cannot effectively remove metals nobler than Pb. The Cu concentration in the MaCE sample is even higher than that in the acid-washed one. The additional HNO₃ cleaning step further purifies the MG-Si powders to 99.9884%, reaching near solar-grade. The purification enhancement by the HNO₃ step was remarkable for Ca, Pb, and Cu but was relatively weak for Zn, Cr, and Ni.

To understand the upgrading effect based on the relationship between the reduction of metals and formation of porosity in MG-SiNWs, there are several features to be considered. First, heterogeneous distribution of metal impurities is notable inside MG-Si. Different solid solubilities of impurity elements in Si mainly cause a non-uniform distribution of metal impurities. During solidification of Si from the molten state, impurities, e.g. Fe, with concentrations exceeding their low solid solubilities likely segregate along the grain boundaries [21,22]. Since the grain boundaries are morphological defects in the crystal structure, the nucleation of AgNPs preferentially occurs at these defect sites, which are energetically more favorable for etching. As a result, a higher Si dissolution rate is observed at grain boundaries than other areas (see SI, Fig. S3); the strong removal of Fe (see Table S1) is thus reasonable during MaCE.

Second, the effect of dissolved metal ions on MaCE of MG-Si should be understood in-depth. During the ‘drilling’ process of AgNPs, metal impurities are dissolved upon exposure to the acidic etchant. Fig. 3(a,b) show that many tiny metal particles spread over the surfaces of MG-SiNWs. Most nanoparticles were identified to be Ag using the energy dispersive X-ray spectrometer installed in the SEM (SEM-EDX) (see SI Fig. S4). Previous work has shown that Ag catalysts located around the bottom of the nanowire are partially dissolved, diffuse upward, and renucleate on the sidewalls of nanowires so as to initiate new etching pathways [17]. Since there are a large number of defective sites near the dopants in heavily doped Si (10¹⁹–10²⁰ cm⁻³), many AgNPs renucleate at the NW surfaces. Here, the doping level of MG-Si is low (B: 6.6 × 10¹⁷ cm⁻³ and P: 3.0 × 10¹⁷ cm⁻³). Therefore, it is reasonable that the metal

7 Ausgewählte Publikationen

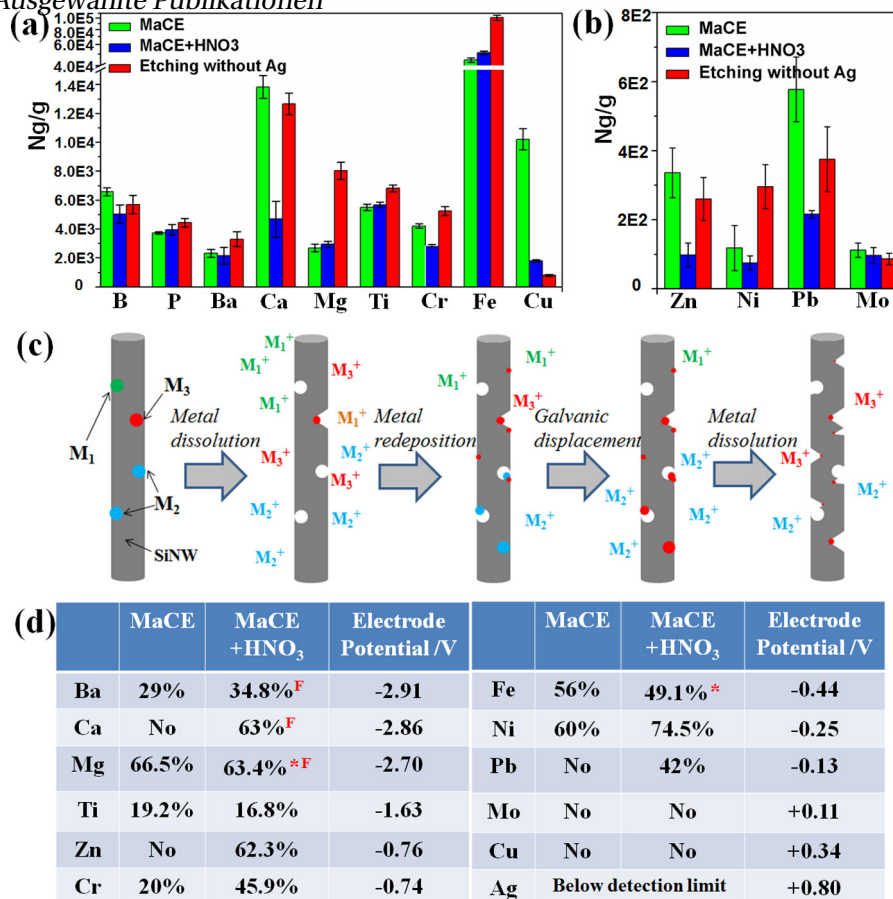


Fig. 2. (a–b) Impurity levels in MG-Si powder treated by three different methods: MaCE (green), MaCE + HNO₃ (blue), and HF + H₂O₂/HNO₃ without Ag deposition (red). (c) Schematic diagrams of the new etching model for MaCE of MG-SiNWs. Three different colors represent three different types of metals: M₁ (Ba, Ca, Mg, Ti, Cr, Zn, Fe, green color), M₂ (Ni, Co, Pb, Mo, blue color) and M₃ (Cu, Ag, red color). M⁺ represents the dissolved metal ions. (d) List of reduction ratios of MG-Si samples treated by MaCE and MaCE+HNO₃ (in comparison with MG-Si etched without Ag). Red-colored 'F' denotes the metal ions reacted with HF to be fluoride precipitates. Red-colored '*' indicates the possibility of contamination from the environment, which causes an increase in reduction ratio upon HNO₃ cleaning. The standard electrode potential data were taken from Ref. 23.

impurities rather than dopants were estimated to form Ag particles nucleated on MG-SiNWs.

In order to confirm our assumption, we conducted etchant contamination experiments during MaCE of ultra-pure EG-Si. The etchants were separately contaminated using metal ions with a concentration of 1 mM, i.e., Ca²⁺, Fe²⁺, Co²⁺, Ni²⁺, Cu²⁺, and Ag⁺. Metals nobler than Ni (or Co) easily nucleated on the Si surface at the expense of dissolution of SiNWs (see SI Fig. S5) [15].

Metal deposition: $M^+ + e^- \leftrightarrow M^0$

$E_0 \geq -0.3$ V vs. NHE (Nobler than Co)

Silicon dissolution: $Si^0 + 6F^- \rightarrow [SiF_6]^{2-} + 4e^-$

$E_0 = -1.24$ V vs. NHE

The NW dissolution rate is known to increase with the standard electrode potential of the metal because the driving force of the NW dissolution is the potential difference between the above two half-cell reactions [23,24]. The SiNWs could be fully surrounded by metals (i.e., Cu, Ag) that have sufficient positive electrode potential. Assuming 0.1 g MG-Si dissolved in 100 mL etchant during MaCE of MG-Si, the concentrations of dissolved metal ions are estimated to vary in a wide range from ~ 20 μ M (for Fe) to $\sim 7.1 \times 10^{-3}$ μ M (for Mo) depending on the original concentration inside MG-Si. In the second etchant contamination experiment, the six kinds of metal ions mentioned above were mixed together. The growth speed of EG-SiNWs was inversely dependent on the mixture concentration, and was reduced from 0.36 μ m/min (without metal ions) to 0.14 μ m/min (mixed metal ions of 1 μ M) and then to 0.08 μ m/min

(10 μ M) (see SI, Fig. S6). Under real conditions, the etching environment during MaCE of MG-Si is far more complicated than that produced by simply mixing the metal ions. The metal impurities are originally non-uniformly distributed, so that their concentrations are locally heterogeneous. Nevertheless, the MaCE of MG-Si was found to create uniformly porous SiNWs.

To understand the influence of metal impurities on the NW morphology, we suggest a new etching principle (shown in Fig. 2(c)) by considering the redox potentials of various metal species as well as their alignment with Si band structures [25–28]. The metal impurities were classified into three types: M₁ for metals with large negative redox potentials (from Ba to Fe listed in Table 1), M₂ for metals with moderate negative potentials (from Ni to Mo), and M₃ for metals with small positive potentials (Cu and Ag). M₁ metals are simply too stable as ions (Ti, Cr, Fe) or as precipitates (MgF₂, CaF₂, BaF₂) in solution to be of much chemical relevance to the surface chemistry of MG-Si. Thus, they have little influence on the evolution of MG-SiNWs. In case of M₂, they predominantly exchange charges with the Si conduction band, and likely soak up the conduction band electrons liberated by the etching reactions. Since M₂ are much easier to be reduced than M₁, they renucleate on the SiNW surfaces, leading to Si dissolution and porosity formation. Due to the instability of M₂ metals, however, they are redissolved in the etchant in repeated renucleation/dissolution cycles. Shallow nanopits can possibly appear on the surfaces of MG-SiNW after such cycles. For M₃ metals, an extra source of Ag⁺ is probable from the

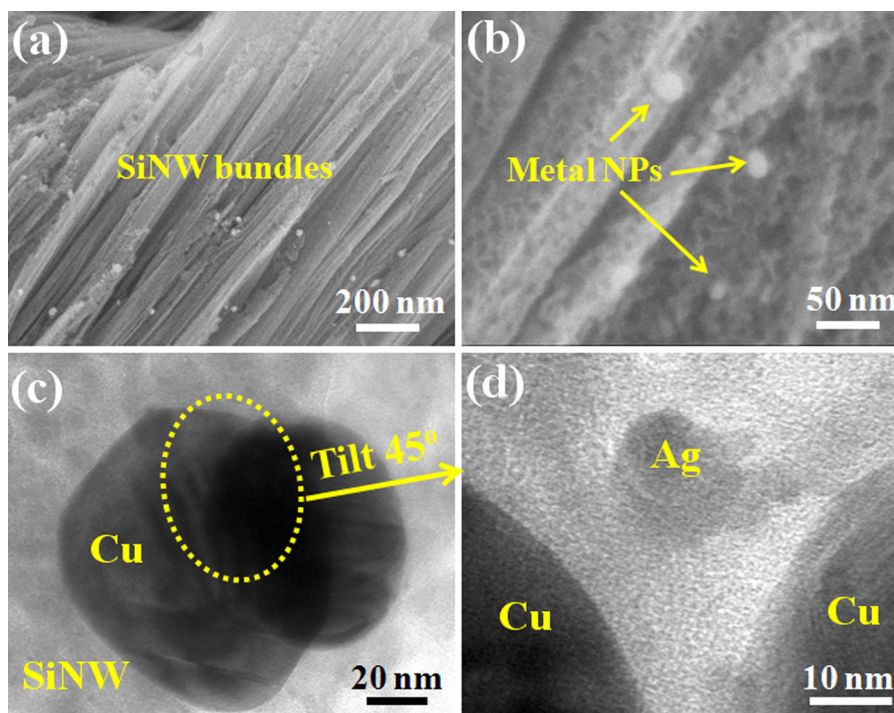


Fig. 3. (a, b) SEM images of MG-SiNW bundles formed after MaCE at low and high magnification. (c) TEM images of metal NPs on MG-SiNWs at low and high magnification. (d) is the magnified view of (c).

dissolution of original Ag catalysts located around the bottoms of SiNWs. The redox potentials of M_3 lie near or below the valence band of Si. Compared to the M_2 metals, M_3 metals not only have repeated etching cycles, but also show higher stability, catalytic activity and the ability to directly initiate etching via hole injection into Si valence band. Deep pores in SiNWs are created by M_3 metals. The metal ions become uniformly distributed because of the diffusion in the etchant after dissolution of metal impurities during etching. Hence, homogeneously distributed pores in MG-SiNWs are created by M_2 and M_3 metals.

The third feature we need to understand is the interaction between metal ions. It is reasonable that galvanic displacement will occur if noble metal M_3 ions surround renucleated M_2 particles. As shown in Fig. 2(c), such a reaction replaces all the renucleated M_2 particles with M_3 particles. Moreover, it promotes the dissolution of original Ag catalysts because M_3 ions become depleted in the etchant, and the amount of Cu is low in MG-Si. As a result, more tiny Ag particles nucleate on the MG-SiNWs than on the EG-SiNWs (see Fig. S1(b)).

To verify our model, we carefully conducted TEM-EDX analysis of MG-SiNWs without HNO_3 treatment. Most tiny metal particles were Ag, without detecting M_1 and M_2 particles, in agreement with a large-area SEM-EDX analysis. Cu particles were also found in a few MG-SiNWs, shown in Fig. 3(c) and Fig. S7. Since there were no Cu ions in the etchant, this provides direct evidence of the dissolution/renucleation model. Unexpectedly, the diameters (60–90 nm) of Cu particles were found to be much bigger than those (~9 nm) of the neighboring Ag particles. Due to the positive electrode potential of Cu, it is reasonable that the renucleation speed is faster, and its displacement speed by Ag is lower than those of M_2 metals. Based on our model, we can conclude that the difficulty of removing a metal by MaCE increases with positive increases in electrode potential. Therefore, the MaCE readily removes M_1 but hardly removes M_2 , and it is almost impossible to remove M_3 . Henceforth, the subsequent HNO_3 cleaning step plays a crucial role in purifying the MG-Si by effectively removing M_2 and M_3 metals.

3. Conclusion

In summary, we developed a new chemical etching model for porous SiNW formation by MaCE of MG-Si. This model takes into consideration various dissolved metal impurities from ‘dirty’ MG-Si and Ag^+ ions from original Ag catalysts in the etchant. The metal ions (nobler than Ni or Co) undergo diffusion and repeated metal renucleation/dissolution cycles, forming SiNWs with homogeneously distributed pores despite heterogeneous metal impurity distribution in MG-Si. Our study not only highlights the importance of controlling the metal ion concentration and selecting metal types for engineering porous features in NW, but also explains the reason for the difficulty in removing noble metals such as Cu. We believe porous MG-SiNWs have great potential for applications in thermoelectrics, lithium ion batteries, sensors and photocatalysts, while keeping fabrication cost extremely low. MaCE could possibly emerge as a new route to purify MG-Si in the near future through further optimization of etching conditions.

Acknowledgements

This work was supported by the National Research Foundation of Korea (NRF) grant funded by the Korean government (MEST) (No. 2011-0028604). We also thank Mr. Jens Beyersdorfer for SEM-EDX characterization. C. Yan acknowledges the support from the ‘‘Thousand Talents Program’’ and the Priority Academic Program Development of Jiangsu Higher Education Institutions (PAPD).

Appendix A. Supplementary data

Supplementary material related to this article can be found, in the online version, at <http://dx.doi.org/10.1016/j.electacta.2014.05.048>.

References

- [1] A.I. Hochbaum, P. Yang, *Chem. Rev.* 110 (2010) 527.
- [2] J.K. Hyun, S. Zhang, L. Luhn, *J. Annu. Rev. Mater. Res.* 43 (2013) 21.1.

7 Ausgewählte Publikationen

- [3] E.C. Garnett, M.L. Brongersma, Y. Cui, M.D. McGehee, *Annu. Rev. Mater. Res.* 41 (2011) 269.
- [4] R. Yan, D. Gargas, P. Yang, *Nature Photonics* 3 (2009) 569–576.
- [5] C.-S. Guo, L.-D. Luo, G.-D. Yuan, X.-B. Yang, R.-Q. Zhang, W.-J. Zhang, S.-T. Lee, *Angew. Chem. Int. Ed.* 48 (2009) 9896.
- [6] X. Li, *Curr. Opin. Solid State Mater. Sci.* 16 (2012) 71.
- [7] H.-D. Um, S.A. Moiz, K.-T. Park, J.-Y. Jung, S.-W. Jee, C.H. Ahn, D.C. Kim, H.K. Cho, D.-W. Kim, J.-H. Lee, *Appl. Phys. Lett.* 98 (2011), 033102:1.
- [8] G. Zheng, F. Patolsky, Y. Cui, W.U. Wang, C.M. Liber, *Nature Biotech.* 23 (2005) 1294.
- [9] A.I. Hochbaum, R. Chen, R.D. Delgado, W. Liang, E.C. Garnett, M. Najarian, A. Majumdar, P. Yang, *Nature* 451 (2008) 163.
- [10] S. Brittman, H. Gao, E.C. Garnett, P. Yang, *Nano Lett.* 11 (2011) 5189.
- [11] M. Ge, J. Rong, X. Fang, C. Zhou, *Nano Lett.* 12 (2012) 2318.
- [12] J.M. Weisse, A.M. Marconnet, D.R. Kim, P.M. Rao, M.A. Panzer, K.E. Goodson, X. Zheng, *Nanoscale Res. Lett.* 7 (2012) 554.
- [13] X. Li, P.W. Bohn, *Appl. Phys. Lett.* 77 (2000) 2572.
- [14] K.-Q. Peng, Y. Wu, H. Fang, X. Zhong, Y. Xu, J. Zhu, *Angew. Chem. Int. Ed.* 44 (2005) 2737.
- [15] Z. Huang, N. Geyer, P. Werner, J.d. Boor, U. Gösele, *Adv. Mater.* 23 (2011) 285.
- [16] Y. Qu, L. Liao, Y. Li, H. Zhang, Y. Huang, X. Duan, *Nano Lett.* 9 (2009) 4539.
- [17] X. Zhong, Y. Qu, Y.C. Lin, L. Liao, X. Duan, *ACS Appl. Mater. Interfaces* 3 (2011) 261.
- [18] X. Li, Y. Xiao, J.H. Bang, D. Lausch, S. Meyer, P.-T. Miclea, J.-Y. Jung, S.L. Schweizer, J.-H. Lee, R.B. Wehrspohn, *Adv. Mater.* 25 (2013) 3187.
- [19] J. Dietl, *Solar Cells* 10 (1983) 145.
- [20] A. Luque, S. Hegedus, *Handbook of photovoltaic science and engineering*, 2nd edition, Wiley-VCH, Weinheim, 2011.
- [21] X. Ma, J. Zhang, T. Wang, T. Li, *Rare Metals* 28 (2009) 221.
- [22] S.A. McHugo, A.C. Thompson, I. Perichaud, S. Martinuzzi, *Appl. Phys. Lett.* 72 (1998) 3482.
- [23] D. R. Lide, ed. *CRC Handbook of Chemistry and Physics* (87th ed.), 2006.
- [24] Y.H. Ogata, K. Kobayashi, M. Motoyama, *Curr. Opin. Solid State Mater. Sci.* 10 (2006) 163–172.
- [25] K.W. Kolasinski, W.B. Barclay, *Angew. Chem. Int. Ed* 52 (2013) 6731.
- [26] K.W. Kolasinski, J.W. Gogola, W.B. Barclay, *J. Phys. Chem. C* 116 (2012) 21472.
- [27] K.W. Kolasinski, *J. Phys. Chem. C* 114 (2010) 22098.
- [28] K. Peng, J. Hu, Y. Yan, Y. Wu, H. Fang, Y. Xu, S.T. Lee, J. Zhu, *Adv. Func. Mater.* 16 (2006) 387.

Black Silicon Photovoltaics

Martin Otto,* Michael Algasinger, Howard Branz, Benjamin Gesemann, Thomas Gimpel, Kevin Füchsel, Thomas Käsebier, Stefan Kontermann, Svetoslav Koynov, Xiaopeng Li, Volker Naumann, Jihun Oh, Alexander N. Sprafke, Johannes Ziegler, Matthias Zilk, and Ralf B. Wehrspohn*

This article presents an overview of the fabrication methods of black silicon, their resulting morphologies, and a quantitative comparison of their optoelectronic properties. To perform this quantitative comparison, different groups working on black silicon solar cells have cooperated for this study. The optical absorption and the minority carrier lifetime are used as benchmark parameters. The differences in the fabrication processes plasma etching, chemical etching, or laser processing are discussed and compared with numerical models. Guidelines to optimize the relevant physical parameters, such as the correlation length, optimal height of the nanostructures, and the surface defect densities for optoelectronic applications are given.

1. Introduction

Micro- and nanostructured silicon surfaces are widely known for their applications in silicon devices, predominantly in photovoltaics,^[1–4] but also for water splitting by photoelectrochemical catalysis,^[5–8] photodiodes,^[9] terahertz emitters,^[10] highly sensitive optical^[11] and chemical detection devices,^[12] and microelectromechanical systems.^[13] A particular class of nanostructured silicon is black silicon (b-Si), defined by their extraordinarily low reflectance over an extremely broad spectral range and for quasi-omnidirectional incidence of light.^[14] Besides the low optical reflectance of the b-Si surfaces, strong light-trapping

(LT) can be achieved for weakly absorbed photons with energies close to the absorption edge of silicon.^[15] These properties of b-Si are particularly useful for photovoltaic applications.

The limiting efficiency of a solar cell is given by the detailed balance of absorption and radiative recombination^[16] and by nonradiative processes like Auger- and impurity recombination.^[17–19] b-Si can help to approach those limits in two ways. On the one hand b-Si improves the coupling of light into the solar cell and the absorption of near band edge photons. This in turn increases the short circuit

current and on a logarithmic scale also the open circuit voltage. On the other hand, due to excellent light-trapping properties b-Si might also allow reducing the solar cell thickness substantially below 100 μm while sustaining a high light absorption. This reduces nonradiative bulk recombination losses that scale linearly with the solar cell thickness^[17,18] and hence, increases the open-circuit voltage. Of course, reducing the solar cell thickness also increases the cost efficiency. Decreasing the amount of required silicon feedstock is a major industry concern as can be seen by the growing interest in kerf-free crystalline silicon solar cell technologies.^[20–22] Unfortunately, besides bulk effects, surface recombination imposes a very critical limit to the solar

M. Otto, B. Gesemann, Dr. X. Li, Dr. A. N. Sprafke, J. Ziegler, Prof. R. B. Wehrspohn
Martin-Luther-University Halle-Wittenberg (MLU)
Heinrich Damerow Str. 4, 06120 Halle, Germany
E-mail: martin.otto@physik.uni-halle.de;
ralf.wehrspohn@physik.uni-halle.de

M. Algasinger, Dr. S. Koynov
Walter Schottky Institut (WSI)
Technische Universität München
Am Coulombwall 4, 85748 Garching, Germany

Dr. H. Branz, Dr. J. Oh
National Renewable Energy Laboratory NREL
15013 Denver West Parkway, Golden, CO 80401, USA

T. Gimpel, S. Kontermann
Fraunhofer Heinrich Hertz Institute (HHI)
Am Stollen 19B, 38640 Goslar, Germany

Dr. K. Füchsel, T. Käsebier, M. Zilk
Friedrich-Schiller-University Jena (FSU)
Institute for Applied Physics
Max-Wien-Platz 1, 07743 Jena, Germany

Dr. K. Füchsel
Fraunhofer Institute for Applied Optics
and Precision Engineering
Albert-Einstein-Straße 7, 07745 Jena, Germany

Dr. V. Naumann
Fraunhofer Center for Silicon Photovoltaics
Walter-Hülse-Str. 1, 06120, Halle Germany

Dr. J. Oh
Graduate School of EEWS (WCU)
and KAIST Institute Nano Century
Korea Advanced Institute of Science and Technology (KAIST)
Yuseong-gu, Daejeon 305-701, Republic of Korea

Prof. R. B. Wehrspohn
Fraunhofer Institute for Mechanics of Materials IWM
Walter-Hülse-Str. 1, 06120 Halle, Germany



DOI: 10.1002/adom.201400395

cell efficiency^[23] especially in thin devices. Hence, an efficient b-Si solar cell can only be obtained if in addition to good optical properties a proper electronic surface passivation can also be obtained. Black-nanostructured silicon surfaces, that are suitable for solar cell applications, have been produced by various methods as shown in **Figure 1** and discussed in detail in section 2. Solar cell results have been published for dry reactive ion etching (RIE),^[24,25] (for cell results see ^[14,26–31]) metal-assisted wet-chemical etching (MACE),^[1,3,5,32–36] fs-laser structuring (L-Si),^[2,11,37–40] and the electrochemical structuring of macroporous silicon (macP-Si).^[7,12,23,24,41–43]

Table 1 summarizes some of the important recent works on b-Si solar cells. One of the first and certainly still one of the best solar cell results on multi- and monocrystalline RIE b-Si were published by Inomata and co-workers^[44] with efficiencies of 16.7% and 17.1%. Their cell concept still incorporated a standard SiN_x layer for passivation and as an additional antireflection coating (ARC). Shortly after, Schnell et al.^[27] and Zaidi et al.^[30] both claimed that the expected increase in electrical current induced by higher absorption was predominantly consumed by enhanced surface recombination due to the enlarged surface area. The cells also suffered from a poor blue response that was explained by near-surface plasma damage.^[27,32] Similar effects were reported by Yuan et al.,^[36] who investigated MACE-structured solar cells. The poor blue response of their MACE b-Si cells could be modeled in terms of a nanoporous low lifetime “dead layer”. Therefore, many groups dealing with b-Si report that damage removal etching (DRE) of nanostructured surfaces in alkaline or acidic solutions can help to recover the charge carrier lifetime and improve the blue response of RIE or MACE-structured solar cells.^[3,19,30,45] However, if thicker damaged surface fractions are removed via DRE, the optical response is compromised due to structural changes.^[3,30] Proper process integration of DRE requires complicated adjustment of the initial black etch to obtain low reflection of the final b-Si surface. Hence, it is more desirable to optimize the black etching step to minimize initial surface damage and contaminations as proposed by Otto et al.^[46] Another idea for improving the blue response and avoiding DRE is to diffuse the emitter first and to texture the front surface in a later step by a RIE-like technique.^[47] This concept leads to a slightly higher cell efficiency, however, in case of this so-called black silicon on emitter (BSOE) cell, the nanostructures were only half as deep as on the reference b-Si cell where the emitter diffusion was carried out after the etching step. Nevertheless, by combining the phosphorus silicate glass (PSG) removal with the black etch, the number of process steps may be minimized that is desirable for industrial applications. For instance, Schäfer and Lüdemann^[48] reported that both saw damage as well as PSG may be removed by low-damage RIE. Such a process can easily be adjusted to result in a b-Si layer.^[25] Recently, Oh et al.^[3] presented an 18.2% efficient b-Si solar cell on a p-type base with a diffused phosphorous emitter at the nanostructured front surface fabricated by Ag-catalyzed MACE structures and alkaline DRE after emitter formation. The nanostructures were passivated by a thermal SiO_2 layer. However, it is known that even n-doped Si may be passivated more effectively by atomic layer deposited (ALD) Al_2O_3 depending on the doping level.^[49] Shortly after, Repo et al.^[50] reported a cell efficiency of 18.7% on n-type Si with diffused



Martin Otto studied physics at the Georg-August-University Göttingen, Germany, and the Centre for Micro Analysis of Materials of the University Autónoma Madrid, Spain. After graduating in 2008, he started his PhD at the Martin-Luther-University Halle-Wittenberg in the field of photovoltaics, with a focus on nanostructured silicon surfaces and thin film deposition under the supervision of Prof. Dr. Ralf B. Wehrspohn. In January 2014 he joined the staff research planning at the Fraunhofer Institute for Mechanics of Materials Halle.



Matthias Zilk received a diploma in physics from the Friedrich-Schiller-Universität Jena, Germany, in 2007. He is currently a doctoral student at the institute of applied physics of the Friedrich-Schiller-Universität. His main research topics are the optical properties of random nanostructures and photon management in solar cells.



Ralf Wehrspohn is working as a Full Professor in Experimental Physics at the University of Halle-Wittenberg and as Director of the Fraunhofer Institute for Mechanics of Materials at Halle/Saale, Germany. His research interests include the fabrication and characterization of nano- and microstructured silicon-based materials.

boron emitter and RIE nanostructure passivated by ALD Al_2O_3 . Currently, these results represent the highest conversion efficiencies reported for b-Si solar cells. Even though in both the cases, the corresponding reference cells still exhibited slightly higher efficiencies, the b-Si cells were not limited by front surface recombination in the nanostructures but due to insufficient passivation at the rear side.^[3,50] All examples mentioned so far rely on diffused emitters forming classic p/n-junction solar cells. Different solar cell concepts are pursued to exploit the optical benefits of b-Si. Füchsel et al.^[51] report on a b-Si solar cell using a semiconductor–insulator–semiconductor (SIS) concept

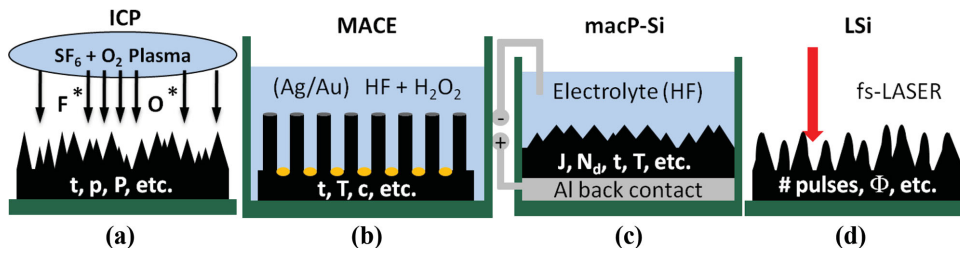


Figure 1. Schematic diagram of the four used blackening methods (not at scale). a) shows the inductive coupled plasma reactive ion etching (ICP-RIE, or short ICP) process in an atmosphere of SF_6 and O_2 ; b) depicts the metal assisted wet chemical etching (MACE) process based on Ag or Au catalyst particles in aqueous solutions of HF and H_2O_2 ; c) shows the electrochemical etch cell used for macro-porous silicon (macP-Si) fabrication; and d) schematically, shows the experimental setup for the fs-laser-treated Si surfaces (L-Si). All schematics indicate the parameters used to prepare distinct surface morphologies in this work.

by sputter deposition of a transparent conducting oxide (TCO) layer over a thin insulator covering the nanostructured surface. Ernst et al.^[43] presented an a-Si:H/c-Si heterojunction solar cell based on a thin ($\approx 33 \mu\text{m}$) macroporous Si absorber. A review on the matter of heterojunction solar cells based on nanowire (NW) arrays was recently published by Song et al.^[52] Ion implantation may also be used for emitter formation in macroporous Si substrates yielding an efficiency of 13.5% on a $\approx 34 \mu\text{m}$ thin

absorber with a b-Si-like front and back.^[53] Structuring b-Si by fs-laser irradiation was presented as a promising concept because under SF_6 atmosphere a hyperdoped sulfur emitter can be implanted in the same process step.^[2,39] A tandem solar cell concept has been proposed wherein the black IR-absorber is placed on the back side of a diffused solar cell.^[40] Recently, back-contact b-Si solar cells have been fabricated that avoid electrically contacting b-Si directly.^[54,55] Apart from all silicon-based

Table 1. Literature overview of several key results on b-Si solar cells.

Author et al.	Year	b-Si method ^{a)}	Additional treatments ^{b)}	Cell type ^{c)}	Wafer material ^{d)}	Emitter	Passivation Scheme	η [%]
Inomata ^[26]	1997	ICP-RIE	SiN_x ARC + FGA	diffused	p/multi/p/mono	n-type	SiN_x	16.7/17.1
Schnell ^[27]	2000	ICP-RIE	SiN_x ARC*	diffused	p/multi	n-type (POCl_3)	SiN_x	10.9/12.2*
Zaidi ^[30]	2001	ICP-RIE	DRE	diffused	p/multi/p/mono	n-type	SiO_2 (≈ 10 [nm])	–
Yoo ^[28]	2006	ICP-RIE	–	diffused	p/multi/p/mono	n-type (POCl_3)	SiO_2 (≈ 10 [nm])	10.2/ 11.7
Sai ^[17]	2007	AAO + ICP-RIE	AAO formation	diffused	p/single	n-type (POCl_3)	–/–	13.9
Koynov ^[118]	2007	MACE	catalyst removal	diffused	p/multi / p/tri-c-Si	n-type (spin-on)	SiO_2 (≈ 10 [nm])	12–14
Yoo ^[31]	2009	ICP-RIE	DRE + SiN_x ARC*	diffused	p/multi / p/mono	n-type (POCl_3)	SiN_x	15.1
Yuan ^[36]	2009	MACE	catalyst removal	diffused	p/single	n-type (POCl_3)	SiO_2 (≈ 20 [nm])	16.8
Huang ^[71]	2011	ICP-RIE	DRE + SiN_x ARC	diffused	p/multi / p/mono	n-type (POCl_3)	SiN_x	17.27
Chen ^[67]	2011	RIE	DRE	diffused	p/mono	n-type (POCl_3)	SiO_2	18.3
Ernst ^[43]	2012	macP-Si ($\approx 33 \mu\text{m}$)	n/a	heterojunction	p/single	a-Si:H	SiO_2 /a-Si:H	7.2
Xia ^[29]	2011	ICP-RIE-like	DRE + SiN_x ARC	diffused	p/multi / p/mono	n-type (POCl_3)	SiN_x	15.7
Füchsel ^[51]	2012	ICP-RIE	–	SIS	p/mono	Sputtered TCO	–/–	8
Oh ^[3]	2012	MACE	catalyst removal + DRE	diffused	p/mono	n-type (POCl_3)	SiO_2	18.2
Shen ^[47]	2013	ICP-RIE-like	SiN_x ARC BSOE concept	diffused	p/mono	n-type (POCl_3)	SiN_x	15.7
Ernst ^[113]	2013	macP-Si ($\approx 33 \mu\text{m}$)	n/a	Epitaxial	n/mono	p-type	SiO_2 / SiN_x	13.1
Ernst ^[53]	2013	macP-Si ($\approx 34 \mu\text{m}$)	n/a	Ion-implanted	n/mono	p-type	SiO_2 / SiN_x	13.5
Repo ^[4]	2013	ICP-RIE	–	Diffused	n/mono	p-type	Al_2O_3	18.7
Ye ^[119]	2014	MACE	DRE	diffused	p/multi	n-type	SiN	18.45
Jeong ^[55]	2013	RIE	–	IBC ^{e)}	n/mono	p-type	SiO_2	13.7
Ziegler ^[54]	2014	ICP-RIE	–	IBC ^{e)}	p/mono	a-Si:H	Al_2O_3	11.2

^{a)}Inductive coupled plasma-reactive ion etching (ICP-RIE); Anodic aluminum oxide (AAO); Metal-assisted chemical etching (MACE); ^{b)}Silicon nitride (SiN_x) passivation and antireflection coating (ARC); Forming gas anneal (FGA) in H_2 -containing atmosphere; Damage removal etching (DRE); In the black silicon on emitter (BSOE) concept b-Si etching is applied after emitter diffusion; ^{c)}Semiconductor insulator semiconductor (SIS) solar cell—very similar to the metal insulator semiconductor (MIS) concept; ^{d)}Doping type (p or n); monocrystalline silicon (c-Si); Multicrystalline silicon (mc-Si); ^{e)}Interdigitated back contact cell (IBC).

homo or heterojunction solar cells, also new concepts including organic emitters have been recently published with more than 13% efficiency.^[56]

Continuous industrial efforts over the last years have been trying to commercialize various b-Si methods, and some commercial success has been achieved. RIE-based methods have been commercialized by several Korean and Germany equipment companies, such as Jusung Engineering, IPS, and Roth & Rau. The dry-textured wafers have been used in production by several PV manufacturers such as Kyocera or Trina Solar. Laser ablation and metal-assisted chemical etching have been pursued by the several U.S. startups, such as SiOnyx, Natcore Technology, and Bandgap Engineering.

1.1. Fabrication Methods for Black Silicon

In this review article, we focus on the four most prominent fabrication methods of b-Si: dry reactive ion etching in an inductive coupled plasma (ICP-RIE),^[15,46,51] electroless MACE with Ag^[3,35,57] and Au^[1,58] catalysts, photoelectrochemical anodization that leads to the formation of macP-Si,^[12] and the irradiation of the surface with femtosecond (fs) laser pulses (L-Si) in vacuum.^[39,40] The various black etching methods (Figure 1) all lead to homogeneous macroscopically b-Si surfaces with a rather low reflectance over the whole absorbing range of silicon as will be shown in section 1.8. However, depending on the available process parameters the micro- or nanostructures have different morphologies that will be presented in this section. The b-Si methods are briefly introduced in the following.

1.2. Black Silicon by Reactive Ion Etching (ICP-RIE)

RIE of silicon with halogen radicals is a well-known process for silicon micromachining.^[59,60] By adding some components to the etching gas that form a passivation layer on silicon, highly anisotropic etching can be achieved.^[61,62] Dry etching of b-Si has been known for decades as undesired byproduct of silicon plasmas. It has been first used by Gittleman et al.^[63] from the RCA laboratories utilizing dry etching in a chlorine plasma to produce nonreflecting b-Si surfaces for, e.g., improved absorbers for solar thermal energy conversion. The anisotropic RIE with a mixture of SF₆ and O₂ gas was studied in detail first by Jansen et al.^[25] In the plasma, the two molecule species SF₆ and O₂ are cracked providing F^{*}- and O^{*}-radicals, respectively (Figure 1a). The fluorine radicals will rapidly attack the silicon surface forming volatile SiF₄. In a competing reaction, the oxygen radicals form silicon-oxyfluoride (SiF₄ + O^{*} → SiO_xF_y) at low (cryogenic) temperatures that acts as an etch stop to F^{*}.^[25,64] On horizontal faces, this passivation layer is etched physically due to ion bombardment from the plasma. However, on vertical sidewalls the sputtering of the passivation layer is weaker due to the directionality of the plasma ions and the sidewalls therefore

remain protected from chemical etching by fluorine radicals. As a result, the overall etching process becomes strongly anisotropic. In this regime precipitates from the gas phase can lead to formation of random nanostructures. Either micromasking by those particles leads to the direct formation of silicon needles as observed by Jansen et al.^[25] or trenching at the particles creates randomly distributed etch pits that eventually overlap and leave needle-like silicon features in-between.^[15] The aspect ratio of the needles can be controlled via the gas pressure which determines the directionality of the ions and the physical etching component by limiting the mean free path of the plasma species. However, the exact formation mechanisms are still under debate^[65,66] and a detailed numerical model describing this instability is still missing. Beyond the random formation of micromasks during the plasma itself, also the tailored fabrication of micromasks for b-Si is possible by silica^[55] or silicon-oxybromide^[67] nanoparticles. A recent review on the plasma-etched b-Si for photovoltaic devices is given by Lin et al.^[68]

The b-Si structures fabricated in this study were made in a single etching step by ICP RIE in a gas mixture of SF₆ and O₂.^[15] Depending on the pressure and time, different b-Si morphologies have been formed (see Figure 2 and Experimental Section).

1.3. Black Silicon by Metal-Assisted Chemical Etching (MACE)

The formation of nanostructures via etching of silicon in aqueous solutions of hydrofluoric acid containing an oxidizing agent like HNO₃ was first described more than 50 years ago.^[69] This particular kind of Si etching, carried out at high dilution and in certain range of HF/oxidant concentrations, is commonly referred to as "Stain Etching" (SE). Typically, the SE forms interference colored films of hydrogenated nano- or mesoporous silicon over the etched Si substrate. After 1990, this process attracted significant interest as potential method for producing luminescent Si films. Provoked by this interest, the common SE was developed further after the discovery that it can be accelerated by adding a metal catalyst.^[70] Shortly after, a simpler variant of this MACE to produce porous Si was studied in more detail by Li and Bohn.^[32] Without application of any electrical potential, photoluminescent nanostructures could be produced on p- and n-type wafers in the dark.^[32]

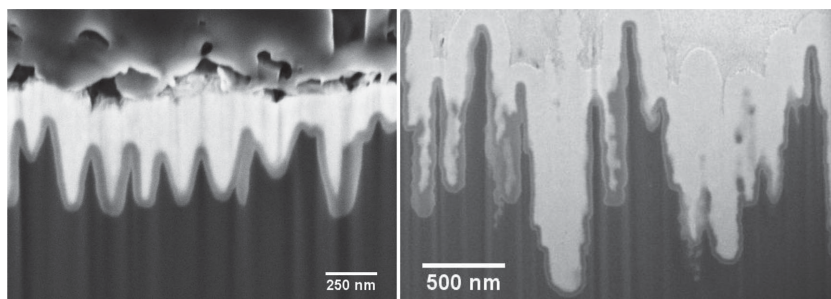


Figure 2. SEM images of the shallow (left) and the deep (right) ICP-RIE nanostructured b-Si surfaces passivated with 35 nm Al₂O₃. The cross-sections were prepared with a focused ion beam (FIB) system. The b-Si substrate (black) is conformally covered by an Al₂O₃ coating (dark gray). Note that for preparation reasons the structures were ALD coated with ZnO:Al (white) and a protective carbon layer (gray) after opto-electronic characterization was completed. In case of the deep structure a FIB-deposited Pt protection layer (light gray) was used.

Therefore, MACE quickly gained popularity and was proposed for various applications in opto-electronics (see also^[32] and references therein). A profound overview on a large variety of MACE processes, their range of parameters and various applications can be found in^[71] and references therein.

Figure 1b illustrates the principle of MACE on the representative example of metal catalyst applied as particles on the Si surface. The H_2O_2 (or other oxidant) from the HF/ H_2O_2 solution is reduced catalytically on the metal surface by consuming electrons. The consumed electrons are restored in the metal via electron transfer from the valence band of silicon through the metal/Si interface. Thus, electronic holes are injected into the semiconductor just below the metal. Subsequently, the holes diffuse to the semiconductor/electrolyte interface close to the particle. This results in local divalent or tetravalent oxidation of Si surface, depending on the local hole concentration (prerequisites for porous Si etching or bulk Si etching, respectively). Then, HF selectively etches the oxidized Si around the metal (mainly at the periphery and below a particle). As a result, the metal particles “sink” into the Si due to the underetching, forming a vertical channel. The overall process is electrochemical in nature, with current flowing between the metal, acting as local cathode and the Si as anode, although an external current source is not applied. The shape of the channel, however, is determined by the etching current distribution in the vicinity of the particles, which itself is strongly dependent on the size, shape, spatial distribution, and kind of the metal particles. In general, the etching direction is towards the Si bulk, although some preferential etching along (100) crystallographic direction has been observed especially for Ag particles.^[35] Due to its underlying catalytic mechanism and the fact that holes originate from H_2O_2 decomposition, the method is working for a wide range of doping levels in n- and p-type Si in combination with many metals^[32] and can be applied to Si substrates with different crystallinity (c-Si, mc-Si, $\mu\text{c-Si}$, and a-Si:H).^[1,72,73] The metal catalyst can be deposited as an ultrathin discontinuous film before black etching by thermal vacuum evaporation or sputtering^[1,57] or by electroplating.^[3,58] Alternatively, the catalysis can be triggered by creating nanoparticles in situ during black etching by the reduction of metal salts.^[35,36] Depending on the metal catalyst (Al, Cu, Fe, Pt, Pd, Au, Ag, etc), its deposition technique, the nanoparticle density and lateral distribution on the wafer surface, the black etching process may lead to very distinct surface geometries (see **Figure 3**). The Si etching rate mainly depends on the temperature and H_2O_2 concentration, whereas the latter may also strongly influence the nanostructure morphology.^[71] The dissolution rate of Si is limited by surface oxidation, as very low HF concentrations are sufficient for immediate etching of the SiO_x .

1.4. Black Silicon by Photoelectrochemical Etching (PEC)

Another method for the electrochemical etching of silicon in an aqueous HF solution is the anodization via an externally

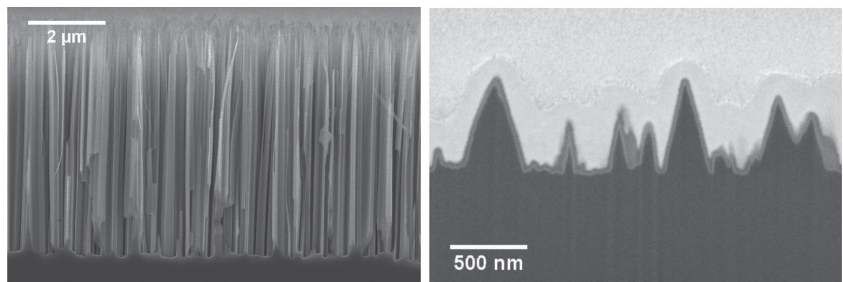


Figure 3. Left: SEM image of passivated long nanowires (NWs) fabricated in a 10 min long Ag-MACE etching step. The NWs are conformally coated with 35 nm Al_2O_3 and have lengths of $\approx 6 \mu\text{m}$ and diameters of about 50–150 nm. Due to the scale, the passivation layer is not well visible. Right: Cross-section of the Au-MACE structured b-Si nanocones (NCs). The b-Si surface (black) is passivated with a 35 nm thick layer of Al_2O_3 (grey), followed by the ZnO:Al coating (white) for better visibility. A Pt protection layer was placed on top (light grey).

applied electric current (Figure 1c). This method produces macP-Si and has been described in detail by Lehmann for both n-type silicon^[74] and p-type material.^[41] To process n-type Si an additional light source is needed for the generation of electronic holes, which is similar to the MACE process, lead to an oxidation of Si atoms at the Si-electrolyte interface. In p-type Si the holes are the majority carriers such that the minimum concentration is fixed to the doping level. Charge carrier injection by light absorption is possible, but not needed. Upon Si oxidation by hole exchange, subsequently, the SiO_x can be dissolved by HF. With larger electronic hole concentrations the pore density increases as the space charge region at the surface becomes thinner.^[41] For constant current and HF concentration at sufficiently low hole concentrations, the pore depth may be controlled by the etching time and temperature. Depending on the electrolyte solution and the galvanic current density etch rates of the order of $0.1\text{--}10 \mu\text{m min}^{-1}$ may be reached in $1 \Omega \text{ cm}$ p-type (100) Si.^[41] Thus, short etching times ($\approx \text{min}$) are sufficient for electrochemical black etching. The pore diameter is controlled by the induced current through the wafer back-contact to the counter-electrode in the electrolyte. This way the 3D-pore shape can be freely modulated as device design requires,^[75] which allows tailoring the optical surface properties within the available parameter range. Under certain conditions, this method can be used for kerf-free wafering of n-type Si and in situ black etching in an one-step-process.^[22] However, if no lithography is applied to predefine the pore positions, randomly emerging pores in p-type Si tend to overlap, as was the case here. Hence, the doping level that defines the average pore distance sets a limit to the minimum achievable feature size. A typical surface structure fabricated by the macroporous Si method is shown in **Figure 4**.

1.5. Black Silicon by Pulsed-Laser Treatment

The formation of surface patterns upon irradiation with pulsed lasers (see Figure 1d) has been first observed in the 1960s^[76] and was found to occur on many materials.^[77] Later the effect was also found for femtosecond laser pulses.^[78,79] The formation of b-Si via fs-laser occurs above a certain fluence threshold and requires a number of pulses hitting the surface.^[37,80–82]

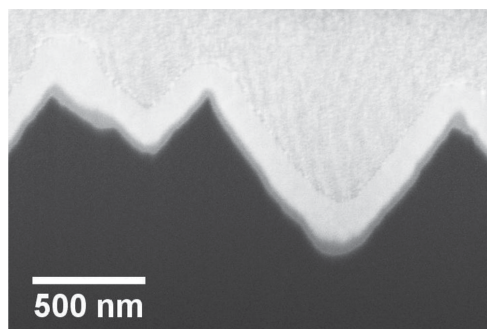


Figure 4. Focused ion beam (FIB) prepared cross-sectional SEM image of the macroporous Si surface (macP-Si) (black). The Al_2O_3 passivation layer (gray) has a thickness of 35 nm and was covered after opto-electronic characterization by a layer of ZnO:Al (white) for better SEM-contrast. A FIB-deposited Pt layer (light gray) protects the surface from the beam halo.

Especially, the fact that doping^[83] and structuring can be performed in a single process step without the need of a predeposited layer of a doping source makes this approach very attractive in solar cell processing. Furthermore, the surface morphology and optical absorption properties of such laser-treated Si surfaces (L-Si) can easily be tuned from the UV into the IR spectral region ($\approx 2.5 \mu\text{m}$).^[40] Both properties depend on the number of pulses, irradiation intensity, structuring atmosphere,^[2,37] and pulse duration^[40] of the laser. Furthermore, the temporal and spatial shape of the laser pulses may be used to control the absorption behavior in the VIS and IR spectral domain.^[39,40] Another advantage is that the laser structuring is independent from the crystal structure. Laser treatment also modifies the crystal structure^[39,84] raising the interest for a working passivation process. Different b-Si surfaces obtained by fs-laser structuring are presented in **Figure 5**.

1.6. Limits of the Fabrication Methods of Black Silicon

The range of applicability is quite large for most of the presented blackening methods. There are no restrictions concerning

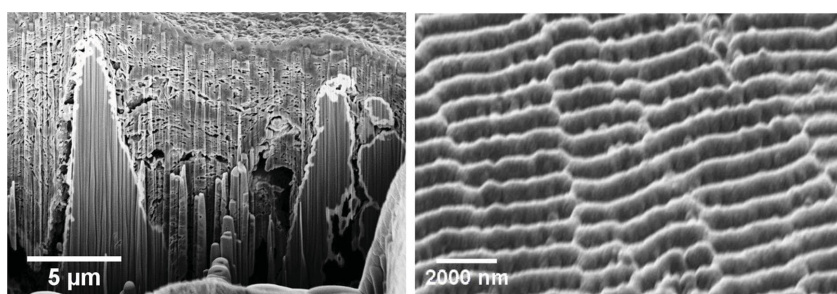


Figure 5. Left: FIB-prepared cross-sections of laser-treated silicon (L-Si) surface structures fabricated by 500 subsequent laser pulses, respectively. The sample is coated with a thicker ZnO:Al layer (white) covering the Al_2O_3 passivation. The "black" L-Si consists of up to 15 μm high Si spikes with aspect ratios of about 3. Right: SEM topview of the laser-treated silicon (L-Si) surface after KOH damage removal etching. The standing wave formation with periodicity of $\approx 800 \text{ nm}$ corresponds to the used laser light wavelength. The surface was coated with 35 nm Al_2O_3 for passivation. After opto-electronic characterization an additional coating of 160 nm ZnO:Al was deposited by ALD.

crystal orientations and doping level of the substrate wafers. In case of the ICP-RIE process this also includes multicrystalline (mc-) and even microcrystalline ($\mu\text{c-Si}$) and amorphous silicon (a-Si), which can mainly be explained by the high isotropy of the fluorine etching reaction, the purely physical etching of the passivation layer. Structuring by fs-laser ablation is also a physical process and therefore is mainly determined by the absorption behavior of the substrate material. Chemically dominated processes may be somewhat more restricted to crystallographic planes. However, MACE also works on mc-, $\mu\text{c-}$, and a-Si.^[72] An exception is the macroporous Si technique that may only be used for pore fabrication on monocrystalline Si substrates in a certain range of doping levels. All four presented methods can be applied selectively on a single wafer side. However, in the experimental part of this study only lifetime samples with bifacially macroscopic identical wafer sides were investigated. There are further technological limits of b-Si technologies that are beyond the scope of the review and which have to be considered for an industrial implementation such as thermal management due to enhanced light absorption, mechanical strength of the nanostructures, structural uniformity over large area or photon loss after encapsulated in glass.

1.7. Surface Passivation Technologies of Black Silicon

To achieve long effective carrier lifetimes that enable solar cells with high open-circuit voltages, surface recombination must be suppressed as far as possible. Thus, effective passivation layers are essential for high efficiency solar cells especially if nanostructured surfaces shall be incorporated. For b-Si nanostructures, SiN, or SiO_2 passivation schemes have been used.^[68] Since 2006 passivation by ALD deposited Al_2O_3 ^[85,86] has been studied extensively for its outstanding performance on (highly doped p-type)^[87] Si. It has been shown that already very thin layers of Al_2O_3 are sufficient to obtain very low surface recombination velocities (SRV).^[88–91] Al_2O_3 offers the unique combination of two complementary passivation effects: first, the coated layer contains a quite high number of negative fixed charges^[92] (up to $Q_{\text{fix}} = -1 \cdot 10^{13} \text{ cm}^{-2}$) that lead to a very strong field effect passivation, and secondly, the interface exhibits a very good chemical quality with interface defect densities as low as $D_{\text{it}} = 4 \cdot 10^{10} \text{ eV}^{-1} \text{ cm}^{-2}$.^[93] In the experimental part of the this study, we use ALD-deposited Al_2O_3 as benchmark (see Experimental Section).

1.8. Optical Properties of Black Silicon

To compare the optical properties of the different b-Si technologies under similar conditions, we have made an experimental comparison with these technologies from different groups world-wide. We processed all samples similar (see Experimental) except the b-Si fabrication step and measured their absorption (**Figure 6**) and in section 1.9 their optoelectronic properties. As reference sample,

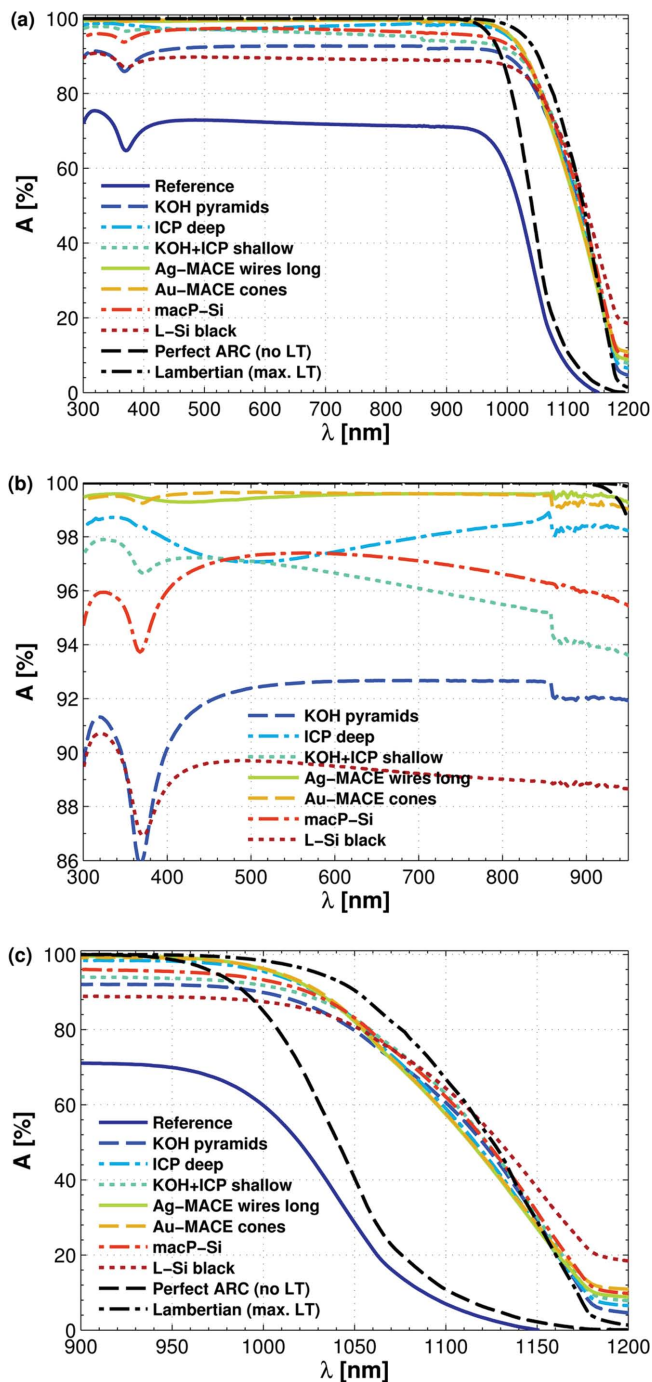


Figure 6. Comparison of the spectral absorption of the investigated black etching methods. Plot a) presents an overview; a zoom into the UV/VIS range is given in (b); and (c) displays the band edge region of Si. Shown are the ICP deep (dash-dotted light blue), the superstructure (dashed cyan), the long Ag-MACE NWs (solid green), the Au-MACE NCs (dashed yellow), the macP-Si (dash-dotted red), and the black L-Si sample (dotted red). The graphs of the experimental (KOH, unstruct.) as well as the numerically simulated reference spectra appear in the same line styles and colors.

we used a planar sample (Reference) and a KOH-treated leading to inverted pyramids (KOH pyramids). The absorption of the KOH sample is about 92% between 450 and 950 nm. Above

1000 nm the texture exhibits the expected light-trapping behavior. For comparison, two theoretical limits are included: the perfect antireflection coating without light trapping and the Lambertian limit as discussed by Yablonovitch.^[94] The perfect antireflection coating was calculated by neglecting the first reflection of incoming light at the sample's surface but taking into account the reflection at the rear Si/air interface. The ergodic limit for light-trapping structures was calculated by assuming a Lambertian scatterer that also acts as a perfect ARC.^[94] Note that it is assumed also in the numerical calculation that are scatters on both sides of the wafer. Since there is no perfect reflector on the backside, the total escape probability of light is increased by a factor of two. Hence, in accordance with the publication of Deckman et al.^[95] bifacial application of light randomizing structures decreases the maximal path-length enhancement to $2n^2$ ($n = 3.5$ for c-Si). The simulations are based on the material data of Si published by Green.^[96] A wafer thickness of 250 μm was assumed. As shown in Figure 6, with a perfect ARC but without any light trapping, the total absorption in the range from 300 to 1180 nm is 84.4%. With Lambertian light trapping, this value increases to 92.7% in the same spectral range. Representative samples are also shown in Figure 6 for the four different b-Si technologies. More details can be found in the supplement information.

The optical absorption measurements of the ICP-RIE treated samples (see Figure 2) show depending on their depth very different properties (see Figure S2, Supporting Information). The deep b-Si structure (ICP deep) has both a better antireflection effect as well as more effective light trapping. Its absorption varies between 97% and 98.7% in the interval of 340 and 515 nm. The light-trapping performance of the ICP deep is as good as the KOH texture under normal incident light but has a better antireflection effect in the VIS and NIR spectral range (Figure 6). The light trapping is close to the $2n^2$ limit. Here, the question arises what happens if one combines the KOH and the ICP-RIE b-Si. Such a superstructure was fabricated by shallow ICP etching of and underlying KOH-textured surface. The combination shows indeed an improved absorption in the UV/VIS compared with the shallow and intermediate structure as well as the KOH texture alone (Figure 6, KOH+ ICP shallow). Its absorption drops from 97.9% at 325 nm to 94% at 900 nm. The superstructure exhibits the strongest light trapping in this study and is closest to the ergodic limit. As in the case of ICP deep, the superstructure KOH+ ICP shallow profits from a lower reflection at long wavelengths. All ICP-RIE structures effectively reduce or virtually completely suppress the reflection peak of Si around 370 nm resulting in a high UV absorption.

The optical absorption spectra of the Au-MACE (Au-MACE cones) and Ag-MACE (Ag-MACE wires long) samples as well as the macP-Si structure are also displayed in Figure 6. As shown in Figure S3, (Supporting Information), these two MACE structures show the highest absorption in the UV and VIS spectral range. For the MACE sample the typical absorption dip of Si at 370 nm is virtually completely suppressed as its absorption drops less than 0.3%. The Au-MACE cone absorption increases to over 99.6% at $\lambda = 500$ nm. The light-trapping properties at the Si band edge are shown in detail in Figure 6(c). The Au-MACE cone and the Ag-MACE wires long show indistinguishable light-trapping behavior being about 3% less effective than the KOH texture at 1100 nm. The macP-Si sample has a maximum

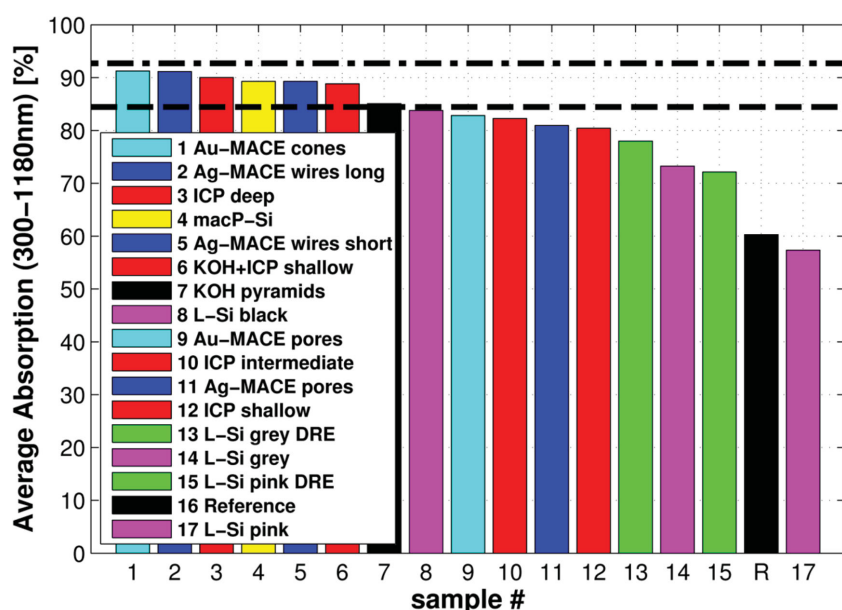


Figure 7. Integrated total optical absorption between 300 and 1180 nm of the black-etched samples passivated with 35 nm Al_2O_3 in comparison with an equally treated sample with KOH random pyramid texture and an unstructured shiny-etched reference. The calculated absorption limits of a perfect antireflection coating with no light trapping (dashed black) and the one with Lambertian light trapping (dash-dotted black line) are also shown. The samples are sorted by absorption efficiency in descending order. Similar processes are grouped by color (Au-MACE: cyan); (Ag-MACE: blue); (ICP-RIE: red); (macP-Si: yellow); (L-Si: magenta); (L-Si+DRE: green); (References: black).

absorption of 97.4% being reached around 550 nm. The absorption slightly decreases to 96% at 900 nm that is 4%–5% more effective than the KOH sample. In comparison with the latter, the macP-Si exhibits a marginally (1.5% at 1100 nm) stronger light-trapping performance and a slightly weaker but still pronounced absorption dip at 370 nm.

Finally, the optical properties of different fs-laser-structured samples were studied (See Figure S4, Supporting Information).

The black sample (*L-Si black*) displays a very similar characteristic like the KOH texture in the UV (Figure 6). In the VIS it absorbs almost 90%. With increasing wavelengths its absorption slightly drops. Note that above 1040 nm *L-Si black* captures more light than the *KOH pyramids* and above 1115 nm even more than the Lambertian scatterer.

In comparison, the Au- and Ag-etched MACE b-Si structures exhibit the highest absorption in the UV and VIS spectral range followed by the deep ICP-etched b-Si. Above 475 nm the macP-Si sample absorbs more light than the superstructure KOH + ICP shallow. LT of all samples in this plot is rather close to the Yablonovitch limit and in all cases very similar for wavelengths greater than 1050 nm. The macP-Si and the superstructure KOH + ICP shallow, both are slightly more effective than the *KOH pyramids* over the whole displayed range. The MACE samples (*Au-MACE cone* and *Ag-MACE wires long*) capture only 3% less normal incident light than the KOH texture around 1120 nm. A summary of all 16 samples of this study concerning their total integrated absorption between 300 and 1180 nm is shown in Figure 7 and a Table with the data is shown in the supplementary information (Table 2 and Table 3).

1.9. Charge Carrier Lifetimes in Black Silicon

Beyond the optical properties of b-Si giving some indications about the maximum short circuit current J_{sc} , the effective carrier lifetime τ_{eff} is the second critical parameter for b-Si structure, giving some indications about the maximum open-circuit voltage V_{oc} . Therefore, the effective lifetime τ_{eff} of all 16 samples was measured determined experimentally by the quasi-steady-state photoconductance (QSSPC) method.^[97] The given lifetime values in this section were measured at an injection level of $\Delta N = 10^{15} \text{ cm}^{-3}$ if not indicated otherwise (Table 3, Figure 8). The lifetime reference (*Reference*) is an unstructured out-of-box wafer that was only cleaned, passivated, and annealed. Its lifetime of more than 3 ms (Figure 8) is comparable with state of the art passivation results based on the similar substrate material with the same doping level and surface passivation quality.^[98] Furthermore, according to the current understanding, the value is close to the intrinsic lifetime limit of $1 \Omega \text{ cm p-type Si}$,^[98] which represents the ultimate limit to the achievable open-circuit voltage in a solar cell.^[99,100] This limitation is noticeable especially for high injection levels indicated by the

drop in τ_{eff} toward $\Delta N = 10^{16} \text{ cm}^{-3}$. The injection level dependence of our reference indicates very stable low light behavior as the lifetime is virtually constant toward lower excess charge carrier densities (Figure S5, Supporting Information). Assuming

Table 2. Geometrical parameters and optical performance indicators of the samples that operate in a wave-optics regime extracted from experimental data combined with simulation.

Sample	$L_c^{a)}$ [μm]	$H^{b)}$ [μm]	$R_{UV/VIS}$ 300–1000 [nm] [%]	$A/A_{\text{Lambert}^{c)}$ 1050–1180 [nm] [%]
Lambertian	–	–	0.0	100
macP-Si	0.360	0.76	3.6	96.2
ICP deep	0.190	1.85	2.1	90.8
Au-MACE nanocones	0.120	0.65	0.6	90.4
Ag-MACE long NWs	0.085–0.100	5.80	0.6	89.3
Ag-MACE short NWs	0.085–0.100	2.55	0.8	72.7
ICP intermediate	0.115	0.55	7.4	59.8
ICP shallow	0.100	0.59	7.5	43.2
Au-MACE nanopores	0.045	0.53	3.5	33.5
Ag-MACE nanopores	0.030	0.55	4.8	25.0

^{a)}Lateral correlation length estimated from 1D FIB cuts as explained in the text;

^{b)}Peak-to-valley height estimated from 1D FIB cuts as explained in the text;

^{c)}Relative absorption performance as compared with a Lambertian scatterer with maximum nonresonant light trapping. The values are renormalized to the absolute absorption of 53.2% in this spectral region.

Table 3. Overview of passivated b-Si samples and references. Shown are the passivation quality in terms of t_{eff} and S_{eff} , and the overall optical absorption and light-trapping performance. The QSSPC data have relative errors of up to 25%.

Sample/Structure	$\tau_{\text{eff}}^{\text{a)}$ [μs]	$S_{\text{eff,max}}^{\text{b)}$ [cm s^{-1}]	$S_{\text{nano}}/S_{\text{ref}}$ [a.u.]	$\gamma_{\text{min}}^{\text{c)}$ $\leq A_{\text{nano}}/A_{\text{ref}}$ [a.u.]	$\delta_{\text{max}}^{\text{d)}$ $\geq D_{\text{S,nano}}/D_{\text{S,ref}}$ [a.u.]	A_{tot} 300–1180 [nm] [%]	$A_{\text{UV/VIS}}$ 300–1000 [nm] [%]	A (LT) ^{e)} 1050–1180 [nm] [%]
Unstructured reference	$3.0 \pm 1.0 \cdot 10^3$	4.1 ± 1.3	1	1	1	60.3	71.3	6.9
KOH pyramids	983 ± 190	12.7 ± 2.8	3.09 ± 0.12	1.7 ± 0.17	1.8 ± 0.2	85.1	91.8	48.9
ICP shallow	1142	11	2.66	$\approx 2-4$	$\approx 0.9-1.3$	80.4	92.5	23.0
ICP intermediate	1597	7.8	1.90	$\approx 2-4$	$\approx 0.6-1.0$	82.2	92.6	31.8
ICP deep	677	18.5	4.49	$\approx 5-10$	$\approx 0.5-0.9$	90.0	97.9	48.3
Superstructure KOH + shallow	890.7	14	3.41	$\approx 3.4-7$	$\approx 0.5-1.0$	88.8	96.0	51.0
Au-MACE nanocones	110.6	113	27.5	$\approx 3-6$	$\approx 5.5-9$	91.3	99.4	48.1
Ag-MACE nanopores	102.4	122	29.7	$\approx 3-5$	$\approx 6-10$	80.9	95.2	13.3
Ag-MACE short NWs	48	261	63.4	$\approx 10-14$	$\approx 4.5-6$	89.3	99.2	38.7
Ag-MACE long NWs	9.1	1374*	334	$\approx 25-45$	$\approx 7-13$	91.1	99.4	47.5
macP-Si	7.6	1635*	398	≈ 2	≈ 200	89.3	96.4	51.2
Laser (pink), [after DRE]	≈ 1.0 [5.6]	12200* [2230]*	2950 [543]	–	–	57.3, [72.1]	67.2 [79.6]	9.7, [34.6]
Laser (gray), [after DRE]	≈ 1.1 [1.7]	11600* [7400]*	2830 [1790]	–	–	73.2, [78.0]	78.9 [84.5]	43.4, [44.2]
Laser (black)	≈ 1.1	1 2200*	2950	≈ 2	≈ 1500	83.8	89.2	54.8
Perfect ARC (no LT)	–	–	–	–	–	84.4	99.5	11.0
Lambertian (max LT)	–	–	–	–	–	92.7	100	53.2

^{a)}For $\Delta N = 10^{15} \text{ cm}^{-3}$. If not indicated otherwise the relative error estimated to be 30%; ^{b)} $S_{\text{eff,max}}$ was calculated by $S_{\text{eff,max}} < W/2\tau$ (Equation (1)) assuming a wafer thickness of $W = 250 \pm 25 \mu\text{m}$. The error of this estimation is lower than 5% as long as $S_{\text{eff}} \leq D_s/(4W)$ with $D_s = 30 \text{ cm}^2 \text{ s}^{-1}$ the minority carrier diffusion constant.^[Sproul94] ^{c)}Measured or conservatively estimated surface enlargement factor $\gamma_{\text{min}} \leq \gamma_{\text{true}} = A_{\text{nano}}/A_{\text{ref}}$. The relative error is estimated to be lower than 50% if not indicated otherwise; ^{d)}Estimation of the maximum number of total recombination active defects relative to the reference which were introduced by black etching $\delta_{\text{max}} \geq \delta_{\text{true}}$. The true number of recombination active defects, $\delta_{\text{true}} = D_{\text{S,nano}}/D_{\text{S,ref}}$ is expected to be inferior to δ_{max} . In accordance to error propagation from [c], the error of δ_{max} is estimated to be lower than 40%; ^{e)}Absorption in the spectral range of 1050–1180 nm. This spectral regime is mostly affected by light trapping in the structures; ^{f)}The SRV may be influenced by either a deteriorated bulk lifetime, or could be limited due to minority carrier diffusion processes.

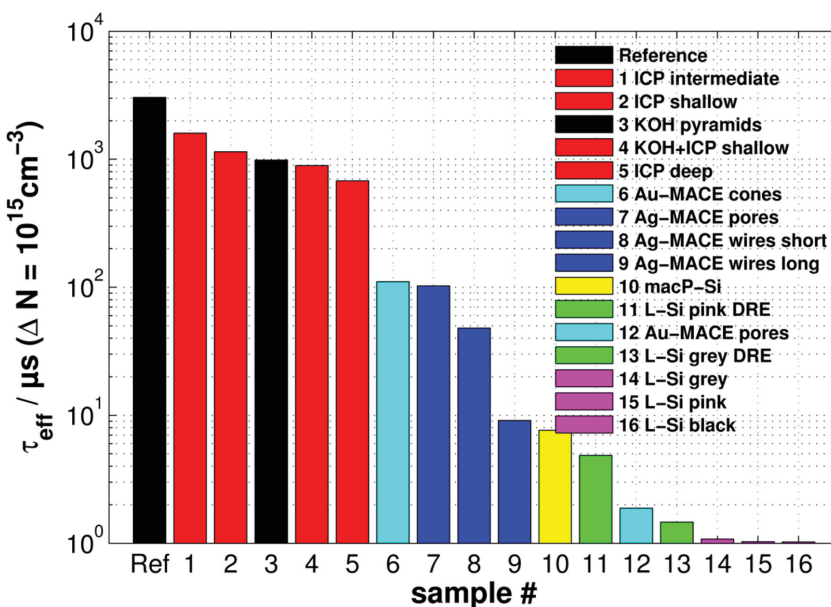


Figure 8. Minority charge carrier lifetimes of b-Si samples and references at an injection level of $\Delta N = 10^{15} \text{ cm}^{-3}$.^[6] All samples were cleaned, passivated with 35 nm Al_2O_3 and annealed. The results are sorted by lifetime in descending order. Similar processes are grouped by color (References: black); (ICP-RIE: red); (Au-MACE: light blue); (Ag-MACE: dark blue); (macP-Si: yellow); (Laser+DRE: green); (Laser: magenta).^[6] For samples treated under direct laser light, the injection level was lower.

infinite bulk lifetime, the measured effective lifetime of 3 ms translates into a maximum surface recombination velocity of $S_{\text{eff}} = 4.1 \pm 0.8 \text{ cm s}^{-1}$. This value is calculated by the worst case approximation after Sproul^[101] ascribing all recombination to the surface:

$$S_{\text{eff}} \equiv S_{\text{eff,max}} \leq W/(2\tau_{\text{eff}}) \quad (1)$$

where W is the wafer thickness and the factor of two accounts for identically structured surfaces on the front and rear side of the wafer (see Supporting Information).

The passivated and annealed KOH textured wafer (*KOH pyramids*) exhibits a lifetime of 0.98 ms at $\Delta N = 10^{15} \text{ cm}^{-3}$, corresponding to $S_{\text{eff}} = 12.7 \text{ cm s}^{-1}$. Like the unstructured reference, its lifetime depends only very weakly on the excess charge carrier density (Figure S5, Supporting Information).

The intermediate b-Si structure (ICP intermediate) with $\tau_{\text{eff}} = 1.6 \text{ ms}$ exhibits the highest lifetime of the dry-etched samples and accordingly has the lowest surface recombination velocity of $S_{\text{eff}} \leq 7.8 \text{ cm s}^{-1}$.

To our knowledge, this is the lowest surface recombination velocity ever reported for a bifacially nanostructured b-Si wafer with a base conductivity of $1 \Omega \text{ cm}$. For the shallow b-Si (ICP shallow) and deep b-Si (ICP deep) structures lifetimes of 1.1 ms ($S_{\text{eff}} \leq 11.3 \text{ cm s}^{-1}$) and $680 \mu\text{s}$ ($S_{\text{eff}} \leq 18.4 \text{ cm s}^{-1}$) were measured, respectively. For the superstructure (KOH + ICP shallow) a value of $\tau_{\text{eff}} = 890 \mu\text{s}$ was obtained. The lifetimes of all ICP-RIE treated samples are independent of the injection level for excess carrier concentrations in the range of $4 \cdot 10^{13} \text{ cm}^{-3} \leq \Delta N \leq 10^{15} \text{ cm}^{-3}$ (Figure S5, Supporting Information).

The MACE nanostructured samples that exhibit the longest carrier lifetimes are the Au-catalyzed nanocones (NC) (*Au-MACE cones*) with $\tau_{\text{eff}} = 111 \mu\text{s}$ and the Ag-etched nanopores (*Au-MACE pores*) with $\tau_{\text{eff}} = 102 \mu\text{s}$. The macP-Si sample exhibits a rather short lifetime of less than $10 \mu\text{s}$. Common to all wet-chemically etched samples is a very weak injection level dependency of the carrier lifetime (Figure S6, Supporting Information).

In contrast to all other sample, the laser-treated samples did not exhibit an increased carrier lifetime after the ALD Al_2O_3 passivation scheme had been applied (Figure S7, Supporting Information). However, a DRE improves the lifetime significantly. The highest lifetime has been achieved for the *L-Si pink DRE* sample with $\tau_{\text{eff}} = 5.6 \mu\text{s}$. All lifetime results are summarized in Table 3 together with the corresponding SRV and the values of the integrated optical absorption. A graphic representation of this table is given in Figure 9.

It shows the measured minority charge carrier lifetimes at an injection level of $\Delta N = 10^{15} \text{ cm}^{-3}$ plotted against the integrated optical absorption between 300 and 1180 nm of the same samples.

2. Discussion of the Optical Properties of Black Silicon

Both, the UV/VIS reflectance and the NIR light-trapping efficiency of the investigated b-Si structures vary significantly among the different b-Si fabrication methods and structures (Figure 7). They depend on the characteristic scales of the topographic features. For characteristic length scales above the wavelength of light (in our study KOH pyramids and laser-processed samples), ray optics can be used. In the opposite case, where the structures are smaller than the wavelength of light (in our study ICP-RIE, MACE, and macP-Si samples), wave-optics has to be considered. We will therefore discuss both classes of structures separately and compare them to numerical simulations. First, we will discuss the antireflection and light-trapping properties of the samples operating in the wave-optics regime and in the following the structures operating in the ray-optics regime.

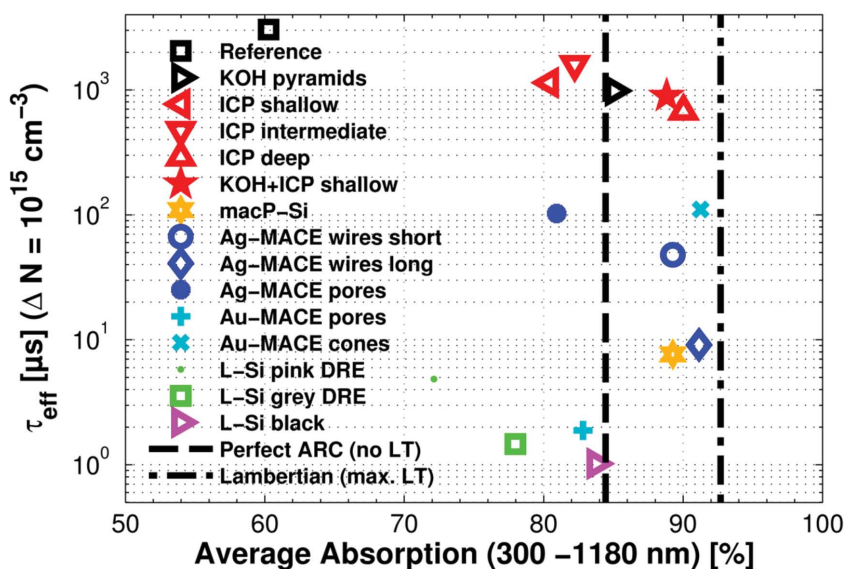


Figure 9. The graph shows the minority carrier lifetimes of the samples at an injection level of $\Delta N = 10^{15} \text{ cm}^{-3}$ plotted against their integrated total absorption between 300 and 1180 nm. [9] For samples treated under direct laser light, the injection level was lower.

2.1. Structures Operating in the Wave Optics Regime

To obtain the characteristic length scales of these samples, 1D height profiles were extracted from cross-sections prepared by FIB milling. From the profiles, the peak to valley height H was measured and the correlation length L_c was determined by fitting a Gaussian function to the 1D autocorrelation function of the profiles. The correlation length L_c was taken to be twice the standard deviation σ of the Gaussian and corresponds approximately to the lateral distance of adjacent peaks and valleys. The geometrical surface parameters are listed in Table 2 together with the average UV/VIS reflectance and the NIR absorption that has been normalized to the Yablonoitch limit. Furthermore, from the cumulative height distribution the depth profile of the silicon fraction was estimated. The results are shown in Figure 10. Please note that all geometrical parameters were extracted from single cross-sections with lengths of about 5–10 μm . Due to such a limited amount of statistical samples, the measured geometrical data, especially the correlation length, are afflicted with large statistical uncertainties. As shown in Table 2, the light-trapping performance of the samples covers the whole range from almost no light trapping, e.g., in case of the *MACE nanopore* samples, to nearly Lambertian light trapping in case of the macP-Si sample. Thereby the light-trapping performance is strongly linked to the correlation length. In general, structures with a large correlation length tend to exhibit a better light-trapping performance than structures with a low correlation length. The influence of the correlation length can be understood from coupled wave theory^[102,103] where it is shown that the coupling between two plane waves with different lateral wave vectors is mediated by the Fourier component of the spatial permittivity distribution corresponding to the difference between the wave vectors. Structures with a very short correlation length relative to the incident wavelength exhibit a broad spectrum of spatial frequencies.

However, most frequencies are above the cut-off $f_c > \frac{2n_{\text{Si}}}{\lambda}$

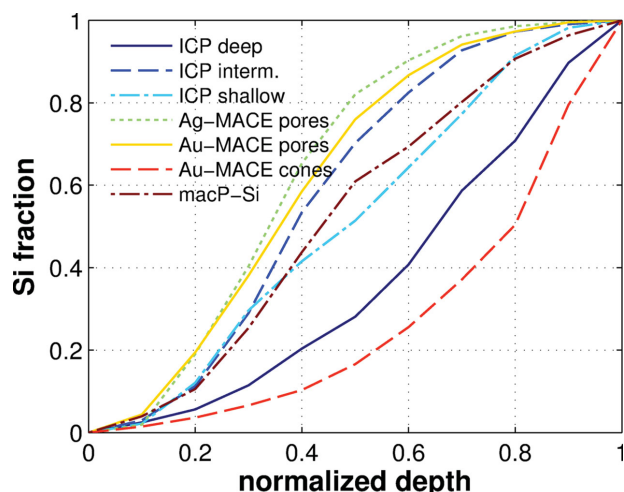


Figure 10. Depth profiles of the silicon fraction of various b-Si structures.

(with the free space wavelength λ and the refractive index of silicon n_{Si}) and will couple to evanescent waves that provide no scattering. The coupling to propagating waves is very weak and hence the fraction of scattered light is low. This is the case of a subwavelength structure like the MACE nanopores. With increasing correlation length the spatial frequency spectrum gets narrower and the amplitude of the lower spatial frequencies will increase. However, coupling might still be weak and thus it takes a long propagation length to scatter a substantial fraction of the incident light. The MACE NWs, the MACE NC, and the ICP structures probably operate in this regime. Thereby, it can be assumed that the ICP shallow and the ICP intermediate structures perform poorly because of the low depth compared with the other structures. The MACE NWs on the contrary are very long and might facilitate multiple scattering that leads to a better light trapping despite the low correlation length. This assumption is supported by the fact that the long NWs perform better than the short NWs. Following this line the ICP deep structure profits both from the large depth and the increased correlation length. However, the behavior of the MACE nanocone sample seems to deviate from this reasoning. The structure performs significantly better than the ICP intermediate structure despite its depth, while its correlation length is only slightly increased. A possible reason for this might be the difference in the depth profiles of the silicon material fraction, as shown in Figure 10. While the MACE nanocone structure exhibits a concave depth profile, the ICP shallow and the ICP intermediate structures both exhibit convex profiles. Finally, the macP-Si structure that has the best light-trapping performance also exhibits the largest correlation length of all samples in this class. Such a large correlation length (i.e., $L_c = \frac{\lambda}{n_{\text{Si}}}$) implies a substantial part of the spatial frequency spectrum being below the cut off and hence efficient coupling to all possible scattering angles can occur even if the depth of the structure is moderate. A further increase of the correlation length should finally lead to a decline of the light-trapping performance when the spatial frequency spectrum becomes too narrow to excite large propagation angles effectively. In this discussion resonant effects, e.g., resonant Mie scattering, were not considered, although those also might occur if

the size of an individual feature is in the order of the scaled wavelength λ/n_{Si} . However, due to the stochastic nature of the b-Si textures it is likely that only a small fraction of the features will be resonant at a given wavelength and hence the overall contribution should be small. Altogether the results of investigated b-Si structures indicate that the correlation length is the key property for the light trapping. Structures with a correlation length significantly smaller than the scaled wavelength λ/n_{Si} do not provide substantial scattering. On the contrary, a structure with a correlation length in the order of the scaled wavelength performs already close to the optimum even with a moderate depth of about twice the scaled wavelength. Structures with intermediate correlation lengths appear to provide some scattering which however seems to depend strongly on the structure depth. Yet, even very deep structures with intermediate correlation length do not match the performance of a structure with a larger correlation length. Not only the light-trapping performance but also the antireflection properties are vastly different between the individual samples as indicated by Table 2. However, unlike the light trapping, the AR properties do not seem to be linked to a single geometrical parameter. For example the structures with the shortest correlation lengths and the structure with the longest correlation length, namely the MACE nanopore samples and the macP-Si sample, exhibit very similar AR properties. Some structures with an intermediate correlation length perform significantly better than those while other structures, namely the ICP shallow and the ICP intermediate structures, perform significantly worse. The antireflection properties of the small structures result from a “moth-eye” effect.^[104] As the lateral features are considerably smaller than the wavelength of the incident light, no back scattering occurs and instead the incident wave experiences some average refractive index that depends on the silicon volume fraction. Due to this effective refractive index gradient there is no abrupt interface between silicon and air and hence Fresnel reflections are strongly reduced.^[105] The efficiency of the gradient-index effect depends on the depth of the structure and the effective refractive index profile. Some effective refractive index profiles and the resulting reflectance behavior are depicted in Figure 11. The best performance is achieved with a quintic profile^[105] that has a continuous first and second derivative. However, also other profiles may work well, even at a thickness of about half the incident wavelength, as long as the initial gradient in n is not too steep (e.g., $\beta \geq 1$ in Figure 10). For structures with $L_c \ll \lambda$ the profile of the effective refractive index could be inferred from the silicon volume fraction by applying an effective medium mixing formula, e.g., as proposed by Bruggeman.^[106] Unfortunately, even the smallest of the investigated structures do not fulfill this criterion. Instead, all structures exhibit some forward scattering in the NIR and most probably even stronger forward scattering in the visible and UV. This means that the structures might appear subwavelength from the air side, but not from the silicon side. Hence, the internal dynamics of the structures is far from plane wave-like and simple effective-medium theory is not applicable. Therefore, the effective refractive index profile will not only depend on the silicon volume fraction but also on the correlation length and other geometrical properties. This behavior has been demonstrated by Boden and Bagnall^[107] who investigated periodic

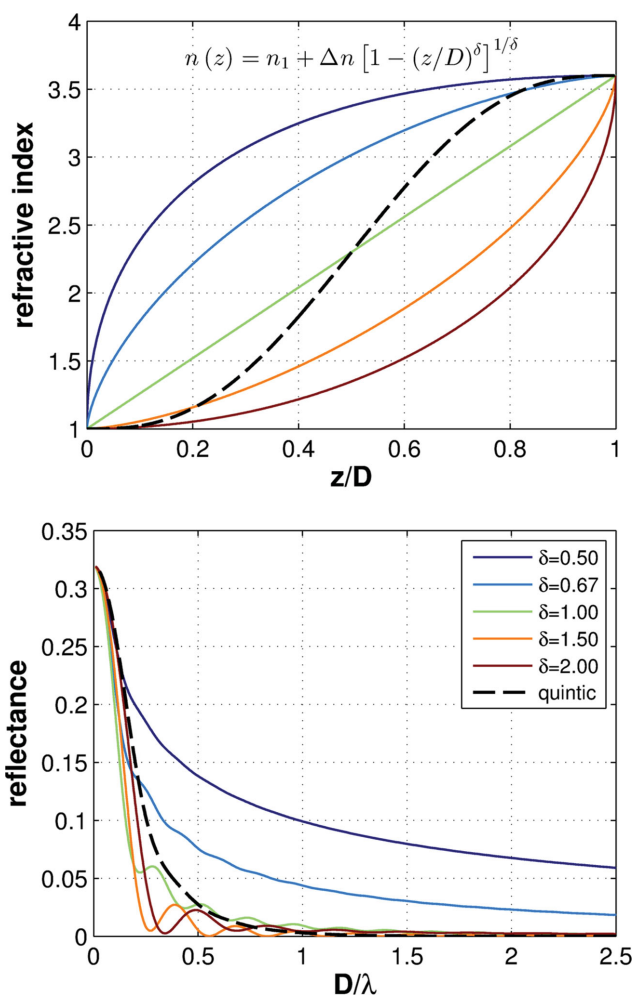


Figure 11. Various refractive index profiles for the transition from air to silicon and resulting reflectance in dependence of the profile depth H with respect to the incident wavelength λ . The propagation depth z is measured from the air side. The quintic profile is given in ref. [90]. The other profiles were obtained from the formula shown in the left graph.

arrays of silicon moth eye structures and found a strong dependence of the optical properties on the period of the arrays in the subwavelength regime. Therefore, it is not possible to deduce a quantitative relationship between the profiles of the silicon fraction depicted in Figure 10 and the refractive index profile. However, we assume that some qualitative similarities exist. Taking this into account we will try to develop a qualitative understanding of the antireflection properties of the various samples. The *MACE nanopore* samples exhibit the shortest correlation lengths and therefore are closest to a real effective medium. From Figure 10 it is apparent that those samples exhibit a mostly convex depth profile of the Si volume fraction with a large initial slope. As this will translate more or less to the effective index profile it might cause the relatively high residual reflectance of 3%–4.5% as demonstrated by the examples given in Figure 11. The absorption spectra of both, the *Ag* and the *Au nanopore* samples, shown in Figure S3 (Supporting Information), are quite flat and depend only weakly on the wavelength. This indicates that the depth H of the samples is

not the limiting parameter. Otherwise, a performance decrease with increasing wavelength would be expected as H/λ approaches some critical value.

An increase of the correlation length significantly above 100 nm deteriorates the AR performance notably even if the structure depth is maintained. This can be observed at both the ICP deep sample and the macP-Si structure. As mentioned before, a larger correlation length is equivalent to a narrower spatial frequency distribution and causes a stronger coupling of the incident light to waves with small transverse wave vectors below the cut-off in air. This in turn can lead to an increased backscattering and higher reflection losses.

To conclude the discussion of the wave-optics b-Si structures the key aspects of the optical properties can be summarized as follows: The light-trapping efficiency of the structures is clearly linked to the correlation length with larger structures performing better. This can be understood in terms of an efficient coupling to scattered waves as soon as a sufficiently large part of the spatial frequency spectrum is below the propagation cut-off in Si. From this argument however, a reversion of the light-trapping efficiency for too large correlations length is expected as soon the spatial frequency distribution gets too narrow to efficiently couple to the large-angle modes in the bulk Si. As this rollover was not observed at the investigated samples, we consider the correlation length of the macP-Si sample close to optimal. In contrast to the light trapping, the AR performance of the samples cannot be linked to a single parameter. Instead there seems to be a complicated interplay of the correlation length, the structure depth and the depth profile of the silicon volume fraction. From the investigated samples, the ones with intermediate correlation length (≈ 100 nm) and a very smooth or a convex material fraction profile perform best while samples with larger correlation length suffer from increased backscattering and the effective-medium-like samples seem to exhibit an refractive index gradient that is too steep. Comparing with the parameters for good light trapping and those for good AR performance, a very fundamental dilemma becomes obvious: The optimum parameters to address these two competing targets are, at least among the investigated samples, essentially disjunctive; meaning that the best light-trapping structure deliver at most a moderate AR performance and vice versa. To achieve the optimum overall performance, the light trapping and AR properties have to be balanced carefully. Especially, any gain by light trapping is of no use if it inflicts additional reflection losses as those affect a very broad spectral range.

2.2. Structures Operating in the Ray Optics Regime

The AR and light-trapping effects of the rather large *L-Si* structures may be understood in terms of geometric ray optics due to repeated reflection and scattering at the inclined surface facets similar to that of the KOH pyramids.^[108] Thereby, the depth of the structure and the inclination of the faces determine the average number of surface interactions an incoming ray might experience before it is finally coupled into the silicon or reflected back out of the structure. The larger this number is the lower is the resulting reflectance of the structure. The optical performance of the *L-Si black* sample is comparable with

the *KOH pyramids* (Figure. 6). However, the *L-Si black* surface has a higher absorption in the NIR ($\lambda > 1040$ nm) and maintains the highest residual absorption for wavelengths well above the optical bandgap of Si^[39,40] ($\lambda \geq 1200$ nm; not shown). This may indicate the presence of optically active defects related to a material modification, e.g., an amorphous Si-phase^[109] with a higher absorption coefficient due to defects. Since, the absorption is caused by defects; these defects also deteriorate the charge carrier lifetime, which is observed for all fs-laser treated Si samples.

3. Discussion of the Electronic Properties of Black Silicon

Depending on the b-Si fabrication method and the process parameters, the resulting carrier lifetimes and thus the effective surface recombination velocity S_{eff} greatly differ. To understand the reasons for the change in effective surface recombination velocity S_{eff} , we first break down S_{eff} into its relevant parameters namely surface area enhancement and surface defect density enhancement. With this model, possible strategies to improve the electronic properties b-Si for the different technologies will be given.

3.1. Model for the Effective Surface Recombination Velocity

To understand the rather complex mechanisms of surface recombination in (nano)structured surfaces, the total number of apparent recombination active defects D_S must be taken into account, which is an essential parameter contributing to S_{eff} . D_S shall include the sum of surface-near and subsurface defects that are not screened by a field effect passivation and offer an energy level anywhere within the bandgap, i.e., D_S is explicitly not only the number of defects in the middle of the gap, as given by D_{it} , and thus, D_S should be greater than D_{it} . $D_{S,\text{nano}}$ includes all such extrinsic and intrinsic defects (i.e., impurities and voids) due to black etching independently of their exact origin. Assuming the unstructured sample exhibits the lowest number of surface defects $D_{S,\text{ref}}$ and possesses no additional “b-Si defects”, the number of defects induced by the b-Si process can be normalized:

$$\delta \equiv D_{S,\text{nano}}/D_{S,\text{ref}} \quad (2)$$

According to Yablonoitch et al.^[100] the surface recombination velocity S_{eff} can be simply modeled as $S_{\text{eff}} = v_{\text{th}} \sigma D_S$, where v_{th} and σ are the thermal velocity of the charges ($\approx 10^7$ cm s⁻¹) and the according capture cross-section ($\approx 10^{-15}$ cm²), respectively. It is further assumed, that all recombination active defects in the sample are located near the surface and thus contained in D_S , which corresponds to the earlier proposed assumption of an infinite bulk lifetime (Equation (1)) that is widely accepted for float-zone Si wafers. This leads to the known worst case approximation for S_{eff} with a relative error of less than 5%, as long as the recombination processes at the surface are not limited by minority charge carrier diffusion through the bulk.^[101] The approximation introduced by Sprouls valid as long as $S_{\text{eff}} < D_a/$

(4 W), with $D_a = 30$ cm² s⁻¹ the minority carrier diffusion constant (here $W = 250$ μm). Accounting for the surface area of the nanostructures as proposed by Hagedorn et al.^[5] and Oh et al.^[6] results in the following expression for the surface recombination velocity:

$$S_{\text{eff}} = \gamma v_{\text{th}} \sigma D_{S,\text{nano}} = \gamma v_{\text{th}} \sigma D_{S,\text{ref}} \delta \quad (3)$$

where $\gamma \equiv A_{\text{nano}}/A_{\text{ref}}$ is the surface enhancement factor,^[6] which becomes unity for the reference sample itself. A_{nano} is the true surface area of the nanostructures while A_{ref} is the planar footprint (i.e., the projected area). To evaluate the obtained surface passivation quality, we may now relate the recombination in the nanostructured surfaces to the reference sample:

$$\left(\frac{S_{\text{nano}}}{S_{\text{ref}}} \right) = \left(\frac{A_{\text{nano}}}{A_{\text{ref}}} \right) \left(\frac{D_{S,\text{nano}}}{D_{S,\text{ref}}} \right) = \gamma \delta \quad (4)$$

It is assumed that v_{th} and σ are identical in all samples. Thus, the effective lifetime τ_{eff} and the respective SRV S_{eff} scale linearly with the enhancement factor of the surface area γ and the ratio of recombination active surface defect states δ introduced by the black etching process. The experimental values of the ratio $S_{\text{nano}}/S_{\text{ref}}$ are listed in Table 3. To separate the individual contributions of an enhanced surface area A_{nano} and additional surface damage, reflected in $D_{S,\text{nano}}$, an estimate of the surface area is required. However, accurately measuring A_{nano} is rather difficult. A few different methods for this task have been proposed in the literature. Mostly only a lower bound for A_{nano} , is obtained that gives a lower limit to the true surface enhancement factor $\gamma_{\text{min}} \leq \gamma$. Correspondingly, the obtained value for the enhancement of the defect density can be considered as an upper limit to the true value $\delta_{\text{max}} \geq \delta$.

3.2. Analysis of the Origin of Recombination-Active Surface Defects in Black Silicon

In Table 3 the analysis of enhancement of the defect density δ_{max} (column 5) as a function of the four different technology is presented and within each technology, the different preparation conditions are also analyzed and compared with the *Unstructured Reference* ($\delta_{\text{max}} = 1$) and the *KOH pyramids* ($\delta_{\text{max}} = 1.8$). For the ICP-RIE etching method, δ_{max} is within the error bars in the order of the same magnitude as the reference ($\delta_{\text{max}} \approx 1$) and almost independent of the etching time and pressure. Thus, the ICP deep and the ICP shallow have about the same δ_{max} but not the same internal surface enhancement γ . This suggests that the ICP-RIE process can be exploited to produce b-Si surfaces that are almost completely free of additional electronic (sub) surface defects. This seems to be at a first sight in contradiction to earlier findings of Schäfer and Lüdemann.^[48] They report that cleaning Si by SF₆ RIE usually results in some subsurface damage. Therefore, we believe that the thermal treatment to activate the Al₂O₃ passivation layers leads to curing of a large fraction of plasma-induced defects. The annealing temperature was about 385 °C that should be rather optimal for a recovery of plasma damage.^[48] Even though the Al₂O₃ activation was carried out in air, curing of defects may be enhanced by

hydrogen diffusion from the Al_2O_3 film into the near-surface bulk as reported by Dingemans et al.^[110] In addition, the coordination of SiO_2 bonds reaches a sufficiently good chemical passivation around 400 °C.^[111] Experiments for the simultaneous optimization of the deposition and annealing temperatures prior to this study showed that keeping both at about 385 °C leads to an improved passivation of ICP-RIE b-Si nanostructures and references. Interestingly, δ_{max} of the superstructure KOH+ ICP shallow is reduced after application of ICP-RIE etching on the KOH texture in comparison with KOH *pyramids*. In the plasma process the surface area is definitely enlarged, while the lifetime is reduced. We therefore speculate that after the KOH etching, on the surface residues remains that act as surface defect centers. These centers are being removed during the plasma etching step since the SF_6 plasma cleans also the surface while nanostructuring it.

At the present state of optimization, MACE samples exhibit a δ_{max} that is about a factor 5–10 higher than that of the *Unstructured Reference* independent of the etching process (MACE nanopores, MACE NWs, MACE NC, as well as catalyst) and independent of laboratory being fabricated. A possible explanation is a defect-rich layer or contamination with deep-level impurities originating from the MACE process that cannot be passivated with Al_2O_3 . Although the nanoporous sponge-like silicon has been completely removed in a mild version of the standard clean 1 (SC1) from the common RCA-cleaning, which is contained in the herein applied RCA cleaning sequence (see Experimental), still an elevated defect density was observed. SC1 dramatically reduces the surface area and defect density and therefore eliminates the photoluminescence of the fibrous layer.^[58] It was also shown that the lifetime could be increased by about one order of magnitude if the SC1 was carried out after MACE and before Al_2O_3 deposition by plasma-assisted ALD.^[58] The process has beneficial effects on the MACE structures independent of the catalyst and the metal deposition technique, whereas the underlying crystalline morphology is not significantly altered by the cleaning procedure. From FTIR measurements it was concluded by Algasinger et al.^[58] that after SC1 the b-Si has a similar surface termination like a planar c-Si wafer. Concerning the dangling bond density at the Si/ SiO_2 interface, a MACE nanocone-like sample exhibited about three times more defects than a planar reference, which correlates approximately with the here measured surface defect enhancement factor δ_{max} of 5–10 determined as upper boundary in this study. Electrically, detected magnetic resonance measurements revealed a hydrogen- or oxygen double-donor-like defect related to MACE.^[58] Note that the optimization of the ALD- Al_2O_3 coating and the successive annealing step at 385 °C was carried out to best suit the ICP-RIE structures^[46] and has not to represent an optimum condition for the other b-Si types such as MACE that may suffer from a completely different nature of defects as described above. As shown recently by Algasinger et al., amorphous silicon might be a much better surface coating than Al_2O_3 leading to minority carrier lifetime of about 1.3 ms being in the same order of magnitude than the ICP-RIE samples in this study.

The macP-Si samples have a significantly higher surface defect density of about $\delta_{\text{max}} = 200$. This high value is not completely unexpected since the doping level of the silicon wafer

is not adequate for macP-Si growth. It has been taken to be comparable with other technologies. macP-Si growth on p-type silicon is stable for doping levels above 10 Ohm cm.^[112] Below this doping level, other growth regimes interfere and will lead to a rather defect-rich, porous subsurface structure of the macropores. It has been shown by Brendel and co-workers^[43,113] that macropores on n-type silicon can have reasonable low SRV in the order of $S_{\text{eff}} \approx 25\text{--}75 \text{ cm s}^{-1}$ for thin 30 μm thick macroporous membranes. This yield similar values of $\delta_{\text{max}} \approx 5\text{--}10$ as for the MACE samples in our study.

For the laser-processed samples, the highest surface defect density of about $\delta_{\text{max}} = 1500$ has been determined. As already discussed in section 5, the strong near infrared absorption points toward a significant defect absorption of the laser-processed silicon. This is also supported by the electronic data in Table 3. By a damage repair etch, an increase in the minority carrier life time of a factor 2–5 has been obtained. However, due to the strong structural changes of the silicon during the laser processing, the defect rich layer is presumably significantly thicker than in all other cases. Therefore, a different post treatment of these structures is necessary such as in situ laser-annealing or hydrogen-treatment. This is supported by recent unpublished solar cell results showing a slightly increased V_{oc} upon hydrogen annealing or if an a-SiN:H passivation layer was deposited by PECVD.

4. Conclusions

We presented an overview of the fabrication methods of b-Si, their resulting morphologies and the current-state-of-the-art of b-Si solar cells. The investigated methods were dry RIE in an inductively coupled SF_6/O_2 plasma (ICP-RIE), MACE, electrochemical etching of macP-Si and femtosecond laser processing in air (L-Si). To perform a systematic and quantitative comparison, different groups working on b-Si solar cells have cooperated for this study. As benchmark parameters, we used the optical absorption being a key parameter for the maximum short-circuit current and the minority carrier lifetime being a key parameter for the maximum open-circuit voltage of a solar cell.

The analysis and corresponding simulations of the optical properties of the different b-Si technologies revealed that the light-trapping performance primarily depends on the lateral correlation length of the b-Si features whereby structures with a large correlation length tend to perform better. This trend was observed to hold at least for feature sizes up to those of macP-Si structures with a correlation length of $L_C = 360 \text{ nm}$. The dependence of the antireflection performance on the geometrical properties of the b-Si surfaces was found to be more complicated. It seems that structures with an intermediate correlation length $L_C = 100 \text{ nm}$ perform best. Structures with larger correlation length suffer from increased backscattering and structures with smaller correlations length tend to exhibit an effective index gradient that is too steep. An important finding is that the optimum overall performance can only be obtained if light trapping is achieved without affecting the antireflection properties. Consequently, the structures that show the highest integrated absorption are not those with the best light trapping but those with the best antireflection properties and some intermediate light trapping with correlations length $L_C = 100 \text{ nm}$. The height of the structures H

is less critical for the optical properties and can be in the range of 500 nm to 5 μm without effecting neither the antireflection nor the scattering properties, significantly. However, the height H and the corresponding surface enhancement factor γ are strongly influencing the surface recombination velocity S and thus the minority carrier lifetime. The analysis and corresponding simulations of the electronic properties of the different b-Si technologies revealed that the critical parameters are the (sub)surface damage D introduced by the nanostructuring technology and the surface enhancement factor γ . It has been shown that for the process scheme used in this study that ICP-RIE leads to a surface damage comparable with that of the reference wafer. Thus, the surface enhancement factor γ , i.e., the height H is the dominant parameter limiting the minority carrier lifetime. Since, the height H is not limiting the optical properties, a combined electro-optic optimum of the height H is about $H = 500$ nm. Please note that each b-Si technology yields a slightly different subsurface damage. Therefore, the damage removal steps and the surface passivation layer have to be optimized for each b-Si technology.

5. Experimental Section

5.1. Substrate Material

For all experiments p-type (100) Si 6" wafers of 250 μm thickness with a doping level of $(1.00 \pm 0.25) \Omega \text{ cm}$ were used. These wafers were used for b-Si etching and served as unstructured process references. As an additional handling reference in each process an extra sample was fabricated by applying all handling steps without conducting the black etching procedure. This way the influence of the black etching process itself could be monitored.

5.2. Black Silicon Fabrication

Bifacial b-Si surface structuring was achieved by the following methods at the indicated institutes:

5.2.1. ICP-RIE Processing

Dry etching was carried out at the Friedrich-Schiller-University in Jena, Germany.^[114] The structures were fabricated in a single etching step by ICP-RIE in a Sentech SI 500 plasma etcher. A gas mixture of SF_6 and O_2 at a flow ratio of 1:1 was used. The shallow and intermediate structures were etched at a process pressure of 4 Pa for etching times t_1 and t_2 ($t_1 < t_2$), respectively, whereas the deep structure was fabricated at 1 Pa during etching time t_1 . The substrates were cooled to -20 °C at process start.

5.2.2. Metal Assisted Chemical Etching (MACE)

Three different MACE methods for fabrication of rather different b-Si surface nanostructures. For Au MACE, Au nanoparticles are formed in situ by reduction of HAuCl_4 by H_2O_2 in the etching solution, while Ag nanoparticles are formed on Si prior to the black etching for Ag MACE.

Nanowires (NWs): The samples with short and long nanostructures were fabricated at the Martin-Luther-University (MLU) in Halle^[57]; Si wafers were first dipped into 5% HF solution for 3 min to remove the native oxide. Subsequently, MACE was carried out by immersing the Si samples into 5 M HF and 10 mM AgNO_3 solution for 1 min to deposit Ag-nanoparticles. Subsequently, an aqueous etchant containing 8.5 vol% HF and 0.9 vol% H_2O_2 was used for black etching. Thereafter, the Si samples were dipped into concentrated HNO_3 for Ag removal. To completely remove the Ag nanoparticles, the cleaning procedure

was repeated two times in total. Finally, the samples were rinsed in deionized (DI) water and dried by N_2 gas blowing. All experimental steps were performed at room temperature inside a fume hood (≈ 20 °C).

Nanopores (NPs): They were produced using Ag and Au nanoparticles as catalysts. The Ag nanoparticles were deposited from aqueous solutions at the national renewable energy laboratory in Boulder, CO, USA^[3]. Ag nanoparticles were first deposited electroless on a Si wafer using 1 mM AgNO_3 and 0.5 vol% HF for 90 s at room temperature. Subsequently, MACE was performed by immersing the Ag nanoparticle-decorated Si wafer in a mixed solution of 12.5 vol% HF and 3 vol% H_2O_2 for 20 s at RT in a sonication bath. Thereafter, the Ag nanoparticles at the bottom of the NPs were removed by treating the wafer in concentrated HNO_3 for 3 min. Between each step, the wafer is carefully rinsed with DI water for at least 3 min. For Au-catalyzed MACE NPs we first immersed a Si wafer in a 0.4 mM HAuCl_4 solution for Au-nanoparticle formation and then add an equal volume of a mixed solution of HF: H_2O_2 : H_2O (1:5:2) in a sonication bath. Herein, Au-MACE was performed for 3 min. After the etch, the Si wafer was rinsed with a DI water and the remaining Au nanoparticles at the bottom of pores were removed by an I_2/KI solution.^[35]

Nanococones (NCs): They were obtained by depositing ultrathin Au films onto Si wafers before black etching at the Walter-Schottky-Institute in Munich, Germany.^[58] All samples were precleaned with acetone and isopropyl alcohol, followed by a HF-dip to remove the native oxide. An ultrathin layer of gold with a nominal film thickness of 1 nm was deposited onto the Si surface by thermal evaporation at a base pressure of $\approx 10^{-6}$ mbar. This leads to a discontinuous film, leaving behind spatially separated Au-clusters of several nanometers in diameter. The Au-catalyzed wet-etching took place in an aqueous solution of HF(50%): H_2O_2 (30%): H_2O with a volume ratio of 1:5:10 at room temperature for 70 s. Due to a much higher etch rate in the vicinity of the Au-catalyst, the particles get under-etched and sink into the Si bulk. This leads to the desired nanocone-like hillocks. As the Au-particles sink deeper into the Si, an evolution of nanoporous Si takes place at the top of the cones. Therefore, an additional postetch treatment is necessary to remove the unwanted porous structures. As previously shown in ref. [58], the SC1 from the common RCA-cleaning sequence is sufficient to remove the nanoporous Si fraction, resulting in a nanostructured Si surface with minimal surface area needed for the beneficial optical properties and a surface defect density comparable with c-Si. In case of the b-Si samples used in this work, the SC1 postetch treatment of the RCA-clean prior to ALD passivation was exploited for the removal of the porous Si. Previously, the gold residues in the as-prepared sample was removed by etching in an aqueous solution of iodine and potassium iodine mixture with a ratio of 1:4:40 (by weight) at room temperature.

5.2.3. Macroporous Silicon

MacP-Si samples were fabricated at the MLU in Halle. An electrochemical etching process without light was applied to produce a single-sided black macroporous Si surface. The doping level of the starting wafer of about p-type $1 \Omega \text{ cm}$ is at the boundary of possible macropore growth still exists in silicon.^[112] Accordingly, a current density of 10 mA cm^{-2} and an HF concentration of 5% were chosen for about 5 min. The sponge-like microporous layer was removed by a KOH dip.

5.2.4. fs-Laser Structuring

The laser structured samples were processed at the Heinrich-Hertz-Institute in Goslar, Germany.^[40] To structure the bifacial samples via fs-laser both sides need to be processed separately. A Mantis seed laser from Coherent with a wavelength of 800 nm is regenerative amplified by a 10 kHz Spitfire system from Spectra Physics. The laser beam is attenuated and focused with a 500 mm lens to fluencies

of 1.6 and 4.0 J cm⁻² on the samples. The process takes place in a fine vacuum ambient at pressures of $p_{L-Si} \leq 0.2$ mbar. Three different structures are realized by varying the scan velocity of the samples underneath the laser spot and therefore the number of pulses hitting each sample spot is varied. With a single pulse per spot the “pink” surface was obtained with a nearly smooth surface structure (1.6 J cm⁻²).^[39] In case of the “grey” sample, five pulses per spot lead to a smooth contoured surface (4.0 J cm⁻²), while sharp conical spikes emerge, when 500 pulses per spot are applied (4.0 J cm⁻²) for the “black” sample.^[40] This surface is the typical structure known as b-Si.

5.2.5. KOH Textures

To compare with the optoelectronic performance of the diverse b-Si surfaces to state of the art industrial processes, random pyramid textures were produced on the same wafers by alkaline etching in KOH:IPA (isopropyl alcohol) solution. For simplicity of the experiment, the bifacial KOH textured wafers were passivated by the same scheme as the black etched samples described below. Therefore, the optical performance was not optimized in this work. The greater interest was in the electronic surface properties like damage introduced during the etching processes. In this work, for better lifetime comparability the KOH random pyramid texture was only passivated with 35 nm Al₂O₃ like the nanostructured samples. This thin layer with a refractive index of ≈ 1.6 only has a slight antireflective effect in the blue spectral range. Thus, we compare our structures to an alkaline texture with a nonoptimized ARC, which can only profit from the geometric light-trapping effect.

5.2.6. Superstructures

An ultimate structure type was obtained by underlying macroscopic KOH textures as a substrate for the ICP-RIE shallow process. We fabricated superstructures by applying the shallow b-Si process to the KOH random pyramids. This way, combined antireflection layer and light-trapping scheme is incorporated in a two step-structuring process.

5.3. Passivation Scheme

The passivation of all wafers has been carried out at the MLU Halle similar to that in ref. [46]. The reference as well as all the etched wafers received an RCA cleaning treatment.^[115] The SC1 and SC2 steps of the RCA cleaning consisted of 5:1:1 solutions of H₂O:H₂O₂:NH₄OH and H₂O:H₂O₂:HCl, respectively. Before applying each RCA cleaning treatment the samples were dipped in 1% HF solution to take off the silicon oxide. All steps were finished by rinsing the samples in DI water. Thus, finishing with the wet-chemical L-SiO₂ (grown in SC2), the samples went directly into the ALD reactor and were coated with 300 ALD cycles of Al₂O₃. The films were synthesized at a temperature of 180 °C from trimethylaluminum (TMA) and H₂O. Precursor pulse lengths were kept equal (250 ms), followed by asymmetric purge times of 1 and 2 s after TMA and H₂O pulses, respectively. The reaction chamber was purged with nitrogen, maintaining the constant gas flow during the whole process. To activate the passivation layers, the wafers were annealed in air ambient for 30 min at 385 °C.

5.4. Characterization

The minority carrier lifetime of the annealed samples was measured with a Sinton WCS 120 lifetime tester in transient or generalized mode depending on the level of measured lifetime. After QSSPC measurements, selected wafers were broken into smaller pieces and optical reflectance and transmittance curves were measured in a λ

950 Spectrometer on unstructured and nanostructured wafer pieces with an integrating sphere of 150 mm diameter covering the full half space of 2π . The measurement spot was 2×4 mm² wide. The reflection was normalized to a Labsphere Spectralon reflectance standard. The spectra were recorded with a resolution of $\Delta\lambda_{VIS} = 2.5$ nm in the VIS and $\Delta\lambda_{NIR} = 10$ nm in the NIR (>860 nm), respectively. The reflection was measured under an angle of incidence of 8°; transmission at an angle of incidence of 0°. The total deposited Al₂O₃ layer thickness, and therefore, the growth per cycle was measured by ellipsometry on the unstructured silicon wafer reference at 211 points on the wafer. Some pieces of the passivated surface structures were characterized by means of SEM, focused ion beam (FIB) to examine the surface morphology arising from the etching treatment. This way, also ALD film growth conformity and homogeneity could be investigated. The Al₂O₃ film thickness on the nanostructured samples was estimated from SEM images of cleaved or FIB-cut edges.

5.5. Simulations

The simulations of a hypothetical perfect ARC without and with Lambertian LT was calculated for a 250 μ m thick silicon wafer. The method was described in detail elsewhere.^[15,116]

Acknowledgements

R.B.W. would like to thank Margrit Hanbücken for the hospitality at CINAM, Marseille for writing this review. M.O. would like to thank Rolf Herold (Fraunhofer IWM, Halle) for the preparation of the FIB cross-sectional images. We gratefully acknowledge funding from the German Federal Ministry of Science and Education (BMBF) within the project STRUKTURSOLAR. This work was also partially supported by a DOE American Recovery and Reinvestment Act (ARRA).

This article is part of the International Year of Light 2015 virtual issue for Advanced Optical Materials.

Received: September 7, 2014

Revised: October 1, 2014

Published online: December 17, 2014

- [1] S. Koynov, M. S. Brandt, M. Stutzmann, *Appl. Phys. Lett.* **2006**, *88*, 203107.
- [2] M. Halbwax, T. Sarnet, P. Delaporte, M. Sentis, H. Etienne, F. Torregrosa, V. Vervisch, I. Perichaud, S. Martinuzzi, *Thin Solid Films* **2008**, *516*, 6791.
- [3] J. Oh, H.-C. Yuan, H. M. Branz, *Nat. Nanotechnol.* **2012**, *7*, 743.
- [4] P. Repo, J. Benick, V. Vähänissi, J. Schön, G. von Gastrow, B. Steinhauser, M. C. Schubert, M. Hermle, H. Savin, *Energy Procedia* **2013**, *38*, 866.
- [5] K. Hagedorn, C. Forgacs, S. Collins, S. Maldonado, *J. Phys. Chem. C* **2010**, *114*, 12010.
- [6] I. Oh, J. Kye, S. Hwang, *Nano Lett.* **2012**, *12*, 298.
- [7] X. Ao, X. Tong, D. Sik Kim, L. Zhang, M. Knez, F. Müller, S. He, V. Schmidt, *Appl. Phys. Lett.* **2012**, *101*, 111901.
- [8] X. Li, Y. Xiao, K. Zhou, C. Yan, P. Wang, S. L. Schweizer, A. N. Sprafke, J.-H. Lee, R. B. Wehrspohn, *Adv. Mater* **2013**, *25*, 3187.
- [9] M. Steglich, M. Zilk, F. Schrepel, A. Tünnermann, E.-B. Kley, *Appl. Phys. Lett.* **2013**, *102*, 111110.
- [10] P. Hoyer, M. Theuer, R. Beigang, E.-B. Kley, *Appl. Phys. Lett.* **2008**, *93*, 091106.
- [11] C. Wu, C. H. Crouch, L. Zhao, J. E. Carey, R. Younkin, J. A. Levinson, E. Mazur, R. M. Farrell, P. Gothoskar, A. Karger, *Appl. Phys. Lett.* **2001**, *78*, 1850.

- [12] B. Gesemann, R. Wehrspohn, A. Hackner, G. Müller, *IEEE Trans. Nanotechnol.* **2011**, *10*, 50.
- [13] H. V. Jansen, M. J. de Boer, S. Unnikrishnan, M. C. Louwerse, M. C. Elwenspoek, *J. Micromech. Microeng.* **2009**, *19*, 33001.
- [14] Y.-F. Huang, S. Chattopadhyay, Y.-J. Jen, C.-Y. Peng, T.-A. Liu, Y.-K. Hsu, C.-L. Pan, H.-C. Lo, C.-H. Hsu, Y.-H. Chang, C.-S. Lee, K.-H. Chen, L.-C. Chen, *Nat. Nanotechnol.* **2007**, *2*, 770.
- [15] M. Kroll, M. Otto, T. Käsebier, K. Fuchsels, R. B. Wehrspohn, E.-B. Kley, A. Tünnermann, T. Pertsch, in *Proc. SPIE* (Eds: R. Wehrspohn, A. Gombert), SPIE, Bellingham, Washington **2012**, 843817.
- [16] W. Shockley, H. J. Queisser, *J. Appl. Phys.* **1961**, *32*, 510.
- [17] T. Tiedje, E. Yablonovitch, G. D. Cody, *IEEE Trans. Electron Devices* **1984**, *31*, 711.
- [18] M. A. Green, *IEEE Trans. Electron Devices* **1984**, *31*, 671.
- [19] E. Yablonovitch, T. Gmitter, *Appl. Phys. Lett.* **1986**, *49*, 587.
- [20] F. J. Henley, in *35th IEEE Photovoltaic Spec. Conf.*, IEEE, Honolulu-Hawaii **2010**, 001184.
- [21] R. Brendel, M. Ernst, *Phys. Status Solidi RRL* **2010**, *4*, 40.
- [22] J. H. Petermann, D. Zielke, J. Schmidt, F. Haase, E. G. Rojas, R. Brendel, *Prog. Photovoltaics* **2012**, *20*, 1.
- [23] M. A. Green, *Prog. Photovoltaics* **1999**, *7*, 327.
- [24] J. I. Gittleman, E. K. Sichel, H. W. Lehmann, R. Widmer, *Appl. Phys. Lett.* **1979**, *35*, 742.
- [25] H. Jansen, M. de Boer, R. Legtenberg, M. Elwenspoek, *J. Micromech. Microeng.* **1995**, *5*, 115.
- [26] Y. Inomata, K. Fukui, K. Shirasawa, *Sol. Energy Mater. Sol. Cells* **1997**, *48*, 237.
- [27] M. Schnell, R. Lüdemann, S. Schäfer, in *28th IEEE Photovoltaic Spec. Conf.*, IEEE, Anchorage, Alaska **2000**, 367.
- [28] J. Yoo, I. O. Parm, U. Gangopadhyay, K. Kim, S. K. Dhungel, D. Mangalaraj, J. Yi, *Sol. Energy Mater. Sol. Cells* **2006**, *90*, 3085.
- [29] Y. Xia, B. Liu, J. Liu, Z. Shen, C. Li, *Sol. Energy* **2011**, *85*, 1574.
- [30] S. H. Zaidi, D. S. Ruby, J. M. Gee, *IEEE Trans. Electron Devices* **2001**, *48*, 1200.
- [31] J. Yoo, G. Yu, J. Yi, *Mater. Sci. Eng. B* **2009**, *159*, 333.
- [32] X. Li, P. W. Bohn, *Appl. Phys. Lett.* **2000**, *77*, 2572.
- [33] L. Tsakalacos, J. Balch, J. Fronheiser, B. A. Korevaar, O. Sulima, J. Rand, *Appl. Phys. Lett.* **2007**, *91*, 233117.
- [34] K. Nishioka, T. Suetu, N. Saito, *Appl. Surf. Sci.* **2009**, *255*, 9504.
- [35] H. M. Branz, V. E. Yost, S. Ward, K. M. Jones, B. To, P. Stradins, *Appl. Phys. Lett.* **2009**, *94*, 231121.
- [36] H.-C. Yuan, V. E. Yost, M. R. Page, P. Stradins, D. L. Meier, H. M. Branz, *Appl. Phys. Lett.* **2009**, *95*, 123501.
- [37] R. Younkin, J. E. Carey, E. Mazur, J. A. Levinson, C. M. Friend, *J. Appl. Phys.* **2003**, *93*, 2626.
- [38] T. Sarnet, M. Halbwx, R. Torres, P. Delaporte, M. Sentis, S. Martinuzzi, V. Vervisch, F. Torregrosa, H. Etienne, L. Roux, S. Bastide, in *Proceedings of SPIE 6881—Commer. Biomed. Appl. Ultrafast Lasers VIII* (Eds: T. Sarnet, M. Halbwx, R. Torres, P. Delaporte, M. Sentis, S. Martinuzzi, V. Vervisch, F. Torregrosa, H. Etienne, L. Roux, S. Bastide), SPIE, Bellingham, Washington **2008**, 688119.
- [39] T. Gimpel, I. Höger, F. Falk, W. Schade, S. Kontermann, *Appl. Phys. Lett.* **2012**, *101*, 111911.
- [40] S. Kontermann, A. L. Baumann, T. Gimpel, K. M. Guenther, A. Ruibys, U. Willer, W. Schade, *MRS Proc.* **2012**, *1405*, mrsf11.
- [41] V. Lehmann, *J. Electrochem. Soc.* **1999**, *146*, 2968.
- [42] C. C. Striemer, P. M. Fauchet, *Appl. Phys. Lett.* **2002**, *81*, 2980.
- [43] M. Ernst, R. Brendel, R. Ferré, N.-P. Harder, *Phys. Status Solidi* **2012**, *6*, 187.
- [44] Y. Inomata, K. Fukui, K. Shirasawa, in *26th IEEE Photovoltaic Spec. Conf.*, IEEE, Anaheim, CA **1997**, 47.
- [45] R. Khandelwal, U. Plachetka, B. Min, C. Moormann, H. Kurz, *Microelectron. Eng.* **2013**, *111*, 220.
- [46] M. Otto, M. Kroll, T. Käsebier, R. Salzer, A. Tünnermann, R. B. Wehrspohn, *Appl. Phys. Lett.* **2012**, *100*, 191603.
- [47] Z. Shen, B. Liu, Y. Xia, J. Liu, J. Liu, S. Zhong, C. Li, *Scr. Mater.* **2013**, *68*, 199.
- [48] S. Schäfer, R. Lüdemann, *J. Vac. Sci. Technol. A* **1999**, *17*, 749.
- [49] B. Hoex, M. C. M. van de Sanden, J. Schmidt, R. Brendel, W. M. M. Kessels, *Phys. Status Solidi RRL* **2012**, *6*, 4.
- [50] P. Repo, A. Haarahiltunen, L. Sainiemi, M. Yli-Koski, H. Talvitie, M. C. Schubert, H. Savin, *IEEE J. Photovoltaics* **2013**, *3*, 90.
- [51] K. Fuchsels, M. Kroll, T. Käsebier, M. Otto, T. Pertsch, E.-B. Kley, R. B. Wehrspohn, N. Kaiser, A. Tünnermann, in *SPIE Photonics Sol. Energy Syst. IV* (Ed: R. B. Wehrspohn), SPIE, Bellingham, Washington **2012**, 843817.
- [52] T. Song, S.-T. Lee, B. Sun, *Nano Energy* **2012**, *1*, 654.
- [53] M. Ernst, H. Schulte-Huxel, R. Niepelt, S. Kajari-Schröder, R. Brendel, *Energy Procedia* **2013**, *38*, 910.
- [54] J. Ziegler, J. Haschke, T. Käsebier, A. N. Sprafke, R. B. Wehrspohn, *Opt. Expr.* **2014**, *22*, A1469.
- [55] S. Jeong, M. D. McGehee, Y. Cui, *Nat. Commun.* **2013**, *4*, 2950.
- [56] P. Yu, C.-Y. Tsai, J.-K. Chang, C.-C. Lai, P.-H. Chen, Y.-C. Lai, P.-T. Tsai, M.-C. Li, H.-T. Pan, Y.-Y. Huang, C.-I. Wu, Y.-L. Chueh, S.-W. Chen, C.-H. Du, S.-F. Horng, H.-F. Men, *ACS Nano* **2013**, *7*, 10780.
- [57] X. Li, Y. Xiao, C. Yan, K. Zhou, S. L. Schweizer, A. Sprafke, J.-H. Lee, R. B. Wehrspohn, *ECS Solid State Lett.* **2012**, *2*, P22.
- [58] M. Algasinger, J. Paye, F. Werner, J. Schmidt, M. S. Brandt, M. Stutzmann, S. Koynov, *Adv. Energy Mater.* **2013**, *3*, 1068.
- [59] G. C. Schwartz, P. M. Schaible, *J. Vac. Sci. Technol.* **1979**, *16*, 410.
- [60] A. J. Perry, R. W. Boswell, *Appl. Phys. Lett.* **1989**, *55*, 148.
- [61] C. P. D'Emic, K. K. Chan, J. Blum, *J. Vac. Sci. Technol. B* **1992**, *10*, 1105.
- [62] V. A. Yunkin, D. Fischer, E. Voges, *Microelectron. Eng.* **1994**, *23*, 373.
- [63] J. I. Gittleman, E. K. Sichel, H. W. Lehmann, R. Widmer, *Appl. Phys. Lett.* **1979**, *35*, 742.
- [64] X. Mellhaoui, R. Dussart, T. Tillocher, P. Lefauchaux, P. Ranson, M. Boufnichel, L. J. Overzet, *J. Appl. Phys.* **2005**, *98*, 104901.
- [65] I. Levchenko, U. Cvelbar, K. Ostrikov, *Appl. Phys. Lett.* **2009**, *95*, 021502.
- [66] R. Dussart, T. Tillocher, P. Lefauchaux, M. Boufnichel, *J. Phys. D. Appl. Phys.* **2014**, *47*, 123001.
- [67] Y. Chen, Z. Xu, M. R. Gartia, D. Whitlock, Y. Lian, G. L. Liu, *ACS Nano* **2011**, *5*, 8002.
- [68] X. Liu, P. R. Coxon, M. Peters, B. Hoex, J. M. Cole, D. J. Fraycet, *Energy Environ. Sci.* **2014**, *7*, 3223.
- [69] R. J. Archer, *J. Phys. Chem. Solids* **1960**, *14*, 104.
- [70] D. Dimova-Malinovska, M. Sendova-Vassileva, N. Tzenov, M. Kamenova, *Thin Solid Films* **1997**, *297*, 9.
- [71] Z. Huang, N. Geyer, P. Werner, J. de Boer, U. Gösele, *Adv. Mater.* **2011**, *23*, 285.
- [72] S. Koynov, M. S. Brandt, M. Stutzmann, *Phys. Status Solidi RRL* **2007**, *1*, R53.
- [73] S. Koynov, M. S. Brandt, M. Stutzmann, *J. Appl. Phys.* **2011**, *110*, 43537.
- [74] V. Lehmann, *J. Electrochem. Soc.* **1993**, *140*, 2836.
- [75] J. Schilling, F. Müller, S. Matthias, R. B. Wehrspohn, U. Gösele, K. Busch, *Appl. Phys. Lett.* **2001**, *78*, 1180.
- [76] M. Birnbaum, *J. Appl. Phys.* **1965**, *36*, 3688.
- [77] H. van Driel, J. Sipe, J. Young, *Phys. Rev. Lett.* **1982**, *49*, 1955.
- [78] H. Varel, M. Wähmer, A. Rosenfeld, D. Ashkenasi, E. E. B. Campbell, *Appl. Surf. Sci.* **1998**, *127–129*, 128.

- [79] A. Borowiec, H. K. Haugen, *Appl. Phys. Lett.* **2003**, *82*, 4462.
- [80] T.-H. Her, R. J. Finlay, C. Wu, S. Deliwala, E. Mazur, *Appl. Phys. Lett.* **1998**, *73*, 1673.
- [81] J. E. Carey, C. H. Crouch, E. Mazur, *Opt. Phot. News* **2003**, *14*, 32.
- [82] C. H. Crouch, J. E. Carey, M. Shen, E. Mazur, F. Y. Génin, *Appl. Phys. A* **2004**, *79*, 1635.
- [83] G. B. Turner, *Appl. Phys. Lett.* **1981**, *39*, 967.
- [84] M. J. Smith, Y.-T. Lin, M.-J. Sher, M. T. Winkler, E. Mazur, S. Gradečak, *J. Appl. Phys.* **2011**, *110*, 53524.
- [85] G. Agostinelli, A. Delabie, P. Vitanov, Z. Alexieva, H. F. W. Dekkers, S. De Wolf, G. Beaucarne, *Sol. Energy Mater. Sol. Cells* **2006**, *90*, 3438.
- [86] B. Hoex, S. B. S. Heil, E. Langereis, M. C. M. van de Sanden, W. M. M. Kessels, *Appl. Phys. Lett.* **2006**, *89*, 042112.
- [87] B. Hoex, J. Schmidt, R. Bock, P. P. Altermatt, M. C. M. van de Sanden, W. M. M. Kessels, *Appl. Phys. Lett.* **2007**, *91*, 112107.
- [88] J. Schmidt, B. Veith, R. Brendel, *Phys. Stat. Sol.- Rap. Res. Lett.* **2009**, *3*, 287.
- [89] G. Dingemans, R. Seguin, P. Engelhart, M. C. M. van de Sanden, W. M. M. Kessels, *Phys. Stat. Sol.- Rap. Res. Lett.* **2010**, *4*, 10.
- [90] A. Richter, J. Benick, M. Hermle, S. W. Glunz, *Phys. Stat. Sol.- Rap. Res. Lett.* **2011**, *5*, 202.
- [91] B. Veith, F. Werner, D. Zielke, R. Brendel, J. Schmidt, *Energy Proc.* **2011**, *8*, 307.
- [92] B. Hoex, J. J. H. Gielis, M. C. M. van de Sanden, W. M. M. Kessels, *J. Appl. Phys.* **2008**, *104*, 113703.
- [93] G. Dingemans, A. Clark, J. A. van Delft, M. C. M. van de Sanden, W. M. M. Kessels, *J. Appl. Phys.* **2011**, *109*, 113107.
- [94] E. Yablonovitch, *J. Opt. Soc. Am.* **1982**, *72*, 899.
- [95] H. W. Deckman, C. B. Roxlo, E. Yablonovitch, *Opt. Lett.* **1983**, *8*, 491.
- [96] M. A. Green, *Sol. Energy Mater. Sol. Cells* **2008**, *92*, 1305.
- [97] R. A. Sinton, A. Cuevas, *Appl. Phys. Lett.* **1996**, *69*, 2510.
- [98] A. Richter, S. W. Glunz, F. Werner, J. Schmidt, A. Cuevas, *Phys. Rev. B* **2012**, *86*, 165202.
- [99] J. Zhao, A. Wang, P. P. Altermatt, S. Wenham, M. A. Green, *Sol. Energy Mater. Sol. Cells* **1996**, *41*, 87.
- [100] E. Yablonovitch, D. Allara, C. Chang, T. Gmitter, T. Bright, *Phys. Rev. Lett.* **1986**, *57*, 249.
- [101] A. B. Sproul, *J. Appl. Phys.* **1994**, *76*, 2851.
- [102] E. Noponen, J. Turunen, *JOSA A* **1994**, *11*, 2494.
- [103] M. G. Moharam, E. B. Grann, D. A. Pommet, T. K. Gaylord, *JOSA A* **1995**, *12*, 1068.
- [104] S. J. Wilson, M. C. Hutley, *Opt. Acta* **1982**, *29*, 993.
- [105] W. H. Southwell, *Opt. Lett.* **1983**, *8*, 584.
- [106] D. A. G. Bruggeman, *Ann. Phys.* **1935**, *416*, 636.
- [107] S. A. Boden, D. M. Bagnall, *Appl. Phys. Lett.* **2008**, *93*, 133108.
- [108] S. C. Baker-Finch, K. R. McIntosh, *Prog. Photovoltaics* **2011**, *19*, 406.
- [109] M. J. Smith, M.-J. Sher, B. Franta, Y.-T. Lin, E. Mazur, S. Gradečak, *J. Appl. Phys.* **2012**, *112*, 083518.
- [110] G. Dingemans, W. Beyer, M. C. M. van de Sanden, W. M. M. Kessels, *Appl. Phys. Lett.* **2010**, *97*, 152106.
- [111] V. Naumann, M. Otto, R. B. Wehrspohn, C. Hagedorf, *J. Vac. Sci. Technol. A* **2012**, *30*, 04D106.
- [112] J.-N. Chazalviel, F. Ozanam, N. Gabouze, S. Fellah, R. B. Wehrspohn, *J. Electrochem. Soc.* **2002**, *149*, C511.
- [113] M. Ernst, R. Brendel, *IEEE J. Photovoltaics* **2013**, *3*, 723.
- [114] M. Kroll, T. Käsebier, M. Otto, R. Salzer, R. B. Wehrspohn, E.-B. Kley, A. Tünnermann, T. Pertsch, in *Proceeding of SPIE* (Eds: R. B. Wehrspohn, A. Gombert), SPIE, Bellingham, Washington **2010**, 772505.
- [115] W. Kern, D. Puotinen, *RCA Rev.* **1970**, *31*, 187.
- [116] M. Otto, M. Kroll, T. Käsebier, M. Ernst, R. Salzer, R. B. Wehrspohn, in *Renew. Energy Environ. Conf. Proc.*, OSAAustin, TX **2011**, JW7.
- [117] H. Sai, Y. Kanamori, K. Arafune, Y. Ohshita, M. Yamaguchi, *Prog. Photovoltaic. Res. Appl.* **2007**, *15*, 415.
- [118] S. Koynov, M. S. Brandt, M. Stutzmann, *Phys. Status Solidi RRL* **2007**, *1*, R53.
- [119] X. Ye, S. Zou, K. Chen, J. Li, J. Huang, F. Cao, X. Wang, L. Zhang, X.-F. Wang, M. Shen, X. Su, *Adv. Funct. Mater.* **2014**, DOI: 10.1002/adfm.201401589.

Large-Area Nanosphere Gratings for Light Trapping and Reduced Surface Losses in Thin Solar Cells

Yuan-Chih Chang , Michael E. Pollard, David N. R. Payne, Alexander Sprafke, Supriya Pillai, and Darren M. Bagnall

Abstract—Light trapping in thin silicon solar cells demands radically different fabrication approaches to standard commercial cells. Weaker optical absorption and increased sensitivity to surface recombination requires light trapping to be achieved over a broader spectral range and, ideally, without texturing the absorber itself. Nano-scale light trapping structures allow the strongest scattering to be tuned to wavelengths, where oblique scattering into the absorber is needed most. Furthermore, applying these structures “externally,” i.e., on a well-passivated planar silicon surface, reduces the surface area and permits optimal electronic conditions to be maintained. Despite these advantages, the challenges of balancing efficiency gain, cost, and lithographic fidelity have prevented the commercial use of nano-scale light trapping schemes. Here, we demonstrate the use of nanosphere lithography for producing high-quality and cost-effective nano-scale light trapping structures suitable for incorporation in thin solar cells. We have successfully fabricated large-area and uniform metal nanospheregrating structures, with embedded dielectric nanospheres, on 30 μm thick c-Si pseudo cells and measured their effectiveness for light trapping. Comparison between simulations and the fabricated pseudo cells’ characteristics highlighted key challenges in fabricating uniform structures, including the impact of air gaps within non-conformal coatings and minor changes in the geometry. Optical characterization via absorption spectroscopy and both spectral and spatially resolved photoluminescence showed a clear enhancement in the short-circuit current density of up to 4.33 mA/cm^2 in comparison with a planar 30 μm thick device and a 3.7 times absorptance enhancement close to the bandgap of Si.

Index Terms—Light trapping, nanostructures, solar cells.

Manuscript received January 23, 2019; revised April 7, 2019; accepted May 9, 2019. This work was supported by the Australian Government through funding provided by the Australian Renewable Energy Agency. The Australian Government, through ARENA, is supporting Australian research and development in solar photovoltaics and solar thermal technologies to make solar energy become cost competitive with other energy sources. (Corresponding author: Yuan-Chih Chang.)

Y.-C. Chang and M. E. Pollard are with the School of Photovoltaic and Renewable Energy Engineering, University of New South Wales, Sydney, NSW 2052, Australia (e-mail: y.chang@unsw.edu.au; m.e.pollard@unsw.edu.au).

D. N. R. Payne and D. M. Bagnall are with the School of Engineering, Macquarie University, Sydney, NSW 2109, Australia (e-mail: david.payne@mq.edu.au; darren.bagnall@mq.edu.au).

A. Sprafke is with the Institute of Physics, Martin Luther University, Halle 06120, Germany (e-mail: alexander.sprafke@physik.uni-halle.de).

S. Pillai is with the School of Photovoltaic and Renewable Energy Engineering, University of New South Wales, Sydney, NSW 2052, Australia, and also with the School of Engineering, Macquarie University, Sydney, NSW 2109, Australia (e-mail: s.pillai@unsw.edu.au).

This paper has supplementary downloadable material available at <http://ieeexplore.ieee.org>.

Color versions of one or more of the figures in this paper are available online at <http://ieeexplore.ieee.org>.

Digital Object Identifier 10.1109/JPHOTOV.2019.2918183

I. INTRODUCTION

SOLAR photovoltaics (PV) is one of the most promising clean and sustainable energy sources. The PV market has maintained steady growth over the last few decades and continues to be dominated by silicon, with record cell efficiencies over 26% recently reported [1]. While these record devices are approaching theoretical limits, mass market efficiencies remain considerably lower. One way to simultaneously increase efficiency and lower material costs is to reduce the thickness of the active layer, therefore leading to thinner, lighter, and potentially cheaper solar cells. Thin solar cells can achieve higher open-circuit voltages provided there is excellent light trapping and surface passivation. Moreover, thinner devices enable lighter and more flexible modules that may be deployed in projects demanding improved aesthetics, low system weight, or building-integrated photovoltaics [2]. Conventional surface texturing can provide significant diffuse scattering for short wavelengths, but the largest requirement is for in-plane scattering at longer wavelengths. Furthermore, diamond-wire sawing, the dominant wafer cutting method in the PV industry, does not create uniformly rough surface damage, which is particularly problematic for acid texturing of mc-Si [3]. Most importantly, rough surfaces of any type lead to a geometric increase in surface recombination. Nano-scale light trapping (LT) structures, such as nano-gratings and plasmonic particle arrays, offer an alternative approach where the wavelength of peak scattering may be tuned to the near-band edge region of the Si absorber without intrinsically affecting the surface passivation. Furthermore, these nanostructures can be applied to many different types of surface (e.g., mc-Si). Over the last decade, numerous light trapping designs based on plasmonic and/or diffractive structures have been reported. However, such LT schemes have not been implemented commercially. The primary barrier to commercialization is the conflict between cost, fabrication control, and expected gain. E-beam lithography (EBL) is favored in fundamental studies as it offers good dimensional feature control and a close match between design and fabrication. However, the high cost and low throughput makes EBL impractical for large area applications [4]–[6]. The use of random plasmonic or dielectric nanoparticle arrays relaxes the fabrication challenges, but simultaneously limits the control over critical performance parameters. Therefore, to make nano-scale LT a competitive technology, a low-cost and scalable fabrication process is necessary.

In general, fabrication methods adopting nanosphere lithography (NSL) or nanoimprint lithography (NIL) have long been

recognized as economically promising [4]–[6]. NIL is based on embossing a target substrate using a master stamp pattern fabricated by other means (e.g., EBL). During imprinting, a thin stamp, usually made from polydimethylsiloxane, is used to press into the curable polymer material on the target substrate to form a negative pattern. After the detachment of the stamp, the patterned polymer layer acts as a mask in the subsequent etching/deposition process. A single stamp can typically be used many times thereby reducing running costs. However, the initial investment in a stamp is expensive and some of the limitations of the techniques used to fabricate the stamp are passed on to NIL (e.g., closely packed nanostructure arrays are challenging to fabricate with EBL). Furthermore, the rapid formation and detachment over a large area without damaging the stamp is challenging. On the other hand, NSL makes use of a mono- or multilayer of nanoparticles, typically consisting of silica or polystyrene spheres arranged in a hexagonal-close-packed lattice, which may then be used as a mask for subsequent processing. The final geometry of the nanostructure is controlled by the initial nanosphere deposition and the following etching/deposition processes. The uniformity of the nanostructure is usually dominated by the initial deposition of the nanospheres [4]–[6]. However, the deposition of large area highly uniform nanosphere arrays is challenging and localized grain boundaries are unavoidable. In this paper, we present NSL fabrication of metallic grating structures with embedded dielectric nanospheres, which can provide light trapping without the need for surface texturing. This process eliminates high cost EBL processing and its associated capital investment, allowing for a broad range of different nanostructures to be fabricated economically and leaving more flexibility for subsequent design/fabrication optimization.

Nano-scale LT schemes have mostly been demonstrated on thick ($>150\ \mu\text{m}$) crystalline silicon (c-Si) or amorphous silicon (a-Si)/microcrystalline silicon ($\mu\text{c-Si}$) thin films [7], [8]. High quality c-Si permits much higher cell efficiency compared with typical thin film silicon (a/ $\mu\text{c-Si}$) solar cells. In recent years, improved fabrication techniques have made thin ($<50\ \mu\text{m}$) and high-quality c-Si viable for lab-scale devices [9]. The diamond wire sawing now common in the PV industry has also allowed for slightly thinner wafers, although the handling of thin wafers remains an issue for production yields [10]. Here, we incorporate large area nano-scale LT structures into thin c-Si pseudo-cells and demonstrate a clear increase in the optical absorption within the active layer. These structures are transferable to any solar technology with minor modifications. Numerical modeling has been used to predict both the optical characteristics for testing the process controllability and for probing the near-field physics to investigate the significance of fabrication imperfections.

II. SAMPLE DESIGN, FABRICATION, AND CHARACTERIZATION

The motivation of this paper was to develop a cost-effective light trapping structure that requires minimal processing, yet avoids direct texturing of the active absorber layer. A rear surface nano-grating structure consisting of metallized embedded

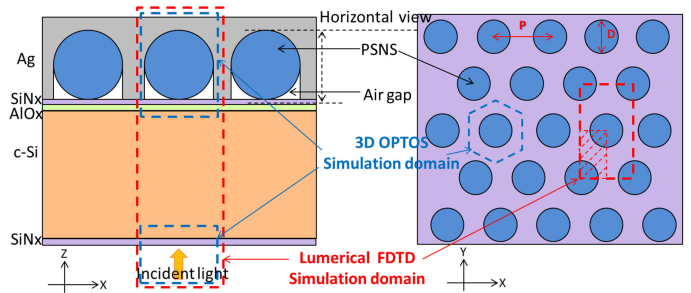


Fig. 1. Schematics of the design structure and simulation domains used in FDTD and OPTOS. The scale in the diagram does not represent its actual size.

nanosphere (NS) was selected (see Fig. 1). This configuration was previously numerically investigated in detail by our group and showed a significant enhancement in simulated photocurrent from a modeled $2\ \mu\text{m}$ thick c-Si solar cell [11], [12]. These structures could potentially act as rear metal contacts for the solar cells as well, in place of planar geometries, although, in this study, we focus on the optical behavior only. Previously reported cell-integrated LT nanostructures require complex fabrication processes (e.g., EBL) which can have an impact on the subsequent device fabrication steps (e.g., absorber growth) [7], [8]. Unlike those structures, rear side nanosphere gratings allow for simple incorporation and can be processed at the final stage of device fabrication. Furthermore, maintaining the planar geometry of the c-Si absorber avoids the concerns of increased surface recombination. In NSL, the formation of regular NS monolayer films is a critical step as the quality of the final nanostructure is mainly determined by the uniformity of the initial NS array. Here, we adopt a robust and repeatable spin coating nanosphere deposition technique. Comprehensive optimization of this technique is reported in previous work [13], [14]. The spin coating process allows wafer-scale polystyrene NS depositions to be accomplished within a few minutes. Although other depositions methods, such as Langmuir–Blodgett coating, can potentially offer higher throughput via batch manufacturing, and may be more suitable at industrial scales, these methods were not investigated here. Finally, as devices become much thinner, as in our case, the benefits of incorporation of LT nanostructures are expected to become more significant.

The fragile nature of the thin c-Si films used here meant that additional mechanical support was required to avoid breakage. In order to maintain the transparency of the front side of the cell, a UV-curing optical adhesive (Norland NOA83H) was used to permanently bond each thin c-Si absorber to a $525\ \mu\text{m}$ thick fused silica wafer. However, the maximum processing temperature for NOA83H (approximately $300\ ^\circ\text{C}$ for 1 h exposure [15]) is about $100\ ^\circ\text{C}$ lower than the temperature usually required for the deposition of a high-quality passivating silicon nitride (SiN_x). A typical process for plasma-enhanced chemical vapor deposition (PECVD) SiN_x passivation layers involves deposition at more than $400\ ^\circ\text{C}$ and may also be followed by a post-deposition anneal. Rear surface passivation was therefore achieved using a two layer stack consisting of 10 nm of aluminum oxide (AlO_x) via atomic layer deposition followed by 55 nm PECVD SiN_x deposited at a lower temperature ($250\ ^\circ\text{C}$).

Fig. 1 shows the schematic of c-Si solar samples with a rear side metallized nanosphere grating. The simulation domains used in the complete optical device modeling (Lumerical FDTD Solutions [16], [17]) and in the three-dimensional formulation of the optical properties of textured optical sheets (OPTOS) [18], [19] method via “JCMwave” [20] are outlined in the same figure. The FDTD method calculates light propagating through the whole structure coherently, thereby taking the interference between each layer and structure into account. Effects due to slight changes in the nanostructure can therefore be visually detected and investigated from the simulated electric fields. However, the full vectorial simulation is computationally intensive for thicker absorber layers. For the OPTOS approach, the optical response of the nanostructured backside and the planar front side of the cell are simulated coherently by finite element method (JCMWave) and Fresnel equations, respectively. To obtain the response of the full structure, these results are incoherently coupled using the OPTOS method. Although interference information may be lost when using this simulation method, it is able to offer a more rapid prediction of the key optical characteristics of the test structure, i.e., absorption and photocurrent enhancement. The decoupling of the surface structure simulation and the bulk absorber achieved using the OPTOS approach allows devices with identical surfaces but different absorber thicknesses to be quickly evaluated. The OPTOS method was therefore used to explore the optical enhancement of the design structures, where optical enhancement is defined as the change in photocurrent density, ΔJ_{ph} . The calculation of J_{ph} was carried out by integrating the simulated absorption in the Si layer ($A(\lambda)$) with the AM 1.5G solar spectrum, along with the assumptions of single electron-hole pair generation per photon and that all electron-hole pairs contribute to the photocurrent. With the additional assumptions of perfectly passivated surfaces and uniform generation throughout the bulk, the maximum possible short-circuit current density (J_{sc}) is therefore equivalent to the calculated J_{ph} given by the following equation [16]:

$$J_{SC} = J_{ph} = e \int \frac{\lambda}{hc} QE(\lambda) \cdot I_{AM1.5}(\lambda) d\lambda \quad (1)$$

where $QE(\lambda)$ is the quantum efficiency of a solar cell at wavelength λ , e is the elementary charge ($\sim 1.6 \times 10^{-19}$ C), h is Planck’s constant, c is the speed of light in the free space, and $I_{AM1.5}$ is the AM 1.5 solar spectrum.

In addition, we define an absorption enhancement factor $AE(\lambda)$ as follows [21]:

$$AE(\lambda) = \frac{A_{test}(\lambda) - A_{ref}(\lambda)}{A_{ref}(\lambda)} \times 100\% \quad (2)$$

where $A_{test}(\lambda)$ is the absorptance of the nanosphere test structure and $A_{ref}(\lambda)$ is the absorptance of a reference (planar) sample. This highlights the spectral range where the absorption is most enhanced.

Complete optical device FDTD modeling was used to investigate the effects due to changes in nanostructures in specific cases of interest. Adopting both simulation techniques together allows us to investigate different aspects of the light trapping property in an efficient, yet suitably accurate way.

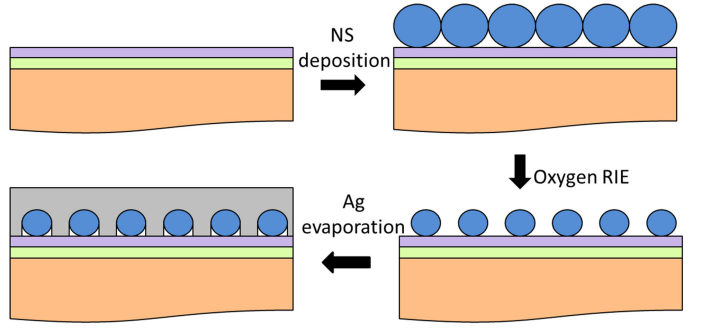


Fig. 2. Schematics of the fabrication flow of the metal nanosphere gratings with embedded dielectric nanospheres.

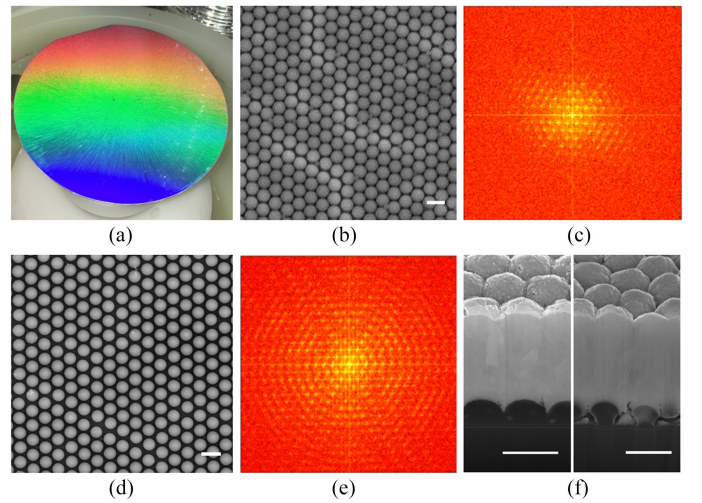


Fig. 3. Images of samples for NS diameter of 746 nm. The scale bar in (b), (d), and (f) is $1 \mu\text{m}$. (a) Photograph of a 4 inch size c-Si coated with NS arrays. The different angle of the arrays relative to the camera leads to a very clear diffraction effect, demonstrating array quality. (b) SEM image of NSs deposited on thin c-Si, and (d) SEM image of NS deposited on thin c-Si after oxygen RIE. The corresponding FFTs of (b) and (d) are shown in (c) and (e), respectively. (f) Focused ion beam (FIB) image of a final sample with an unetched 746 nm NS array (left) and etched down to 627 nm in diameter size, 746 nm in periodicity NS array (right).

Fig. 2 shows the fabrication procedure of the dielectric embedded metal nanosphere grating structure on a $30 \mu\text{m}$ thick c-Si substrate. First, a uniform polystyrene nanosphere (PSNS) monolayer was deposited by a concentration-controlled spin-coating method [14]. This allowed a broad range of NS arrays to be fabricated quickly at low cost, using NS of various diameters. In this study, PSNSs of diameter 500, 746, and 960 nm were used. Strong diffraction, evident in the optical image of Fig. 3(a), indicates the large area uniformity of the deposited NS array. A scanning electron microscope (SEM) image of the as-deposited NS array on silicon is shown in Fig. 3(b), along with a fast Fourier transform (FFT) of this image in Fig. 3(c). The latter shows the lattice structure in the frequency domain. When a uniform hexagonal NS array is present in the SEM image, regular hexagonal patterns are clearly visible at spatial frequencies corresponding to the periodicity of the array and reflecting the symmetry of the lattice. Although grain boundaries still appear

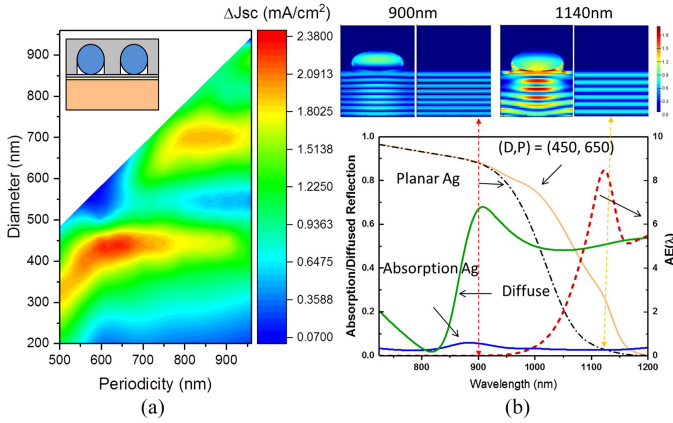


Fig. 4. (a) Highest possible J_{sc} (mA/cm²) enhancement for a 30 μm Si absorber for different NS diameters and periodicities embedded in a Ag layer at the rear of the cell. (b) Absorption/diffuse reflection spectra of the planar structure and the nanosphere grating design, (D, P) = (450, 650), giving the highest J_{sc} improvement. The diffuse reflection spectra were simulated with a non-absorbing Si. D is the diameter of the NS and P is the periodicity of the grating. E-field-profiles in the presence of simulated structures and in the planar reference along the x-z plane at 900 and 1140 nm are shown.

in the corresponding SEM image [see Fig. 3(b)], closely packed NSs with slightly varying grain orientation and size can actually prove beneficial for LT, thanks to the isotropic and spectrally broadened response [22]. Tuning of the NS diameter was accomplished by a low power oxygen reactive ion etching (RIE) plasma etch, the results of which are shown in Fig. 3(d). The etching parameters were carefully chosen to avoid roughening the surface of the NS, a detrimental effect previously observed in our earlier study [21]. Finally, a 2.5 μm thick Ag layer was deposited as the back-reflector via thermal evaporation [see Fig. 3(f)].

Although the process described here includes vacuum-based methods (RIE, evaporation) that are typically considered high-cost for PV, the rapid development of industrial tools is beginning to enable these advanced processes. For example, there is currently great interest in applying “black silicon” texturing in industry. Tools producing “black silicon” via RIE are already viable and can process hundreds of wafers per batch [23]. This rapid innovation in manufacturing tools could potentially drive the high-cost of vacuum-based process down by batch processing.

III. SIMULATION RESULTS

Fig. 4(a) shows a color-coded surface plot of the maximum short-circuit current density enhancement (ΔJ_{sc}) from a 30 μm thick c-Si structure implementing the proposed nanosphere grating. The data were calculated using OPTOS and uses a planar sample as the baseline reference. The J_{sc} enhancement is seen to peak when the NS diameter is approximately 100–200 nm smaller than the array periodicity, which correlates well with our previous numerical studies [11], [12]. Although only three sizes of NSs were considered for fabrication, the simulation results indicate that similar enhancement (red region) can be achieved over a relatively wide process window making these structures tolerant against fabrication imperfections. Further simulations

were conducted with a semi-infinite silicon absorber that was modeled as lossless, by artificially setting the imaginary part of the refractive index to zero. This was to better understand the resonant and short wavelength (<900 nm) behavior of the nanosphere grating and reveal any parasitic absorption in the Ag layer. It was found that when the nanosphere grating design offers a relatively high J_{sc} enhancement (e.g., with a periodicity of 650 nm and NS diameter of 450 nm), the incoming light is scattered most at about 900 nm, where the absorption in Ag is strongest, which agrees with our previous results recently reported [24] and is shown in Fig. 4(b). However, when calculating the strongest absorption enhancement, the silicon absorption must of course be considered. The highest absorption enhancement is seen to be more than 8 times greater than a planar device at the same resonant wavelength, i.e., ~ 1140 nm. To better understand this, the steady-state electric field (E-field) within a unit cell of the optical device is plotted in Fig. 4(b) for wavelengths of 900 and 1140 nm, both with the embedded NS and for a planar device. Although the NS is strongly scattering at both wavelengths (green curve), more light is re-directed into the Si layer at 1140 nm, while the electric field intensity in Si at 900 nm remains similar to that of a planar cell. Furthermore, compared with 1140 nm, 900 nm is strongly absorbed in 30 μm of planar Si. Indeed, the $1/e$ absorption depth at 900 nm is close to 30 μm meaning only approximately 36% of the incident light reaches the rear surface. The absorption enhancement due to the rear surface nanosphere grating is therefore much greater for wavelengths (>1100 nm), where the incident light is very weakly absorbed ($A(\lambda) < 1\%$).

IV. EXPERIMENTAL RESULTS

Several techniques were used to determine the optical properties of the 30 μm thick experimental samples. Standard absorptance measurements (1-R-T) were first carried out using a UV-Vis spectrophotometer (Perkin Elmer Lambda 950) to provide an initial comparison of different NSs. Fig. 5 shows the spectrally resolved absorptance enhancement over planar rear metal samples for nanosphere gratings with different periodicities. All embedded NS devices show clear enhancement at long wavelengths. However, there is also some spurious “absorption” at long wavelengths, well beyond the bandgap of c-Si. This may be due to the parasitic absorption in the non-active layers (NS array and Ag back-reflector) and/or potential lateral waveguiding that contribute to the measurement. The highest enhancement is obtained for samples with an unetched array of 746 nm diameter NS, resulting in an average absorptance of 80.7% from 300 to 1200 nm. Compared with the planar control samples (with metal) with an average absorptance of 69.6%, there is an absolute increase of 11.1%, which could potentially lead to an increase in short-circuit current of up to 4.33 mA/cm² (J_{sc} of the control samples is 34.86 mA/cm²). However, it should be noted that this “best” result could be misleading, with the increased absorption potentially being parasitic. Near-infrared photoluminescence (PL) imaging and spectra, which are almost entirely selective to absorption in the silicon, were therefore used to confirm the absorption enhancement in Si.

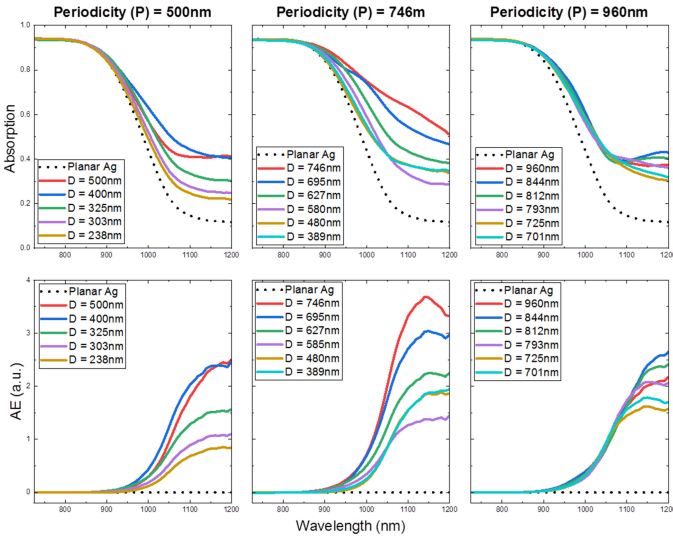


Fig. 5. Absorbance and absorbance enhancement (AE) of fabricated samples. The measurements were carried out from 300 to 1200 nm. However, the figure here shows data beyond 800 nm only as the absorption spectra are nearly identical in UV and visible light region and no light trapping effects are expected.

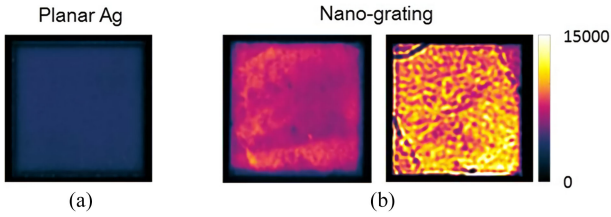


Fig. 6. PL image of fabricated samples without (a) and with (b) nanosphere grating back-reflectors. In (b), the left PL image shows the design [(D, P) = (480, 746)] providing the weakest enhancement and the right PL image shows the design [(D, P) = (627, 746)] providing the strongest enhancement. D is the diameter of the NS and P is the periodicity of the grating.

PL is very useful for determining light trapping efficiency [25] as the emission can be filtered to be selective to the silicon absorber alone, thereby excluding any parasitic absorption in other layers. All experimental samples were PL imaged under one-sun equivalent exposure conditions. Post-processing and analysis of the PL images of the whole illumination area was then performed with LumiTools [26]. Fig. 6 shows the representative PL images, where it can be seen that the introduction of the nanosphere grating almost doubles the PL counts. The area-averaged PL enhancement (ΔPL) from the fabricated samples and simulated short-circuit current density enhancement (ΔJ_{sc}) from structured and planar control samples are compared in Fig. 7. In general, the trends from the PL measurement results are in good agreement with those from the simulation results, albeit shifted toward slightly larger NS diameters [27]. This implies good control of the fabrication process and supports the potential of such nanostructures to be produced at commercial scales. Furthermore, it is believed that the difference between the fabrication and simulation trends is mainly due to the distorted shape of the polystyrene NS, which results in a larger feature size in the final device. In general, a closer match between the

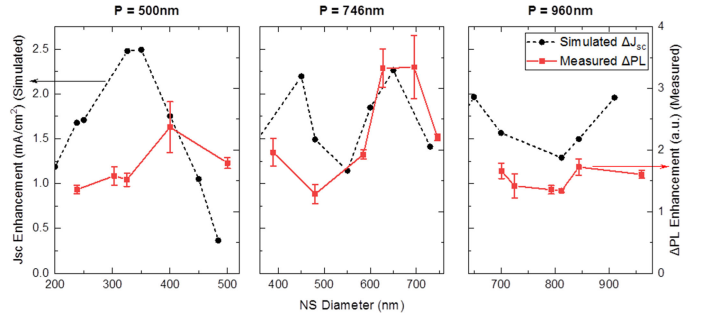


Fig. 7. Area-averaged PL intensity enhancement of fabricated samples and simulated J_{sc} enhancement from 3-D OPTOS simulation. From left to right, it shows the comparison results of nanosphere grating for 500, 746, and 960 nm periodicity, respectively. The black dashed line is simulated J_{sc} enhancement and the red solid line is PL intensity enhancement measured from fabricated samples.

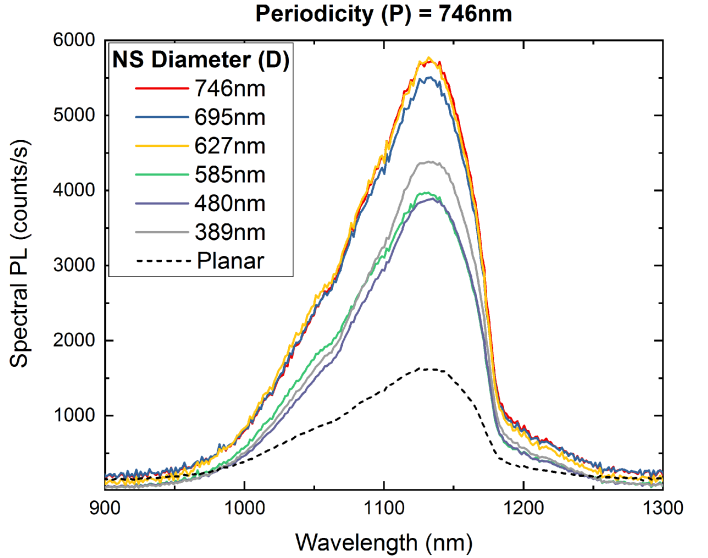


Fig. 8. Spectral PL measurement results of fabricated samples for different NS sizes clearly showing enhanced performance over the planar geometry.

simulation and fabrication results can be expected from Fig. 7 when the trends of area-averaged PL imaging enhancement are offset by slightly decreasing the NS diameter (i.e., 20–50 nm) verifying our claim that the actual NS feature size in the fabricated samples may be slightly larger than that included in the simulation. This was confirmed by FIB and is discussed in the next section. Our results nevertheless support the potential of such nanostructures to be implemented for light trapping.

Finally, spectrally resolved PL measurements were used to measure the long wavelength (close to bandgap) performance of our test structures, as shown in Fig. 8 ($P = 746$ nm) and the Supplementary information ($P = 500$ nm and $P = 960$ nm). The spectral PL measurements were carried out using a custom-built micro-PL system [28]. Each sample was measured at 36 points across the center area (~ 1 cm²). The illuminated area is about 1.53×10^{-3} cm² with a power density of 4.9 W cm⁻². The approximate photon flux is therefore 4.64×10^{19} photons s⁻¹ · cm⁻², putting the sample under high injection conditions

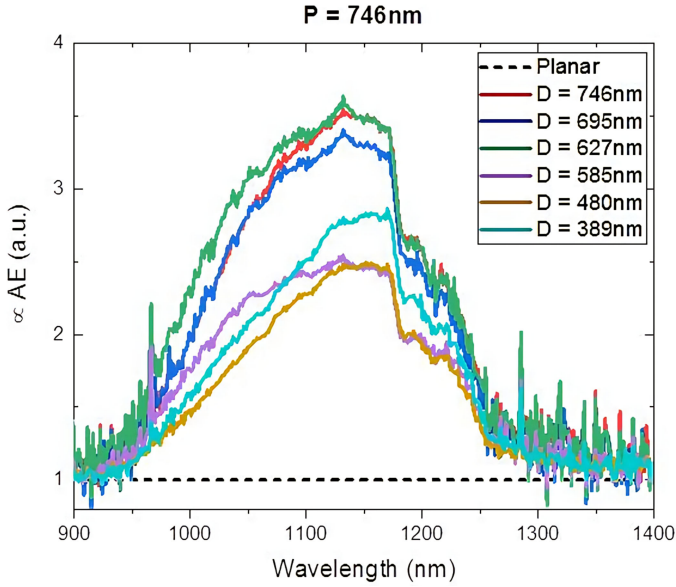


Fig. 9. Spectral PL calculated absorbance enhancement (\propto AE). Spectra PL data of each nanosphere grating design was normalized at 900 nm.

for all measurements. The emission from samples both with and without the nanosphere grating structure peaks at about 1130 nm, typical of silicon. The results indicate that the LT structures clearly enhance the PL emission, which corresponds to increased absorption in the active silicon absorber according to reciprocity.

The observed PL signal is related to the black body emission, absorbance and the quasi-Fermi energies of the measured sample by the following equation [29]:

$$I_{\text{PL}} = \text{BB}_i \cdot A_i \cdot \exp\left(\frac{V}{kT}\right). \quad (3)$$

Here, I_{PL} is the measured PL signal, BB_i is the black body emission of the measured sample, A_i is its absorbance, and V is the separation of quasi-Fermi energies.

The “useful” absorbance enhancement (\propto AE) can therefore be calculated from the spectrally resolved PL results by dividing the PL response of the test structure by that of the reference (planar) sample. Fig. 9 ($P = 746$ nm) and Supplementary images (C, D) show the \propto AE calculated from the measured spectral PL. Up to ~ 3.7 times absorbance enhancement was observed. This value is close to the peak \propto AE value obtained from earlier standard absorbance measurements, which indicates that the primary contribution to the simulated J_{sc} enhancement is indeed from absorption in the silicon itself.

Compared with the planar device, the embedded NS array showed up to 4.3 times higher PL counts in PL imaging and 4 times higher spectral PL counts (integrated from 900 to 1200 nm), which leads to an increase in implied open-circuit voltage [30]. From the enhancements observed from both the maximum possible short-circuit current density (J_{sc}) and implied open-circuit voltage (iV_{oc}), the fabricated nanosphere grating structure has therefore been shown to be capable of cost-effectively boosting efficiency in solar cells with absorber layers that are not suitable for texturing (e.g., micron-thick c-Si/GaAs).

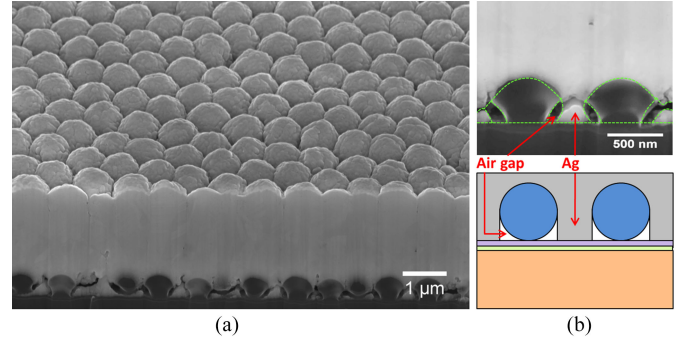


Fig. 10. (a) FIB image of the final samples with NS array (periodicity = 746 nm, NS diameter = 627 nm when measured after oxygen RIE). Some of the air gaps is partly missing and filled by Ag. (b) Exemplary high-resolution FIB images of the sample shown in (a) along with the schematic of its initial design structure. The resulting (cupcake-like) NS have a diameter of ~ 567 and ~ 462 nm in height with air gaps. The shape of the final NS is traced using dotted lines.

TABLE I
NS DIAMETER MEASUREMENT RESULTS OF REPRESENTATIVE SAMPLES

NS grating design (D,P)	After RIE etching	Final feature
(i) Unetched NS array (746, 746)	746 \pm 8	730 \pm 13
(ii) Strongest Δ PL design (627, 746)	627 \pm 6	604 \pm 31
(iii) Weakest Δ PL design (480, 746)	480 \pm 30	408 \pm 27

The NS diameter was determined from its Feret diameter by analyzing relative SEM/FIB images in ImageJ. The unit used in this table for both diameter (D) and periodicity (P) is nanometer (nm).

V. DISCUSSION

To confirm the origin of the inconsistency between the trends for the simulated and fabricated samples in Fig. 7, the fabricated samples were further characterized by FIB. Fig. 10 shows a representative FIB image of a finished sample consisting of etched NSs coated with Ag. First, while the NS array has been conformally coated by the Ag film without distorting the array uniformity [see Fig. 10(a)], closer observation under the SEM reveals that the shape of each NS is distorted to a semi-“cupcake” appearance [see Fig. 10(b)]. This distortion likely occurred during the metallization as there is no NS deformation observed prior to metal evaporation. The final cupcake-like NS are compressed in the vertical direction, with a smaller height and larger width compared with their measured diameters after RIE. The analysis of the NS size before and after metallization was initially conducted using the Feret diameter, which includes information from both axes. This information is presented in Table I. It should be noted though that this results in an apparent NS feature size that is smaller, not larger, than the RIE-etched NS diameter, in contradiction to the optical response presented in Fig. 7. However, the increase in the feature width is expected to play a dominant role, as this axis is aligned with the plane of polarization of the incident light. The net result of the NS distortion is therefore a shift in the resonance peak toward longer wavelengths.

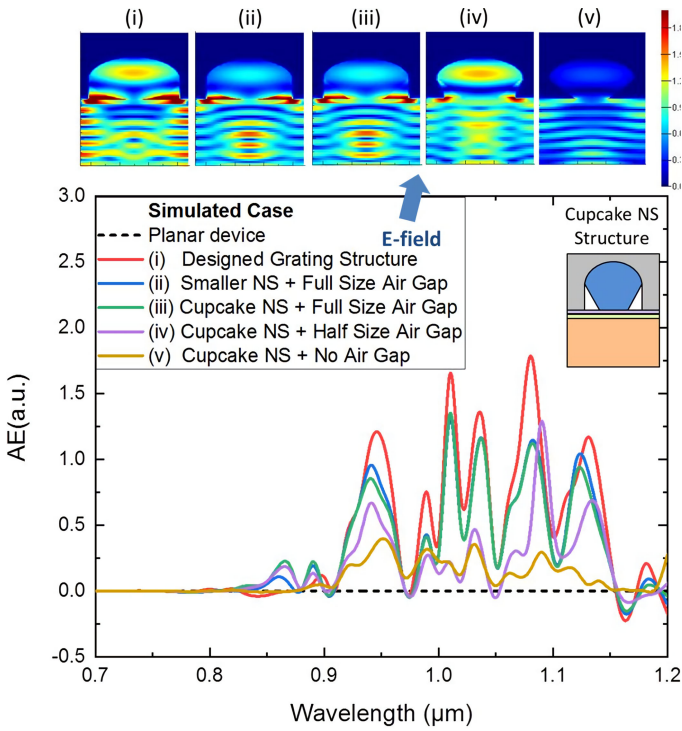


Fig. 11. Complete optical device simulated absorptance enhancement (AE) of different distorted NS nanostructures in comparison with a $30\ \mu\text{m}$ thick planar device. *E*-field-profiles in the presence of simulated structures along the *x-z* plane at the peak resonant wavelength (1080–1090 nm) are shown. The effects of NS distortion and air gap existence on resonance strength are shown for different configurations through these *E*-field images.

TABLE II
SIMULATED EFFECTS OF NS DISTORTION ON SHORT-CIRCUIT CURRENT DENSITY ENHANCEMENT

Simulated Case	ΔJ_{sc} (mA/cm ²)
(i) Design (Ideal) Grating Structure	2.14
(ii) Smaller NS + Full Size Air Gap	1.78
(iii) Cupcake NS + Full Size Air Gap	1.89
(iv) Cupcake NS + Half Size Air Gap	1.15
(v) Cupcake NS + No Air Gap	0.74

Simulations were carried out from 700 to 1200 nm using complex optical device modeling in Lumerical FDTD Solutions. The short-circuit current density of the planar device is $17.23\ \text{mA}/\text{cm}^2$.

A further important deviation from the ideal case is that the air gaps included in the original design are partially or even entirely missing in some cases. The air gaps can strongly affect the photocurrent, as has been previously observed in our simulations [11], [12]. Therefore, the change of NS shape and the missing air gap may also contribute to the inconsistency. We investigated the effects of these mismatches between the simulation model and the fabricated devices via FDTD modeling.

Based on the general features observed in the cross-sectional FIB images of Fig. 10, several test structures were simulated to investigate the effects due to shape changes, size reductions, and missing air gaps. Fig. 11 shows the AE spectra of those test structures. It indicates that the size and shape change of the NS do not cause serious impacts to the light trapping (see Table II).

Although there is a slight shift and decrease in the magnitude of the resonant peaks, it still provides considerable absorption enhancement. In contrast, the effect of the missing air gaps is far more critical, the worst case being when the air gaps are fully filled by the Ag. The electric field intensity at a resonant wavelength of approximately 1085 nm and simulated ΔJ_{sc} results (see Table II) show that a nanosphere grating without air gaps barely improves the LT relative to a planar rear mirror. Although the design was not perfectly replicated in the fabricated samples, the similar trends in Fig. 10 indicate that extreme distortion, i.e., complete absence of the air gaps, should not exist in our samples.

A likely cause of the NS shape distortion is the substrate holder heating during the thermal Ag evaporation process. During this process, the substrate and substrate holder both rise in temperature due to radiant heat from the source. This may cause a temperature gradient in the polystyrene NS. With a continuing rise in temperature, the NS being polystyrene may eventually melt/deform at the point of contact to the spacer layer [31], [32].

This study therefore highlights that there should be a careful choice of the NS materials used. Silica nanospheres (SNS) have a much higher melting point ($\sim 1713\ ^\circ\text{C}$) compared with that of polystyrene ($\sim 240\ ^\circ\text{C}$) and were the first choice in this study due to their higher compatibility with PV device processing. However, the reduction of SNS size via RIE etching involves fluorinated gases such as sulfur hexafluoride (SF_6) and tetrafluoromethane (CF_4), which can also attack the SiN_x and potentially degrade the surface passivation. To obtain good control of the fabrication process using SNS, further investigation on alternative passivation and/or subsequent NS size reduction processes is required. Using a substrate cooling function in the evaporator would be a much simpler and preferred solution. Finally, in order to make LT nanostructures for industrial scale PV, lower cost metals such as aluminum should be considered, although the light trapping may be greatly reduced in comparison with Ag [11]. Al–Ag alloys may also be a possible economic alternative. Despite the technical challenges, the results from this study demonstrate that properly designed metal grating structures can provide significant benefits over traditional planar rear metal reflectors for thin photovoltaic devices.

VI. CONCLUSION

In conclusion, this paper demonstrated a promising approach for the cost-effective and controlled fabrication of LT nanostructures in thin c-Si solar cells. These structures do not directly texture the silicon surface and therefore permit optimal surface passivation. We showed proof-of-concept photocurrent improvement of up to $4.33\ \text{mA}/\text{cm}^2$ by incorporating metal nanosphere gratings into $\sim 30\ \mu\text{m}$ thick c-Si pseudo cells and up to ~ 3.7 times absorptance enhancement in comparison with a planar Ag device structure. Clear enhancements were observed in both spatially and spectrally resolved PL measurements, indicating that the increased absorption is predominantly in the silicon layer and not parasitic. Furthermore, the fabricated samples showed good agreement with simulations, indicating

good control of the robust nanosphere lithography process. Although challenges remain, such as nanosphere deformation and batch processing, this paper demonstrated the feasibility of large-area light trapping nanostructures that may be applied to any commercial thin-film photovoltaic technology.

ACKNOWLEDGMENT

Responsibility for any views, information, or advice expressed herein is not necessarily accepted by the Australian Government.

REFERENCES

- [1] M. Green *et al.*, "Solar cell efficiency tables (version 51)," *Prog. Photovolt., Res. Appl.*, vol. 26, no. 1, pp. 3–12, Jan. 2018.
- [2] A. Shah, "Thin-film silicon solar cells," in *Practical Handbook of Photovoltaics*. Amsterdam, The Netherlands: Elsevier, 2012, pp. 207–282.
- [3] M. Rentsch *et al.*, "Texture etching technologies for diamond-wire-sawn mc-Si solar cells," *Photovolt. Int.*, vol. 38, pp. 56–66, 2018.
- [4] M. R. Goncalves, "Plasmonic nanoparticles: Fabrication, simulation and experiments," *J. Phys. D, Appl. Phys.*, vol. 47, no. 21, May 2014, Art. no. 213001.
- [5] F. Sohrabi and S.M. Hamidi, "Fabrication methods of plasmonic and magnetoplasmonic crystals: A review," *Eur. Phys. J. Plus*, vol. 132, no. 1, pp. 1–21, Jan. 2017.
- [6] P. Colson *et al.*, "Nanosphere lithography: A powerful method for the controlled manufacturing of nanomaterials," *J. Nanomater.*, vol. 2013, pp. 1–19, 2013.
- [7] P. Mandal and S. Sharma, "Progress in plasmonic solar cell efficiency improvement: a status review," *Renewable Sustain. Energy Rev.*, vol. 65, pp. 537–552, Nov. 2016.
- [8] Y. H. Jang *et al.*, "Plasmonic solar cells: From rational design to mechanism overview," *Chem. Rev.*, vol. 116, no. 24, pp. 14982–15034, Dec. 2016.
- [9] J. Montgomery, "Four new approaches to ultrathin silicon," *Renewable Energy World*, Jul. 8, 2013. [Online]. Available: <https://www.renewableenergyworld.com/articles/2013/07/four-new-approaches-to-ultrathin-silicon.html>
- [10] K. Gurnett and T. Adams, "Ultra-thin semiconductor wafer applications and processes," *III-Vs Rev.*, vol. 19, no. 4, pp. 38–40, May 2006.
- [11] C. Disney, S. Pillai, C. Johnson, Q. Xu, and M. Green, "Plasmonic rear reflectors for thin-film solar cells: Design principles from electromagnetic modelling," *Proc. SPIE*, vol. 9178, 2014, Art. no. 91780J.
- [12] C. Disney, S. Pillai, C. Johnson, and M. Green, "Self-assembled nanostructured rear reflector designs for thin-film solar cells," *ACS Photon.*, vol. 2, pp. 1108–1116, 2015.
- [13] Y. Chang, D. Payne, M. Pollard, S. Pillai, and D. Bagnall, "Nanosphere lithography for improved absorption in thin crystalline silicon solar cells," *Proc. SPIE*, vol. 9668, 2015, Art. no. 966849.
- [14] Y. Chang, M. Pollard, D. Payne, S. Pillai, and D. Bagnall, "Nanosphere lithography for fast and controlled fabrication of large area plasmonic nanostructures in thin film photovoltaics," in *Proc. Asia-Pac. Sol. Res. Conf.*, Dec. 2016.
- [15] "Norland Products." [Online]. Available: <https://www.norlandprod.com/adhesiveindex2.html>. Accessed on: May 29, 2019.
- [16] K.-H. Brenner, "Aspects for calculating local absorption with the rigorous coupled-wave method," *Opt. Express*, vol. 18, pp. 10369–10376, 2010.
- [17] Y. Chang, D. Payne, M. Pollard, and D. Bagnall, "Optimization of plasmonic back reflectors for ultra-thin crystalline silicon photovoltaics," in *Proc. 31st Eur. Photovolt. Sol. Energy Conf. Exhib.*, 2015, pp. 1321–1326.
- [18] N. Tucher *et al.*, "Optical simulation of photovoltaic modules with multiple textured interfaces using the matrix-based formalism OPTOS," *Opt. Express*, vol. 24, no. 14, pp. A1083–A1093, Jul. 2016.
- [19] N. Tucher *et al.*, "Optical performance of the honeycomb texture—A cell and module level analysis using the OPTOS formalism," *Sol. Energy Mater. Sol. Cells*, vol. 173, pp. 66–71, Dec. 2017.
- [20] J. Pomplun, S. Burger, L. Zschiedrich, and F. Schmidt, "Adaptive finite element method for simulation of optical nano structures," *Phys. Status Solidi*, vol. 244, no. 10, pp. 3419–3434, Oct. 2007.
- [21] Q. Xu, C. Johnson, C. Disney, and S. Pillai, "Enhanced broadband light trapping in c-Si solar cells using nanosphere-embedded metallic grating structure," *IEEE J. Photovolt.*, vol. 6, no. 1, pp. 61–67, Jan. 2016.
- [22] E. Wang, S. Mokkaapati, T. Soderstrom, S. Varlamov, and K. Catchpole, "Effect of nanoparticle size distribution on the performance of plasmonic thin-film solar cells: Monodisperse versus multidisperse arrays," *IEEE J. Photovolt.*, vol. 3, no. 1, pp. 267–270, Jan. 2013.
- [23] D. Payne *et al.*, "Understanding the optics of industrial black silicon," *Proc. AIP Conf.*, vol. 1999, no. 1, 2018, Art. no. 050007.
- [24] C. Disney, S. Pillai, and M. Green, "The impact of parasitic loss on solar cells with plasmonic nano-textured rear reflectors," *Sci. Rep.*, vol. 7, no. 1, Dec. 2017, Art. no. 12826.
- [25] C. Barugkin *et al.*, "Light trapping efficiency comparison of Si solar cell textures using spectral photoluminescence," *Opt. Express*, vol. 23, no. 7, pp. A391–A400, Apr. 2015.
- [26] D. Payne, C. Vargas, Z. Hameiri, S. Wenham, and D. Bagnall, "An advanced software suite for the processing and analysis of silicon luminescence images," *Comput. Phys. Commun.*, vol. 215, pp. 223–234, Jun. 2017.
- [27] R. L. Chin *et al.*, "Insights into bulk defects in n-type monocrystalline silicon wafers via temperature-dependent micro-photoluminescence spectroscopy," in *Proc. IEEE 7th World Conf. Photovolt. Energy Convers.*, Jun. 2018, pp. 2524–2527.
- [28] H. Hoffer, O. Breitenstein, and J. Haunschild, "Short-circuit current density imaging via PL image evaluation based on implied voltage distribution," *IEEE J. Photovolt.*, vol. 5, no. 2, pp. 613–618, Mar. 2015.
- [29] A. Delamarre, L. Lombez, and J. F. Guillemoles, "Characterization of solar cells using electroluminescence and photoluminescence hyperspectral images," *Proc. SPIE*, vol. 8256, 2012, Art. no. 825614.
- [30] B. Hallam, B. Tjahjono, T. Trupke, and S. Wenham, "Photoluminescence imaging for determining the spatially resolved implied open circuit voltage of silicon solar cells," *J. Appl. Phys.*, vol. 115, no. 4, Jan. 2014, Art. no. 044901.
- [31] H. Djidjelli and D. Benachour, "Effects of recycling on mechanical and thermal properties of polystyrene," *Macromol. Symp.*, vol. 127, no. 1, pp. 181–185, Feb. 1998.
- [32] F. Rouabah, D. Dadache, and N. Haddaoui, "Thermophysical and mechanical properties of polystyrene: Influence of free quenching," *ISRN Polym. Sci.*, vol. 2012, pp. 1–8, Feb. 2012.

Authors' photographs and biographies not available at the time of publication.

Ultrathin CIGSe Solar Cells with Integrated Structured Back Reflector

Thomas Schneider,* Johanna Tröndle, Bodo Fuhrmann, Frank Syrowatka, Alexander Sprafke, and Roland Scheer

To reduce the thickness of $\text{CuIn}_{1-x}\text{Ga}_x\text{Se}_2$ (CIGSe) solar cells, light management concepts must be used. One concept is the combination of an Al/indium-tin-oxide (ITO) reflector/contact and an optical scattering element at the back side of the device. Herein, nanostructured substrates, obtained by laser interference lithography and lift-off process, are covered with an Al/ITO back contact. Structure dimensions are a pitch of $1.96\ \mu\text{m}$ and heights of $100\text{--}700\ \text{nm}$. Solar cells with $600\ \text{nm}$ CIGSe absorber having this integrated structured back reflector exhibit an increase in J_{SC} of up to $3.2\ \text{mA cm}^{-2}$ compared with the Mo reference sample of identical thickness. To understand this optical gain, 3D finite-difference time-domain (FDTD) simulations are performed. To this end, a model is built to simulate structure formation. It is shown that locally enhanced optical absorption can be achieved by the integrated structured back reflector. It is also shown that parasitic absorption in the back ITO diffusion barrier needs to be minimized.

1. Introduction


Reducing the thickness of thin-film solar cells reduces the total cost of ownership of solar module production. Theoretically, a $500\ \text{nm}$ $\text{Cu}(\text{In,Ga})\text{Se}_2$ (CIGSe) solar cell allows more than 20% efficiency.^[1–4] However, this requires a very low back contact recombination velocity and advanced optical light management. The standard molybdenum back contact is generally attributed with a high recombination velocity^[5–7] and has a poor optical reflectivity.^[8] In ref. [9], a ZrN layer on top of molybdenum having a reflectivity of 60% was used with the result of increased quantum efficiency at long wavelengths. An even

higher reflectivity and higher gain in photocurrent could be achieved by an Au back reflector applied by post-deposition recontacting after removing the Mo layer.^[10] In addition to cost aspects, Au is not suitable for direct deposition of CIGSe thin films at high temperatures due to the chemical reactivity with the chalcogen species during CIGSe deposition. The latter is also true for other highly reflective metals such as Ag, Cu, and Al.^[11] Instead, these metals have to be encapsulated by a transparent and conductive diffusion barrier layer. Bissig et al. investigated an Al/InZnO back contact for solar cells with an absorber thickness of $2.1\ \mu\text{m}$ and were able to increase the short-circuit density up to $1.4\ \text{mA cm}^{-2}$ compared with a sample with Mo back contact, despite the relatively high

absorber thickness.^[12] According to former work on transparent back contacts, the transparent conductor indium-tin-oxide (ITO) is a good candidate as a transparent back contact^[13] and as a diffusion barrier.^[14] Recently, ref. [15] showed an experimental gain in short-circuit current density of $4.9\ \text{mA cm}^{-2}$ in a structure Mo/Ag/ITO/ $0.5\ \mu\text{m}$ CIGSe with respect to the reference structure of Mo/ $0.5\ \mu\text{m}$ CIGSe. Al/ITO-based solar cells can be prepared up to at least $600\ ^\circ\text{C}$ without Al diffusion inside the absorber while providing high reflectivity at long optical wavelengths.^[16] This raises the question of the electronic properties of the ITO/CIGSe contact. Keller et al. investigated $650\ \text{nm}$ CIGSe bifacial solar cells with a hydrogen-doped In_2O_3 back contact^[17] and quantified the back-contact recombination velocity to the range of $10^7\ \text{cm s}^{-1}$. This value dropped by application of an $\text{Al}_2\text{O}_3 + \text{NaF}$ precursor layer stack as confirmed by a strongly increased rear-side external quantum efficiency (EQE) at short wavelengths. Unfortunately, the $5\ \text{nm}$ Al_2O_3 conformal layer reduces the fill factor (FF).^[17] Although a flat optical reflector enhances the long-wavelength EQE upon front-side illumination to some extent, light scattering is required in addition to approach the Yablonovitch limit.^[18] Yin et al. used ITO as transparent back contact and applied both dielectric SiO_2 nanoparticles on top of ITO and an external Ag mirror behind the substrate glass achieving a very high short-circuit current density of $32.4\ \text{mA cm}^{-2}$ with an absorber thickness of only $390\ \text{nm}$.^[19] This was an important step toward a structured and reflecting back contact for CIGSe solar cells. Kovacic et al. performed optical simulations with a $500\ \text{nm}$ absorber in a complete solar module stack with different back-contact metals in combination with

T. Schneider, J. Tröndle, Dr. A. Sprafke, Prof. R. Scheer
Martin-Luther-University Halle-Wittenberg
Institute of Physics
Von-Danckelmann-Platz 3, 06120 Halle (Saale), Germany
E-mail: thomas.schneider@physik.uni-halle.de

Dr. B. Fuhrmann, F. Syrowatka
Interdisziplinäres Zentrum für Materialwissenschaften (IZM)
Martin-Luther-University Halle-Wittenberg
Heinrich-Damerow Straße 4, 06120 Halle (Saale), Germany

 The ORCID identification number(s) for the author(s) of this article can be found under <https://doi.org/10.1002/solr.202000295>.

© 2020 The Authors. Published by Wiley-VCH GmbH. This is an open access article under the terms of the Creative Commons Attribution License, which permits use, distribution and reproduction in any medium, provided the original work is properly cited.

DOI: 10.1002/solr.202000295

an internal and external structure.^[20] The results show that solar cells with a 500 nm CIGSe absorber can even surpass the J_{SC} value of a standard Mo-based CIGSe solar cell with a 1800 nm thick absorber layer. Al_2O_3 was used in the simulations as diffusion barrier for the back-contact metals. For real devices, however, a different configuration has to be used because the Al_2O_3 is electrically isolating and local openings or thinning of the Al_2O_3 would compromise its diffusion barrier properties.

In this article, the functionalities of optical scattering, optical reflectivity, and electric conductivity of the back contact are fully integrated into the solar cell stack using a structured Al/ITO rear contact. The CIGSe thickness was chosen to be 600 nm as this thickness prevents pin-holes (in contrast to thinner CIGSe) but renders the back contact highly critical in terms of absorption and recombination (in contrast to thicker CIGSe). The growth of CIGSe on the nanostructured back contact is investigated, the solar cell parameters for different structure heights are determined, and optical simulations are carried out.

2. Experimental Section

Figure 1 gives a principle sketch of the applied thin-film structure. Commercial coated soda-lime glasses with 500 nm Mo layers on top of a SiO_xN_y diffusion barrier layer were used for all samples as substrate. SiO_2 nanostructures are formed by photolithography using lift-off technology. The lift-off approach was selected due to higher reproducibility. For this purpose, a negative photo-resist (AR N4240 with diluter AR 300:12 from Allresist) is deposited by spin-coating. The photoresist is illuminated by Fresnel-type laser interference lithography, baked, and developed (AR 300:475). This leads to pillar-like structures of photoresist on a hexagonal lattice. SiO_2 layers of varying thickness are deposited by e-beam deposition. Lift-off is carried out in acetone at 50 °C for 30 min in an ultrasound bath. The results are hexagonally ordered holes in SiO_2 of variable shape and size with a pitch of 1.96 μm . Structures with 197, 550, and 700 nm SiO_2 thicknesses can be seen in the upper row of Figure 2 showing scanning electron microscopy (SEM) images.

Two sample sets were fabricated with roughly the same structural dimensions. The structure heights are 101, 197, 282, 550,

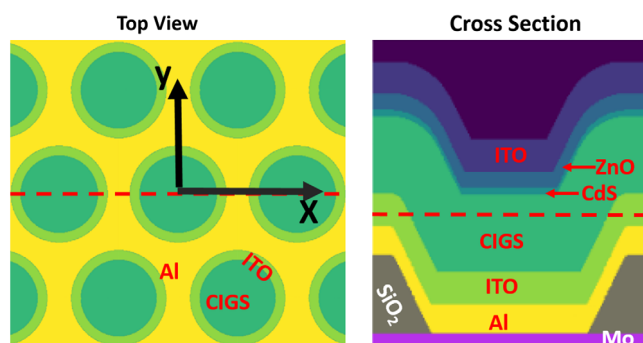


Figure 1. Schematics of the prepared solar cell with SiO_2 structure elements, aluminum metal reflector, and ITO transparent back contact underneath an ultrathin CIGSe solar cell with 0.6 μm CIGSe layer. The red dashed lines in the left picture show the axis of the right cross-section picture and vice versa.

and 700 nm for sample set 1 and 100, 174, 296, and 499 nm for sample set 2 as determined by spectral ellipsometry measurements on unstructured SiO_2 layers deposited in the same preparation processes. An aluminum layer of 110 nm thickness was deposited on top of the SiO_2 nanostructures using e-beam evaporation followed by 250 nm ITO sputtering. CIGSe layers were grown simultaneously on each sample set using the three-stage deposition process resulting in 600 nm thick layers. The chemical composition is $GGI = [Ga]/([In] + [Ga])$ of 0.37 for the first set of samples and 0.3 for the second set. The $CGI = [Cu]/([In] + [Ga])$ is 0.84 for both sample sets as determined using energy-dispersive X-ray spectroscopy measurements. The GGI depth profile was determined using Glow Discharge Optical Emission Spectroscopy (GDOES) with a commercial GDA 750 of Spectrum Analytik GmbH. The substrate temperature was chosen to be 480 °C because higher average V_{OC} values were found at this temperature for Al/ITO-based back contacts.^[16] Directly after CIGSe growth, the samples were subjected to a 1 nm NaF post-deposition-treatment by thermal evaporation of NaF at a sample temperature of 450 °C without breaking the vacuum. The solar cells were finished by chemical bath deposition of ≈ 45 nm CdS, 123 nm i-ZnO sputtering, and 240 nm ITO sputtering. Small solar cells of ≈ 10 mm² area are defined by chemical etching of the front contact. For this purpose 10% HCl was applied manually to the front surface, locally removing the ITO/ZnO/CdS layers.

The finished solar cells were characterized using a home-built sun simulator using a halogen lamp. The intensity of the lamp was adjusted by matching the current of a Si reference solar cell to the current anticipated under AM1.5G conditions. EQE measurements were also investigated using a home-built system. Focus-ion-beam (FIB) preparation was carried out using a versa3D from FEI. The layer growth was computed separately for each layer using a self-written Fortran program. 3D finite-difference time-domain (FDTD) simulations were performed using the software package Meep.^[21]

3. Results and Discussion

3.1. Structure Transposition

As a result of the lift-off process, periodic openings in the SiO_2 layer are formed. These openings are surrounded by conical walls. The conical shape of the walls is due to the fact that the diameter of the pillars—consisting of photoresist plus SiO_2 deposit—grows upon prolonged SiO_2 deposition. As the pillars form a shadow for the SiO_2 deposition, the deposited sample surface decreases upon prolonged SiO_2 deposition. For large SiO_2 thickness, the conical walls form a sharp tip. This is the case for the 700 nm SiO_2 thickness in Figure 2. Having achieved these SiO_2 openings after lift-off, conformal coverage of the structured back contact would lead to a transposition of the structure to the successively deposited layers. In the lower row of Figure 2, SEM cross-sections of complete solar cells are shown. After Al and ITO deposition, the structure height appears to be transposed—meaning that there is no change in structure height and the structure is replicated. This is no longer the case for the CIGSe deposition. Here, the mobility of the deposited species on

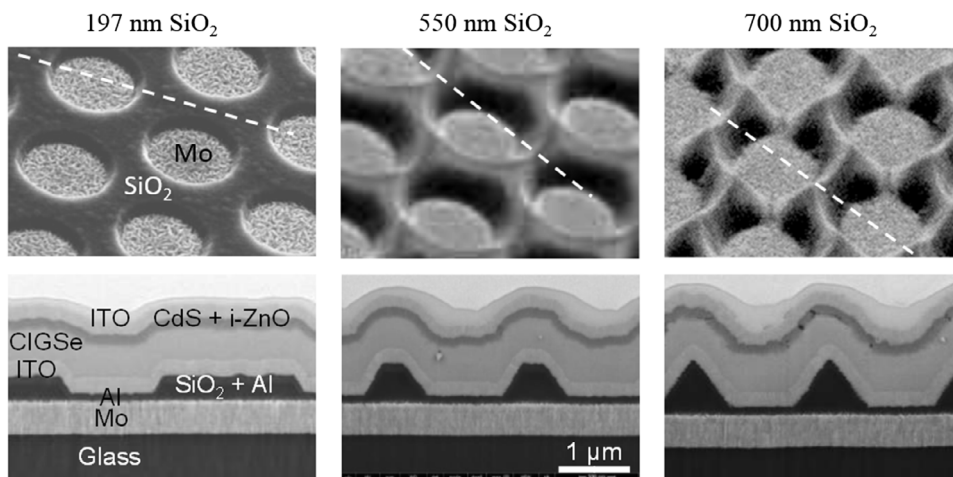


Figure 2. (Top) SEM images of structured SiO_2 layers on a molybdenum back contact for structure heights of 197, 550, and 700 nm. Dashed lines give the orientation of the cross-sections below. (Bottom) SEM images (tilt angle 52°) of FIB prepared cross-sections of the complete structures comprising molybdenum, SiO_2 , Al, ITO, CIGSe, CdS + i-ZnO, ITO. (The specimens were covered in addition by platinum to preserve the top layer from preferred ion etching.) Aluminum and SiO_2 appear with the same shade of gray and cannot be discriminated.

the growth surface may limit the structure transposition to some extent. For low SiO_2 thickness, conformal coverage is greatly achieved; the largest structure height of 700 nm shows a smoothing effect: the structure height of the CIGSe layer is less than of the Al back contact. Surface smoothing can be understood considering adatom surface diffusion^[22] and re-evaporation.^[23] The smoothing has to be considered in optical simulations. Nevertheless, a larger angle of the front interfaces is achieved with respect to the flat sample surface using higher SiO_2 structures. Therefore, incoming light will be scattered in larger angles. We note that the achieved structure is the geometric negative of the pillar structure in ref. [19] producing the same structure height.

The 3D structure of the samples was reconstructed using a self-written computer program with the following model. A sketch of the working principle of the model can be seen in Figure S1, Supporting Information. Two different growth modes were implemented. First, a growth purely in the normal direction of the flat substrate, and second, a growth in the normal direction of the inclined sample surface. In the following, these two growth modes will be denoted as vertical growth and normal growth. The growth of each material layer was described by a mixed growth mode of the two elementary growth modes. The nature of the growth progress can be tuned to mimic the real layer growth by manipulating the portions of the two elementary growth processes used in the calculation. The algorithm for this is the following: the two growth modes were applied in sequence, growing a larger number of sub-layers thinner than the targeted material layer. The resulting thickness of the newly modeled sub-layer is d_{normal} for normal growth and d_{vertical} for vertical growth. The fraction between these two quantities is defined by $\beta = d_{\text{normal}} / (d_{\text{normal}} + d_{\text{vertical}})$. The growth algorithm for each material layer is terminated when the total volume of the material matches the volume measured on the flat reference.

Using the SEM pictures, values for β were extracted for each material by visual comparison. A value of $\beta = 0.5$ was extracted

for CIGS and a value of $\beta = 0.3$ was determined for ZnO, both ITO layers, and Al. It must be noted that the determination for Al is especially error-prone due to its small thickness. No value could be extracted for CdS because the layer was difficult to identify in the SEM cross-sections. This also increases the uncertainty for the determination of β for both CIGSe and ZnO. Overall, a good match of the grown layers and the calculated ones could be achieved. Figure 1 is created from the calculated 3D structure for the solar cell with a 550 nm structure height. Sever et al. developed a calculation model for the layer growth on structured surfaces and used it for a thin-film Si solar cell.^[24] The calculation strategy using the two elementary growth modes connected by a parameter basically is identical to the one used there. Therefore, it is possible to compare the values, although the computational representation of the layers differs from the one used here. A value of $\beta = 0.2$ was found for ZnO and $\beta = 0.3$ for Si. Kovacic et al. applied this model onto a CIGSe absorber and obtained a value of $\beta = 0.3$ for CIGSe.^[20] Two remarks have to be made regarding the determined value for the CIGSe in our work. First, the CIGSe top interface has an additional random structure caused by the crystal size which makes it difficult to determine a precise value for β . An absolute error for β of 0.1 is therefore estimated. Second, the exact growth of the CIGSe is possibly process dependent, e.g., the process temperature affects atom diffusion and crystal size during the deposition process.

3.2. Solar Cell Performance

Figure 3 shows the solar cell parameters for both sample sets. Only the values of the best solar cell for each sample are shown. The results for a 700 nm structure are omitted, due to strong shunting of this sample. Because of this observation, this sample thickness was not repeated in sample set 2. This shunting could be caused by pinholes in the CIGSe layer of this structure. A possible cause could be a cracking of the CIGSe layer at the sharp top edge of these samples caused by mechanical stress through

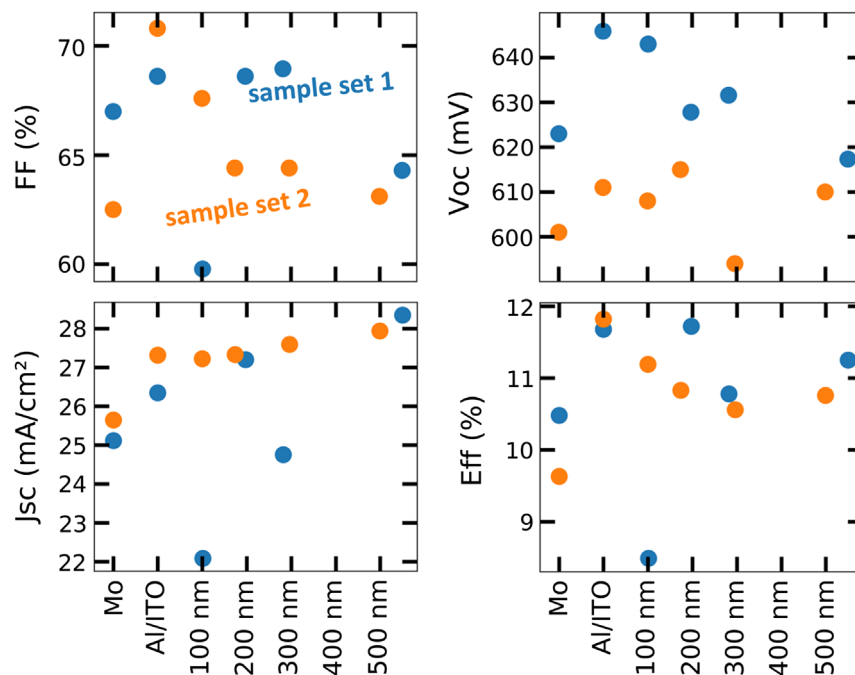


Figure 3. Solar cell parameters of reference sample with Mo back contact, a sample with flat Al/ITO back contact, and structured back contacts with different SiO₂ layer thicknesses for sample sets 1 and 2.

different thermal expansion coefficients of the different materials. However, no such thing was observable from SEM cross-sections.

The FF and V_{oc} values are obtained from J - V measurements. The J_{sc} values are calculated from the EQE curves using the tabulated AM1.5G spectrum. Samples of the sample set 1, in general, show a higher V_{oc} than the samples of the second set. This could be explained by the higher GGI of set 1 or by a better absorber quality. The different GGI gradients as determined by GDOES measurements are shown in Figure S2, Supporting Information. The samples with Al/ITO back contact for most samples show a higher V_{oc} compared with the respective Mo reference. A similar result has been reported in ref. [16], although there the V_{oc} difference was more pronounced. Representative J - V curves are shown in Figure S3, Supporting Information. The shunt resistance determined from the dark J - V curves is above $20 \text{ k}\Omega \text{ cm}^2$ for all solar cells. Despite this high shunt resistance, a small slope can be seen in the illuminated J - V -curves for 0 V. This indicates problems with carrier collection. A relatively strong crossover can be seen when comparing the dark with the illuminated case. Those effects are visible independent of the used back contact. No trend can be seen for both V_{oc} and the FF when comparing different structure heights.

Regarding J_{sc} , however, a clear trend is visible: the flat Al/ITO samples show an increased J_{sc} of 1.2 and 1.7 mA cm^{-2} compared with the Mo sample. In combination with the structured back contact, J_{sc} further increases. This gain increases with increasing structure height. For the 500 nm structures, a total gain of 3.2 and 2.3 mA cm^{-2} is achieved compared with their corresponding Mo references. Two outliers from this trend can be seen in sample set 1. By optical inspection, the 101 nm sample appears to exhibit an incomplete lift-off of the photoresist

pillars. Its poor FF and J_{sc} may be explained by photoresist remainings. A similar problem could also explain the poor performance of the 282 nm sample of sample set 1.

The overall efficiency is not increased by the structuring process. Almost all structured solar cells display a decreased efficiency compared to their corresponding flat reference with Al/ITO back contact. The increased J_{sc} caused by structuring is offset by losses in the other PV-parameters. The sample number is, however, too low to conclusively state if the losses in FF and V_{oc} are systematic or if they are caused by the additional handling involved compared with their flat references. The comparison of the flat substrates shows an absolute increase in efficiency of 1.2% for sample set 1 and 2.2% for sample set 2 when comparing the Al/ITO back contact with the corresponding Mo reference. The Al/ITO reference cell of sample set 2 shows the highest efficiency of 11.8%.

Figure 4 shows the measured EQE curves for both sample sets. A solar cell with Mo back contact and the same window structure but with a $2.8 \mu\text{m}$ absorber is also given for comparison. Experimental details of the sample preparation for this specific sample are given in the Supporting Information. The unstructured solar cells with Al/ITO rear contact show a distinct peak at $\approx 900 \text{ nm}$. This peak is due to an increased light absorption within the absorber layer caused by interference of light entering the solar cell with light reflected at the back contact. The 900 nm peak disappears with increasing structuring height. A second peak is visible for the flat sample of set 2 at 820 nm. The curves for the 101 and 282 nm samples of set 1 both show a decreased EQE over the full spectra (the complete data set is given in Figure S4, Supporting Information). This could hint to electrical problems caused by an incomplete lift-off. For wavelengths above 900 nm, an increase in the EQE is visible with

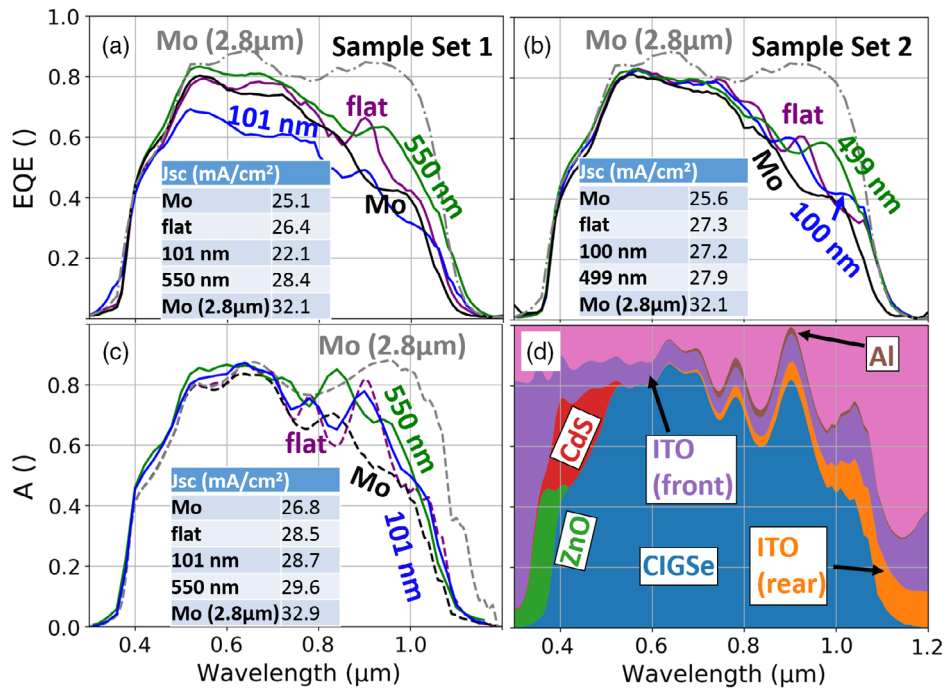


Figure 4. EQE of solar cells with different back contacts for a) sample set 1 and b) sample set 2. An additional CIGSe solar cell with a 2.8 μm absorber and a Mo back contact is shown in both figures for comparison. c) Calculated absorption within the CIGSe layer of a complete solar cell. The dashed lines are calculated using the transfer-matrix-method for an unstructured sample with an Al/ITO back contact (purple), a Mo back contact (black), and a solar cell with Mo back contact with a 2.8 μm absorber (gray). The other curves are from FDTD calculations for the structural dimensions of sample set 1. d) Calculated relative absorption within the separate solar cell layers for an unstructured solar cell with Al/ITO back contact. (The complete EQE measurements and simulations can be found in the Figure S1, Supporting Information).

increasing structure height. This trend is better visible for sample set 2. A small increase in the EQE with increasing structure height is also visible for shorter wavelengths around 600 nm. This could be caused by reduced reflectance at the front interface by the structure. In addition, layer thickness variation of the CdS between different samples can cause a difference for short wavelengths. The best structure reaches about 88% of the J_{SC} value of the given 2.8 μm absorber thickness reference. The band gap of the Al/ITO-based solar cells appears to be lower in comparison to the Mo-based samples. As shown later in the next section, these differences can be explained by optical simulations. The EQE curves of sample set 1 show overall more variation over the whole spectral range. These differences could be explained by a partial unsuccessful lift-off process which is related to the failure of the 101 nm structure. The results of set 2 are therefore probably more representative for the actual influence of the structures on the EQE.

The gain in J_{SC} due to the combination of reflectance and scattering is slightly below the gain in ref. [19], however there, the CIGSe thickness was only 390 nm. This proves the working principle of integration of optical scattering and reflectance in a thin-film solar cell.

3.3. Optical Simulations

For the FDTD simulations, structure models based on sample set 1 were constructed according to the method described in

Section 3.1. The GGI profile extracted from GDOES measurements given in Figure S2, Supporting Information, was implemented in the simulations. For 1D and 3D simulations, the GGI gradient was implemented by dividing the CIGS layer into sub-layers with different GGI according to the GGI gradient. The optical data for an arbitrary GGI value was interpolated from the optical properties found in ref. [25]. The optical coefficients were extracted for both ITO layers as described in ref. [16]. The optical data for the other layers are taken from the literature.^[25–27] The local absorption was calculated for the two polarization directions in x and y direction (the x - and y -axis are defined in Figure 1). The overall absorption was calculated by summing up the local absorptions of the two polarizations. In general, the difference in global absorption in the CIGSe layer for the two polarizations was found to be very small (<0.01%) for all wavelengths. The calculated wavelength-dependent absorption within the CIGSe layer is plotted in Figure 4c. Reference curves were calculated in 1D using the transfer-matrix-method for the unstructured solar cell with Al/ITO back contact as well as for two solar cells with Mo back contact having an absorber thickness of 0.6 and 2.8 μm. These are also given in Figure 4c. The overall shapes of the calculated absorption curves are in close agreement to the corresponding EQE spectra, with the exception of a peak at 820 nm, which is visible for the 550 nm structure in simulations but does not appear in the experiment. This peak might be visible in the 499 nm structure of sample set 2. The previously mentioned apparent difference between the band gaps of samples with Mo back contact in comparison to samples with Al/ITO

back contact is also visible in the simulations. This difference can, therefore, be explained by an increased absorption for the Al/ITO back-contact samples in comparison to the Mo back-contact samples. The peaks are generally more pronounced in the simulations than in the experiment, with EQE values generally lower than the calculated absorption at the peak positions. This can be explained to some extent by the additional random structure caused by the crystal structure of the layers. This structure will apply some additional random scattering and therefore reduce the sharpness of interference peaks. 2D FDTD simulations have been performed additionally to estimate the influence of this surface roughness, which is not included in the other simulations. The layer interfaces were directly extracted from SEM cross-sections. A constant GGI of 0.37 was used for simplicity. The results can be seen in Figure S5, Supporting Information. The reduced peak height in the experiment can only be explained to a smaller degree by surface roughness caused by the crystal size of the layer. The rest of the difference could be related to recombination losses including back-contact recombination losses. In addition, some discrepancies can be seen at around 620 nm with lower EQE values than for the calculated absorption. Theoretically, the overall absorption of all samples should be similar to the 2.8 μm sample in this range. Most of the absorption will happen near the front interface in this wavelength range. Those losses could be therefore related to bulk recombination and recombination within the p-n junction. Further experiments are necessary to understand the electrical losses. In particular, the back-contact recombination velocity for the Al/ITO back contact needs to be determined. The J_{SC} values derived from the EQE are lower by 1.7 mA cm^{-2} for the Mo sample, 2.1 mA cm^{-2} for the Al/ITO sample, and 1.2 mA cm^{-2} for the 550 nm sample compared with the obtained J_{SC} values. Those differences are caused by electrical losses as well as by errors of the simulation caused, for example, by the usage of tabulated CIGSe material properties which may differ from the material properties of the CIGSe used in the experiment. In addition, the values are probably underestimated to some degree by the reduced reflectance through the front surface structuring as seen in Figure S5, Supporting Information.

In summary, the simulation show some additional absorption for shorter wavelength when the SiO_2 structures are added, which are probably related to a decreased front-side reflectivity.

This effect can however not be observed in the EQE results of sample set 2. Therefore, this effect may be overemphasized by the simulation because the sample roughness caused by the crystal size is not considered. This roughness for itself already leads to a reduced reflectance as can be seen in Figure S5, Supporting Information. Most of the experimental gains are seen for longer wavelengths. Therefore, it is likely that a light-path enhancement by scattering is the main cause for the increased short-circuit current by the structure. Compared to a simulated solar cell with 2.8 μm CIGSe layer thickness, 88% of the current density can be achieved with the integrated structured back reflector using 550 nm structure height.

Figure 5a,b shows the local absorption for a solar cell with a 550 nm structure height at a wavelength of 940 nm. The respective plot for the unstructured sample is shown in Figure 5c for comparison. Locally increased absorption caused by interference is visible in the unstructured case. This local absorption is enhanced for the structured case by additional local maxima in the heights of the structure. On the other hand, in the valley, the CIGSe layer exhibits a decreased absorption. Both observations can be explained by scattering of light at the front interface of the structure. Light is scattered from the “valley-region” to the height region. The additional path length through the CIGSe layer caused by the increased angles to the surface normal may already explain the increase in absorption. The portion of the front interface which is curved instead of flat increases with increasing structure height. Therefore, this scattering effect is more pronounced for higher structures. In addition, a smaller region of increased absorption is found in the center of the valley. This local field enhancement is probably caused by light coming directly from the front interface, interacting with light reflected at the conical walls. Overall, this inhomogeneous absorption can lead to regions of the solar cell operating under different illumination conditions. This could have a negative influence on the solar cell parameter. The significance of this is however unclear.

Figure 4d shows the absorption within the different solar cell layers. There are two strong absorption losses related to the non-optimized ITO used in our laboratory. Parasitic absorption occurs in the front ITO for a wide wavelength range. In addition, parasitic absorption occurs within the rear ITO at long wavelengths. This limits the possible gain achievable through the

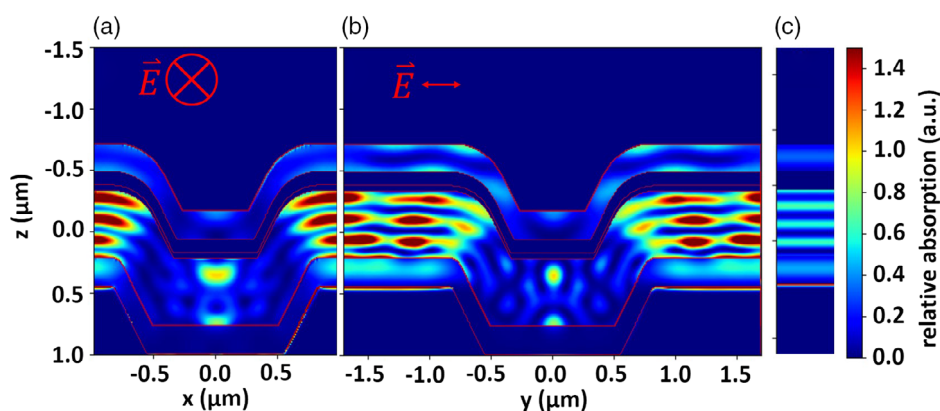


Figure 5. a,b) Calculated local absorption within a solar cell corresponding to the 550 nm structure height sample from sample set 1. The used axes are shown in Figure 1. c) The same data calculated for a flat solar cell with the same layer thicknesses. All pictures share the same color scale, which shows the local absorption within a volume element in arbitrary units.

structuring and could be mitigated by improved material properties and parameters. The relative parasitic absorption of the incoming solar energy within the rear ITO layer, for energies below the bandgap of the CIGSe, was calculated to 3.8% in the flat case, 3.8% for the 101 nm structure, and 4.2% for the 550 nm structure. As experimentally shown in ref. [16], a decrease in the ITO rear thickness from 200 to 100 nm leads to an increased J_{SC} of 0.5 mA cm^{-2} already in the unstructured case.

The simulations of Kovacic et al. on 2D sine-like structures with highly reflective back contact but without parasitic absorption in the rear oxide layer showed the highest increase in J_{SC} for a pitch of $0.8 \mu\text{m}$ and 300 nm structure height.^[20] This suggests that smaller pitches than the here used $1.96 \mu\text{m}$ may lead to higher J_{SC} values. However, absorption effects in the diffusion barrier material ITO layer need to be considered, which may also influence the optimum structure. This optimal structure must confine the light inside the CIGSe without increasing the parasitic ITO absorption.

4. Conclusions

CIGSe solar cells with Al/ITO back reflector were successfully prepared on a nanostructured substrate. Compared with the Mo reference cell, an increase in J_{SC} up to 3.2 mA cm^{-2} was obtained by combining both the Al/ITO back contact and the rear nanostructuring. The I - V curves show further, that the average V_{oc} is increased by $\approx 20 \text{ mV}$ when an Al/ITO back contact is used instead of the standard Mo back contact for 600 nm thick CIGSe. The growth of the solar cell layers was studied using SEM cross-sections. The overall structure is only partly transposed to the front side of the solar cell. A simple model was used to reconstruct the layers in 3D. 3D optical simulations were used to calculate the changes in absorption within the CIGSe layer. A good match was found between simulations and experimental EQE curves. The simulations reveal that further optical gain can be achieved by reduced parasitic absorption within the ITO layers. Compared to a $2.8 \mu\text{m}$ CIGSe solar cell with Mo rear contact and the same window layers, the best structure reaches according to experiment already 88% of the J_{SC} value. It is expected that this value can be further improved by both reducing the ITO diffusion barrier thickness and through optimization of the structural dimension of the rear nanostructure.

Supporting Information

Supporting Information is available from the Wiley Online Library or from the author.

Acknowledgements

The authors gratefully acknowledge the funding through the BMBF project StrukturSolarII (Nr: 03EK3570B). Open-access funding enabled and organized by Projekt DEAL.

Conflict of Interest

The authors declare no conflict of interest.

Keywords

alternative back contacts, layer growth, optical simulations, ultrathin CIGSe solar cells

Received: June 10, 2020

Revised: July 28, 2020

Published online: August 13, 2020

- [1] L. M. Mansfield, A. Kanevce, S. P. Harvey, K. Bowers, C. Beall, S. Glynn, I. L. Repins, *Prog. Photovoltaics* **2018**, *26*, 949.
- [2] R. Scheer, H.-W. Schock, *Chalcogenide Photovoltaics – Physics, Technologies, and Thin Film Devices*, Wiley VCH, Weinheim **2011**.
- [3] J. Goffard, C. Colin, F. Mollica, A. Cattoni, C. Sauvan, P. Lalanne, J. Guillemoles, N. Naghavi, S. Collin, *IEEE J. Photovoltaics* **2017**, *7*, 1433.
- [4] J. Krc, M. Sever, A. Campa, Z. Lokar, B. Lipovsek, M. Topic, *Thin Solid Films* **2017**, *633*, 193.
- [5] E. Jarzembowski, F. Syrowatka, K. Kaufmann, W. Fränzel, T. Hölscher, R. Scheer, *Appl. Phys. Lett.* **2015**, *107*, 051601.
- [6] B. Vermang, J. T. Wätjen, V. Fjällström, F. Rostvall, M. Edoff, R. Gunnarsson, I. Pilch, U. Helmersson, R. Kotipalli, F. Henry, D. Flandre, *Thin Solid Films* **2014**, *582*, 300.
- [7] G. Birant, J. D. Wild, M. Meuris, J. Poortmans, B. Vermang, *Appl. Sci.* **2019**, *9*, 677.
- [8] E. Jarzembowski, B. Fuhrmann, H. Leipner, W. Fränzel, R. Scheer, *Thin Solid Films* **2017**, *633*, 61.
- [9] J. Malmström, S. Schleussner, L. Stolt, *Appl. Phys. Lett.* **2004**, *85*, 2634.
- [10] Z. J. Li-Kao, N. Naghavi, F. Erfurth, J. F. Guillemoles, I. Gérard, A. Etcheberry, J. L. Pelouard, S. Collin, G. Voorwinden, D. Lincot, *Prog. Photovoltaics* **2012**, *20*, 582.
- [11] K. Orgassa, H. W. Schock, J. H. Werner, *Thin Solid Films* **2003**, *387*, 431.
- [12] B. Bissig, R. Carron, L. Greuter, S. Nishiwaki, E. Avancini, C. Andres, T. Feurer, S. Buechler, A. Tiwari, *Prog. Photocool. Res. Appl.* **2018**, *26*, 894.
- [13] T. Nakada, Y. Hirabayashi, T. Tokado, D. Ohmori, T. Mise, *Solar Energy* **2004**, *77*, 739.
- [14] C. M. Liu, W. L. Liu, W. J. Chen, S. H. Hsieh, T. K. Tsai, L. C. Yang, *J. Electrochem. Soc.* **2005**, *152*, 234.
- [15] L. Gouillart, A. Cattoni, J. Goffard, F. Donsanti, G. Patriarche, M. Jubault, N. Naghavi, S. Collin, *Thin Solid Films* **2019**, *672*, 1.
- [16] T. Schneider, R. Scheer, in *Proc. 36th European Photovoltaic Solar Energy Conf.*, WIP Wirtschaft und Infrastruktur GmbH & Co Planungs KG, Marseille, France **2019**, p. 684.
- [17] J. Keller, W.-C. Chen, L. Riekehr, T. Kubart, T. Törndahl, M. Edoff, *Prog. Photovoltaics* **2018**, *26*, 846.
- [18] E. Yablonoitch, *J. Opt. Soc. Am.* **1982**, *72*, 899.
- [19] G. Yin, M. W. Knight, M.-C. van Lare, M. M. Solà Garcia, A. Polman, M. Schmid, *Adv. Opt. Mat.*, **2017**, *5*, 1600637.
- [20] M. Kovacic, J. Krc, B. Lipovsek, W.-C. Chen, M. Edoff, P. J. Bolt, J. van Deelen, M. Zhukova, J. Lontchi, D. Flandre, P. Salomé, M. Topic, in *36th European Photovoltaic Solar Energy Conf.*, **2019**, p. 654.
- [21] A. Oskooi, D. Roundy, M. Ibanescu, P. Bermel, J. D. Joannopoulos, S. G. Johnson, *Comput. Phys. Commun.* **2010**, *181*, 687.
- [22] T. B. T. To, V. B. de Sousa, F. D. A. Aarão Reis, *Phys. A* **2018**, *511*, 240.
- [23] T. Karabacak, *J. Nanophoton.* **2011**, *5*, 052501.
- [24] M. Sever, J. Krč, M. Topič, *Thin Solid Films* **2014**, *573*, 176.
- [25] G. Yin, Ph.D Thesis, Technical University of Berlin, **2015**.
- [26] K. M. McPeak, S. V. Jayanti, S. J. P. Kress, S. Meyer, S. Iotti, A. Rossinelli, D. J. Norris, *ACS hotonics*, **2015**, *2*, 326.
- [27] K. Orgassa, *Coherent Optical Analysis Of The ZnO/Cds/Cu(In,Ga)Se2 Thin Film Solar Cell*, Shaker Verlag, Aachen **2004**.

Femtosecond laser-written high-efficiency blazed phase gratings in the volume of soda lime glass for light management in solar modules

Markus Muchow,^{1,2} Torsten Büchner,^{2,3,4} Alexander Sprafke,⁵ and Gerhard Seifert^{2,3,6,*}

¹Anhalt University of Applied Science, Electrical and Electronic Engineering, Mechanical and Industrial Engineering, Bernburger Str. 57, 06366 Köthen, Germany

²Centre of Innovation Competence SiLi-nano, Martin Luther University Halle-Wittenberg, Karl-Freiherr-von-Fritsch-Str. 3, 06120 Halle (Saale), Germany

³Fraunhofer-Center for Silicon-Photovoltaics CSP, Otto-Eißfeldt-Str. 12, 06120 Halle (Saale), Germany

⁴now with: boraident GmbH – Nano-Technologies in Glass, Koethener Str. 33a, 06118 Halle (Saale), Germany

⁵Martin Luther University Halle-Wittenberg, Institute of Physics, μ MD Group, Heinrich-Damerow-Straße 4, 06120 Halle, Germany

⁶Fraunhofer-Institute for Silicate Research ISC, Gottlieb-Keim-Str. 62, 95448 Bayreuth, Germany
[*gerhard.seifert@physik.uni-halle.de](mailto:gerhard.seifert@physik.uni-halle.de)

Abstract: Highly efficient volume phase gratings have been fabricated in low-iron soda lime glass using femtosecond (fs) laser pulses with 1030 nm wavelength and 270 fs pulse duration. Optical simulations based on rigorous coupled-wave analysis theory were performed to determine optimal grating parameters and designs for the application of the gratings for light management in solar modules, suggesting a very effective blazed-like design. Several of such blazed phase gratings have been fabricated and analyzed by measuring their diffraction efficiencies into first and higher orders. Up to 77% of the incoming light in the wavelength region relevant for silicon-based photovoltaics were diffracted by these gratings. Typical induced refractive index changes between 0.002 and 0.006 were derived by comparing the experimental efficiencies with the simulation results.

©2015 Optical Society of America

OCIS codes: (050.1950) Diffraction gratings; (050.7330) Volume gratings; (320.7130) Ultrafast processes in condensed matter, including semiconductors; (140.3390) Laser materials processing; (320.7090) Ultrafast lasers.

References and links

1. T. Yamada, H. Nakamura, T. Sugiura, K. Sakuta, and K. Kurokawa, "Reflection loss analysis by optical modeling of PV module," *Sol. Energy Mater. Sol. Cells* **67**(1), 405–413 (2001).
2. J. Schneider, M. Turek, M. Dyrba, I. Baumann, B. Koll, and T. Booz, "Combined effect of light harvesting strings, anti-reflective coating, thin glass, and high ultraviolet transmission encapsulant to reduce optical losses in solar modules," *Prog. Photovolt. Res. Appl.* **22**(7), 830–837 (2014).
3. J. Müller, B. Rech, J. Springer, and M. Vanecek, "TCO and light trapping in silicon thin film solar cells," *Sol. Energy* **77**(6), 917–930 (2004).
4. G. Seifert, I. Schwedler, J. Schneider, and R. B. Wehrspohn, "Light management in solar modules," in *Photon Management in Solar Cells*, eds. R.B. Wehrspohn, U. Rau, A. Gombert (Wiley-VCH 2015), pp. 323–347.
5. J. Jaus, M. Duell, J. Eckert, F. Adurodija, B. Li, R. A. Mickiewicz, and D. M. Doble, "Approaches to improving energy yield from PV modules," *Proc. SPIE* **7773**, 77730S (2010).
6. L. Kuna, G. C. Eder, C. Leiner, and G. Peharz, "Reducing shadowing losses with femtosecond-laserwritten deflective optical elements in the bulk of EVA encapsulation," *Prog. Photovolt. Res. Appl.* **23**(9), 1120–1130 (2015).
7. E. N. Glezer, M. Milosavljevic, L. Huang, R. J. Finlay, T.-H. Her, J. P. Callan, and E. Mazur, "Three-dimensional optical storage inside transparent materials," *Opt. Lett.* **21**(24), 2023–2025 (1996).
8. W. Watanabe, T. Toma, K. Yamada, J. Nishii, K. Hayashi, and K. Itoh, "Optical seizing and merging of voids in silica glass with infrared femtosecond laser pulses," *Opt. Lett.* **25**(22), 1669–1671 (2000).
9. S. Richter, S. Döring, A. Tünnermann, and S. Nolte, "Bonding of glass with femtosecond laser pulses at high repetition rates," *Appl. Phys. A* **103**(2), 257–261 (2011).
10. I. Miyamoto, A. Horn, J. Gottmann, D. Wortmann, and F. Yoshino, "Fusion welding of glass using femtosecond laser pulses with high-repetition rates," *J. Laser Micro/Nanoeng.* **2**(1), 57–63 (2007).
11. T. Tamaki, W. Watanabe, J. Nishii, and K. Itoh, "Welding of transparent materials using femtosecond laser pulses," *Jpn. J. Appl. Phys.* **44**(5), L687–L689 (2005).

#251568

© 2015 OSA

Received 21 Oct 2015; revised 2 Dec 2015; accepted 2 Dec 2015; published 18 Dec 2015

28 Dec 2015 | Vol. 23, No. 26 | DOI:10.1364/OE.23.033540 | OPTICS EXPRESS 33540

12. K. M. Davis, K. Miura, N. Sugimoto, and K. Hirao, "Writing waveguides in glass with a femtosecond laser," *Opt. Lett.* **21**(21), 1729–1731 (1996).
13. C. Hnatovsky, R. S. Taylor, E. Simova, P. P. Rajeev, D. M. Rayner, V. R. Bhardwaj, and P. B. Corkum, "Fabrication of microchannels in glass using focused femtosecond laser radiation and selective chemical etching," *Appl. Phys., A Mater. Sci. Process.* **84**(1–2), 47–61 (2006).
14. D. Wortmann, J. Gottmann, N. Brandt, and H. Horn-Solle, "Micro- and nanostructures inside sapphire by fs-laser irradiation and selective etching," *Opt. Express* **16**(3), 1517–1522 (2008).
15. C. Voigtländer, D. Richter, J. Thomas, A. Tünnermann, and S. Nolte, "Inscription of high contrast volume Bragg gratings in fused silica with femtosecond laser pulses," *Appl. Phys., A Mater. Sci. Process.* **102**(1), 35–38 (2011).
16. I. V. Ciapurin, L. B. Glebov, and V. I. Smirnov, "Modeling of phase volume diffractive gratings, part 1: transmitting sinusoidal uniform gratings," *Opt. Eng.* **45**(1), 015802 (2006).
17. T. Clausnitzer, T. Kämpfe, F. Brückner, R. Heinze, E. B. Kley, A. Tünnermann, O. Parriaux, and A. V. Tishchenko, "Highly dispersive dielectric transmission gratings with 100% diffraction efficiency," *Proc. SPIE* **6883**, 68830U (2008).
18. J. W. Chan, T. R. Huser, S. H. Risbud, and D. M. Krol, "Modification of the fused silica glass network associated with waveguide fabrication using femtosecond laser pulses," *Appl. Phys., A Mater. Sci. Process.* **76**(3), 367–372 (2003).
19. W. Watanabe, T. Tamaki, Y. Ozeki, and K. Itoh, *Progress in Ultrafast Intense Laser Science VI* (Springer Berlin Heidelberg, 2010), Ch. 9.
20. V. Liu and S. Fan, "S⁴: A free electromagnetic solver for layered periodic structures," *Comput. Phys. Commun.* **183**(10), 2233–2244 (2012).
21. M. G. Moharam, T. K. Gaylord, and R. Magnusson, "Criteria for Raman-Nath regime diffraction by phase gratings," *Opt. Commun.* **32**(1), 19–23 (1980).
22. M. Muchow, T. Büchner, and G. Seifert, "Femtosecond laser-induced optical microstructures inside glass volume for light management in solar modules," in *Proc. of 29th EU PVSEC* (2014), pp. 214–217.
23. D. M. Krol, "Femtosecond laser modification of glass," *J. Non-Cryst. Solids* **354**(2), 416–424 (2008).
24. R. Berlich, J. Choi, C. Mazuir, W. V. Schoenfeld, S. Nolte, and M. Richardson, "Spatially resolved measurement of femtosecond laser induced refractive index changes in transparent materials," *Opt. Lett.* **37**(14), 3003–3005 (2012).
25. S. M. Eaton, M. L. Ng, R. Osellame, and P. R. Herman, "High refractive index contrast in fused silica waveguides by tightly focused, high-repetition rate femtosecond laser," *J. Non-Cryst. Solids* **357**(11), 2387–2391 (2011).
26. F. Hashimoto, T. Yoshino, Y. Ozeki, and K. Itoh, "Large increase in refractive index inside silica glass after the movement of voids caused by femtosecond laser pulses," *Jpn. J. Appl. Phys.* **53**(4), 042601 (2014).

1. Introduction

Light management approaches are crucial to further increase the efficiency of photovoltaic devices [1–3]. One topic that is currently under investigation within the research community is the optimization of light management in solar modules, i.e. to redirect light that is incident on optically non-active module components, such as front side contacts, to the area of the solar cell absorber material [4]. Currently, the photovoltaic market is dominated by crystalline silicon solar cells with front side metallization. The front contacting scheme usually consists of three bus bars (width of about 1 - 2 mm) and grid fingers (width of about 50 - 100 μm) that together cover 5-10% of the active cell area causing shadowing of the absorber material. Furthermore, light impinging onto the spaces between adjacent cells of the module is usually lost for the solar-to-electrical power generation, too. A promising approach to redirect this light to the absorber material is to apply appropriate diffractive microstructures to the part of the solar modules above the cells, i.e. the encapsulation foil or the cover glass [5] like shown schematically in Fig. 1. Recently, volume optics within the EVA polymer encapsulation fabricated by fs laser pulses have been demonstrated [6].

However, when considering long-term stability or vertical distance to the absorber material, it appears advantageous to create diffractive microstructures by fs laser irradiation in the cover glass rather than in the encapsulation polymer.

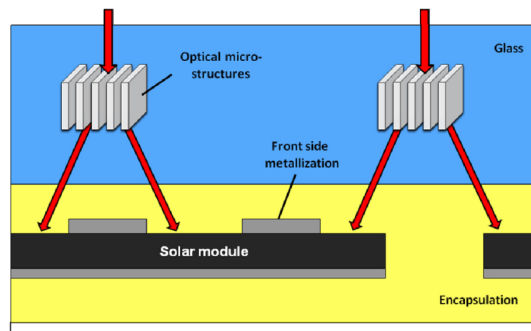


Fig. 1. Sketch of optical microstructures and the light management in a solar module around the front side metallization.

A lot of work has been done on volume modification of transparent dielectrics using focused ultrashort laser pulses. Various interesting applications such as optical memory [7,8], microwelding [9–11], waveguide formation [12] and selective etching [13,14] have been investigated. Furthermore, modifications in fused silica arranged as volume bragg gratings with low grating periods and high period stability were investigated for use as reflection elements [15–17]. From this work, it is well-known that laser-induced nonlinear processes on the molecular scale in glass have the potential to create pure refractive index changes of long-term stability. With properly chosen laser parameters, focused fs pulses can generate an electron plasma in the focal volume, inducing a permanent structural change on the molecular level. In fused silica, for instance, the large molecular ring structures composed of several SiO₂ molecules can break and recombine into smaller rings, thereby increasing both density and refractive index locally [18]. Filamentations, occurring as a result of the dynamic balance between self-focusing through Kerr-effect and defocusing through the created electron plasma [19], can be utilized to generate structural modifications with lengths far beyond the Rayleigh length of the laser beam.

In this study, we follow this approach by fabricating high-efficient phase gratings with fs laser pulses inside soda lime glass with the goal to reduce optical losses in solar modules by redirecting the incoming light onto the active area of standard silicon solar cells. Optical simulations based on rigorous coupled-wave analysis (RCWA) theory were performed to determine efficient phase grating designs and parameters. Optimized diffraction gratings were then inscribed with a fs laser into the glass and characterized. The induced refractive index changes were determined by comparing the diffraction efficiencies of the fabricated phase grating with the simulation results.

2. Experimental

The phase gratings have been fabricated using a Yb:KGW laser system (PHAROS, LightConversion) emitting 270 fs laser pulses with a wavelength of 1030 nm. The laser features a maximum repetition rate of 350 kHz; for this study, the repetition rate was set to 20 kHz. The Gaussian fs laser pulses were focused in the volume of 3.2 mm thick low iron soda lime glass (used as front glass in solar modules and provided by f | solar GmbH) using either an aspherical lens (AL) with numerical aperture (NA) of 0.4 or 0.5, or a 63x microscope objective (MO) with a NA of 0.65 was used. The focussing optic is mounted above a motorised xy-table (maximum speed: 100 mm/s, step resolution: 0.5 μm) with vacuum chuck which positioned and fixed the glass substrate samples. Laser pulse energy was varied using an adjustable $\lambda/2$ plate combined with a thin film polariser, hence the polarisation of the incoming laser light hitting the sample was linear. The focus position could be varied to arbitrary depths in the glass volume. The induced micromodifications in the glass were characterized using an optical microscope in phase contrast mode (Olympus BX61).

The length of the refractive index changes, with a typical diameter of 2 – 3 μm , was varied within a range from 25 to 150 μm in a depth of 650 μm into the glass by changing the laser pulse energy, see Fig. 2(a). The influence of spherical aberration on the modification length was taken into account. The modification thresholds for persistent refractive index changes were found to be at around 1 μJ for a single fs laser pulse, depending only slightly on the used focusing optics. The lengths of the modification increased with higher pulse energies until reaching a saturation level between 100 and 150 μm at 6 – 11 μJ . In Fig. 2(b) an optical micrograph cross section of single modifications is shown.

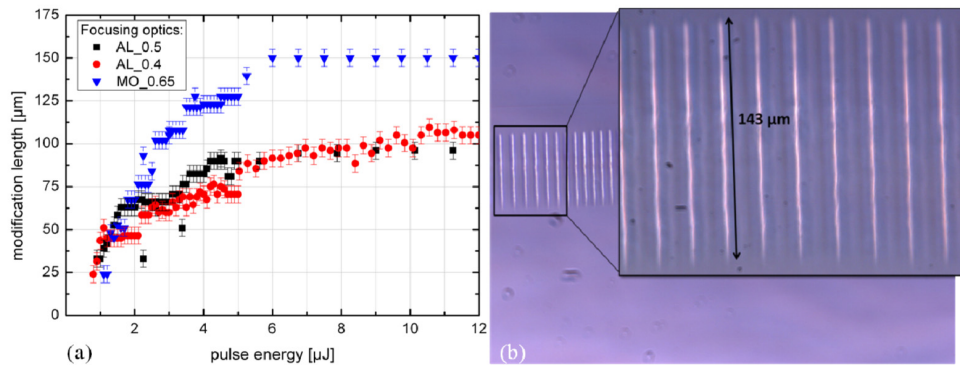


Fig. 2. (a) Pulse energy dependence of induced modification length for three different focusing optics (b) Phase contrast microscope image of a cross section of induced refractive index changes.

In the results presented in this work, the laser repetition rate was set to 20 kHz. A dedicated computer program was used for the irradiation which controls the translation stage and the electronic laser shutter in a way that the shutter is opened while the stage with the mounted sample is moved. By partially overlapping subsequent single fs laser pulses in one dimension with a stage speed of 20 mm/s resulting in a pulse-to-pulse distance of 1 μm , we were able to induce refractive index changes that form a one dimensional phase grating, see sketch in Fig. 3(a). Writing a large number of such parallel, equally spaced lines into the glass volume, phase gratings could be fabricated. The diffraction efficiencies of the phase gratings were measured using a CCD camera by comparing the light intensity I_0 after passing through unstructured glass and the intensity of the 0th diffraction order $I^{0\text{th}}$ after passing through the phase grating. The intensity difference ($I_0 - I^{0\text{th}}$) is apparently equal to the sum of intensities diffracted into higher orders of diffraction when only a negligible difference in reflection between treated and untreated glass is existent. In this study the change in reflection between unirradiated regions and areas containing phase gratings was measured to be $< 1\%$, validating the above assumption of low reflection. In this work, we will usually discuss the diffraction efficiency defined as

$$\eta_D(\lambda) = \frac{I_0(\lambda) - I^{0\text{th}}(\lambda)}{I_0(\lambda)} \quad (1)$$

Laser diodes with wavelengths of 405, 514, 635 and 785 nm have been used in connection with isotropic optical fibers to characterize the diffraction efficiencies of the fabricated gratings in the wavelength region interesting for photovoltaic use. The illumination was checked for equal intensity in p- and s- polarization with respect to the grating orientation in all cases to ensure comparability with the numerical simulations (see below).

3. Results and discussion

3.1 Simulation results

In our study we performed optical simulations based on rigorous coupled-wave analysis (RCWA), also called Fourier Model Method (FMM), using a freely available software package [20] to determine efficient phase grating parameters. The package solves Maxwell's equations in layered periodic structures and the results contain the spectra for the different diffraction orders. Our first approach for the simulations were rather 'simple' 1D phase gratings, which can be characterized by the following parameters: induced refractive index Δn , modification length l , grating period a , modification width b , see Fig. 3(a). The refractive index of the unmodified soda lime glass was determined to 1.52 by transmission and reflection measurements,; the incidence angle was kept constant at 0° in the simulations while the wavelength of the incoming plane wave has been varied. Every calculation has been conducted for s- and p-polarized incoming light, then summed up and normalized. As a typical and instructive example, a phase grating with parameters $a = 6 \mu\text{m}$, $b = 3 \mu\text{m}$, and $\lambda = 785 \text{ nm}$ has been chosen. The diffraction efficiency η_D (see Eq. (1)) was calculated in dependence of modification length ($l = 0 \dots 300 \mu\text{m}$), and refractive index change ($\Delta n = 0.001 \dots 0.01$). The results are given as a contour plot in Fig. 3(b), where the colour coding for η_D is given as legend at the right side of the figure.

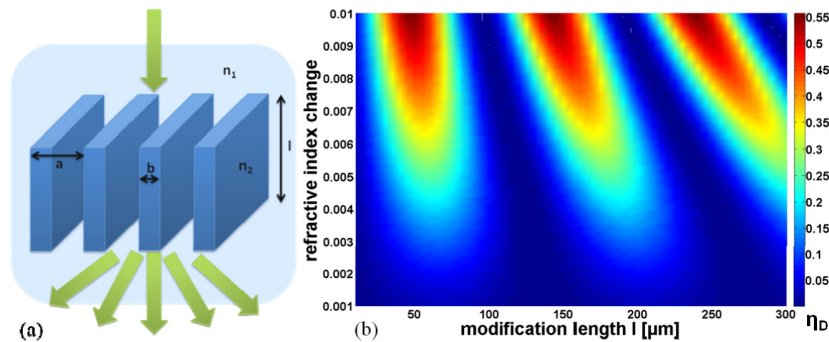


Fig. 3. (a) Sketch of a simple phase grating (b) η_D for a phase grating with $a = 6 \mu\text{m}$, $b = 3 \mu\text{m}$, $\lambda = 785 \text{ nm}$.

The simulation results for this 'simple' phase grating reveal that an overall diffraction efficiency into higher orders of about 55% can be achieved when suitable parameters for length l (about 50, 150 and 250 μm) and refractive index change $\Delta n = 0.01$ are used. Furthermore, a periodic behaviour can be observed for η_D when the length of the modifications increases. This can be understood qualitatively as to be due to the phase delay the traversing light is acquiring on its way through the modified regions; when the light diffracted in the bottom part of the structure length is delayed by $\lambda/2$ relative to that diffracted in the top part, destructive interference will suppress diffraction into higher orders. This effect has a strong impact on the design of efficient gratings, since modification lengths around the efficiency maxima have to be created. Also, we note that our structure appears to be in the thin grating regime (Raman-Nath regime) [21] which, however, is not to be expected considering its geometrical extensions and similar gratings acting as thick gratings [16].

In an attempt to maximize the diffraction efficiency η_D , we performed various simulations with other geometry parameters. It turned out that larger dimensions ($a > 6 \mu\text{m}$, $b > 3 \mu\text{m}$) only decreased the peak efficiency, while smaller dimensions could in principle provide higher efficiency in some cases. As our setup, however, cannot produce finer lines ($b_{\text{min}} \approx 2 \mu\text{m}$) with sufficiently high Δn , such gratings could not be fabricated in this study. Respecting these experimental constrains, the grating design discussed above is the relative optimum achievable by way of 'simple' gratings in this work.

3.2 Comparison with fabricated phase gratings

The diffraction efficiency calculated above is comparable to a recently reported value of about 50% for a phase grating under illumination at 405 nm wavelength [22]. To compare in detail the simulation results presented in section 3.1 with experimental values, we produced phase gratings corresponding to the calculations, i.e. having a grating period of $a = 6 \mu\text{m}$ and grating line width of $b = 3 \mu\text{m}$. A modification length of $150 \mu\text{m}$ was achieved by focusing fs laser pulses with an energy of $6 \mu\text{J}$ through MO 0.65 into the glass substrate. Laser diodes with emission wavelengths of 405, 514, 635 and 785 nm have been used to irradiate the gratings and characterize their diffraction efficiencies. For comparison, simulations for the same wavelengths have been performed. In Figs. 4(a)–4(d) the experimental and simulation results of the diffraction efficiency η_D for the investigated wavelengths are plotted as a function of modification length. By correlating the experimental values with the corresponding calculation results (phase grating parameters $a = 6 \mu\text{m}$, $b = 3 \mu\text{m}$) at a modification length of $150 \mu\text{m}$ and the respective wavelength, we were able to determine a wavelength dependent refractive index change in a range of $\Delta n = 0.0049 - 0.0061$.

The corresponding calculations are represented as red dashed lines in Fig. 4. Furthermore, the simulation results for an average value of the determined refractive index increases for the four investigated wavelengths are displayed (black lines) while experimentally measured values of the diffraction efficiency are presented as red dots. Analyzing the fabricated phase grating, we were able to experimentally obtain a maximum value of η_D of 54% at 405 nm illumination, decreasing with increasing wavelength and reaching 19% at 785 nm. This means that up to 54% of the incoming light is being diffracted into higher diffraction orders. When considering the determined refractive index changes we received by correlating the experimental with the corresponding simulation results, the range of the induced refractive index can be specified to $\Delta n = (5.5 \pm 0.6) \cdot 10^{-3}$. This range is in considerable agreement with the refractive index increase of 0.01 reported for single ultrashort laser pulse processing of fused silica [23]. With regards to the intended application of the presented gratings in solar modules, we prioritized writing speed over precision in our experiments. Nevertheless we found good diffraction efficiencies even for somewhat imprecise gratings when evaluating our results. Reasonable writing speed is an important factor to improve the light management of already completely built solar modules by way of a laser post-treatment.

The decrease in efficiency with increasing wavelength can also be observed in the calculated results while the periodic behavior of η_D with the modification length l is maintained for different wavelengths. Looking for an optimization of the total diffraction efficiency, a further increase of the induced refractive index changes as well as an extension of the modification length to about $170 \mu\text{m}$ would be beneficial for all four wavelengths investigated. In our experiments, however, neither an increase of laser pulse energy nor a change of the focusing optics enabled us to extend the modification length beyond $150 \mu\text{m}$, see Fig. 2. Also, an increase of the refractive index change to more than 0.006 could not be achieved.

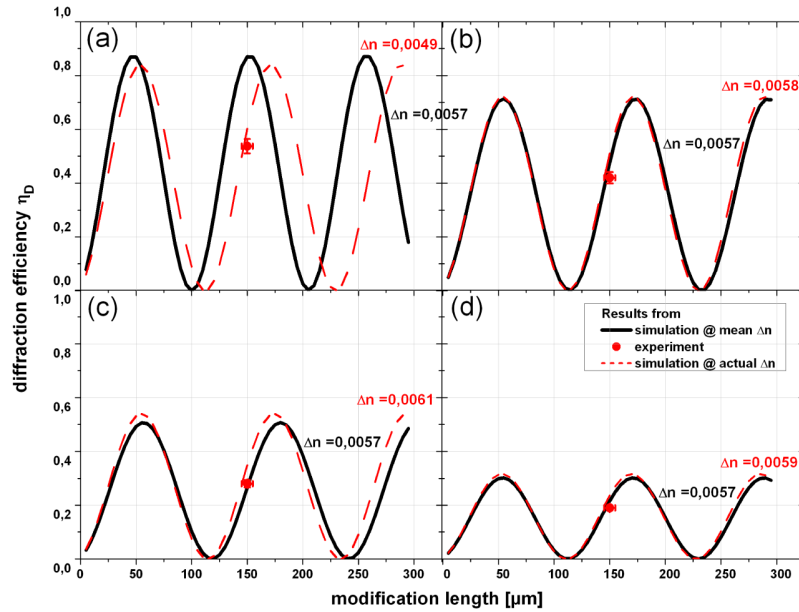


Fig. 4. Experimental and simulation results of η_D for a phase grating with $a = 6 \mu\text{m}$, $b = 3 \mu\text{m}$ and $l = 150 \mu\text{m}$ at wavelength (a) 405 nm (b) 514 nm (c) 635 nm and (d) 785 nm.

Overall, the results of the optical simulations are in good agreement with the experiment results of the fabricated phase grating. Therefore, it appears reasonable to estimate the value of the refractive index change induced in soda lime glass by fs laser pulses. More generally, this method provides a sufficient precise and reliable tool to determine the laser-induced refractive index changes in transparent materials, which are otherwise often difficult to measure experimentally due to their small values. Another approach addressing this problem reported by Berlich et al. [24] is to use an iterative Fourier transform technique to spatially resolve an accurate estimate of the refractive index profile with high spatial resolution.

3.3 Optimized blazed design

Having optimized the parameters of a ‘simple’ phase grating through numerical simulations, the next step is to look for a more effective grating design. Our basic idea was to fabricate blazed gratings with an approximately triangular cross section, in order to favour diffraction into larger angles and to suppress the 0th order. This is apparently beneficial for the intended application, e.g. guiding incoming light around the front side metallization of solar cells. We have conducted various calculations for such blazed phase gratings for the whole interesting wavelength range and then evaluated their total diffraction efficiency by extracting a spectrally averaged η_{PV}

$$\eta_{PV} = \frac{1}{R} \int_{300nm}^{1100nm} \eta_D(\lambda) d\lambda \quad \text{with } R = \int_{300nm}^{1100nm} d\lambda. \quad (2)$$

Simulations for a two-, three- and four-step blaze design were performed revealing an increasing efficiency with larger number of steps. However, we chose to work with the three-step blazed phase grating in order to facilitate fabrication. The design is shown schematically in Fig. 5(a).

The calculated total diffraction efficiency η_{PV} (see Eq. (2)) for a pertinent grating with $a = 8 \mu\text{m}$, $b = 2 \mu\text{m}$ and $l = 150 \mu\text{m}$ (the two shorter grating blocks have lengths of 100 and 50 μm) is shown in Fig. 5(b). The obtained values of η_{PV} reveal that about 70% averaged diffraction efficiency can be reached when using a modification length in the range of 100 – 150 μm and

a Δn of 0.006 as was achieved for the simple grating. Furthermore, the high-efficiency region turns out to be rather broad indicating a robust design structure with respect to slight variations of the modification length.

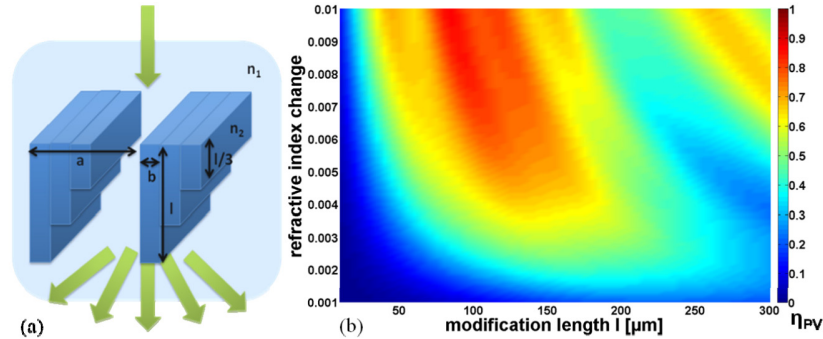


Fig. 5. (a) Sketch of a three-step blazed phase grating (b) η_{PV} for a three-step blazed phase grating with $a = 8 \mu\text{m}$, $b = 2 \mu\text{m}$, $\lambda = 300 - 1100 \text{ nm}$.

Due to this attractive properties, a three-step blazed grating with the above-mentioned parameters has been realized by writing grating lines with different laser pulse energies just next to each other leading to different modification lengths and achieving the desired blaze design. It has been produced with pulse energies of 8.0, 3.0 and 1.5 μJ leading to the requested modification lengths of 150, 100 and 50 μm inside the glass volume. Experimentally measured and calculated diffraction efficiencies η_D for the four investigated wavelengths are presented in Figs. 6(a)–6(d) as a function of the modification length. Correlation of the experimental (red dots) and simulated results at the respective wavelengths determine a wavelength dependent refractive index change of $\Delta n = 0.0017 - 0.0029$. The calculations involving the actual refractive index change are represented as red dashed lines while the simulation results for the mean refractive index increase are displayed as black lines in Fig. 6.

Experimentally, up to 77% of the incoming light could be diffracted into higher diffraction orders, i.e. in the case of $\lambda = 405, 514 \text{ nm}$. A decrease in efficiency with increasing wavelength can be observed both in calculated and experimental results. But even for longer wavelengths, up to 43% of the incoming light is diffracted into higher orders. Slight deviations between experimental and calculated results are observed at wavelengths of 405 and 785 nm. These variations may, at least partially, be due to deviations of the actual shape of the laser-generated structures from the geometrically idealized blaze grating design used in the simulations. In addition, there appears to be a wavelength dependence of the induced refractive index, indicating a smaller Δn at the shortest wavelength used (405 nm). By comparing the experimental and calculated results for the three-step blazed grating, the (average) induced refractive index change was determined to be $\Delta n = (2.3 \pm 0.6) \cdot 10^{-3}$.

Compared to the ‘simple’ grating, the determined value of Δn for the blazed grating is smaller by roughly a factor of 2. One possible reason for this difference is the variation of pulse energy to generate the different refractive index filament lengths of 150, 100 and 50 μm , which may cause different Δn in the three adjacent blocks; the simulation can then apparently provide only an effective average value. Another aspect is the close proximity of the three blocks which might cause different modification conditions when writing the second and third block. And finally, since the absorption of the incoming laser pulses and therefore the modification of the material is a strongly nonlinear effect, already small variations of laser input parameters such as focal width might have a significant impact on Δn .

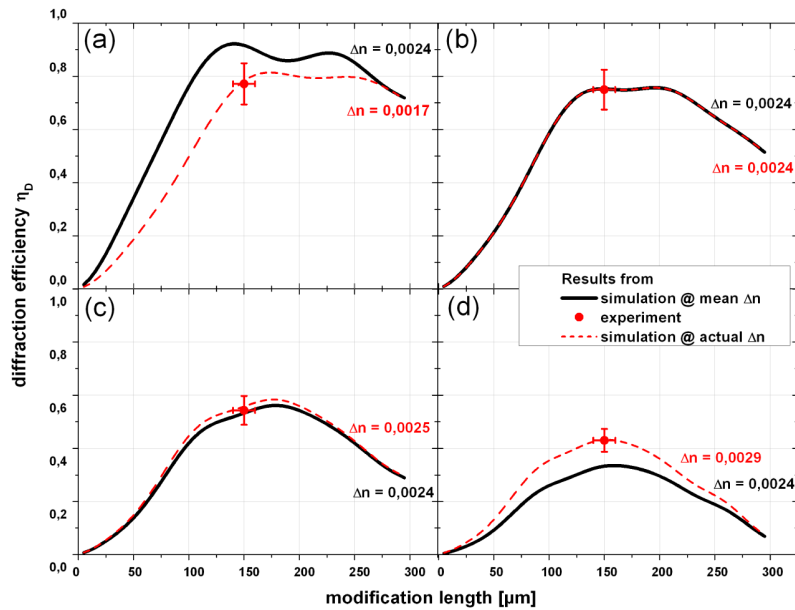


Fig. 6. Experimental and simulation results of η_D for a three-step blazed phase grating with $a = 8 \mu\text{m}$, $b = 2 \mu\text{m}$ and $l = 150 \mu\text{m}$ at wavelengths (a) 405 nm (b) 514 nm (c) 635 nm and (d) 785 nm.

For the addressed application of light management in photovoltaics, optimal functionality requires that already the diffraction angle of the first order is large enough to redirect all incoming light normally incident on a contact finger to a position aside from it. If we consider a typical, $70 \mu\text{m}$ wide contact finger and a vertical distance of 2 mm from grating to finger (i.e., grating created about 1 mm below glass surface), the minimum angle required for the first diffraction order would be 2.0° . For a diffraction grating with $8 \mu\text{m}$ grating period, as shown in this work, even the shortest wavelength (405 nm) features already a diffraction angle of 2.9° for the 1st order. Larger wavelengths and higher diffraction orders lead to higher angles, so that the three step blazed grating design as described above appears to be well suited for our intended application of improving the light management in solar modules.

Assuming an area shadowed by contacts of typically 5% and a typical cell conversion efficiency of 20% , the potential for improvement can be estimated to about 1% increase of absolute solar power conversion efficiency. To achieve this, it would be desirable to generate higher Δn which, according to our simulations, could cause diffraction efficiencies above 90% . Principally, such an increase of Δn appears possible: Eaton et al. measured the induced refractive index in their fabricated waveguides to 0.02 when using high-repetition laser pulses (500 kHz) [25], and just recently, Hashimoto et al. demonstrated that they were able to create high refractive index changes of up to 0.03 with low repetition rate laser sources (1 kHz) [26]. They assume that the movement of generated voids in the glass network distributes to a strong densification and therefore to a high induced refractive index. It will be an aspect of future work to utilize these effects for the fabrication of light management microstructures in glass.

4. Conclusion and outlook

In conclusion, we have demonstrated that we can create efficient phase gratings in the volume of soda lime glass using femtosecond laser pulses. Up to 54% of the incoming light with a wavelength of 405 nm at normal incidence can be diffracted into higher diffraction orders when a 'simple' phase grating design with optimized grating parameters is used. Optical simulations based on rigorous coupled-wave analysis theory were performed to determine the

most efficient phase grating parameters. By comparing the experimental efficiencies with the simulation results, we found the induced refractive index change to be $(5.5 \pm 0.6) \cdot 10^{-3}$.

As a next step, we conducted various calculations for a blazed grating design as a promising layout for high-efficient phase gratings. Evaluating the simulation results, we fabricated a three-step blazed transmission grating which showed diffraction efficiencies of up to 70% for incoming white light, addressing the spectral region relevant for photovoltaics. By comparing the experimental and simulated results, the induced average refractive index increase was determined to $(2.3 \pm 0.6) \cdot 10^{-3}$ for the blazed phase grating design. Hence, our optical simulations deliver a reliable tool to determine the induced change in refractive index which is otherwise difficult to measure experimentally because of its low magnitude and small spatial extent. An attractive application for the gratings presented here is their use in solar modules as elements to guide light around shadowed areas. The respective potential for an increase of solar cell efficiency can be estimated to 1% absolute (5% relative) when the whole module is processed for precisely adjusted light management microstructures.

Currently, the quantitative effect on photo current of high-efficient phase gratings integrated into the front glass of miniature solar modules is under investigation, accompanied by an evaluation of the functionality under varying incidence angles. These results will be reported in a forthcoming publication.

Acknowledgments

The authors would like to thank the German Federal Ministry for Education and Research (“Bundesministerium für Bildung und Forschung”) for the financial support within the joint research graduate school ‘StrukturSolar’ of Anhalt University of Applied Sciences and Martin-Luther-University Halle-Wittenberg (Förderkennzeichen: 03SF0417A) and the Centre for Innovation Competence SiLi-nano® (Förderkennzeichen: 03Z2HN12). The help from f | solar GmbH in providing the solar glasses is gratefully acknowledged.

Automated spray coating process for the fabrication of large-area artificial opals on textured substrates

Alexander N. Sprafke,¹ Daniela Schneevoigt,^{1,*} Sophie Seidel,¹ Stefan L. Schweizer,¹ and Ralf B. Wehrspohn^{1,2}

¹ Institute of Physics, Martin-Luther-University Halle-Wittenberg, Germany

² Fraunhofer Institute for Mechanics and Materials IWM, Halle, Germany

*daniela.schneevoigt@physik.uni-halle.de

Abstract: 3D photonic crystals, such as opals, have been shown to have a high potential to increase the efficiency of solar cells by enabling advanced light management concepts. However, methods which comply with the demands of the photovoltaic industry for integration of these structures, i. e. the fabrication in a low-cost, fast, and large-scale manner, are missing up to now. In this work, we present the spray coating of a colloidal suspension on textured substrates and subsequent drying. We fabricated opaline films of much larger lateral dimensions and in much shorter times than what is possible using conventional opal fabrication methods.

© 2013 Optical Society of America

OCIS codes: (050.5298) Diffraction and gratings - Photonic crystals; (160.5298) Materials - Photonic crystals; (310.1860) Thin films - Deposition and fabrication; (310.6845) Thin films - Devices and applications; Light management in solar cells.

References and links

1. E. Yablonovitch, "Inhabited spontaneous emission in solid-state physics and electronics," *Phys. Rev. Lett.* **58**(20), 2059–2062 (1987).
2. S. John, "Strong localization of photons in certain disordered dielectric superlattices," *Phys. Rev. Lett.* **58**(23), 2486–2489 (1987).
3. M. Peters, A. Bielawny, B. Bläsi, R. Carius, S. W. Glunz, J. C. Goldschmidt, H. Hauser, M. Hermle, T. Kirchartz, P. Löper, J. Üpping, R. B. Wehrspohn, and G. Willeke, *Photonic Concepts for Solar Cells in Physics of Nanostructured Solar Cells* (V. Badescu, and M. Paulescu, eds., Nova Science Pub, Inc., 2009), pp. 1–42.
4. A. N. Sprafke and R. B. Wehrspohn, "Light trapping concepts for photon management in solar cells," *Green* **2**(4), 177–187 (2012).
5. A. S. Dimitrov and K. Nagayama, "Continuous convective assembling of fine particles into two-dimensional arrays on solid surfaces," *Langmuir* **12**, 1303–1311 (1996).
6. A. Mihi, M. Ocana, and H. Miguez, "Oriented colloidal-crystal thin films by spin coating microspheres dispersed in volatile media," *Adv. Mater.* **18**, 2244–2249 (2006).
7. D. Allard, B. Lange, F. Fleischhaker, R. Zentel, and M. Wulf, "Opaline effect pigments by spray induced self-assembly on porous substrates," *Soft Materials* **3**(23), 121–131 (2006).
8. J. Üpping, A. Bielawny, R. B. Wehrspohn, T. Beckers, R. Carius, U. Rau, S. Fahr, C. Rockstuhl, F. Lederer, M. Kroll, T. Pertsch, L. Steidl, and R. Zentel, "Three-dimensional photonic crystal intermediate reflectors for enhanced light trapping in tandem solar cells," *Adv. Mater.* **23**, 3896–3900 (2011).
9. D. J. Norris, E. G. Arlinghaus, L. Meng, R. Heiny, and L. E. Scriven, "Opaline photonic crystals: How does self-assembly work?," *Adv. Mater.* **16**, 1393–1399 (2004).
10. A. Blanco, E. Chomski, S. Grabtchak, M. Ibisate, S. John, S. W. Leonard, C. Lopez, F. Meseguer, H. Miguez, J. P. Mondia, G. A. Ozin, O. Toader, and H. M. van Driel, "Large-scale synthesis of a silicon photonic crystal with a complete three-dimensional bandgap near 1.5 micrometers," *Nature* **405**, 437–440 (2000).
11. M. Egen, R. Voss, B. Griesbock, and R. Zentel, "Heterostructures of polymer photonic crystal films," *Chem. Mater.* **15**, 3786–3792 (2003).

12. M. Egen, and R. Zentel, "Surfactant-free emulsion polymerization of various methacrylates: Towards monodisperse colloids for polymer opals," *Macromol. Chem. Phys.* **205**, 1479–1488 (2004).
 13. K. Bittkau, R. Carius, A. Bielawny, and R. B. Wehrspohn, "Influence of defects in opal photonic crystals on the optical transmission imaged by near-field scanning optical microscopy," *J Mater Sci: Mater Electron* **19**, 203–207 (2008)
-

1. Introduction

3D photonic crystals [1, 2], such as artificial opals, are a promising material class for the use in advanced light management concepts for solar cells. Their special photonic band structure leads to strong wavelength-dependent and directional reflection and transmission properties which may be exploited in solar cells for innovative angular-selective or energy-selective filters, as well as reflective and diffractive backside structures [3, 4]. The optical properties of artificial opals can be designed within a broad range, as opals of many varieties can be easily synthesized experimentally by the self-assembly of monodisperse nanoscaled colloids, without the need for costly instruments [5–7]. The transmission, reflection and photonic dispersion characteristics of the opal are defined by the material and size of the colloids. Inverted opals are of particular interest for the applications mentioned above as they exhibit a complete photonic band-gap. E. g., we recently presented the first successful integration of an inverted opal structure as an intermediate reflective layer in a micromorph tandem solar cells [8]. We could show, that the electrical current of the top cell was significantly enhanced by the 3D photonic crystal structure.

Artificial opals are commonly synthesized from colloidal suspensions. Using conventional methods, either the suspension is drop coated onto the substrate or the substrate is dipcoated into the suspension and subsequently slowly pulled out [9–11]. During the deposition process the substrate is in contact with a reservoir of the colloidal suspension. The crystallization of the opaline film takes place in the meniscus which forms between the liquid phase of the solution and the gas phase of the ambient atmosphere. The combination of the evaporation of the solvent and capillary forces at the substrate surface creates a flow of the suspension which drives the colloids to the crystallization front and advances the crystal growth. However, the disadvantage of the drop and the dip coating fabrication method is their long duration which takes up several hours up to days and the rather small area of the obtained opaline film.

For a successful integration of advanced light management concepts using artificial opals in the photovoltaic industry a low-cost, fast, and large-scale technique to produce extensive opaline films of high quality is needed. The work presented by Zentel *et al.* shows that the fabrication of artificial opals by simply spraying the colloidal suspension onto the substrate is a promising method to comply with these demands [7]. Using a spray coating method enables one to deposit very thin layers of the colloidal suspension onto the substrate. Therefore, the drying process, i. e. the evaporation of the solvent and the concurrent opal crystallization, in principle occurs over the whole area of the substrate simultaneously. This is in contrast to the fabrication methods mentioned above in which the drying process advances along the substrate surface. Thus, the spray coating method offers a huge time saving component compared to the conventional methods. Additionally, this method needs no expensive equipment and obviously can be upscaled easily. However, Zentel *et al.* applied the spray coating process to porous and rather small substrates, such as sheets of paper. Also, they executed the spraying process by manually applying the spraying device, an airbrush, to a sheet of paper. These issues apparently make the application to the solar cell production process impossible in which techniques have to comply with non-porous, smooth as well as textured, and large-area substrates in a controllable and reproducible manner. Here, we report on important upgrades to the approach of Zentel *et al.* and on the successful implementation of an automated process

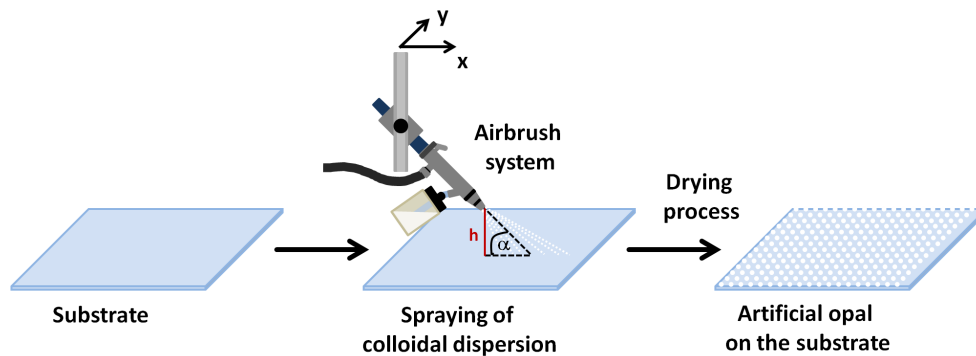


Fig. 1. Schematic illustration of the fabrication process of an artificial opal by spray coating.

for spray-induced self-assembly of extensive artificial opals on non-porous substrates, i. e. glass substrates (size $15 \times 21 \text{ cm}^2$) and aluminium foil. We achieved to reproducibly fabricate opaline films of up to $10 \times 20 \text{ cm}^2$ prepared on a glass substrate within 1–2 hours. Also, we present a summary on the parameters which influence the resulting opaline films, such as the solid content of the colloidal dispersion, the drying process, the substrate material, and the dispersion agent.

2. Materials and methods

The principle of our spray coating process is simple (see Fig. 1). A suspension of highly monodisperse nanoscaled polymethyl methacrylate (PMMA) colloids is sprayed onto the substrate. During the drying sequence the dispersion agent evaporates and the subsequent flow of the agent leads to the crystallization of the opal. As building blocks for the artificial opaline films highly monodisperse PMMA spheres ($d \approx 240 \text{ nm}$) dissolved in deionized water are used. These colloidal dispersions with varying solid content per weight are provided by our project partner Institute of Organic Chemistry at the University of Mainz [12]. The substrates are commercially available glass slides with sizes of up to $15 \times 21 \text{ cm}^2$ and conventional aluminium foil. As the substrate surface has to be wettable to achieve a uniform distribution of the colloidal dispersion after the spraying process, the substrates need to be pretreated. The glass substrates are treated with a 7M NaOH solution prior to the spraying process, whereas the aluminum foil does not need to be treated as the oxide layer of the untreated foil provides the needed wettability. This effect can be amplified by tempering the aluminum foil at 300°C , as the thickness of the oxide layer is increased by the tempering.

The experiments were performed using a commercially available airbrush system by Badger to spray the colloidal dispersion onto a substrate. The airbrush device is implemented in a self-constructed apparatus, which mechanically triggers the dispersion flow and the movement of the airbrush in the x - and y -direction via a computer software. The distance h and the angle α between the substrate and the airbrush can be adjusted (see Fig. 1). We used an angle of $\alpha = 45^\circ$ and a distance of $h = 14 \text{ cm}$ for all experiments. The airbrush is moved laterally over the substrate with a velocity of 9000 mm/min . The pressure used by the airbrush was set at 1 bar. The drying of the evenly distributed colloidal dispersion on the substrate was performed in an oven under ambient atmosphere.

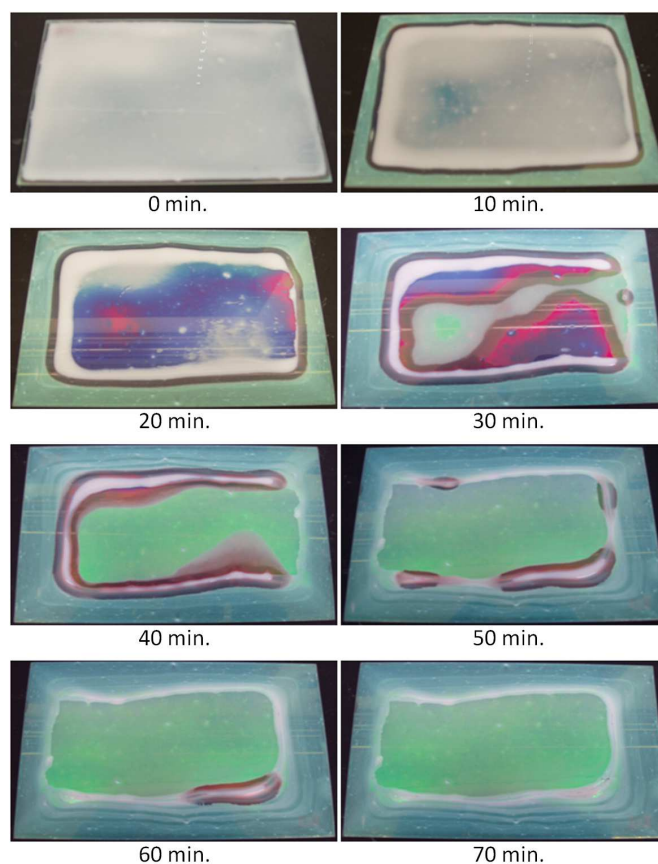


Fig. 2. Course of the drying sequence on a glass substrate. In this example, an approximately $10 \times 15 \text{ cm}^2$ opal has formed after 70 min. on a $15 \times 21 \text{ cm}^2$ glass substrate.

3. Results and discussion

To achieve artificial opals of high quality via spray coating, process parameters such as the solid content of the colloidal dispersion, the substrate material and the dispersion agent need to be optimized. Most important is the understanding of the drying process, i. e. the evaporation of the solvent and the concurrent opal crystallization, which is strongly affected by the choice of the aforementioned parameters. Therefore, an extensive investigation of the influence of these parameters on the spray coating process was carried out in order to achieve a more precise understanding of the crystallization mechanisms and to gain a better control over the fabrication process of artificial opals on non-porous substrates by spray coating.

3.1. Drying process

The drying process is the most crucial process step during the self-organized crystallization of the artificial opal. The visible course of the drying sequence on a glass substrate is illustrated in Fig. 2. The colloidal dispersion is distributed very evenly on the substrate by the spray deposition (0 min. in Fig. 2). The drying process does not take place simultaneously over the whole substrate as it is the case for porous substrates [7]. The drying rather starts from the

edges of the substrate and then advances to the center (10 min. in Fig. 2). Additionally, there are spots in the central part of the substrate where drying occurs while other parts still seem to be unaffected (20–60 min. in Fig. 2). The evaporation of the dispersion agent and thus the crystallization of the opal takes place at the advancing fronts which form a meniscus between the liquid phase and the ambient air just above the substrate surface. However, the advancing crystallization fronts found here (≈ 1 cm) are laterally much broader than the ones occurring in the conventional fabrication methods ($\ll 1$ mm), thus leading to quick crystallization durations. After approximately 70 minutes an inner area of approximately $10 \times 15 \text{ cm}^2$ with high reflectance in the green spectral range and an outer area with low reflectance have formed on the substrate (70 min. in Fig. 2). The optical reflectance of these two distinguishable areas are plotted in Fig. 3 (a) for comparison. The reflectance peaks at around $\lambda = 535 \text{ nm}$ originate from the photonic stop gap of the artificial opal. While the peak positions are located at the same wavelength, the peak heights differ strongly for the two regions. The reflectance of the inner region achieves a value of $R \approx 47\%$, but for the outer region the maximum is at only $R \approx 18\%$. SEM cross-sections of these two areas reveal that the PMMA spheres are packed in hexagonal closest packing in the inner area (see Fig. 3 (b)), i. e. an opal has formed, whereas almost no closest packing of the spheres can be detected in the outer area, furthermore the structure here seems to be amorphous (Fig. 3 (c)). Therefore, the synthesized artificial opal is laterally limited to the inner area by the drying process. But in comparison to other fabrication methods on non-porous substrates already an immense upscaling of the opal size was achieved with the automated spray coating presented here.

The drying sequence was examined for different ambient temperatures between 5°C and 80°C in an oven, but no influence of the temperature on the resulting opaline films was found. This needs to be investigated further, as it is not understood why the temperature seems not to have an influence on the drying process in these samples.

The contraction of the colloidal dispersion during the drying process additionally leads to the formation of cracks in the artificial opal, which divide the crystal in several microdomains of approximately $50 \times 50 \mu\text{m}^2$ maximum in size (see Fig. 4). These cracks also occur for other fabrication methods and can not be prevented [13]. However, depending on the proposed design this is not disadvantageous as a certain electrical conductivity of the films often is required when considering possible applications in solar cells. E. g., after inverting opaline films with a suitable filling material the needed conductivity can be provided mainly by these cracks [8].

3.2. Solid content of the colloidal dispersion

Colloidal dispersions with concentrations of 19%, 10% and 5% by weight were sprayed onto glass substrates under identical conditions and dried at 26°C in an oven for 1.5 hours. The resulting opaline films are shown in Fig. 5. The sample which was prepared with the colloidal dispersion of 19% by weight reveals the most even and homogeneous surface with an intense reflectance in the green spectral range (see Fig. 5 (a)). The opaline films prepared with colloidal dispersions of lower concentrations are much more inhomogeneous, i.e. many bright and dark spots are visible within the green reflecting surface. The film which was prepared with the lowest concentration (5%) revealed the lowest quality with the highest number of impurities and crumbs (see Fig. 5 (c)). This sample also has the lowest reflectance and the opaline surface appears stained.

For a quantitative evaluation of the visible appearance reflectance spectra of the opaline films were measured, see Fig. 6 (a). In this graph the reflectance is plotted against the wavelength of light λ for the different concentrations. The spectra were normalized to the reflectance spec-

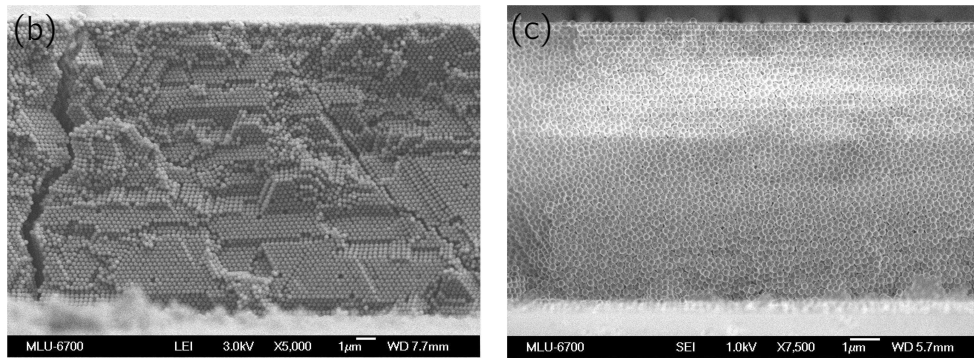
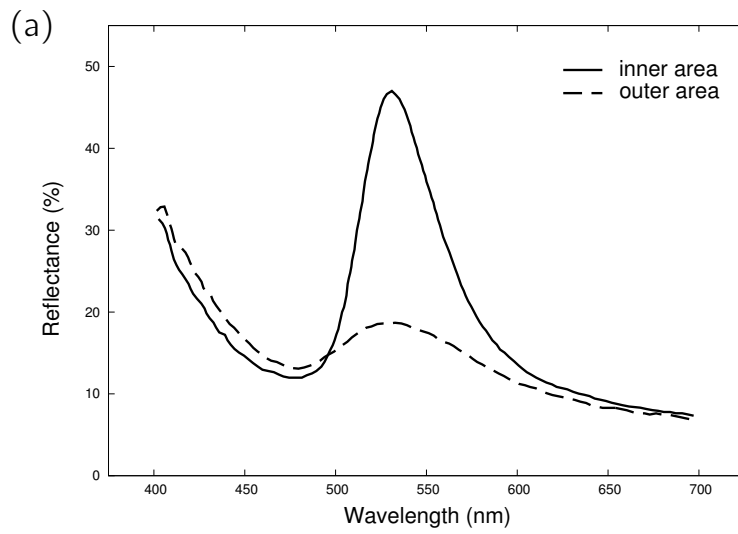


Fig. 3. (a) Reflectance spectra of the spray coating deposited opaline film from the inner (full line) and outer region of the substrate which is presented in Fig. 2. SEM cross-sectional views: Cross-section of the (a) inner region (5000x magnification) and (b) outer region (7500x magnification).

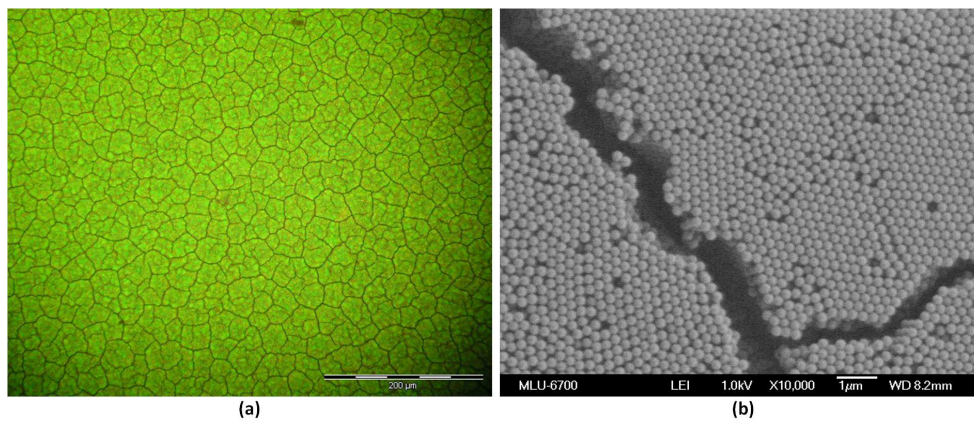


Fig. 4. Cracks in the opaline structure: (a) Optical microscope image in reflection (200x magnification), (b) SEM image (10000x magnification).

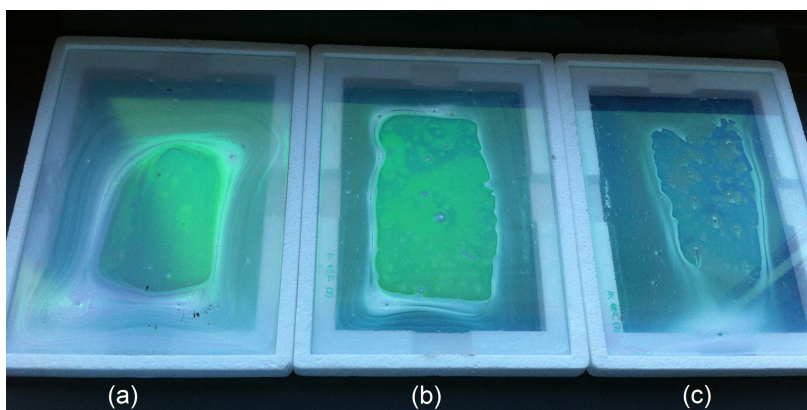


Fig. 5. Samples prepared with different concentrations of the colloidal dispersion: (a) 19%, (b) 10% and (c) 5% by weight.

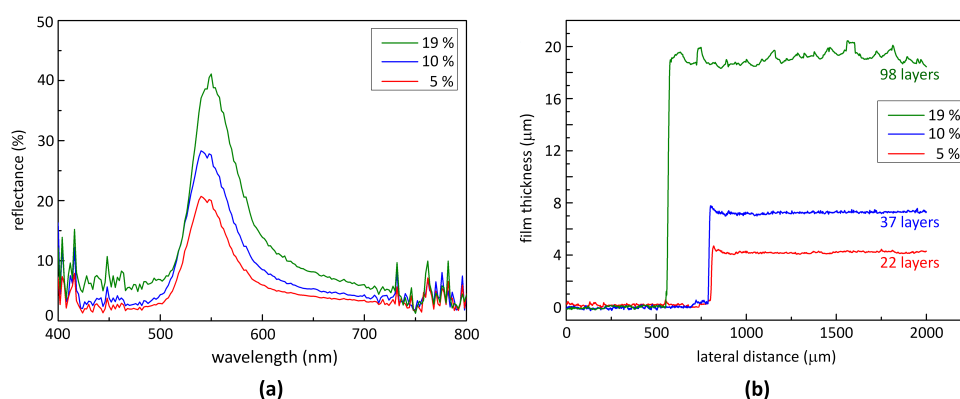


Fig. 6. (a) Reflectance and (b) thickness of the opaline films prepared with colloidal dispersions of varying solid content.

trum of the bare glass substrate. All three samples clearly reveal an increased reflectance in the green spectral range. The spectral position of the peak maximum of the sample which was prepared with the colloidal dispersion of 19% by weight is at a wavelength of $\lambda = 550\text{ nm}$, whereas the position is slightly shifted to $\lambda = 548\text{ nm}$ for the other samples. The position of the reflectance peaks corresponds to the spectral position of the stop gap of an artificial opal consisting of PMMA spheres with a diameter of 250 nm. We also observe that with an increasing concentration by weight of the colloidal dispersion the maximum peak value of the reflectance rises clearly (see Fig. 6 (a)).

The thickness of the opaline films was determined with the help of a profilometer. A diamond stylus is moved laterally across the sample for a specified distance and a profil of the surface is generated. The opaline film was removed from the substrate at some spots so the edge between opaline film and substrate can be gauged. The film thickness can then be extracted from the diagram Fig. 6 (b). It was found, that with a higher concentration of the colloidal dispersion, the thickness of the opaline films increases. The opaline film which was prepared with the colloidal dispersion of 19% by weight consists of approximately 98 layers of PMMA colloids on a lateral average. Whereas the opaline film which was prepared with

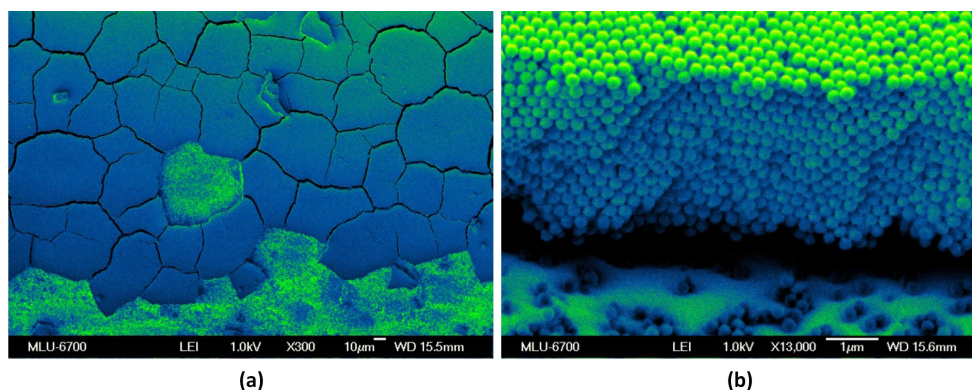


Fig. 7. Artificial opal deposited onto aluminium foil: (a) SEM top view (300x magnification), (b) SEM cross-sectional view (13000x magnification).

the colloidal dispersion of 5% by weight only consists of approximately 22 layers of PMMA colloids. Since the same volume of colloidal dispersion was deposited onto every substrate during the spraying process, the solid content of the colloidal dispersion determines the number of PMMA spheres which arrive on the substrate and compose the crystal. Thus, the thickness of the resulting opaline films is scaled with the content of colloids in the deposited suspension. To fabricate artificial opals of a certain thickness and peak-value of the reflectance the solid content of the colloidal dispersion needs to be adjusted as well as the volume of the deposited colloidal suspensions, e. g. by adjusting the velocity or the pressure of the airbrush.

3.3. Substrate material

Also the substrate material has an important influence on the drying mechanisms and thus the resulting opaline films. It has been shown before that for porous substrates, such as sheets of paper, the drying takes place simultaneously over the entire substrate as the dispersion agent is soaked up by the substrate material and the thereby generated liquid flow drives the colloids towards the crystallization front of the opal [7]. However, for non-porous substrates, such as glass substrates, the drying sequence is very different from that of porous substrates. The drying sequence on glass substrates is described in Sec. 3.1. But it remains unclear whether a different non-porous substrate will lead to different results.

Besides on large-area glass substrates we performed first spray coating experiments on conventional commercially available aluminium foil. In contrast to the smooth surface of a glass substrate aluminium foil exhibits a textured surface. The fabrication of 3D photonic crystals on this textured and conducting foil is of potentially high interest for photovoltaic applications. E. g., the aluminium foil may be used as a backside mirror which at the same time acts as an electrical back contact. A photonic crystal structure may add useful light trapping properties to such a backside structure, such as bragg reflection or diffraction.

It was possible to obtain opaline films on aluminium foil substrates, too, which turn out to be very similar to those fabricated on glass substrates. SEM images of the obtained structures are shown in Fig. 7 (a) and (b). Despite the rough texture of the aluminium foil the grown opaline films is crystalline after only a few monolayers and exhibits a smooth top surface. The opaline area is divided into microdomains due to the formation of cracks which is analogue to the case of the deposition onto glass substrates. However, the photonic crystal structures spall very easily from the substrate. On the one hand, this behaviour may

account to a less strong adhesion of the structures to the aluminium foil due to a weaker adhesion strength of the PMMA spheres to the aluminium oxide surface. On the other hand, a possible reason may be that the aluminium foil bends and distorts very easily when handling the samples leading to large mechanical strains inside the opaline structure and subsequent peeling off of the substrate. Because of the high potential of this approach further investigation and optimization of the spray coating deposition process on aluminium foil has to be conducted.

3.4. Dispersion agent

In addition, also the dispersion agent has an influence on the drying process. The colloids used in this work are dispersed in deionized water. The high surface tension of this dispersion agent (see Tab. 1) could lead to the observed contraction of the colloidal dispersion during the drying sequence. Therefore, the exchange of the dispersion agent for the PMMA colloids is a good possibility to manipulate the drying process. To fabricate even larger opaline films of similar or better quality, the dispersion agent must have a low surface tension. This property presumably prevents the contraction of the colloidal dispersion during the drying sequence. Also, the vapor pressure of the dispersion agent is an important parameter. If the vapor pressure is too high, i. e. the dispersion agent is very exhalable, the dispersion agent may be in the gaseous phase directly after leaving the airbrush system and before reaching the substrate. Such a property obviously is unfeasible.

Table 1. Surface tension and vapor pressure of several solvents.

	Surface tension at 20° C [mN]	Vapor pressure at 20° C [mbar]
Water	72.75	23
Ethanol	22.55	58
1-Propanol	21.4	20.3
2-Propanol	21.7	42.6
p-Xylene	30	8.89

Ethanol was tested as a dispersion agent because of its low surface tension (see Table 1), but it was found to evaporate too fast. The PMMA spheres do not have enough time to arrange themselves in closest packing. A mixture of ethanol and water leads to the same problems, if the ratio of ethanol is higher than 50%. A higher ratio of water however leads to the known contraction of the colloidal dispersion during the drying sequence. Because of their promising characteristics 1-Propanol and p-Xylene were tested (see Table 1), but were found to corrode the polymethyl methacrylate and thus destroy the spheres. So none of the tested solvents is an applicable dispersion agent. Nevertheless, further experiments showed, that 2-Propanol is a promising candidate, since it does not affect the PMMA spheres, but it needs to be examined further how this solvent effects the drying mechanisms.

3.5. Discussion

In comparison to the most common fabrication method for opaline films at present, the dipcoating process, our automated spray coating process presented here offers an immense upscaling of the obtained size of the films (as needed for implementation in solar cells). The size of artificial opals fabricated via dipcoating is technically limited to a few square millimeters, whereas our results suggest that using the automated spray coating, in principle square meter large areas

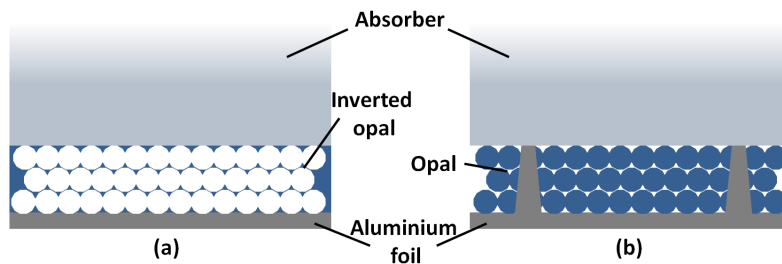


Fig. 8. Possible implementations of a backside foil on solar cells. The backside foil is applied to the backside of the absorber. (a) Photonic crystal structure (here: inverted opal) consists of an electrically conducting material and the foil acts as a large scale backside contact. (b) Photonic crystal structure (here: opal) is isolating, electrical contacts are laser-fired into the absorber material.

of opaline films can be produced. Additionally, artificial opals can be produced much faster via spray coating. The fabrication of an opaline film of $156 \times 156 \text{ mm}^2$ (size of a conventional solar cell) via dipcoating would require approximately 48 hours (using a pull velocity of 3.25 mm/h). Only 1–2 hours are needed for an opaline film of the same size via spray coating. This is due to the different drying process of the two fabrication methods. In the case of the spray coating the crystallization takes place in multiple, laterally broad fronts ($\approx 1 \text{ cm}$) which start from the edges and advance towards the center of the sample, whereas during the dipcoating the crystallization takes place in just one vertically advancing meniscus ($\ll 1 \text{ mm}$) which leads to much longer fabrication durations.

Imperfections within the crystal structure of the opal possess a crucial impact on the optical quality of the opal as it is apparent from the optical spectra in Fig. 3 (a). Opaline films deposited by our spray coating technique exhibit an area of low quality at the edge region of the substrate which is much larger than that of opals deposited by other methods, e. g. the dip coating technique. However, the extent of this area is not dependent on the absolute size of the substrate except for small substrates with dimensions similar to that of the low quality edge region. Thus, the appearance of low quality areas is not a disadvantage when considering applications involving large-area substrates as it is the case in the photovoltaic industry.

Applying 3D photonic crystals to the backside of a solar cell is a promising light management approach for light path enhancement. Light that is not absorbed during the first round through the solar cell would be either Bragg reflected or diffracted by the photonic crystal structure back into the cell. While the reflection is spectrally broadband, the diffraction is resonant, i. e. spectrally narrow and can be tuned to critical spectral ranges (near the electronic band gap of the absorber material). Therefore, the probability of light absorption and thus the efficiency of the solar cells is increased by such a backside structure [3,4].

Incorporating new concepts, such as light management by opals, directly into existing solar cell production lines involves several drawbacks which the photovoltaic industry commonly is not willing to take. E. g., the preparation of photonic crystals onto a solar cell absorber means an extra process step which is tied to increased production complexity, cost, and time. Also, the probability of defects introduced into the cell is increased because of additional thermal and mechanical exposures.

In the case of a backside structure, we propose that these drawbacks can be avoided by implementing the backside structure as a foil. This backside foil is fabricated in a process which is separate from the solar cell production process. It consists of a flexible substrate and a photonic crystal and is applied to the absorber after its fabrication, e. g. by glue assembly.

The independent fabrication cuts down possible additional damaging impacts on the absorber material. Using aluminium foil as a substrate in combination with our presented spray coating technique for the preparation of opaline films as shown in paragraph 3.3, the proposed backside foil is not limited to a certain type of solar cells. Depending on the desired optical and electrical properties of the backside foil the photonic crystal may be a conventional opal, e. g. as deposited, or an inverted opal, e. g. obtained by atomic layer deposition and subsequent dissolving of the PMMA spheres. Aluminium as a substrate material offers several advantages. It is a low cost metal, it is well-known and already in use in the photovoltaic industry. It acts not only as a substrate for the opaline film but also as a backside mirror for light that was not absorbed in the absorber or bragg reflected or diffracted by the opal structure. Since the proposed backside foil additionally has to act as an electrical backside contact, aluminium as a substrate material is advantageous, too. There are different ways to electrically contact the absorber. If the photonic crystal is made of a transparent electrically conductive material, such as Al:ZnO or ITO, the whole backside foil acts as a large-scale backside contact as sketched in Fig.8 (a). In that case, the formation of cracks in the opaline film as shown in paragraph 3.1 is of great advantage, since they provide a low resistance contact to the absorber. If the opal is electrically isolating, electrical contacts can be achieved by laser-firing the aluminium into the absorber material (see Fig.8 (b)). This strategy enables localized selective electrical contacts if needed and avoids unwanted short-circuits.

4. Conclusion

In conclusion, we presented the fabrication of extensive artificial opals on non-porous smooth and textured substrates, such as glass substrates and aluminium foil, by a low-cost, automated spray coating process. In addition to an immense time saving, a large upscaling of the opal size was achieved in comparison to other fabrication methods on non-porous substrates. We obtained opaline films of up to approximately $10 \times 15 \text{ cm}^2$ within fabrication durations of approximately 70 min. The size limiting process is the drying sequence, which leads to the formation of an opal in the inner region of the substrate and a not closest packed formation of the spheres at the outer regions of the substrate. The investigated parameters solid content of the sprayed colloidal dispersion, substrate material, and dispersion agent have been shown to play an important role in the spray coating process influencing properties of the opaline films such as thickness, lateral size, optical properties, and overall quality. Using optimized values of these parameters will enable one to even increase the achieved lateral dimensions of the opal and precisely control its properties. For the incorporation of advanced light management concepts with 3D photonic crystals into innovative solar cell devices we propose the use of a backside foil which is applied to the absorber. This foil is made of an aluminium foil substrate and an opaline film deposited with the spray coating method. The backside foil is fabricated in a separate process step, thus making this concept feasible for the photovoltaic industry.

Acknowledgments

This work has been carried out by the Infravolt-Consortium. Financial support by the German Federal Ministry of Education and Research (BMBF) within the projects Infravolt and Struktur-solar is gratefully acknowledged (as well as the German Science foundation within the project PAK 88 Nanosun). We like to thank our partners from the Research consortium for stimulating discussions in particular the Institute of Organic Chemistry at the Johannes Gutenberg-University Mainz.

We thank Sabrina Lehmann and Julia-Maria Osinga for their experimental assistance and Claudia Stehr and Susanne Wille for their excellent technical support.



Strategy for tailoring the size distribution of nanospheres to optimize rough backreflectors of solar cells

STEFAN NANZ,^{1,*} AIMI ABASS,² PETER M. PIECHULLA,³
ALEXANDER SPRAFKE,³ RALF B. WEHRSPHON,^{3,4} AND CARSTEN
ROCKSTUHL^{1,2}

¹*Institute of Theoretical Solid State Physics, Karlsruhe Institute of Technology, 76131 Karlsruhe, Germany*

²*Institute of Nanotechnology, Karlsruhe Institute of Technology, 76021 Karlsruhe, Germany*

³*Institute of Physics, Martin Luther University Halle-Wittenberg, 06120 Halle (Saale), Germany*

⁴*Fraunhofer Institute for Microstructure of Materials and Systems, 06120 Halle (Saale), Germany*

*stefan.nanz@kit.edu

Abstract: We study the light-trapping properties of surface textures generated by a bottom-up approach, which utilizes monolayers of densely deposited nanospheres as a template. We demonstrate that just allowing placement disorder in monolayers from identical nanospheres can already lead to a significant boost in light-trapping capabilities. Further absorption enhancement can be obtained by involving an additional nanosphere size species. We show that the Power Spectral Density provides limited correspondence to the diffraction pattern and in turn to the short-circuit current density enhancement for large texture modulations. However, in predicting the optimal nanosphere size distribution, we demonstrate that full-wave simulations of just a c-Si semi-infinite halfspace at a single wavelength in the range where light trapping is of main importance is sufficient to provide an excellent estimate. The envisioned bottom-up approach can thus reliably provide good light-trapping surface textures even with simple nanosphere monolayer templates defined by a limited number of control parameters: two nanosphere radii and their occurrence probability.

© 2018 Optical Society of America under the terms of the [OSA Open Access Publishing Agreement](#)

OCIS codes: (050.1970) Diffractive optics; (350.6050) Solar energy; (310.6845) Thin film devices and applications.

References and links

1. S. Reber, M. Arnold, D. Pocza, and N. Schillinger, "ConCVD and ProConCVD: development of high-throughput CVD tools on the way to low-cost silicon epitaxy," Proceedings of the 24th European Photovoltaic Solar Energy Conference (2009), Hamburg, Germany.
2. T. Rachow, N. Milenkovic, B. Steinhauser, J. Benick, S. Janz, M. Hermle, and S. Reber, "Solar cells with epitaxial or gas phase diffused emitters above 21% efficiency," *Energy Procedia* **77**, 540–545 (2015).
3. H.-P. Wang, D.-H. Lien, M.-L. Lien, C.-A. Lin, H.-C. Chang, K.-Y. Lai, and J.-H. He, "Photon management in nanostructured solar cells," *J. Mater. Chem. C* **2**, 3144–3171 (2014).
4. S. Mokkapati and K. R. Catchpole, "Nanophotonic light trapping in solar cells," *J. Appl. Phys.* **112**, 101101 (2012).
5. C. Eisele, C. Nebel, and M. Stutzmann, "Periodic light coupler gratings in amorphous thin film solar cells," *J. Appl. Phys.* **89**, 7722–7726 (2001).
6. R. Dewan and D. Knipp, "Light trapping in thin-film silicon solar cells with integrated diffraction grating," *J. Appl. Phys.* **106**, 074901 (2009).
7. A. Abass, K. Q. Le, A. Alu, M. Burgelman, and B. Maes, "Dual-interface gratings for broadband absorption enhancement in thin-film solar cells," *Phys. Rev. B* **85**, 115449 (2012).
8. C. Rockstuhl, F. Lederer, K. Bittkau, and R. Carius, "Light localization at randomly textured surfaces for solar-cell applications," *Appl. Phys. Lett.* **91**, 171104 (2007).
9. S. Fahr, T. Kirchartz, C. Rockstuhl, and F. Lederer, "Approaching the Lambertian limit in randomly textured thin-film solar cells," *Opt. Express* **19**, A865–A874 (2011).
10. S. Jain, V. Depauw, V. D. Miljkovic, A. Dmitriev, C. Trompoukis, I. Gordon, P. V. Dorpe, and O. E. Daif, "Broadband absorption enhancement in ultra-thin crystalline Si solar cells by incorporating metallic and dielectric nanostructures in the back reflector," *Prog. Photov. Res. Appl.* **23**, 1144–1156 (2015).
11. M.-C. van Lare and A. Polman, "Optimized scattering Power Spectral Density of Photovoltaic Light-Trapping Patterns," *ACS Photonics* **2**, 822–831 (2015).

12. C. Trompoukis, I. Massiot, V. Depauw, O. E. Daif, K. Lee, A. Dmitriev, I. Gordon, R. Mertens, and J. Poortmans, "Disordered nanostructures by hole-mask colloidal lithography for advanced light trapping in silicon solar cells," *Opt. Express* **24**, A191–A201 (2016).
13. M. Kroll, S. Fahr, C. Helgert, C. Rockstuhl, F. Lederer, and T. Pertsch, "Employing dielectric diffractive structures in solar cells – a numerical study," *Phys. Stat. Sol. (a)* **205**, 2777–2795 (2008).
14. C. Rockstuhl, S. Fahr, and F. Lederer, "Absorption enhancement in solar cells by localized plasmon polaritons," *J. Appl. Phys.* **104**, 123102 (2008).
15. S. Pillai, K. R. Catchpole, T. Trupke, and M. Green, "Surface plasmon enhanced silicon solar cells," *J. Appl. Phys.* **101**, 093105 (2007).
16. C. Rockstuhl, S. Fahr, F. Lederer, K. Bittkau, T. Beckers, and R. Carius, "Local versus global absorption in thin-film solar cells with randomly textured surfaces," *Appl. Phys. Lett.* **93**, 061105 (2008).
17. M. A. Green and S. Pillai, "Harnessing plasmonics for solar cells," *Nat. Photon.* **6**, 130–132 (2012).
18. C. Battaglia, C.-M. Hsu, K. Söderström, J. Escarré, F.-J. Haug, M. Charrière, M. Boccard, M. Despeisse, D. Alexander, M. Cantoni, Y. Cui, and C. Ballif, "Light trapping in solar cells: Can periodic beat random?" *ACS Nano* **6**, 2790–2797 (2012).
19. M. Peters, C. Battaglia, K. Forberich, B. Bläsi, N. Sahraei, and A. G. Aberle, "Comparison between periodic and stochastic parabolic light trapping structures for thin-film microcrystalline silicon solar cells," *Opt. Express* **20**, 29488–29499 (2012).
20. P. Kowalczywski, A. Bozzola, M. Liscidini, and L. C. Andreani, "Light trapping and electrical transport in thin-film solar cells with randomly rough textures," *J. Appl. Phys.* **115**, 194504 (2014).
21. U. W. Paetzold, M. Smeets, M. Meier, K. Bittkau, T. Merdzhanova, V. Smirnov, D. Michaelis, C. Waechter, R. Carius, and U. Rau, "Disorder improves nanophotonic light trapping in thin-film solar cells," *Appl. Phys. Lett.* **104**, 131102 (2014).
22. A. Oskooi, P. A. Favuzzi, Y. Tanaka, H. Shigeta, Y. Kawakami, and S. Noda, "Partially disordered photonic-crystal thin films for enhanced and robust photovoltaics," *Appl. Phys. Lett.* **100**, 181110 (2012).
23. S. Wiesendanger, M. Zilk, T. Pertsch, C. Rockstuhl, and F. Lederer, "Combining randomly textured surfaces and photonic crystals for the photon management in thin film microcrystalline silicon solar cells," *Opt. Express* **21**, A450–A459 (2013).
24. S. Fahr, C. Rockstuhl, and F. Lederer, "Engineering the randomness for enhanced absorption in solar cells," *Appl. Phys. Lett.* **92**, 171114 (2008).
25. E. R. Martins, J. Li, Y. Liu, J. Zhou, and T. F. Krauss, "Engineering gratings for light trapping in photovoltaics: The supercell concept," *Phys. Rev. B* **86**, 041404(R) (2012).
26. E. R. Martins, J. Li, Y. Liu, V. Depauw, Z. Chen, J. Zhou, and T. F. Krauss, "Deterministic quasi-random nanostructures for photon control," *Nat. Commun.* **4**, 2665 (2013).
27. F. Priolo, T. Gregorkiewicz, M. Galli, and T. Krauss, "Silicon nanostructures for photonics and photovoltaics," *Nat. Nanotechnol.* **9**, 19–32 (2014).
28. X. Guo, D. Wang, B. Liu, S. Li, and X. Sheng, "Enhanced light absorption in thin film silicon solar cells with Fourier-series based periodic nanostructures," *Opt. Express* **24**, A408–A413 (2016).
29. R. Yu, Q. Lin, S.-F. Leung, and Z. Fan, "Nanomaterials and nanostructures for efficient light absorption and photovoltaics," *Nano Energy* **1**, 57–72 (2012).
30. X. Meng, V. Depauw, G. Gomard, O. E. Daif, C. Trompoukis, E. Drouard, C. Jamois, A. Fave, F. Dross, I. Gordon, and C. Seassal, "Design, fabrication and optical characterization of photonic crystal assisted thin film monocrystalline-silicon solar cells," *Opt. Express* **20**, A465–A475 (2012).
31. S. Wiesendanger, M. Zilk, T. Pertsch, F. Lederer, and C. Rockstuhl, "A path to implement optimized randomly textured surfaces for solar cells," *Appl. Phys. Lett.* **103**, 131115 (2013).
32. F. Pratesi, M. Burreli, F. Riboli, K. Vynck, and D. S. Wiersma, "Disordered photonic structures for light harvesting in solar cells," *Opt. Express* **21**, A460–A468 (2013).
33. T. Okamoto, K. Shinotsuka, E. Kawamukai, and K. Ishibashi, "Self-assembly method for controlling spatial frequency response of plasmonic back reflectors in organic thin-film solar cells," *Appl. Phys. Express* **10**, 012301 (2017).
34. T. Itoh and N. Yamauchi, "Surface morphology characterization of pentacene thin film and its substrate with under-layers by power spectral density using fast Fourier transform algorithms," *Appl. Surf. Sci.* **253**, 6196–6202 (2007).
35. C. Rockstuhl, S. Fahr, K. Bittkau, T. Beckers, R. Carius, F.-J. Haug, T. Söderström, C. Ballif, and F. Lederer, "Comparison and optimization of randomly textured surfaces in thin-film solar cells," *Opt. Express* **18**, A335–A342 (2010).
36. N. Sahraei, K. Forberich, S. Venkataraj, A. G. Aberle, and M. Peters, "Analytical solution for haze values of aluminium-induced texture (AIT) glass superstrates for a-Si:H solar cells," *Opt. Express* **22**, A53–A67 (2014).
37. S. J. Fonash, *Introduction to Light Trapping in Solar Cell and Photo-detector Devices* (Academic Press, 2015), 1st ed.
38. S. M. George, "Atomic Layer Deposition: An Overview," *Chem. Rev.* **110**, 111–131 (2010).
39. S. Wiesendanger, T. Bischoff, V. Jovanov, D. Knipp, S. Burger, F. Lederer, and C. Rockstuhl, "Effects of film growth modes on light trapping in silicon thin film solar cells," *Appl. Phys. Lett.* **104**, 231103 (2014).
40. J.-P. Berenger, "A perfectly matched layer for the absorption of electromagnetic waves," *J. Comput. Phys.* **114**, 185–200 (1994).

41. M. Green and M. Keevers, "Optical properties of intrinsic silicon at 300 K," *Prog. Photov. Res. Appl.* pp. 189–192 (1995).
42. Z. Holman, M. Filipic, A. Descoedres, S. D. Wolf, F. Smole, M. Topic, and C. Ballif, "Infrared light management in high-efficiency silicon heterojunction and rear-passivated solar cells," *J. Appl. Phys.* **113**, 013107 (2013).
43. P. B. Johnson and R. W. Christy, "Optical constants of the noble metals," *Phys. Rev. B* **6**, 4370–4379 (1972).
44. K. Jäger, D. Linssen, O. Isabella, and M. Zeman, "Ambiguities in optical simulations of nanotextured thin-film solar cells using the finite-element method," *Opt. Expr.* **23**, A1060–A1071 (2015).
45. S. G. Romanov, S. Orlov, D. Ploss, C. K. Weiss, N. Vogel, and U. Peschel, "Engineered disorder and light propagation in a planar photonic glass," *Sci. Rep.* **6**, 27264 (2016).
46. J. Pomplun, S. Burger, L. Zschiedrich, and F. Schmidt, "Adaptive finite element method for simulation of optical nano structures," *Phys. Stat. Sol.* **244**, 3419–3434 (2007).
47. ASTM, "Standard tables for reference solar spectral irradiances: Direct normal and hemispherical on 37° tilted surface," (2012). West Conshohocken (PA): American Society for Testing and Materials. Available from <https://www.astm.org>.

1. Introduction

Thin-film silicon solar cells are being revisited by several groups and companies world-wide due to their better materials and energy efficiency and thereby possibly lower production cost. Whereas ten years ago, focus was mainly on PECVD-based microcrystalline technologies, nowadays, thin film crystalline solar cells are being prepared by high-throughput casting or high-temperature CVD processes [1, 2]. Thin-film cells can be made to be mechanically flexible and more portable. A thinner absorber layer also implies a shorter diffusion path for the generated minority carriers to reach the semiconductor junction, which in turn may translate to a better internal quantum efficiency (IQE) of the solar cell. However, for weakly absorbing materials such as c-Si, a thinner active material may lead to incomplete light absorption, which leads to a lower short-circuit current density [3, 4].

To address the incomplete absorption problem in thin-film devices, several possibilities have been proposed. Many approaches involve the usage of nanostructures which are either periodic [5–7] or random [8–12], placed at the back [13] or front side of the cell, or both [14]. These nanostructures enhance light absorption by improving light incoupling from air/glass superstrate to the higher-index absorber layer and also by increasing the effective light path within the absorber (light trapping). Metallic nanostructures have also been proposed for providing absorption enhancement by exploiting their various modes with strong scattering cross-section and large near-field enhancement [15–17]. However, with such lossy metallic structures there is also significant parasitic absorption, which leads to a lower absorption in the silicon layer.

Introducing disorder in light-trapping surface textures has been demonstrated to possibly lead to a spectrally broader absorption enhancement in photovoltaic devices [18–21]. Having disorder populates the Fourier spectrum of the geometry, which in turn leads to more available light scattering pathways across an extended spectral domain. However, not every disordered structure is equally useful as light absorption may instead be impaired [22]. Not just the availability, but also the scattering strength to the different pathways is important. Disorder may also enhance light scattering within the escape cone and may weaken with that the resonant optical response, resulting in less absorption enhancement. Therefore, obtaining the most out of disorder for light trapping purposes requires care and remains a major design challenge, especially due to huge computational costs in numerically addressing the problem. Furthermore, reliable large-area fabrication of optimum disordered light-trapping surface textures is highly demanding.

In an attempt to deduce and realize optimal light-trapping textures, many strategies have been explored. Among them is the combination of photonic crystal structures with disordered layers, e.g. using several layers with ordered and disordered structures [23]. Fahr *et al.* explored how statistical parameters that describe a surface texture can be tuned to ensure an optimal scattering pattern for absorption enhancement [24]. Martins *et al.* proposed a deterministic way to deduce an optimum quasi-periodic surface profile by superposing periodic gratings [25, 26]. Supercells resulting from several superposed grating periods may have a richer Fourier spectrum than single

periodic cells, thus providing a more broadband diffraction response while still retaining distinct diffraction orders [27, 28]. Though one can deduce with these approaches a favorable surface texture possessing the desired scattering response, the resulting textures are typically difficult to fabricate and often rely on relatively expensive top-down methods [29, 30].

Recently, a bottom-up strategy to define rough textures utilizing dielectric nanospheres with tailored radius sizes as building blocks has been proposed [31]. These nanospheres are grown in the liquid phase and the resulting colloidal dispersion is deposited onto a substrate. The properties of the solution and deposition method are tuned such that the deposited nanospheres form a monolayer on the substrate. This monolayer of nanospheres then defines a rough surface which serves as a template for a backreflector in solar cells. A similar approach with a disordered photonic crystal was already discussed [32]. There, they considered holes in a dielectric medium with correlated and uncorrelated positional disorder. Also, colloidal particles have been shown to enhance the absorption in organic thin-film solar cells [33].

Here, we demonstrate how favorable scattering properties for light trapping can be reliably obtained with the nanospheres-based bottom-up approach by utilizing nanospheres of only two different sizes. The resulting textures possess a Fourier spectrum that favors oblique scattering of normal incident light in a broad wavelength range, which in turn provides a large enhancement in absorption if the texture is an integrated part of a thin-film solar cell. This in turn yields an enhanced short-circuit current density when considering the full solar cell stack. One can hereby circumvent the need for full-wave simulations in a large parameter regime but still work towards optimizing the surface textures to be of use in thin-film solar cells.

For the analysis we use the well-known Power Spectral Density (PSD) [11, 34]. This quantity, which is the absolute square of the Fourier transform of the height profile, provides the amplitudes of the spatial frequencies, i. e. the grating vectors, that are available in the corrugated surface. It is hence a useful tool for our purposes in tailoring the nanosphere sizes via optimizing the amplitudes of the relevant grating vectors. Other measures such as the haze, which is basically the fraction of the specular and diffracted light, exist as well [35, 36], but they suffer from the inability to clearly distinguish the angular distribution and treat textures that scatter light into large oblique angles, which is generally favorable, comparable to textures that scatter the light into weakly oblique angles.

2. Strategy and simulations

2.1. General considerations

In this work, we consider the case of a simplified thin-film c-Si cell depicted in Fig. 1(a). We particularly discuss in this section the scattering properties we wish to achieve for an optimum light trapping rear-side texture. We also discuss how one can achieve a comparable response from textures obtained with the nanosphere-based bottom-up approach.

Before we proceed in discussing how to deduce nanosphere size distributions of interest, we first outline the desired scattering response that we aim to achieve. As the goal is absorption enhancement, one essentially seeks to utilize the disordered surface texture to scatter light into oblique angles within the light-absorbing medium [37]. For first order diffraction scattering processes, an incident wave with parallel wave vector $\vec{k}_{||,inc}$ will only be scattered to a certain mode $\vec{k}_{||}$ if the scattering texture height profile possesses a Fourier component with wavevector \vec{G} , fulfilling $\vec{k}_{||,inc} + \vec{G} = \vec{k}_{||}$. To significantly scatter (near) normal incident light to oblique angles via a first order diffraction scattering process, the surface texture must therefore possess Fourier components pertaining to sufficiently large $|\vec{G}|$. However, for the purpose of rear-side textures, height-profile Fourier components corresponding to $|\vec{G}| > k_0 n_{Si}$ can result in significant parasitic absorption losses as they facilitate scattering to plasmonic modes that are evanescent in the relevant spatial domain. These plasmonic evanescent modes may encompass strong

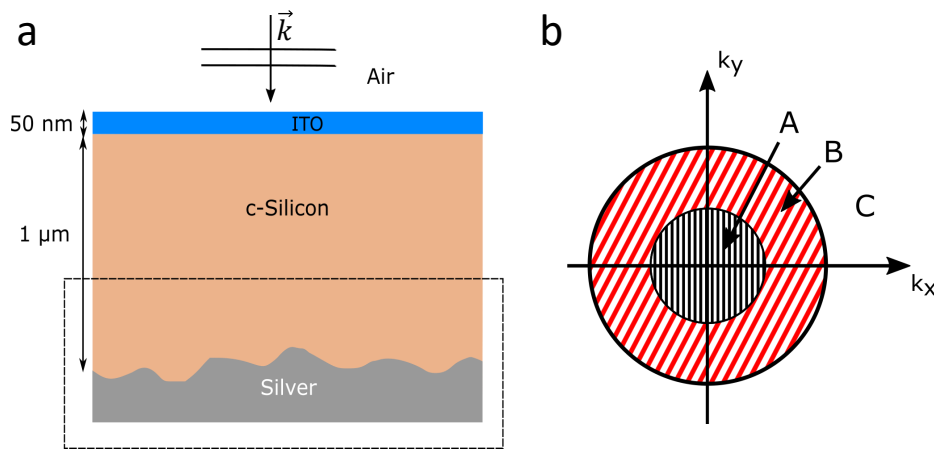


Fig. 1. a) A two-dimensional slice through the three-dimensional geometry of the considered thin-film solar cell used for full-wave FEM simulations with normal incident plane waves. Above the silver rough back-reflector whose height profile we are optimizing in this work, $1 \mu\text{m}$ of c-Si is considered. To reduce reflections at the front side, a 50 nm Indium tin oxide (ITO) anti-reflection layer is deposited on top of the silicon. The geometry in the dashed box was used for full-wave diffraction simulations, i.e. when calculating the angular spectrum. The entire three-dimensional geometry was considered when analyzing the short-circuit current density. b) To judge the quality of a rough surface, the Fourier spectrum was divided into three regions: A, for angles smaller than the angle of total internal reflection (TIR) at a silicon-air interface; B, for angles larger than the TIR angle, considering only propagating modes; C, evanescent wave vector components. We aim to tailor the diffraction spectrum to have its major contributions in region B.

parasitic absorption supported at the metal-dielectric interface that overshadows the absorption enhancement in the light absorbing media if one is not careful. Thus, our considerations above let us conclude that we require a height profile for our texture that possesses a Fourier spectrum as shown in Fig. 1(b), in which the Fourier distribution forms an annulus.

The outer and inner radius of the target annulus region are subject to optimization. The optimization requires to consider the intrinsic absorption response of the solar-cell material and the incoming solar irradiation. The Fourier spectra of a light trapping texture should be chosen in a way to account for the wavelength range where the absorption enhancement is most beneficial. For example, photons with energy significantly higher than the bandgap are already absorbed to a large extent within the first few hundred nanometers. In this wavelength regime, one only needs to ensure good anti-reflection properties of the front surface. Light trapping is most relevant for photons with energy close to the bandgap of the absorber, which experience a weak material absorption response. Although one should aim for the wavelength regime where a mere double pass through the absorber layer is not enough to ensure complete absorption, one should still prioritize the wavelength range where the solar spectrum offers the most photons.

Based on our discussion above, the main target wavelength region to enhance absorption is approximately 600–900 nm, for the case of thin-film c-Si cells. In order to provide a proof-of-principle demonstration of how one can design a light trapping structure for this wavelength regime, we aim to tailor the Fourier spectrum of our scattering surface in the shape of an annulus with the wavelength of 700 nm in mind. The inner radius of the target annulus distribution shall correspond to the angle of total internal reflection at a c-Si/air interface for this wavelength.

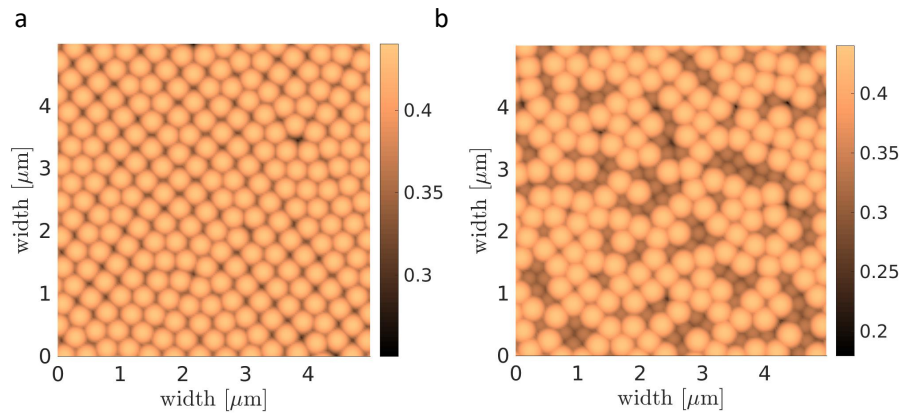


Fig. 2. a) Example monolayer consisting of nanospheres with only one radius (170 nm) and an isotropic coating layer with thickness 100 nm. Parts of the monolayer form a hexagonal pattern, whereas others are disordered. b) Example monolayer with 60 % of nanospheres with radius 170 nm and 40 % nanospheres with radius 120 nm. Again, a 100 nm thick isotropic layer has been added. The small nanospheres lead to the vanishing of any remaining order of the bigger nanospheres.

For the outer radius, the largest propagating spatial frequency was chosen to avoid large losses through parasitic absorption in the metal.

2.2. Methodology

Having identified a target scattering characteristic, we proceed to investigate surfaces that can be obtained with a nanosphere-based bottom-up approach. In this work, we consider only nanosphere monolayers that are densely arranged, i.e. where neighboring nanospheres always touch each other, but nevertheless positional randomness is allowed. This constraint enables in principle a hexagonal close-packing of the nanospheres in the case of only one radius size, but also, and this is what we are focusing on here, a disordered monolayer. Surface textures arising from such monolayers are of particular interest as the statistical characteristics of the geometrical features would depend only on the nanospheres sizes and relative concentration of the nanosphere species. Though by doing so we restrict the degrees of freedom, the dense nanosphere monolayer distribution can provide a Power Spectral Density (PSD) distribution that approaches the target annulus profile distribution as will be shown below. Examples of monolayers using different nanosphere distributions can be seen in Figs. 2(a) and 2(b).

Our numerical height profile generation works as follows: We first generate a set of spheres with the desired radii in random order. The number of generated spheres is determined by the area of the box that we want to cover, ensuring that enough spheres are generated to cover the complete box, while also generating not too much to not distort the initialized nanosphere size distribution. The suitable number of nanospheres is different for different fractions of big and small nanospheres and determined individually for each configuration. We then initialize a random x-coordinate for each nanosphere while the initial y-coordinate is always set to the same value on one of the edges of the box. Then, the nanospheres are gradually moved towards the opposite side of the box until they either reach the opposite edge or touch another already placed nanosphere. After this, the nanosphere is moved along the x-direction to check if there is a position where it could be moved even further in y-direction to ensure uniform filling along the x-axis. The filling finishes when no not-deposited nanosphere is remaining or when the box

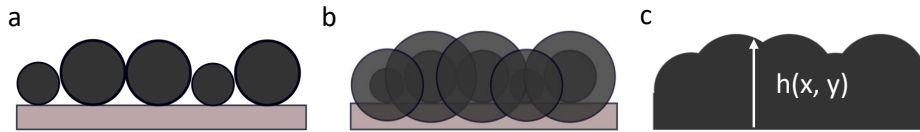


Fig. 3. Procedure to generate the rough surface template. Displayed is a two-dimensional cross-section of the three-dimensional height profile. a) Nanospheres are placed in a monolayer with the restriction that every nanosphere touches at least one other nanosphere. Overlapping nanospheres are not allowed. b) To mimic the isotropic coating by atomic layer deposition, the nanospheres are radially enlarged. c) The last step is to homogenize the resulting structure. The height profile is then the maximal height resulting from the enlarged nanospheres.

is full. For cases where too many nanospheres could not be placed in the box or the box was not filled, the result was discarded and restarted with an adapted number of nanospheres. A two-dimensional cross-section of such a nanosphere monolayer is shown in Fig. 3(a).

To build the surface texture template, the nanosphere monolayer is subsequently coated in an isotropic manner, which can be experimentally done via atomic layer deposition [38]. The isotropic coating thickness is chosen to be 100 nm to avoid texture smoothing, which would result in a decrease of surface amplitude and in turn would lead to weaker scattering [39]. Numerically, the isotropic coating can be deduced by first enhancing every nanosphere radially, as shown in Fig. 3(b). The final height profile can then be calculated by retrieving the continuous surface which is represented by the highest point of the enhanced nanospheres at each position (Fig. 3(c)). Since we are not interested in the zeroth order scattering strength, we set the average height of our profiles to zero. As a last step, we cut a small strip of the height profile on each side to avoid edge effects that encompass the placing process, and we apply a periodification to the height profile at the computational domain edges to be able to handle the scattering problem numerically; 50 nm on two adjacent sides of the height profile are modified in order to have a continuous transition to the next unit cell.

For the finite-element simulations, we place Perfectly Matched Layers (PMLs) in z -direction at the top and bottom of the computational domain to avoid unphysical reflections from the boundaries [40]. In the x - y -plane periodic boundary conditions are enforced. We simulate for p -polarized plane waves incident from the positive z -direction. The minimum and maximum finite-element degrees were chosen to be 2 and 3, respectively. The maximum mesh sidelength of the computational domain was 200 nm in the x - y -plane and varied along the z -axis for the different materials and also inside one material to ensure a sufficient fine mesh near the corrugated interface. We chose as maximum vertical mesh sizes 140 nm to 150 nm in silver, 50 nm to 80 nm in c -Si, 20 nm in ITO and 50 nm in air. The refractive indices for crystalline silicon [41], ITO [42], and silver [43] have been taken from published data.

2.3. Tailoring scattering properties

The simplicity in predicting the resulting height profile allows one to exploit knowledge of the scattering process in determining the nanospheres' size of interest. Along with the knowledge of the height profile, one has access to the Fourier picture of the geometry, which can be used to identify guidelines to deduce parameter regions of interest for the nanosphere compositions. One of the predictors of whether the scattering facilitated by a Fourier component with wavevector \vec{G} is significant, is the PSD. The PSD(\vec{G}) is defined as the absolute square of the two-dimensional discrete Fourier transform of the height profile $h(x, y)$ [34],

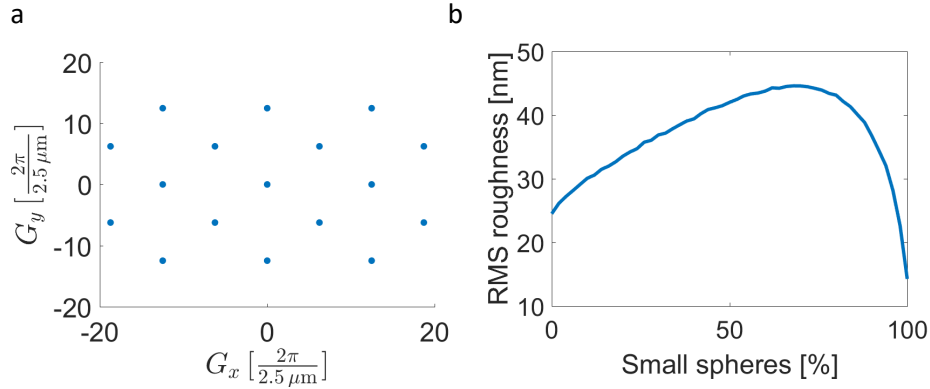


Fig. 4. a) Diffraction pattern of an ideal hexagonal monolayer of single-sized nanospheres with radius of 170 nm. The blue dots indicate the available discrete diffraction channels. b) Average root mean square (RMS) roughness of a surface consisting of nanospheres with 170 nm radius and an increasing portion of nanospheres with 120 nm radius. The graph shows the average of 20 generated height profiles for each portion of larger and smaller nanospheres in steps of 2 %. By increasing the portion of the small nanospheres, the RMS roughness first increases up to a portion of approx. 70 % of nanospheres, before it quickly drops; this is due to smearing out of the surface features accompanying the diminishing influence of the bigger nanospheres.

$$\text{PSD}(\vec{G}) = \frac{1}{L_x L_y} \left| \sum_m \sum_n h(x_m, y_n) e^{-i(G_x^m x_m + G_y^n y_n)} \Delta L \right|^2. \quad (1)$$

L_x and L_y are the considered widths of the rough surface in x and y direction and G_x^m and G_y^n are the spatial frequencies in x and y direction that belong to the diffraction orders m and n , respectively. ΔL is the minimal step width of the generated discrete height profile. Due to the discreteness of the transformation, G_x^m (and similarly G_y^n) can also be written as $G_x^m = \frac{2\pi}{L_x} m$. As an example, Fig. 4(a) shows the PSD of a hexagonal sinusoidal grating. The PSD must be calculated for a simulation window much larger than the correlation length of the disordered structure to ensure statistical significance and stability of the Fourier distribution [44].

In general, the PSD is a useful predictor for the diffraction efficiency in the limit of shallow textures [11], meaning that the wavelength incident to the rough surfaces is much larger than the amplitude modulation of the texture. For our setup, the wavelength in c-Si is, assuming a vacuum wavelength of 700 nm, approximately 185 nm. A measure for the strength of the amplitude modulation is the root mean-square (RMS) roughness, shown in Fig. 4(b) for the nanosphere size combination 170 nm and 120 nm and increasing portion of the 120 nm sized nanospheres. The RMS roughness almost doubles its value up to around 45 nm when small nanospheres are gradually added, which is only around four times smaller than the wavelength. This suggests that the PSD prediction will be less reliable in such conditions when the portion of the two nanosphere sizes are almost the same.

Even with a dense nanosphere monolayer comprising of only identical nanospheres, one can already obtain an annulus-like shaped distribution when a disordered placement is allowed. Figure 5(a) shows the PSD profile of a surface texture consisting of one nanosphere size species. The PSD profile was made for a $10 \times 10 \mu\text{m}^2$ for the case of a $r_{\text{main}} = 170$ nm. The nanosphere

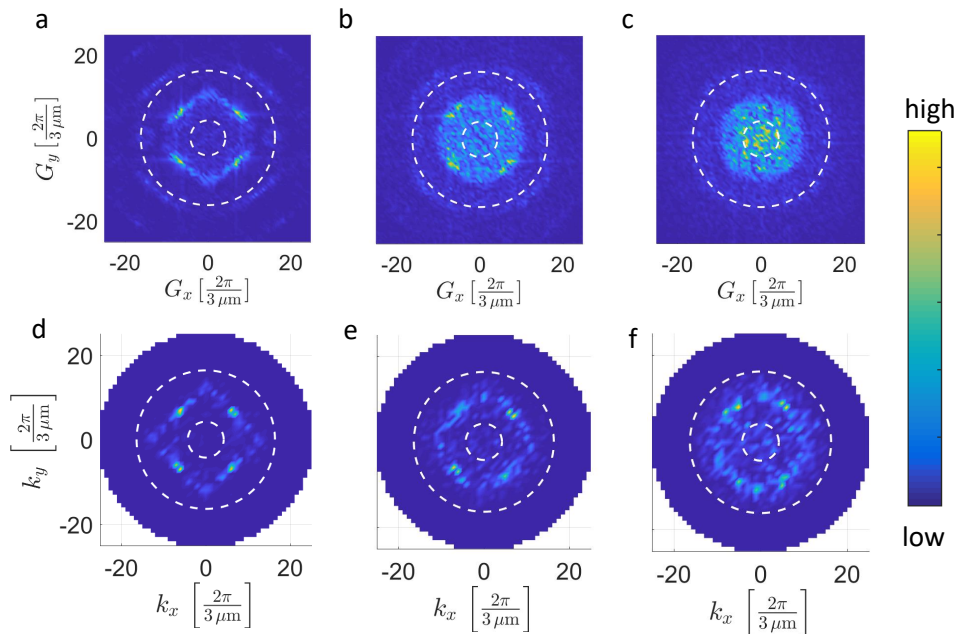


Fig. 5. Plots of the PSD (5(a)–5(c)) and the diffracted angular spectra (5(d)–5(f)) at a wavelength of 700 nm for three different portions of small nanospheres. The white dashed rings mark the annulus sketched in Fig. 1(b) with optimized inner and outer radius. Figures 5(a)–5(c) show PSD plots of disordered monolayers where the radius of the main nanosphere species is $r_{\text{main}} = 170$ nm and the perturbing nanospheres have $r_{\text{pert}} = 120$ nm, and Figs. 5(d)–5(f) show diffraction plots of such monolayer configurations, respectively. For the PSD plots, the average height of the height profiles was set to zero to remove the zeroth order component, and in the diffraction plots, the zeroth order is not shown. Percentages of the perturbing nanospheres are: a, d: 0%; b, e: 10%, and c, f: 40%. For the small perturbations of 0% and 10%, the PSD and diffraction components are mainly located centrally in the previously defined annulus region, whereas for higher perturbations, the PSD pattern transforms into a disk.

radius determines both the amplitude of the height profile and the average correlation length, which in turn affects the scattering strength and the Fourier components that are populated. Smaller radii lead to surface textures with weaker scattering strength but populate Fourier components with large $|\vec{G}|$, while larger radii lead to stronger scattering strength but more population of Fourier components at smaller $|\vec{G}|$. Choosing the radius $r_{\text{main}} = 170$ nm is not based on a systematic analysis, it is merely a plausible choice taking into account the previously discussed requirements of the height profile. The choice can be motivated by the fact that it leads to a population of the Fourier distribution in our target Fourier annulus region in the spectral region of interest. Furthermore, this radius indeed provides strong scattering in the directions and wavelength range of interest reaching around 74% as will be shown below. By having placement disorder while maintaining a dense arrangement, one actually observes a ring-shaped broadening (cf. Fig. 5(a)) of the main peaks of the Fourier distribution compared to a purely ordered system. Allowing placement randomness thus already promises to provide significant boost to light trapping.

To ensure a spectrally broadband enhancement effect, one of course is interested in broadening the ring-like spectra. One can further broaden the annulus-shaped Fourier distribution obtained

by allowing another nanosphere size species to generate the monolayer. A similar strategy was chosen in [45], where two different sphere sizes have been used to engineer the light propagation in a photonic glass. Interestingly, by just considering a distribution of two nanosphere sizes, one can already obtain a sufficiently broad annulus-like distribution of surface texture Fourier components as demonstrated in Figs. 5(b) and 5(c) when another nanosphere size species is successively introduced in the monolayer. Naturally, as the amount of the other nanosphere size species is increased, the PSD profile is also populated at low $|\vec{G}|$ where scattering would be near-normal. The second nanosphere size species is considered to have a radius $r_{\text{pert}} = 120$ nm. The motivation to use a smaller nanosphere size is to avoid a PSD profile that is too dominant at low $|\vec{G}|$ which would naturally occur if bigger nanospheres are added.

A large PSD in the annulus region would not itself guarantee that also the scattering strength is stronger in the annulus, as also only the available number of scattering channels could be increased. When additionally looking at the RMS roughness in Fig. 4(b) when increasing the portion of perturbing small nanospheres, we can settle this question. By increasing the portion of small nanospheres, the RMS roughness starts from 24 nm for no perturbing nanospheres added and increases up to 44 nm for 68% of small nanospheres; for higher portions of small nanospheres, the RMS roughness will go down again. These values compare to the RMS roughness value of Asahi-U profiles, which have a RMS roughness of 35 nm [11]. The RMS roughness is a measure of how strong a surface scatters, but does not specify the angular frequencies at which this happens. But together with the PSD, we can conclude that by adding perturbing small nanospheres, we increase the total scattering strength in the target annulus region, as we intended.

To confirm the scattering properties, we calculate the scattering of normal incident waves impinging on a c-Si/Ag textured interface with the commercial FEM solver JCMsuite [46]. Our simulation domain for the diffraction calculations essentially consists only of the dashed box region in Fig. 1(a) with only the real part of the refractive index of c-Si considered. The surface texture is assumed to be transferred perfectly to an Ag substrate. In practice, one can achieve the same effect by applying a metal coating on the nanosphere monolayers. If the metal coating is thick enough, the fact that the nanospheres themselves are made of a dielectric material can be neglected. Jäger *et al.* demonstrated that one can obtain a statistically meaningful result when modeling the scattering property of a disordered texture by considering a periodified cut of the domain that spans at least five times the lateral feature size (LFS) [44]. In our case, the LFS, in a good approximation, can be considered to be the distance between two nanospheres with the same radius of the prevalent nanosphere species. For portions of the larger nanospheres between 50% and 100%, this means that $LFS \approx 2r_{\text{main}} = 340$ nm. If the smaller nanospheres are the dominant portion, $LFS \approx 240$ nm. We choose the computational domain size to be at least $2.5 \times 2.5 \mu\text{m}^2$, which is around seven times larger than the LFS. Hence, statistical validity of our results is ensured.

Figures 5(d)–5(f) show the angular distribution of the diffraction efficiency at a wavelength of 700 nm. As can be seen in Figs. 5(a) and 5(d), the diffraction efficiency follows well the PSD profile for the case of identical nanospheres in the monolayer. As the percentage of small nanospheres is increased, the annulus in the diffraction profile broadens. It is also noticeable that the diffraction still preserves its annulus shape while the PSD completely turns into a disk as the two portions of the nanosphere size species are becoming equal. This indicates that the diffraction, even when considering larger fraction of the small nanospheres, continues to be determined by the larger nanospheres; the smaller nanospheres only act as a perturbation by broadening the annulus.

Despite discrepancies between the diffraction efficiency and $\text{PSD}(\vec{G})$ displayed in Fig. 5, we found that the integration of the $\text{PSD}(\vec{G})$ within the target annulus region is still a useful figure of merit to predict the absorption enhancement capability. To be more exact, this figure of merit is defined by

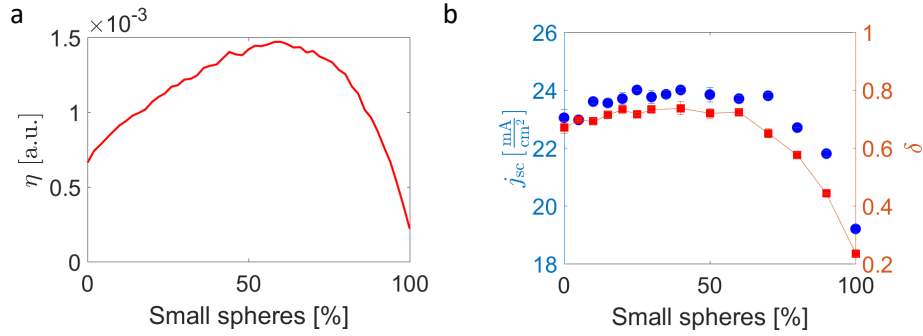


Fig. 6. Comparison between the contributions of the PSD and the diffraction components, both summed up in the annulus region B indicated in Fig. 1(b). a) By increasing the portion of the small nanospheres, the sum of the PSD components in the annulus (η) doubles its value up to around 60 % of small nanospheres due to the introduction of more Fourier components by the perturbing nanospheres, and then decreases rapidly as the smaller nanospheres generate a less rough surface morphology. b) The diffraction efficiency in the annulus (δ , red squares) shows the same tendency, but with a less pronounced peak. The short-circuit current density j_{sc} (blue dots) shows a similar behavior with a peak at around 50 %. The increase of j_{sc} from 0 % to 50 % amounts to $1.1 \frac{\text{mA}}{\text{cm}^2}$. Each datapoint of η is the average of three simulations, and each j_{sc} datapoint is the average of at least two simulations. The error bars indicate the uncertainty of the averages.

$$\eta = \sum_{\substack{G_x^m, G_y^n, \\ k_{\text{TIR}} < G_{\parallel} < k_{\text{inc}}}} \text{PSD}(G_x^m, G_y^n), \quad (2)$$

where $G_{\parallel} = \sqrt{(G_x^m)^2 + (G_y^n)^2}$ is the in-plane spatial frequency for diffraction channel (m, n) . The formula states that those components of the PSD are summed up which fulfill the criterion that the in-plane spatial frequency lies in the interval between the wavevector of total internal reflection and the largest non-evanescent mode. This interval, as discussed before, is most beneficial for light-trapping purposes.

Figure 6(a) depicts a plot of η versus the portion of smaller nanospheres in the monolayer. η was calculated for 20 iterations of the same size fraction of the nanospheres in steps of 2 %. A distinct peak around 60% of smaller nanospheres is seen. The dependency of the figure of merit η on the percentage of smaller nanospheres is comparable to the diffraction efficiency δ within the annulus region, calculated by

$$\delta = \sum_{\substack{k_x^m, k_y^n, \\ k_{\text{TIR}} < G_{\parallel} < k_{\text{inc}}}} |\vec{E}_{\text{ref}}(k_x^m, k_y^n)|^2 \frac{k_z}{k_{\text{inc}}}. \quad (3)$$

Here, $\vec{E}_{\text{ref}}(k_x^m, k_y^n)$ is the spectral representation of the reflected field above the surface, and it is implicitly assumed that the incident field has a unit magnitude so that the normalization factor in δ can be omitted. δ hence gives the portion of the total diffraction efficiency which goes into the target region.

Figure 6(b) (red squares) gives the plot of integrated diffraction efficiencies versus the portion of the small nanospheres. Every datapoint is the average of at least three simulations using

different height profiles with the same fraction of nanosphere sizes. The red line in Fig. 6(b) is a guide to the eye. A common trend can be seen with a broad plateau peak at small nanosphere percentages between around 30 % and 60 %. The observation that the diffraction is relatively insensitive for the perturbing nanospheres in this percentage regime indicates that the degree of disorder does not change much for these percentages; having 30 % perturbing small nanospheres and adding another 10 % does neither further broaden the diffraction spectrum nor decrease the scattering strength of the available Fourier components.

2.4. Full-wave simulations

To validate the performance of our textures, we proceed to calculate the impact of the different textures on the absorption in the c-Si thin-film solar cell stack shown in Fig. 1(a). We consider a solar cell structure with a silver back reflector, 1 μm thick c-Si absorber layer, and a 50 nm thick anti-reflection layer (Indium tin oxide, ITO [42]). This multilayer structure is not supposed to be realized experimentally exactly in this scheme, as a corrugated back surface and a flat front surface are hard to achieve with current techniques and we are also omitting the usually used TCO layer between the metal back reflector and the c-Si layer. However, for our purposes of providing a strategy for optimizing the rough back reflector, it is sufficient: The TCO layer would not significantly influence the diffraction properties and a textured front side of the cell would narrow down the applicability of the analyses compared to just a flat front side.

Our simulation domains vary in size, but are at least 2.5 μm by 2.5 μm large to ensure statistically stable results. We simulate for the absorption between 300 nm and 1100 nm in steps of 10 nm with normal incident plane waves.

The macroscopic quantity of interest is the short-circuit current density j_{sc} . To obtain j_{sc} , we calculated the absorption in the silicon layer by integrating the divergence of the Poynting vector over the volume of the c-Si layer using JCMSuite:

$$A(\lambda) = \int_V \vec{\nabla} \cdot \vec{S}(\lambda) dV. \quad (4)$$

The short-circuit current density is afterwards calculated by weighting the absorption efficiency with the solar cell spectrum [10]:

$$j_{sc} = e \int_{300\text{nm}}^{1100\text{nm}} QE \cdot A(\lambda) \cdot \phi(\lambda) d\lambda. \quad (5)$$

$\phi(\lambda)$ is the AM 1.5G solar irradiation photon number spectrum [47], e is the elementary charge, and we further assume optimal photon conversion into electrons and holes, thus the quantum (i.e. collection) efficiency $QE = 1$.

Comparing the sum of all PSD components in the annulus (Fig. 6(a)) with the diffraction components in the annulus (red squares in Fig. 6(b)), we see that both quantities follow the same trend, but the slopes and the pronounciation of the peaks are considerably different. Beginning at 0 % small nanospheres, the components in the annulus increase slowly when the portion of small nanospheres is increased since more Fourier components caused by the perturbing nanospheres do emerge. The zeroth order (not shown) will, at the expense of the annulus components, decrease as the roughness of the surface is increased. At around 50 %, the integrated diffraction efficiency δ reaches a plateau. This plateau can also be seen in the short-circuit current density (blue dots in Fig. 6(b)), whereas the PSD contributions still increase up to a portion of 60% small nanospheres. The trend in the short-circuit current density thus follows closely the trend seen in the integrated diffraction efficiency at 700 nm. The uncertainty from three diffraction simulations at each datapoint is very small; insofar, we can conclude that for obtaining values for the short-circuit current density with low uncertainties, only a few simulations are needed also.

A 1 μm thick c-Si layer on top of a flat silver substrate and with a 50 nm ITO layer yields a short-circuit current density of $j_{\text{sc}} = 15.3 \frac{\text{mA}}{\text{cm}^2}$. For the same stack with a backreflector made from a hexagonally ordered monolayer with one nanosphere size species with radius 170 nm, the short-circuit current density is $j_{\text{sc}} = 21.1 \frac{\text{mA}}{\text{cm}^2}$. For the disordered case (but still retaining only one nanosphere size), the average short-circuit current density amounts to $23.0 \frac{\text{mA}}{\text{cm}^2}$. This means that the relative increase of the short-circuit current density by giving up the hexagonal order amounts to 9 %. Introducing perturbing nanospheres will then increase the short-circuit current density even more. It is apparent from Fig. 6(b) that the short-circuit current density exhibits a similar dependency trend as the diffraction efficiency at 700 nm. Though the latter one is more expensive to calculate than the PSD, it is, at least for the height profiles considered here, a better predictor of the short-circuit current density increase than the PSD. Nevertheless, due to the fast availability of the PSD for a large number of height profiles, the PSD still can be used as a first guess for the target nanosphere size distribution.

We observe from our simulations a maximum value of $j_{\text{sc}} = 24.1 \frac{\text{mA}}{\text{cm}^2}$ at a portion of 60 % perturbing nanospheres. This is an enhancement of 58 % compared to the flat surface, 13.7 % compared to the hexagonal ordered surface and 4.8 % compared to the single nanosphere-size case without order. The uncertainty of the short-circuit current density values for the disordered cases is of the order of $0.1 \frac{\text{mA}}{\text{cm}^2}$, which indicates that the results are statistically stable.

3. Summary and conclusions

We present a strategy how one can reliably obtain a favorable light-trapping surface texture from a bottom-up fabrication approach based on colloidal nanospheres. The generated surface texture can be ensured to possess an optimal Fourier distribution for light trapping, by having a relatively simple nanosphere size distribution comprising of only two radii. An annulus shaped Fourier spectrum, which favors scattering to oblique angles in the target wavelength range for enhancement, is obtained. We discuss how analyzing the Power Spectral Density of the height profile generated from a monolayer of identical nanospheres can give guidance in choosing the nanospheres' radii. We show that the diffraction efficiency in the target wavelength range for light trapping is a better predictor for the optimum nanosphere monolayer parameters than the PSD.

We proceed to demonstrate the application of such surface textures in a thin-film c-Si cell, and obtained a short-circuit current density enhancement of 13.7 % compared to the hexagonal ordered surface and 4.8 % compared to the disordered single nanosphere-size monolayer. Further optimization of the radius choice is still possible and promises an even stronger short-circuit current enhancement. This work opens the possibility to obtain a highly efficient light trapping structure in a technology that is directly ready for upscaling in a cost effective manner.

Funding

German Research Foundation (priority programme SPP 1839 'Tailored Disorder'); Karlsruhe School of Optics and Photonics.

Acknowledgments

We are grateful to the company JCMwave for their free provision of the FEM Maxwell solver JCMsuite, with which the simulations in this work have been performed.

Disclosures

The authors declare that there are no conflicts of interest related to this article.

Fabrication of Nearly-Hyperuniform Substrates by Tailored Disorder for Photonic Applications

Peter M. Piechulla, Lutz Muehlenbein, Ralf B. Wehrspohn, Stefan Nanz, Aimi Abass, Carsten Rockstuhl, and Alexander Sprafke*

Disordered optical substrates play a key role in photonic applications. Furthermore, structures of correlated, in particular hyperuniform, disorder are an emerging new class of photonic material enabling new ways of *k*-space engineering. Yet, there are little to no feasible technologies that allow fabrication of tailored disordered structures to facilitate a tailored optical response. This work reports on a scalable method to fabricate substrates of tailored correlated disorder by self-stabilized colloid deposition. Easy-to-access experimental parameters allow to tune lateral and vertical statistics of the disordered patterns. In addition, a model is presented that allows accurate prediction of mono- as well as polydisperse particle patterns. Correlation of disorder of the prepared patterns is investigated by means of the structure factor and optical measurements.

1. Introduction

Fabrication of disordered micro- and nanostructured interfaces remains a key challenge in optics and photonics. Scalable technologies for industries, such as photovoltaics and solid-state lighting, are particularly at stake. To maintain or even excel conversion efficiencies of current solar cells, suitable and flexible interface texturing approaches are crucial to facilitate optimal light management in upcoming cell designs. Micro- and nanostructured interfaces allow, e.g., to increase material efficiency in photovoltaic devices, as absorber thicknesses are becoming thinner.^[1,2] Deterministic approaches, such as electron beam

lithography, provide great flexibility but are slow and expensive, and are therefore not feasible. Conventional scalable techniques, for instance random etching processes such as chemical wet etching^[3,4] or plasma dry etching,^[5,6] operate in a small window of parameters, thus offering only limited freedom of design and the statistics of fabricated disordered interfaces is more or less fixed. Bottom up, self-organized colloid deposition is a promising candidate for scalable interface texturing.^[7–9] There are a number of both theoretical and experimental studies on how structures fabricated by colloid deposition can be used for light management in photonic devices such as solar cells.^[10–15]

Colloid-defined samples are mostly used to produce strictly periodic structures, such as hexagonal photonic crystals and nanoparticle arrays.^[7–9] However, partly ordered and disordered structures have been shown to possibly perform significantly better than perfectly ordered structures in recent studies.^[15–20] Nevertheless, a colloid-based deposition technique to prepare disordered structures with the ability to tailor its topographical statistics, and thus a tailored optical response, is still missing.

In this work, we investigate the scalable deposition of disordered arrangements of colloidal nanoparticles that self-organize on a substrate to create disordered topographies of defined statistics. The fabricated substrates may serve as templates in a subsequent fabrication process, e.g., etching, nanosphere lithography, or overcoating with optical materials such as absorber layers for solar cells or light generation layers for solid-state lighting. Irregular deposition of colloids is often governed by unwanted effects, such as ordering into regular periodic patterns, autostratification, or separation of particle sizes due to surface tension or depletion forces.^[9,21–24] Here, we introduce a self-stabilized particle deposition process to overcome these effects. The process allows us to control lateral and vertical structure dimensions by setting size distribution and interparticle spacing of a sub-monolayer of particles through experimentally easy-to-access parameters. By understanding the deposition process and the resulting statistics, we can predict the topography and thereby enable optimization of these structures for a specific application without the need for laborious trial-and-error experiments.

The pattern structure of the substrates fabricated by our procedure is of correlated disorder and reveals features that resemble hyperuniformity.^[25,26] Like glasses, disordered

P. M. Piechulla, L. Muehlenbein, Prof. R. B. Wehrspohn, Dr. A. Sprafke
Institute of Physics
Martin Luther University Halle-Wittenberg
06120 Halle, Germany
E-mail: alexander.sprafke@physik.uni-halle.de

Prof. R. B. Wehrspohn
Fraunhofer Institute for Microstructure of Materials and Systems IMWS
06120 Halle, Germany

S. Nanz, Prof. C. Rockstuhl
Institute of Theoretical Solid State Physics
Karlsruhe Institute of Technology
76131 Karlsruhe, Germany

Dr. A. Abass, Prof. C. Rockstuhl
Institute of Nanotechnology
Karlsruhe Institute of Technology
76021 Karlsruhe, Germany

 The ORCID identification number(s) for the author(s) of this article can be found under <https://doi.org/10.1002/adom.201701272>.

DOI: 10.1002/adom.201701272

hyperuniform structures of correlated disorder show no periodic arrangement of their building blocks, while maintaining a short-range order. A hidden long-range order is given by the absence of density fluctuation on larger length scales. The relevance of correlated and in particular hyperuniform disorder in several fields of research, in particular in photonics, has been discovered just in the past decade.^[16,26–32] However, only few works have been published on bottom-up approaches to achieve structures of tailored correlated or nearly-hyperuniform disorder.^[33,34]

Being able to fabricate structures of correlated disorder with tailored statistics bears the potential of a whole new class of materials through novel ways to manipulate *k*-space.^[16,35–41] In terms of optics, to mention one example, one could bring together the advantages of periodic and disordered structures, i.e., enable a strong, grating-like but spectrally broadband diffraction. To the best of our knowledge, this is the first time that the fabrication of 2D patterns of strongly correlated disorder for optical applications in the visible and near-infrared spectral range by a practicable, cheap, and scalable technique with the ability to tailor key parameters of the achieved patterns such as the average distance of its building blocks is reported.

In the following, we first introduce our self-stabilized nanosphere deposition process scheme and present the fabricated patterns together with their optical properties. Then, we review the involved interparticle and particle–substrate potentials responsible for the pattern growth. Based on these, we develop a model that enables accurate prediction of the obtained patterns using monodisperse and even polydisperse colloidal dispersions. Furthermore, we investigate the statistical nature of the disordered patterns in terms of the structure factor. Our findings are confirmed by replicating the optical scattering response observed experimentally.

2. Experimental

2.1. Particle Deposition Process

To fabricate the nanostructured substrates, we start with conventional microscope slides covered with a thin Al₂O₃ layer (thickness 10 nm). Functionalization of the substrate surface plays a key role in the deposition process as the surface charges of the Al₂O₃ layer give rise to an electrostatic force for attracting and immobilizing nanospheres. The need for such a layer poses only a minor requirement on substrates for real-world applications as Al₂O₃ or an alternative functionalization layer can be

deposited by several means, i.e., magnetron-sputter deposition, solution-based deposition, or atomic layer deposition (ALD), on many different kind of substrates,^[42–44] in case of atomic layer deposition even on almost arbitrary surface topographies with extreme aspect ratios. The substrates are then immersed into a colloidal dispersion of polymethylmethacrylate (PMMA) nanospheres with a predefined particle size statistics and ionic strength (see also sketch in **Figure 1a**). In this work, we have used colloidal dispersions with nominal nanosphere diameters of $D = 350$ nm and $D = 499$ nm. The nanospheres attach to the substrate due to opposite charge signs of particle and substrate surface are immobilized. The remaining dispersion is then removed, leaving behind a particulate surface with randomly positioned nanospheres. Drying of the structures can lead to significant aggregation, mainly due to surface tension, which is significant compared to particle adhesion on the sub-micrometer length scale.^[45–47] To prevent the structure from collapsing, lyophilization is applied to remove the solvent.

Figure 1b shows a photograph of a fabricated sample. Homogeneity of deposition of this process is high up to the edge of the substrate. We succeeded to prepare homogeneous samples on glass slides of an area of up to 15×20 cm² without having to adapt the process. We do not see any restrictions to scale this process up to even larger substrate areas in an industrial environment.

2.2. Results

Figure 2a–c shows SEM images of substrates prepared according to the deposition scheme described above using different durations of immersion into the colloidal solution. The nanospheres attach to the substrate surface on a timescale of a few minutes and the coverage finally saturates after 40 min. After this time, no increase of nanosphere density is observed (see **Figure 2d**). The position of the nanospheres seems random as the spheres do not arrange into a periodic pattern. Still, they are evenly distributed over the substrate surface sharing a common average interparticle distance d .

Here, d denotes the interparticle surface-to-surface distance, which can be adjusted via the ionic strength μ of the dispersion solution, i.e., by adding small amounts of KCl to the suspension. **Figure 2e–g** shows SEM images of samples for which μ has been varied. Though all samples have been exposed to the respective colloidal dispersion for the same amount of time, the average distance between the particles and thus their density on the surface clearly differs. The higher μ is tuned, the smaller the

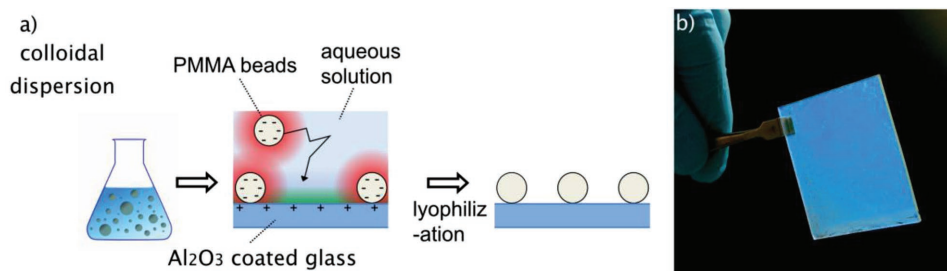


Figure 1. a) Sketch of the particle deposition process. b) Photograph of fabricated sample.

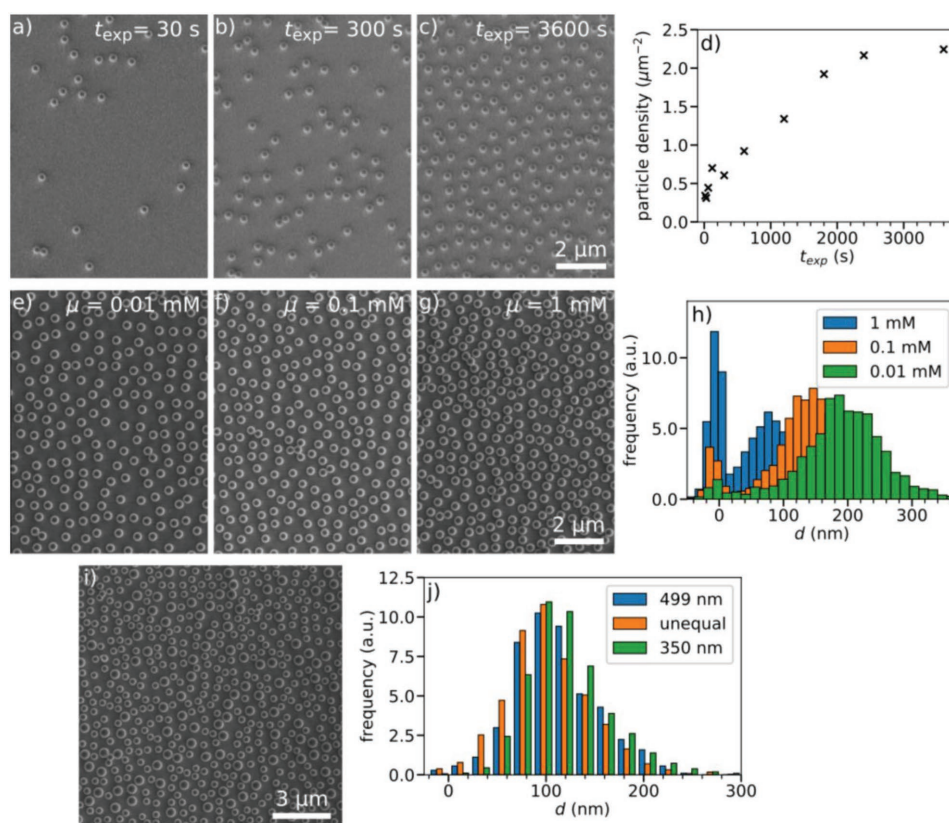


Figure 2. a–c) Scanning electron micrographs (top view) of substrates after 30, 300, and 3000 s exposure to a colloidal dispersion with nanospheres of $D = 350$ nm. d) Nanosphere density on the substrate surface plotted against exposure time. e–g) Images taken after saturated nanosphere deposition at different ionic strengths μ of the dispersion. h) Histogram of the nearest neighbor distances of the samples shown to the left. i) A substrate prepared with a colloidal dispersion containing $D = 350$ nm and $D = 499$ nm nanospheres with a number ratio of 4:1. j) Histogram of nearest neighbour distances (equal and unequal) of sample in (i).

final average interparticle distance d_0 . The positions of the particles have been extracted from a number of such micrographs (7000 to 10 000 particles for each ionic strength) by digital image recognition^[48] and the nearest neighbor distance histograms have been plotted as a quantitative measure in Figure 2h. For all ionic strengths μ , the histogram shows a bimodal distribution of nearest neighbor distances. The impression from the SEM images is confirmed and a dependence of the mode value of the interparticle distance on the ionic strength is clearly visible. We observe a shift in the average nearest neighbor distances d_0 as the ionic strength μ is increased. Adjusting μ between $0.01\text{--}1 \times 10^{-3}$ M let us tune d_0 in the range from $\approx 60\text{--}200$ nm. We note that this behavior is only little dependent on the nanosphere diameter (not shown). The peak around a surface-to-surface separation of $d = 0$ nm is attributed to particles found in aggregates. Though some of the aggregates may have formed during deposition or already before inside the dispersion, variations in the drying process seem to have a strong impact on the density of these aggregates. However, we find that the occurrence of aggregates is not a major issue in our patterns as only few particles are affected. Whereas in the samples shown in Figure 2h we have aggregation rates ranging from 1.5% (0.01×10^{-3} M) up to around 5% (1×10^{-3} M), we find that after careful optimization, we are able to achieve typical aggregation rates below 1%.

The independence of the average interparticle distance d_0 from the nanosphere diameter D enables the preparation of colloidal substrates with arbitrary predefined nanosphere size distributions that still hold a common average interparticle distance (see Figure 2i), in which $D = 350$ nm and $D = 499$ nm nanospheres have been deposited in a ratio of 4:1. The histogram in Figure 2j indeed reveals that the interparticle distance (surface-to-surface) d , between like as well as unlike particles, all peak at a common value of $d_0 = 100$ nm.

To evaluate the optical properties of our fabricated substrates, we measured their forward scattering response. We find a rotational-symmetric ring-like scattering pattern, (see Figure 3a) which shows a photograph of the forward scattered light imaged onto a screen. For this particular light wavelength ($\lambda = 405$ nm), the individual PMMA nanospheres have a scattering pattern with a maximum at a polar scattering angle of $\theta = 0^\circ$ and monotonically falling off intensity for increasing θ (see also Figure 7a), which is also expected for a complete random, i.e., uncorrelated, arrangement of scatterers. Here, in contrast, e.g., for the case of a sample prepared with 350 nm nanospheres (green line in Figure 3b) we observe suppressed scattering for an angular range of $\theta \approx 5^\circ\text{--}30^\circ$ and a new scattering maximum at $\theta = 45^\circ$. This peak shifts to smaller θ when 499 nm nanospheres are added (orange line for a mixture of 4:1, and blue line for purely 499 nm nanospheres).

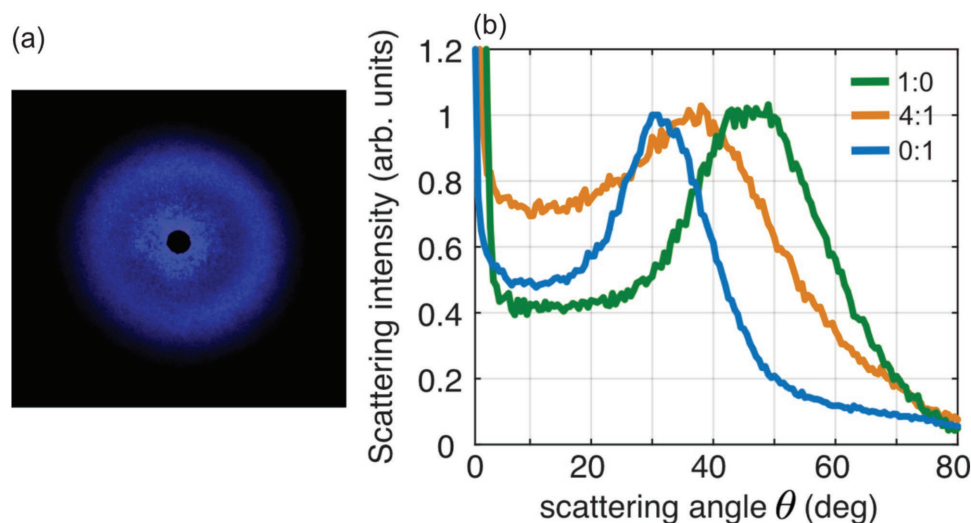


Figure 3. a) Photograph of light ($\lambda = 405$ nm) scattered by a sample fabricated by our self-stabilized nanosphere deposition procedure (PMMA nanospheres diameter: $D = 499$ nm). The black circular area in the center is due to a beam block for nonscattered laser light. b) Angular resolved scattering intensity of substrates prepared with different size distributions of the colloidal dispersion. The number ratios of $D = 350$ to $D = 499$ nm nanospheres is 1:0 (green line), 4:1 (orange line), and 0:1 (blue line).

3. Discussion

In the following, we will first review the involved interactions that are needed for the understanding of the deposition of the nanospheres. Based on these interactions, we will introduce a simple model, which enables us to predict the statistics of our samples. Furthermore, we will discuss the structural properties of the nanoparticle patterns by means of the structure factor and investigate their optical scattering response.

3.1. Interaction Potentials

The PMMA particles are sulfate-stabilized and carry a negative surface charge density throughout a wide range of experimental conditions. The thin layer of Al_2O_3 covering the substrate forms positive surface charges in pH neutral conditions.^[49,50] As the particle deposition takes place in a liquid bath with virtually no agitation, surface tension and convective forces are negligible. Thus, primarily electrostatic surface charges give rise to interparticle and particle–substrate interactions while sedimentation and diffusion drive particle motion.

The interaction potentials are described by the Derjaguin–Landau–Verwey–Overbeek (DLVO) theory^[51]

$$W_{\text{DLVO}}(d) = W_{\text{el}}(d) + W_{\text{vdw}}(d) \quad (1)$$

with $W_{\text{el}}(d) \propto e^{-\kappa d}$ and $W_{\text{vdw}} \propto -\frac{1}{d}$

with surface-to-surface separation d of two interacting objects and the Debye screening length $1/\kappa$. For particle–substrate interactions, in our case particles and substrate carry opposite charge signs, both van der Waals potential W_{vdw} and electrostatic potential W_{el} are negative. Thus, the nanospheres are always attracted to the substrate surface. Particle–particle interactions are governed by charge-like

repulsion, which stabilizes the colloidal dispersion by preventing particles from aggregation. The extend of this repulsive potential is characterized by κ and can be controlled via the ionic strength μ of the dispersion.^[47] However, effects of van der Waals forces and the effect of curved surfaces on electrostatic and van der Waals forces are not included in κ . We therefore propose to characterize the particle pair interaction by the equilibrium separation at which the pair potential exhibits a local minimum (see **Figure 4a**), in literature often referred to as the secondary minimum.^[51] For the parameter range considered here, the depth of the potential minimum is in the order of $1 k_{\text{B}}T$.

The path of an individual particle is determined by a rather complex electrostatic potential landscape due to the substrate and nearby particles.^[52,53] However, the most important component of this potential landscape is the pair interaction potential. Calculating this potential gives access to the qualitative relations of the controllable parameters ionic strength μ and particle diameter D and the resulting interparticle distance (surface-to-surface separation) d_0 on the surface. The dependence of the equilibrium interparticle distance d_0 on ionic strength and particle diameter is shown for a wide range of parameters in **Figure 4b**. The particle size range of 50 nm to 1 μm covers the typical sizes for optical applications in the subwavelength visible to the near-infrared spectral range. The limits of ionic strength are deduced from practical considerations: An ionic strength lower than 10^{-5} M is difficult to achieve experimentally due to dissolved gases (e.g., CO_2) and dissociation of surface groups by surface charges.^[47] On the other end, high ionic strengths ($>10^{-2}$ M) will reduce the height of the potential barrier and lead to particle aggregation up to the point of colloidal instability, i.e., irreversible aggregation. According to **Figure 4b**, the equilibrium separation spans over about two orders of magnitude with the variation of ionic strength but is only little sensitive to the nanoparticles size. Only for particle diameters smaller than about 100 nm a reduction of equilibrium

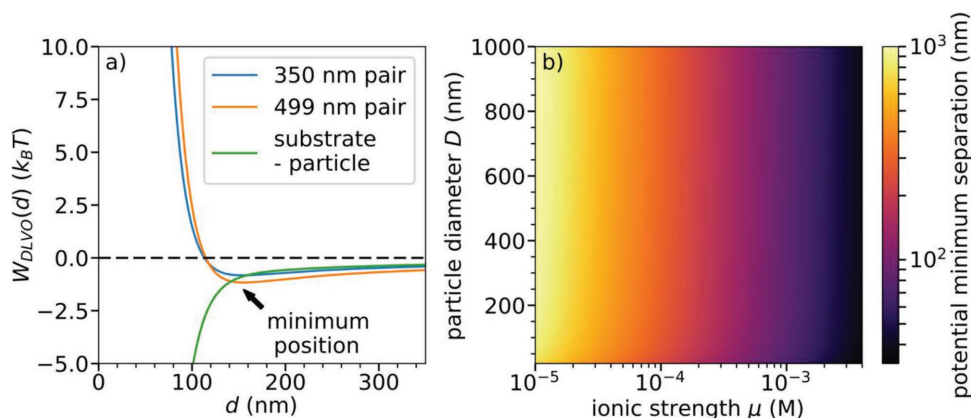


Figure 4. a) Exemplary interaction potentials according to Equation (1) for interparticle interaction (pairs of equal size particles, 350 nm and 499 nm diameter nanospheres, respectively) and 350 nm particle– Al_2O_3 substrate interaction. Potentials have been calculated using typical values for the surface charge densities of sulfate-stabilized PMMA particles^[49] and Al_2O_3 .^[50] b) Interaction potential minimum position versus particle diameter D and ionic strength μ .

separation can be observed with decreasing particle diameter. This is in agreement with our experimental finding that irrespective of nanosphere diameter D , the average interparticle distance d_0 remains constant (see Figure 2j).

In **Figure 5**, the experimentally found mode value of nearest neighbor distances, i.e., the average interparticle distance d_0 , is plotted against the ionic strength μ along with minimum positions from calculated pair potentials. The qualitative agreement indicates that pair potentials and the resulting equilibrium separations are indeed an essential component to the understanding of the deposition process. The deviations, in particular in the low ionic strength regime, are partly due to the practical difficulties when working with low ionic strengths, partly due to the influence of the substrate. As a result, for PMMA particles dispersed in an aqueous solution and deposited on Al_2O_3 -functionalized surfaces, the typical particle separations can be controlled in a range of about 60–200 nm. We note that the presented method is not restricted to the use of PMMA nanoparticles. The prerequisites are that the nanoparticles carry a surface charge, which is of opposite sign than that of the substrate. This enables electrostatic (attractive) substrate–particle and (repulsive) particle–particle interaction. This imposes only a minor requirement on the choice of nanoparticle material since nanoparticles can be easily functionalized with (charged)

surfactants by wet-chemical means or are already functionalized with surfactants during their fabrication process.

3.2. Particle Deposition Process

While pair potentials have been identified as a major element in the deposition process, they are only one component of a more complex potential landscape a particle experiences when diffusing close to a particle covered substrate.^[53] Accurate data for surface potentials of particles and substrate to simulate the deposition realistically are not trivial to acquire.^[49] However, a common way to predict patterns of a particle covered surface is the random sequential adsorption (RSA) model. In this work, instead of calculating the RSA parameters from raw material data, we propose to extract the parameters from our experiments. As the qualitative relations are given above, one would need a calibration similar to Figure 5a to predict particle patterns from arbitrarily composed colloidal dispersions. The calibration can be reconstructed from a limited set of experimentally determined results, as for instance the influence of particle size is small.

In the RSA model, particles are sequentially placed on a plane at random positions (x_i, y_i) . Each nearby particle m modulates the probability of the i th particle to stick at the given

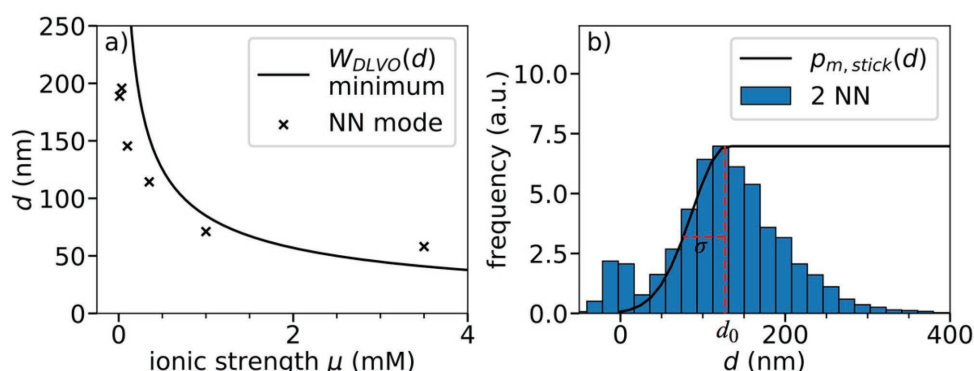


Figure 5. a) Mode value of nearest neighbor distances (NN mode) from fabricated samples along with calculated minimum positions in pair interaction potential. b) Two nearest neighbor histogram of particles deposited at $\mu = 3.5 \times 10^{-4}$ M KCl and a fitted sticking probability function $p_{m,stick}(d)$.

position by a sticking probability function $p_{m,\text{stick}}$ or being discarded otherwise

$$p_{\text{stick}}(\mathbf{x}_i, \mathbf{y}_i) = \prod_m p_{m,\text{stick}}(\mathbf{x}_i, \mathbf{y}_i) \quad (2)$$

We assume that particle–substrate attraction is only important at the very vicinity to the substrate surface, so that a particle will stick to the substrate on approach but its path through the liquid is solely influenced by other nearby particles. In the most simple case, the force a particle experiences when approaching another particle is inversely proportional with distance d , thus the potential will scale with $1/d^2$, while the probability for a particle to have a certain energy is $\propto e^{-E/k_B T}$. Consequently, a half-Gaussian probability is assumed for a particle to be found close to another one. This directly transfers to the sticking probability, given the case that the particle is also close to the substrate

$$p_{\text{stick}}(\mathbf{x}_i, \mathbf{y}_i) = \begin{cases} e^{-\frac{(d_m(\mathbf{x}_i, \mathbf{y}_i) - d_0)^2}{2\sigma^2}} & d_m \leq d_0 \\ 1 & d_m > d_0 \end{cases} \quad (3)$$

where $d_m(\mathbf{x}_i, \mathbf{y}_i)$ denotes the surface-to-surface distance to the neighboring particle m . We extract the parameters σ and d_0 from histograms derived from experimental data as shown in Figure 5b. In accordance with the assumptions for $p_{m,\text{stick}}$, one can distinguish two sides of the nearest neighbor distance distribution: The right shoulder being caused by the random nature of the deposition process and the left by the soft-shell nature of the particles due to the pair potential, as opposed to colloidal hard spheres.

3.3. Verification of the Deposition Model and Structural Properties

An intuitive and common tool to characterize colloidal structures that has been borrowed from X-ray and neutron scattering experiments is the structure factor $S(\mathbf{q})$. In short, the structure factor describes the distribution of spatial frequencies a certain structure provides. $S(\mathbf{q})$ is related to the pair correlation function $g(r)$ by a Fourier transform, but can also be deduced directly from real-space representations such as SEM images from N particle positions $\mathbf{r}^{[54]}$

$$S(\mathbf{q}) = \frac{1}{N} \sum_{i,j} e^{-i\mathbf{q}(\mathbf{r}_i - \mathbf{r}_j)} \quad (4)$$

A similar expression yields the partial structure factors for two unequal types of particles α and β ^[54]

$$S_{\alpha\beta}(\mathbf{q}) = \frac{1}{N} \sum_{j=1}^{N_\alpha} \sum_{i=1}^{N_\beta} e^{-i\mathbf{q}(\mathbf{r}_i - \mathbf{r}_j)} \quad (5)$$

To fully determine a system, the partial structure factor for every combination of particle types has to be calculated, e.g., three functions for a bidisperse particle composition, which summed up give the total structure factor $S_{\text{total}}(\mathbf{q}) = S_{\alpha\alpha}(\mathbf{q}) + 2S_{\alpha\beta}(\mathbf{q}) + S_{\beta\beta}(\mathbf{q})$.

In Figure 6a, the 2D representation ($\mathbf{q} = q_x \hat{\mathbf{e}}_x + q_y \hat{\mathbf{e}}_y$) of the structure factor of a monodisperse ($D = 350$ nm) sample is plotted. Due to the isotropic nature of the pattern in real space, the structure factor is invariant to rotation. We therefore show in Figure 6b the angular average of $S(\mathbf{q})$ over all \mathbf{q} of the same length. Here, $S(|\mathbf{q}| = q)$ is compared for the experimentally (black) and simulated (red) determined patterns. We find very good agreement between experiment and simulation. This indicates that our introduced nanosphere pattern generation algorithm correctly reproduces the statistics of the experimentally fabricated patterns.

In the low q limit, both simulation and experimental curves show similarly low values close to zero. $S(\mathbf{q})$ from the experiment additionally shows high peaks near $q = 0$, which is potentially due to aggregates that are not included in the deposition model, and are therefore absent in $S(\mathbf{q})$ for simulated positions. Small values of S for $q \rightarrow 0$ indicate correlated disordered structures as this property reveals the suppression of long-range order and while not truly hyperuniform, i.e. reaching $S = 0$ for $q \rightarrow 0$, imply large-scale correlated disordered structures.^[29] Large-scale correlated disorder is a feature of all samples fabricated by our deposition method after saturation of the particle surface density. Simply speaking, this means that interaction of the structure with external quantities, e.g., light waves, is suppressed in this region. This depicts an important physical property since this could lead to the inhibition of propagation of light, i.e., the formation of bandgaps, in media which are not crystalline but random.

The appearance of correlated disorder is only achieved after sufficiently long exposure of the substrate to the colloidal dispersion. The evolution of a particle pattern with time is documented in Figure 6c–f, which shows the structure factor S for the samples shown in Figure 2e–g. At low exposure times ($t_{\text{exp}} = 30$ s), particles are scattered randomly over the surface, resulting in a structure factor with no correlation, which is similar to a gas. As exposure time is increased ($t_{\text{exp}} = 300$ s), the particle density increases with still no apparent order in the real space image but a decreasing structure factor for low q values can be observed. For longer exposure times ($t_{\text{exp}} = 3600$ s) the particle density eventually saturates and an evenly distributed particle pattern is visible in the real space SEM image as well as a structure factor that has low values for $q \rightarrow 0$, i.e., a strongly correlated disordered structure has formed.

We have shown above that the average interparticle distance d_0 between next neighbors is independent of particle size. Therefore, only one set of parameters σ and d_0 for a certain ionic strength μ should be sufficient to even simulate particle patterns using polydisperse colloidal dispersions. The particle pattern in Figure 2i has been deposited with a mixture of nanospheres with a number ratio of $n_{350 \text{ nm}}:n_{499 \text{ nm}} = 4:1$. The total structure factor S_{total} deduced from SEM images is plotted in Figure 6f. Again, patterns of correlated disorder are achieved even in the polydisperse case. The angular average of S_{total} along with the partial structure factors S_{11} , S_{22} , and S_{12} is plotted in Figure 6g (index 1: 350 nm particles, index 2: 499 nm). Using the same set of parameters (σ , d_0) as above, a particle pattern has been simulated, resulting in structure factors shown in Figure 6h, which are in good agreement with the experimental curves.

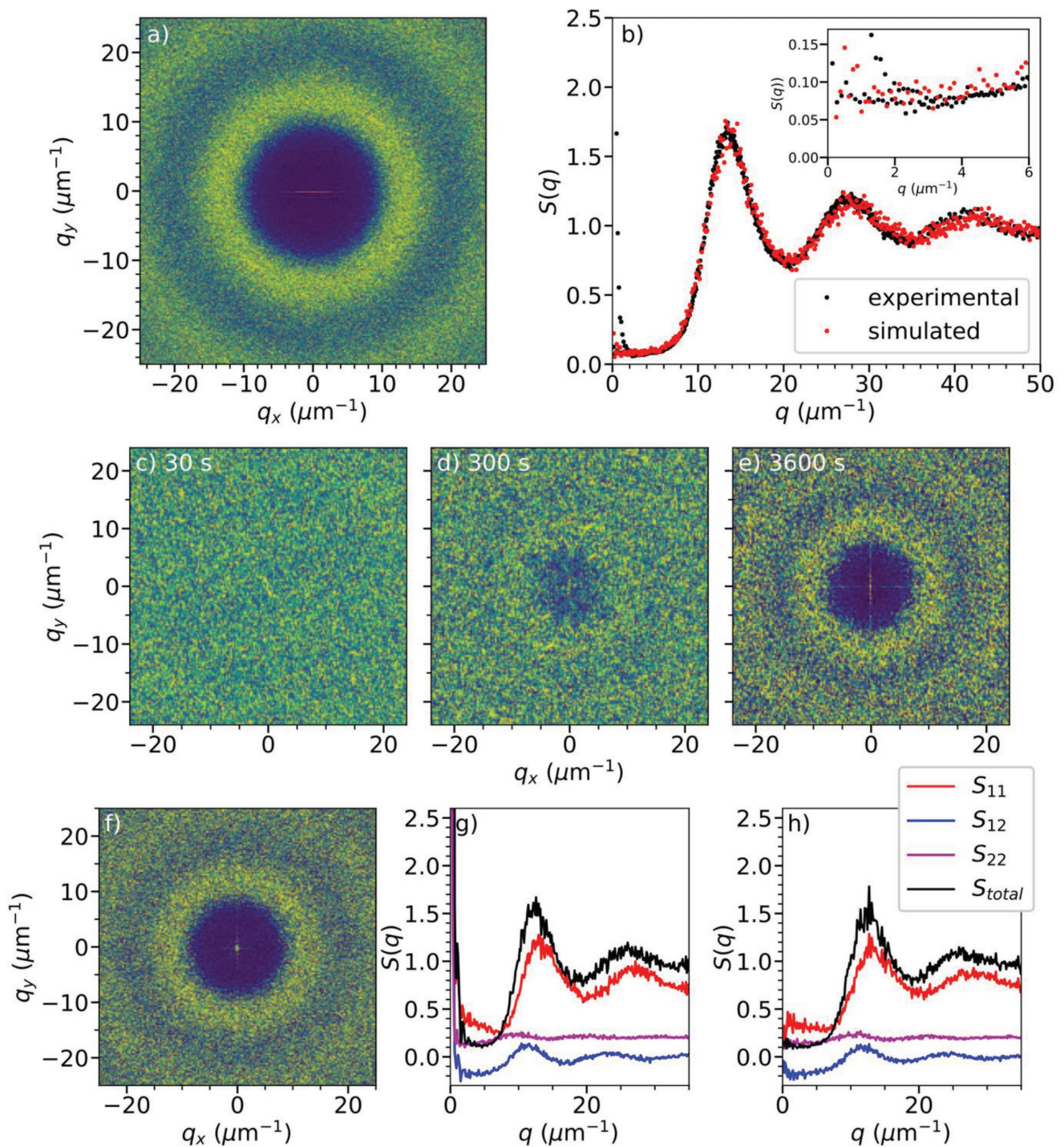


Figure 6. a) Structure factor S extracted from the positions of a sample with 350 nm nanospheres deposited at 3.5×10^{-4} M. b) Angular average of S for simulated and real positions. c–e) Structure factor S extracted from samples after varying exposure times to a colloidal dispersion. f) Total structure factor of a sample prepared with a bidisperse mixture of particles with number ratio $n_{350 \text{ nm}} : n_{499 \text{ nm}} = 4:1$. Partial structure factors deduced from g) experiment and h) simulation (index 1:350 nm particles, index 2:499 nm particles).

3.4. Optical Properties

Assuming negligible near-field interaction and multiple scattering between the nanospheres, one can predict their light scattering response from the angular scattering pattern of the

individual scatterers together with the structure factor S of the sample. This is in analogy to X-ray and neutron scattering experiments, where the scattering patterns of solids are deduced from the form factor (scattering of individual atoms and molecules) and the structure factor. Considering our case, these

assumptions are still justified: Calculations (not shown) reveal that for both sphere sizes >96.8% of all scattered light is either backscattered into the substrate or forward scattered into a cone with an opening angle of $\theta = 65^\circ$. The value of $\theta = 65^\circ$ follows from simple geometric considerations for which a cone with this opening angle placed in the center of a particle will not intersect a neighboring particle even if the surface-to-surface distance is only 50 nm. This leaves an amount of scattered light of <3.2% that may interact with neighboring spheres, which we find to be sufficiently low to neglect multiple scattering. Considering near-field interaction between neighboring particles, we note that we are not in resonance with an electromagnetic mode of the particles, thus no enhanced electromagnetic fields are expected, which may give rise to near field coupling. Furthermore, the first mode that would play a role would be a magnetic dipole resonance. A distinct feature of this mode are ring currents, i.e., ring-shaped electric fields, which are, in the case of spheres, localized within the sphere and barely leak out, which makes it even less likely for a sphere to couple to its neighbor.

The scattered intensity I of a structure with known structure factor S is^[55]

$$I(k_{\parallel}) \propto \sum_{\alpha, \beta}^m E_{\alpha}(k_{\parallel}) E_{\beta}(k_{\parallel}) \cdot S_{\alpha\beta}(k_{\parallel}) \quad (6)$$

with the scattering amplitudes E_m of particle type m , the projection of the wave vector of light \mathbf{k} onto the plane of the substrate,

$k_{\parallel} = |\mathbf{k}| \sin\theta$, with θ being the polar scattering angle, and $k_{\parallel} = q$ for normal incidence.

In **Figure 7a**, we have plotted the scattering patterns of individual PMMA spheres with diameter $D = 350$ nm and $D = 499$ nm, respectively, placed on a glass substrate. The patterns have been averaged over the azimuthal angle, but we note that there is only very little dependence on this angle. As expected, forward scattering of the individual particles has a maximum into the $\theta = 0$ direction and the intensity quickly falls off for increasing θ except for a little bump in the range of $\theta = 60^\circ$ for the 499 nm particle, which is a known phenomenon due to interference of light scattered by the individual sphere.^[56] We then modeled nanosphere patterns with the RSA algorithm as described above to simulate samples that have been prepared with $D = 499$ nm nanospheres only, a mixture of nanospheres with $D = 350$ nm and $D = 499$ nm of a ratio of 4:1, and $D = 350$ nm nanospheres only. The derived structure factors are plotted in **Figure 7b,c** (partial structure factors S_{11} , S_{22} , and S_{12}), and d , respectively. Inserting the angular scattering patterns of the individual particles and the corresponding structure factors into Equation (6), we obtain the angular scattering response plotted in **Figure 7e** together with experimental measurements.

We find good agreement between the predictions based on the structure factor and experiment. In particular, suppressed scattering for an angular range close to the optical axis and the

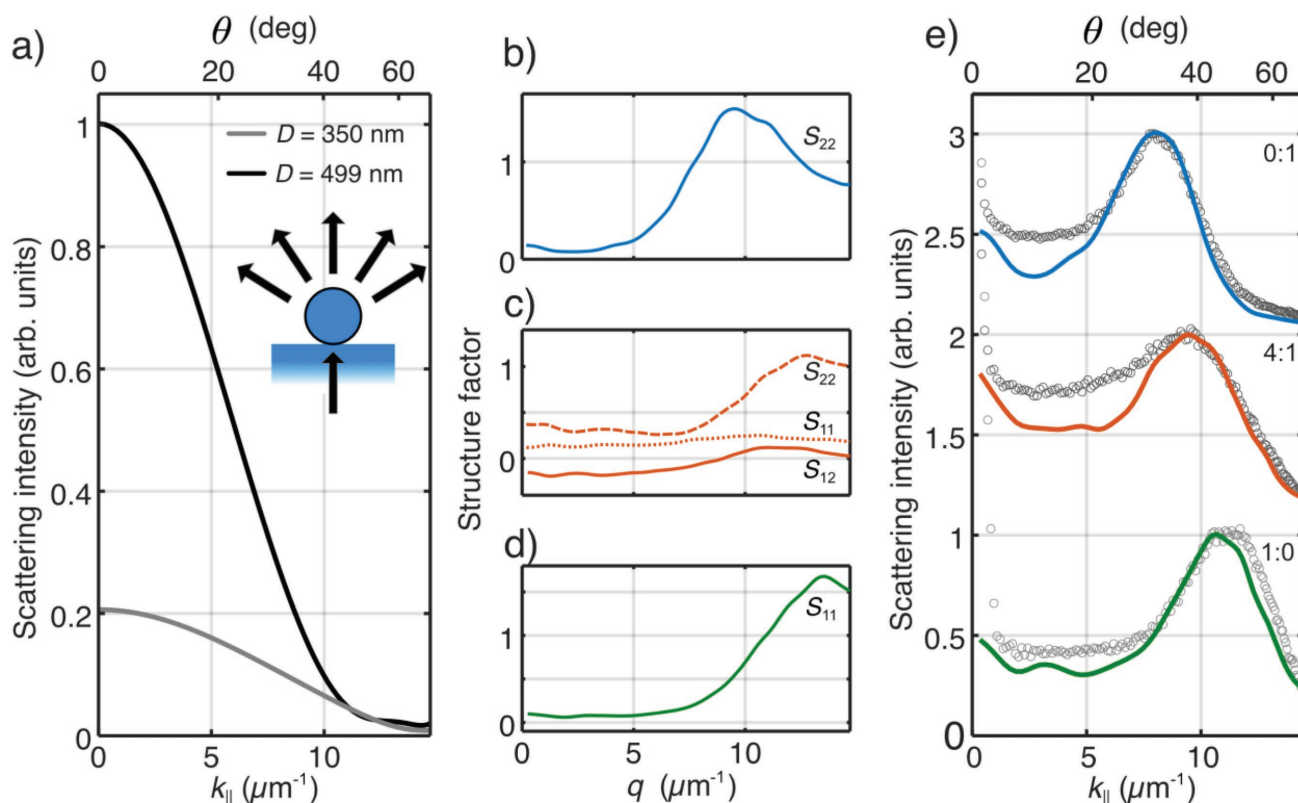


Figure 7. a) Simulated scattering pattern of individual PMMA nanospheres with diameter $D = 350$ nm (gray line) and $D = 499$ nm (black line), $\lambda = 405$ nm. $S(q)$ deduced from RSA algorithm to model a sample containing b) only $D = 499$ nm, c) $D = 499$ nm and $D = 350$ nm of a number ratio of 1:4, and d) only $D = 350$ nm nanospheres. e) Scattering pattern derived from the simulated individual scattering pattern and the RSA structure factor along with experimental measurements (circles). The blue, orange, and green lines correspond to the structures of the same colors shown to the left.

distinct maximum off the optical axis could be reproduced. For instance, in the case of the sample with $D = 350$ nm nanospheres only, we find suppressed scattering between $\theta \approx 8^\circ$ – 30° and a scattering peak at $\theta = 43.0^\circ$. This is a direct consequence of our statement above that the structures are of correlated disordered with low values of the structure factor for a certain ranges of q around $q = 0$. Since the structure factor is rotational symmetric in the plane of the substrate, the scattering pattern holds the same symmetry, thus, the scattering pattern reveals a ring-like scattering maximum as has been observed experimentally (see Figure 3a). Adding larger spheres, this peak shifts to smaller angles, $\theta = 37.0^\circ$ for the sample with a number ratio of 4:1, and $\theta = 30.5^\circ$ for 499 nm spheres only.

Suppression and enhancement of scattering is a result of destructive and constructive interference of light waves scattered by each nanosphere. This is similar to the case of diffraction of a grating with two important distinctions: One is that here diffraction is rotational symmetric due to the isotropic arrangement of scatterers. The other one being the fact that there is not one discrete next neighbor distance but a distribution of next neighbor distances leading to a broadening of the diffraction peak. Still, the analogy with a grating gives an intuitive explanation of the shift of the scattering peak to smaller angles with the addition of larger nanospheres: Since the surface-to-surface distance approximately stays constant, the center-to-center distance increases with larger spheres. As in the case of a grating with periodicity, a larger correlation length leads to a smaller angle of diffraction.

The variation of the scattering maximum as discussed above provides a simple example on tailoring the optical response of a structure of correlated disorder. We chose to keep the ionic strength μ of the colloidal dispersion constant and tune the ratio of small and large nanospheres instead to obtain a scattering maximum at an angle θ , which lies approximately in the center between the two monodisperse cases. To find the correct ratio of nanospheres, we used the RSA algorithm to generate nanosphere patterns, derived their structure factor and then calculated the scattering pattern. Measurement of the sample fabricated with the predicted ratio confirms our proposed strategy

4. Conclusion

In summary, we have presented a scalable, self-stabilized bottom-up fabrication technique for 2D nanostructured strongly correlated disordered substrates. Tuning easy-to-access experimental parameters such as the size distribution of colloids and the ionic strength of the dispersion, we are able to produce particle patterns of tailored disorder. We developed a particle deposition model, which enables to predict the statistics of the obtained nanoparticle patterns. The agreement of the statistics of experiment and simulation confirms that our presented approach depicts a desirable tool to predict possible particle patterns. Therefore, our approach opens the path to tailor physical material properties such as the optical response based on simulated structures without the need for tedious experimental parameter scans. Fabrication of truly hyperuniform structures through further optimization of the deposition process constitutes an important direction for future work. As

particle aggregates introduce unwanted long-range density fluctuations, this may be achieved by a complete suppression of aggregates, e.g. through improved surface chemistry of particles and substrate.

In this work, we used the initially deposited PMMA nanospheres as optical scatterers. We note that one could use these nanospheres only as a template instead, e.g., for lithography processes, to prepare different kind of scatterers. Preparing scatterers based on plasmonic metals or high-refractive index materials with stronger scattering intensities or more exotic angular scattering patterns with our presented deposition procedure opens up the way to a completely new class of tailored optical materials.

5. Experimental Section

Standard microscope slides were cleaned in a combined wet chemical and oxygen plasma protocol. The glass surfaces were functionalized with aluminum oxide films by means of ALD.^[43] In the thermal ALD process, substrates were exposed to alternating pulses of trimethylaluminum (TMA, $\text{Al}(\text{CH}_3)_3$) and water (200 ms pulse duration, 100 pulses each) at 180°C . The reaction chamber was purged with nitrogen for 2 s in between pulses.

PMMA particles of various sizes were bought from Microparticles Berlin GmbH. By supplier specification, the particles were monodisperse with a coefficient of variation of 2.3%. The stock colloidal dispersion was first treated in an ultrasonic bath to break up reversible aggregates and then centrifuged at low g factor to remove irreversible aggregates. The colloidal dispersion was then diluted with a mixture of MicroPure water (18 M Ω), potassium chloride solution (KCl), and isopropyl alcohol (IPA, 30%). The latter has experimentally been proven to provide more evenly distributed particles, presumably due to better substrate wetting. The amount of potassium chloride was adjusted to achieve the desired ionic strength in the resulting dispersion. The glass samples were horizontally exposed (Al_2O_3 face up) to the colloidal dispersion for 5 to 6 h unless noted otherwise, which ensured particle saturated surfaces. Substrates were removed from the colloidal dispersion and stirred in a bath of deionized water for at least one minute to remove excess particles that were not attached to the surface, without allowing them to dry in between.

After a dip in fresh deionized water, the samples were horizontally placed on an aluminum block that had previously been cooled to -20°C . The block including the samples was placed in a desiccator and a vacuum was applied to sublimate the residue water, after which the samples were ready for characterization.

Scanning electron micrographs were taken with a field emission microscope (FEI Versa 3D) at 2 keV. The exemplary images shown above were taken from samples as prepared. For the large area image recognition, samples were sputter coated with 15 nm gold in order to avoid charging effects. For each particle size, a template image was cropped from the respective micrograph and used for template matching in a custom Python program based on the OpenCV library.^[48] About 35 000 to 45 000 particle positions were read from images of $138 \times 92 \mu\text{m}^2$ unless otherwise noted.

For the implemented RSA algorithm, an effective fill fraction FF_{eff} was defined, that was the share of the substrate covered by particles with an extended radius $r_{\text{ext}} = D/2 + d_0$. FF_{eff} can be determined from SEM images; we set FF_{eff} as a stop criterion for the algorithm.

To calculate the angular scattering spectrum of the individual PMMA spheres on glass substrate, we rigorously solved Maxwell's equations in 3D with appropriate source, material and boundary condition settings, using the time-harmonic finite-element solver JCMsuite.^[57]

Acknowledgements

This work was funded by the Deutsche Forschungsgemeinschaft (DFG) through program DFG-SPP 1839 "Tailored Disorder". S.N. also

acknowledges support by the Karlsruhe School of Optics & Photonics (KSOP). The authors thank Claudia Stehr for her excellent technical support.

Conflict of Interest

The authors declare no conflict of interest.

Keywords

colloidal deposition, disorder, k-space engineering, scattering interfaces, tailored disorder

Received: November 25, 2017

Revised: January 22, 2018

Published online:

- [1] S. V. Boriskina, M. A. Green, K. Catchpole, E. Yablonovitch, M. C. Beard, Y. Okada, S. Lany, T. Gershon, A. Zakutayev, M. H. Tahersima, V. J. Sorger, M. J. Naughton, K. Kempa, M. Dagenais, Y. Yao, L. Xu, X. Sheng, N. D. Bronstein, J. A. Rogers, A. P. Alivisatos, R. G. Nuzzo, J. M. Gordon, D. M. Wu, M. D. Wisser, A. Salleo, J. Dionne, P. Bermel, J.-J. Greffet, I. Celanovic, M. Soljacic, A. Manor, C. Rotschild, A. Raman, L. Zhu, S. Fan, G. Chen, *J. Opt.* **2016**, *18*, 073004.
- [2] International Technology Roadmap for Photovoltaic (ITRPV), 8th ed., **2017**, <http://www.itrpv.net> (accessed: September 2017).
- [3] K. E. Bean, *IEEE Trans. Electron Devices* **1978**, *25*, 1185.
- [4] Z. Huang, N. Geyer, P. Werner, J. de Boor, U. Gösele, *Adv. Mater.* **2011**, *23*, 285.
- [5] M. Steglich, T. Käsebier, M. Zilk, T. Pertsch, E.-B. Kley, A. Tünnermann, *J. Appl. Phys.* **2014**, *116*, 173503.
- [6] M. Gaudig, J. Hirsch, T. Schneider, A. N. Sprafke, J. Ziegler, N. Bernhard, R. B. Wehrspohn, *J. Vac. Sci. Technol. A* **2015**, *33*, 05E132.
- [7] J. C. Hulthen, R. P. Van Duyne, *J. Vac. Sci. Technol. A* **1995**, *13*, 1553.
- [8] T. R. Jensen, M. D. Malinsky, C. L. Haynes, R. P. Van Duyne, *J. Phys. Chem. B* **2000**, *104*, 10549.
- [9] A. N. Sprafke, D. Schneevoigt, S. Seidel, S. L. Schweizer, R. B. Wehrspohn, *Opt. Express* **2013**, *21*, A528.
- [10] S. Nanz, A. Abass, P. Piechulla, A. N. Sprafke, R. Wehrspohn, C. Rockstuhl, in *Light, Energy and the Environment*, OSA Congress, **2016**, p. PTh2A.3.
- [11] S. Wiesendanger, M. Zilk, T. Pertsch, C. Rockstuhl, F. Lederer, *Opt. Express* **2013**, *21*, A450.
- [12] S. Wiesendanger, M. Zilk, T. Pertsch, F. Lederer, C. Rockstuhl, *Appl. Phys. Lett.* **2013**, *103*, 131115.
- [13] J. Eisenlohr, J. Benick, M. Peters, B. Bläsi, J. C. Goldschmidt, M. Hermle, *Opt. Express* **2014**, *22*, A111.
- [14] Y. Chang, D. N. R. Payne, M. E. Pollard, S. Pillai, D. M. Bagnall, *Proc. SPIE* **2015**, *9668*, 1.
- [15] C. Trompoukis, I. Massiot, V. Depauw, O. El Daif, K. Lee, A. Dmitriev, I. Gordon, R. Mertens, J. Poortmans, *Opt. Express* **2016**, *24*, A191.
- [16] *Amorphous Nanophotonics* (Eds: C. Rockstuhl, T. Scharf), Springer, Berlin, Germany **2013**.
- [17] E. R. Martins, J. Li, Y. Liu, V. Depauw, Z. Chen, J. Zhou, T. F. Krauss, *Nat. Commun.* **2013**, *4*, 2665.
- [18] F. Pratesi, M. Burresti, F. Riboli, K. Vynck, D. S. Wiersma, *Opt. Express* **2013**, *21*, A460.
- [19] A. Oskooi, P. A. Favuzzi, Y. Tanaka, H. Shigeta, Y. Kawakami, S. Noda, *Appl. Phys. Lett.* **2012**, *100*, 181110.
- [20] K. Vynck, M. Burresti, F. Riboli, D. S. Wiersma, *Nat. Mater.* **2012**, *11*, 1017.
- [21] K. Nagayama, *Colloids Surf. A* **1996**, *109*, 363.
- [22] M. Yamaki, J. Higo, K. Nagayama, *Langmuir* **1995**, *11*, 2975.
- [23] A. K. Atmuri, S. R. Bhatia, A. F. Routh, *Langmuir* **2012**, *28*, 2652.
- [24] Y. Mao, M. E. Cates, H. N. W. Lekkerkerker, *Physica A* **1995**, *222*, 10.
- [25] D. A. Keen, A. L. Goodwin, *Nature* **2015**, *521*, 303.
- [26] D. S. Wiersma, *Nat. Photonics* **2013**, *7*, 188.
- [27] G. M. Conley, M. Burresti, F. Pratesi, K. Vynck, D. S. Wiersma, *Phys. Rev. Lett.* **2014**, *112*, 143901.
- [28] H. H. Sheinflux, Y. Lumer, G. Ankonina, A. Z. Genack, G. Bartal, M. Segev, *Science* **2017**, *356*, 953.
- [29] S. Torquato, F. H. Stillinger, *Phys. Rev. E* **2003**, *68*, 041113.
- [30] R. D. Batten, F. H. Stillinger, S. Torquato, *J. Appl. Phys.* **2008**, *104*, 033504.
- [31] Y. Jiao, T. Lau, H. Hatzikirou, M. Meyer-Hermann, J. C. Corbo, S. Torquato, *Phys. Rev. E* **2014**, *89*, 022721.
- [32] R. Xie, G. G. Long, S. J. Weigand, S. C. Moss, T. Carvalho, S. Roorda, M. Hejna, S. Torquato, P. J. Steinhardt, *Proc. Natl. Acad. Sci. USA* **2013**, *110*, 13250.
- [33] J. Ricouvier, R. Pierrat, R. Carminati, P. Tabeling, P. Yazhgur, *Phys. Rev. Lett.* **2017**, *119*, 208001.
- [34] G. Zito, G. Rusciano, G. Pesce, A. Malafronte, R. Di Girolamo, G. Ausanio, A. Vecchione, A. Sasso, *Phys. Rev. E* **2015**, *92*, 050601.
- [35] E. Martins, J. Li, Y. Liu, J. Zhou, T. Krauss, *Phys. Rev. B* **2012**, *86*, 041404.
- [36] E. R. Martins, J. Li, Y. Liu, V. Depauw, Z. Chen, J. Zhou, T. F. Krauss, *Nat. Commun.* **2013**, *4*, 2665.
- [37] M. Castro-Lopez, M. Gaio, S. Sellers, G. Gkantzounis, M. Florescu, R. Sapienza, *APL Photonics* **2017**, *2*, 061302.
- [38] Z. Ma, S. Torquato, *J. Appl. Phys.* **2017**, *121*, 244904.
- [39] N. Lawrence, J. Trevino, L. Dal Negro, *J. Appl. Phys.* **2012**, *111*, 113101.
- [40] N. Yu, P. Genevet, M. A. Kats, F. Aieta, J.-P. Tetienne, F. Capasso, Z. Gaburro, *Science* **2011**, *334*, 333.
- [41] L. S. Froufe-Pérez, M. Engel, P. F. Damasceno, N. Muller, J. Haberko, S. C. Glotzer, F. Scheffold, *Phys. Rev. Lett.* **2016**, *117*, 1.
- [42] J. A. García-Valenzuela, R. Rivera, A. B. Morales-Vilches, L. G. Gerling, A. Caballero, J. M. Asensi, C. Voz, J. Bertomeu, J. Andreu, *Thin Solid Films* **2016**, *619*, 288.
- [43] M. Otto, M. Kroll, T. Käsebier, R. Salzer, A. Tünnermann, R. B. Wehrspohn, *Appl. Phys. Lett.* **2012**, *100*, 191603.
- [44] P. Hanarp, D. S. Sutherland, J. Gold, B. Kasemo, *Colloids Surf., A* **2003**, *214*, 23.
- [45] Y. Reyes, Y. Duda, *Langmuir* **2005**, *21*, 7057.
- [46] J. Aizenberg, P. V. Braun, P. Wiltzius, *Phys. Rev. Lett.* **2000**, *84*, 2997.
- [47] P. Hanarp, D. Sutherland, J. Gold, B. Kasemo, *Nanostruct. Mater.* **1999**, *12*, 429.
- [48] G. Bradski, *Dr. Dobb's J. Software Tools* **2000**, *120*, 122.
- [49] S. H. Behrens, D. G. Grier, *J. Chem. Phys.* **2001**, *115*, 6716.
- [50] R. Sprycha, *J. Colloid Interface Sci.* **1989**, *127*, 1.
- [51] J. N. Israelachvili, *Intermolecular and Surface Forces*, Academic Press, Cambridge, MA, USA **1992**.
- [52] Z. Adamczyk, M. Zembala, B. Siwek, J. P. Warszyński, *Colloid Interface Sci.* **1990**, *140*, 123.
- [53] M. R. Oberholzer, J. M. Stankovich, S. L. Carnie, D. Y. C. Chan, A. M. Lenhoff, *J. Colloid Interface Sci.* **1997**, *194*, 138.
- [54] H. Liu, S. J. Paddison, *Phys. Chem. Chem. Phys.* **2016**, *18*, 11000.
- [55] *Neutrons, X-rays, and Light: Scattering Methods Applied to Soft Condensed* (Eds: P. P. Lindner, T. T. Zemb), Elsevier, Amsterdam, NL **2002**.
- [56] C. F. Bohren, D. R. Huffman, *Absorption and Scattering of Light by Small Particles*, Wiley-VCH, Weinheim, Germany **2007**.
- [57] J. Pomplun, S. Burger, L. Zschiedrich, F. Schmidt, *Phys. Status Solidi B* **2007**, *244*, 3419.

Tailored Light Scattering through Hyperuniform Disorder in Self-Organized Arrays of High-Index Nanodisks

Peter M. Piechulla, Bodo Fuhrmann, Evgeniia Slivina, Carsten Rockstuhl, Ralf B. Wehrspohn, and Alexander N. Sprafke*

Arrays of nanoparticles exploited in light scattering applications commonly only feature either a periodic or a rather random arrangement of its constituents. For the periodic case, light scattering is mostly governed by the strong spatial correlations of the arrangement, expressed by the structure factor. For the random case, structural correlations cancel each other out and light scattering is mostly governed by the scattering properties of the individual scatterer, expressed by the form factor. In contrast to these extreme cases, it is shown here that hyperuniform disorder in self-organized large-area arrays of high refractive index nanodisks enables both structure and form factor to impact the resulting scattering pattern, offering novel means to tailor light scattering. The scattering response from the authors' nearly hyperuniform interfaces can be exploited in a large variety of applications and constitutes a novel class of advanced optical materials.

and solid-state lighting devices,^[4,5] spectral molecular fingerprint detection,^[6,7] or colored surfaces in architecture and design.^[8–10] The key challenge in ongoing research is the ability to tailor the optical response from these interfaces in a quite sophisticated manner to meet the demands of specific applications. This fundamental scientific goal is accompanied by the engineering challenge of scalable fabrication of nanophotonic interfaces. As today's manufacturing capabilities fall far behind proposed theoretical approaches due to the costs and complexity of their fabrication, prevalent structures are those of highest feasibility instead, for example in crystalline silicon solar cells pyramidal surface textures by alkaline etching still are of industry standard.^[11] While

1. Introduction

Micro- and nanostructured interfaces for electromagnetic scattering continue to play a major role in photonics due to their particularly wide range of existing as well as prospective applications, for example, for light management in solar cells^[1–3]

advanced techniques such as electron beam lithography provide high flexibility in terms of producing nanostructures with quite a deterministic geometry, these fabrication technologies are generally slow and expensive, thus, for example, applied to solar cells at most feasible for proof-of-concept or research purposes.

In this work, we focus on the implementation of photonic scattering interfaces consisting of an array of identical scatterers. The angle-resolved scattering (ARS) response of such a structure generally depends a) on the arrangement of the scatterers, for example regularity of the array and distances between the scatterers, as well as b) on the properties of the scatterers it is made of, for example size, shape, and involved materials. The first property is described by the structure factor S , the latter property by the form factor f , and under the assumption of the first Born approximation, it is $ARS \propto |f|^2 S$.^[12,13] However, either of these two quantities usually determines the angular scattering profile of established scattering interfaces almost completely. The strong spatial correlations present in a periodic array cause the structure factor to compact into a Dirac delta distribution. Hence, scattering from periodic arrays is only allowed into a small fraction of all available angular directions, the well-defined diffraction orders, while any other direction is prohibited as S is zero otherwise. A fully random arrangement of scatterers is here in stark contrast. There, no particular direction is enhanced nor suppressed due to the arrangement of the scatterers and the scattering response of the array essentially becomes identical to that of the individual scatterer.

Between these two diametrically opposed types of spatial configurations lies the parameter space of correlated disorder, which received increased interest from the photonics

P. M. Piechulla, R. B. Wehrspohn, A. N. Sprafke
Institute of Physics

Martin Luther University Halle-Wittenberg
06120 Halle, Germany

E-mail: alexander.sprafke@physik.uni-halle.de

B. Fuhrmann


Interdisciplinary Center of Materials Science
Martin Luther University Halle-Wittenberg
06120 Halle, Germany

E. Slivina, C. Rockstuhl

Institute of Theoretical Solid State Physics
Karlsruhe Institute of Technology
76131 Karlsruhe, Germany

C. Rockstuhl

Institute of Nanotechnology
Karlsruhe Institute of Technology
76021 Karlsruhe, Germany

 The ORCID identification number(s) for the author(s) of this article can be found under <https://doi.org/10.1002/adom.202100186>.

© 2021 The Authors. Advanced Optical Materials published by Wiley-VCH GmbH. This is an open access article under the terms of the Creative Commons Attribution-NonCommercial License, which permits use, distribution and reproduction in any medium, provided the original work is properly cited and is not used for commercial purposes.

DOI: 10.1002/adom.202100186

community in recent years.^[14–18] On the one hand, a spectrally broadband operation and robustness in fabrication makes the use of disorder attractive. On the other hand, structural correlations enable effective means for directional and spectral enhancement or suppression of scattering. A special class of disorder is the hyperuniform disordered (HuD) case for which large-scale density fluctuations vanish as they do in periodic systems but a disordered and isotropic spatial configuration is maintained.^[18,19] HuD structures have recently seen increasing interest in applications and experimental realizations due to their unique properties such as isotropic band gap formation.^[18–26]

In this work, we will show how a hyperuniform configuration of scatterers enables a new leverage to tailor light scattering by enabling both S and f to significantly shape the resulting scattering response of the array. The lack of large-scale density fluctuations represents a hidden symmetry and, just as long-range translational symmetry in periodic systems, leads to a strong suppression of small-angle scattering. However, the disorder present in our structures on short length-scales relaxes the bounds of S for larger scattering angles up to the extent of random structures, thus leaving the composition of the scattering pattern to f .

As scattering elements we choose TiO₂ nanodisks. Low-loss high refractive index nanoparticles are renowned for their large scattering cross sections, thus constitute ideal scattering elements for this study.^[27] Furthermore, high-index nanoparticles have received considerable attention from the metamaterials community in recent years as they allow, for example, the study of magnetic in addition to electrical resonances at optical frequencies.^[27–29] These Mie-type resonances give rise to novel ways for near and far field manipulation such as nonlinear frequency generation^[29,30] and wavefront shaping.^[31,32] Nanodisks have been investigated in particular due to their rather simple fabrication while allowing good control over spectral features via the geometry of the disks. Based on findings of our previous work,^[33] in addition to the above we report on a novel scalable method to fabricate substrates covered with TiO₂ nanodisk arrays of tailored nearly hyperuniform disorder by a self-organized nanosphere deposition process.

2. Sample Fabrication Scheme

The procedure to fabricate large-scale TiO₂ arrays of tailored disorder relies on a nanosphere deposition technique that we have published elsewhere.^[33] By exploiting the nanospheres as a template in a subsequent dry-etching process, we significantly extend our approach by the ability to obtain disk-shaped nanoparticles. The developed process scheme allows controlled

etching of TiO₂, which is a material of particular interest to the photonics community due to its high refractive index in the visible spectral range, and is, to the best of our knowledge, here reported on for the first time.

The fabrication scheme (see **Figure 1**) starts with standard microscopic slides that are functionalized with a Al₂O₃/TiO₂/Al₂O₃ multilayer with thickness 13.8, 231.0, and 19.5 nm, respectively. We use atomic layer deposition (ALD) since this method allows great control over film thickness and produces dense layers. The thin top layer serves a double purpose. First, the surface charges of the Al₂O₃ film are essential for immobilizing the nanospheres in the subsequent nanosphere deposition. Second, this layer transforms into a hard mask imprinted by the nanospheres. The thick TiO₂ layer provides the material of the nanodisks. The thin bottom layer serves as an etch stop to prevent overetching and damage to the substrate.

In the next step we apply our nanospheres deposition using PMMA nanospheres (diameter $D = 499 \pm 10$ nm) in aqueous dispersion. In short, this technique exploits the electrostatic interactions of surface-charged nanospheres with each other and with the top Al₂O₃ layer. The nanospheres (negatively charged) are driven toward the substrate (positively charged) and are immobilized as soon as they adsorb on the substrate surface. The nanospheres repel each other, thus modifying the probability of the location of adsorption for another nanosphere. After a certain density of adsorbed nanospheres is reached, no more nanospheres will attach since the repelling forces due to already adsorbed nanospheres become dominant. Therefore, our deposition process is not only self-organized but also self-limiting, which makes it very cost-effective. A prepared dispersion can be applied multiple times since only a tiny fraction of nanospheres is used up during one deposition. By precisely setting the ionic strength of the dispersion, here via the addition of KCl, screening of the nanosphere surface charges within the aqueous dispersion can be controlled, providing an effective lever to control the resulting nanosphere density on the substrate. Details and theoretical background of our nanosphere deposition method are presented elsewhere.^[33]

After the nanosphere deposition, the substrate is rinsed in deionized water and directly transferred to ethylene glycol and heated to 144 °C to slightly soften the nanospheres and increase the particle-substrate bond. This step prevents particle aggregation due to surface tension of the liquid film during drying. After rinsing with water and drying in air, the samples undergo an additional tempering step (30 min at 155 °C) to change the nanospheres' shape to a dome-like structure such that the area below a nanosphere is fully covered with PMMA (Figure 1c).

The transition from the nanosphere pattern to a Al₂O₃ hard mask is performed via reactive ion-etching (RIE). As shown by Dekker et al., Al₂O₃ prepared by ALD provides an excellent hard

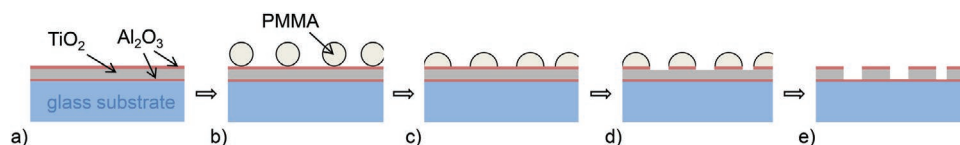


Figure 1. Fabrication scheme of disordered TiO₂ nanodisk arrays. a) The substrate is functionalized with a Al₂O₃/TiO₂/Al₂O₃ layer stack. b) Then a self-organized nanosphere deposition process is applied and c) the substrate is tempered. The resulting domes serve as a template for the following d) 2-step dry-etching process after which e) arrays of TiO₂ nanodisks are obtained.

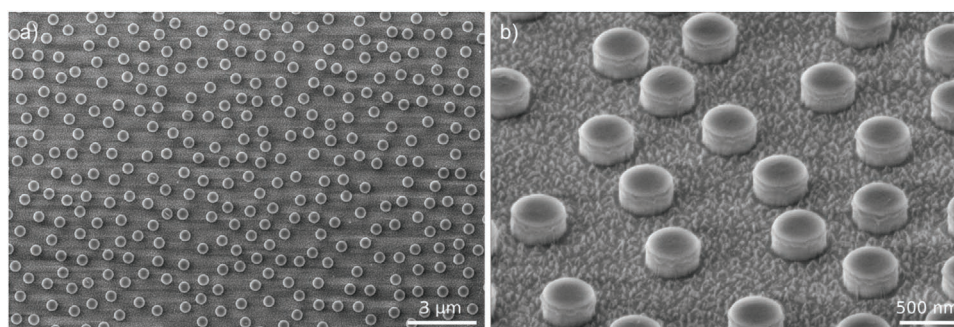


Figure 2. Scanning electron micrographs of a fabricated TiO₂ nanodisk array on glass substrate in a) top view and b) viewed at 52° inclination from normal. The disk density of this sample is 1.15 μm⁻² and the characteristic center-to-center distance is $r_0 = 828$ nm.

mask for dry etching processes due to its chemical stability and superior film quality even in thin layers.^[34] Due to the low volatility of AlF₃, Al compounds can not be etched by fluorine-based dry chemistry without a significant physical component. However, they are readily etched in chlorine chemistry.^[34–37] Based on this, we developed the hard mask patterning process (see Section 5 for technical details). The plasma is ignited in a BCl₃/Ar atmosphere with a low DC bias to achieve a sufficient Al₂O₃ over PMMA etching selectivity of ≈0.4.^[37] The etch rate of Al₂O₃ was found to be ≈1.1 nm s⁻¹ and the etch time was chosen to be 29 s, which results in slightly overetching the hard mask layer while keeping the PMMA nanospheres sufficiently intact, which are afterward removed in a pure O₂ plasma.

Unlike Al₂O₃, TiO₂ is etched by fluorine chemistry. Based on the work of Choi et al.,^[38] a CF₄-O₂-based process has been developed resulting in a TiO₂ etch rate of ≈1.5 nm s⁻¹ and a TiO₂ over Al₂O₃ selectivity of ≈29. Hence, the top hard mask layer was sufficiently thick. For the 231.0 nm TiO₂ layer, we etched for 240 s, that is longer than actually needed. However, the Al₂O₃ etch stop layer beneath limits the etch depth and thereby increases repeatability of the manufacturing process (Figure 1e). The requirements of high selectivity, high aspect ratios, and smooth surfaces are difficult to meet in fluorine-based TiO₂ etching compared to, for example, silicon processes,^[39,40] as parameters for vertical sidewalls and good selectivity also lead to self-masking effects and, thus, rough surfaces. In our case, etching down to the etch stop layer reduces the roughness to an acceptable level for our investigations and produced relatively smooth surfaces (see Figure 2b) compared to previously published results.^[41,42] We note that reactive ion etching processes have been successfully applied in industrial process chains and therefore do not principally impede the scalability of our fabrication method.^[43,44]

3. Results and Discussion

The key objective of this study is to combine scattering properties of the individual TiO₂ nanodisk (form factor f) with those introduced by positional correlations of their disordered arrangement (structure factor S). Therefore, we choose the geometric parameters of the nanodisk arrays such that the spectral features due to form and structure factor overlap. For the form factor, these are the dimensions of the individual nanodisk, that is diameter D and height h . For the structure factor, it is the

characteristic distance r_0 between the nanodisks, which is the typical next-neighbor center-to-center distance, or more precisely, the first maximum of the pair correlation function $g_2(r)$ of the point configuration of the array.^[19] In reciprocal space, r_0 corresponds to the first maximum q_0 of the structure factor, see also discussion below.

Given the refractive index of our amorphous TiO₂, $n \approx 2.54–2.31$ for a wavelength range of $\lambda = 450–1000$ nm, preliminary calculations using the finite-element method (FEM) predict a number of multipolar resonances in the visible and near-infrared spectral region for individual nanodisks of about 230 nm height and 500 nm diameter. Accordingly, the nearest available particles size from stock, $D = 499$ nm, was chosen for the template fabrication. For the structural resonances to spectrally coincide with the resonances of the individual nanodisks, r_0 needs to be of the same order as the wavelength. We have previously demonstrated how r_0 can be varied by the deposition conditions. Furthermore, we are able to statistically predict particle patterns based on a modified random sequential adsorption (RSA) model of soft spheres near the saturation density.^[33] Thus, we experimentally fabricated a set of samples comprising glass substrates covered with disordered TiO₂ nanodisk patterns with desired geometrical dimensions. Additionally, one pattern that ideally shows no structural correlations, that is of random disorder, was fabricated by exposing the functionalized substrate to the nanosphere dispersion for only a short period of time such that the particle density is far from saturation. In the following we discuss the properties of such samples first from a structural and later from an optical perspective.

3.1. Structural Properties

We successfully fabricated disordered arrangements of TiO₂ nanodisks. Exemplary images of the fabricated TiO₂ nanodisk structures are shown in Figure 2. We determine an average nanodisk diameter of 455.0 ± 5.4 nm and an average height of 231.0 nm. We attribute the nanodisk diameter dispersion to the size dispersion of the nanospheres used to prepare the mask template. In comparison to the nanospheres (499 nm diameter), the disks are around 10 % smaller in diameter, which is a result of the tempering process prior to pattern transfer. The error on disk height is negligible due to the excellent control of ALD deposition over layer thickness.

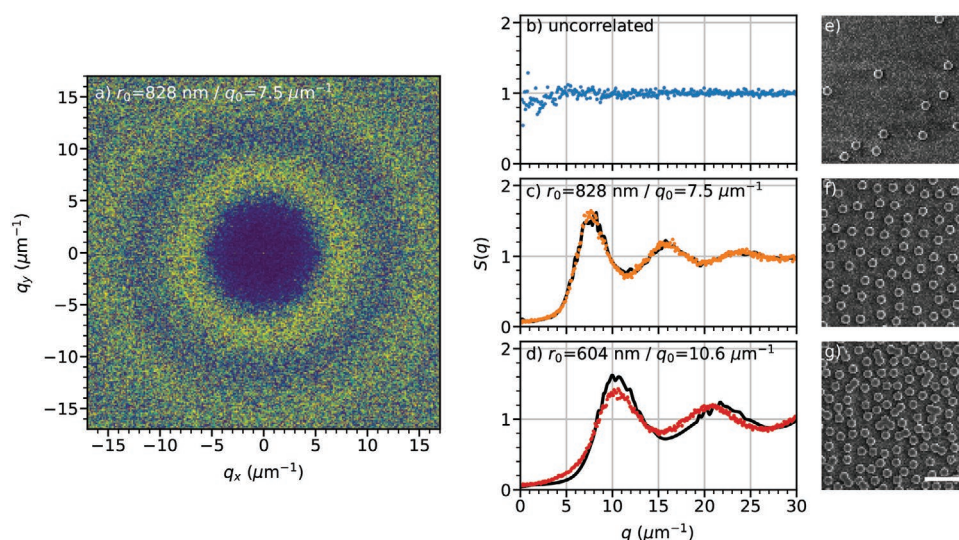


Figure 3. a) Typical structure factor $S(\mathbf{q})$ for a fabricated disordered pattern. b–d) Angular average $S(q)$ for the uncorrelated pattern and two correlated patterns from experiment (dots) and simulations (solid black lines). e–g) Exemplary electron micrographs (detail) corresponding to structure factors to their left (scale bar: 2 μm).

The disks are homogeneously distributed across the entire substrate surface in a disordered pattern (see characterization methods in Section 5 for pattern extraction). The statistics of our patterns can be appropriately captured in Fourier space. We consider the size dispersion of the disks sufficiently small to consider the structure factor instead of the spectral density. However, the latter would be a more appropriate quantity to characterize polydisperse particle patterns.^[45] The (static) structure factor of a N -point pattern \mathbf{r}_i is^[46,47]

$$S(\mathbf{q}) = \frac{1}{N} \sum_{i,j} e^{-i\mathbf{q}(\mathbf{r}_i - \mathbf{r}_j)} \quad (1)$$

with wave vectors \mathbf{q} . In this work, we write \mathbf{q} for wave vectors that lie in the plane of the nanodisk array and \mathbf{k} for wave vectors of propagating free-space light modes which in general have a component perpendicular to the array plane. The point patterns are isotropic, thus S is rotationally symmetric, exemplary shown in **Figure 3a**. The angular average $S(q) = S(|\mathbf{q}| = \sqrt{q_x^2 + q_y^2})$ is plotted for typical samples in **Figure 3b–d** together with $S(q)$ of predicted patterns.

Figure 3b shows $S(q)$ for the sample on which the nanosphere deposition was stopped prior saturation. As a result, spatial correlations are negligible and $S(q) \approx 1$ for all q and we will refer to this pattern in the following as uncorrelated. The deviation from unity near $q = 0$ stem from the fact that particles maintain a minimum distance, which becomes relevant at finite densities. However, the random nature of the process prevails.

The particle patterns of the samples corresponding to **Figure 3c,d** are saturated and reveal strong correlations, that is $S(q)$ clearly deviates from unity. Each structure factor $S(q)$ of these patterns holds a characteristic peak $S_{\text{max}} = S(q_0)$ at around $q_0 = 7.5 \mu\text{m}^{-1}$ and $q_0 = 10.6 \mu\text{m}^{-1}$, corresponding to a characteristic next-neighbor distance of about $r_0 = 828 \text{ nm}$ and $r_0 = 604 \text{ nm}$, respectively, that is also indicated in the figure. For the

sparsely coated saturated sample (**Figure 3c,f**), we find excellent agreement between our modified RSA model^[33] and experiment, whereas for the densely coated sample (**Figure 3d,g**) a lower value of S_{max} and a slight shift of about $-0.1 \mu\text{m}^{-1}$ compared to the prediction can be observed. A possible explanation for this deviation in the denser sample is the occurrence of aggregates, that is touching particles, which is not accounted for in our deposition model. To experimentally achieve a certain characteristic distance r_0 , we carefully adjust the electrostatic potential landscape in which the nanospheres move through during the deposition process and a rather shallow potential minimum (in the order of $-k_B T$) gives rise to a preferred next neighbor distance.^[33] However, as soon as two spheres touch each other, irreversible aggregation occurs. Thus, the smaller the characteristic distance aimed for, the higher the probability of aggregate formation, which is supported by our observations in numerous other experiments. Furthermore, aggregates would also explain increased values of $S(q)$ for $0 < q < q_0$ in comparison to our model, as aggregate formation occurs in a random Poisson-like manner and, therefore, enhances long-range particle density fluctuations. Therefore, aggregation and its effect on the resulting structure factor should be taken into account when considering high particle densities. For the samples used in this work, the number share of particles present in configurations of two or more touching particles was found to be 2.6%, 3.0%, 9.5%, and 31.2% for $r_0 = 828, 713, 649,$ and 604 nm , respectively. Due to the strong increase in aggregation for $r_0 = 604 \text{ nm}$, the pattern may be dubbed over-saturated. Nevertheless, the general shape of the structure factor is still preserved (**Figure 3d**). Furthermore, we note that the final structure was obtained by patterning a flat layer. Therefore, all nanosphere aggregates result in in-plane nanodisk aggregates, that is a binary height profile with no component in the third dimension.

For our samples of correlated disorder, $S(q)$ becomes small for q approaching zero, which is equivalent to a suppression of

density fluctuations on large length scales. When $S(q \rightarrow 0) = 0$, structures are referred to as hyperuniform, and stealthy hyperuniform when $S(q)$ vanishes for an entire range of q around the origin.^[19,48] In real world structures, the strict criterion of $S(q \rightarrow 0) = 0$ can obviously not be achieved due to fundamental aspects such as finite size and temperature effects to the least. A practical criterion that has recently been proposed is the hyperuniformity metric^[19,49]

$$H = \frac{S(q \rightarrow 0)}{S_{\max}} \quad (2)$$

A system is considered as effectively hyperuniform if H is of the order of 10^{-4} ,^[49] which is stricter than the requirement for nearly hyperuniform patterns with H on the order of 10^{-2} .^[50] In our case, $H \approx 0.032$ and the lower limit of the structure factor is $S(q \rightarrow 0) \approx 0.05$, which is slightly lower than values found for 2D random sequential adsorption of hard sphere patterns.^[51] Therefore, we consider the structures shown here nearly hyperuniform disordered.

Besides fundamental reasons, we suspect further limitations similar to those applying to conventional RSA patterns hindering the achievement of lower degrees of hyperuniformity. In RSA patterns, a strictly sequential adsorption of particles onto the substrate surface is assumed and except the condition that particles must not overlap no interaction potential is accounted for. Thus, the precise position of an adsorbed particle carries a rather large amount of randomness leading to density fluctuations at large length scales, that is $S(q \rightarrow 0) > 0$. In our case, the particles interact with each other via repulsive electrostatic and attractive van-der-Waals forces.^[33] The probability for a particle to adhere in the vicinity of already attached particles with a characteristic distance—which we are able to set experimentally—is therefore modulated and leads to increased correlations of particle positions. Additionally, the adsorption of particles is not strictly sequential so there might be some degree of coordination while particles are mobile. However, the particle ensemble cannot achieve a collective configuration to minimize potential energy since they are immobilized as soon as they touch the substrate. Thus, density fluctuations are not fully suppressed and it can therefore be assumed that H in our nanosphere deposition will be at least identical or, as observed here, smaller to the RSA case. At this point, the limits of H in self-organized bottom-up techniques like ours are still an open question. Nevertheless, the relative stealthiness of our patterns, that is $S(q)$ being rather small for a range of q 's around the origin, has a strong impact on their scattering properties as we will show in the next section.

3.2. Optical Properties

3.2.1. Numerical Method

To numerically reproduce the optical response of our fabricated TiO_2 nanodisk arrays, we apply the first Born approximation,^[12] that is the exciting light field for each scatterer is assumed to be the unperturbed incoming light field \mathbf{E}_{in} . Throughout this work we consider plane wave irradiation through a transparent substrate of refractive index $n^- = 1.52$ occupying the $z \leq 0$ half

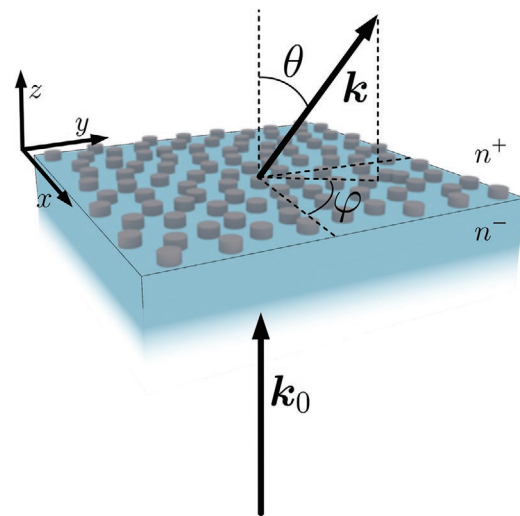


Figure 4. Sketch of the notation used throughout this work. The nanodisk array lies in the xy -plane on a glass substrate and the incoming light is travelling through the substrate at normal incidence with regard to the array plane.

space. The $z > 0$ half space is vacuum with $n^+ = 1$, see **Figure 4** for notation. The plane wave with field amplitude \mathbf{E}_0 is x -polarized and normally incident onto an infinite array of identical scatterers covering the substrate, that is $\mathbf{E}_{\text{in}}(\mathbf{r}) = E_0 \hat{\mathbf{x}} e^{i(k_0 z - \omega t)}$.

The scattered far field ($kr \gg 1$) of an individual scatterer can be expressed as an outgoing spherical wave (we omit the harmonic time dependence $e^{-i\omega t}$ in the following)^[12,52]

$$\mathbf{E}_s(\mathbf{r}) = E_0 \frac{e^{ikr}}{r} \mathbf{f} \quad (3)$$

$\mathbf{f} = \mathbf{f}(\hat{\mathbf{E}}_0, \mathbf{k}_0, \mathbf{k})$ is the form factor and describes the normalized scattered field amplitude of an individual scatterer for a given polarisation $\hat{\mathbf{E}}_0 = \mathbf{E}_0 / |\mathbf{E}_0|$ and incoming and scattered wave vectors \mathbf{k}_0 and \mathbf{k} , respectively. Furthermore, $|\mathbf{f}|^2 = \frac{d\sigma}{d\Omega}$ is the differential scattering cross section or radiation pattern of the individual particle. \mathbf{f} can be readily obtained by various means, for example analytically by Mie theory in case of a spherical particle, or by rigorously solving Maxwell's equations with techniques such as FEM. We write f_0 for x -polarized irradiation normal to the array plane, that is $f_0(\mathbf{k}) = \mathbf{f}(\hat{\mathbf{x}}, k\hat{\mathbf{z}}, \mathbf{k})$. Using the angular spectrum representation of Equation (3) in its asymptotic limit ($kr \rightarrow \infty$),^[53] we find the normal incidence transmission and reflection of an infinite array of identical scatterers in terms of the form factor to be

$$T = \frac{n^+}{n^-} \left| t \hat{\mathbf{E}}_0 + \rho \frac{2\pi}{ik^+} f_0^+ \right|^2 \quad (4)$$

$$R = \left| r \hat{\mathbf{E}}_0 + \rho \frac{2\pi}{ik^-} f_0^- \right|^2 \quad (5)$$

with areal density of scatterers ρ , Fresnel's transmission and reflection coefficients t and r of the bare substrate interface, wave numbers k^+ and k^- in substrate and vacuum, and $f_0^\pm = f_0(\mathbf{k} = \pm \mathbf{k}_0)$, respectively.

Scattering into the directions normal to the array plane, $\mathbf{k} = \pm k\hat{z}$, depends on f_0 and ρ , but not on the particular spatial arrangement of scatterers. Interference of these fields with $t\hat{\mathbf{E}}_0$ and $r\hat{\mathbf{E}}_0$ (Equations (4) and (5)) determines the normalized power P_{sca} that undergoes off-normal scattering, $P_{\text{sca}} = 1 - T - R$ (neglecting absorption). However, for off-normal scattering structural phase relations have to be accounted for by modulating $|f_0|^2$ by the structure factor $S(q = k_{\parallel})$, with the projection k_{\parallel} of the scattered wave vector \mathbf{k} onto the array plane.^[13] Using $P_{\text{sca}} = \int_{\Omega} \text{ARS} \, d\Omega$, with integration of the angle-resolved scattering ASR over the unit sphere Ω except for $d\Omega = d\Omega(\mathbf{k} \pm k\hat{z})$, we can now write down the ARS response of the array at normal incidence as

$$\text{ARS} = \frac{P_{\text{sca}}}{\int_{\Omega} |f_0|^2 S \, d\Omega} |f_0(\mathbf{k})|^2 S(k_{\parallel}) \quad \mathbf{k} \neq \pm k\hat{z} \quad (6)$$

The numerical approach described here significantly simplifies the computational efforts to predict the optical response of our structures. The structure factor S in Equation (6) can be taken either from experiment, for example by evaluating SEM pictures, or, if sufficient knowledge of the fabrication process is available, from theoretical modeling such as our modified RSA approach.^[33] Instead of numerically solving Maxwell's equations for a computational domain large enough to sufficiently approximate the statistics of a disordered array of scatterers, only the scattering response of the individual scatterer is calculated rigorously. We shortly discuss the applicability of the first Born approximation to our structures at the end of the discussion, see below. Furthermore, our approach is restricted to planar arrays of non-overlapping identical scatterers and we note that a more general formalism for the effective electromagnetic wave properties of disordered composites was recently derived from first principles.^[54]

3.2.2. Angle-Resolved Scattering Response

Figure 5 illustrates how arranging identical TiO₂ nanodisks into a nearly HuD pattern has a remarkable impact on the resulting angular scattering response. For two different wavelengths we compare the ARS of the uncorrelated pattern in the top row and a nearly HuD pattern (characteristic distance $r_0 = 828$ nm) in the bottom row. Additionally, corresponding numerical results after the approach described above are plotted using f_0 calculated by FEM and S taken from our modified RSA modeling algorithm.

For the uncorrelated sample, it is $S \approx 1$ for all q 's (see Figure 3b), thus its ARS essentially remains that of the individual nanodisk but scaled by the number of illuminated particles. Scattering is strongest at $\theta = 0^\circ$ and quickly decreases as θ increases. In contrast to this, scattering is very different for the nearly HuD pattern with a maximum at significantly larger angles and being mostly confined within a ring-shaped area. Spatial correlations in these structures, for example expressed through the existence of the characteristic distance of neighbors r_0 , leads to similar optical phase differences for off-normal scattered light waves. Thus, destructive as well as constructive interference occurs and even though translational symmetry is missing, intensity maxima (ring-shaped area) or minima (angular area inside ring) appear well pronounced. Opposed to the well-know diffraction of an optical grating, which is based on interference as well, constructive interference occupies a much larger solid angle due to a range of similar but not exactly equal distances between scatterers. For example, for $\lambda = 540$ nm we find that $\int_{\theta} \int_{\varphi=0}^{2\pi} \text{ARS} \, d\Omega = 80\%$ of forward scattering is confined within $\theta < 48^\circ$ for the uncorrelated case, while the same amount is confined within $25^\circ < \theta < 56^\circ$ for the nearly HuD case.

In contrast to irradiation with unpolarized light, we here observe experimentally as well as numerically a φ -dependency

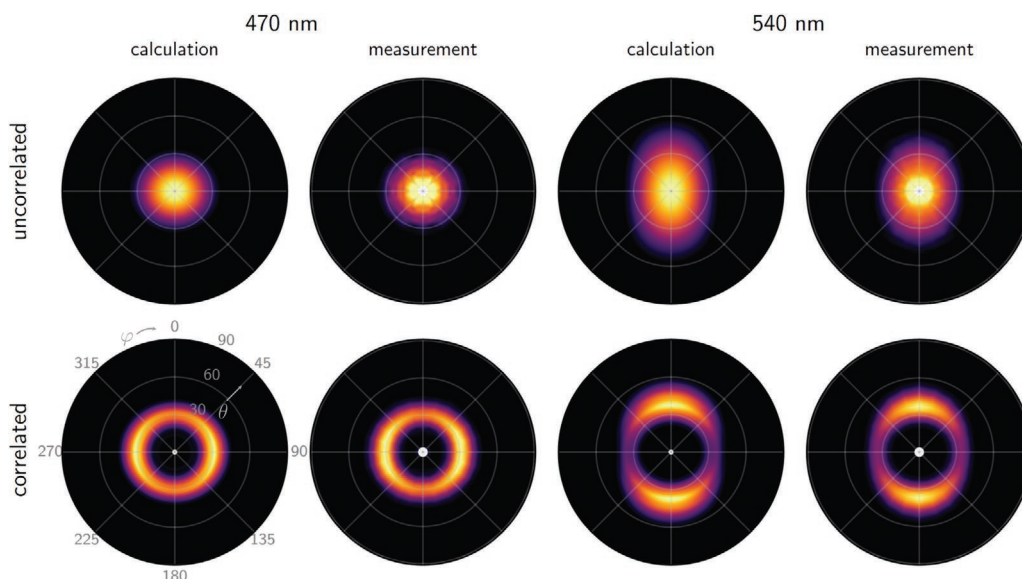


Figure 5. Measured and calculated ARS(θ, φ) in forward direction of an uncorrelated (top row) and nearly HuD array of nanodisks (bottom row). S and SEM of the uncorrelated and correlated sample are shown in Figure 3b,e and c,d, respectively. The incoming light is x-polarized.

of the scattering response, which is very subtle for most part of the investigated spectral range but is slightly visible at $\lambda = 470$ nm and well observed for $\lambda = 540$ nm. In particular, for the nearly hyperuniform sample it can be seen that for $\lambda = 470$ nm scattering reaches out further into the y - than into the x -direction, and even more pronounced for $\lambda = 540$ nm but perpendicular to the former, that is reaching out further into the x - than into the y -direction. The same anisotropy is also present for the uncorrelated sample, but less pronounced.

To elucidate our observations, we look into the φ -dependency in more detail in **Figure 6**. Plotted is the power scattered into the xy - and yz -plane in forward direction, $P(\varphi_0, \lambda) = \int_{\theta=0}^{\pi/2} \int_{\varphi=\varphi_0-\Delta\varphi/2}^{\varphi_0+\Delta\varphi/2} \text{ARS}(\lambda) d\Omega$ with $\varphi_0 = 0^\circ$ and 90° , respectively, and $\Delta\varphi = 3.5^\circ$, of the uncorrelated sample together with FEM simulations of a single TiO_2 nanodisk on glass substrate. Furthermore, we performed a multipole expansion analysis of a single TiO_2 nanodisk. As multipole expansion is only defined for a scatterer embedded in a homogeneous medium, we analyze a TiO_2 nanodisk with identical geometrical dimensions in vacuum (dashed lines). Comparing $P(\varphi_0, \lambda)$ for the isolated disc in vacuum with the case of the disk on glass substrate, we find only minor deviations, particularly for the spectral feature at $\lambda = 540$ nm. This indicates that the removal of the substrate has only little impact on the optical properties of the disk and insights obtained from the multipole expansion considering the isolated disc can be applied to the substrate case.

The multipole expansion reveals that for our chosen nanodisk dimensions a plethora of modes ranging from magnetic and electric dipoles up to octupoles contribute significantly to the scattering response within the spectral range of interest (see Figure S1, Supporting Information). None of the spectral features found in the scattering spectra can be accounted to a single mode but a mix of several modes. However, comparing the power emitted by the sum of electric dipole, quadrupole, and octupole with the sum of their magnetic counterparts, $P_{\text{el}}(\varphi_0, \lambda)$ and $P_{\text{mag}}(\varphi_0, \lambda)$, respectively (colored dashed lines in

Figure 6), reveals that scattering at $\lambda = 470$ nm is predominately caused by electric modes, whereas at $\lambda = 540$ nm it is predominately caused by magnetic modes.

The electric moments excited in the nanodisks share an equatorial plane that is oriented perpendicular to the one shared by the magnetic moments, according to the geometry of our experiment the yz - and the xz -plane, respectively. Therefore, since their equatorial planes are also the planes of preferred scattering, excitation of these two kinds of modes explains the observed φ -anisotropy observed in Figure 5. However, as both kinds of modes emit into small θ s, the discussed effect is only significant at larger θ s. As scattering concentrates at rather small θ s for the uncorrelated case, the dependency of the scattering pattern on the nature of the excited mode is only weak. But arranging the same nanodisks into a nearly HuD pattern strongly emphasizes this effect. Due to its structure factor, small-angle scattering is suppressed, hence giving an enhanced spatial contrast to differentiate between the natures of the excited modes. To be specific, for TiO_2 disks arranged in an uncorrelated pattern the ratio $P(\varphi_0 = 0^\circ, \lambda)/P(\varphi_0 = 90^\circ, \lambda)$ at $\lambda = 540$ nm is 2.2, but it more than doubles to 5.2 in the nearly HuD case.

3.2.3. Spectral Dependence of Scattering Response

In **Figure 7**, we capture the spectral dependence of scattering in near HuD TiO_2 nanodisk arrays by plotting the calculated and experimentally measured ARS against wavelength λ and forward scattering angle θ . As the φ -dependency was discussed in the previous section and for the sake of clarity, the values are averaged over φ . The top row shows the scattering response of the uncorrelated array, that is essentially the unmodified response of the individual TiO_2 nanodisk, the centre and bottom rows show the scattering response of two nearly HuD arrays with different characteristic distances $r_0 = 828$ nm, and $r_0 = 604$ nm, respectively. Both of them have been discussed

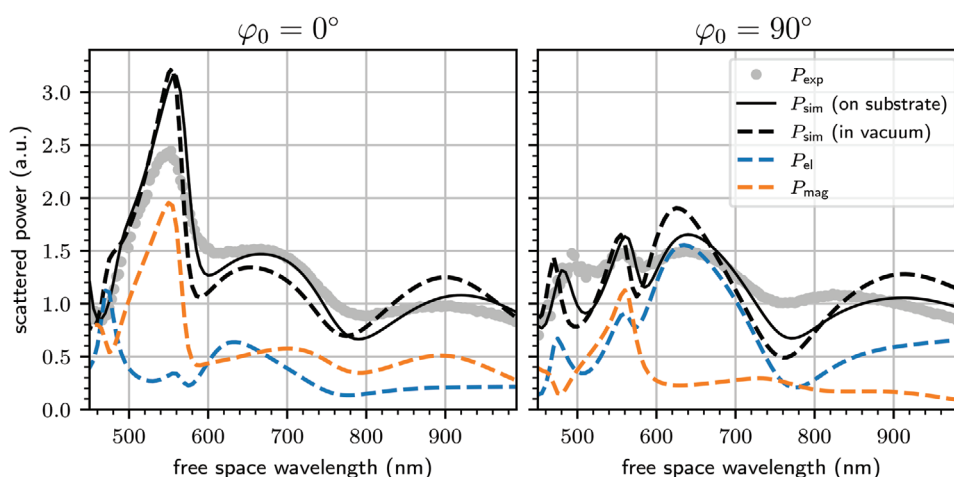


Figure 6. Forward scattering $P(\varphi_0, \lambda)$ into the plane defined by $\varphi_0 = 0^\circ$ (xz -plane) and $\varphi_0 = 90^\circ$ (yz -plane). Experimental data of the uncorrelated sample together with simulations of a TiO_2 nanodisk on glass substrate as well as without substrate. Additionally, $P_{\text{el}}(\varphi_0, \lambda)$ and $P_{\text{mag}}(\varphi_0, \lambda)$ is plotted, that is the radiation power of the sum of electric and magnetic dipole, quadrupole, and octupole, respectively, derived from multipole expansion analysis of the same nanodisk without substrate (see also Supporting Information).

in Figure 3. As indicated above for single wavelengths, experimental and calculated ARS agree as well for the whole considered spectral range.

The unmodified scattering response of the uncorrelated pattern is characterized by spectrally broadband forward scattering with its maximum at $\theta = 0$. The strongest scattering response is around $\lambda = 560$ nm, which can be attributed to the simultaneous excitation of the magnetic dipole, quadrupole, and octupole mode (see Figure S9, Supporting Information). The center row of Figure 7 shows the scattering response of the nearly HuD sample that was also under study in the previous section. In accordance to the observations for single wavelengths,

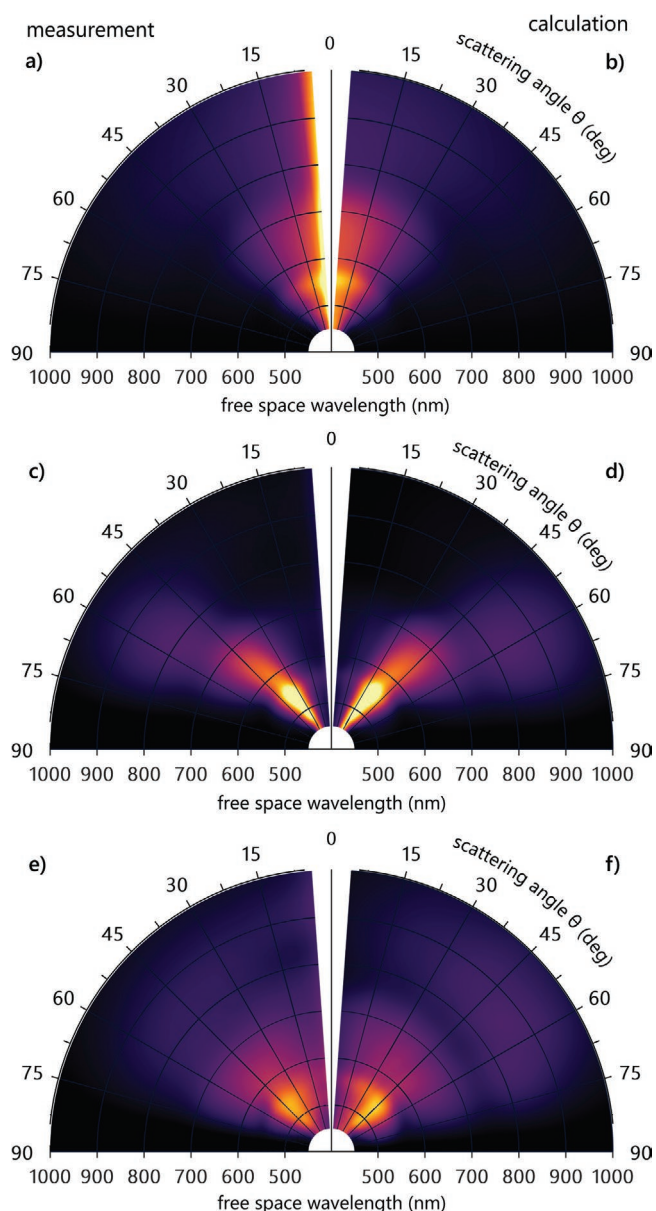


Figure 7. Measured (left column) and calculated (right column) φ -averaged angle-resolved scattering response $ARS(\theta, \lambda)$ in forward direction of (top row) the uncorrelated TiO_2 nanodisk array, and the nearly HuD array with (centre row) $r_0 = 828$ nm, and (bottom row) $r_0 = 604$ nm. Color scaling is identical for (a) and (b) and (c–f), respectively.

the ARS is modified for the whole considered spectral range as well, that is transformed into a ring-shaped pattern with a scattering maximum $\theta \neq 0$. Surprisingly, the angular range covered by the ring stays almost constant for a rather large spectral bandwidth. To be precise, for $\lambda = 450 - 750$ nm the major part of scattered light stays within $30^\circ < \theta < 50^\circ$, for $\lambda = 800 - 1000$ nm, the ring radius rather abruptly increases to occupy an angular range of $50^\circ < \theta < 70^\circ$.

Scattering in both periodic and (nearly) HuD structures is based on structural phase-induced interference, therefore it is intuitive to compare the two. In Figure 8a we plot the same S as in Figure 3c but converted q to the corresponding scattering angle θ for each wavelength λ . Since S is a property of the arrangement of scatterers within the array, it is invariant with regards to constant q 's, and, thus, its course for varying θ and λ is determined through $\theta = \arcsin\left(\frac{\lambda q}{2\pi}\right)$ (assuming normal incidence).

This general relation is fundamental for periodic structures, such as optical gratings, since it sets the only angular directions periodic structures are allowed to scatter into as long as q exactly equals a multiple of reciprocal grating vectors. The black line in Figure 8a follows $S_{\max} = S(q_0)$ of the HuD array. Considering a periodic pattern with periodicity $a = r_0$, this line would also represent its (first) diffraction order. The most distinct difference between S of a periodic and a HuD structure is that the first consists of a set of Dirac delta functions while the latter is a continuous function. This implies the existence of a cutoff wavelength $\lambda_c = a$, for the periodic structure, that is for wavelengths $\lambda > \lambda_c$, off-normal scattering is disabled since then all scattered waves become evanescent in the normal direction. In contrast to this, the continuous nature of S of a HuD structure leads to a pronounced spectral broadening of any features of S as clearly visible in Figure 8a. For $\lambda_c > r_0$, that is when light with wavelengths longer than the one corresponding to S_{\max} , non-vanishing values of S still stretch over a considerable angular and spectral range enabling scattering. For example, light waves corresponding to $S(q = 6 \mu\text{m}^{-1}) = 0.5 \cdot S_{\max}$ are able to propagate in free space up to $\lambda = 1050$ nm. In case of a truly stealthy HuD structure, for which $S(q) = 0$ for some finite $q < Q$, a cutoff wavelength exists as well, but in contrast to the periodic case, this wavelength can in principle be much longer than the characteristic next-neighbor distance of scatterers within the array.

However, by comparing Figure 7c/d and Figure 8a, the ARS cannot be traced back to the structure factor alone. Indeed, we find that the form factor f has to be taken into account as well. In Figure 8b we plot the radiation pattern $|f_0|^2$ of the individual nanodisk. Since we focus on the angular dependence for now, $|f_0|^2$ is normalized by its maximum value for each wavelength, that is by its value in forward direction ($\theta = 0$). In this representation, the angular dependencies of the different involved multipoles become visible. For $\lambda < 800$ nm, scattering is confined roughly within $\theta < 45^\circ$ but abruptly widens up to $\theta = 75^\circ$ for $\lambda > 800$ nm. Multipole expansion analysis reveals that this is due to the electric and magnetic dipole modes being the dominant modes excited in our nanodisks for $\lambda > 800$ nm (see overlaid full and dashed white lines in Figure 8b). The resulting scattering pattern of the individual nanodisk depends on the detailed interference of all excited

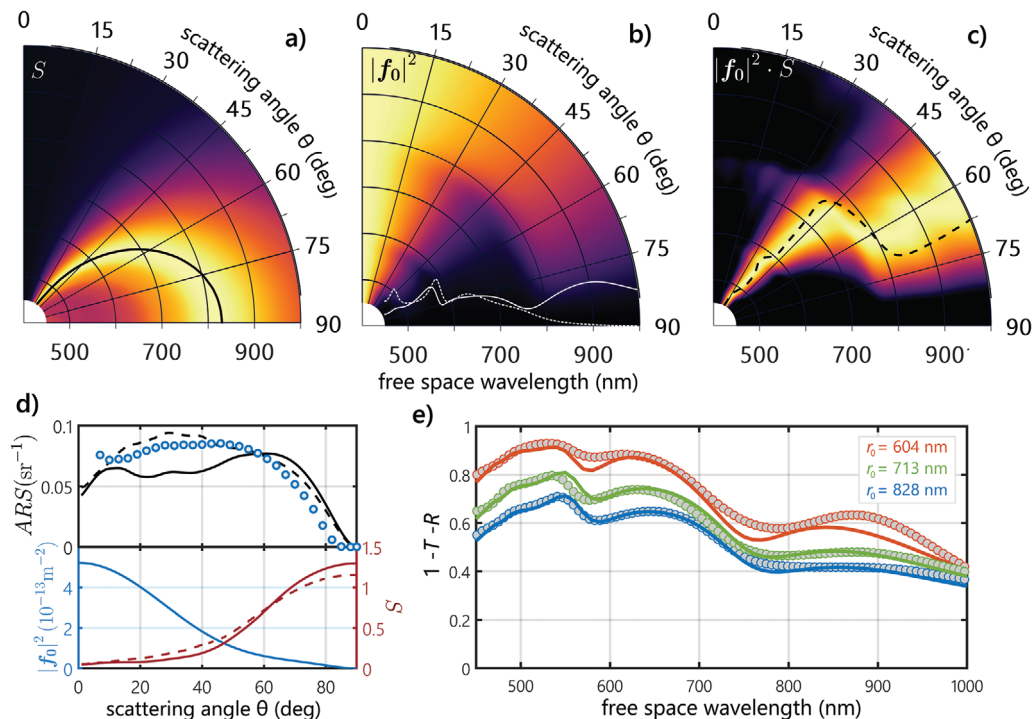


Figure 8. a) $S(\lambda, \theta)$ of our nearly HuD pattern with $r_0 = 828$ nm. b) φ -averaged $|f_0|^2$ normalized by its maximum value for each wavelength. The overlaid white line indicates the contribution of electric and magnetic dipole modes, $|a_1|^2 + |b_1|^2$, the dashed line the contribution of higher order modes, $\sum_{i=2,3} |a_i|^2 + |b_i|^2$. c) ARS of the nearly HuD array normalized by its maximum value for each wavelength. The dashed black line indicates a contour line of the data shown in (b) at $|f_0|^2 = 0.35$. d) Experimental (circles) and calculated (black) ARS, $|f_0|^2$, and S (all for $\lambda = 700$ nm) of the sample shown bottom in Figure 7. Full and dashed lines of ARS and S indicate use of simulated and experimental array patterns, respectively. e) Experimental (circles) and calculated (lines) $1 - T - R$ of different nearly HuD samples with characteristic next-neighbor distances r_0 .

multipoles.^[55] In contrast to higher order modes, such as quadrupole and octupole modes, the radiation pattern of pure dipole modes does not hold a θ -dependence, that is does not possess any radiation lobes. Therefore, as long as dipole modes are dominant their radiation pattern is only little affected by interference with higher-order modes and they keep their angularly broad scattering. This is not the case for $\lambda < 800$ nm, as electric and magnetic quadrupoles as well as octupoles are excited, resulting in a scattering pattern that is confined to a smaller θ -range.

The final ARS of scatterers with form factor f arranged into an array with structure factor S is proportional to their product, $|f_0|^2 \cdot S$ (Equation (6)), which we plot in Figure 8c. Essentially, this is the same data as shown in Figure 7d, but again we normalize to the maximum value at each wavelength to better visualize the resulting main direction of scattering. Additionally, a contour line of the normalized radiation pattern of the individual nanodisk (Figure 8c) is overlaid following the value of $|f_0|^2$ at the absolute scattering maximum of this sample, ($\lambda = 560$ nm, $\theta = 35^\circ$, see Figure 7d). In this representation, it becomes visible that the angular scattering properties of our nearly HuD structures is indeed not only governed by S . Comparing the contour line and the course of maximum scattering (light-yellow regions in Figure 8c) reveals that the angular dependence of the individual scatterer is clearly imprinted into the angular dependence of the array.

This is in stark contrast to diffraction in periodic structures. In these, the impact of f is limited to the intensity of a diffraction order, but f never affects the direction of propagation. However, our observations are as well in contrast to truly random structures, in which f alone determines the scattering pattern since in those structures is $S = 1$. In fact, instead either S or f dominating the scattering response, tailored disorder structures such as our HuD structures enable a precise interplay between f and S .

An example of how delicate this interplay can be reveals another sample with the same TiO_2 nanodisks but different characteristic distance $r_0 = 604$ nm. Its experimentally measured ARS is plotted in Figure 7e and we observe a rather uniform scattering response with regards to λ and θ . With S from our modified RSA modeling we were not able to theoretically reproduce the ARS as good as it is the case for the other samples. We found better agreement using the experimentally evaluated S (deduced from SEM pictures), the resulting ARS is shown in Figure 7e. This can also be observed in Figure 8d, where we plot $|f_0|^2$, S , and the resulting ARS for $\lambda = 700$ nm. It can be recognized how the slight deviations between simulated (full line) and experimental (dashed) S lead to a closer agreement between ARS of theory and experiment. The need to use the experimental S is due to the high share of aggregates (30.2%) in this sample as pointed out above in the discussion on structural properties. The occurrence of aggregates is

random, which shifts S slightly toward unity and, for the case shown in Figure 8d, increases scattering up to $\theta = 70^\circ$.

We point out that many experimentally obtained disordered interfaces generally carry intrinsic correlations to some extent due to fabrication conditions and constraints, that is S , or any other appropriate representation of a structure in Fourier space, deviates from the value of a truly random structure. As an example, it is known that black silicon surface textures prepared by dry-etching have certain correlation lengths that can be controlled through fabrication parameters, moreover, it has been shown that their correlation length correlates with the light-trapping abilities of these kind of textures in solar cells.^[2,56] However, as long as S has no tendency toward zero for $q \rightarrow 0$ and f concentrates scattering into an angular region of small θ s, which is the case for most nanoparticles commonly used in the field of nanophotonics, these structures will still scatter mostly into the forward direction since their $|f_0|^2$ and S are both large. To suppress scattering into small θ s, S has to be as small as possible in the corresponding q -range, but large otherwise, which essentially describes S of a nearly HuD structure. Therefore, we can identify (nearly) HuD as a key element to achieve high efficiency large-angle scattering.

Concerning array properties, specular transmission and reflection depend only on the areal nanodisk density ρ but are independent of S , see Equations (4) and (5). This counter-intuitive result is a direct consequence of the first-Born approximation which we apply within the framework of our numerical approach, as it neglects any kind of coupling between scatterers that could change f in, for example, dependence of distance to neighboring scatterers. However, throughout this work and also in Figure 8e, where we plot $P_{\text{sca}} = 1 - R - T$ for different nearly HuD samples made of the same nanodisks but different S and ρ , we find good agreement between numerical and experimental results. We take the observed agreement as a strong indication that the assumption of negligible inter-particle coupling in our samples is sufficiently justified. We attribute the deviations between the numerical and experimental values in case of the dense sample (orange) in Figure 8e to the high number of aggregates in this sample.

However, since P_{sca} depicts the amount of light scattered, but does not imply how the angular scattering response looks like, Figure 8e also reveals the potential of (nearly) HuD structures to build highly efficient scattering interfaces with a scattering response on demand (see also Supporting Information). The scattering response is up to the interplay between f and S and can be tailored by adapting both precisely. It implies that one could change f by using another scatterer geometry, and S by refining the fabrication process to suppress the occurrence of aggregates at high densities and enhance hyperuniformity, or use even another suitable process to enable the fabrication of desired S .

4. Conclusion

In summary, we achieved to prepare high-index nanodisk arrays of strong correlated disorder with a novel fabrication method. The developed technique is scalable and allows control over important properties of the array, such as nanodisk

height and diameter, and characteristic next-neighbor distance, through easy-to-access experimental parameters. Moreover, we could show that the disorder of the arrangement of the nanodisks is nearly hyperuniform, leading to rather unusual light scattering properties. While control over the angular scattering response of conventional scattering interfaces, either periodic or random, is essentially limited by either the structure or the form factor, near hyperuniform disorder enables both quantities to substantially impact the response. This particular ability, in consequence, leads to a fundamentally novel approach to tailor light scattering through tailoring both structure and form factor toward a scattering response on demand and paves the way to a new class of optical materials.

5. Experimental Section

Nanodisk Array Fabrication: Standard 1 mm thick 76×26 mm object slides (soda-lime glass) were coated by thermal atomic layer (ALD) deposition in a Beneq TFS-200 ALD tool. First, the 13.8 nm etch stop layer of Al_2O_3 was deposited by alternating pulses of trimethylaluminum ($\text{Al}(\text{CH}_3)_3$) and water (250 ms pulse duration, 100 pulses per precursor, 3 s purge) at 180°C .^[57] Then, a 231.0 nm layer of TiO_2 was deposited at 120°C by 3633 alternating pulses of TiCl_4 and water (pulse duration 200 ms). This layer provides the material the nanodisks are made of. In more detailed studies on the optical properties of ALD grown TiO_2 found in literature,^[58–60] deposition temperatures below $\approx 165^\circ\text{C}$ produce smooth, amorphous films with negligible optical losses in the visible spectrum compared to higher deposition temperatures, which agrees well with our observations by electron microscopy and spectroscopic ellipsometry. To complete the layer stack (please note Figure 1a), a layer of 19.5 nm Al_2O_3 was deposited by ALD (165 cycles, otherwise same deposition parameters as above).

A dispersion of PMMA nanospheres with diameter of 499 ± 10 nm (microParticles GmbH, Berlin, Germany) was first treated in an ultrasonic bath for 30 min to break up reversible aggregates and then diluted with a mixture of MicroPurewater (18 M Ω cm) and 30% isopropyl alcohol (p.a. grade). Potassium chloride (KCl) was used to carefully adjust the ionic strength of the dispersion (typically in the range of 10^{-5} to 10^{-3} M). The ALD coated substrates were exposed to the dispersion for 18 h and rinsed in deionized water afterward. The samples were then rinsed in ethylene glycol multiple times to remove all water since Al_2O_3 surfaces can degrade in hot aqueous solutions during the subsequent tempering step.^[61]

Pattern transfer was performed via RIE in an Oxford Plasmalab 100 System. For the Al_2O_3 etch process, BCl_3 and Ar were used in a ratio of 30:20 sccm at a pressure of 10 mTorr. The inductively coupled plasma (ICP) power was 2500 W and the capacitively coupled plasma (CCP) power was 63 W, resulting in a dc-bias of -89 V.^[37] For the TiO_2 etch process the gas of $\text{CF}_4:\text{O}_2:\text{Ar}$ was 40:6:10 sccm with the pressure kept constant at 15 mTorr. The ICP power was 1800 W and the CCP power was 41 W, resulting in a dc-bias of -81 V.

Characterization: For the microstructural characterization, SEM images were recorded with a field emission microscope (FEI Versa 3D) at 4 kV. Disk positions were extracted from images of $104 \times 70 \mu\text{m}^2$ area via template matching, corresponding to about 2.000 Disks for the uncorrelated pattern and 16.000 for the most dense.^[33,62] Briefly, the image of a sample particle was scanned over the original SEM image and tested for similarity at every point. Some disk pairs exhibit nominal surface-to-surface distances ≤ 0 nm (see e.g., Figure 3g) due to slight merging of the PMMA particles during tempering. Those pairs were defined as disks in aggregates.

The ALD layers were optically characterized on silicon reference samples using a spectroscopic ellipsometer (J.A. Woollam M2000V). Due to the low absorption of TiO_2 the refractive index could reasonably approximated by Cauchy's equation with

$n(\lambda_{\text{um}}) = 2.281 + 0.024/\lambda_{\text{um}}^2 + 0.006/\lambda_{\text{um}}^4$, for example, $n(\lambda = 0.45 \mu\text{m}) \approx 2.54$ and $n(\lambda = 1.0 \mu\text{m}) \approx 2.31$.^[59,60]

Angular resolved scattering measurements were performed using a custom-made goniometer setup. White light of a halogen lamp was collimated, linearly polarized (where applicable) and directed onto the respective sample. The scattered light was collected and focused onto a fiber bundle by a single lens with an aperture corresponding to an acceptance angle of $\approx 3.5^\circ$. in steps of $\Delta\theta = 3^\circ$. A monochromator (Horiba iHR550) in conjunction with a silicon photodetector (Thorlabs DET210) and a lock-in amplifier (Stanford Research Systems SR830) was used to detect the light at the fiber output in the range of 450–1000 nm. Directly transmitted light at $\theta = 0^\circ$ without sample was recorded as reference $I_{\text{ref}}(\psi, \lambda)$ for each linear polarization angle ψ and for unpolarized light, in order to characterize the system response. The presented data are $I(\theta, \psi, \lambda) = (I_{\text{raw}}(\theta, \psi, \lambda) - I_{\text{dark}})/(I_{\text{ref}}(\psi, \lambda) - I_{\text{dark}})$. Integrations over the forward-scattering half-space were $\int_{4^\circ}^{90^\circ} I(\theta, \psi, \lambda) \sin\theta d\theta$, where the $\sin\theta$ accounts for stronger representations of larger angles.

Numerical Methods: Point configurations were predicted via a random sequential adsorption scheme in a Monte Carlo type code. The soft-sphere behavior of the charged colloidal particles was taken into account by modulating the probability of a particle to adhere on the substrate at a given random position within an extended radius of neighboring particles.^[33] Considering the extended radius, the saturation density in the experiment was slightly higher than in the hard-sphere case but approximately constant over a variety of number densities. It could therefore be kept constant for the prediction of patterns. Optimizations of the algorithm regarding computation time were inspired by the work of Zhang et al.^[51]

To calculate the angular resolved scattering response of a single nanodisk, the form factor $f(\vec{E}, \mathbf{k}_0, \mathbf{k})$, we rigorously solved Maxwell's equations in 3D with appropriate source, material, and boundary condition settings using the time-harmonic finite-element solver JCMsuite.^[63] To obtain the angular resolved scattering response of an infinitely extended array of identical nanodisks, f is combined with the structure factor $S(q)$ of the point configuration of the particular array via our numerical approach based on Born's approximation (Equations (4)–(6)). Multipole decomposition was performed using an integrated function of JCMsuite that applies the multipole expansion to the scattered fields and solves for the corresponding coefficients using an algorithm presented by Santiago et al.^[64]

Supporting Information

Supporting Information is available from the Wiley Online Library or from the author.

Acknowledgements

This work was funded by the Deutsche Forschungsgemeinschaft (DFG) through priority program SPP 1839 "Tailored Disorder"- project number 278744673. The authors thank Claudia Stehr for her excellent technical support.

Open access funding enabled and organized by Projekt DEAL.

Conflict of Interest

The authors declare no conflict of interest.

Data Availability Statement

The data that support the findings of this study are available from the corresponding author upon reasonable request.

Keywords

hyperuniformity, metasurfaces, nanophotonics, tailored disorder

Received: January 27, 2021

Revised: April 26, 2021

Published online: June 1, 2021

- [1] P. Spinelli, M. Verschuuren, A. Polman, *Nat. Commun.* **2012**, *3*, 692.
- [2] M. Otto, M. Algasinger, H. Branz, B. Gesemann, T. Gimpel, K. Fuchsels, T. Käsebier, S. Kontermann, S. Koynov, X. Li, V. Naumann, J. Oh, A. N. Sprafke, J. Ziegler, M. Zilk, R. B. Wehrspohn, *Adv. Opt. Mat.* **2015**, *3*, 147.
- [3] T. Schneider, J. Tröndle, B. Fuhrmann, F. Syrowatka, A. Sprafke, R. Scheer, *Solar RRL* **2020**, *4*, 2000295.
- [4] J. H. Son, J. U. Kim, Y. H. Song, B. J. Kim, C. J. Ryu, J.-L. Lee, *Adv. Mat.* **2012**, *24*, 2259.
- [5] J. Y. Park, B. J. Kim, C. J. Yoo, W. J. Dong, I. Lee, S. Kim, J.-L. Lee, *Sci. Rep.* **2020**, *10*, 2045.
- [6] S.-Y. Ding, J. Yi, J.-F. Li, B. Ren, D.-Y. Wu, R. Panneerselvam, Z.-Q. Tian, *Nat. Rev. Mat.* **2016**, *1*, 16021.
- [7] J. Langer, D. Jimenez de Aberasturi, J. Aizpurua, R. A. Alvarez-Puebla, B. Auguie, J. J. Baumberg, G. C. Bazan, S. E. J. Bell, A. Boisen, A. G. Brolo, J. Choo, D. Cialla-May, V. Deckert, L. Fabris, K. Faulds, F. J. Garcia de Abajo, R. Goodacre, D. Graham, A. J. Haes, C. L. Haynes, C. Huck, T. Itoh, M. Käll, J. Kneipp, N. A. Kotov, H. Kuang, E. C. Le Ru, H. K. Lee, J.-F. Li, X. Y. Ling, et al., *ACS Nano* **2020**, *14*, 28.
- [8] K. Chung, S. Yu, C.-J. Heo, J. W. Shim, S.-M. Yang, M. G. Han, H.-S. Lee, Y. Jin, S. Y. Lee, N. Park, J. H. Shin, *Adv. Mat.* **2012**, *24*, 2375.
- [9] B. Bläsi, T. Kroyer, O. Höhn, M. Wiese, C. Ferrara, U. Eitner, T.-E. Kuhn, *Proc. 33rd European PV Solar Energy Conf.*, Amsterdam, The Netherlands, September **2017**, 2630.
- [10] X. Liu, Z. Huang, J. Zang, *Nano Lett.* **2020**, *20*, 8739.
- [11] G. M. Wilson, M. Al-jassim, W. K. Metzger, S. W. Glunz, P. Verlinden, G. Xiong, L. M. Mansfield, B. J. Stanbery, K. Zhu, Y. Yan, J. J. Berry, A. J. Ptak, F. Dimroth, B. M. Kayes, A. C. Tamboli, R. Peibst, K. Catchpole, M. O. Reese, C. S. Klinga, P. Denholm, M. Morjaria, M. G. Deceglie, J. M. Freeman, M. A. Mikofski, D. C. Jordan, G. Tamizhmani, D. B. Sulas-Kern, *J. Phys. D: Appl. Phys.* **2020**, *53*, 493001.
- [12] M. Born, E. Wolf, A. B. Bhatia, P. C. Clemmow, D. Gabor, A. R. Stokes, A. M. Taylor, P. A. Wayman, W. L. Wilcock, *Principles of Optics: Electromagnetic Theory of Propagation, Interference and Diffraction of Light*, 7th ed., Cambridge University Press, Cambridge, **1999**.
- [13] T. Zemb, P. Lindner, *Neutron, X-rays and Light. Scattering Methods Applied to Soft Condensed Matter*, North-Holland, Amsterdam **2002**.
- [14] K. Vynck, M. Burrelli, F. Riboli, D. S. Wiersma, *Nat. Mater.* **2012**, *11*, 1017.
- [15] D. S. Wiersma, *Nat. Photonics* **2013**, *7*, 188.
- [16] *Amorphous Nanophotonics* (Eds: C. Rockstuhl, T. Scharf), Springer, Berlin, Heidelberg **2013**.
- [17] F. Riboli, N. Caselli, S. Vignolini, F. Intonti, K. Vynck, P. Barthelemy, A. Gerardino, L. Balet, L. H. Li, A. Fiore, M. Gurioli, D. S. Wiersma, *Nat. Mater.* **2014**, *13*, 720.
- [18] S. Yu, C. Qiu, Y. Chong, S. Torquato, N. Park, *Nat. Rev. Mater.* **2021**, *6*, 226.
- [19] S. Torquato, *Phys. Rep.* **2018**, *745*, 1.
- [20] M.-J. Sun, X.-Y. Zhao, L.-J. Li, *Opt. Lett.* **2018**, *43*, 4049.
- [21] M. Castro-Lopez, M. Gaio, S. Sellers, G. Gkantounis, M. Florescu, R. Sapienza, *APL Photonics* **2017**, *2*, 061302.

- [22] O. Leseur, R. Pierrat, R. Carminati, *Optica* **2016**, 3, 763.
- [23] M. Florescu, S. Torquato, P. J. Steinhardt, *Proc. Natl. Acad. Sci. USA* **2009**, 106, 20658.
- [24] W. Man, M. Florescu, E. P. Williamson, Y. He, S. R. Hashemizad, B. Y. C. Leung, D. R. Liner, S. Torquato, P. M. Chaikin, P. J. Steinhardt, *Proc. Natl. Acad. Sci. USA* **2013**, 110, 15886.
- [25] M. Florescu, P. J. Steinhardt, S. Torquato, *Phys. Rev. B* **2013**, 87, 165116.
- [26] M. M. Milosevic, W. Man, G. Nahal, P. J. Steinhardt, S. Torquato, P. M. Chaikin, T. Amoah, B. Yu, R. A. Mullen, M. Florescu, *Sci. Rep.* **2019**, 9, 20338.
- [27] A. I. Kuznetsov, A. E. Miroshnichenko, M. L. Brongersma, Y. S. Kivshar, B. Luk'yanchuk, *Science* **2016**, 354, aag2472.
- [28] M. Decker, I. Staude, M. Falkner, J. Dominguez, D. N. Neshev, I. Brener, T. Pertsch, Y. S. Kivshar, *Adv. Opt. Mat.* **2015**, 3, 813.
- [29] S. Kruk, Y. Kivshar, *ACS Photonics* **2017**, 4, 2638.
- [30] K. Koshelev, S. Kruk, E. Melik-Gaykazyan, J.-H. Choi, A. Bogdanov, H.-G. Park, Y. Kivshar, *Science* **2020**, 367, 288.
- [31] M. Jang, Y. Horie, A. Shibukawa, J. Brake, Y. Liu, S. M. Kamali, A. Arbabi, H. Ruan, A. Faraon, C. Yang, *Nat. Photonics* **2018**, 12, 84.
- [32] L. Wang, S. Kruk, K. Koshelev, I. Kravchenko, B. Luther-Davies, Y. Kivshar, *Nano Lett.* **2018**, 18, 3978.
- [33] P. M. Piechulla, L. Muehlenbein, R. B. Wehrspohn, S. Nanz, A. Abass, C. Rockstuhl, A. Sprafke, *Adv. Opt. Mater.* **2018**, 6, 1701272.
- [34] J. Dekker, K. Kolari, R. L. Puurunen, *J. Vac. Sci. Technol. B* **2006**, 24, 2350.
- [35] *Dry Etching for Microelectronics* (Ed: R. A. Powell), Vol. 4, North-Holland, Amsterdam **1984**.
- [36] S.-M. Koo, D.-P. Kim, K.-T. Kim, C.-I. Kim, *Mater. Sci. Eng. B* **2005**, 118, 201.
- [37] S. J. Yun, A. Efremov, M. Kim, D.-W. Kim, J. W. Lim, Y.-H. Kim, C.-H. Chung, D. J. Park, K.-H. Kwon, *Vacuum* **2008**, 82, 1198.
- [38] K.-R. Choi, J.-C. Woo, Y.-H. Joo, Y.-S. Chun, C.-I. Kim, *Vacuum* **2013**, 92, 85.
- [39] A. A. Garay, S. M. Hwang, C. W. Chung, *Thin Solid Films* **2015**, 587, 20.
- [40] H. Jansen, M. de Boer, R. Legtenberg, M. Elwenspoek, *J. Micro-mech. Microeng.* **1995**, 5, 115.
- [41] I. Hotovy, S. Hascik, M. Gregor, V. Rehacek, M. Predanoc, A. Plecenik, *Vacuum* **2014**, 107, 20.
- [42] R. Adzhri, M. K. M. Arshad, M. F. M. Fathil, U. Hashim, A. R. Ruslinda, R. M. Ayub, S. C. B. Gopinath, C. H. Voon, K. L. Foo, M. N. M. Nuzaihan, A. H. Azman, M. Zaki, in *2015 IEEE Regional Symposium on Micro and Nanoelectronics*, IEEE, Piscataway, NJ, **2015**, pp.1–4.
- [43] P. Piechulla, J. Seiffe, M. Hofmann, J. Rentsch, R. Preu, presented at *26th European PV Solar Energy Conf. and Exhibition*, Hamburg, Germany, September **2011**.
- [44] A.-K. Volk, N. Tucher, J. Seiffe, H. Hauser, M. Zimmer, B. Blasi, M. Hofmann, J. Rentsch, *IEEE J. Photovoltaics* **2015**, 5, 1027.
- [45] R. Dreyfus, Y. Xu, T. Still, L. A. Hough, A. G. Yodh, S. Torquato, *Phys. Rev. E* **2015**, 91, 012302.
- [46] H. Liu, S. J. Paddison, *Phys. Chem. Chem. Phys.* **2016**, 18, 11000.
- [47] S. M. Allen, E. L. Thomas, R. A. Jones, *The Structure of Materials*, Wiley, New York **1999**.
- [48] S. Torquato, F. H. Stillinger, *Phys. Rev. E* **2003**, 68, 041113.
- [49] J. Kim, S. Torquato, *Phys. Rev. B* **2018**, 97, 054105.
- [50] S. Torquato, O. U. Uche, F. H. Stillinger, *Phys. Rev. E* **2006**, 74, 061308.
- [51] G. Zhang, S. Torquato, *Phys. Rev. E* **2013**, 88, 053312.
- [52] J. Keller, *Proc. Symp. Appl. Math.* **1964**, 16, 145.
- [53] L. Mandel, E. Wolf, *Optical Coherence and Quantum Optics*, Cambridge University Press, Cambridge **1995**.
- [54] S. Torquato, J. Kim, *Phys. Rev. X* **2021**, 11, 021002.
- [55] G. Mie, *Ann. Phys.* **1908**, 330, 377.
- [56] M. Steglich, T. Käsebier, M. Zilk, T. Pertsch, E.-B. Kley, A. Tünnermann, *J. Appl. Phys.* **2014**, 116, 173503.
- [57] M. Otto, M. Kroll, T. Käsebier, R. Salzer, A. Tünnermann, R. B. Wehrspohn, *Appl. Phys. Lett.* **2012**, 100, 191603.
- [58] J. Aarik, A. Aidla, T. Uustare, V. Sammelselg, *J. Cryst. Growth* **1995**, 148, 268.
- [59] J. Aarik, A. Aidla, A.-A. Kiisler, T. Uustare, V. Sammelselg, *Thin Solid Films* **1997**, 305, 270.
- [60] D. Saha, R. Ajimsha, K. Rajiv, C. Mukherjee, M. Gupta, P. Misra, L. Kukreja, *Appl. Surf. Sci.* **2014**, 315, 116.
- [61] K. Tadanaga, N. Yamaguchi, A. Matsuda, T. Minami, M. Tatsumisago, *J. Adhes. Sci. Technol.* **2008**, 22, 387.
- [62] OpenCV library, <http://opencv.org/> (accessed: October 2020).
- [63] J. Pomplun, S. Burger, L. Zschiedrich, F. Schmidt, *Phys. Status Solidi B* **2007**, 244, 3419.
- [64] X. G. Santiago, M. Hammerschmidt, S. Burger, C. Rockstuhl, I. Fernandez-Corbaton, L. Zschiedrich, *Phys. Rev. B* **2019**, 99, 045406.

Antireflective Huygens' Metasurface with Correlated Disorder Made from High-Index Disks Implemented into Silicon Heterojunction Solar Cells

Peter M. Piechulla,^{*,#} Evgeniia Slivina,^{*,#} Derk Bätzner, Ivan Fernandez-Corbaton, Prerak Dhawan, Ralf B. Wehrspohn, Alexander N. Sprafke, and Carsten Rockstuhl



Cite This: *ACS Photonics* 2021, 8, 3476–3485



Read Online

ACCESS |



Metrics & More

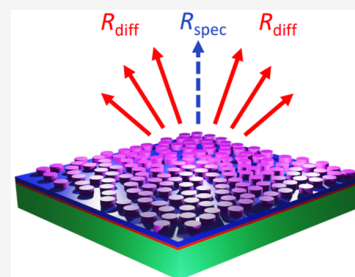


Article Recommendations



Supporting Information

ABSTRACT: A large variety of different strategies has been proposed as alternatives to random textures to improve light coupling into solar cells. While the understanding of dedicated nanophotonic systems deepens continuously, only a few of the proposed designs are industrially accepted due to a lack of scalability. In this Article, a tailored disordered arrangement of high-index dielectric submicron-sized titanium dioxide (TiO₂) disks is experimentally exploited as an antireflective Huygens' metasurface for standard heterojunction silicon solar cells. The disordered array is fabricated using a scalable bottom-up technique based on colloidal self-assembly that is applicable virtually irrespective of material or surface morphology of the device. We observe a broadband reduction of reflectance resulting in a relative improvement of a short-circuit current by 5.1% compared to a reference cell with an optimized flat antireflective indium tin oxide (ITO) layer. A theoretical model based on Born's first approximation is proposed that links the current increase in the arrangement of disks expressed in terms of the structure factor $S(q)$ of the disk array. Additionally, we discuss the optical performance of the metasurface within the framework of helicity preservation, which can be achieved at specific wavelengths for an isolated disk for illumination along the symmetry axis by tuning its dimensions. By comparison to a simulated periodic metasurface, we show that this framework is applicable in the case of the structure factor approaching zero and the disks' arrangement becoming stealthy hyperuniform.



KEYWORDS: *scalable, hyperuniformity, tailored disorder, Mie resonators, Kerker condition, metamaterials*

Efficient light coupling between a device and its surrounding is key to maximize the performance of any optoelectronic system. This is particularly true for silicon solar cells, where the large discontinuity of the permittivity from air to silicon causes severe reflection losses. Optical losses are indeed one of the main causes that prevents us currently from reaching the detailed-balance limit,^{1,2} which constitutes the upper bound of achievable device efficiency.

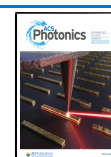
Common strategies to reduce losses include the use of flat antireflective coatings and surface textures, or combinations thereof, for example, pyramidal textures with an added conformal coating. The latter approach has been overwhelmingly successful as industry standard for decades, albeit it may not be applicable for every device. For example, it requires comparably thick wafers, while thin absorbers are attractive for flexible devices and to lower material consumption. Also, it relies on silicon as the absorber material because the pyramids are etched in a self-organized process along specific crystallographic axes. The approach is not applicable to promising alternative materials, such as perovskites, that may soon be industrialized.^{3,4} Silicon pyramids imply a corrugated interface, while very often a flat interface is preferred in the following fabrication steps. For example, in solution-processed perovskite-silicon tandem solar cells, the

pyramidal surface profile poses additional challenges in optimizing the electrical functionality of the perovskite top-cell.^{5–7} Alternatives to pyramidal textures must, therefore, be explored, that come with greater flexibility with respect to the design of a device. If, for instance, the tandem is bound to a flat configuration, a light in-coupling structure could be added on top of the perovskite top cell.

That challenge has been accepted, and a number of nanophotonic concepts have been proposed not only to improve light incoupling on the front interface, but for a much broader spectrum of objectives, including light trapping, spectrum splitting in tandem devices, or colored photovoltaics.^{8–12} As building blocks, submicron-sized disks or pillar-shaped scattering elements have attracted a lot of attention during recent years because of their ability to support multipolar Mie resonances.^{13,14} This allows to control

Received: April 20, 2021

Published: November 11, 2021



the propagation of light in quite a drastic and deterministic manner. The shape of such submicron-sized disks (henceforth referred to as disks) can be tuned to carefully overlap electric and magnetic modes to control scattering characteristics.^{15–18} Inspired by the original work of Kerker et al., complete suppression of back scattering can be achieved, making these disk-based Huygens' metasurfaces ideal for use as antireflective coatings.^{19–21} This bears the question of how to arrange the scattering elements. Disordered arrangements have been shown to possess a superior broadband response,^{22–25} whereas periodic arrangements can be made entirely subwavelength, thereby suppressing all off-axis scattering.¹⁹ As we will show, the latter can be achieved also in a disordered arrangement if spatial correlations are tuned appropriately.^{26,27}

The design of the metasurface proposed in this Article was inspired by our previous work²⁸ on a similar but periodic arrangement of disks, whose antireflective properties were designed and analyzed from the perspective of the helicity of the scattered light. Preserving the helicity of the incident light, plus a sufficiently high degree of rotational symmetry along the illumination axis, are sufficient conditions to ensure zero specular reflection from a general system.²⁹ The most general way to achieve helicity preservation is by means of electromagnetically dual systems, that is, systems with equivalent electric and magnetic responses.³⁰ In a more restricted and practical setting, helicity preservation can be achieved for on-axis illumination of high-permittivity disks. The aspect ratio of the disks can be tuned into the Huygens scattering regime where the electric and magnetic dipolar responses are balanced. Then, the condition of discrete rotational symmetry $2\pi/n$, with $n \geq 3$, can be met by arranging the disks in a square or hexagonal lattice on top of a substrate. While this approach nulls the specular reflection at a single or at most at a few discrete wavelengths, it turns out that the effect is all together rather broadband and suitable to the relevant spectral range for a solar cell.²⁸ In a disordered system, the concept of discrete rotational symmetry is not exactly applicable. However, if the pattern is tailored appropriately, one can speak of an effective continuous rotational symmetry ($n \rightarrow \infty$) and, consequently, establish a one-to-one relationship in the long wavelength limit between the helicity preservation and the antireflective properties of the coated solar cell.

Despite the initially discussed advantages of photonic structures, the proposed designs were barely even considered to be implemented on an industrial scale. On the one hand, wafer-based silicon solar cells are still dominant and the standard pyramidal texture already poses a tough benchmark. On the other hand, fabrication of newly designed structures often relies on expensive top down fabrication methods such as e-beam lithography. Also, many fabrication techniques require specially prepared substrates, for example, polished surfaces. Clearly, scalability is essential for a structure to be used in a real world application. Techniques like nanoimprint lithography^{31,32} are in principle scaleable, and the first promising results were published for solar cells in the subcentimeter range.³³ However, to the best of our knowledge, so far no results for disk-based photonic structures were published for solar cells with multiple square centimeter area.

In this publication, we will show for the first time by means of experiments and simulations that a dielectric disk-based antireflective coating (Figure 1) can improve the performance of a solar cell of standard industrial design, where the point of departure is a nontextured, damage-etched surface. We

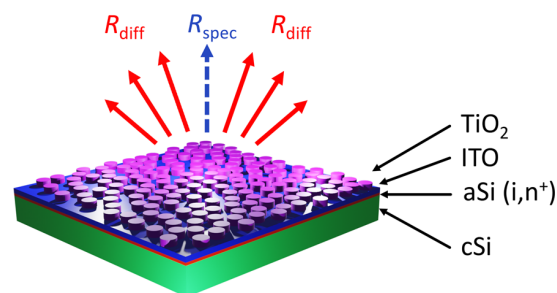


Figure 1. Schematic illustration of the solar cell structure considered in this work. R_{diff} and R_{spec} denote the diffuse and specular parts of reflectance as discussed in the text below. The disks were deposited on fully processed heterojunction technology (HJT) rear-emitter solar cells for which the front surface of a flat unpolished silicon wafer was passivated by amorphous silicon (aSi) intrinsic and n^+ -doped layers. A transparent conductive indium tin oxide (ITO) film serves as both an antireflection coating (ARC) and a front contact (see [Methods](#) for more details). Additionally, devices included screen-printed contact fingers (not shown) but no busbar.

consider silicon solar cells as a platform to demonstrate feasibility. However, we note that through our fabrication process the disks can be applied to any surface, in principle irrespective of topography or material. Moreover, a structure composed of dielectric disks can potentially be integrated into the solar module, which was numerically shown in ref 34. The design of the disks is inspired by the concept of helicity preservation which, as we will show, also works in conjunction with a disk pattern of correlated disorder in the long wavelength limit. Differences to a similar but periodic system are revealed by supporting simulations thereof.

RESULTS AND DISCUSSION

Details of our novel colloid-based nanofabrication method are documented in [Methods](#) and in previous publications.^{18,35} We fabricated arrays of disks on top of the ITO front contact of flat heterojunction solar cells, as shown in [Figure 2](#). Like-sized disks of 370 nm in diameter and 122 nm in height ([Figure 2](#), left) cover the entire surface of the sample in a disordered dense pattern ([Figure 2](#), center). The process is not affected by any previously present structures (see [Supporting Information, Figure S1](#), for disk patterns on pyramids) and covers the entire $39 \times 39 \text{ mm}^2$ sample. This includes areas of uneven surface profile due to residue roughness after damage removal etch and contact fingers (see photograph, [Figure 2](#), right). Some edge effects are visible, which are likely due to residues from laser-cutting the samples from full scale industrial type solar cells, as the sample size was limited due to laboratory scale fabrication equipment for atomic layer deposition (ALD) for titanium dioxide (TiO_2) film deposition and reactive ion etching (RIE) for thin film structuring. We note that the relatively thick TiO_2 layer and therefore slow ALD deposition could also be achieved by faster means such as plasma-enhanced chemical vapor deposition^{36,37} (PECVD) or sol-gel³³ deposition. Furthermore, directional plasma etching processes are known to work in high-throughput inline machines.^{38,39} The pattern formation process is based on self-organization of colloids and can be realized with very basic equipment. We fabricated multiple samples coated with disk arrays of varying densities and further analyzed their optical and electrical properties by measuring broadband reflectance, current–voltage characteristic, and quantum efficiency (see [Methods](#) for more details).

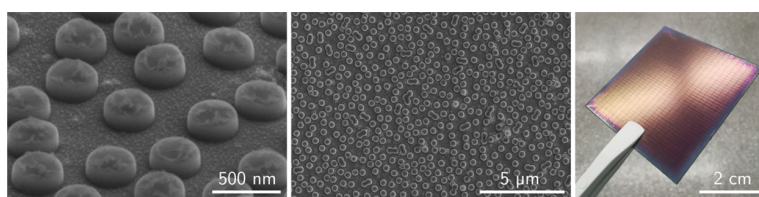


Figure 2. (Left, Center) Electron micrographs of disks deposited on top of a solar cell on different magnification stages. The left figure highlights the features of the individual disks, while the center image highlights the uniformity of the samples. (Right) Photograph of a $39 \times 39 \text{ mm}^2$ coated solar cell.

To simulate the optical response, the disordered nature of our disk pattern is accommodated by using Born's first approximation. Far-field scattering contributions of the individual disks are conveniently superposed by a multiplication of the structure factor as an array property with the form factor squared as a property of the individual disk. Though this approach neglects any near-field interaction and multiple scattering effects, it allows reasonable predictions of the response for the presented case and will prove a useful tool of analysis. In this work, we obtain the structure factor from digitized scanning electron microscopy (SEM) images, whereas the form factor is the mere result of a simulation of a single disk by means of the finite element method (FEM; see [Methods](#)). For all simulations in this publication, we only consider reflection and scattering at the front side of the device and assume the silicon absorber to occupy the lower half-space.

In [Figure 3](#) we use the described approach to predict the reflectance of a disk pattern deposited on top of an actual solar

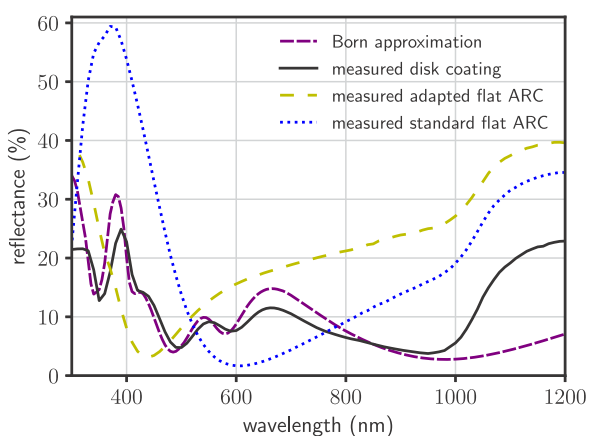


Figure 3. Reflectance of a disk pattern calculated via Born approximation and finite element simulation of a single disk. Measured reflectances of a disk coated sample and an adapted flat ARC (50 nm ITO) the disk structure is based on. A standard flat ARC reference (80 nm ITO) is shown for comparison.

cell. The measured disk sample reflectance curve (see [Methods](#) for details on measurements) includes all major features predicted by the calculation, but shows an increased reflectance above 1000 nm. This is caused by reflectance at the back side of the solar cell that has not been considered in the simulation. A detailed analysis of the measured absorption in the wavelength range around 1000 nm could help to assess the light-trapping capabilities of our disk structure. However, the structure was not optimized for light trapping and, given the relatively thick wafers, the experimental setup is not well suited for such an investigation. We, therefore, refer to the

recent work of Slivina et al. for a detailed numerical analyses for similar but periodic light-trapping structures.³⁴ Otherwise, the most prominent deviation of about 4%_{abs} is found around 650 nm and may be the result of slight differences between the model parameters of the FEM simulation and the real disks. For instance, the surface roughness on top of the disks ([Figure 2](#), left) is not included in the simulation. Also, for the Born approximation, the disks are assumed to be perfectly aligned within one plane. This is in contrast to the experiment that is not conducted with polished silicon wafers.

The ITO front contact of the disk-coated solar cells has been adapted to 50 nm to enable good functionality of the disk structure as ARC, compared to a standard flat ARC reference with 80 nm ITO, that is optimized for maximum current at air mass 1.5 global tilted irradiance (AM1.5G⁴⁰).²⁸ Measured reflectances for both flat ARCs are shown for reference in [Figure 3](#) as well. For the 50 nm ARC, the minimum in reflectance is shifted to a shorter wavelength compared to the 80 nm ARC. However, adding the disk coating reduces the reflectance also at longer wavelengths. Though the standard 80 nm ARC reflectance is lower at the optimal wavelength around 600 nm, throughout most of the spectrum, we observe lower reflectances for the measured disk sample, thereby clearly showing the effect of the disk structure. We note that, according to our previous work,²⁸ this result is expected to be robust to small variations of the disks' dimensions up to approximately 20%. However, a purposeful design of the disks is still essential (see [SI, Figure S8](#) for a counterexample).

Impact on Optoelectronic Properties. We further analyzed the optoelectronic properties of a series of solar cells. In order to observe in the most direct way the effect of the disk coating and possible side effects due to processing, we here compare the optimally coated device to an untreated sample with adapted flat ARC. More comprehensive results are shown at a later stage. The left graph in [Figure 4](#) shows the measured current–voltage characteristics of the untreated and the coated cell with an optimal disk density of $3.0 \mu\text{m}^{-2}$ exhibiting the highest increase in J_{SC} (for details on IV characterization, see [Methods](#)). The extracted parameters characterizing these cells are shown in [Table 1](#). The short circuit current of the coated cell was improved significantly and increased by 14.0%_{rel} in comparison to the untreated sample. Due to the increase of current at the maximum power point I_{MP} , the efficiency of the cell $\eta = P_{\text{max}}/P_{\text{in}}$ was increased by 10.4%_{rel} with the nominal incident power $P_{\text{in}} = 1.521 \text{ W}$. The fill factor $FF = P_{\text{max}}/(V_{\text{OC}} \cdot I_{\text{SC}})$ of the coated cell was found to be 2.7%_{abs} lower than the one of the untreated sample. However, this is not stemming from the properties of the coating, but rather the higher V_{MP} of the untreated cell. This can be attributed to the untreated sample not being subjected to any processing, which could potentially cause a small

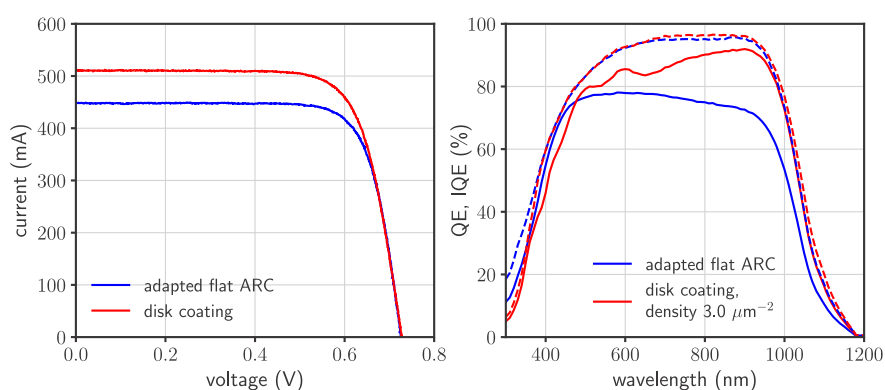


Figure 4. (Left) Current–voltage characteristics of the untreated (adapted flat ARC) sample and coated sample. (Right) External (solid lines) and internal (dashed lines) quantum efficiencies.

Table 1. Cell Parameters Comparing Untreated (Adapted Flat ARC) and the Best Disk Coated Sample, with the Estimated Uncertainty for the Current from Repeated Measurements of Around 0.5%

	untreated sample	disk coating
$I_{SC,meas}$ (mA)	448	511
J_{SC} (mA/cm ²)	29.5	33.6
V_{OC} (V)	0.726	0.728
I_{MP} (mA)	420	473
V_{MP} (V)	0.598	0.586
P_{max} (W)	0.251	0.277
η (%)	16.5	18.2
FF (%)	77.2	74.5

reduction in V_{MP} of the coated sample. However, the cell parameters determined from IV characteristics strongly indicate the overall positive effect of the coating, boosting short-circuit current and efficiency of the device.

We characterized the spectral behavior of the coated solar cell with respect to the untreated sample (adapted flat ARC) by measuring external (QE) and internal (IQE) quantum

efficiencies (see Methods), shown in the right graph in Figure 4. As expected, the coated cell with optimal disk density shows significant improvement in QE in the most part of the considered spectral region in comparison with the adapted flat ARC sample which has the same ITO thickness of 50 nm. Note that the QE of the latter will not be directly comparable to the QE of a standard flat ARC (see SI, Figure S3) due to the mismatch of reflectance and IQE. The QE of a disk coated device is lower than that of the adapted flat ARC cell only at wavelengths below 500 nm. The region between $\lambda_0 = 350$ nm and $\lambda_0 = 500$ nm is the only part of the spectrum where the reflectance of the coated cell is higher than the reflectance of adapted flat ARC cell (see Figure 3), which leads to higher QE of the latter. Additionally, the TiO₂ disks introduce some parasitic absorption in the wavelength range below $\lambda_0 = 380$ nm.

To exclude the effect of the reflection losses in the analysis, we considered the IQE of these cells. Starting from $\lambda_0 = 380$ nm, both devices show comparable performance within measurement uncertainty. Only at shorter wavelengths, the IQE of the coated cell is lower than the IQE of the flat adapted ARC cell due to parasitic absorption in the disks.

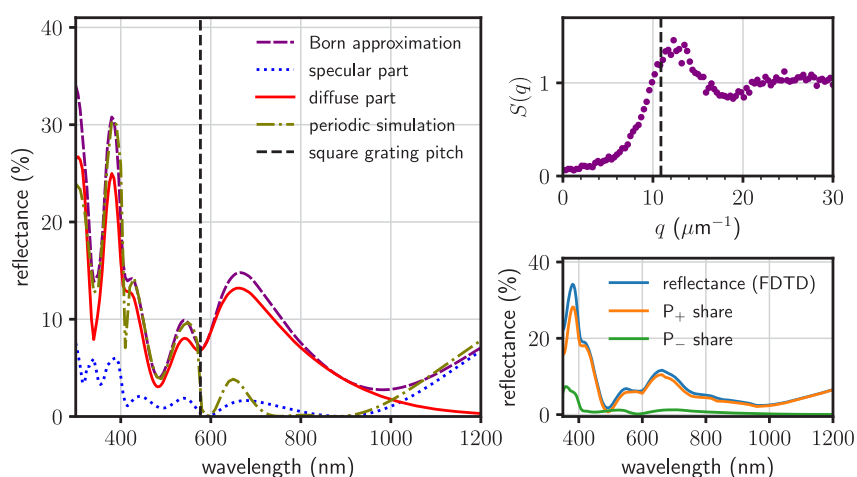


Figure 5. (Left) Decomposition of total reflectance (calculated via Born approximation) into specular and diffuse parts, and comparison to a disk pattern in a square array (with grating pitch of 577 nm). (Right, top) Structure factor of the disk pattern calculated from a digitized SEM image. The dashed line marks q corresponding to 577 nm vacuum wavelength. (Right, bottom) Simulated reflectance via finite-difference time-domain (FDTD) method of a disordered disk arrangement similar to the experiment and decomposition into normalized reflected powers of fields of positive and negative helicity, P_+ and P_- , respectively. The incident field had negative helicity (right circular polarized light).

Specular and Diffuse Reflectance. In a previous work by Slivina et al., it was numerically shown that periodic disk arrangements can significantly reduce reflectance losses in a solar cell.²⁸ Using the same finite element approach, we rigorously simulated the reflectance of a periodic structure with equivalent disk density, based on a disk model with identical parameters, as in the disordered case. In passing we note that, for the Born approximation that describes the disordered sample, we only considered the real part of the refractive index for TiO₂. This is not a severe assumption, as the imaginary part of TiO₂ anyhow is mostly small in the spectral region of interest. These results compared to results obtained for the disordered sample are shown in Figure 5 (left). Comparison to experimental results are shown in Figure 3. At wavelengths below 577 nm, the Born approximation and periodic simulation are almost congruent and both agree reasonably well with the measured disk sample, except for wavelengths below 350 nm. In this range, absorption in the TiO₂ disks becomes significant, which is not included for the Born approximation, hence, the deviation.

The wavelength range above 577 nm, where we observe the strongest deviation between a periodic simulation and the Born approximation, is also of great importance to the device performance due to the strong solar irradiance in this range. To further elucidate the increased reflectance above 577 nm, we decompose the calculated reflectance via Born approximation (see eq 10 in Methods and Figure 1) into specular and diffusive parts, as shown in Figure 5 (left). The diffusive contribution by far outweighs the specular, which is particularly true in the range from 600 to 1000 nm. From eq 12 it is clear that scattering and therefore diffusive reflection can only occur when $q = k_0 \sin \theta$ is satisfied and $S(q) \neq 0$. The structure factor $S(q)$ for the disordered particle pattern (Figure 5, right, top) peaks at around $q \approx 12.5 \mu\text{m}^{-1}$ and for large q converges to 1. Toward smaller q it decays from the peak value down to about $S_{\text{min}} \approx 0.06$ for reasons discussed elsewhere in more detail.^{18,35,41} In Figure 5 (right, top) we also marked the length of the wave vector corresponding to a vacuum wavelength $\lambda_c = 577 \text{ nm}$, which can only be affected (scattered) by structure factor components with $q \leq k(\lambda_c)$. At $q = k(\lambda_c)$, the structure factor $S(q)$ is relatively large; however, for longer wavelengths, the relevant range for scattering is restricted to even smaller q . We, therefore, observe reduced scattering for longer wavelengths due to $S(q)$ being small at small q . Note, that for a periodic grating with the smallest grating vector $|q| = q_c = 2\pi/577 \text{ nm}$, all $S(q < q_c)$ vanish. In contrast to our disordered sample, the periodic disk arrangement from the simulation (Figure 5, left) does not support any propagating modes besides the zeroth order, hence, the lower reflectance starting from 577 nm.

The possible exact rotational symmetries as initially required for helicity preservation in an ordered system (see the first section of this paper) are lost in a disordered system, hereby not meeting one of the conditions for zero reflection. Additionally, nonspecular reflections are possible due to the diffuse components allowed by $S(q) \neq 0$, but the theorem for zero reflection²⁹ is only applicable to the specular component. Crucially though, disorder if tailored appropriately can also end up overcoming both obstacles. A subclass of point configurations where

$$S(0 < q \leq Q) = 0 \quad (1)$$

in the range Q around the origin is called stealthy hyperuniform.²⁶ Periodic systems trivially meet this condition, however, also disordered systems can be tailored to do so and are then called disordered stealthy hyperuniform. They do not possess Bragg peaks and are fully isotropic and therefore exhibit effective continuous rotational symmetry.⁴² Then, on the one hand, the diffuse component of the total reflection is completely suppressed and on the other hand, the continuous rotational symmetry $2\pi/n$ with $n \rightarrow \infty$ meets the requirement for zero specular reflection. Note that condition (1) is in many cases a weaker requirement than periodicity.

To discuss the results in Figure 5 (left) in light of this knowledge, we also calculated the optical response of the disordered structure upon plane-wave illumination at normal incidence with right-hand circular polarization, that is, negative helicity. These calculations were performed using the finite-difference time-domain (FDTD) method (see Methods). The backscattered light (reflectance) was decomposed into positive and negative helicity components, P_+ and P_- (Figure 5, right, bottom), similar to the decomposition for periodic structures in ref 28. At wavelengths shorter than 577 nm, which corresponds to the square lattice constant, the periodic system scatters in multiple diffraction orders, which greatly contribute to the mixed helicity of the reflected light (see ref 28). For the disordered system, a continuum of scattering channels is open with the same effect, that is, P_+ and P_- contribute to the reflectance (Figure 5, right, bottom). However, the differences in reflectance between periodic and disordered systems are more pronounced in the wavelength region between $\lambda_0 = 577 \text{ nm}$ and $\lambda_0 = 1000 \text{ nm}$. For the periodic system, only the zeroth diffraction order is present, and all reflected light is of flipped helicity (P_+ , see ref 28). It follows that the backscattered power will decrease as the degree of helicity preservation of the system increases. In contrast, $S(q)$ of the disordered system is still considerably higher than 0 (e.g., $S(q = 2\pi/(800 \text{ nm})) \approx 0.48$), and the main contribution to reflectance is again the diffuse part, thereby allowing reflected light of the same helicity as the incident light. Nevertheless, the bottom right panel of Figure 5 shows that the reflectance is mostly dominated by the component of flipped helicity. The differences between the disordered system and the periodic system diminish as the relative contribution of the specular part to the backscattered light increases (in particular, from $\lambda_0 = 1000 \text{ nm}$ on). For such longer wavelengths, $S(q)$ is decaying (e.g., $S(q = 2\pi/(1200 \text{ nm})) \approx 0.18$), and we enter the regime where the disordered system is sufficiently stealthy. The reflection losses at $\lambda_0 = 1200 \text{ nm}$ are similar to the losses at 800 nm. But in the $\lambda_0 = 1200 \text{ nm}$ region, the reflection losses are almost exclusively due to the specular part of the reflectance with flipped helicity (P_+), and the reflected power corresponding to the scattered field of the same helicity as the incident field (P_-) approaches zero, resembling the helicity decomposition of the periodic system.²⁸ It is in this long wavelength region that the reflection loss for our disordered system has a one-to-one relation to the changed helicity component. We suspect that reducing $S(q)$ also for larger q would extend such a one-to-one relation toward lower wavelength regions. Additionally, the results indicate that, even in the diffusive region of the spectrum, improved helicity preservation of the system would result in reduced reflectance, although not in a one-to-one relation. Note that the effect of the decaying $S(q)$ is complemented by a decreasing scattering cross-section of the individual disk with increasing wavelength.

The delicate interplay between $S(q)$ and individual scattering response is analyzed in depth in ref 18.

Given the other device characteristics remain largely intact after disk fabrication, the short circuit current is the single most relevant parameter to assess the performance of the coating. Assuming the internal quantum efficiency of the disk coated sample also remains unchanged compared to an untreated cell with $\text{IQE}_{\text{ref}}(\lambda_0)$ (see Figure 4), we can estimate the short circuit current density of a solar cell

$$J_{\text{SC}} = e \int_{300\text{nm}}^{1200\text{nm}} \phi_{\text{AML.SG}}(\lambda_0) \text{IQE}_{\text{ref}}(\lambda_0) (1 - R(\lambda_0)) d\lambda_0 \quad (2)$$

where $\phi_{\text{AML.SG}}(\lambda_0)$ denotes the incident photon flux and e is the elementary charge. Table 2 shows calculated J_{SC} values from reflectance curves of the Born approximation and the periodic simulation.

Table 2. Calculated Current Densities and Current Losses for the Disordered Sample (from Reflectance Calculation via Born Approximation) and Periodic Sample (Rigorous Simulation of Reflectance)

	current density (mA/cm ²)		current loss (mA/cm ²) $\lambda_0 > 577$ nm	
	total	$\lambda_0 > 577$ nm	specular	diffuse
Born approximation	33.44	25.15	-0.23	-2.01
periodic simulation	35.42	27.26	-0.30	0
ΔJ_{SC}	-1.98	-2.11	0.07	-2.01

As expected, the current density is lower for the disordered sample (Born approximation) due to the higher reflectance. Considering only the current contribution from wavelengths $\lambda_0 > 577$ nm, we can infer that the difference in total current is accounted for by differences in reflectance in this range. However, the current loss due to specular reflectance beyond 577 nm is comparably low for both cases, while the loss due to diffusive reflectance at the disordered sample is about -2.01 mA/cm². Therefore, the difference in performance of both antireflective structures is primarily a consequence of the nonzero structure factor components in the low q range.

The simulated periodic system has been optimized with the prerequisite of a square grating, albeit the optimal parameters may not be the same for the disordered arrays of disks. As shown above, the share of absorbed incident photons ($1 - R$) is directly related to the short circuit current density J_{SC} which is therefore the single most relevant device parameter in judging the antireflective coating. For the reflectance R we use the calculated curves such as shown in Figure 5. Instead of using structure factors $S(q)$ from fabricated samples, however, we predicted a series of particle patterns within the bounds of the deposition technique (see ref 35) and forecast the response of those patterns.

Figure 6 shows the calculated J_{SC} of a series of such predicted patterns with varying disk density. The highest current is achieved at a disk density of about $3.0 \mu\text{m}^{-2}$. This is the density previously discussed in depth. A series of experiments with varying disk density is also shown in Figure 6 along with the measured current density for a standard flat ARC. The measured data essentially confirms the trends as well as the optimum of the prediction. The highest measured current densities are slightly lower than calculated, however,

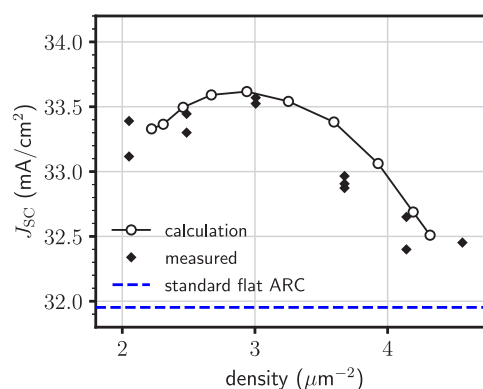


Figure 6. Short circuit current density versus disk density for simulated correlated disorder disk patterns (open circles, solid line is a guide to the eyes) and measured short circuit current densities (black squares). Additionally, the median current density of a series of samples with standard flat antireflective coating (80 nm ITO) is shown (blue dashed line).

given the differences between measured and calculated reflectance (Figure 3), some deviations were to be expected. Also, there is some degree of uncertainty in predicting the particle patterns from which reflectances are calculated.³⁵ Namely, the deposition model does not include any aggregation of particles which tends to increase the values of $S(q)$ for small q , as discussed in ref 18 in more detail. Therefore, we expect higher diffuse scattering contributions at wavelengths $\lambda_0 > 600$ nm and consequently higher current losses in the measurement compared to the predicted pattern, as discussed above.

Notably, for all considered disk densities the current is higher for both calculation and measurement compared to the standard flat ARC reference, which corresponds to the measured reflectance in Figure 3. The highest measured difference of about 1.6 mA/cm^2 ($+5.1\%_{\text{rel}}$) is found at $3.0 \mu\text{m}^{-2}$. Considering the change in current for the samples before and after disk deposition, the increase is even more decisive with 4.1 mA/cm^2 ($+14.0\%_{\text{rel}}$). Another benchmark would be a double ARC stack, consisting of a MgF_2 layer on top of the ITO layer (each with optimized thickness), for which we estimate a current density increase of 1.5 mA/cm^2 ($+4.7\%_{\text{rel}}$) compared to the standard flat ARC^{43,44} (see SI, Figure S7 for reflectance and details). However, the effect of encapsulation of the solar cell in a module tends to annihilate the advantage of the double ARC, while this is not the case for an optimized disk structure.³⁴ Additionally, the total current density for the periodic simulation in Table 2 and the corresponding discussion suggest that even higher current is possible to reach with the disk structure by further reducing the structure factor for small q .

CONCLUSION

We have demonstrated the successful implementation of a TiO_2 dielectric disk-based disordered AR coating in solar cells of standard industrial design by using a scalable bottom-up technique.¹⁸ Robustness of this deposition technique with respect to the surface morphology allows to avoid special preparation of the substrate, which, in addition to scalability, makes it an attractive technique to fabricate disordered particle coatings. Our measurements show significant reflection suppression in the spectral range relevant for solar cells, and

we observe 5.1%_{rel} improvement of the short-circuit current in comparison to a standard (optimized for AM1.5G irradiance) flat ARC reference device.

Additionally, we corroborate our experimental results with a theoretical model based on Born's first approximation which takes into account the disordered nature of the disk coating. Our results show that most of the reflected light is of changed helicity with respect to the helicity of the incident light. As the stealthiness of the disk coating increases ($S(q)$ decreases) with increasing wavelength, the reflectance becomes equal to the power of the changed helicity component. These findings support the purposeful design of the coatings based on dielectric high-index nanoparticles targeting helicity preservation, even though the existence of nonspecular components reduces the effectiveness as compared to a periodic system in the nondiffracting region.²⁸ Moreover, our design is exemplary and is neither restricted to the materials used nor to a particular solar cell stack and can be applied to other systems.

METHODS

Sample Fabrication. The experiment is based on industrial type heterojunction technology (HJT) solar cells fabricated from 150 μm Czochralski silicon (cSi) wafers. Instead of a pyramidal standard texture, a mostly flat surface was achieved by adapting the wet-chemical damage etch process. The HJT solar cells used in the experiment were rear emitter cells that were passivated with amorphous silicon (aSi). The thicknesses of the front passivation (intrinsic aSi and n^+ doped aSi) and ITO layers can be found in ref 28 and similar passivation (intrinsic aSi and p^+ doped) and ITO layers were applied to the rear side. Two alternative types of front ITO layers were used. The reference devices with 80 nm ITO layers were optimized for efficiency under standard conditions. The disk coating was based on 50 nm ITO layers with higher doping levels and carrier concentration to compensate for the loss in conductivity due to the lower thickness. A total of 81 sample with dimensions 39 \times 39 mm^2 were laser-cut from fully processed 156 mm solar cells (including contact fingers) to match the processing capabilities for the subsequent disk fabrication process.

Details of the disk fabrication have been published elsewhere.¹⁸ Briefly, it is based on self-organizing colloidal particles that are deposited onto a functionalized surface and the patterns thereof are subsequently transferred to a TiO_2 layer via RIE. On top of the front ITO layer, TiO_2 layers of 105.5 nm thickness were deposited via ALD at 120 $^\circ\text{C}$ using alternating pulses of titanium tetrachloride (TiCl_4) and water (1800 pulses each) in a Beneq TFS-200 thermal ALD tool. Additionally, a thinner 16.8 nm layer of aluminum oxide (Al_2O_3) was deposited (120 $^\circ\text{C}$, 150 pulses of trimethylaluminum (TMAI) and water, each) as functionalization for the particle deposition process. The samples were exposed to a dispersion of 350 nm diameter poly(methyl methacrylate) (PMMA) particles (microParticles Berlin GmbH, Germany), which formed an evenly distributed arrangement on the surface.³⁵ The particles were tempered briefly (30 min at 135 $^\circ\text{C}$) for improved covering of the surface, such that they could serve as an etch mask for RIE. This process step was likely the reason for the slight increase of disk diameter (370 nm) compared to particle diameter. The etch process was carried out in two steps: First, the Al_2O_3 layer was structured using a Chlorine-containing plasma. Second, the structured Al_2O_3 was used as hard-mask in a fluorine-based process to

selectively etch TiO_2 . The ITO contact beneath is only weakly etched in Fluorine-plasmas and served as an etch-stop layer.

IV Characterization. For each of the laser-separated samples (see Sample Fabrication) the IV characterization was performed under standard test conditions of 1 kW/m^2 mean irradiance and a cell temperature in the range of 25 ± 1 $^\circ\text{C}$ (adjusted via calibration) using a dedicated setup for bus barless cells⁴⁵ in order to compare them (see Table 1) with the focus on I_{SC} , which is influenced by the coating. The coated cells were characterized within one month after separation from full-sized cells, however, the smaller than usual samples led to unstable voltage readings due to a mechanical problem with the voltage probe wire, while not affecting the current measurement. For those samples discussed in terms of voltage, we repeated the IV characterization within four months after separation. The current was scaled in order to account for handling of the samples and differences in the calibration, as well as the possible degradation of the samples in the time span between the measurements. The scaling factor a is the ratio of short circuit currents $I_{\text{SC},i}$:

$$a = \frac{I_{\text{SC},1\text{m}}}{I_{\text{SC},4\text{m}}} \quad (3)$$

where indices $i = 1\text{m}$ and $i = 4\text{m}$ denote the delays between separation and measurement. The corrected currents presented in Figure 4 and in Table 1 were then obtained by dividing the measured values with a , which corresponds to an average change (reduction) in the short-circuit current $\Delta_{\text{rel}}I_{\text{SC}} = 1 - a = 0.64\%$ within three months between the measurements, which is slightly above the estimated uncertainty for the current.

Reflectance and Quantum Efficiencies. Reflectance was measured using a PerkinElmer Lambda 750 UV/vis/NIR spectrophotometer. QE measurements were performed using PV Measurements, Inc. Solar Cell Spectral Response/QE/IPCE Measurement System, Model QEX7 with black back sheet as a background. In order to account for signal instabilities during the QE measurement, we scaled the raw data with respect to J_{SC} , obtained from the IV characteristic. This was carried out by calculating the short circuit current from the QE data, $J_{\text{SC,QE}}$, and subsequently calculating the scaling factor $b = J_{\text{SC,QE}}/J_{\text{SC}}$ where J_{SC} is the value taken from Table 1:

$$J_{\text{SC,QE}} = e \int_{300\text{nm}}^{1200\text{nm}} \phi_{\text{AM1.5G}}(\lambda_0) \cdot \text{QE}(\lambda_0) d\lambda_0 \quad (4)$$

where e is the elementary charge and $\phi_{\text{AM1.5G}}$ is the incident photon flux. The scaled external (QE_s) and internal (IQE_s) quantum efficiencies were then calculated using the following equations:

$$\text{QE}_s = \text{QE}/b \quad (5)$$

$$\text{IQE}_s = \frac{\text{QE}_s}{1 - R} \quad (6)$$

where R is the measured reflectance.

Numerical Methods and Material Information. The numerical simulations discussed in this paper were done using the finite element method (FEM) with commercial software JCMSuite.⁴⁶ Refractive indices for cSi and ITO used in calculations were taken from literature.^{47,48} Refractive index data for aSi, TiO_2 , and Al_2O_3 were obtained by means of

ellipsometry, and corresponding n and k values are provided in the SI.⁴⁹

Additional simulations of a $3 \times 3 \mu\text{m}^2$ unit cell containing 27 disks under periodic boundary conditions were performed using the FDTD method (free software Meep⁵⁰). The disks were arranged to match the experimentally determined structure factor⁵¹ (see SI for details).

Calculation of Reflectance. The disks are arranged in a two-dimensional pattern in a plane perpendicular to the incident field propagating in z -direction. Coupling between disks is therefore considerably lower than in three-dimensional pattern of similar scatterer density, and we consider the individual disks only to be excited by the incident field $\mathbf{E}_{\text{in}} = \mathbf{E}_0 e^{i(k_0 z - \omega t)}$ and employ the first Born approximation⁵² to calculate the scattering response of our disk layer.¹⁸ In the far field, the scattered electric field of an individual scatterer has the form of a spherical wave⁵³

$$\mathbf{E}_s(\mathbf{r}) = E_0 \frac{e^{ikr}}{r} \mathbf{f} \quad (7)$$

where the time dependence $e^{-i\omega t}$ has been omitted. The form factor $\mathbf{f} = \mathbf{f}(\hat{\mathbf{E}}_0, \mathbf{k}_0, \mathbf{k})$ describes the normalized field amplitude for an incident field with polarization $\hat{\mathbf{E}}_0 = \mathbf{E}_0/|\mathbf{E}_0|$, where \mathbf{k}_0 and \mathbf{k} denote the incoming and scattered wave vectors, respectively. In this work, we obtain \mathbf{f} via finite element simulation, using a model with identical parameters to those of the periodic simulation, except for neglecting absorption by the disks for numerical reasons (see below).

Considering now only the scattering components perpendicular to the disk plane in forward direction with $\mathbf{k}^+ = n_{\text{Si}} k_0 \mathbf{e}_z$ (silicon half-space) and backward direction $\mathbf{k}^- = -k_0 \mathbf{e}_z$ (air half-space) of an individual disk illuminated with a linearly polarized plane wave with $k_0 \mathbf{e}_z$, we can use the angular spectrum (eq 7) in its asymptotic limit to calculate specular transmission and reflection⁵⁴

$$T_{\text{spec}} = n_{\text{Si}} \left| t \hat{\mathbf{E}}_0 + \rho \frac{2\pi}{i|\mathbf{k}^+|} \mathbf{f}(\mathbf{k} = \mathbf{k}^+) \right|^2 \quad (8)$$

$$R_{\text{spec}} = \left| r \hat{\mathbf{E}}_0 + \rho \frac{2\pi}{i|\mathbf{k}^-|} \mathbf{f}(\mathbf{k} = \mathbf{k}^-) \right|^2 \quad (9)$$

where t and r denote the Fresnel transmission and reflection coefficients of the planar layer stack and ρ is the density of the disks. Since the interaction between the disks is neglected, T and R do not depend on the particular arrangement of disks, but only on the density ρ . All scattered fields of the individual disks in normal direction are in phase and interfere with $t \hat{\mathbf{E}}_0$ and $r \hat{\mathbf{E}}_0$ of the planar stack if polarizations match. If absorption within the scattering structure is neglected, energy conservation demands that

$$1 - T_{\text{spec}} - R_{\text{spec}} = T_{\text{diff}} + R_{\text{diff}} = P_{\text{diff}} \quad (10)$$

with T_{diff} and R_{diff} denoting diffusive contributions to transmission and reflection, and P_{diff} is the normalized scattered power excluding specular components. On the other hand, the scattered power must be equivalent to the integral of the angular resolved scattering (ARS) over the unit sphere Ω (excluding $d\Omega = d\Omega(\mathbf{k} = \mathbf{k}^\pm)$), with $P_{\text{diff}} = \int_{\Omega} \text{ARS} d\Omega$. The ARS now is obtained by modulating the individual

scattering response $|\mathbf{f}|^2$ with the structure factor $S(q = k_{\parallel})$, where k_{\parallel} is the projection of the scattered wave vector \mathbf{k} to the disk pattern plane and needs to be scaled in order to satisfy eq 10:

$$\text{ARS} = \frac{P_{\text{diff}}}{\int_{\Omega} |\mathbf{f}|^2 S d\Omega} \cdot |\mathbf{f}(\mathbf{k})|^2 S(k_{\parallel}) \quad \mathbf{k} \neq \mathbf{k}^\pm \quad (11)$$

The diffusive part of the reflectance is obtained by integrating over the half-sphere Ω' in air,

$$R_{\text{diff}} = \int_{\Omega'} \text{ARS} d\Omega \quad \mathbf{k} \neq \mathbf{k}^- \quad (12)$$

For the periodic case, reflectance was calculated from the ratio of the power scattered into the upper half-space to the power of the incident field as

$$R_{\text{periodic}} = \frac{\sum_{\mathbf{k}_r} |\tilde{\mathbf{E}}(k_{r,x}, k_{r,y})|^2 \cdot \cos(\theta_r)}{|\mathbf{E}_0|^2} \quad (13)$$

where \mathbf{k}_r are the wave vectors of the reflected electromagnetic waves, θ_r are the angles between these wave vectors and the z -axis, \mathbf{E}_0 is the amplitude of a normally incident and linearly polarized plane wave, and the angular spectrum of the scattered field $\tilde{\mathbf{E}}(k_{r,x}, k_{r,y})$ is determined via Fourier transform of the field in real space obtained from full-wave simulations.

■ ASSOCIATED CONTENT

Supporting Information

The Supporting Information is available free of charge at <https://pubs.acs.org/doi/10.1021/acsp Photonics.1c00601>.

Disks deposited on a textured surface as demonstration of robustness of the fabrication technique; Optical material data used for simulations; Quantum efficiencies for various disk densities and a reference device; Short circuit current density before/after comparison of disk-coated cells; Comparison of double ARC with standard flat ARC; Reciprocal space optimized sample for FDTD simulations; Results of the FDTD simulation for disks with increased height (PDF)

■ AUTHOR INFORMATION

Corresponding Authors

Peter M. Piechulla – Institute of Physics, Martin Luther University Halle-Wittenberg, 06120 Halle, Germany; orcid.org/0000-0002-9495-1709;

Email: peter.piechulla@physik.uni-halle.de

Evgeniia Slivina – Institute of Theoretical Solid State Physics, Karlsruhe Institute of Technology, 76131 Karlsruhe, Germany; orcid.org/0000-0003-4645-1491;

Email: evgeniia.slivina@kit.edu

Authors

Derk Bätzner – Meyer Burger Research AG, Hauterive 2068, Switzerland

Ivan Fernandez-Corbaton – Institute of Nanotechnology, Karlsruhe Institute of Technology, 76344 Eggenstein-Leopoldshafen, Germany; orcid.org/0000-0003-2834-5572

Prerak Dhawan – Institute of Theoretical Solid State Physics, Karlsruhe Institute of Technology, 76131 Karlsruhe, Germany

Ralf B. Wehrspohn – Institute of Physics, Martin Luther University Halle-Wittenberg, 06120 Halle, Germany
Alexander N. Sprafke – Institute of Physics, Martin Luther University Halle-Wittenberg, 06120 Halle, Germany
Carsten Rockstuhl – Institute of Theoretical Solid State Physics, Karlsruhe Institute of Technology, 76131 Karlsruhe, Germany; Institute of Nanotechnology, Karlsruhe Institute of Technology, 76344 Eggenstein-Leopoldshafen, Germany

Complete contact information is available at:
<https://pubs.acs.org/10.1021/acsp Photonics.1c00601>

Author Contributions

*These authors contributed equally to this work.

Notes

The authors declare no competing financial interest.

ACKNOWLEDGMENTS

This work was funded by the Deutsche Forschungsgemeinschaft (DFG) through Program DFG-SPP 1839 “Tailored Disorder”, second period (RO 3640/6-2 and WE4051/19-2, Project 278744673), under the Germany’s Excellence Strategy via the Excellence Cluster 3D Matter Made to Order (No. EXC-2082/1–390761711), and the KIT through the “Virtual Materials Design” (VIRTMAT) Project. The authors are grateful to the company JCMwave for their free provision of the FEM Maxwell solver JCMsuite.

REFERENCES

- (1) Shockley, W.; Queisser, H. J. Detailed balance limit of efficiency of p–n junction solar cells. *J. Appl. Phys.* **1961**, *32*, 510.
- (2) Ehrler, B.; Hutter, E. M.; Berry, J. J. The Complicated Morality of Named Inventions. *ACS Energy Lett.* **2021**, *6*, 565–567.
- (3) Rong, Y.; Hu, Y.; Mei, A.; Tan, H.; Saidaminov, M. I.; Seok, S. I.; McGehee, M. D.; Sargent, E. H.; Han, H. Challenges for Commercializing Perovskite Solar Cells. *Science* **2018**, *361*, No. eaat8235.
- (4) Galagan, Y. Perovskite Solar Cells: Toward Industrial-Scale Methods. *J. Phys. Chem. Lett.* **2018**, *9*, 4326–4335.
- (5) Chen, D.; Manley, P. Nanophotonic Light Management for Perovskite–Silicon Tandem Solar Cells. *J. Photonics Energy* **2018**, *8*, 022601.
- (6) Hou, Y.; et al. Efficient Tandem Solar Cells with Solution-Processed Perovskite on Textured Crystalline Silicon. *Science* **2020**, *367*, 1135–1140.
- (7) Schulze, P. S. C.; Bett, A. J.; Bivour, M.; Caprioglio, P.; Gerspacher, F. M.; Kabakli, Ö. Ş.; Richter, A.; Stolterfoht, M.; Zhang, Q.; Neher, D.; Hermle, M.; Hillebrecht, H.; Glunz, S. W.; Goldschmidt, J. C. 25.1% High-Efficiency Monolithic Perovskite Silicon Tandem Solar Cell with a High Bandgap Perovskite Absorber. *Sol. RRL* **2020**, *4*, 2000152.
- (8) Stavroulakis, P. I.; Boden, S. A.; Johnson, T.; Bagnall, D. M. Suppression of Backscattered Diffraction from Sub-Wavelength ‘Moth-Eye’ Arrays. *Opt. Express* **2013**, *21*, 1–11.
- (9) Florescu, M.; Gkantzounis, G. Hyperuniform Disordered Structures for Enhanced Light Absorption. *Proc. SPIE 10527* **2018**, 105270J.
- (10) Sprafke, A.; Pollard, M.; Piechulla, P.; Bagnall, D.; Hoex, B.; Conibeer, G.; Wehrspohn, R. B. Mie resonators as rearside light trapping structures in planar crystalline silicon solar cells. *Light, Energy and the Environment 2018 (E2, FTS, HISE, SOLAR, SSL)*; OSA, 2018; paper OT3C.5, DOI: 10.1364/OSE.2018.OT3C.5.
- (11) Yamanchili, S.; Verlage, E.; Cheng, W.-H.; Fontaine, K. T.; Jahlka, P. R.; Kempler, P. A.; Saive, R.; Lewis, N. S.; Atwater, H. A. High Broadband Light Transmission for Solar Fuels Production Using

Dielectric Optical Waveguides in TiO₂ Nanocone Arrays. *Nano Lett.* **2020**, *20*, 502–508.

(12) Garnett, E. C.; Ehrler, B.; Polman, A.; Alarcon-Llado, E. Photonics for Photovoltaics: Advances and Opportunities. *ACS Photonics* **2021**, *8*, 61–70.

(13) Donie, Y. J.; Smeets, M.; Egel, A.; Lentz, F.; Preinfalk, J. B.; Mertens, A.; Smirnov, V.; Lemmer, U.; Bittkau, K.; Gomard, G. Light Trapping in Thin Film Silicon Solar Cells via Phase Separated Disordered Nanopillars. *Nanoscale* **2018**, *10*, 6651–6659.

(14) Spinelli, P.; Polman, A. Light Trapping in Thin Crystalline Si Solar Cells Using Surface Mie Scatterers. *IEEE J. Photovoltaics* **2014**, *4*, 554–559.

(15) Staude, I.; Miroshnichenko, A. E.; Decker, M.; Fofang, N. T.; Liu, S.; Gonzales, E.; Dominguez, J.; Luk, T. S.; Neshev, D. N.; Brener, I.; Kivshar, Y. Tailoring Directional Scattering through Magnetic and Electric Resonances in Subwavelength Silicon Nanodisks. *ACS Nano* **2013**, *7*, 7824–7832.

(16) van de Groep, J.; Polman, A. Designing Dielectric Resonators on Substrates: Combining Magnetic and Electric Resonances. *Opt. Express* **2013**, *21*, 26285–26302.

(17) Rahimzadegan, A.; Arslan, D.; Suryadharma, R. N. S.; Fasold, S.; Falkner, M.; Pertsch, T.; Staude, I.; Rockstuhl, C. Disorder-Induced Phase Transitions in the Transmission of Dielectric Metasurfaces. *Phys. Rev. Lett.* **2019**, *122*, 015702.

(18) Piechulla, P. M.; Fuhrmann, B.; Slivina, E.; Rockstuhl, C.; Wehrspohn, R. B.; Sprafke, A. N. Tailored Light Scattering through Hyperuniform Disorder in Self-Organized Arrays of High-Index Nanodisks. *Adv. Opt. Mater.* **2021**, *9*, 2100186.

(19) Spinelli, P.; Verschuuren, M. A.; Polman, A. Broadband Omnidirectional Antireflection Coating Based on Subwavelength Surface Mie Resonators. *Nat. Commun.* **2012**, *3*, 692.

(20) Spinelli, P.; Lenzenmann, F.; Weeber, A.; Polman, A. Effect of EVA Encapsulation on Antireflection Properties of Mie Nanoscatterers for C-Si Solar Cells. *IEEE J. Photovoltaics* **2015**, *5*, 559–564.

(21) Stevens, L.; Tucher, N.; Höhn, O.; Hauser, H.; Müller, C.; Bläsi, B. Broadband Antireflection Mie Scatterers Revisited—A Solar Cell and Module Analysis. *Opt. Express* **2019**, *27*, A524–A535.

(22) Oskooi, A.; Favuzzi, P. A.; Tanaka, Y.; Shigetani, H.; Kawakami, Y.; Noda, S. Partially disordered photonic-crystal thin films for enhanced and robust photovoltaics. *Appl. Phys. Lett.* **2012**, *100*, 181110.

(23) van Lare, M.-C.; Polman, A. Optimized Scattering Power Spectral Density of Photovoltaic Light-Trapping Patterns. *ACS Photonics* **2015**, *2*, 822–831.

(24) Pratesi, F.; Buresi, M.; Riboli, F.; Vynck, K.; Wiersma, D. S. Disordered Photonic Structures for Light Harvesting in Solar Cells. *Opt. Express* **2013**, *21*, A460–A468.

(25) Tavakoli, N.; Spalding, R. J.; Gkantzounis, G.; Wan, C.; Röhrich, R.; Kontoleta, E.; Florescu, M.; Sapienza, R.; Koenderink, F.; Lladó, E. A. Hyperuniform Designs for Enhanced Light Trapping in Ultrathin Single and Tandem Solar Cells (Conference Presentation). *Photonics for Solar Energy Systems VIII*; SPIE, 2020; p 113660A, DOI: 10.1117/12.2554441.

(26) Torquato, S. Hyperuniform States of Matter. *Phys. Rep.* **2018**, *745*, 1–95.

(27) Klatt, M. A.; Lovrić, J.; Chen, D.; Kapfer, S. C.; Schaller, F. M.; Schönhöfer, P. W. A.; Gardiner, B. S.; Smith, A.-S.; Schröder-Turk, G. E.; Torquato, S. Universal Hidden Order in Amorphous Cellular Geometries. *Nat. Commun.* **2019**, *10*, 811.

(28) Slivina, E.; Abass, A.; Bätzner, D.; Strahm, B.; Rockstuhl, C.; Fernandez-Corbaton, I. Insights into Backscattering Suppression in Solar Cells from the Helicity-Preservation Point of View. *Phys. Rev. Appl.* **2019**, *12*, 054003.

(29) Fernandez-Corbaton, I. Forward and Backward Helicity Scattering Coefficients for Systems with Discrete Rotational Symmetry. *Opt. Express* **2013**, *21*, 29885–29893.

(30) Fernandez-Corbaton, I.; Zambrana-Puyalto, X.; Tischler, N.; Vidal, X.; Juan, M. L.; Molina-Terriza, G. Electromagnetic Duality

Symmetry and Helicity Conservation for the Macroscopic Maxwell's Equations. *Phys. Rev. Lett.* **2013**, *111*, 060401.

(31) Bottein, T.; Wood, T.; David, T.; Claude, J. B.; Favre, L.; Berbézier, I.; Ronda, A.; Abbarchi, M.; Grosso, D. Black[®] Titania Coatings Composed of Sol–Gel Imprinted Mie Resonators Arrays. *Adv. Funct. Mater.* **2017**, *27*, 1604924.

(32) Verschuuren, M. A.; Megens, M.; Ni, Y.; van Sprang, H.; Polman, A. Large Area Nanoimprint by Substrate Conformal Imprint Lithography (SCIL). *Adv. Opt. Technol.* **2017**, *6*, 243–264.

(33) Visser, D.; Chen, D. Y.; Désières, Y.; Ravishankar, A. P.; Anand, S. Embossed Mie Resonator Arrays Composed of Compacted TiO₂ Nanoparticles for Broadband Anti-Reflection in Solar Cells. *Sci. Rep.* **2020**, *10*, 12527.

(34) Slivina, E.; Bätzner, D.; Schmagel, R.; Langenhorst, M.; Lehr, J.; Paetzold, U. W.; Lemmer, U.; Rockstuhl, C. The Annual Energy Yield of Mono- and Bifacial Silicon Heterojunction Solar Modules with High-Index Dielectric Nanodisk Arrays as Anti-Reflective and Light Trapping Structures. *Opt. Express* **2021**, *29*, 34494–34509.

(35) Piechulla, P. M.; Muehlenbein, L.; Wehrspohn, R. B.; Nanz, S.; Abass, A.; Rockstuhl, C.; Sprafke, A. Fabrication of Nearly-Hyperuniform Substrates by Tailored Disorder for Photonic Applications. *Adv. Opt. Mater.* **2018**, *6*, 1701272.

(36) Battiston, G. A.; Gerbasi, R.; Gregori, A.; Porchia, M.; Cattarin, S.; Rizzi, G. A. PECVD of Amorphous TiO₂ Thin Films: Effect of Growth Temperature and Plasma Gas Composition. *Thin Solid Films* **2000**, *371*, 126–131.

(37) Lee, W. G.; Woo, S. I.; Kim, J. C.; Choi, S. H.; Oh, K. H. Preparation and Properties of Amorphous TiO₂ Thin Films by Plasma Enhanced Chemical Vapor Deposition. *Thin Solid Films* **1994**, *237*, 105–111.

(38) Volk, A.-K.; Tucher, N.; Seiffe, J.; Hauser, H.; Zimmer, M.; Blasi, B.; Hofmann, M.; Rentsch, J. Honeycomb Structure on Multi-Crystalline Silicon Al-BSF Solar Cell With 17.8% Efficiency. *IEEE J. Photovoltaics* **2015**, *5*, 1027–1033.

(39) Piechulla, P.; Seiffe, J.; Hofmann, M.; Rentsch, J.; Preu, R. Increased Ion Energies for Texturing in a High-Throughput Plasma Tool. *Proc. of 26th European Photovoltaic Solar Energy Conference and Exhibition, EUPVSEC*, 2011; DOI: 10.4229/26thEUPVSEC2011-2CV.2.16.

(40) Gueymard, C. A.; Myers, D.; Emery, K. Proposed Reference Irradiance Spectra for Solar Energy Systems Testing. *Sol. Energy* **2002**, *73*, 443–467.

(41) Torquato, S.; Uche, O. U.; Stillinger, F. H. Random Sequential Addition of Hard Spheres in High Euclidean Dimensions. *Phys. Rev. E* **2006**, *74*, 061308.

(42) Yu, S.; Qiu, C.-W.; Chong, Y.; Torquato, S.; Park, N. Engineered Disorder in Photonics. *Nat. Rev. Mater.* **2021**, *6*, 226–243.

(43) Meiners, B.-M.; Holinski, S.; Schäfer, P.; Hohage, S.; Borchert, D. Investigation of anti-reflection-coating stacks for silicon heterojunction solar cells. *Proc. of 29th European Photovoltaic Solar Energy Conference and Exhibition, EUPVSEC*, 2014; pp 1020–1023, DOI: 10.4229/EUPVSEC20142014-2AV.3.22.

(44) McIntosh, K. R.; Baker-Finch, S. C. OPAL 2: Rapid Optical Simulation of Silicon Solar Cells. *2012 38th IEEE Photovoltaic Specialists Conference*, Austin, TX, U.S.A., June 3–8, 2012, IEEE, 2012; pp 000265–000271, DOI: 10.1109/PVSC.2012.6317616.

(45) Bassi, N.; Clerc, C.; Pelet, Y.; Hiller, J.; Fakhfour, V.; Droz, C.; Despeisse, M.; Levrat, J.; Faes, A.; Bätzner, D. GridTouch: Innovative Solution for Accurate IV Measurement of Busbarless Cells in Production and Laboratory Environments. *Proc. of 29th European Photovoltaic Solar Energy Conference and Exhibition, EUPVSEC*, 2014; p 1180, DOI: 10.4229/EUPVSEC20142014-2BV.8.24.

(46) Pomplun, J.; Burger, S.; Zschiedrich, L.; Schmidt, F. Adaptive Finite Element Method for Simulation of Optical Nano Structures. *Phys. Status Solidi B* **2007**, *244*, 3419–3434.

(47) Schinke, C.; Christian Peest, P.; Schmidt, J.; Brendel, R.; Bothe, K.; Vogt, M. R.; Kröger, I.; Winter, S.; Schirmacher, A.; Lim, S.; Nguyen, H. T.; MacDonald, D. Uncertainty analysis for the coefficient

of band-to-band absorption of crystalline silicon. *AIP Adv.* **2015**, *5*, 067168.

(48) Holman, Z. C.; Filipič, M.; Descoeur, A.; De Wolf, S.; Smole, F.; Topič, M.; Ballif, C. Infrared Light Management in High-Efficiency Silicon Heterojunction and Rear-Passivated Solar Cells. *J. Appl. Phys.* **2013**, *113*, 013107.

(49) Jellison, G. E.; Modine, F. A. Parameterization of the Optical Functions of Amorphous Materials in the Interband Region. *Appl. Phys. Lett.* **1996**, *69*, 371–373.

(50) Oskooi, A. F.; Roundy, D.; Ibanescu, M.; Bermel, P.; Joannopoulos, J. D.; Johnson, S. G. Meep: A flexible free-software package for electromagnetic simulations by the FDTD method. *Comput. Phys. Commun.* **2010**, *181*, 687–702.

(51) Uche, O. U.; Stillinger, F. H.; Torquato, S. Constraints on Collective Density Variables: Two Dimensions. *Phys. Rev. E* **2004**, *70*, 046122.

(52) Born, M.; Wolf, E.; Bhatia, A. B.; Clemmow, P. C.; Gabor, D.; Stokes, A. R.; Taylor, A. M.; Wayman, P. A.; Wilcock, W. L. *Principles of Optics: Electromagnetic Theory of Propagation, Interference and Diffraction of Light*, 7th ed.; Cambridge University Press, 1999.

(53) Keller, J. Stochastic Equations and Wave Propagation in Random Media. *Proc. Symp. Appl. Math.* **1964**, *16*, 145–170.

(54) Mandel, L.; Wolf, E. *Optical Coherence and Quantum Optics*; Cambridge University Press: Cambridge, U.S.A., 1995.

Danksagung

Die (fast) letzte Seite meiner Habilitationsschrift möchte ich nutzen, um Danke zu sagen. Die Einsichten dieser Arbeit sind keine Sololeistung, sondern das Ergebnis eines gemeinschaftlichen Engagements und der Unterstützung durch Beiträge meiner geschätzten Kollegen.

Ein besonderer Dank geht an Prof. Ralf B. Wehrspohn. Durch die langjährige Zusammenarbeit habe ich nicht nur bedeutende fachliche Unterstützung erfahren, sondern auch wertvolle Einblicke in die Forschungslandschaft Deutschlands erhalten. Sein Vertrauen in meine Fähigkeiten und die mir gebotenen Möglichkeiten haben maßgeblich zum Gelingen meiner Habilitation beigetragen.

Ein riesiger Dank geht an die vielen Nachwuchswissenschaftlerinnen und Nachwuchswissenschaftler, an deren Ausbildung ich mitwirken durfte: Dr. Peter Piechulla war in den Untersuchungen zur hyperuniformen Unordnung von Beginn an zentraler Diskussionspartner. Unsere tollen Ergebnisse auf diesem Gebiet beruhen auf seiner Exzellenz im Labor und seiner wissenschaftlichen Sorgfalt. Für diese unerlässliche Zusammenarbeit bin ich ihm tief dankbar. Im weiteren danke ich Dr. Maria Gaudig, Dr. Martin Otto, Dr. Johannes Ziegler, Dr. Xiaopeng Li, Dr. Daniela Schneevoigt, Dr. Thomas Schneider und Dr. Markus Muchow. Ihre Forschungsbeiträge durch harte Laborarbeit und wissenschaftliche Expertise im Bereich der periodischen Strukturen und des schwarzen Siliziums waren von entscheidender Bedeutung. An dieser Stelle danke ich auch allen Studierenden, die ich in ihrer Master- und Bachelorarbeit betreuen durfte.

Meinem langjährigen Bürokollegen, Dr. Stefan Schweizer danke ich herzlich für die Unterstützung im Universitätsalltag und die unzähligen bereichernden Diskussionen über Physik sowie ~~Gott~~ und die Welt. Ein ebenso herzlicher Dank geht an Claudia Stehr, der guten Seele der Gruppe μ MD. Ein großes Dankeschön geht an Prof. Jörg Schilling für die fruchtbaren Diskussionen und die wertvolle Zusammenarbeit mit seiner Gruppe sowie die Gelegenheit, an seiner Seite die Lehre in der Physik an der MLU mitzugestalten. Im weiteren danke ich Richard Schalinski, Dr. Juliana Martins de Souza e Silva, Dr. Haojie Zhang, Dr. Paul Miclea, Dr. Bodo Fuhrmann, Dr. Benni Gesemann, Murilo Santos und Simone Stahn.

Ich danke auch meinen externen Kollaborationspartnern, allen voran Prof. Carsten Rockstuhl vom KIT. Die Zusammenarbeit mit ihm und seinen Mitarbeitern Dr. Aimi Abass, Dr. Evgeniia Slivina und Dr. Prerak Dhawan, war besonders fruchtbar.

Dankbar bin ich auch meinen Freunden und meiner Familie. Danke für Eure Unterstützung. Und Euer Aushalten. Oder einfach dafür, dass Ihr mir mein regelmäßiges Abtauchen abseht.

Lebenslauf

Persönliche Daten

Dr. rer. nat. Alexander Nicolas Sprafke
Geboren am 18.10.1979 in Oberhausen

Dienstlich

Fachgruppe Mikrostrukturbasiertes Materialdesign μ MD
Institut für Physik, Martin-Luther-Universität Halle-Wittenberg
Heinrich-Damerow-Straße 4, 06120 Halle (Saale)
+49 345 5528470, alexander.sprafke@physik.uni-halle.de

Privat

Puschkinstraße 16, 06108 Halle (Saale)
+49 179 7819252, alexsprafke@gmail.com

Wissenschaftlicher Werdegang

aktuelle Position

Gruppenleiter Photonenmanagement
Institut für Physik, Martin-Luther-Universität Halle-Wittenberg

1/2020 - 3/2021

Vertretungsprofessur Mikrostrukturbasiertes Materialdesign μ MD
Institut für Physik, Martin-Luther-Universität Halle-Wittenberg

10/2017 - 12/2019

Gruppenleiter Photonenmanagement in Solarzellen
Institut für Physik, Martin-Luther-Universität Halle-Wittenberg

9/2016 - 9/2017

Visiting Research Fellow (DFG Forschungsstipendium)
School for Photovoltaic and Renewable Energy Engineering
Universität von New South Wales, Sydney (Australien)

3/2012 - 8/2016

Gruppenleiter Photonenmanagement in Solarzellen
Institut für Physik, Martin-Luther-Universität Halle-Wittenberg

1/2006 - 12/2011

Wissenschaftlicher Mitarbeiter (Promotion zum Dr. rer. nat.)
Fachgruppe Nanostruktur-Optik, 1. Physikalisches Institut A, RWTH Aachen.
Dissertation: Optische Nahfeld-Wechselwirkungen von Plasmonen mit ihrer Umgebung

10/1999 - 6/2005

Studium der Physik (Abschluss: Dipl.-Phys.), RWTH Aachen
Diplomarbeit: Photochrome Silbernanopartikel eingebettet in Titanoxid

Halle (Saale), den 26. August 2022

Dr. Alexander Sprafke

Eidesstattliche Erklärung

Diese Habilitationsschrift wurde selbstständig und ohne fremde Hilfe verfaßt. Andere als die angegeben Quellen und Hilfsmittel wurden nicht benutzt und die den benutzten Werken wörtlich oder inhaltlich entnommenen Stellen wurden als solche kenntlich gemacht.

Halle (Saale), den 26. August 2022

Dr. Alexander Sprafke